An Experimental Investigation of Cavity Flow

Richard M Cannon

Thesis Submitted to the Faculty of Engineering,
University of Glasgow, for the Degree of Doctor of Philosophy

University of Glasgow
Department of Aerospace Engineering

December 2003

ABSTRACT

Understanding and controlling the flowfield in and around a cavity has challenged researchers for a number of years. The presence of a cavity on a body has been observed to significantly increase the mean drag, cause flow-induced vibrations and give rise to strong acoustic production. Of particular interest here are the flow structure and dynamics associated with open shallow rectangular cavities at low Mach numbers for various length-to-depth ratios. At the Reynolds number investigated, it is the presence of convective instabilities through the process of feedback disturbance that gives rise to a globally unstable flowfield.

Using an instrumented wing model with a cut-out an experimental investigation of a cavity flowfield exhibiting 'fluid-dynamic' phenomenon has been completed. A post-processing module for the PIV image data was constructed which optimised the data fidelity and accuracy while improving upon velocity spatial resolution. These improvements were necessary to capture the flow scales of interest and minimise the measurement error for the presentation of velocity, velocity-derivative and turbulent statistics.

It is shown that the hydrodynamic instability that is intrinsic to the cavity flowfield at these inflow conditions organises the oscillation of small- and large-scale vortical structures. The impingent scenario at the downstream edge is seen to be crucially important to the cavity oscillation and during the mass addition phase a jet-edge is seen to form over the rear bulkhead and floor. In some instances this jet-like flow is observed to traverse the total internal perimeter of the cavity and interact with the shear layer at the leading edge of the cavity, this disturbs the normal growth of the shear layer and instigates an increase in fluctuation. The coexistence and interplay between a lower frequency mode dominant within the cavity zone and the shear layer mode is seen to shed large-scale eddies from the cavity. This modulation imposes a modification to the feedback signal strength such that two distinct states of the shear layer are noted. Concepts for the passive reduction of internal cavity fluctuation are successful although modifications to the shear layer unsteadiness are encountered; an increase in drag is implied.

NOTATION

A, B	empirical constants
a	speed of sound, m/s
C_D	drag coefficient
C_o	image contrast, $C_o = I^p_{mean} - I^B_{mean}$
C_P	pressure coefficient, $Cp = \left(P_C - P_S\right)/(P_T - P_S)$
C_f	skin friction coefficient
c	random error gradient
c_τ	total measurement error, pixels
D	cavity depth, mm
D_A	aperture diameter, mm
$\mathbf{d}$	displacement vector, $\mathbf{d} = d_x\mathbf{i} + d_y\mathbf{j}$
d	actual displacement, pixels
$\hat{d}$	measured displacement, pixels
d_c	diameter of the cylinder / height of floor section in configuration 3 / height of vertical fence in configurations 4, 5 and 6, mm
d_p	seeding particle diameter, μm
d_r	diameter of pixel, μm
d_τ	particle image diameter, μm
Δd	measured displacement error, pixels, $\Delta d = \hat{d} - d$
E, F	empirical constants
F_A	lens focal length, mm
f	frequency, Hz
$f^\#$	f-number, $f^\# = F_A/D_A$
H	boundary layer shape parameter, $H = \delta^*/\theta$
I	intensity
K	length of pixel area, pixels
k	wave number
L	cavity length, mm
l_δ	local length scale

M_I	magnification
M	Mach number, $M = U/a$
m	mode number
N	sample size
$NV, T\%$	domain size, percentage tolerance for post-processing algorithm rules
N_i	mean number of particle images on a square tile, where K = 32 pixels
N_i^*	min. number of particle images on a square tile, where K = 32 pixels
N_*	mean number of particle images on the CCD
P_C, P_S, P_T	channel static pressure, static pressure and total pressure, N/m^2
P_{ij}	probability of track between particles i and j
P_i^*	probability of no track match
R	range, $R^* = \lvert *_{\max} \rvert - \lvert *_{\min} \rvert$
Re	Reynolds number, Re = $\rho U_\infty x/\mu$
R_c	radius of rigidity between particle movement
R_s	radius of interest for image 1, pixels
R_n	radius of flow coherence, pixels
R_{II}	correlation value
SPL	sound pressure level, dB
St	Strouhal number, $St = fx/U_\infty$
s	standard deviation
s^2	variance
$t, \Delta t$	time, time delay, s
T	temperature, K
TI	turbulent intensity
U_∞	freestream velocity, m/s
$\mathbf{u}$	velocity vector, $\mathbf{u} = u_{\mathbf{i}} + v_{\mathbf{j}}$
u, v, w	velocity components for x, y, z directions, m/s
u', v', w'	velocity fluctuation for x, y, z directions, m/s
W	cavity width, mm
x, y, z	Cartesian coordinates

Greek symbols

α	confidence parameter
β	fundamental of the most unstable frequency of the cavity shear layer
Δ_{IJ}	spacing between measurement points
Γ	circulation, m^2/s
δ	boundary layer height, mm
δ^*	boundary layer displacement thickness, mm
ε	error
ϕ	streamline, s^{-1}
γ	empirical phase between instabilities in the shear layer and pressure waves, a function of L/D
λ	wavelength of laser light, nm
μ	dynamic viscosity, kg/ms
μ_{pop}	population mean
θ	boundary layer momentum thickness, mm
ρ	density, kg/m^3
σ^2_{pop}	population variance
υ	kinematic viscosity, m^2/s
ω	vorticity, s^{-1}
ξ	empirical ratio of shear layer velocity and freestream velocities a function of M_∞
ζ	real part of complex wave vector in x-direction, from Block 1976.

Superscripts

B	background
N	noise
n	iteration number
P	particle

Subscripts

a	acoustic
bias	bias contribution
c	cylinder
chord	wing chord as length parameter
L	cavity length as length parameter
max	maximum value
mean	average value
min	minimum value
px	measured in pixels
x, y, z	relative direction
θ	momentum thickness at cavity leading edge as length parameter
∞	freestream conditions
1,2	respective image pair number

Abbreviations

AT	Anatomy building wind tunnel
CCD	charged coupled device
CPP	correct particle pickup
DC	direct correlation
DOF	depth of field
DSR	dynamic spatial range
DVR	dynamic velocity range
DWO	discrete window offset
DyR	dynamic range
FFT	fast fourier transform
FRTT	forward/reverse tile-testing
HPT	Handley-Page wind tunnel
IPP	incorrect particle pickup
PIV	particle image velocimetry
PTV	particle tracking velocimetry
rms	root mean square
SNR	signal-to-noise ratio

ACKNOWLEDGEMENTS

I am sincerely grateful for all the support and encouragement extended to me by my supervisor Dr. Richard Green. I would also like to thank Dr. Eric Gillies for many insightful and interesting chats regarding fluid mechanics. Funding from the Engineering and Physical Sciences Research Council is gratefully acknowledged.

Most importantly, I thank my family and close friends, especially to my mum and dad for their enduring support, encouragement and motivation.

CONTENTS

LIST OF TABLES AND FIGURES

CHAPTER 1: AN INTRODUCTION TO CAVITY FLOW

This chapter is used to introduce the salient features of cavity flow with specific focus being given to the behaviour of the flow at low subsonic speeds. A summary of the pertinent research publications is included and some of the unresolved issues are identified and discussed. This chapter ends with an appraisal of what this particular experimental investigation hopes to achieve and introduces some specific industrial applications.

1.0 General Introduction

A cavity configuration illustrates that a simple geometry does not necessarily imply a simple flow behaviour. The presence of a cavity in a surface bounding a fluid flow can cause large fluctuations of pressure, velocity and density in the flow in its vicinity, as well as strong propagating acoustic waves. For many cases involving cavity flow it is possible to give rise to self-sustained oscillations, as experienced by Soundhaus in 1854 during an investigation of edge-tones. These cavity oscillations are the origin of the acoustic production that may cause flow-induced vibrations (if the structure is sufficiently flexible) and alter the mean drag. For most applications the inclusion of a cavity is pernicious. A schematic of some common cavity flow interactions is shown in figure 1.1.

One of the first dedicated investigations of flow oscillations caused by surface cut-outs was pursed by King et al. 1958 in which the application was to improve the flow quality through the test-section of a slotted wall wind-tunnel. Nowadays the most commonly associated problem of cavity flows is to bomb-bay doors on aircraft. In such cases the internal pressure oscillations may affect the dynamics and safety of store release, increase the radar profile of the aircraft, cause accelerated structural fatigue around the store compartment and affect nearby electronic equipment, Krishnamurty 1955 and Heller and Bliss 1975 and Heller et al. 1996 for example. More diverse applications of the cavity problem do exist, for instance the pressure vents (cavities) on the Space Shuttle have been seen to cause extremely high internal noise levels during ascent that may affect the actual payload specifications, Tanner 1984. For a typical passenger airliner, for example the A320, the increase in drag associated with slots and cutouts (usually for instrument housing) on the skin surface accounts for 3% of the total drag. A

737-SP adapted to an airborne observatory requires a telescope to be housed inside a square cavity, Srinivasan 2000. In this instance the 2% drag increase caused by the cavity is acceptable although the sound pressure levels generated at the rear bulkhead of the cavity cause vibrations in the telescope itself, which then requires an aerodynamic control strategy to suppress the structural vibrations. There are similar issues for laser targeting devices whereby the turbulent density fluctuation inside the shear layer imposes structural vibration and also causes the refractive index to vary at high Mach number (thereby increasing scattering losses), Sutton 1969 and Shen 1979. However, there are applications in which the uncontrolled cavity flow regimes are beneficial such as increasing the convective heat transfer rates between electronic chips, Sparrow 1983.

In the application of high-speed trains the join between two coaches will cause a cavity to exist, see figure 1.2. It is expected that the shear layer interaction with the slower moving internal flow causes large vortical structures to be cast off downstream along the train skin. This typically causes the downstream boundary layer to thicken and increases the profile drag, there are also issues concerning vortical interaction with other structures that increase the radiated noise form the train, which can become severe at high-speeds, Takehisa 1998. Such problems are currently faced by the Maglev and Skinkanson train projects in Japan[1] where the top speeds are currently 550km/h and 300km/h respectively. Due to environmental concerns there is ongoing research aimed at reducing the radiated noise from these inter-car gaps, bogies and pantograph assemblies, Frémion et al. 2000 and Noger et al. 2000 respectively.

A brief background containing relevant research material that has progressed the understanding of cavity flow is now given.

1.1 The classification of Cavity Flow

The problem of self-sustained oscillations in impinging flows is unique in fluid mechanics and as such has been the subject of much research over many years; Komerath et al. 1987 provides a good review. For a cavity subjected to freestream parallel conditions the upstream boundary layer separates at the leading edge of the cavity and causes a free-shear layer to develop across the open mouth of the cavity. For

[1] See for instance www.rtri.or.jp

such a separation Kelvin-Helmholtz instabilities, Betchov 1967 are inherent and cause amplification in the initial disturbance as it progresses downstream. This shear layer will then reattach either to the rear bulkhead of the cavity or downstream of the cavity itself, as shown in figure 1.1. As the vorticity in the shear layer exits the cavity domain, the shear layer bends into the cavity itself forcing fluid to enter the cavity that causes a pressure pulse to be sent upstream inside the cavity. Oscillation of the shear layer permits mass efflux from the cavity also.

Flow oscillations are born out of the evolving organised structure in the cavity shear layer that are generated by the selective amplification of extraneous disturbances. These oscillations may be self-sustained, implying the existence of a feedback mechanism that can be the result of aerodynamic and/or acoustic effects. Since there are a number of permutations possible for the cavity flow regimes they are now classified according to the definition of Rockwell and Naudascher 1978. In essence there are three interactions possible: fluid dynamic, arising from the intrinsic instability of the flow; fluid-resonant, influenced by resonant waves; and fluid elastic, requiring a coupling with the motion of a solid boundary.

(i) Fluid-dynamic interactions

Purely fluid-dynamic oscillations involve coupling between the shear layer developed over the cavity and the flow inside the cavity. The selective amplification of the shear layer is not a pre-requisite to instigate feedback. However, pressure waves from the downstream corner must travel upstream and agitate the leading edge, causing vorticity fluctuations and thus enhanced disturbances through shear layer amplification. This interaction is observed so long as the cavity length to acoustic wavelength remains very small. Standing acoustic modes are not involved and the need for flow compressibility is not necessary.

(ii) Fluid resonant interactions

For a fluid resonant cavity to exist, the acoustic wavelength must be the same order of magnitude or smaller than the cavity length or depth. These are the flow oscillations that are controlled by the acoustic modes of the cavity. The Helmholtz resonator is the perfect example since it is a large volume with a short cavity face. An open sunroof on a vehicle, Kook et al. 1997 and aircraft landing gears, Tam et al. 1978 are examples of

possible fluid-resonant interactions. Such interactions are subjected to further classification that is determined by the direction of the waves produced. When the length-to-depth ratio (L/D) is sufficiently large longitudinal oscillatory modes may exist and the cavity flow is generalized to 'shallow', as illustrated in figure 1.3. If the L/D ratio is small transverse waves may be present and the cavity is denoted as 'deep'. The most appropriate simplification for this study was given by Heller et al. 1971 in which it was stated that any L/D smaller than unity is 'deep' and any other is 'shallow'.

(iii) Fluid-elastic interactions

When there are interactions between the shear layer oscillation and the elastic boundaries of the cavity, fluid-elastic interactions may exist. Thus the inertia, elastic and damping characteristics of the structure have a decisive influence on the dynamics of the flow itself. An example of this would be Goldman et al. 1968 who used freely oscillating control surfaces with a specific rigidity to improve the stability performance of re-entry vehicles. The data for unstable shear layers of finite thickness past flexible cavities would provide insight into the basic coupling between fluid-dynamic and fluid-elastic oscillations, Rockwell et al. 1978.

For higher freestream Mach numbers it is possible for fluid resonant oscillations to exist alone or with fluid-dynamic interactions (and even fluid-elastic interactions). In these instances it is difficult to determine when standing waves will occur since it is complicated by the behaviour of the cavity shear layer and the mass exchange at the cavity trailing edge. Since the determination of the cavity regime is ambiguous it is more reasonable to pursue classification based solely on the pressure trace on the cavity floor, Plentovich et al. 1993. These flowfield types are now included for completeness.

When the shear layer bridges the open face of the cavity it is identified as being 'open', (see figure 1.4), which is broadly the case for $L/D < 8$. This flow state can be identified when the static pressure distribution on the cavity floor is nearly uniform, in comparison to other states. It is possible for open cavity flow to exhibit resonance in a high Mach number flow, which is caused by the reinforcement of the shear layer instabilities and the upstream travelling pressure waves. Conversely, missile bays on fighter aircraft experience 'closed' cavity flow (frequently when $L/D > 13$) whereby the stagnation

streamline that previously bridged the open face of the cavity now impinges on the cavity floor, thus forming two well defined regions of recirculation. This can be identified by a mean static pressure distribution with low pressure at the upstream corner a pressure plateau in the middle section and high pressure to the aft. For a missile bay the separating store has been seen to experience a large pitching moment that turns the store nose into the cavity (to catastrophic effect). It has not yet been clearly defined if acoustic tones can exist within the 'closed' cavity flow structure, although they are not commonly observed.

1.1.1 Mach number

As the Mach number increases from low subsonic flow to supersonic flow the reflected acoustic waves will begin to predominate the feedback mechanism. The existence of shock waves causes the directivity of the sound to increase and forces the shear layer to oscillate in a more orderly manner. An approximate limit that bounds fluid-dynamic and fluid-resonant behaviour was discovered by Block 1976 who described it as an expression that related cavity L/D to Mach number using two empirical constants (adapted from Rossiter 1966). A change in Mach number is seen to affect the limits of 'open' and 'closed' cavity flow although the largest changes are discovered in the so-called 'transitional' regime that bridges these two flow states. In the absence of shock waves transitional flow can be easily defined from the static pressure measurement on the cavity floor, where the distinction can be made by inspection of the inflection points in the pressure coefficient profile, see figure 1.4. With high Mach numbers the transitional regime is categorized more rigorously according to the shock wave locations.

In the supersonic flow regime closed cavity flow can be clearly identified by the location of an impingement shock at the leading corner of the cavity and a shock wave at the aft wall of the cavity. As the length of the cavity decreases the shock waves collapse into one single shock wave located at the point of shear layer impingement on the cavity floor, this is termed 'transitional-closed' flow. With a further (small) decrease in cavity length this single shock wave splits into a series of compression waves indicating shear layer deflection with no stagnation impingement, this is called 'transitional-open' flow. The acoustic properties of these transitional flow regimes

remain undetermined, Tracey et al. 1997. Further reductions in cavity length force the flow back to an open regime which is characterized by oblique shock waves at the leading and trailing edges of the cavity that respond to shear layer deflection with a periodic travelling wave pattern over (and under) the shear layer itself, Heller and Bliss 1975. A complete description of these physical feedback mechanisms for supersonic cavity flow with the aid of Schlieren optical spark photography is given in Heller et al.1996 and Zhang et al. 1998.

1.1.2 Reynolds number

As the Reynolds number increases the energy transforming and dissipating scales become more distinct from one another. This is because more small-scale structures are generated which then intervene between the process of energy extraction and viscous dissipation. Over the Reynolds number range the large eddy structures remain similar even though the small-scale content is changed considerably. The general conclusion is that beyond the transition region there is no significant influence of Reynolds number to be seen. Roshko 1976 has demonstrated that it is possible to maintain similarity in a free-shear layer flow for Reynolds number ranging from 600 to 850,000. A study by Sarohia 1977 indicated the lack of sensitivity of oscillatory characteristics of a cavity flow to changes in Reynolds number, although the oscillatory behaviour was affected by the upstream boundary layer height (that is when $\delta/D < 0.5$). Ho et al. 1984 later emphasised that a relationship between Reynolds number and the formation of coherent structures in a free-shear layer does indeed exist with reference to the stability theory of Hussain et al. 1977. Therefore for the purposes of this study (knowing *a priori* that there are no acoustic resonance effects) the Reynolds number is presented in terms of the upstream boundary layer momentum thickness. This is an appropriate definition since the change of the separating boundary layer at the cavity leading edge to an inflection profile and its stability thereafter are intrinsically linked to the initial state of the boundary layer.

1.2 The Cavity Problem

From the first extensive report on cavity flow by Krishnamurty 1955 to the latest full-field investigation by Lin et al. 2001, efforts are continually being made to understand, model and modify the behaviour of cavity flow. Such an interest remains because

techniques for predicting the dominant frequency of operation or calculating the amplitude of a particular oscillatory mode remain under development. Through these investigations much has been learned about the nature of cavity oscillations and some of the more interesting observations from the literature are now included.

1.2.1 Early benchmark work

As previously stated Krishnamurty 1955 undertook the first study of tones generated by cavity flow in a blowdown tunnel, and with this made the most significant observation about cavity oscillations. He discovered that the wavelength of the cavity oscillations were proportional to the cavity length except in the case where the cavity length was so small that the shear layer could not impinge on the downstream wall (and no tone would be generated). Sarohia 1977 was able to map this relationship between oscillations and cavity length using linear stability theory with some success (the amplitude data was obviously poor), Kook et al. 2002 and Hankey et al. 1980 later provided more rigorous clarification. Another early benchmark study was conducted by Roshko 1955 who was able to identify the stagnation pressure caused by the shear layer impingement on the downstream wall as the main contributor to the drag caused by a cavity. Plumbee et al. 1962 then conducted the largest study of that time by presenting results from both experimental and theoretical work. He studied the response of the cavity through the Mach number range of 0.2 to 5 where it was noted that the discrete tone frequency increased with Mach number, but it was not linear, and the static pressure in the cavity increased with increasing cavity depth. It was then expected that short cavities would exhibit depth modes in resonance and shallow cavities would display lengthwise modes. The theoretical description used by Plumbee et al. 1962 considered the shear layer turbulence as the driving mechanism for the cavity which was contrary to the observations of both Krishnamurty 1955 and later Heller et al. 1971 who noted that the oscillations in the cavity were much stronger when the shear layer was laminar as opposed to turbulent.

East 1966 noticed that cavity resonance would only be produced when the shear layer oscillations were amplified through acoustic coupling between the shear layer pressure fluctuations and the cavity modes. His experimental results were in good agreement with Plumbee et al. 1962 and confirmation of these observations was later provided by Tam et al. 1978 and Ahuja et al. 1995.

1.2.2 Prediction of cavity oscillation

Using high-speed shadowgraph motion pictures Rossiter 1966 was able to visualise discrete vortices being shed periodically from the cavity leading edge, which was confirmation of earlier postulations made in Rossiter 1962 about cavity wave interactions and confirmation of experimental results from Rossiter 1964. From these studies it was possible to fit an empirical equation to the experimental data although no explanation was given regarding the physical mechanisms at work, equation 1.1. This equation would recognise available oscillation frequencies but not determine the actual operating mode.

$$St_L = \frac{fL}{U_\infty} = \frac{m - \gamma}{\frac{1}{\xi} + M_\infty} \qquad [1.1]$$

where, $m = 1,2,3,...$, $\gamma = 0.25$, $\xi = 0.66$ and St_L is the Strouhal number for that particular mode.

Rossiter's equation represented his observations that approximately one-quarter period after a shear layer vortex hit the trailing edge and left the cavity, a new vortex would be shed from the leading edge, thus $\gamma = 0.25$. ξ represents the convection of the shear layer structures as a fraction of the freestream velocity. The formula and the underlying instability process are similar to that which occurs in edgetones, Powell 1961. Rossiter 1966 was in agreement with Plumbee et al. 1962 when he identified the principal source of acoustic radiation being close to the trailing edge of the cavity. At the same time Spee 1966 was able to illustrate from his subsonic Schlieren photographs that the periodic inflow and outflow at the trailing edge of the cavity was accompanied by lateral displacement of the shear layer, although he was unable to verify Rossiter's observation that discrete vortex shedding was occurring at the leading edge. The first verification for this shedding came from McGregor et al.1970 who also included balance data that measured a 250% increase in drag when cavity resonance occurred. In a simplification to Rossiter's equation (equation 1.1), Heller et al. 1971 demonstrated that the temperature (thus the speed of sound) approached stagnation values inside the cavity. Using the remaining empirical constants it was possible to accommodate either fluid-dynamic or fluid-resonant interactions within this formula, however at low Mach numbers the dependence of the shear layer instability characteristics on the frequency of oscillation reduced the accuracy of prediction.

1.2.3 The feedback mechanism

Heller and Bliss 1975 presented the next benchmark report regarding self-excited cavity oscillations. In this report a complete description of the feedback mechanism was given in which a typical cavity cycle would see discrete vortices cast off from the leading edge and convected downstream at a fraction of the freestream speed. An impulsive disturbance is then generated when the vortex reaches the downstream edge and travels back upstream to initiate the formation of a new vortex at the leading edge. Therefore by using this rear bulkhead 'pseudopiston' analogy a direct relation for the frequency of the shear layer oscillation was possible although in reality it is necessary to incorporate an additional frequency-dependent time delay to account for phase lags induced by the fluid-structure interactions at the edges. Heller also noted the effects of stronger wave receptivity of higher Mach numbers. Values for the convection speed of shear layer vortices have seen some change although the best prediction criterion has probably been described by Ahuja et al. 1995. It should be noted that Heller and Bliss 1975 viewed the spatial amplification rate of the cavity wave travelling downstream as a function of the finite-thickness shear-layer instability characteristics (for values of $M_\infty < 2.0$).

Although the subject is not free from controversy, there are certain aspects of the complete feedback mechanism that are now generally accepted. The generic description of the physical mechanisms of self-excited cavity oscillations given by Rockwell et al. 1978 (updated in Rockwell et al. 1979, 1983 and 1998) is adopted here. This is described as follows and is adapted from the original description given by Rossiter 1964:

(i). There is an interaction of a vorticity concentration(s) with the downstream corner.
(ii). A disturbance travels upstream from this downstream corner to the shear layer separation position at the upstream corner.
(iii). There is a conversion from this upstream influence to a fluctuation in the shear layer as it arrives at the corner.
(iv). There is an amplification of this fluctuation in the shear layer as it develops in the streamwise direction.

For the design of oscillation suppression devices the role of the downstream corner geometry could clearly be seen and direct manipulation of the mass exchange stroke at the downstream corner was indeed successful, Ethembabaoglu 1973 and Maurer 1976.

1.2.4 Numerical predictions

There were two common approaches of modelling the complex interactions associated with cavity flow to predict the modes of oscillation. Fluid-dynamic interactions were typically predicted from the 'feedback' phase angle condition already described (equation 1.1) and King et al. 1958, Martin et al. 1975 and Rockwell 1977 pursed other numerical studies performed in the this manner. King et al. 1958 modelled the shear layer as being infinitesimally thin since this was a good approximation for his 2d flow over a perforated slot. Martin et al. 1975 and Rockwell 1977 went to great efforts in modelling the shear layer as accurately as they could although the drawback was that no description of an impingement surface was included, prohibiting the collection of useful amplitude data and resonance effects. Rockwell 1977 and Sarohia 1977 provided the most important work of that time by providing an equation that would determine if self-sustained oscillation would occur and if so the capability to determine the predominate mode.

The other approximation used was to model the shear layer as being infinitesimally thin so that the inclusion of fluid-mass exchange, wave propagation and elastic effects could be facilitated. From the studies of King et al 1958 (where this condition is valid), Bilanin et al. 1973 and Block 1976 it was established that these models were particularly good at predicting fluid resonance (when a number of coexisting frequencies are evident) and at high Mach number where the wave effects are strongest (as predicted by Heller and Bliss 1975). The analysis of Bilanin and Covert 1973 yielded a relation for the Strouhal number with the same general form as the Rossiter equation, but with no empirical constants. It was found that there was excellent agreement the range $0.8 < M_{\infty} < 3.0$ even though there was no coupling between the cavity wave structure and the shear layer motion.

Block 1976 extended the work of Bilanin and Covert 1973 to include wave reflections from the floor of the cavity and the prediction found good agreement with previous

experimental studies by East 1966 and Covert 1970. Of particular interest in this study was the observed coupling between the lengthwise and depthwise modes at particular Mach number and L/D ratio. This allowed Block to determine the maximum-amplitude Mach number as when there was reinforcement in the two directions of oscillation. This is given in equation 1.2 and indicated in figure 1.5, it may be seen that this maximum amplitude criterion is prevalent when $L/D < 2.0$.

$$M = \frac{\frac{1}{\zeta}\frac{L}{D}}{4m\left[1 + A\left(\frac{L}{D}\right)^{B}\right] - \left(\frac{L}{D} - 0.514\right)} \qquad [1.2]$$

where, $m = 1,2,3,...$, $A = 0.65$, $B = 0.75$ and ζ represents the longitudinal wave number, determined by Block 1976.

In a similar fashion Tam 1976 also modelled the acoustic modes of a cavity and derived a minimum Mach number below which flow-induced cavity tones could not become self-sustained. Further development of this model by Tam and Block 1978 to combine the effects of longitudinal and transverse waves then found evidence that it was possible for tones to be generated by the normal mode resonance mechanism for $M_\infty < 0.2$.

Numerical prediction then changed to the full solution of the unsteady Navier-Stokes equations where Hankey et al. 1980 determined that the maximum intensity of pressure oscillations over an open cavity occurred at a Mach number of one. Brandesis 1982 used a similar approach to make some observations about the behaviour of the shear layer for different cavity lengths at supersonic speeds. Investigations then continued with Ghadder et al.1986, Zhang et al. 1988, Najm et al. 1991 and Pereira et al. 1993, who each provided computational solutions for their particular cavity flow problem. In each case it was realised that there were interactions between the internal cavity structure and the shear layer, to further quantify this Pereira et al. 1995 used Laser-Doppler anemometry in conjunction with a numerical simulation. Using this he discovered that large amplitude organised oscillations were due to fluid-dynamic instabilities, while the visualisation and unsteady prediction elucidated the instability process as involving a complex coupling between the shear layer and the recirculating flowfield dynamics. Using large eddy simulation Takakura et al. 1996 investigated the unsteady features of supersonic flow past a cavity ($\mathrm{Re}_L = 843000$ for $L/D = 2.0$) where

it was evident there was a formation of a wall jet flow along the vertical and bottom faces of the cavity.

1.2.5 The origin of jitter

Plumbee et al. 1962 was the first to notice a low frequency interaction of the shear layer vortices with the downstream cavity corner, which was then properly investigated by Rockwell et al. 1979 and Knisely and Rockwell 1982. In these studies it is observed that an approaching vortical structure may experience one of three possible events: complete clipping, whereby the structure is swept down into the cavity; partial clipping, which results in severing of the vortex; or escape, involving deformation of the vortex while it is swept intact over the downstream corner. Each possible event (or 'jitter') is illustrated in figure 1.6, taken from Rockwell et al. 1979. It was also determined that there was a substantial increase in transverse velocity just upstream of the edge and that each event at the downstream corner would have a consequence at the leading edge via the internal pressure wave propagation. These may be the origin of several instability frequencies present within the shear layer that do not exist when the downstream edge is removed.

In the absence of resonance the organised nature of the shear layer oscillation is relaxed and it is the presence of other coexisting agents that determine the oscillatory process of the cavity shear layer at the downstream edge. This eddy shedding that can be observed from the recirculation zone may be caused by the modulation of the shear layer imposed by the larger (more energetic) recirculation region. It is possible that there is some level of phase compatibility through other nonlinear interactions between the shear layer and the recirculation region that commits the edge interaction to a certain fate (complete clipping, partial clipping or escape). If this is the case then in the description of the feedback mechanism it is important to monitor the shear layer amplification to the jitter event such that better understanding can be found (and control may be enforced). Such research requires the accumulation of full flowfield information although this experimental data remains, at best, sparse.

1.3 Cavity Acoustics

Even though it is possible to predict the possible frequencies of cavity oscillations over a large Mach number range the capability of predicting cavity noise tone is far from complete. There continues to be much interest in such predictions since high amplitude

oscillations may produce tones that produce acoustic fatigue; measurements that are now commonly requested by environmental law. For the cavity there is a general understanding of the nearfield noise generated and the pressure fluctuations within the cavity, while prediction methods have been reported. See for example Moore 1977, Lepicovsky et al. 1985 and Vakili et al. 1993.

It is the generation of a shear tone that facilitates the amplification of other tones for a cavity. This shear tone is generated by the instabilities in the separated shear layer that interact with a downstream edge causing pressure waves that are propagated back upstream to the point of initial separation. If the upstream propagating disturbance is in phase with the instability formed at shear separation, then amplification will occur, Ethembabaoglu 1973 and Rockwell 1977. Woolley et al. 1974 was able to stipulate a criterion for tone selection by realising they would only be generated in modes where the integrated amplification was greater than unity. There are three possible types of interaction that the shear tone may take with the underlying cavity structure: these are cavity tone, Helmholtz resonance and cavity resonance. These are now explained.

(i) Cavity tone

The presence of a cavity under the shear layer imposes a condition stating the mass of fluid inside the cavity must remain constant (at least for incompressible flow). This means that the periodic mass addition and removal at the trailing edge of the cavity will have a direct affect on the movement of the shear layer at the upstream separation position. At certain frequencies this unsteady mass stroke at the upstream station may amplify the instability in the shear layer and cause the generation of a tone. Since this feedback depends on the presence of a cavity, it is referred to as a cavity tone, Sarohia 1977 and Courtney 1994. Some aerodynamic frame noise on trains and noise associated with turbo-machinery is generated by cavity tones. The challenge here is then to isolate the cavities or grooves causing the noise and determine at what speed the cavity tone becomes excited. It is then possible to quieten the structure, Maruta et al. 2000 and Sagawa 1999.

(ii) Helmholtz resonance

The generation of Helmholtz resonance for a cavity is dependent on the volume of the cavity. Therefore if the frequency of the shear tone across the opening of the cavity is

close to or equal to the Helmholtz resonance frequency, amplification of the shear tone will occur, Elder 1978 and Nelson et al. 1983. A popular example of this is the 'wind throb' phenomenon when a vehicle cabin with an open window or sunroof causes a low frequency high-pressure oscillation inside the cabin itself. It is possible to exceed 130dB in the passenger cabin in such a fashion without exceeding 70mph, Inagaki 2002.

(iii) Cavity resonance

A shear tone is generated when two frequencies of the cavity couple together and cause an increase in the generated tone, East 1966 and Elder 1978. As previously noted by Block 1976 for values of $L/D < 2.0$ it is possible for depthwise resonance mode and the feedback mode to couple together and increase the amplitude of oscillation at distinct Mach numbers, as described by equation 1.2. In such an instance it is the vortical shedding in the shear layer that is purely reinforced by the oscillations of the duct resonance mode. Such interactions have been seen to exist in aircraft landing wheel wells, Bliss et al. 1976.

The sound produced by nominally steady, high Reynolds number flow over an aperture or cavity in a wall often consists of a sequence of discrete tones, Howe 1997. Tonal amplitude is solely dependent on flow speed and can change abruptly between modes as the flow speed is varied; in fact Rossiter 1962, East 1966 and Komerath 1987 all noticed mode switching effects in their data. The main theoretical models used for estimating sound generation have already been briefly explained (Heller et al. 1971, Bliss et al. 1976 and Block 1976), while in each instance good agreement was found for the Mach number range of interest there was no generic prediction scheme found. The most notable recent progress has been made by Hardin et al. 1993 and Kriesels 1995 and Ahuja et al. 1995 who has performed the most extensive study of farfield sound generation to date (for the purpose of validating new aeroacoustic codes). From these studies it was confirmed that shallower cavities radiate sound more uniformly, whereas deeper cavities appear to be more directional. It was also implied that it might be possible to eliminate all cavity tones by thickening the upstream boundary layer, while narrower transitional cavities tend more towards closed flow (where the potential for resonance is reduced). Tracey et al. 1997 although in agreement with Rossiter 1966 and Block 1976 that resonant frequencies decrease with increasing L/D, has demonstrated

that resonance is still possible for closed cavity flow, which has concerns for missile bay applications. Henderson et al. 2001 has used a computational investigation of subsonic and transonic open turbulent flows to provide acoustic data that is in good agreement with past experimental studies, while Tam et al. 2001 have pursued the development of specific computational aeroacoustic (CAA) codes to determine sound pressure levels around various geometries.

The prediction of cavity noise is far from complete because this phenomenon is seen to be a strong function of upstream boundary layer state, while the sound generated is highly dependent on the three-dimensional flow state, Lele 1997. For instance Ahuja et al. 1995 sound pressure level (SPL) results pertaining to narrow three-dimensional cavities are in direct contradiction to the findings of Block 1976, possibly caused by the difference in boundary layer momentum thickness at the cavity leading edge.

1.4 The cavity energy source

The origin of the energy required to maintain cavity oscillations requires clarification. As briefly mentioned earlier Plumbee et al. 1962 suggested that the energy was a result of broadband turbulence, while Tam and Block 1978 postulated that the energy transfer to the cavity came purely from the shear layer instabilities. Some clarification of this problem has recently came from Disimile et al.1998 and 2000 who determined that although there was transfer of energy between oscillation frequencies as the cavity span was decreased, the total energy obtained from the mean flow was increased. This was measured in relative sound pressure level, (RSPL) taken to represent the acoustic energy. By measuring the upstream boundary layer using a hot-wire probe the maximum dissipation was seen to occur at an energy region responsible for viscous forces, thus leaving little energy for fluid-dynamic excitation. With the shear layer containing vortical structures with energy two orders of magnitude greater, coupling to oscillations is more tenable. It appears that the hypothesis of Tam and Block 1978 is now well supported.

1.5 Three-dimensionalities

Two-dimensional cavity flow implies that the flow is uniform across the entire span. As a result, a coherent shear layer is expected to form across the entire span of the cavity. For three-dimensional cavities closed systems of recirculating flow cannot exist. Hunt et

al. 1978, and so the flow regimes are considerably more complicated with fluid entering the cavity and vorticity being shed from it. It is expedient for an experimental set-up to try and predict the level of encroachment or interaction that three-dimensional effects would bring.

Several researchers have examined the case of a fully three-dimensional rectangular cavity in the past. In the work of Friesing 1971, Gaudet et al. 1973 and Young et al. 1981 the purpose of the research was simply to ascertain drag data that may be used for design purposes and as such no explanation was given about the flow regimes present. For Sinha et al. 1982 and Kaufman et al. 1983 the purpose of their investigations was very specific to their particular applications and no discussion was given to the origins of three-dimensionalities. The work performed by Plentovich 1990 and Ahuja et al. 1995 did present pressure distribution measurements and made efforts to understand the effects of cavity width on the direction and amplitude of tones at high Mach number. Given the nature of these studies it was sufficient to state that reductions in span do not affect the main frequency of oscillation while Q-factor[2] increases. Roshko 1955 measured the presence of spanwise gradients only for completeness. This leaves the work of Maull and East 1963, Rockwell et al. 1980 and a dedicated study by Savory 1993 and Disimile 2000 as the only work to actively purse the description of three-dimensionalities in subsonic flow conditions.

Using oil flow visualization and surface static-pressure distributions Maull and East 1963 found strong evidence to suggest regular three-dimensional flow across the cavity floor. An example of the cellular structures visualised are shown in figure 1.7. In these experiments it was found that for particular L/D ratios this spanwise cellular structure would collapse causing increased fluctuations in the lengthwise oscillations. It was also discovered that large values of L/W did not necessarily imply the damping of spanwise effects. A later study by East 1966 reported no discernable changes to the cavity oscillations by the spanwise effects although the range of L/D and L/W covered was not as extensive.

---

[2] Q-factor is the quality factor, which is the ratio of the centre frequency to the bandwidth of the surrounding peaks.

Miksad 1972 measured the three-dimensional character of free-shear layers and discovered that the spanwise variation in wavelength is associated with the streamwise location in the flow and to the primary wavelength. Using the hydrogen bubble technique Rockwell et al. 1980 was able to record the spanwise variation of a free-shear layer along the mouth of a cavity where the oscillation were better defined because vortex pairing in the shear layer was inhibited, as shown in figure 1.8. It was discovered that there was strong coupling between longitudinal and spanwise vortices that caused severe, but ordered, spanwise distortion of the primary vortex. This was found to be in agreement with stability study carried out by Browand 1979 and data from Breidenthal 1979 and 1980.

When calculating drag for cavities over a number of configurations Savory et al. 1993 noticed that the pressure distribution on the floor of the cavity showed remarkable lateral uniformity with no noticeable three-dimensionality (as opposed to the studies above). Disimile et al. 2000 studied the effects of cavity span on the flow oscillations that occur in a low-speed open cavity (with $L/D = 1.0$). He noticed that a state of fluid-dynamic resonance was observed at small L/W ratio that progressed to fluid-acoustic resonance as L/W increased. This was determined as a depth mode acoustic response using a relationship adopted from East 1966. No relationship between the acoustics of the cavity and the formation of spanwise vorticity has ever been pursued.

1.6 Flow Control

With the exception of studies to design wind instruments and other sound sources, the objective of most work concerning cavity flow is to achieve the eventual suppression of oscillations and thus sound generation. In the initial study by King et al. 1958 to reduce the instability caused by slots on wind tunnel walls Mabey 1970 found a practical solution by covering the slots with perforated screens. With the addition of a spoiler at the trailing edge of the cavity Rossiter 1966 found that oscillations were suppressed. In fact the addition of the spoiler served to destroy the interaction between the shear layer vortices and the trailing edge and as such reduced feedback to the cavity leading edge. The optical distortion and vibration caused by the shear layer at high Mach number as noted by Shen 1979 was alleviated for a particular Mach number ($M_\infty = 3.2$) with installation of a wedge shaped lip at the cavity trailing edge. Another possible solution

to this problem was demonstrated by Parmentier et al. 1973 who used directional upstream mass injection to reduce the impact of the shear layer at the cavity trailing edge. Miksad 1972 disproved the notion that relaminarisation of the boundary layer at the leading edge would be beneficial by suppressing shear layer amplification. He calculated that the shear layer would once again become turbulent-inflectional at approximately 27 times the laminar boundary layer height downstream.

Heller and Bliss 1975 documented a variety of suppression devices for transonic/supersonic flow that intended to either stabilize the shear layer and/or prevent the periodic trailing edge mass addition process. Shear layer stabilization was achieved either through the introduction of vorticity from an upstream-vortex generator (spoilers) or by the provision of an inherently stabilizing trailing edge geometry (slanted rear bulkhead). Both of these examples were successful and are included in figure 1.9a and b. The slanting trailing edge is successful because the stagnation streamline is not perpendicular to the rear bulkhead and as such compensating the impingement angle with an angled surface will force the shear layer into a steadier state by virtue of weaker growth amplification. A detached cowl, shown in figure 1.9c suppresses the mass addition and removal process by causing enough lift such that the shear layer is accelerated over the cowl itself. The location and orientation of this cowl is very critical to the operating Mach number. Reductions in fluctuating pressure coefficients of more than one hundred percent and attenuations of SPL by 35dB have been achieved by using appropriate combinations of these devices, Rockwell 1978 and Franke and Carr 1975. The acoustic pressure loads experienced by current fighter and attack aircraft is higher than ever since more severe manoeuvres are possible. Jacobs 1990 used a linear model with non-dimensional scaling to develop a universal design tool that predicts the size of sawtooth spoiler required to reduce the SPL within a given cavity and operational Mach number range.

Sarohia 1976 studied the effect of mass flow injection at the leading edge of a cavity and discovered that it was possible to delay the onset of a given mode of oscillation. Experimental studies by Sarno et al. 1994 and Vakili et al. 1994 have shown that attenuation of cavity flow oscillations in this manner is possible when the instability characteristics of the shear layer are directly affected. Therefore by thickening the shear layer the preferred vortex roll-up frequency is shifted outside the natural frequencies of

the cavity. Navier-Stokes simulations of passive control techniques have also been pursed although no comparison to experiments has been made, Zhang et al. 1999. For both active and passive suppression schemes once the device is located and orientated at the desired location, success can only be assured over a small Mach number, L/D and L/W range.

By changing the geometry of the downstream impingement edge Pereira et al. 1994 was able to modify the 'clipping' fate of the impinging vortex as previously defined by Rockwell et al. 1979 and Knisely and Rockwell 1982. Using LDA it was determined that by facilitating nearly perpendicular impingement of the stagnation streamline on the rear cavity bulkhead the primary vortex would increase in size. It was also noticed that any geometrical changes to the downstream corner did not affect the dominant frequency of oscillation, indicating that the primary recirculating flowfield has very little effect on the inner shear layer structure.

Kuo et al. 2001 reported that banking the floor of the cavity itself could change the oscillation characteristics of the shear layer. They found that by sloping the floor of the cavity (higher on the leading edge side) and thus imposing an adverse pressure gradient on the primary vortex, the oscillation of the shear layer was significantly reduced. Another interpretation on the success of floor banking would be that by constricting the primary vortex in the upstream portion of the cavity the shear layer vortical structures are generally incipient, thus less prone to low frequency modulation.

Gharib 1987 has demonstrated that it is possible to excite a naturally nonoscillating shear layer through addition of Tollmien-Schlichting waves to the upstream boundary layer that transform into Kelvin-Helmholtz waves. The success of this work has motivated several more studies on active control of cavity oscillations using low-dimensional systems. For further reference (and review), the most success so far has been attributed to Kergerise et al. 1999 and 2002 for self-tuning of weapons bays using a flap assembly. There has been no deviation of strategies based on gain/phase/delay controllers although more sophisticated model-based schemes may be expected soon, Rowley et al. 2000.

1.7 The aerodynamics of trains

In this work particular interest is given to the study of airflow between the inter-coach spacing on trains. It is therefore appropriate to include a brief summary concerning the aerodynamics of trains and the expected benefits that a study on inter-car gaps would bring to a complete train configuration.

The total resistance of motion for a train is composed of rolling mechanical resistance, air momentum drag (for combustion and air conditioning) and aerodynamic resistance, Gawthorpe 1978. The coefficient of drag (based on frontal area) can range from ~1 for streamlined trains to ~15 for freight trains. Taking the case of a streamlined train operating between 250-300 km/h isolated in the open with no crosswinds, it can be expected that 75-80% of the total resistance is caused by external aerodynamic drag. Breaking this up into constituent parts, about 30% of the aerodynamic drag is caused by skin friction, about 8-13% by nose and tail pressure drag, 38-47% by bogie and associated interference drag, and 8-20% by pantograph and roof equipment drag, Peters 1983 and Schetz 2001. Some cavity areas around the train are shown in the schematic of figure 1.10.

The reduction of pressure drag possible on the nose and tail sections is very small once the general profile is long and slender and without sharp edges, Schetz 2001. If a particular nose shape (for instance the aero-wedge, Gawthorpe 1998) generates pressure waves that exceed environmental requirements in tunnels the problem is dealt with by modifying the geometry of the tunnel entrance and exits rather than sacrifice drag reduction by modifying the nose shape. To reduce the rolling resistance a more radical change has been pursed based on magnetic levitation (or Maglev) technology. Using electromagnetic suspension (EMS) the vehicle undercarriage either wraps around the track or rides within a trough with approximately 10mm (full-scale) levitation ground clearance, Pulliam et al. 1996. From the initial studies by Germany in the 1930's Maglev trains are now at full-scale test demonstrations in France, Germany, US and Korea. Japan has already set a deadline for commercial availability in 2004 while China are already operating a 430km/h service in Shanghai[3]. It is to be expected then that any

[3] See for instance www.transrapid.de

future improvements in train efficiency will come solely from a reduction in the drag caused by pantograph and roof equipment and skin friction.

Reducing the effects of viscous drag on high-speed rolling trains, such as the ICE (InterCity Express) and TGV (train à grande vitesse) is still a very important problem for rail researchers. Direct manipulation of the boundary layer by application of Large Eddy Break-up devices (LEBU) and vane vortex generators (VVG) have fallen short on reliability although longitudinal riblets have found good application on the train surface, Guezennec et al. 1985 and Bechert et al. 1997 respectively. For experimentalists the complications are that the flat plate law does not hold for a discontinuous fusiform[4] body like the train and there are scaling effects for friction measurement that are not yet understood, Baker 1985. In fact the typical argument embraced by rail researchers regarding drag reduction is to maintain a thin boundary layer around the train, Gawthorpe 1983. However it is plausible that unimpeded boundary layer development along the train surface will decrease the skin friction, although this will increase the boundary layer displacement thickness and as such increase pressure drag at the tail.

It has been shown in several studies (most notably in Gaylard et al. 1994) that there is significant thickening of the boundary layer by bogies and inter-car gaps caused by low-energy fluid being fed into the boundary layer. Based on the results of Sockel 1996 for an ICE it can be seen that these cavities (and possibly other skin protrusions) are causing the boundary layer to double in thickness over a 100m span (where the boundary layer height has been measured at approximately 1500mm). At this position along the train the effective cross-sectional area is expected to have increased by around 14-20% from the growth of the boundary layer. These values are expected to be much larger at the tail of a high-speed train where the total length is commonly in excess of 200m. So although a thick boundary layer is beneficial for reduced viscous drag its growth should not be left unchecked along the entire length of the train. Essentially there remains an optimal balance between the constituent aerodynamic drag components even though the body is in fact streamlined.

---

[4] Tapering at each end, spindle shaped

Another issue worth mentioning is the level of noise generated by a typical high-speed train. In this case the rolling noise of the train is exceeded by the aerodynamic noise from inter-car gaps, pantograph recesses and bogies, all of which may be modelled as cavities, Noger et al. 2000 and see figure 1.10. It is expected that some fraction of the noise generated by the pantograph is in fact caused by vortex escape from the inter-car gaps and as such requires some control. In some cases the electrical connection between the pantograph and the overhead cables can actually be lost due to these oscillations. New environmental laws in Japan state that the noise generated by a passing train must be less than 75dB at a distance 25m from the track wayside. This has recently restricted the top-speed of all their high-speed trains; in particular the Skinkanson (flagship) train, which was forced to operate at 220km/h. Noise reductions were subsequently reduced below the safe limit when particular attention was paid to pantograph assemblies and the vortical escape from the inter-car gap, Sagawa et al. 1999 and references cited within.

As an example of the detrimental impact that a cavity can have at this geometrical scale and this Reynolds number range it was found in a study by Saunders et al. 1993 that the drag caused by a compliment of fully loaded ore wagons in transport was in fact the same as that generated by empty unsheeted wagons. Therefore after delivery the benefit of the reduction in weight (or rolling resistance) was augmented by the increase in profile drag encountered by towing a cascade of cavities.

1.8 The Present Work

Previous quantitative measurements of the unsteady flow between the upstream corner and the downstream corner of the cavity have involved pointwise measurements and in most cases it is the time-averaged or phase-averaged data that is presented. It then seems suitable to pursue the measurement of cavity vortical interactions using Particle Image Velocimetry (PIV) for a wing with a cutout. As previously stated there are substantial amounts of cycle-to-cycle variation of the flow pattern for a typical cavity oscillation, which may be caused by a low frequency modulation in the internal cavity structure interacting with the shear layer at the downstream corner of the cavity. It would therefore be progressive to obtain instantaneous measurements over the entire

region for a range of L/D thus providing comparable quantitative measurement of the coexisting structures, growth, and their interaction with the shear layer.

Prior to the study of the cavity flowfield a post-processing module is designed that can adequately measure the spatial scales of interest. Any increase in the spatial resolution that this system provides over traditional systems must not compromise the accuracy of the measurements and procedures are introduced that seek to maintain both accuracy and fidelity. Consequently, any improvements must be mindful of the dynamic range metric, which can be maximised through software modifications and experimental procedures. The development of a popular PTV scheme to a hybrid PIV-PTV scheme is completed and tested. This gives more flexibility in the investigation of cavity flow and promises better system spatial resolution. A decent appraisal of the new algorithms are finalized with two test-cases, the near wake of the circular cylinder and the shear layer region of the cavity at $L/D = 2.0$.

A sample set of instantaneous velocity data is accumulated for the cavity at various L/D. This is of sufficient size so that the statistical average and deviation can be presented with good confidence while the wind-tunnel testing process remains efficient. Of primary importance is the coexisting oscillation between the separated shear layer and the recirculation zone within the cavity walls. The use of instantaneous flowfield data gains an insight into the coupling processes between the different scales and an appreciation of the cycle-to-cycle variation in the oscillation. With a rotation of the wind-tunnel model, an insight into the cavity three-dimensional effects can be interpreted and the level of encroachment these structures have on the normal plane data can be measured.

The flowfield within an inter-car gap for a train is studied using simple geometrical modifications to the clean cavity cases. Of particular interest is the reduction of skin friction downstream of the gap and a suppression of the migration of large vortical structures from the gap. Finally, two other passive control strategies are tested and comments made.

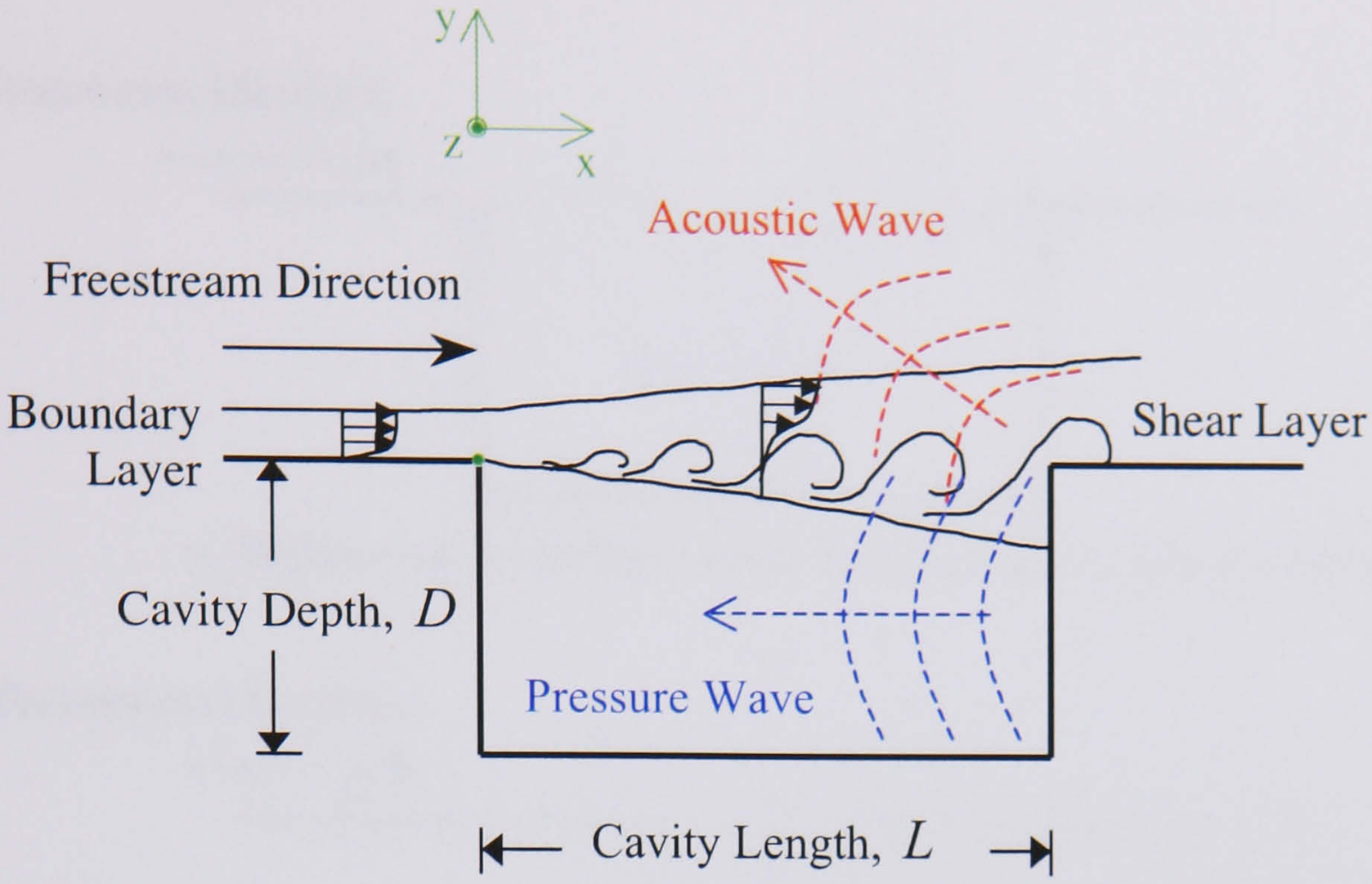

Figure 1.1. The presence of a cavity in freestream flow conditions causes the boundary layer to separate at the leading edge of the cavity and roll-up into a shear layer. It is the interaction of the shear layer at the downstream corner that produces pressure wave feedback inside the cavity and acoustic propagation into the farfield. The green dot indicates the origin of the coordinate axis (shown above). Freestream direction will be from left to right unless otherwise stated.

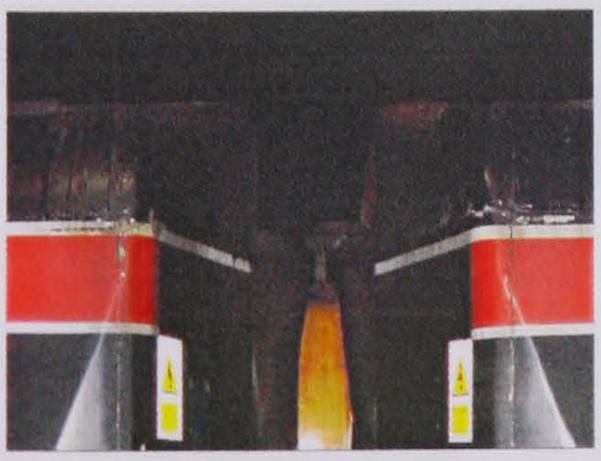

a. Train gap approximating a clean cavity with $L/D = 1.0$.

b. An Inter-car gap with protrusion evident on the cavity floor.

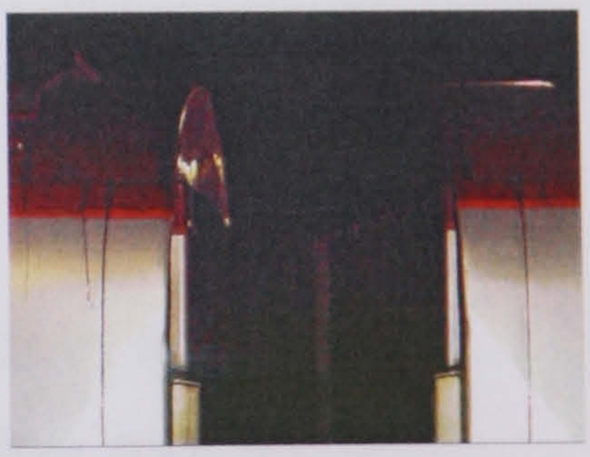

c. Train gap with a sloping floor configuration with $L/D \approx 1.5$.

Figure 1.2. Some inter-car gap configurations for common passenger trains.

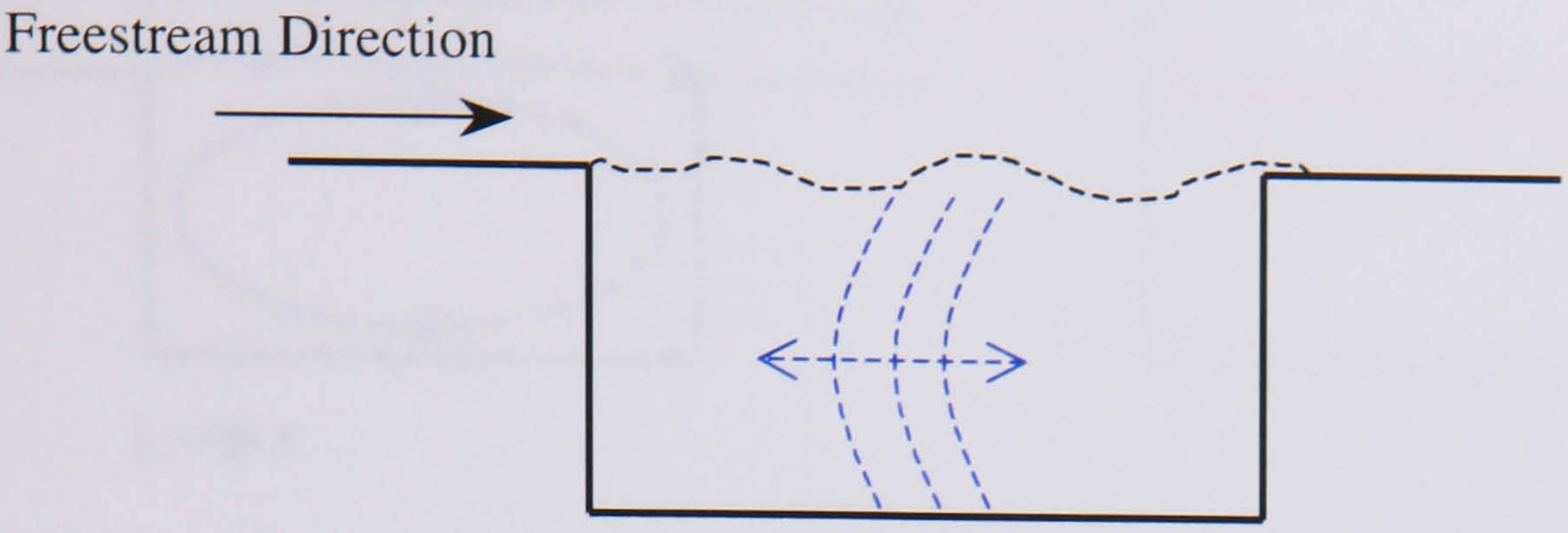

a. Shallow cavity influenced by longitudinal oscillatory modes.

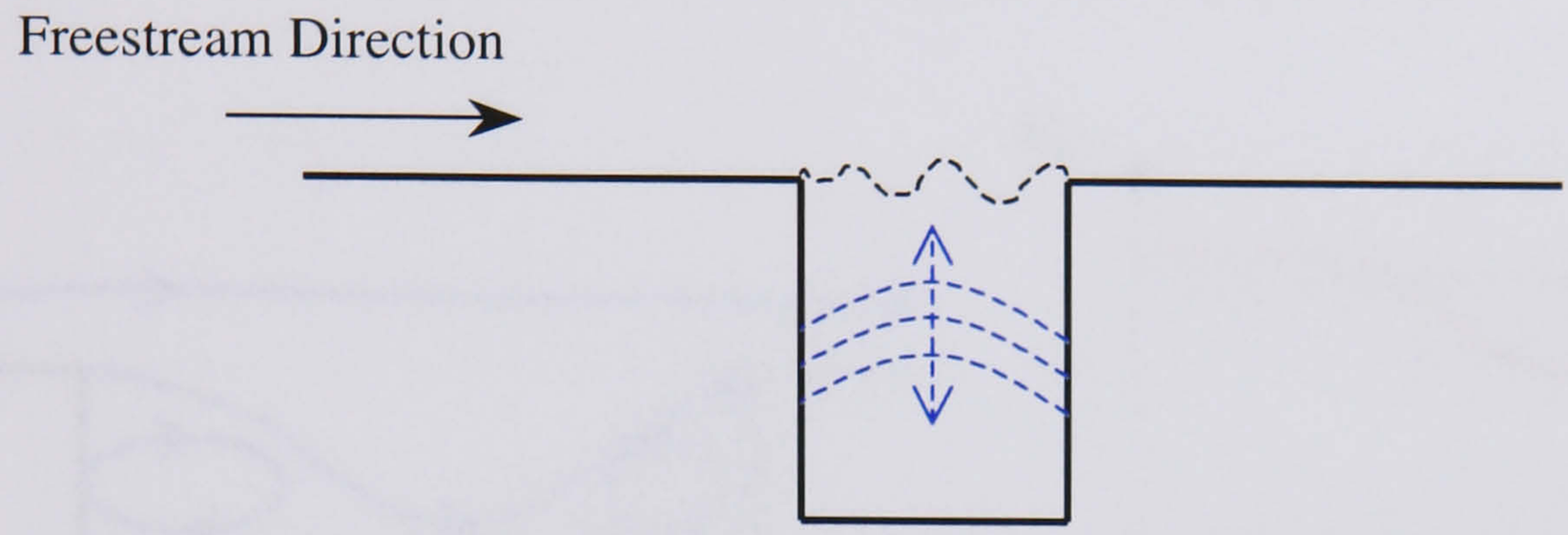

b. Deep cavity exhibiting acoustic depth modes.

c. Shallow cavity in resonance.

Schlieren photograph for $M_\infty = 0.7$

© Rowley et al. 2000

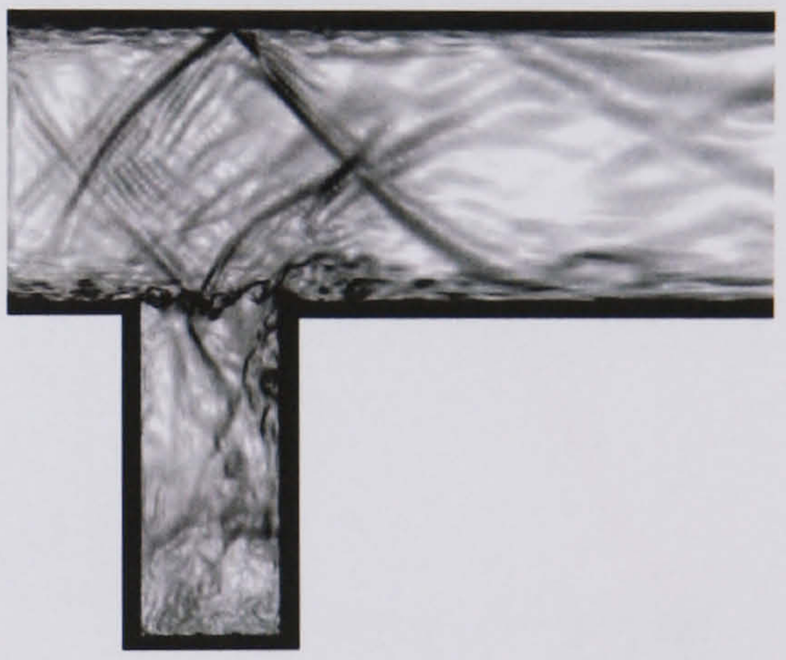

d. Deep cavity in duct mode.

Channel flow with $L/D = 0.5$

© Colonius et al. 1999

Figure 1.3. Shallow and deep cavities in fluid resonance. The oscillatory flow of shallow cavities are strongly influenced by the characteristics of the shear layer and it is the internal dimensions of the cavity that affect the oscillations of a depth mode.

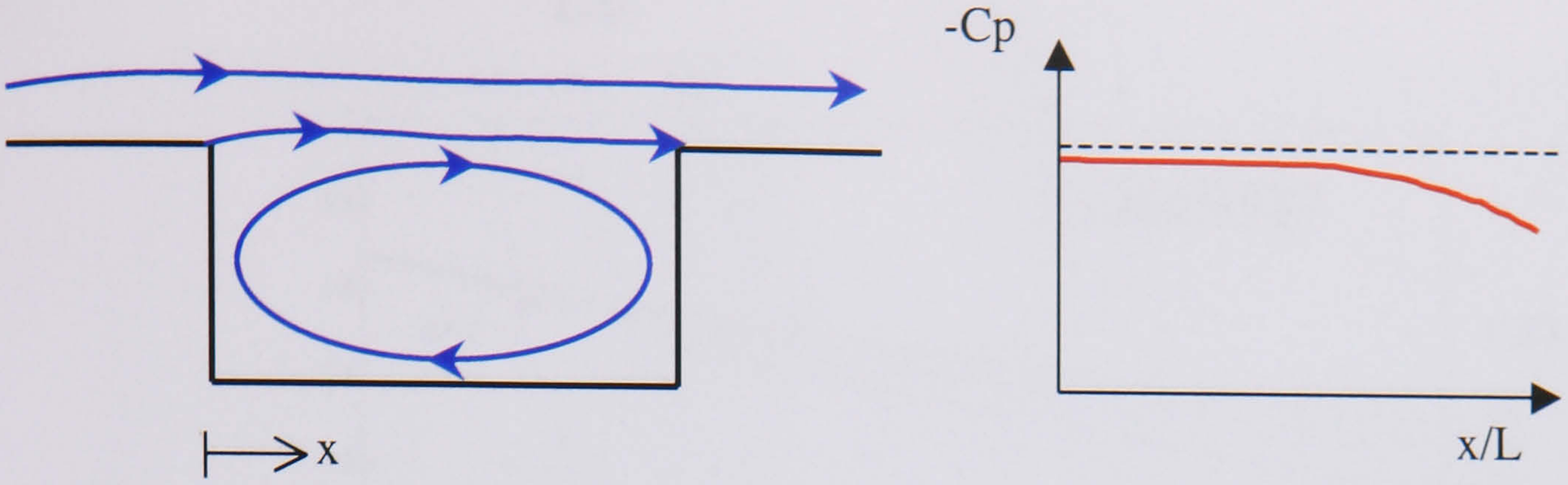

a. Open cavity flow. The shear layer bridges the open face of the cavity. The static pressure profile on the cavity floor is very weak.

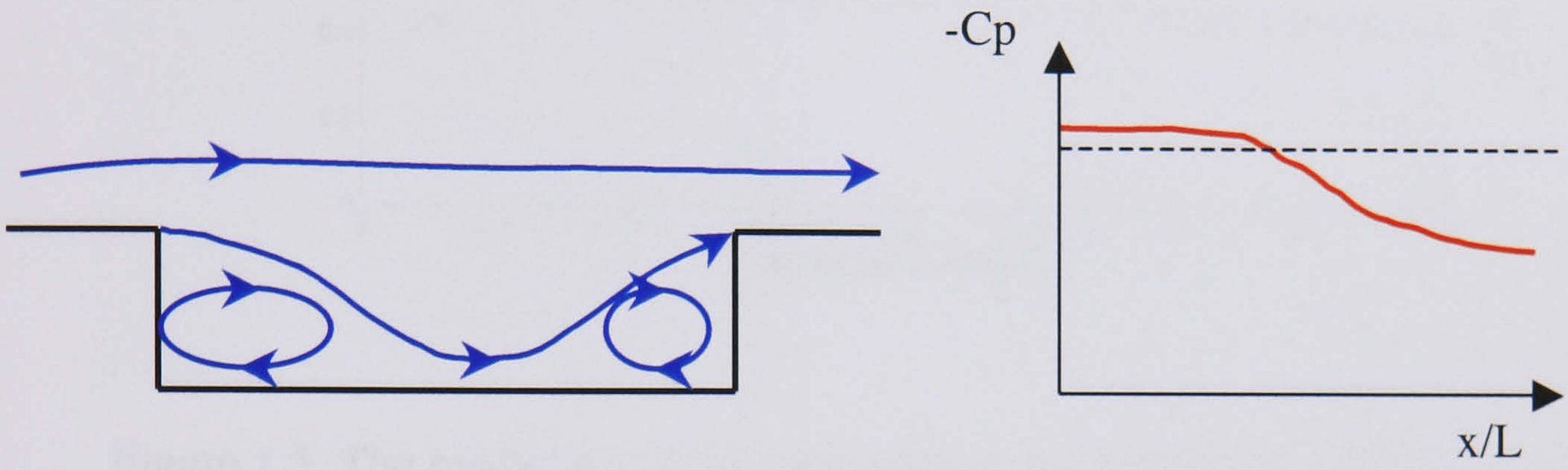

b. Transitional cavity flow. The stagnation streamline is deflected into the cavity

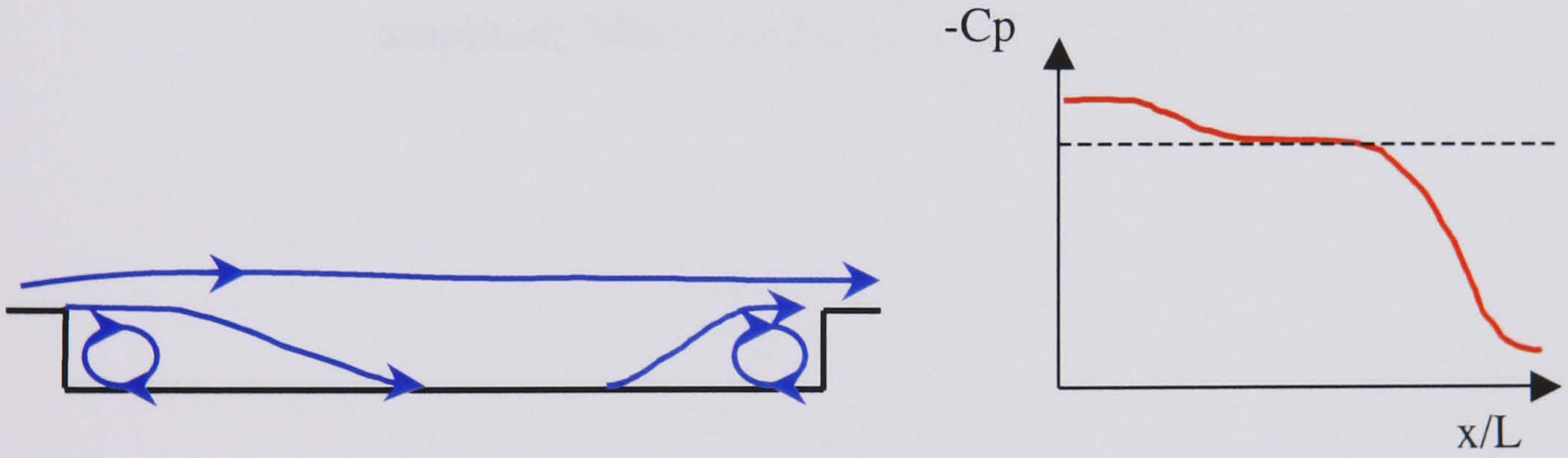

c. Closed cavity flow. The stagnation streamline impinges onto the cavity floor creating two distinct separating regions, one downstream of the forward face and one upstream of the rear face.

Figure 1.4. Open, transitional and closed cavity flow descriptions. The general behaviour of streamlines (including the stagnation streamline) is illustrated to the left hand side and the pressure coefficient profiles associated with the description are included to the right. It is the formation of the plateau pressure region that determines closed cavity flow.

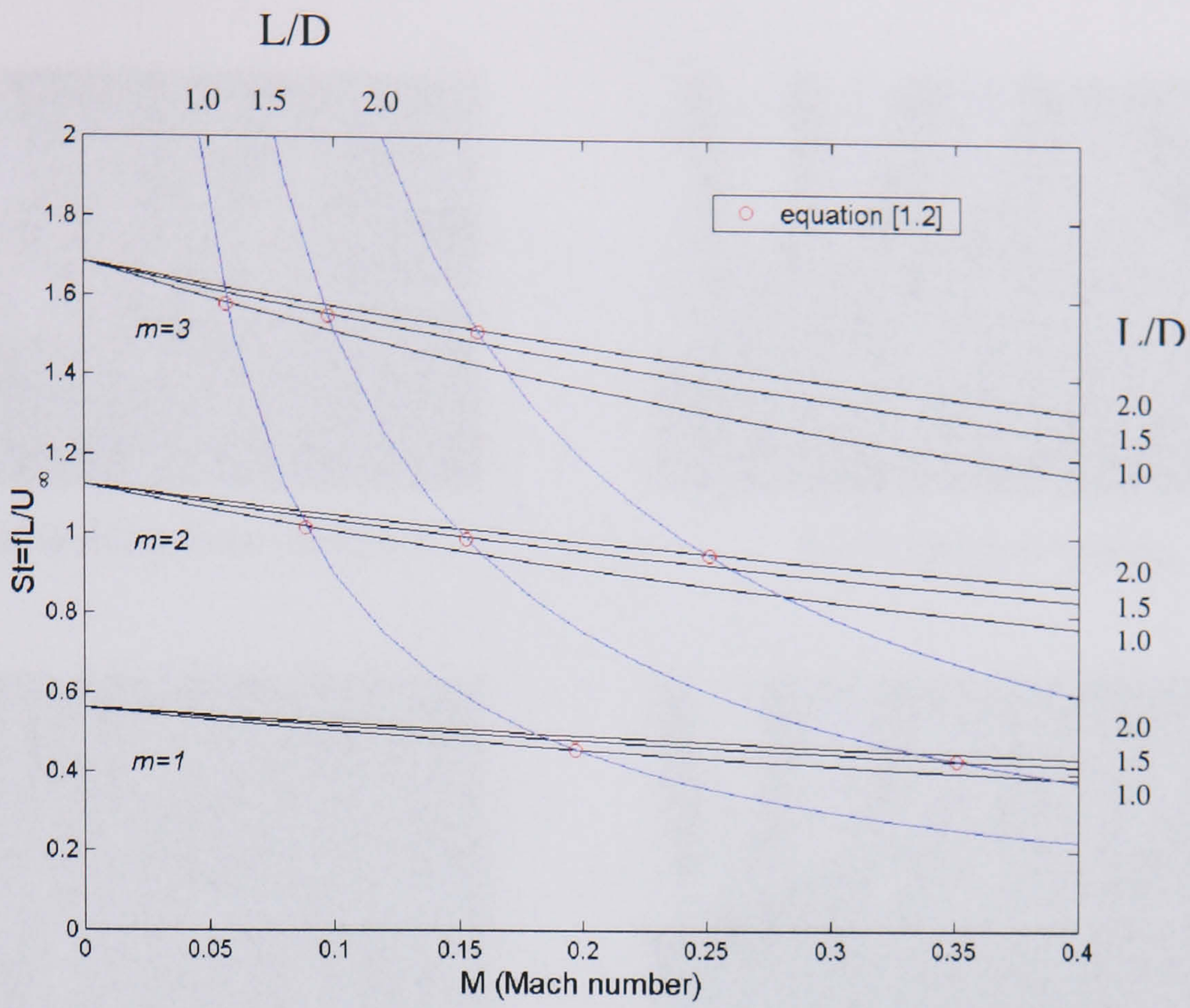

Figure 1.5. The prediction of Strouhal number for lengthwise vortical-acoustic oscillation (black lines) and depthwise standing-wave modes (blue lines) based on cavity L/D for a range of Mach numbers. The red dots indicate the maximum amplitude Mach number as defined by Block 1976.

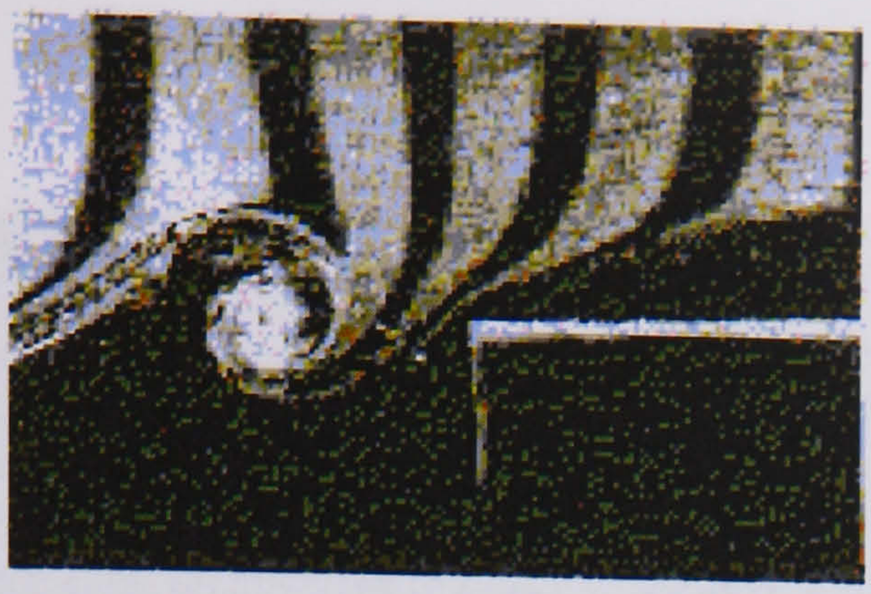

a. The approaching flow structure.

b. Complete clipping.

c. Partial clipping.

d. Escape of vortex.

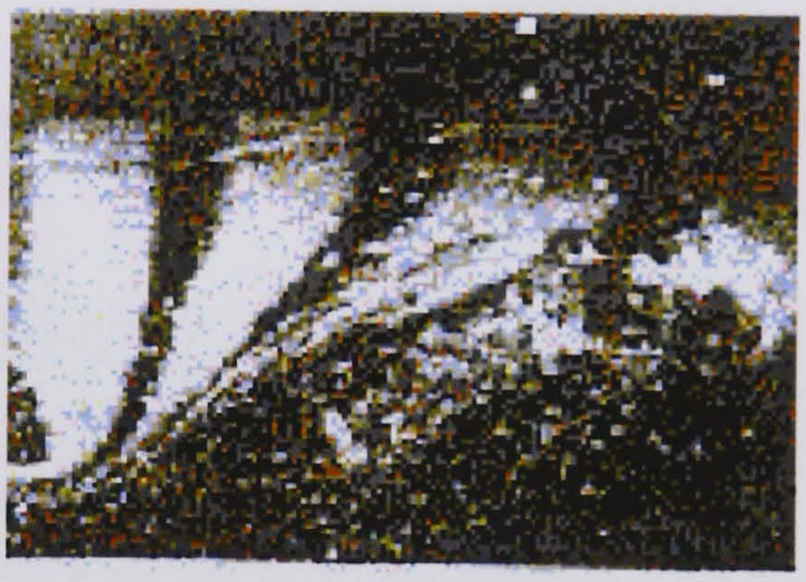

e. Flow without edge.

Figure 1.6. An approaching vortical structure to the downstream corner may experience one of three possible fates, described as 'jitter'. Complete clipping (b) describes the approaching vortex (a) as being swept into the cavity. Partial clipping (c) is the instance where the vortex is severed by the downstream corner causing a partial vortex to be cast over the cavity face and convected downstream. Complete escape of the vortex (d) is also possible and is noted when the vortical structure skips over the rear face deformed but intact. Pictures from Rockwell et al. 1979.

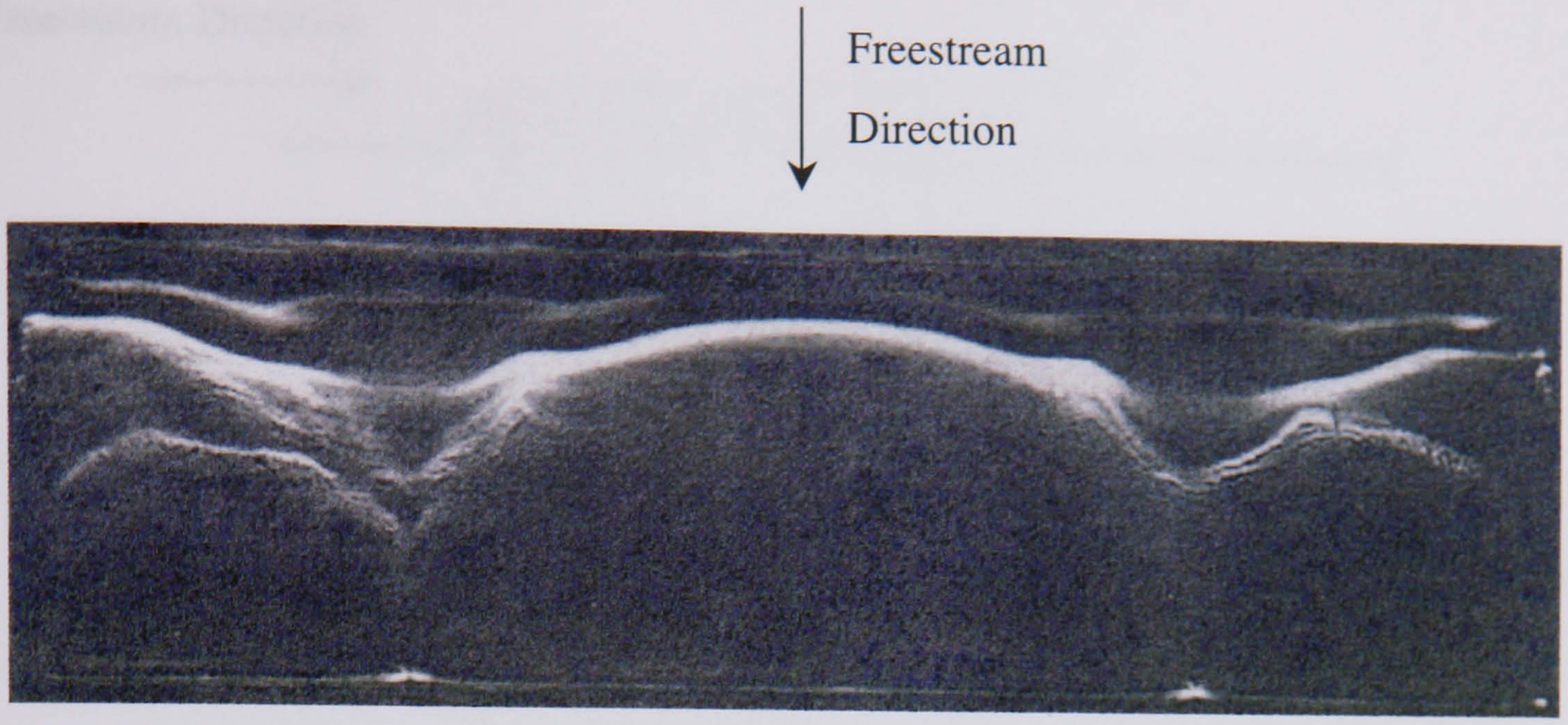

Figure 1.7. Oil pattern formed on the floor of the cavity. The effect of changing the span was to change the number of cells present both on the cavity floor and on the downstream wall (not shown). Picture from Maull and East 1963.

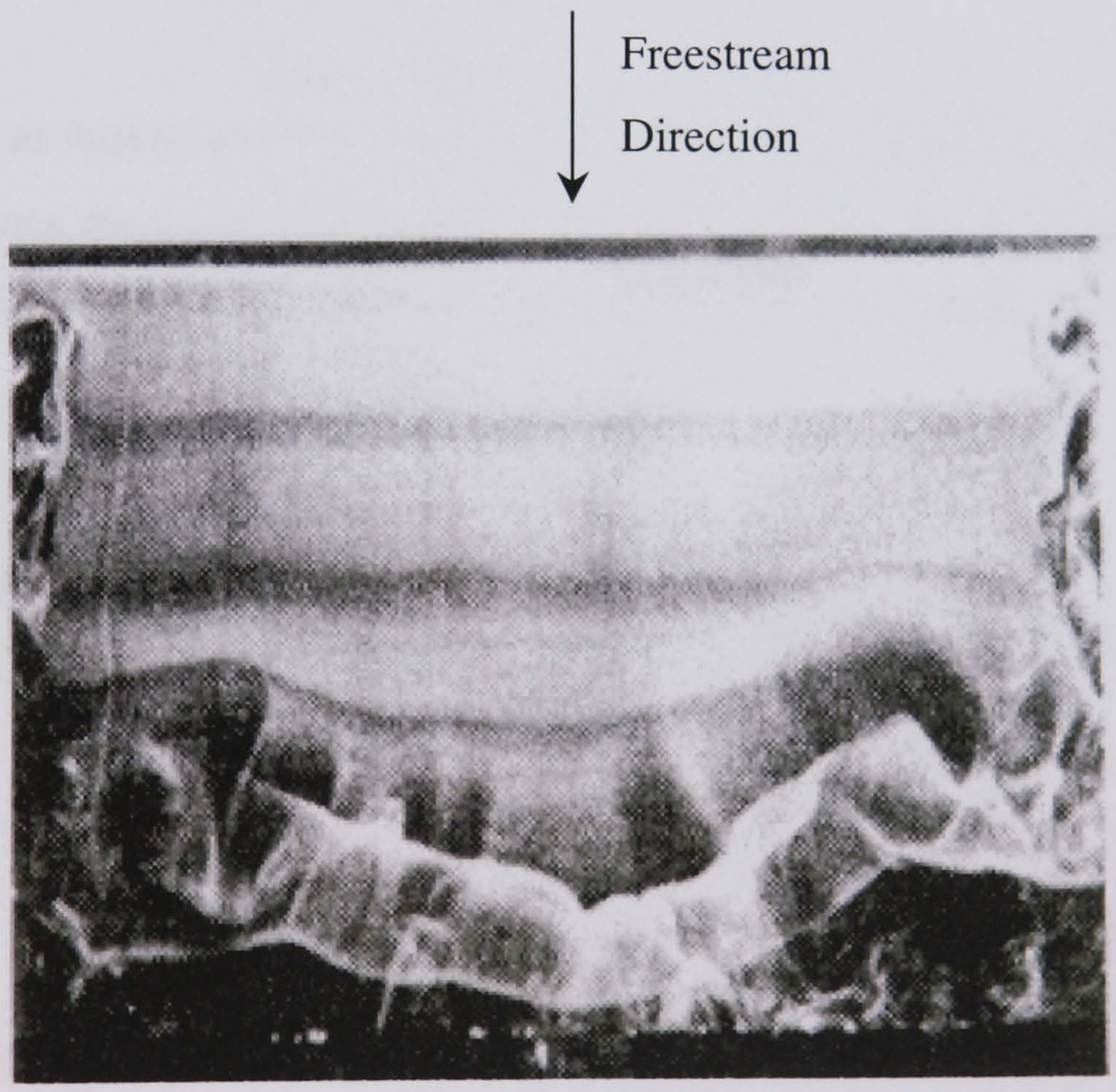

Figure 1.8. A depiction of the curvature of the core of the primary vortex and associated streamwise vorticity. The impinging nature of the vortex on the downstream edge would be analogous to partial clipping. Picture from Rockwell et al. 1980

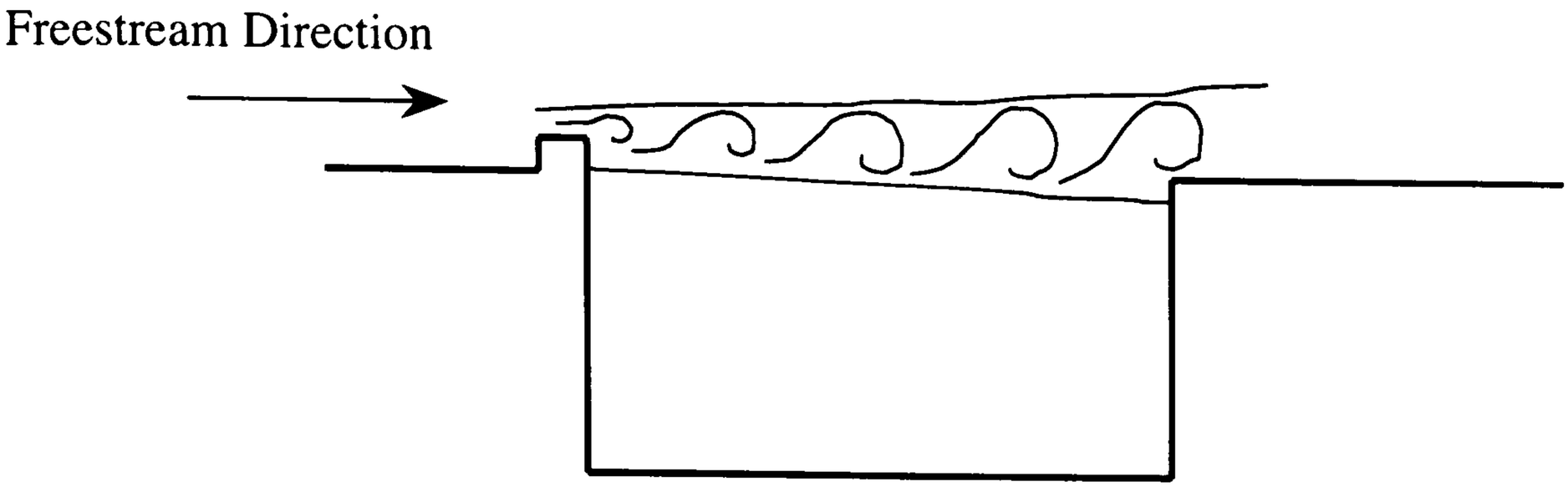

a. Upstream Spoiler. The addition of a vortex generator modifies the growth of the shear layer as it travels downstream, thus reducing the feedback strength to the shear layer origin.

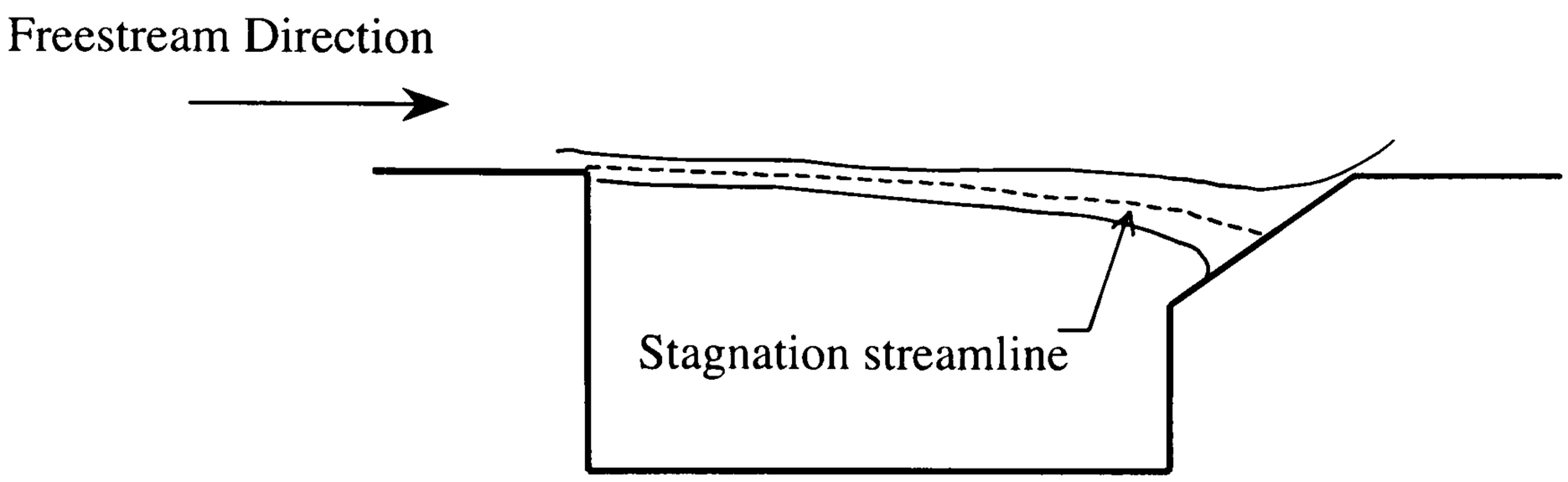

b. Slanted rear bulkhead. Flow impingement on the rear bulkhead must have some curvature since there is a velocity gradient across the shear layer. The angle of the stagnation streamline can be balanced with a change in impingement angle, yielding a more steady state.

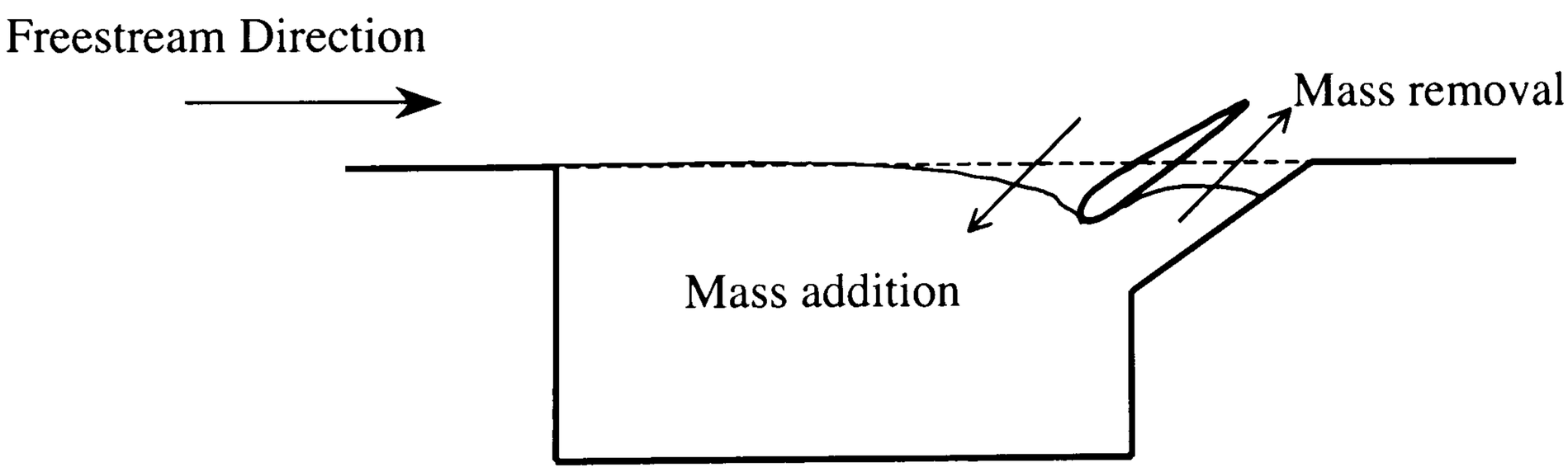

c. Slanted rear bulkhead with detached cowl. The optimum cowl position for subsonic speeds is above the plane of the cavity. Mass addition at the trailing edge is suppressed by effectively operating two mass strokes at the same time.

Figure 1.9. Some concepts that have been used for suppressing the oscillations inherent in cavity flow.

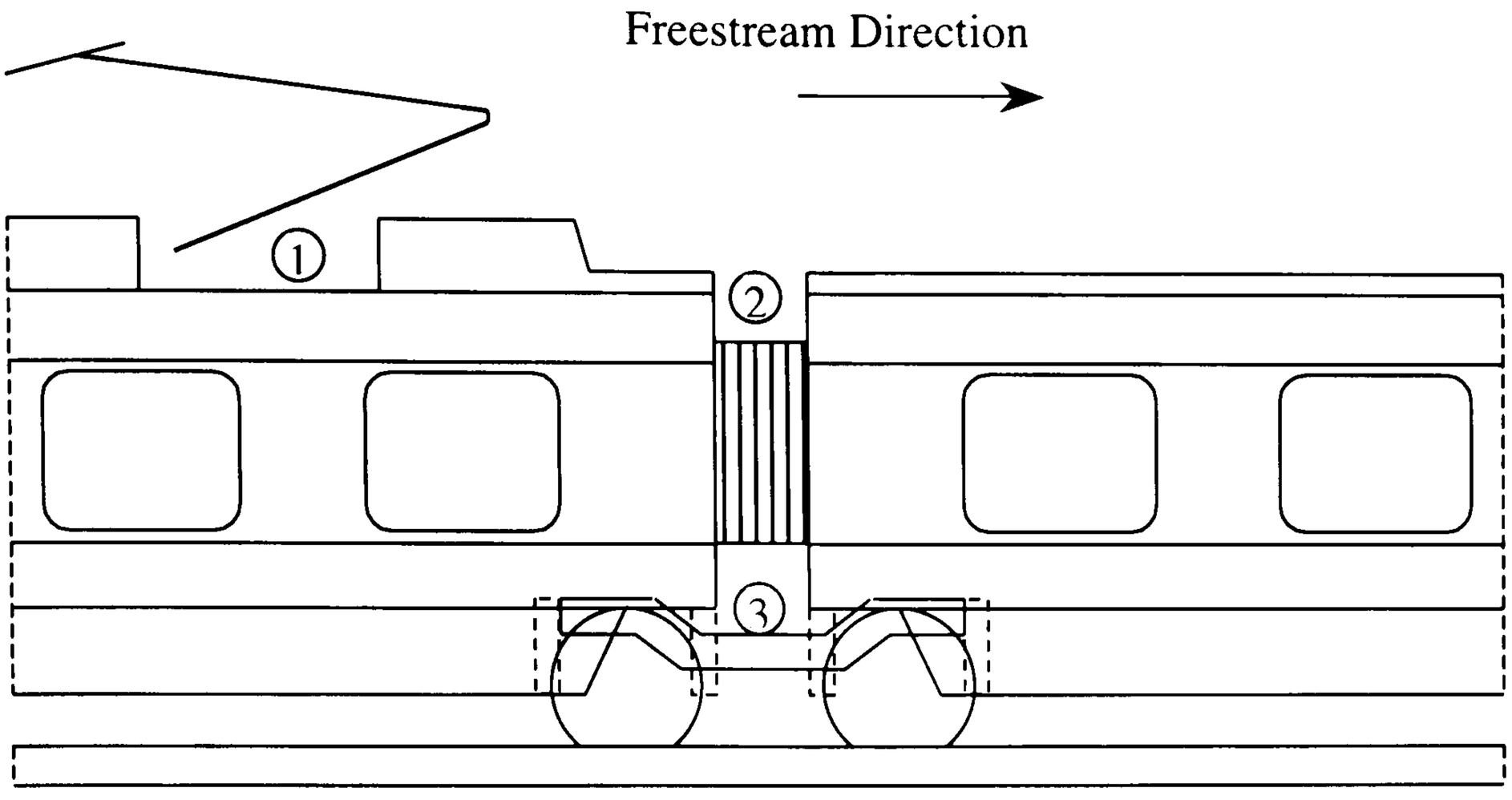

Figure 1.10. Examples of the cavity flow scenario for a normal high-speed train configuration.

1. Pantograph and cavity, estimated to generate 37% of the total aerodynamic drag from the above configuration, from Considine 1998.
2. Inter-car gap, pressure drag imposed by flow stagnation accounts for 3% of the total drag. The effects on downstream skin-friction caused by the thickening of the boundary layer over the cavity are substantial, Gaylard et al. 1994.
3. Bogie and cavity cascade, accounts for 50% of the total aerodynamic drag from the above configuration. The load bearing and powered part of the bogie are mounted onto a series of cavities for support.

CHAPTER 2: THE DEVELOPMENT OF A DIGITAL PARTICLE IMAGE VELOCIMETRY SYSTEM

The interplay of the flow in and around a cavity is known to have a broad range of length scales and a number of periodic oscillations that interact to yield a non-linear (unsteady) fluid flow problem. While this type of challenge brings out the strength of the PIV method by being able to sample the entire flowfield instantaneously it also exposes its weakness associated with measurement error. Another relevant issue is the choice of using a fully digital system for this type of problem, which although ideal for capturing large data ensembles lacks the final accuracy of a wet-film system. It is the purpose of this chapter to qualify the approach made in investigating the cavity flowfield and to implement different approaches for improving the performance of the system.

This chapter begins with a description of the image capture system available at the University of Glasgow with a brief mention of the typical analysis procedures implemented for PIV. The development of the software to improve the accuracy over the entire dynamic range of the system is described and the expected measurement errors for these new procedures are quantified. In this study the error analysis is performed using synthetic images (or Monte Carlo simulations) to provide a more reliable estimation of the errors. A new post-processing methodology is presented that serves to preserve the quality of measurement and there is a brief mention of the flow derivatives used. The penultimate section documents the development of a new hybrid PIV-particle tracking method that will allow better spatial representation of the important turbulent statistics for the cavity problem. This chapter ends with an estimate of the statistical confidence and expected derivative errors.

2.0 General introduction

Flow visualization has always been an integral tool in fluid mechanics; Yang 2001 provides a compendium of visualization approaches using interesting fluid flow interactions. Evolving from a qualitative imaging system to one that will provide quantitative measurements of complex instantaneous velocity fields has only been possible over the last twenty years. With recent scientific and technical advances in

optics, lasers, electronics, video and computer techniques particle imaging has been able to evolve quickly and are now a popular family of non-intrusive quantitative flow visualisation schemes that provide instantaneous velocity field information for fluid flow. PIV has become a well-known and effective technique for measuring two-dimensional flow fields instantaneously. It was introduced in the 1970's as the laser speckle technique, Barker and Fourney 1977 and Simpkins and Dudderar 1978 and since then many investigations have been carried out to improve its performance. The performance of a PIV system is defined by its spatial resolution, detection rate and accuracy.

PIV consists of obtaining the velocity of a fluid by measuring the movement of tracer particles suspended in the flow. Typically flows are seeded with micro particles and a planar region of the flow is illuminated with a high intensity strobe, usually a pulsed laser. The tracer positions can then be recorded as a function of time in doubly or multiple exposure photographs, the visible particles can then be used to measure the tracer displacement. Knowledge of the strobe period with the physical displacement of the tracer particles will then yield the local velocity. A typical PIV set-up for a wind tunnel is shown in figure 2.1. For correlation PIV the image is broken up into measuring volumes, or tiles as shown in figure 2.2, which allows the velocity to be evaluated at discrete positions throughout the image plane. The resulting velocity field consists of vectors on a rectangular grid with each vector representing a spatially averaged velocity measurement.

PIV is traditionally distinguished from laser speckle velocimetry (LSV) and particle-tracking velocimetry (PTV) by the seeding concentration used, Adrian 1984. LSV was conceived as an extension to speckle metrology and uses a very high seeding density that causes an interference pattern to occur in the image plane of the camera. This speckle pattern may then be interrogated to resolve the particle displacements, see Grant 1994 for a complete review. In ideal operating conditions for PIV the tracer concentration is high enough such that a large number of particles exist within a specified measuring volume that is considered to contain adequately uniform flow, Lourenco et al. 1986. This local velocity is then taken to be the average velocity over the measuring volume. In its simplest form PTV follows the progress of an individual particle through a series of instantaneous observations or pictures; as used by Prandtl in

1934 to more sophisticated applications by Agüi et al. 1987. Using a low seeding density with a simple PTV algorithm ensures that individual particles are not confused with one another, although there is currently scope for improving the spatial resolution of PTV by raising the seeding density used. The merits of this PTV approach are discussed later.

There are several methods in use that will resolve the local velocity within a measuring volume for PIV. Young's fringe, auto-correlation and cross-correlation may all be used to extract velocities from sequentially double- or multi-exposed particles on a single picture. Autocorrelation is the digital implementation of the Young's fringe analysis and is a popular procedure for the calculation of tracer displacement, although complexities arise when trying to resolve the directional ambiguity, Burch et al. 1968 and Liu et al. 1991. For double/multi- exposed PIV images on double/multiple pictures the gradient method can be used to address the compromise between accuracy and processing speed by using simple image plane subtraction or addition correlation, Tan et al. 2001. Cross-correlation has useful application in both single and multi-exposure capture systems, Cho 1989. Using multiple-pictures this technique removes the directional ambiguity inherent in both the Young's fringes and auto-correlation techniques, Utami et al. 1991. Using this type of fast image acquisition became popular with the advent of the digital camera since a single traditional SLR camera cannot capture two sequential pictures in the time frame required. Although there are advantages to this Digital PIV (DPIV) technique, such as eliminating the need for the photographic and opto-mechanical processing steps, there remain significant challenges and constraints to the PIV user regarding the inherent bias errors involved when using a CCD chip.

Photographic film has a tremendous resolving power with a 125mm x 100mm piece of film containing as much as 3Gbytes of information. A current state of the art dual-exposure progressive scan interline CCD camera will contain 4.2Mbytes of information. This mismatch in available information will have an impact on the accuracy of DPIV. although it has been perhaps the single main aim of the research community to improve the spatial resolution of results using 'super-resolution' algorithms, Keane et al. 1995. For image processing, spatial resolution is taken to mean the ability to distinguish between images of two different particles in the image plane that are originally distinct or separated in the object plane. For PIV the term spatial resolution relates to the

smallest velocity structures that can be resolved or measured in the flow field, or using the definition of Adrian 1988 is just the size of the interrogation spot in the fluid. A physical measurement volume side length of K_{phy} (μm) will be able to identify structures of the order,

$$l_\delta = \frac{K_{phy}}{M_I} = \frac{Kd_r}{M_I} \qquad [2.1]$$

where, K is the side length of the interrogation area in pixels and d_r is the diameter of the pixels on the CCD array, μm

The spatial resolution is always bounded by the size of the measurement volume, which is determined by the intersection of the illumination light sheet with the interrogation spot density distribution. This minimum resolvable scale is crucially important in DPIV and some super-resolution techniques used to measure smaller length scales are included in later sections. Although there are rigid constraints concerning the usage of a DPIV system it remains a viable competitor to wet-film PIV since these systems require a significant amount of optimisation at the image capture stage. In fact it may take several experimental iterations to establish whether there is sufficient light, proper focusing, adequate seeding and an appropriate laser time delay because they are non-integrated and non real-time. It is these economical and efficiency reasons that have caused the common mode of operation for PIV systems to migrate to fully digital systems.

There are three modular stages involved with the application of a PIV system from wind tunnel to flow derivative. The capture of the seeded images from a camera synchronised with a laser is the first and most crucial stage of the system. Any inadequacy of image quality with the capture of the scattered light from the particles will result in an irrecoverable loss in accuracy. Secondly the calculation of the velocity vectors from image interrogation is performed with the final stage being the evaluation of other quantitative flow information. The total performance of the whole system is dependent on each of these steps. If the intention is to apply DPIV to a measurement problem characterized by 3D motion with broad ranges in length scale (such as the flow in and around that of a cavity), then close attention must be paid to achieving the best possible accuracy given a certain sampling resolution, Fincham and Spedding 1997. It is the

intention in the remainder of this chapter to document the modifications made to the current DPIV system that will improve both spatial resolution and accuracy. The third performance criterion of detection rate is not a predominate issue although it will be addressed at appropriate points in the text if the computational cost becomes especially excessive.

2.1 Image capture

The current image capture system at the University of Glasgow is capable of performing several modes of operation since the system has at its disposal two lasers and two cameras. The illumination source is provided by a pair of Spectra-Physics GCR-130-10 frequency doubled, double-pulsed Nd:YAG lasers running at a nominal repetition rate of 10Hz with a wavelength of 532nm. With this laser unit operating in a single pulsed mode the manufacturer reports an approximate pulse power of 240 mJ. The images are recorded using two 8-bit Kodak Megaplus ES1.0 digital cameras, of 1k x 1k resolution, operating in a triggered double exposure mode with a 60% pixel fill ratio. To enhance the fill ratio an array of microlenses are deposited on the sensor that will improve the light sensitivity of each pixel. The images are captured using two National Instruments PCI 1424 digital frame grabbers, the cameras, frame grabbers and laser synchronisation are managed using a Pentium 3 (1 GHz) PC through a LabVIEW interface.

A Brewster plate beam combiner may be used to produce two collinear beams for a twin laser set-up. In this instance the lasers may be operated in single-pulsed or double-pulsed modes and polarizing filters fitted to the camera lens may be used to distinguish between each laser head if necessary. The laser is then delivered into the wind tunnel test-section using a beam-shaping telescope with cylindrical lens. The minimum time delay between two pulses using a single laser head is 35μs while both lasers operating in single pulse mode can provide a minimum time delay of 12μs (using the beam combiner to set up collinear planes of illumination). The pulse length is 8ns. The output energy of the laser is sufficient to illuminate a 250x250mm object region using a lens f-number of 4.2 (written $f^{\#}4.2$). Each experimental scenario used will be explained more precisely in chapter 4. Both Nikon 50mm fixed focal length lenses and Navitar Zoom lenses are available and suitable for the size of CCD chip used on the Kodak ES1.0. The Nikon lenses provide an f-number range of $f^{\#}2.8$ to $f^{\#}16$ while the Navitar zoom lens

extends from 18mm to 108mm, with a range of $f^{\#}2.5$ to $f^{\#}16$. At maximum zoom (108mm) the effective f-number reduces to $f^{\#}4.2$ for a fully open aperture. Experiments are calibrated using a 5mm pitch graticule slide placed in the field of view. Based on this image a conversion between pixel displacements and spatial displacements is possible. Additionally a transfer function is computed which accounts for camera lens distortion (that is stretching and rotation) as the displacements are projected into the physical domain.

Seeding is provided by a C.F. Taylor smoke generator. This unit vaporizes Shell Ondina E.L. oil to provide an oil mist with a nominal particle diameter of 2mm. Höcker et al 1990, Meyers 1991 and Melling 1997 have pursued investigations into ideal tracer particle diameter. They concluded a particle diameter of approximately 1mm would follow the flow faithfully, their results indicate there is very little difference for the particle diameter used here. Seeding was introduced through the breather slot which ensured a good seeding concentration in the closed return wind-tunnels. If it can be assured that the particles are neutrally buoyant, are effectively exposed instantaneously (no blurring and no saturation) and there is no optical distortion or contamination of the scattered light before it reaches the pixel array (caused by lens aberrations or unclean glass surfaces) then there are no errors associated with the general wind-tunnel set-up. This then means that the error of the velocity measurement is solely dependent on the accuracy by which the particle positions can be determined on the image sensor.

2.2 Image analysis

A simple appraisal of the error sources present when determining the particle position on the image sensor shows that inadequate pixel resolution can give rise to mean bias error while imperfections in the particles, the recording process, electronic noise in the camera, the interrogation method and the peak location technique is responsible for random errors in the system. If the hardware of the system has already been designed then improvements to the accuracy of the system can only be accomplished with changes to the interrogation method and the peak location technique (reducing the mean bias error is an issue for section 2.3). It is then possible to minimize these error types with an optimized implementation of the PIV technique and improved analysis procedures after the image capture procedure. This section deals with these issues.

2.2.1 Optimising the PIV technique

The displacement information calculated by a standard double-exposure correlation analysis can only deliver first order information (that is no rotation or deformation). Therefore if the curvature of the particles cannot be recovered then it is prudent to reduce the time delay between successive image captures such that the measured displacement and the real displacement are more similar (see figure 2.3). When there is a broad range of velocities present within the measured flowfield a compromise must be made.

To resolve the local velocity within a measuring volume for DPIV the cross-correlation algorithm is used since the digital system is capable of capturing multi sequential images. For correlation analysis Keane and Adrian 1990 and 1992 have demonstrated that there are several criteria necessary to guarantee an adequate signal-to-noise ratio (SNR) and thus guarantee accuracy for the mean velocity over the tile. Of particular importance is the velocity variation error within the measuring volume or 'gradient biasing'. Because the smaller displaced particle pairs have a higher probability of remaining in the second image tile the result may be biased towards lower values. This can be alleviated by an adequate seeding tile density (N_i) optimised inter-pulse delay and correct optical depth of field (DOF), see Keane 1991 and 1995, Willert 1991 and Grant 1997 for more details. The measurement bias is enhanced when a velocity gradient exists across the interrogation window, which causes the correlation peak to broaden and deviate from the $d_\tau / \sqrt{2} d_r$ cross-sectional profile expected and may even split the peak into several peaks, Westerweel 1993a (d_τ is the physical particle image diameter). Keane 1995 and Westerweel 1997a give practical solutions for this problem.

2.2.2 The correlation algorithm

The displacement can be estimated using the discrete cross-correlation function that statistically finds the best match between any two-image tiles; this direct formulation is given in equation 2.2.

$$R_{II} = \sum_{i=-K_x}^{K_x} \sum_{j=-K_y}^{K_y} I_1(i,j) I_2(i+x, j+y) \qquad [2.2]$$

The variables I_1 and I_2 are the intensity values of the tiles and R_{II} is the correlation value. As illustrated in figure 2.4 the correlation plane typically comprises a single peak

and a number of smaller peaks, Keane 1992. The distance between the highest detected peak and the centre of the tile then provides the average particle displacement. Since this function is a true measure of the best statistical match of image pairs in the measurement volume the correlation peak may be measured to sub-pixel accuracy using a variety of methods, see Westerweel 1993a for further reading on this issue. To reduce the computational cost with little reduction in accuracy it is typical to implement the convolution theorem such that the direct correlation is replaced with a Fast Fourier Transform (FFT), Nussbaumer 1982, Utami 1991 and Huang 1993a. Since the image data has no complex part it is possible to further quicken this calculation time by stacking the transform, Press et al. 1993. Therefore the basic calculation of 1000 vectors can be reduced from 180 seconds (direct correlation) to 0.5 seconds (circular/FFT correlation)[1]. Finally, a weighting function is used (that is the convolution of the sampling weighting functions) to remove the bias artefact associated with the frequency domain. In this study it is also beneficial to quantify the degree of correlation between samples and this is provided by a normalization of the correlation plane data. For the direct correlation the technique employed by Raffel 1998 is used and for the circular correlation a first order accurate method derived by Brigham 1974 is used.

2.2.3 The need for further improvement

The primary limitation of conventional PIV is imposed by the velocity gradients present within the flow to be measured, Huang 1993a and b. For optimal PIV performance (see section 2.2.1 and references therein) the velocity gradient across any interrogation tile cannot exceed the diameter of the imaged particles themselves (that is $|\Delta\mathbf{u}|/\mathbf{u} < d_\tau$). The most obvious solution to this problem is to reduce the camera field of view by increasing magnification, which is fine as long as the field of view remains large enough to image the region of interest within the flowfield (usually not the case). Both Willert 1991 and Prasad et al. 1992 have investigated the effect of velocity gradient and spatial resolution on accuracy and have suggested two other approaches for coping with velocity gradients. The first approach is to actually predict the deformation present in the flow while the second is to simply reduce the pixel area of the interrogation tiles used. These two approaches are now briefly discussed.

---

[1] Pentium 3 (700MHz) PC

Predicting the deformation present in the flow can be achieved using two distinct methods. The first approach was introduced by Huang 1993b in which groups of particles are tracked and their deformation measured (termed particle image pattern). Using a different approach Jambunathan et al. 1995 used an improved cross correlation technique that would iteratively rebuild the second image such that elevated levels of deformation could be tolerated. As a recent extension to these two approaches Nogueria et al. 1999 and 2001b developed local field correction PIV (LFCPIV) that improves spatial resolution by manipulating the actual particle pattern using the displacement field from a previous evaluation. This system avoids instabilities caused by wavelengths smaller than the interrogation window by using proprietary weighting in the correlation process, while the resolution is limited only by the average distance between particle pairs. This technique represents the most sophisticated and successful algorithm using this type of approach. Even though these techniques have experienced considerable success (especially in shearing flows) their algorithms remain complicated and rely on velocity fields with low deformation and small velocity dynamic ranges. Even though there have been recent advances towards a much simpler algorithm this technique is not chosen for this study.

By simply increasing the spatial resolution of the velocity vector map it is possible to cope better with excessive velocity gradients within the flowfield. This approach has been converged upon by several researchers over recent years and has been given the name 'super-resolution'. This type of approach was initially proposed by Keane et al. 1995 (adapted from Guezennec and Kiritsis 1990) to bridge the quality issues between photographic film and CCD such that large sample sizes of data could be acquired with good accuracy. Therefore, although current CCD technology does not facilitate these super-resolution techniques to comprehensively optimise a PIV system it can improve the spatial resolution of a vector field by up to an order of magnitude. The most important issue for a super-resolution scheme is to maintain accuracy in the velocity measurement as the spatial resolution increases. Since there may be considerable reductions in the l_δ measurable in the flowfield and it can be added in a modular fashion to a traditional correlation process it is the chosen method for coping with velocity gradients in this study. A complete description of the implemented super-resolution method is given in section 2.2.5 while this issue of measurement fidelity is

given further consideration using reference to synthetic imaging (or simulated image) results.

2.2.4 Synthetic imaging

To properly conclude the accuracy of a particular PIV algorithm it is important to test the procedures on an image environment that is fully controlled. Normal experimental conditions are not ideal in such instances since the noise incurred will obviate the system's true accuracy. In such a scenario it can be expected that the recorded optical images will not be perfect circular distributions but will instead be irregular in shape as a result of background speckle, aberrations of the lenses or noise in the image-recording medium. Videographic media will impact noise to image also through electronic noise in the circuits and shot noise in the photo detection process. Highly idealized experimental conditions have found some application in testing a system, Fincham and Spedding 1997 but essentially the errors are inferred rather than calculated. By using synthetic images rather than real ones, all the parameters involved can be controlled and varied as needed in order to systematically study their influence. The objective is then to produce realistic images that are numerous enough to accumulate reliable statistics of the results for any given test case. This approach has been taken by several researchers to date, including and Keane and Adrian 1992 and Keane et al. 1995.

The synthetic (or Monte Carlo) simulation generates images fields of randomly located particles, governed by Poisson statistics (Bendat 1958) embedded in some kind of flow field. The imposed three-dimensional flowfield then displaces the particles over a pre-determined time-delay to the their final location via. Lagrangian integration, thus generating pairs of image fields for analysis. The mean particle image size, $(d_\tau/d_r)_{mean}$, distribution, R^p and the particle image density, N_i is specified with the simulated laser sheet thickness (thus simulating the optical DOF). The continuous images of all particles have a two-dimensional Gaussian shape with the discrete pixel gray values of the discrete image found through integration of the continuous image for each pixel. The bit depth is set at 8 bits per pixel (256 gray levels) with the light sheet illumination intensity modeled as a top-hat function. Controlling the size of the field of view and inter-pulse delay serves to modulate the in-plane motion, out-of-plane displacement and the inter-tile velocity gradient. Alternatively these parameters may be preset and the

synthetic CCD size and inter-pulse delay are automatically determined. Other image parameters are the mean grey level maximum intensity of the particle pixels, I^P_{mean}. the mean grey level intensity of the background pixels, I^B_{mean} and the standard deviation of the image noise, s^N. The contrast for a particular image is the difference between the mean grey level of the particle pixels and the background, thus $C_o = I^P_{mean} - I^B_{mean}$. It is also helpful to impose a function that allows the synthetic image to be seeded with non-colliding particles.

The imposed velocity field should represent challenging spatial and velocity dynamic ranges to accentuate the error type under investigation. In particular isolated Burgers vortices make excellent test cases since there is a significant variation in vorticity permitting detailed analysis of the effects of the local fluid deformation. The method of 'kinematic simulation', Fung et al. 1992 and Westerweel et al. 1997b, yields a velocity field with the kinematic characteristics of isotropic turbulence, which is ideal for exposing bias error and testing super-resolution algorithms.

Each simulation will result in a characteristic variation of error with displacement. The error in displacement is $\Delta d = \hat{d} - d$, where, $\hat{d}$ represents the measured displacement and d represents the actual displacement.

$$rms(e_1) = \sqrt{\frac{\sum_{k=1}^{N} (\Delta d)^2}{N-1}} \qquad [2.3]$$

$$rms(e_2) = \sqrt{\frac{N\sum_{k=1}^{N} \hat{d}(i,j)^2 - \left(\sum_{k=1}^{N} \hat{d}(i,j)\right)^2}{N(N-1)}} \qquad [2.4]$$

$$mean(e) = \frac{1}{N}\sum_{k=1}^{N} \Delta d(i,j) \qquad [2.5]$$

For the errors, equation [2.3] represents the rms error from the real displacement, equation [2.4] represents the rms error from the local measurement mean and equation [2.5] represents the average mean error. All results are based on sample sizes of more than 500,000 vectors, which is approximately 1000 individual vector fields (with a typical processing time of ~100 minutes[2])

A simplified representation for the performance characteristics of any DPIV system can be developed from a non-dimensional analysis. Of particular interest here is the analysis

[2] Pentium 3 (700MHz) PC

from Keane and Adrian 1992 and Stitou et al. 2001b and demonstrates how critical an imposed noise source, (noise intensity/image contrast) can be on the correlation process and on subsequent individual particle identification required for hybrid PIV-PTV. The noise in synthetic images is typically modelled as Gaussian additive noise because of its predictability, generality and similarity to actual camera noise. In real applications the error sources that contribute to noise may be more efficiently and appropriately quantified through experimental observation. This can then allow the noise to be modelled more accurately thus making the need for extensive parametric noise studies redundant. Therefore, following the work of Stitou et al. 2001b and using the particle identification technique summarized in section 2.6.1 experimental values for the noise source are estimated to be $I^{P}_{mean} = 80$ and $I^{B}_{mean} \approx 16$, thus $C_o = 64$.

Each algorithm used or developed was also tested on the standard image database, Okamoto et al. 2000[3].

2.2.5 Super-resolution PIV

For this study a DPIV system without a super-resolution module will deliver a spatial resolution of approximately $10^{-2}m^{-1}$, which is a considerable disadvantage since Laser Doppler Anemometry (LDA) and hot wire anemometry have a resolving power of 100 and 1000 times higher, Willert 1991 and Adrian 1991. The criterion for this super-resolution system is clear, to deliver as high a spatial resolution as possible without a reduction in the measurement accuracy, Keane 1995, Vogt 1996 and Westerweel 1997b. To do this the current algorithms should be reviewed and adapted.

Super-resolution techniques may be categorized into several distinct definitions, Nogueira, 2001a. Hybrid systems are those that apply conventional correlation PIV techniques for the first iterations and then switch to particle tracking (PTV) for improved spatial resolution, Cowen et al. 1997 among others. Multigrid PIV uses circular correlation in an iterative procedure that continually reduces the size of the interrogation window, the discrete window shifting (DWO) stage benefits from an increase in SNR for a given tile size, Soria 1996, Hart 1999, Scarano and Reithmuller 1999 and 2000 and Lecordier et al. 1999. Multigrid direct correlation PIV (or DCPIV)

[3] Examples may be found on http://vsj.or.jp/piv/

is analogous to the former procedure but can use a more flexible shape of interrogation window, Fincham and Spedding 1997. Recent work performed by Gui and Merzkirch 1998 and 2000 to allow arbitrary sized windows to be used with circular correlation (i.e. not radix-2) are bringing the strengths of the Multigrid PIV and DCPIV strategies closer together although both will continue to suffer from bias errors (known as peak locking). Preventative strategies for this are available and mentioned in section 2.3.

The foundation of the current study is based on the discrete window offset (DWO) technique first proposed by Keane and Adrian 1993 and then applied to DPIV by Westerweel et al. 1997b and has since found application in all the most robust super-resolution techniques. The classical performance limitation for PIV is between the dynamic range and the spatial resolution (termed the 'one quarter rule'); this can be negated by the DWO procedure. DWO is a scheme that uses the initial correlated displacement field as an input to a second pass whereby each of the second interrogation tiles are offset by the previous integer displacement information. The residual displacement is then only the fractional amount of the particle-image displacement, thus it avoids the elevated rms error expected from large particle displacements since, $\Delta d \propto (d \times d_\tau)$, for a more detailed analysis see Westerweel 1993a. This improved performance is possible since window shifting minimizes the in-plane loss of pairs and thus increases the detectability of the displacement correlation peak. Measurements of both low and high turbulent intensity benefit from this type of analysis and it can be expected that a three-fold reduction in signal noise is possible.

It has been observed here that Δd depends on the particle image diameter d_τ and the interrogation window size K, thus the DWO algorithm may be combined with a reduction of the window size in such a way that the variation of the measurement error remains at a constant level. Therefore DWO with a reduced interrogation window size would yield a result with an improved spatial resolution for the same SNR, thus preserving measurement fidelity. Figure 2.5 illustrates the DWO procedure with interrogation tile reduction. The smaller scale structures observed are now more apparent because of the improved spatial sampling. It was also found that the DWO algorithm used in conjunction with reduced tile sizing could work efficiently as an iterative scheme. In this each window offset was driven by the previous local

measurement to the convergence of a particular local displacement. It was found that the most expedient way to avoid non-converging window displacements (and hence reduce computation time) was to limit the number of iterations possible and to validate each iterative prediction using the local displacement. This is called iterative discrete window offset (ITDWO). A similar scheme called window displacement iterative multigrid (WIDIM) has been developed by Scarano et al. 1999 and 2000.

It was observed here that a higher seeding density was required for ITDWO to be truly effective, since smaller boxes contain less particle information. Through simulation it was seen that the optimal seeding density, N_i for a standard tile (32x32 pixels) in a strong velocity gradient must increase from ~12 particle pairs to greater than 20 particle pairs per tile, this is in line with the probability results of Keane et al. 1995 and Westerweel et al. 1997b. If an inadequate seeding density is encountered, ITDWO would stop and that particular position would be flagged for post-processing attention.

When the velocity gradient is excessively high the SNR decreases and the correlation plane will start to splinter and separate. In such instances it is beneficial to restore the signal strength, preserve measurement fidelity and maintain the local spatial resolution. The best way to achieve this is to instruct the calculation to perform an adaptive Multigrid PIV pass, or tile skewing, first mentioned by Lecordier et al. 1999. Adaptive multigrid analysis increases the SNR of the correlation by skewing the interrogation tiles into the local flowfield. Figure 2.6 shows the progression of the calculation from initial correlation to tile skewing during ITDWO. The new dimension of the interrogation tile is a function of the local velocity and typically leads to elongated tile dimensions that further preserve the in-plane motion. Figure 2.7 demonstrates a global application of the second iteration step of the tile skewing technique used here for the case of flow over the rear portion of a hatchback car. This figure also contrasts the increase in SNR for a result composed only of ITDWO-DC to one that has used additional tile skewing during window offset. It can be seen that there are global increases in the signal strength over the whole flowfield with sustained improvements in the thick shear layer region. The only stipulation required for this procedure is a minimum tile dimension such that the measurement volumes are prevented from converging to streaklines when one velocity component dominates (for example in

freestream conditions). Florio et al. 2002 has recently presented a more flexible algorithm that seeks to integrate the strengths of the approaches developed.

In conclusion to this section a comparison between the standard correlation procedure and the new super-resolution technique is illustrated in figure 2.8. Using an instantaneous result from the cavity study ($L/D = 3.0$ and figure 2.8a) some measure of the optimization present in the experiment can be predicted, as indicated in figure 2.8b. Without any improvements in spatial resolution it is clear to see that the most important regions in a typical cavity flowfield are not being measured correctly. The proportion of the flowfield that is poorly sampled is dramatically reduced when applying the algorithms described in this section. Even though the benefits of such a well-optimized experiment are obvious the spatial resolution improvements for a digital system is known to magnify the bias errors present in the system. Techniques to suppress these errors are now given.

2.3 Suppression of peak locking and estimated dynamic range

In the pursuit of accuracy for DPIV it is the effects of peak locking that may cause the greatest accumulation of measurement error, Nogueria et al. 2001a. Incurring locking errors is a consequence of those systems that use low-resolution techniques to sample the PIV image. Thus with the advent of the DPIV, locking errors have obviously been accentuated at the price of speed and ease of use. These errors will systematically bias the calculated displacements toward integral values, inflicting a measurement accuracy of ±0.5 pixels, which is unacceptable for flowfields with high velocity dynamic ranges. In this study effort must be made to reduce peak locking effects to a minimum since some portions of the flowfield inside the cavity amount to particle displacements that are typically small, sometimes only fractions of a pixel in length. There have been three sources of peak locking identified to date, these are from the CCD sensor geometry, from the chosen interrogation tile dimensions and from the subpixel estimation.

2.3.1 Sensor geometry

Nowadays it is common to record PIV images directly onto image sensors (viz. CCD arrays). It is then that the discretization of the image may no longer match the Nyquist sampling criterion and the measurement precision becomes a function of the physical

geometry of the image sensor. The number of pixels defining a particular particle and the pixel fill ratio (fraction of the pixel which is light sensitive) now become important parameters in the experiment, Fincham and Spedding 1997.

The relationship between particle diameter and measurement accuracy is strongly coupled. If there are too few pixels characterizing the particles then bias error will dominate the sub-pixel accuracy and peak locking is inflicted on the measured displacement. If there is too much spatial sampling of the particle then the measurement error is dominated by increased random error, Westerweel 1999. In this scenario the user must find the proper balance between these two-error types prior to the experiment, that is, at the juncture when the bias error is equivalent to the random error. Using synthetic image simulations with an isotropic turbulence model it is possible to quantify this prediction. The mean bias error may be quantified by taking a sufficient number of vector fields (in this case 500) and the random error may be estimated by calculating the deviation from the calculated mean value, defined as $rms(e_2)$. These findings are presented in figure 2.9, which confirm the above error behaviour and suggest that the limit $1.6 < d_\tau / d_\tau < 1.9$ is the optimum particle diameter for peak locking suppression without respect to the correlation procedure. In order for this relationship to remain true any deviation from a 100% pixel fill ratio must be met with a similar increase in laser illumination, Wernet and Pline 1993.

It is already known from Prasad 1992 that the random error is related to the particle diameter by a constant representing electronic noise and the correlation procedure, while a lower random error is expected for the direct correlation. In this study a random error gradient of $c = 0.07$ is encountered when the FFT is used, as opposed to $c = 0.055$ when the direct method is chosen. To confirm the reliability of the synthetic results the flow through an empty wind-tunnel test-section at $U_\infty = 28\text{m/s}$ with $TI \approx 0.31\%$ (see appendix A) and using a high magnification Navitar zoom lens ($M_I = 0.26$) was completed. By changing the particle pixel diameter (by varying $f^\#$) an estimate of the total measurement error could be made to an uncertainty of ± 0.02 pixels. These results are included in figure 2.10. It appears that there is an expected dip in the error range indicated by the simulated results and the error values are very similar, although the random error component appears to be slightly underestimated. Since there is adequate

credibility given to the simulated data results the predefined optimum particle diameter range should be sought for better accuracy.

Stipulating the laser wavelength, λ and the physical size of a CCD pixel, d_τ and noting the seeding particle size, d_p then following the working by Adrian 1984 and Goodman 1968 a relationship between, $f^\#$ and image magnification, M_I may be expressed. For peak locking suppression when $M_I = 0.1$ (for a field of view of 90 x 90mm) the camera should be set-up such that $f^\# > 10$. Early experimental tests indicated that the laser illumination was only sufficient for $f^\# \approx 5.6$, which is not optimal and yields an error estimate of approximately 0.17 pixels. For the majority of the image capture performed it was possible to use this value of f-number (twin laser set-up), although towards the end of this study a lower f-number had to be used (single laser set-up). Figure 2.11 illustrates the test matrix completed in this study using the magnification, particle diameter and f-number data only. The measurement accuracy has been compromised by this reduction in particle image diameter although none of the data accumulated at these reduced f-numbers were used in the presentation of turbulent statistics. It should be noted that the notion of defocusing the camera in order to increase the effective size of the imaged particles is severely flawed, Browand and Plocher 1985. Although this causes an apparent increase in measurement clarity, it is usually the case that the systematic errors are then being obscured by elevated random errors.

2.3.2 Particle truncation

Associated with the interrogation window size this error source has an amplified effect on measurements when super-resolution techniques are being used. As the perimeter of an interrogation tile decreases with respect to the area of the tile a larger fraction of the particles are being truncated at the tile perimeter, this causes a loss in correlation peak symmetry and a locking bias towards zero displacement. A correction for recovering the symmetry, first noted by Huang 1997 is given by Nogueria et al 2001a and is adopted here. The procedure is to converge the sub-pixel estimate to a stable result using a symmetric correlation and a bi-parabolic interpolator to suppress random error: usage of this algorithm appends Symmetric (or S) to the technique already in use. A simple error analysis using simulated images (with no additive noise) is shown in figure 2.12. It can be seen that for small window sizes SDCPIV outperforms FFTPIV because of this peak

locking suppression. It seems then that better accuracy can be attained by any super-resolution strategy if the final iterative passes are calculated using SDCPIV. In summary, it would then be typical to find a calculation scheme that begins with an ITDWO super-resolution scheme using a direct correlation that switches to a symmetric correlation at the final stage of the iteration (given the name ITDWO-DC-SDCPIV).

So far the improvements in spatial resolution and the preservation of accuracy have been made without regard for the computational cost. Therefore, at this point the behaviour between normalized CPU time and rms error ($rms(e_1)$) for several possible interrogation strategies is presented in figure 2.13 (the spatial resolution is predefined). The optimal super-resolution calculation is described by ITDWO-FFT-SDCPIV since ITDWO-DCC-SDCPIV delivers only marginal improvements in accuracy for a large increase in computational cost. In real time the calculation times for one vector field was 2.5 minutes and 10.4 minutes respectively[4]. ITDWO-FFT-SDCPIV is then the chosen strategy for super-resolution PIV in this study.

2.3.3 Subpixel estimation

When the resolution of the particle diameter (d_τ/d_r) is greater than 1.8 the sensor geometry is no longer a source of error and the difference in sub-pixel estimates is less than 0.1 pixels, Willert and Gharib 1991, Prasad et al. 1992, Westerweel 1993a, Lourenco and Krothapalli 1995 and Cowen and Monismith 1997. As shown in figure 2.11 the particle diameter is below this value and the specifics of the sub-pixel operator are now more important.

Efforts for decreasing the random error in sub-pixel estimation have already been made although the systematic errors remain (matching the functional form of the curve to the actual particle profile). It was found here that in the particle diameter range of $0.7 < d_\tau/d_r < 1.5$ both Cardinal interpolation (or Whittaker's reconstruction), Stearns and Hush 1990 and a thin shell smoothed spline function perform equally well. However, it is the more generic choice of Gaussian peak-fitting, Westerweel 1993a that is the best function fit for such a particle diameter limit, although there exists a well-documented bias against integer pixel values. It should be noted that if the recursive

---

[4] Pentium 3 (700MHz) PC

iterations of the symmetric super-resolution technique are successful (stable) it would eventually record a null real displacement at which there is no difference between any sub-pixel estimators.

2.3.4 Dynamic range

The dynamic velocity range (DVR) is defined as the maximum range that can be measured with a fixed set of instrumental parameters divided by the minimum resolvable velocity measurement, Adrian 1997. Whereas the accuracy and spatial resolution describe the usefulness of a PIV system the dynamic velocity range encapsulates the measurement range of a particular system. Moreover the dynamic spatial range (DSR) is the field of view of the object space divided by the smallest resolvable spatial variation. From the interpretation of the PIV uncertainty principle by Adrian 1986 it can be expected that the capability of a PIV system may then be described by,

$$(DVR) \times (DSR) = DyR = \frac{K_{CCD}}{c_\tau d_\tau} \qquad [2.6]$$

where K_{CCD} is the dimension in the recording plane, in this case the size of the CCD chip, which determines its capacity to hold information, and DyR is the overall dynamic range metric for the system. The constant c_τ is a measure of the ability of the analysis procedure to determine the correct displacement between images. The larger the value of DyR the more suited the PIV system is to resolving small-scale variation embedded in larger scale motion. It can be expected that a standard 35mm film (TMAX400) will have a DyR metric of 62610, which is ideal for measuring several decades of a turbulent spectrum. A standard DPIV configuration will yield a DyR value of approximately 5000.

By using a twin-camera set-up whereby each camera views one half of the image plane at the same magnification, the physical area (K_{CCD}) of the recording plane can be doubled (the vector fields are later interlaced). For a specified spatial resolution, the implementation of the super-resolution scheme with additional bias error reduction (ITDWO-FFT-SDCPIV) increases the ability of the system to reconstruct the actual velocity field (thus reducing c_τ). In addition to this, the whole experiment may be re-optimized when algorithms such as the tile-skewing algorithm are being used, since a

larger velocity range may be accommodated within a given image area. As a direct effect of these changes, the dynamic range value has been increased to approximately 21000 without any modifications to the hardware of the system. An illustration of these improvements is presented in figure 2.14 where the displacement histogram of two separate experimental tests (one optimized, one non-optimized) for a cavity with $L/D = 2.0$ is shown. It is clear that without optimization the data suffers from severe peak locking effects.

2.4 Post-processing methodology

The vector output from PIV can be classified into two groups (1) false measurements or spurious vectors (2) correct measurements with uncertainty, as defined by Westerweel 1994. Spurious vectors tend to originate from interrogation windows that have insufficient particle pairs or a low signal-to-noise ratio, resulting in the peak detection algorithm pointing to an incorrect peak on the correlation plane. This causes highly localized deviations from the surrounding flow nature. Spurious vectors may also originate from any parameter that detracts from ideal experimental conditions, such as turbulence, seeding inhomogeneities, bad focusing, stray light etc. If unchecked these 'wild vectors' will reduce the quality of the results and preclude the calculation of derived flow properties. Some false vectors can clearly be identified in figure 2.15, which illustrates the flow downstream of a cambered aerofoil with gurney flap. It is important that the PIV system is able to automatically detect these bad vectors and replace them with a suitable estimate.

The approach taken for the removal of these wild vectors may fall into one of two categories, namely reliability or post-interrogation. Reliability checking either measures the SNR of each measurement, Keane and Adrian 1990 or determines the quality of the correlation, Huang and Fielder 1993a. In both instances it is quite difficult to impose a global tolerance that will suffice for any problem and as such valid vectors may be rejected. Thus reliability checking is seldom used in isolation. Post-interrogation data validation is usually performed by a close neighbourhood scheme that calculates the local mean and variance and compares this to a preset tolerance that then determines acceptability. Some relevant techniques that determine these residuals for detection and replacement are Raffel et al. 1992, Westerweel 1994, Fujita and Kaizu 1995 and Raffel and Kompenhans 1996. When there are a high proportion of bad vectors in the local

neighbourhood (roughly when there are >5% bad vectors in the whole image) the failure of this type of algorithm is anticipated.

A much-improved way of dealing with false vector detection and replacement was proposed by Nogueira et al. 1997b. For improved detection, zones of local coherence are iteratively identified within the measurement using a preset tolerance $T\%$ and then validated by the count of a particular zone, NV. It has been shown that both $T\%$ and NV have a low sensitivity making it a very robust operator. For the correction stage an interpolating filter defined as 'C' in Nogueira et al. 1997 was used here. This replacement and interpolating scheme is used for comparison in this section.

Each validation methodology so far described essentially operates as a low pass filter, therefore it can be expected that sometimes too few measurements are checked or too many measurements are replaced, ultimately reducing the quality of results. However, the richest source of information about the flow itself remains on the image plane and it is reasonable to expect that fidelity of the velocity vector map can be improved using more effective means of extracting data from the images. This technique is called FRTT (forward/reverse tile testing), Green et al. 2000 and operates using both correlation and neighbourhood comparisons to improve fidelity through validation. This technique is distinct from the DWO strategy proposed by Westerweel et al. 1997 since that is concerned with increased accuracy for improved fidelity. FRTT is now described in more detail.

The FRTT algorithm shares the same methodology as the post-interrogation techniques already described, in that a tolerable level of coherence must exist between clusters of vectors. The difference with FRTT lies in the driving principle behind the validation method, where the comparisons are made with two grid-shifted correlation positions, as shown in figure 2.16 and not between the original vector set. The displacement vector of the central tile locates these extra measurement positions in a forward and reverse shifting manner. Therefore these new tile positions should correspond to the physical particle movement in the flow and as such a degree of flow similarity is expected between each result. Any deviation from these three individual correlations forces the replacement algorithm to be implemented. A procedural description of the technique is as follows:

(1) The displacement vector for a specific tile is calculated using the normal technique. This position is named the central tile.

(2) Both a forward tile and reverse tile are located based on the projection of the central tile's displacement vector in a positive and negative sense. These two directions account for out-of and into tile motions between the two exposures.

(3) The displacement vector for the forward and reverse tiles are calculated and compared to the central tile value. If there is suitable coherence between each result then the central tile result is preserved and the calculation moves forward to the next tile. If there is not suitable agreement then further work is necessary: It follows,

(a) If the central vector shares a common motion with either the forward or reverse measurement then the central tile result is preserved.

(b) If both the forward and reverse vectors are in agreement but not the central tile then the central tile result is deemed erroneous and requires replacement. The original central correlation plane is then re-scanned for peaks of 'high-detectability' and if such a peak is discovered in proximity to the average location of the forward reverse displacements, it is taken as the displacement with good quality. If this is not the case the central value is replaced with the average of the forward reverse displacements.

(c) When all three vectors disagree then it can be expected that the SNR in that particular region is poor and is probably caused by seeding inhomogeneities (for a well optimized experiment). To improve the signal a larger tile size is selected (4 pixel increase for DC, while the tile size is doubled for FFT) and the process is repeated. If no agreement is found after several iterations the vector is replaced by an interpolated value using filter 'C' from Nogueria et al. 1997.

This validation methodology has been slightly modified from the FRTT procedure described in Green et al. 2000 so that accuracy and spatial resolution are better preserved. Each validation decision is designated a particular flag such that the quality of the result may be monitored, especially important when the tile sizes are forcibly increased. The system requires only one input parameter, which dictates the level of tolerance between neighbouring vectors. Using the central tile displacement and the amount of tolerable shear possible without correlation peak splintering. Grant 1997 it is possible to preset the metric, although its effectiveness is broadly insensitive to change.

In Green et al. 2000 it has been shown that FRTT is ideal for regions in the flow where the seeding is sparse ($N_i < 7$) and thus where large groups of spurious vectors will exist. Although in the current study the seeding concentration is much higher there will still exist seeding inhomogeneities that will locally reduce the N_i value toward this range. Additionally, the cavity problem displays a larger velocity dynamic range than that covered in the publication and there are more spatial wavelengths evident that will distort the performance of the replacement algorithm. Therefore for completeness, sparsely seeded and instantaneous Taylor-Green vortex interactions were modeled to compare the modified FRTT scheme to the coherence scheme already mentioned. For this study the effects of seeding density and displacement range (defined as $R^d = |d_{\max}| - |d_{\min}|$) are covered, these results are presented in figure 2.17. By increasing the seeding density within an experiment it can be expected that the rms error will reduce as the SNR of each interrogation tile increases, and this is confirmed by the 'basic analysis' curve shown in the figure, here $R^d = 16$. It can be seen that the FRTT scheme is consistently more accurate than the coherence scheme over the seeding concentration range specified, with the largest contrast in performances between $3 < N_i < 7$). This confirms the previous study in Green et al. 2000. To quantify the behaviour of the replacement strategies the velocity range within the flowfield was changed while the seeding concentration was set at $N_i = 16$. Since the FRTT scheme interrogates the raw image plane at the appropriate positions a good estimate of the correct velocity is typically acquired (at some computational cost). Although the interpolating filter used for the coherence has been proven to have excellent performance over an extensive frequency range (see Nogueria et al 1997) some errors are inevitable especially when the spurious points are clustered and/or coherent. The FRTT scheme manages to improve upon the filter scheme because it re-samples the flowfield and has a structured heuristic to follow.

For the synthetic model used in this study the seeding was distributed in a random manner throughout the image. This type of modelling therefore favours validation schemes that can seek out bad vectors in an otherwise correct local neighbourhood. For real flow interactions, seeding is typically forced from vortex structures leading to clusters of bad vectors, such as that shown in figure 2.15. Using this test case a final observation was made on the ability of FRTT and coherence with this more realistic

problem. As shown in figure 2.18 the coherence algorithm still performs very well with approximately 90% of the bad vectors automatically identified and replaced. However, in figure 2.19 it is shown that the FRTT scheme makes a correct decision about every central vector while the reconstruction of the vector field is superior in clusters of bad data.

2.5 Vector field operators

The planar velocity field obtained by standard (2D) PIV can be used to estimate other fluid mechanically relevant quantities by means of differentiation or integration. For derivative computation a compromise has to be made between the order of the filter, the number of points used for derivation, the frequency response and the noise amplification, Lecuona et al. 1997 and Foucaut 2002 among others. The purpose of the derivative computation here is for maximum feature extraction with minimum error.

There have been numerous studies concerning the accuracy of various computational methods used to calculate flow derivatives. Agüi and Jimenez 1987, Sinha and Kulhman 1992 and Spedding and Rignot 1993 are the most pertinent studies regarding PIV. The adaptive Richardson's extrapolation principle from Fouras and Soria 1998 is used here.

The purpose of this algorithm is to minimize the total derivative error by reducing the truncation error to the upper limit of the measurement error. The grid state of the derivative is shown in appendix B.

Vorticity

Vorticity measures the rotation of the fluid. Each of the vorticity components can be computed from correspondingly measured in-plane velocity vector field data using its basic definition, Batchelor 1967. With a standard PIV system one component is measured at one time, denoted by ω_z[5], which is pointing in the positive z-direction of an x-y-z Cartesian coordinate frame,

$$\omega_z = \frac{\partial v}{\partial x} - \frac{\partial u}{\partial y} \qquad [2.7]$$

[5] In section 4.2 the vorticity in the y-direction is calculated by illuminating the x-z plane

where u and v are the velocity component in the x- and y-directions of the x-y-z coordinate frame respectively.

Shear Stress

Shear stress represents the irreversible viscous transfer of momentum in a fluid. Shear stress forces shear strain, which is the non-rigid body deformation of a fluid element. For the standard PIV system used here one component is measured, denoted by τ_{xy}, given by the following expression,

$$\tau_{xy} = \mu\left(\frac{\partial u}{\partial y} + \frac{\partial v}{\partial x}\right) \qquad [2.8]$$

Streamlines

A streamline φ_n is defined as a path whose tangent at any point is aligned with the velocity vector at that point.

$$\varphi = udx - vdy \qquad [2.9]$$

It was found that a well conditioned second order polynomial (usually termed γ_{13}^2) fit to the two orthogonal velocity components should be used to smooth the data, Press et al. 1993. This type of smoothing prior to the streamline calculation suppresses the random error transmission from velocity to streamlines. Although this increases the bias error a confidence estimate (the Cholesky factor) is monitored, allowing good feature extraction.

2.6 A hybrid PIV-PTV technique

The spatial difference between particle tracking velocimetry and correlation particle image velocimetry is the localization of the measured velocity within the limit of the traceability of particles, as opposed to a mean velocity measurement based on a group of particles. This is depicted in figure 2.20. With this increase in spatial resolution it is also possible to neglect the 'gradient biasing' error of PIV that was mentioned in section 2.2, allowing improved measurement of highly deformed flows. The price to pay is a more complex algorithm with longer computing times yielding low reliability in comparison to PIV. However, these disadvantages have recently been alleviated by the development of hybrid PIV-PTV, Cowen and Monismith 1997, Shan and Gharib 1998 and Zimmer et al. 1999. In this procedure the standard tracking algorithm is preceded by

a correlation analysis allowing an improvement in computation cost while increasing the performance reliability, Stitou et al. 2001b. The distinction with the hybrid PIV-PTV analysis required here is that for the first time the PTV module must be able to cope with PIV imaging conditions and not vice versa, as with these other methodologies. With such a system it would be possible to present turbulent statistics with improved accuracy and up to a 9-fold increase in spatial sampling. A typical hybrid strategy is summarized in figure 2.21.

There are two typical performance indicators for the evaluation of a PTV module; reliability, which is a measure of accuracy and yield, which is a measure of the spatial resolution success. These are defined as follows,

$$\text{Reliability} = \frac{\text{number of correct vectors determined by tracking method}}{\text{total number of vectors determined by tracking method}} \qquad [2.10]$$

$$\text{Yield} = \frac{\text{number of correct vectors determined by tracking method}}{\text{total number of true vectors}} \qquad [2.11]$$

Classical PTV algorithms such as Kobayashi et al. 1989 and Hassan and Canaan 1991, used a low density of distributed particles to present simplistic and reliable techniques, although low rates of recovery were expected. For this particular hybrid scheme the seeding concentrations are an order of magnitude greater and as such a successful particle identification system must be implemented. When the seeding concentrations are at this level the incorrect identification of a particle on the image plane is just as detrimental to the tracking process as a missed particle. A measure of the particle identification success is included as,

$$CPP = \frac{\text{number of correctly identified particles}}{\text{total number of particles}} \qquad [2.12]$$

$$IPP = \frac{\text{number of incorrectly identified particles}}{\text{total number of particles}} \qquad [2.13]$$

where CPP is the ratio of correct particle pickup and IPP is the ratio of incorrect particle pickup. The required performance of a hybrid system is now included.

2.6.1 Requirements of the hybrid system

The usefulness of a hybrid PIV-PTV scheme in this study is obvious, it can be used to improve the fidelity of the presented turbulent statistics. Since the velocity data is being supplemented with a multigrid analysis it may be possible to neglect the need to

redistribute the velocity data onto a regular grid using the methods of Agüi and Jimenez 1987, Spedding and Rignot 1993 or Stitou and Riethmuller 2001a for instance. This is convenient since the improvement in accuracy gained from the hybrid analysis is not then obviated by interpolation error, Hesselink 1988 and Cowen and Monismith 1997.

The proposed technique is simple, after each particle is successfully tracked its location is shuffled into the centre of the nearest 't-tile' (or measurement volume), see figure 2.22. These t-tiles (or 'bins') are much smaller than the interrogation tiles used in super-resolution PIV and as such any vector relocation may be regarded as interpolation with zero-order. It would be advantageous if each t-tile area would yield one velocity measurement per image pair, and by assuming homogeneous seeding it is possible to assess the potential for such a scenario, as shown in figure 2.23. From inspection of this data it may be seen that for a seeding density of $N_i \approx 25$ a t-tile dimension of $6x6$ pixels will just about fulfil the criteria, which is advantageous since this matches the minimum seeding conditions for super-resolution PIV. Because the t-tile size presented so far is not calibrated, it is important to look at the physical shift required for each individual cavity case. This data is collated in table 2.2. For a $6x6$ pixel t-tile the maximum vector movement is 0.25mm (one half of the physical t-tile length), which is encountered for the $L/D = 3.0$ cavity case. The remaining data in this table illustrates the relocation error present for other t-tile dimensions; this is included for the purposes of chapter 5. In conclusion, it appears that this method of presenting turbulent statistics is viable as long as the assumption of homogeneous seeding is not overly optimistic. To investigate this assumption a sequence of 110 image pairs were interrogated (for a cavity with $L/D = 3.0$) and the number of particles within each t-tile (of $6x6$ pixels) from the first frame image was recorded, this data is shown in figure 2.24. From this it appears that there is sufficient seeding being entrained into the cavity, although portions of the flowfield are clearly not evenly seeded. Therefore, at these seeding concentrations for this type of flowfield the statistical sample size and the number of images captured will clearly not be the same.

2.6.2 Particle detection

A particle density of $N_i = 25$ will invoke a 54% probability of particle overlap for a 3-point sub-pixel estimation scheme. This implies that a suitable particle identification

scheme must be able to discriminate between contiguous particle images. Less important image facets to this study are out-of-focus particles, flocks and lineaments. Particle detection is broken up into two stages, that is general particle identification (pixel estimate of particle location) and particle peak location (the sub-pixel calculation). These are now discussed.

2.6.2.1 Particle identification

The subtle difference between a particle identification scheme that provides good yield and reliability and bad yield and reliability is in its *CPP* and *IPP* performance. This is illustrated by a test case in figure 2.25 where the same tracking algorithm (Barnard and Thompson 1980) has been implemented using particle data identified from two different schemes. It is clear from this simple test case that tracking algorithms will only deliver good yield and reliability if the particle identification scheme preceding it is successful. If *CPP* can be preserved while *IPP* is minimized the particle identification scheme is deemed successful.

Particle identification schemes that have found application in traditional PTV operate by simply subtracting globally (standard threshold binarization, STB) or locally (multiple threshold binarization, MTB) weighted intensity values. Such schemes will not be successful when high seeding concentrations are prevalent. More pertinent methods are those proposed by Maas et al. 1993, called here MTB_M and Ohmi and Li 1999, called here $M_{OR}TB$. Although these methods can cope with the PIV imaging conditions the particle diameter range expected here ($1.0 \leq d_\tau / d_r \leq 1.5$) seriously reduces their effectiveness. In this study it was found that dynamic threshold binarization (DTB), Ohmi and Li 2000 and particle mask correlation (PMC), Etoh and Takehara 1998 were the most reliable and robust schemes available. DTB is successful since it uses an adaptive contrast thresholding, thus allowing less bright particles to be identified also, although it faltered for small particles. PMC was found to return the highest values of *CPP* since it uses a 3-point Gaussian fit for identification using a correlation match but this also makes it very susceptible to noise, causing an elevated number of *IPP*. Each of the particle identification schemes mentioned so far were tested on the standard image database and the results are posted in table 2.2

The particle identification scheme used here is a mixture of the DTB and PMC methods and is called reconstruction threshold binarization (RTB). This is now briefly mentioned. As with DTB the RTB algorithm works on a contrast threshold value to identify local dominant intensity peaks. Since this requires a global threshold value to be set it is beneficial to initially correct the image for uneven illumination using a white top hat procedure with improved rendering. A weighted morphological structuring element (an image template) is then used to identify the most prominent intensity peaks for that particular contrast value and see if they are morphologically particle like. This stage is equivalent to the analysis performed in the PMC scheme. After each contrast level has been interrogated the images is scanned for contiguous particles. By using the spline fitting technique suggested by Fincham and Delerce 1999 within the neighbourhood of particle clusters it is possible to increase the spatial resolution of the primary particle neighbourhood to more clearly identify possible particle overlap. When particles are identified in this manner there may be a high particle peak detection error since the particle is typically under sampled (causing large random error) but the *CPP* has been improved which sustains the yield and reliability. The RTB performance is included at the foot of table 2.2.

Using a series of simple synthetic images with a particle diameter range of $1.0 \leq d_\tau / d_r \leq 2.0$ is a convenient way to compare the performance between PMC, DTB and RTB. Figure 2.26 indicates the response of the filters for images with zero noise and figure 2.27 represents those with realistic noise added. It can be expected that the performance of both the PMC and RTB operators will be overestimated since all particles are described by a Gaussian profile in a simulated image. Therefore as expected in figure 2.26 the *CPP* values for PMC and RTB are very similar, although *IPP* for RTB is slightly higher. When a noise source is imposed, as shown in figure 2.27 the benefits of the PMC filter are quickly reduced with a 25-fold increase in *IPP* and some loss in *CPP* performance. The DTB operator reduces in effectiveness almost linearly as the seeding concentration increases, caused by the increasing proportion of contiguous particles present in the flow. The best performer is RTB, which is able to provide a 95% *CPP* for only 8% *IPP* at the seeding concentration expected in the experiments.

2.6.2.2 Particle peak location

After the object data has been located on the image plane the sub-pixel particle peak location is calculated. Most particle profile fitting schemes will have similar accuracy when the peak is well sampled (that is $d_\tau / d_r > 2.0$), Lourenco and Krothapalli 1995 , however this choice is reduced when the seeding concentration is high. Five-point sub-pixel estimation routines cannot be used since this will increase the fraction of overlapping particles. It is generally accepted from the analytic work carried out by Westerweel 1993a and b and from the numerous synthetic image simulations, Willert and Gharib 1991, Prasad et al. 1992 Cowen and Monismith 1997 and Stanislas et al. 1999 and 2000, that the Gaussian sub-pixel peak fitting operation is optimal for the current experimental conditions. In a study performed here it was found that typical Gaussian fitting and a less established method of bidimensional Gaussian fitting[6], Udrea et al. 1996 and Press et al. 1993, recurrently delivered the lowest errors or 'tracking bias' as defined by Westerweel 1993a, see figure 2.28. Between these two operators it is the typical Gaussian peak fitting routine that suffers least from tracking bias in this particle diameter range. This was the method used by the hybrid system and has an accuracy of approximately 0.12 pixels for $N_i = 25$.

It was found that the bidimensional Gaussian peak fitting technique had a significant accuracy advantage over other sub-pixel estimators when the flow is in high shear and/or when there is a high seeding concentration, $N_i > 30$, although there is a high computational cost.

2.6.3 A particle tracking algorithm

The PTV module required for measurement in a cavity must be able to cope with fluid flow subjected to strong deformations, which are modelled here as rotation, shear and expansion. An ideal tracking module is one that uses the multigrid PIV to speed up the tracking calculation without depleting the yield and reliability of the original tracking system. It is also important not to inherit any if the inadequacies of the PIV step into the PTV step. Uemura et al 1989, Kobayashi et al 1989 and Nishino et al. 1989 presented the first tracking algorithms. The binary image cross correlation (BICC) method from Uemura et al. 1989 became known as the high speed two-frame tracking method

[6] Using a Nelder-Meade (downhill simplex) non-linear fitting method, Nelder and Meade 1965

because it tracked particles using a strict highest similarity pattern. Quick calculation times were achieved[7] because the algorithm used the binarized image plane output (typically from STB), but there was very little permitted deformation from parallel flow. BICC has remained a good benchmark for other tracking algorithms. Both Kobayashi et al 1989 and Nishino et al. 1989 used the classical four-frame in-line tracking methods, which delivered a low yield with good reliability.

Two-frame particle cluster matching operates using a deformation index to represent the movement of the target particle neighbourhood in which both rotation and shearing is permitted. Some relevant works are Ohyama et al 1993, Okamoto et al. 1995 and Ishikawa et al. 1997. The velocity gradient tensor method by Ishikawa et al. 2000 and Yamamoto et al. 1996 is probably one of the best tracking algorithms available, although its success remains susceptible to non-paired particles. The spring model tracking technique (SMT) proposed by Okamoto et al. 1995 is a similar scheme to the those mentioned above and calculates the deformation index by relating particles to one another using a series of spring-models. The smallest total spring force yields the tracked particle. This method is relatively easy to implement and is used for comparative purposes in this section.

There exist other tracking algorithms that are either optimized for one type of fluid deformation or have strict stipulations for effectiveness. For example Song et al. 1999 uses Delaunay triangulation to follow rotation only and Labonté 1999 uses a neural network scheme to cope with strong out-of-plane components. In this vein, Baek and Lee 1996 have utilized probability tracking (adapted from Banard and Thompson 1980 image recognition procedure) that is tolerant of rotation, shear and expansion but cannot cope with non-pairing particles. After efforts by Ohmi and Dao Hai Lam 1998 and Ohmi et al. 2000 this algorithm is more resilient and is the tracking scheme adopted here. Because of the functionality of the procedure it will dramatically benefit from a PIV precursor step, it is named Barnard and Thompson tracking (BTT) in this report.

BTT is based on the iterative estimation of positive match probability, P_{ij} and no match probability P_i^* that measures the matching degree (the nomenclature of Ohmi et al. 2000

[7] 1200 vectors in 5 seconds for a Pentium 3 (700MHz) PC

is used here). The principle particle i in the first frame initially preselects its neighbouring particles in the second frame using a locality condition based on some radius R_c, as shown in figure 2.29a. Then P_{ij} denotes the probability of particle i in the first frame-matching particle j in the sectioned second frame area, while at the same time the probability of the second frame particle disappearing is P_i^*. The probabilities are normalized at the end of each iteration,

$$\sum_j P_{ij} + P_i^* = 1.0 \qquad [2.14]$$

There are several way to estimate the initial probabilities such that convergence times are improved (that is the definition of $P_{ij}^{(0)}$ and $P_i^{*(0)}$), and for this study both the normalized cross-correlation coefficient and local FRTT parameters were used to good effect. The particle matching probability is updated by using the probability values of the neighbouring particles (first frame particle k to second frame particle l) defined to exist within a radius R_n of the principle particle i, as seen in figure 2.29b.

$$P_{ij}^{(n)} = P_{ij}^{(n-1)}\left(A + B\sum_k\sum_l P_{kl}^{(n-1)}\right) \qquad [2.15]$$

It is this insistence of quasi-parallel particle motion (k to l) within the globally predefined radius value R_n that must remain with another radius defined as R_c (called the relaxation area) that causes a reduced performance of this algorithm; this is shown for completeness in figure 2.29c. $P_{ij}^{(n)}$ denotes the updated probability for that iteration n. Using the updated value of no match probability (via the new method stated by Ohmi et al. 2000) the next iteration may be implemented after simple re-normalization of $P_{ij}^{(n)}$ and $P_i^{*(n)}$. Both A and B ($A = 0.3$ and $B = 3.0$) are weighting constants predicted by Barnard and Thompson 1980. Using this version of the technique it can be expected that a first frame global particle density of N_* will require $O\left(N_*^3\right)$ probability tracks to be formed. Images acquired in this study (for $N_i = 25$) will require approximately 20^8 minutes to calculate.

By using the hybrid analysis a better estimation of R_s can be endorsed that improves convergence times by reducing the number of possible second frame particles j, while R_n and R_c may be better estimated to increase yield and reliability. Since the local

[8] 700MHz Pentium 3 PC

direction of motion is known from the PIV pass (ITDWO-FFT) the search radius R_s can be reduced and set to an offset position, as seen in figure 2.30. The offset is taken as the locally interpolated displacement for that particle, but the new value of R_s is more complicated to decipher. To increase the probability of a correct track, as discussed by Keane et al. 1995 the second search radius area should be of approximate size.

$$R_s \approx \sqrt{\frac{2\,|\mathbf{d}_{px}|^2}{\pi} + \left(\frac{d_\tau}{d_r}\right)^2} \qquad [2.16]$$

where, $\mathbf{d}_{px} = d_{x\mathbf{i}} + d_{y\mathbf{j}}$ and is the local vector pixel displacement for that particle (spline interpolated from the PIV results) .

Although the probability study performed by Keane et al 1995 was for a different type of super-resolution system the seeding concentration used are similar and as such the relationship works well. A correct value of R_n should encapsulate the common quasi-rigid motion of the second frame particles while maintaining enough particles to enable the probability calculation to converge on a solution (as opposed to a no match particle). Essentially R_n should be larger than R_c although as the seeding concentration increases these two values can become more similar. It was found that the calculation of the correct matching area benefits from an observation of the extensional strain, ε_{xy}. A good compromise was found in the equation,

$$\left\{ \begin{array}{rcl} R_n = \left(1.5 - |\varepsilon_{xy\,px}|\right) R_s & \Leftrightarrow & R_n > 1.2R_s \\ R_n = 1.2R_s & \Leftrightarrow & R_n < 1.2R_s \end{array} \right\} \qquad [2.17]$$

Strictly speaking, a local increase in strain corresponds to a smaller area of particles obeying the common motion heuristic and the radius of motion similarity should be decreased with respect to a variable that describes the local strain rate (that is $R_n \propto \varepsilon_{xy}$).

It is possible to control the tracking in this manner because the seeding concentration is high enough such that any local changes in R_n is not detrimental to the probability convergence since there will always be sufficient number of particles, this is also maintained by the lower limit $R_n > 1.2R_s$.

The quasi-rigidity threshold R_c indicates the degree of flexibility within which a particle can wonder from the predetermined vector of the principle particle. It is therefore the relaxation of similar movement allowed within the radius R_n. It can be

expected that the improved estimate of R_n from the PIV analysis makes R_c less important for good tracking. The optimal value for R_c is then adapted from the improvements stipulated by Ohmi et al. 2000. In this instance the local flow speed is scaled proportionally to R_c in the fashion,

$$R_c = E + F\,|\mathbf{d}_{px}| \qquad [2.18]$$

where $E = 2.0$ and is image dependent and $F = 0.2$, which is a proportionality constant. The proportionality term clearly helps to increase the reliability of the system particularly in strong shearing flows.

The current project of interest is that of cavity flow and as such any test case for the tracking procedure must contain strong regions of shear and rotation. Therefore the Barnard and Thompson algorithm was tested using instantaneous pictures of the Taylor-Green vortex interaction, shown in figure 2.31, which is an analytical solution of the Navier-Stokes equation. This problem is ideal because a comprehensive study of the standard scheme and the hybrid driven tracking scheme can be evaluated with respect to the wave number, k. In all cases $CPP = 100\%$ and $IPP = 0\%$.The response to seeding concentration is shown in figure 2.32. In this instance it appear as if the Hybrid BTT technique can maintain a good yield over a satisfactory seeding concentration range, which is principally due to the reduction in R_s imparted by the hybrid technique causing the number of possible second
frame particles to be reduced. In contrast, with the BTT tracking set at $R_s = 16$ clusters of spurious data or no-match particles will exist within regions of strong velocity gradient.

The results shown in figure 2.33 are ideal for illustrating the hybrid BTT's ability to establish optimal values of the neighbourhood radii. In particular, determining an accurate value for R_n means that the tracking can carefully establish areas of locally coherent flow and follow it precisely, thus the common motion heuristic is not violated and higher wave numbers can be followed with better success. In addition to this there is quite an improvement in computational time for the hybrid BTT. Figure 2.34 shows that for the expected PIV seeding concentration the convergence times will improve by at least a factor of 5, which is important since it will be used mainly to calculate turbulent statistics. Using a full set of images the hybrid algorithm can process a

Reynolds stress calculation (using t-tiling) in 8.2 hours (for $L/D = 2.0$), whereas the standard BTT procedure takes 45.7 hours.

Motivated by the work of Ishikawa et al. 2000 the hybrid BTT scheme was further compared to the SMT and BICC schemes using synthetic models exhibiting expansion, shear and rotation in isolation. The results from these tests are extensive although the main finding is evident using only figure 2.35. It is shown in this figure that the performance of the other tracking schemes is acceptable for the conditions they were designed for although only the hybrid BTT scheme that can operate with a high yield recovery in the presence of PIV imaging conditions.

2.7 Confidence and the estimation of error

There remain a few experimental issues pertaining to the measurement of cavity flow with DPIV. These are the quantification of the uncertainty of turbulent statistics and the actual error in velocity and vorticity estimates.

When first and second moment calculations of the velocity data are being presented the uncertainty in the turbulent statistics must be addressed. So for a given a sample space of size N, the confidence interval for the computed statistic (i.e. mean variance etc.) must be calculated. If it can be assumed that the sample space is always larger than 30, sampling theory dictates that it is not important if the variance of the sample is known or unknown and a normal distribution can be used, Walpole 1998. If we further assume that the sample variance (observation relative to the sample mean), $\sigma_{\hat{d}}^2$ is used in place of the population variance, σ_{pop}^2 and $\langle \hat{d} \rangle$ (the sample mean) is used as an estimate of μ_{pop} (the population mean), we can be $(1-\alpha)100\%$ confident that the error will not exceed a specified amount ε when the mean sample size, N_μ is,

$$N_\mu = \left(\frac{z_{\alpha/2}\, s_{\hat{d}}}{\varepsilon} \right)^2 \qquad [2.19]$$

where $z_{\alpha/2}$ is the $z-value$ of the normal distribution leaving an area of $\alpha/2$ to the right, α is the confidence parameter and $s_{\hat{d}}$ is the standard deviation computed from the sample space.

The number of samples required to report the standard deviation to a given accuracy level is independent of the local turbulence level, Grant and Owens 1990. The $(1-\alpha)100\%$ confidence interval for σ_{pop}^2 of a normal population can also be calculated and suitably rearranged to [2.20] if it can be assumed that the number of sample required for the mean is always less than that required for the standard deviation (valid when the measured turbulence intensity remains below 30%).

$$N_\sigma = \frac{N_\mu}{2s_{\hat{d}}^2} \qquad [2.20]$$

where N_σ is the number of samples required for the standard deviation while adopting the same confidence levels and accuracy as stated in equation [2.19].

Using a hot-wire measurements were made in the shear layer at $x/L = 0.1$ for $L/D = 3.0$ and $\mathrm{Re}_\theta = 1664$ ($\mathrm{Re}_L = 275000$) since the shear layer region is the source of the highest sample standard deviation in the flow regime. A value of $\sigma_{pop}/\mu_{pop} \approx 0.1$ was measured at this particular location. A confidence level of 95% was selected with an expected error level in the mean velocity of 5%. In such an instance the number of samples required for the mean velocity to satisfy these conditions is $O(10^2)$ and the number of samples required for the variance of velocity fluctuation of the sample to be within 5% of that of the population is $O(10^3)$. This was seen to be the case throughout the entire shear region; the exact measurements are presented in table 2.3.

To confirm these estimates the test case described above was measured using the DPIV system to capture 1000 image pairs. Figure 2.36 shows the convergence of the mean velocity, $\langle \mathbf{u} \rangle$ mean vorticity, $\langle \omega \rangle$ and the turbulent intensity. From this it can be seen that the mean velocity varies by less than 5% after approximately 100 samples. For the mean vorticity the same level of accuracy can be observed after approximately 250 samples and the turbulent stress requires more than 800 samples, as expected. However, such a large amount of image storage for variance calculation is prohibitive to the testing procedure. Therefore it was decided that a fixed sample size of $N = 250$ would be used and accuracy of measurement ultimately calculated (at the 95% confidence level). These results are presented to the right of table 2.3 and indicate that it is possible to maintain accuracy to within 10% if the sample size is reduced to 250.

An estimate for the total uncertainty associated with a velocity measurement can be calculated by adding the variances of the various known contributors, Soria 2002. The ratio of vorticity bias error to the exact value for a thirteen point least-squares fit is related to the sample separation, Fouras and Soria 1998, and is given by,

$$\varepsilon_{\omega_{bias}} = \frac{\omega_{bias}}{\omega_{\max}} = -0.748\left(\frac{\Delta_{IJ}}{l_\delta}\right)^{1.96} \qquad [2.21]$$

where Δ_{IJ} is the distance between adjacent velocity measurements (taken in this case as 16 pixels) and l_δ is an appropriate measure of the local length scale. The ratio of the uncertainty in the in-plane velocity vector to the uncertainty in the out-of-plane vorticity for a thirteen point least-squares fit is given by the following relationship

$$\lambda_\omega = \sqrt{\frac{1}{5}}\frac{l_\delta}{\Delta_{IJ}} \qquad [2.22]$$

so that $\varepsilon_{\omega_{rand}} = \lambda_\omega \varepsilon_{u_{rand}}$ and is specific to the scheme used here, see section 2.5.

The random and bias components of the velocity and vorticity error may therefore be estimated at any point in the domain. For this example the two points in the cavity shear layer will be once again used, the results are included in table 2.4. For the calculation of the total error in velocity measurement, ε_u it is assumed that the scale error and temporal error are both <<1%, thus leaving only the error in displacement measurement. This error has already been calculated in section 2.3 and is now given the value 0.14 pixels ± 0.05 pixels in the 95% confidence limit (ITDWO-FFT-SDCPIV), following a benchmark working from Soria 1996. The complete results are shown in table 2.5. Table 2.4 shows that although it is possible to image the whole cavity flowfield it is difficult to get reliable measurements in all regions using the same image. In particular the vorticity accuracy within the shear layer at $x/L = 0.1$ has a possible bias error of up to 48.3%. Such elevated errors are caused by the difference of scales present between shear layer separation and shear layer interaction with the rear face of the cavity. The example chosen for this study ($L/D = 3.0$) represents the test case with the largest accumulated errors since the resolution (pixels/mm) is at its lowest.

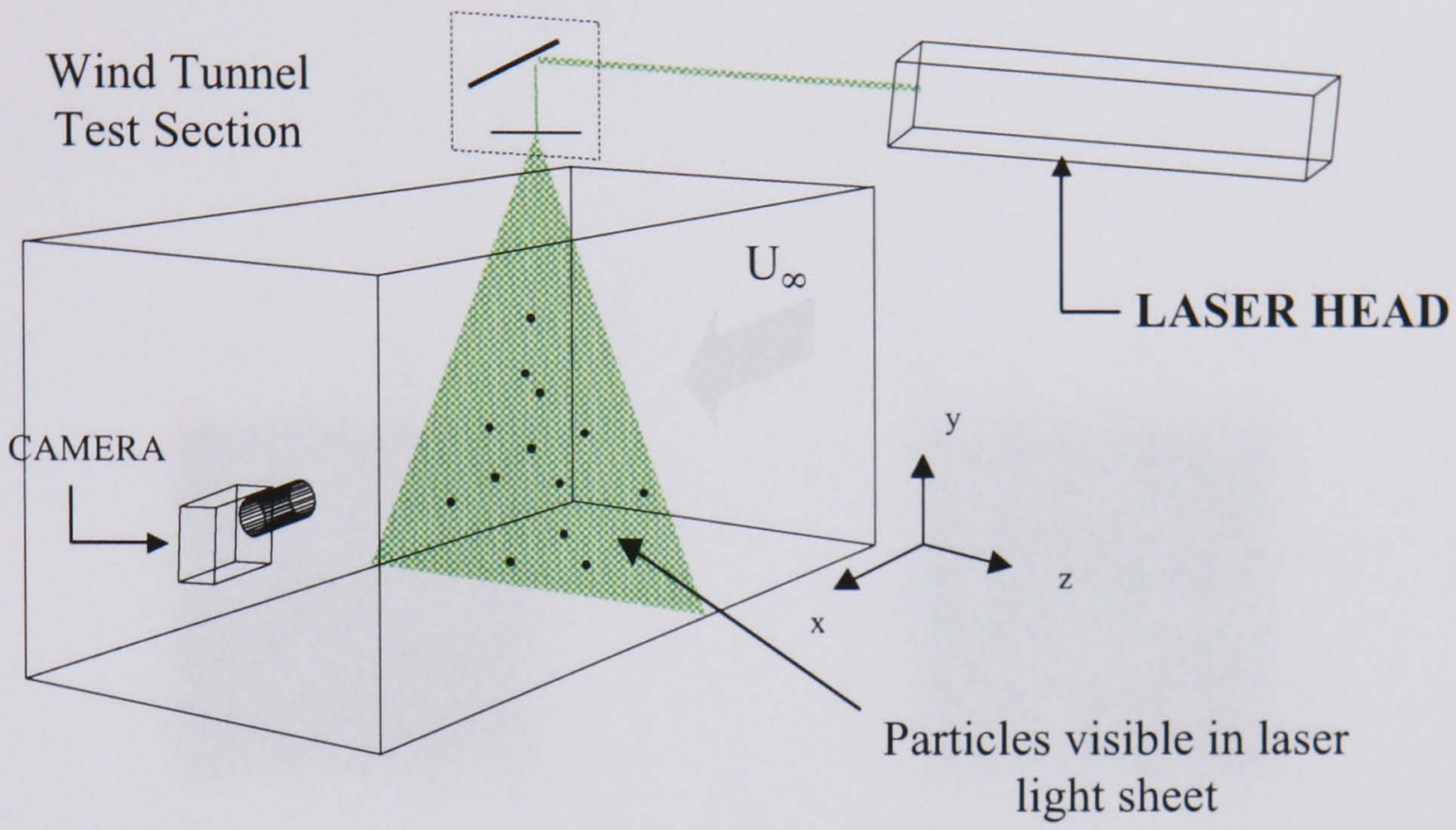

Figure 2.1. An illustration of a typical PIV set-up in a wind tunnel. In this scenario the particles are moving through a laser light sheet while being recorded by a camera situated in the wind-tunnel itself.

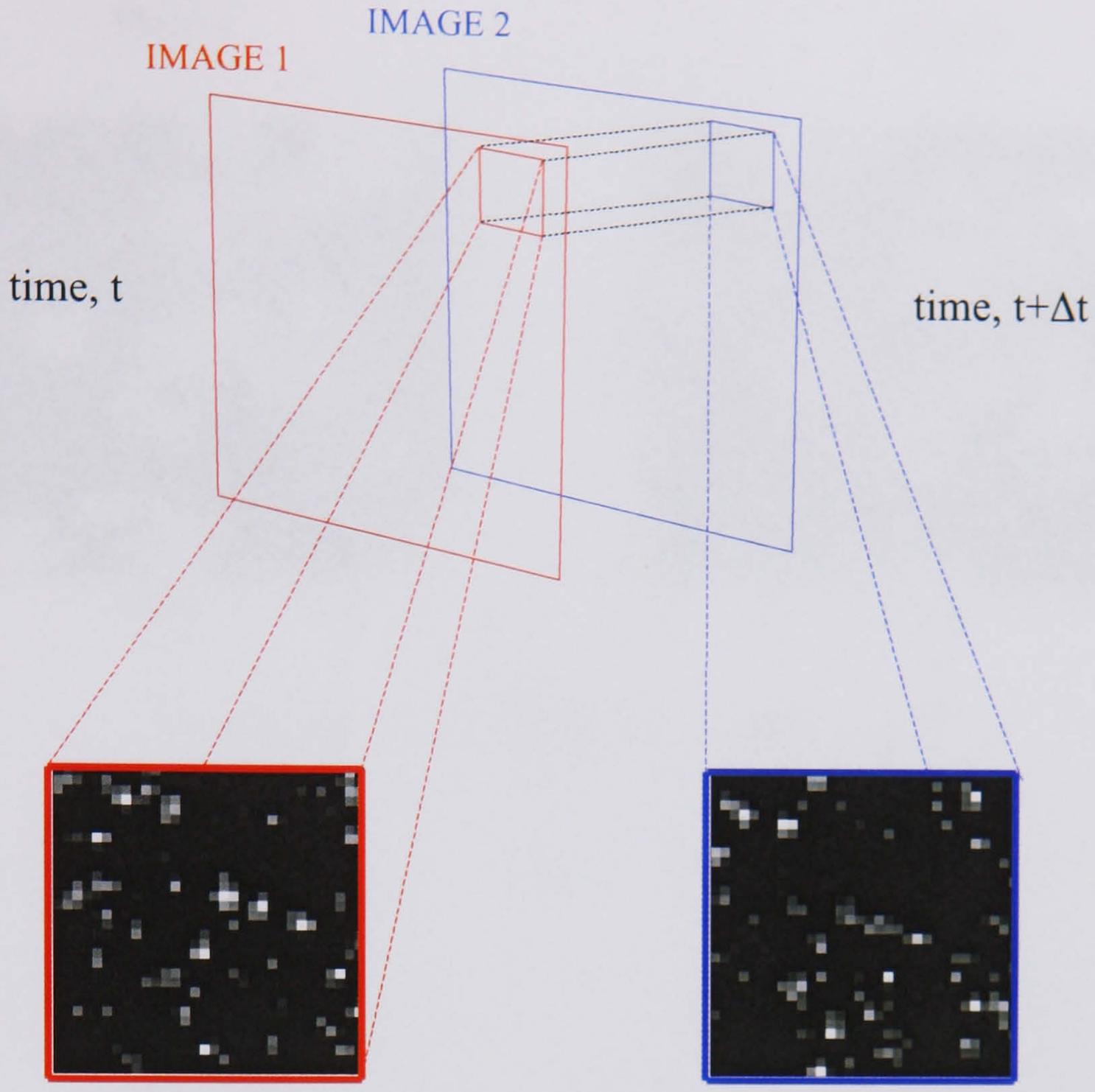

Figure 2.2. Image 1 is captured at a set time, *t* with image 2 captured a small time increment later, $t+\Delta t$. The two images are then each split into a number of interrogation tiles. Each image 1 tile is then individually correlated with its image 2 tile partner.

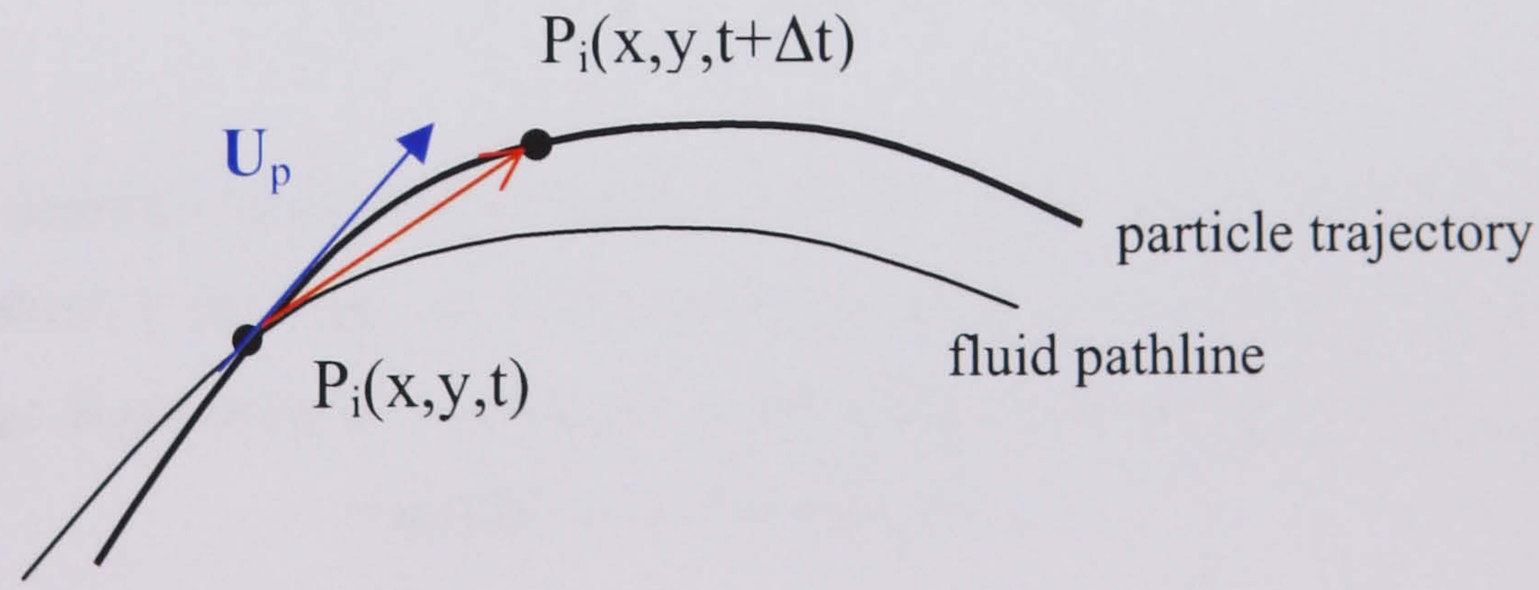

Figure 2.3. It is the red vector that indicates the actual measured velocity between the first position $P_i(x,y,t)$ and the second position $P_i(x,y,t+\Delta t)$. This is an approximation to the actual velocity at that point, $\mathbf{U}_p$, it's accuracy is determined by the laser pulse delay Δt.

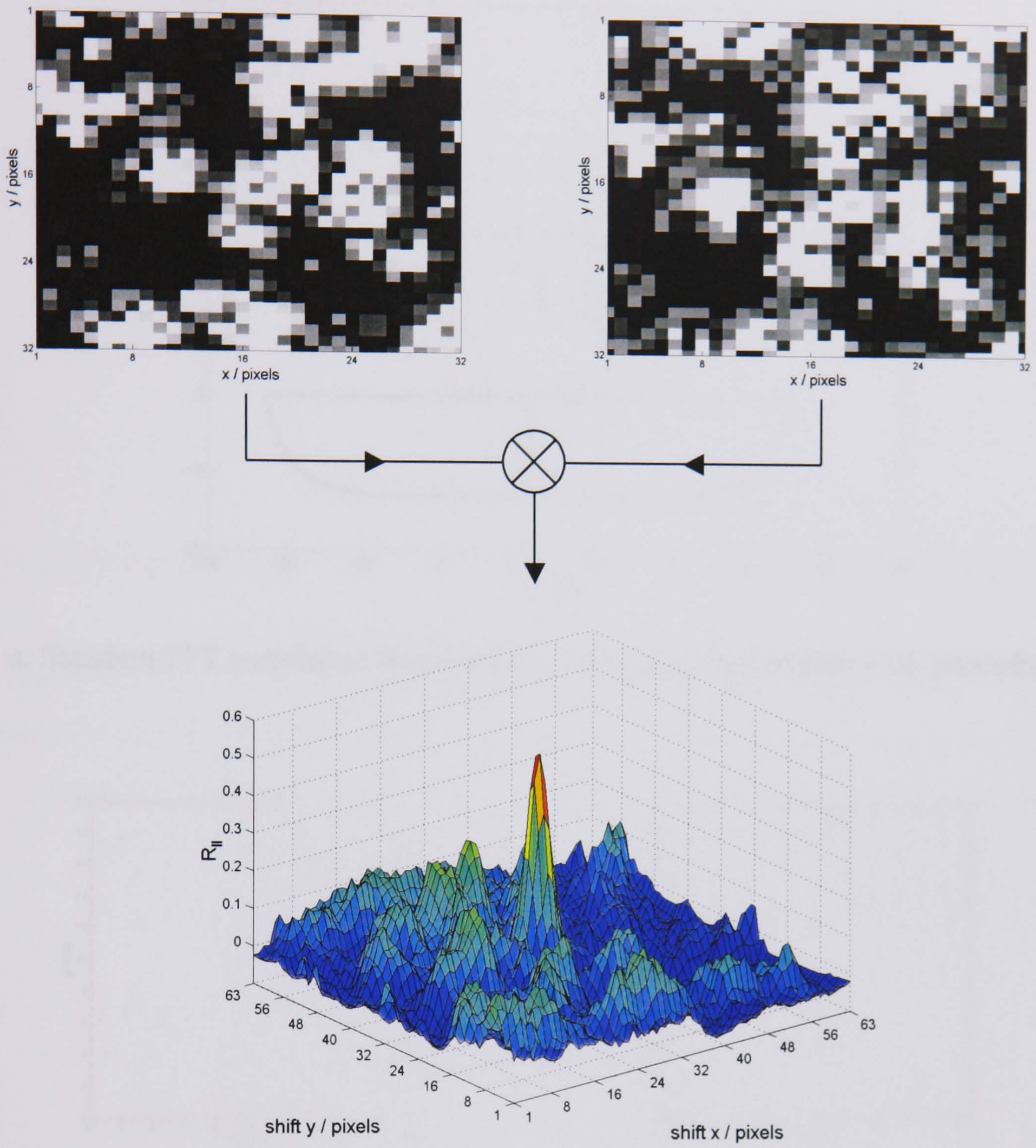

Figure 2.4. The standard correlation procedure used for image analysis. In this instance the direct correlation is used and reveals a correlation plane larger than the image plane itself. The average displacement is measured as the offset of the highest correlation peak from the centre of the tile.

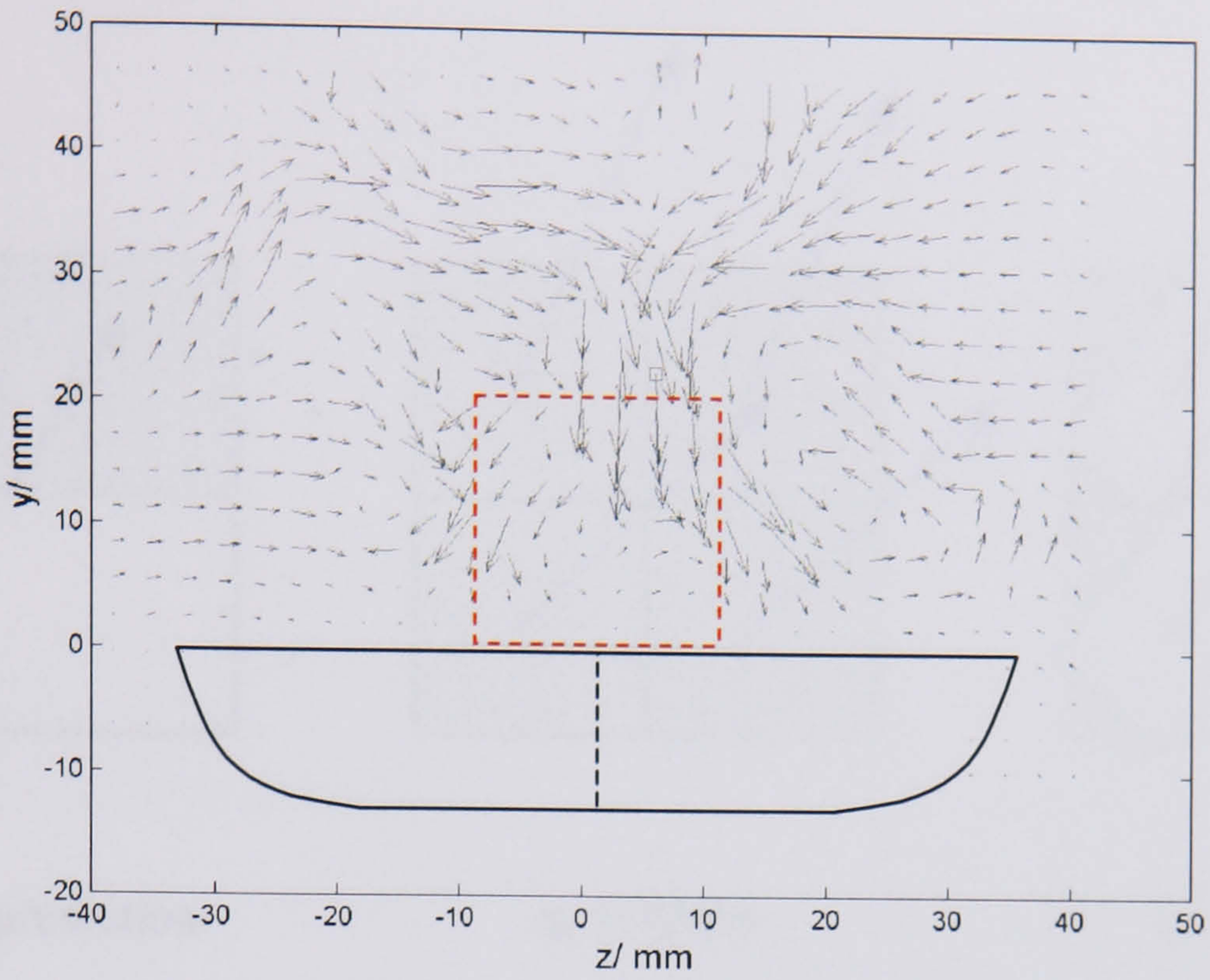

a. Standard FFT correlation result from a 32x32 pixel interrogation tile procedure.

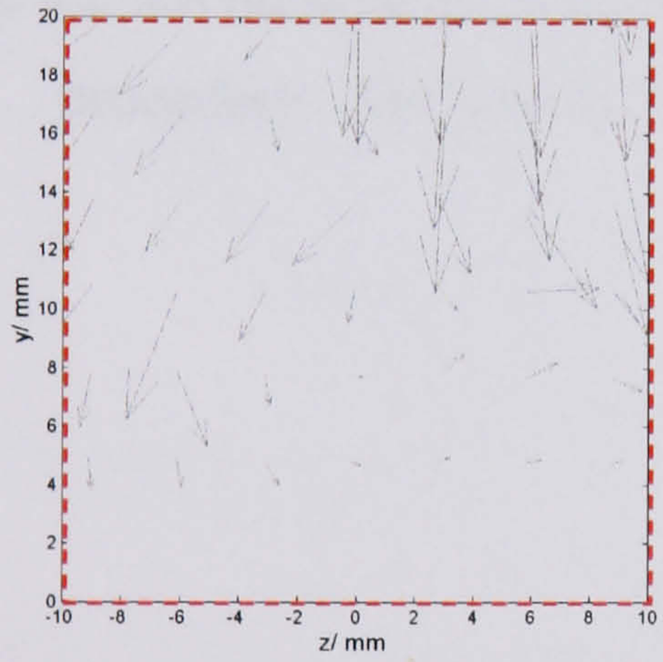

b. Standard FFT treatment for a 32x32 pixel tile yielding approximately 1 vector every 2mm.

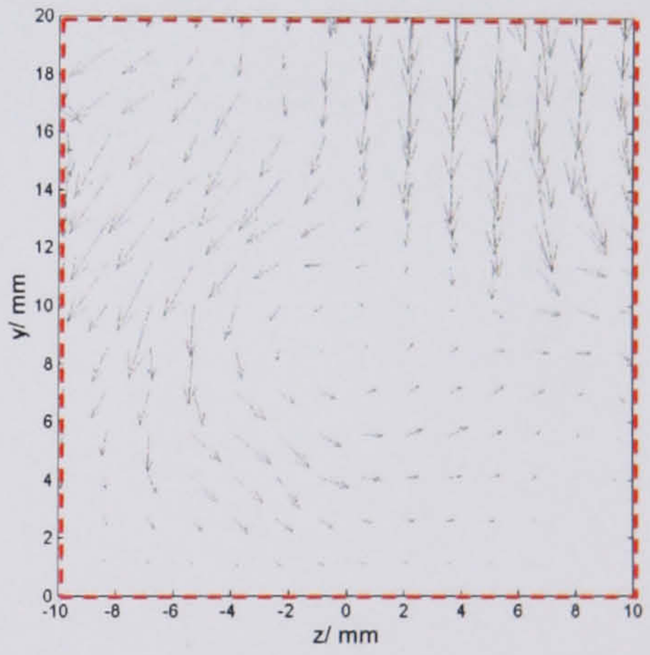

c. Implementing the DWO (FFT) treatment yields a velocity measurement every 1mm.

Figure 2.5. Instantaneous flowfield experienced over the deck of a ship with open deck cargo (equivalent to a backward facing step), the flow is through the light sheet and shows from port to starboard at $x/X = 0.4$. The region indicated by the dashed box is shown magnified in (b) and (c).

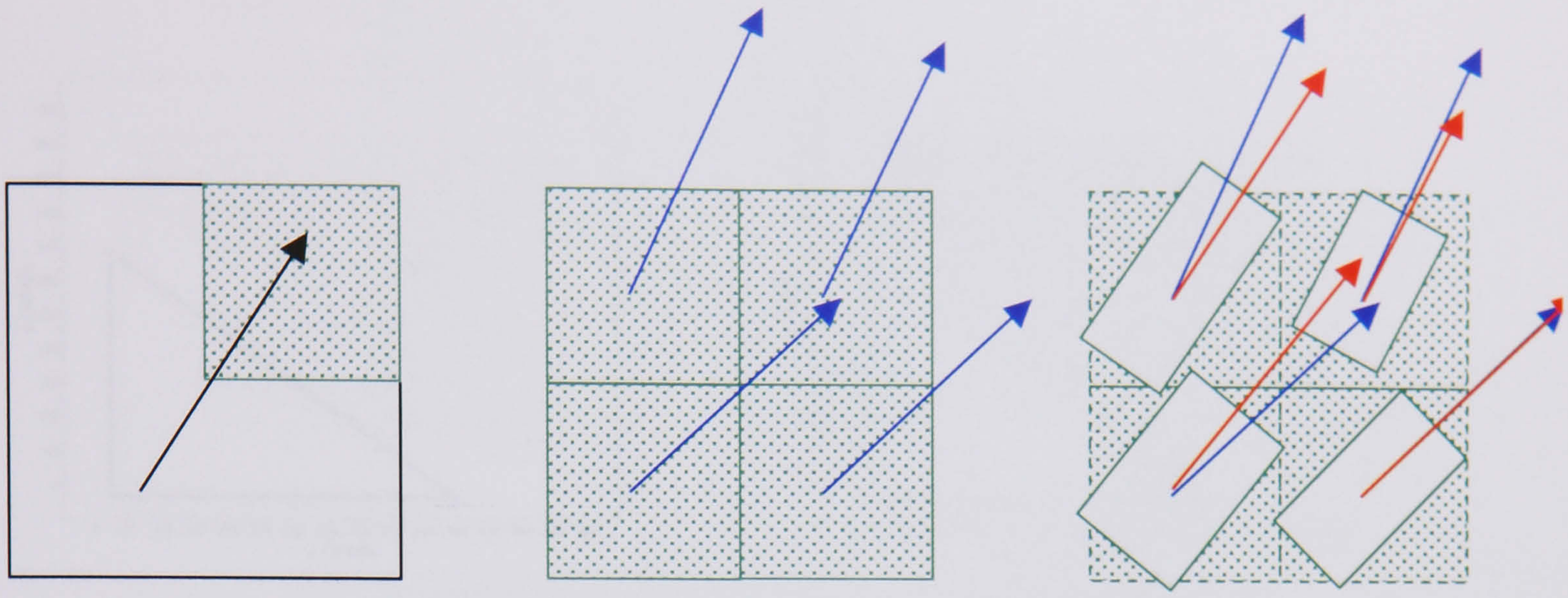

a. Initial prediction. b. ITDWO c. Tile skewing

Figure 2.6. Application of successive super-resolution techniques to build a result with improved spatial resolution and good signal strength. Showing the progression of only the top left hand segment from the standard interrogation tile to the tile skewing procedure. The spatial resolution has been increased by a factor of 16.

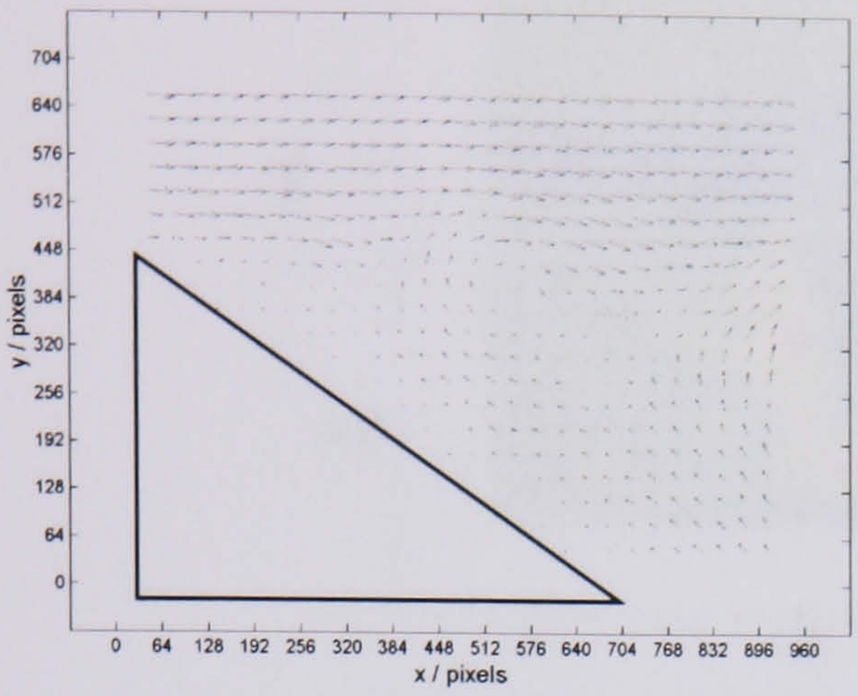

a. Flowfield measured behind a hatchback car model using ITDWO-DC.

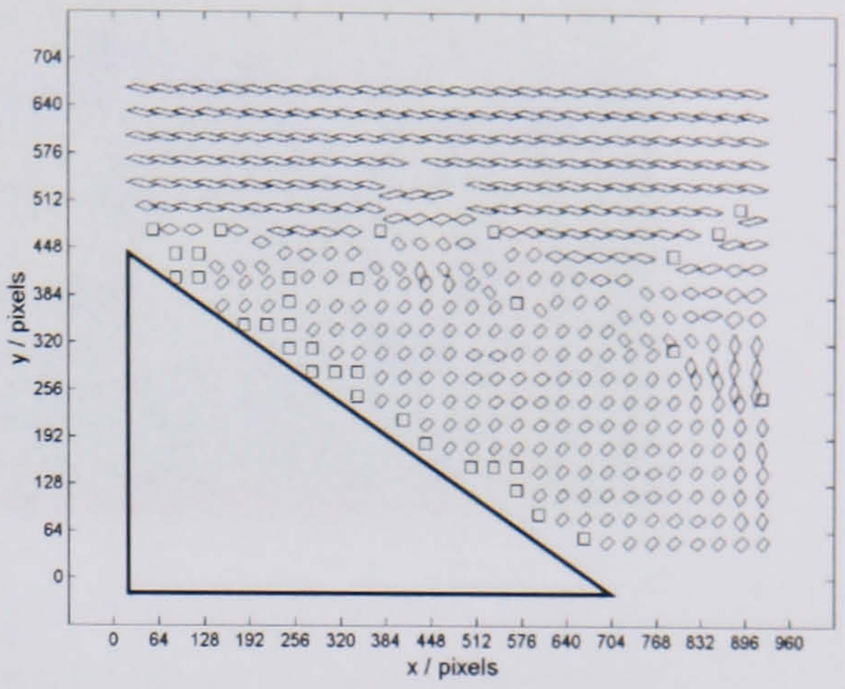

b. First iteration result of the tile-skewing algorithm showing reorientation of the tile into the local flow direction.

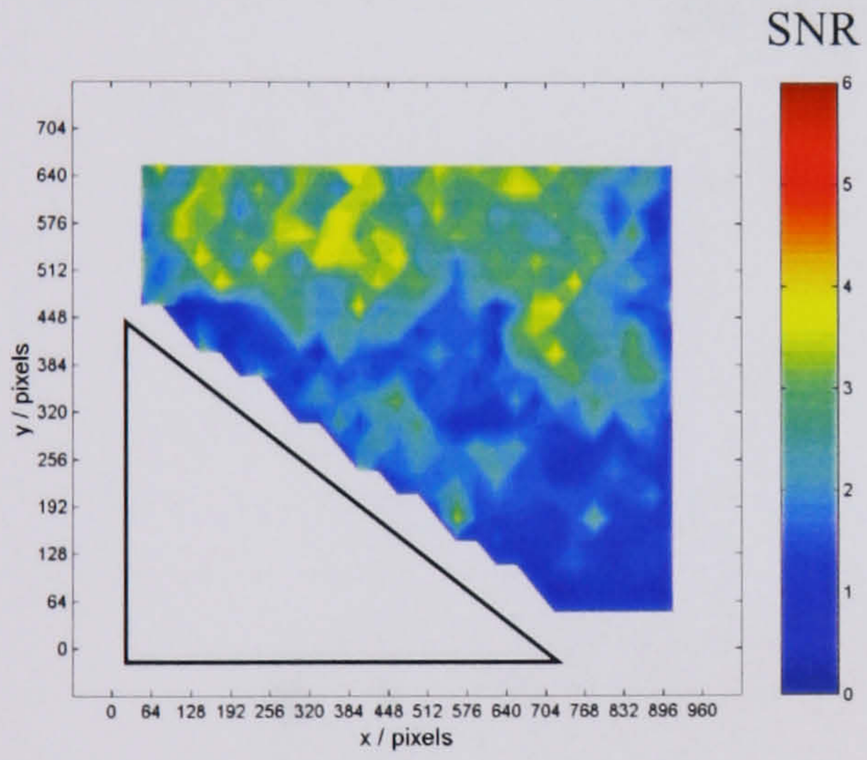

c. SNR of ITDWO-DC algorithm.

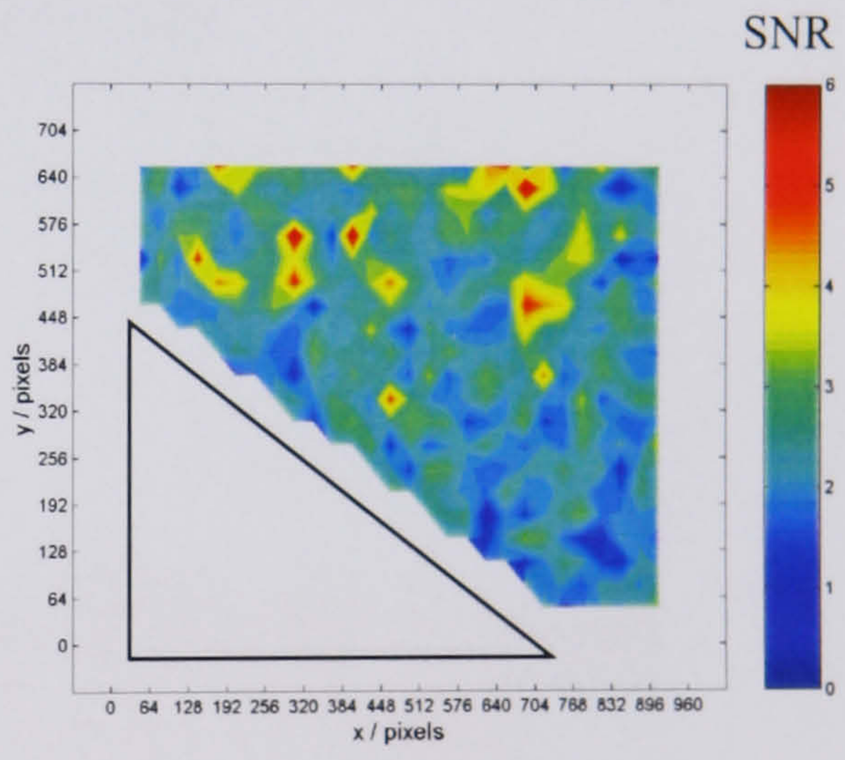

d. SNR of ITDWO-DC algorithm with tile skewing.

Figure 2.7. Flowfield measured behind a hatchback car model for a flow from left to right. Using the result from (a) tile skewing may be performed, shown in (b) which increases the signal strength across the measurement domain, as shown in (c) and (d). An increase in signal strength may be interpreted as an increase in accuracy.

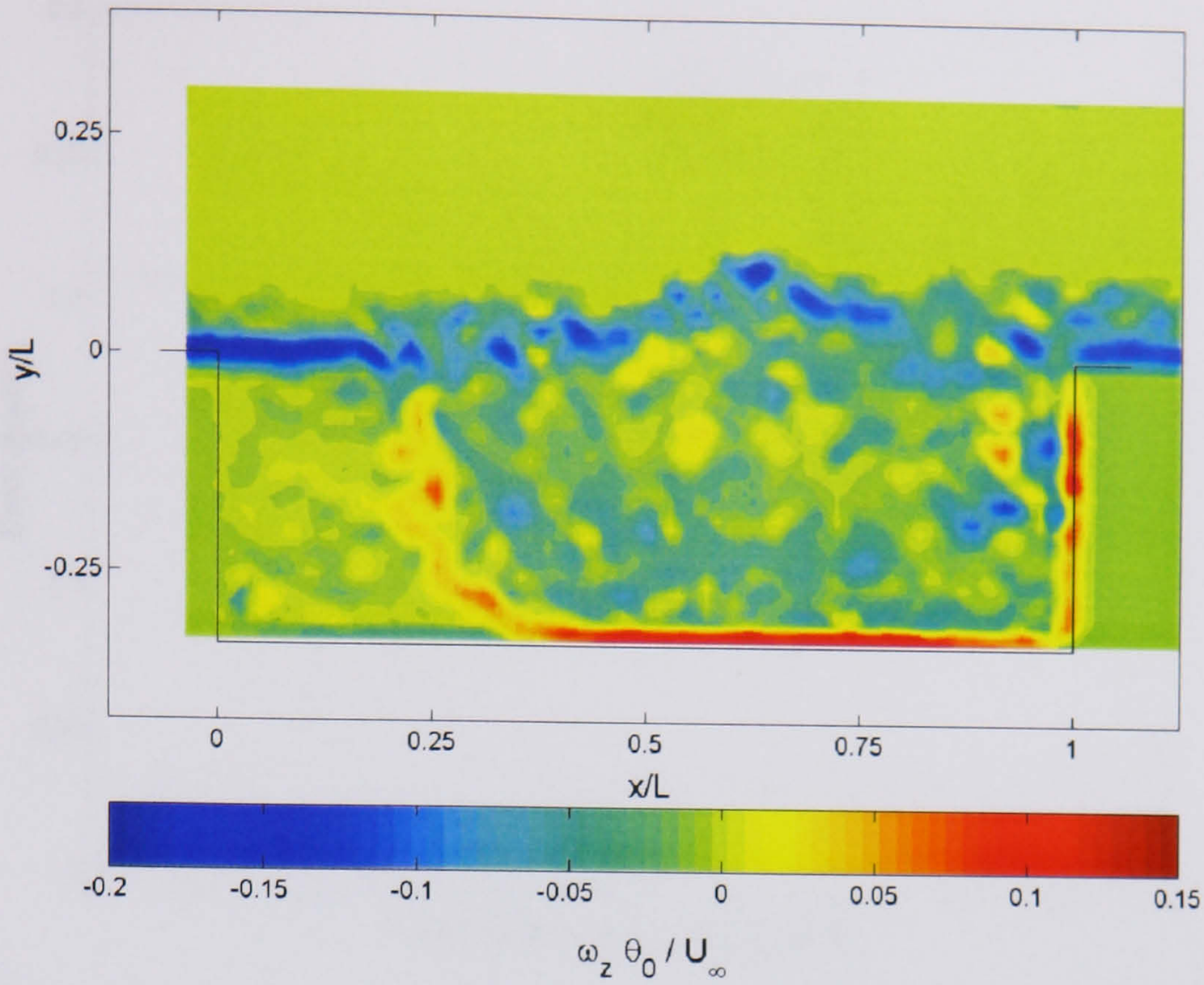

a. Vorticity calculated for a clean cavity configuration with $L/D = 3.0$. The flow is travelling from left to right.

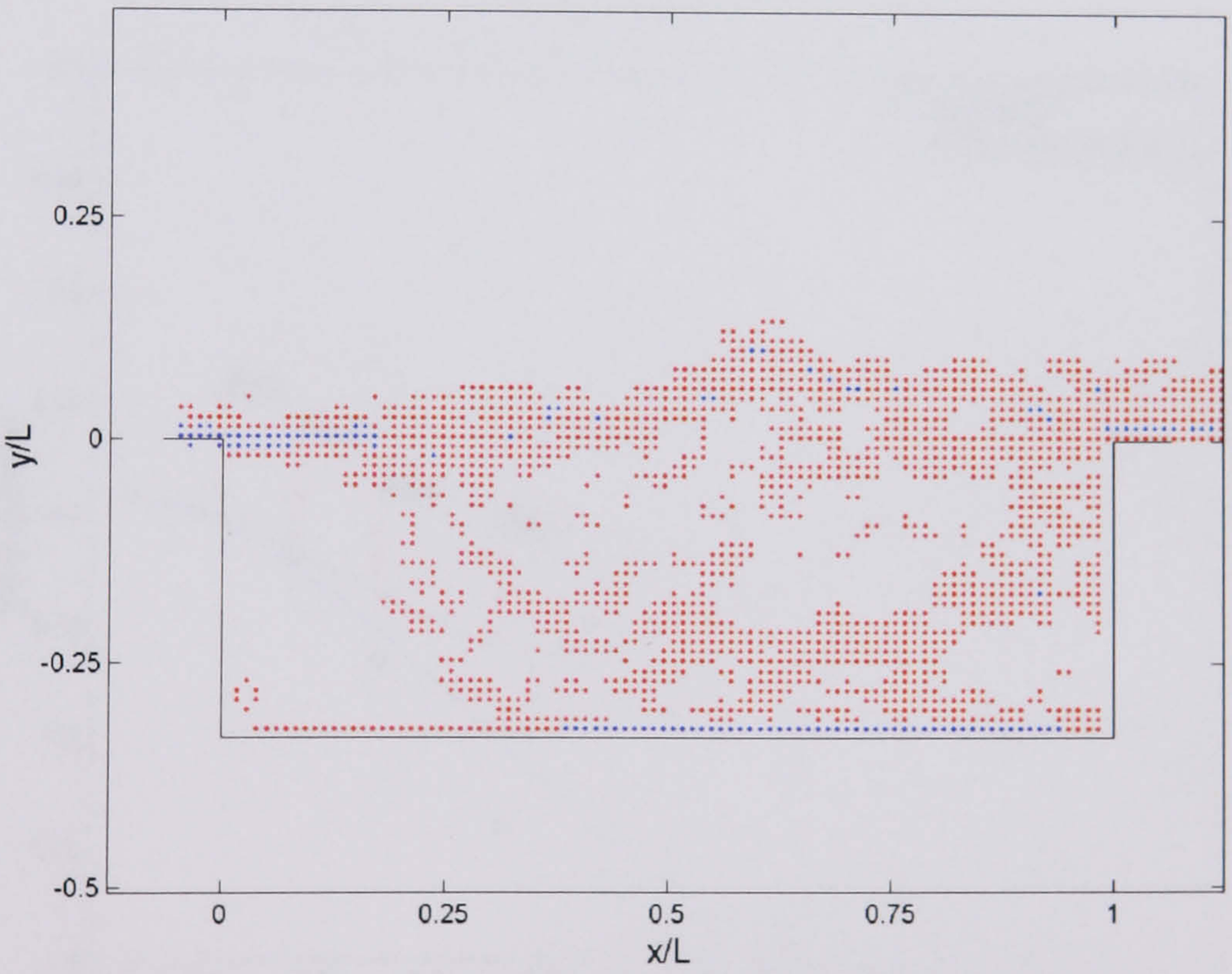

b. Dots indicating where the criteria for correct correlation sampling break down due to the magnitude of the inter-tile velocity gradient.

• : normal pass. • : ITDWO pass with tile skewing

Figure 2.8. Super-resolution techniques applied to real clean cavity test case.

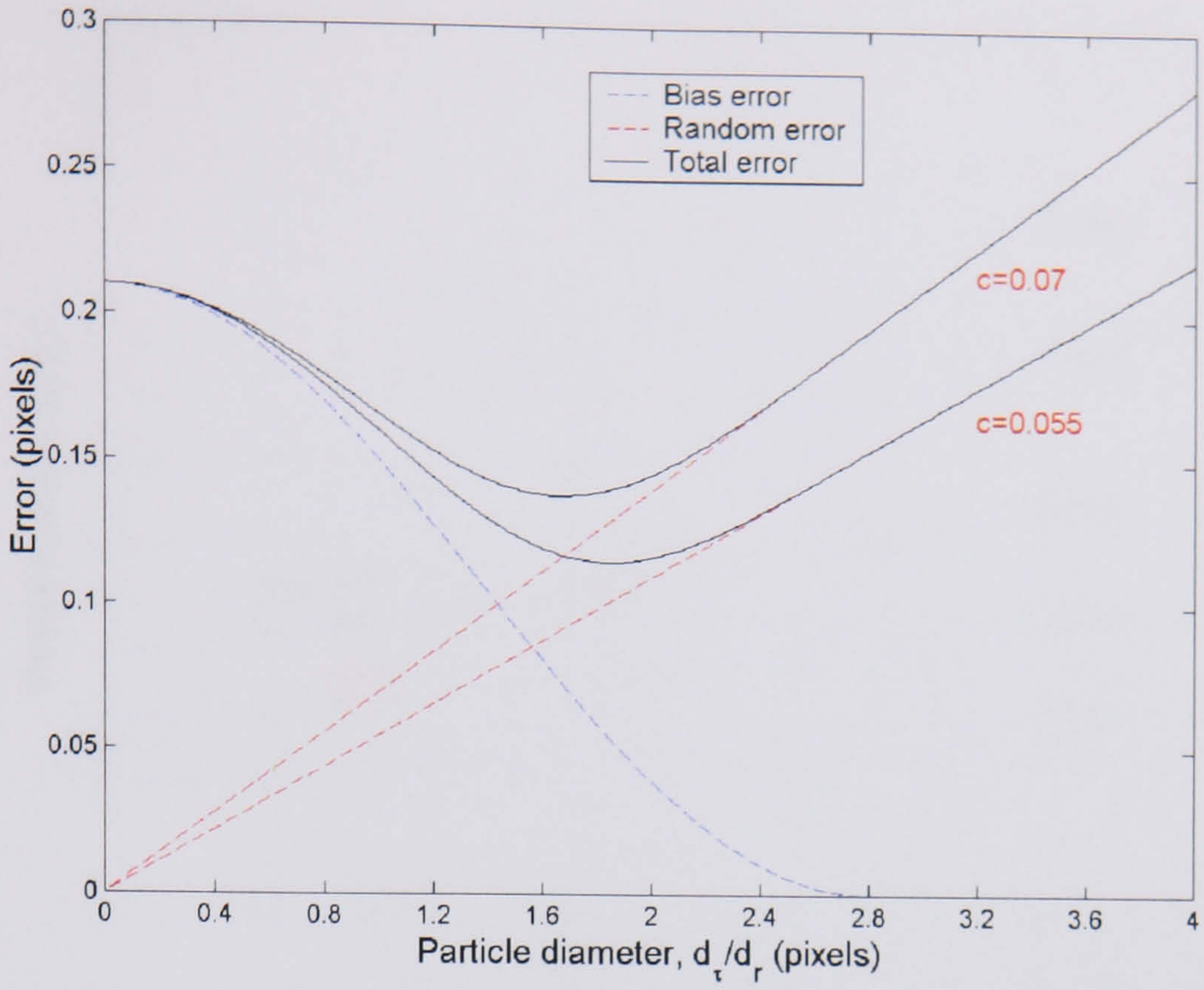

Figure 2.9. The behaviour of bias error and random error components with respect to particle diameter. The different gradients of the random error component shown correspond to circular, $c = 0.055$ and direct correlation, $c = 0.07$ methods.

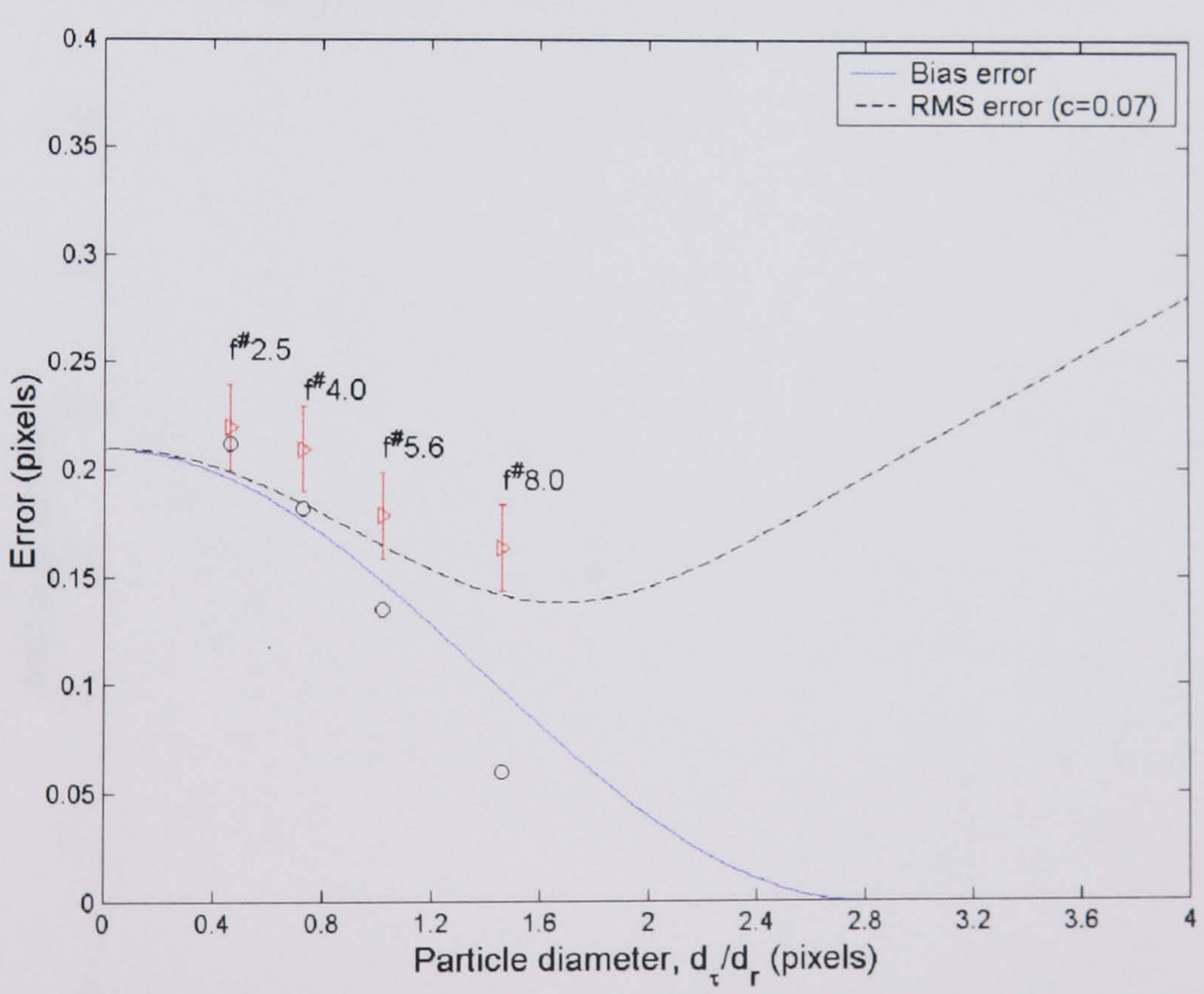

Figure 2.10. Comparison of the rms error component with experimental results. The triangles and dots indicate the total error (with error bars) and sample-averaged results for each f-number test respectively. Because the *SNR* is lower for actual experiments the random error component is increased, although deviations in the bias error component are not expected.

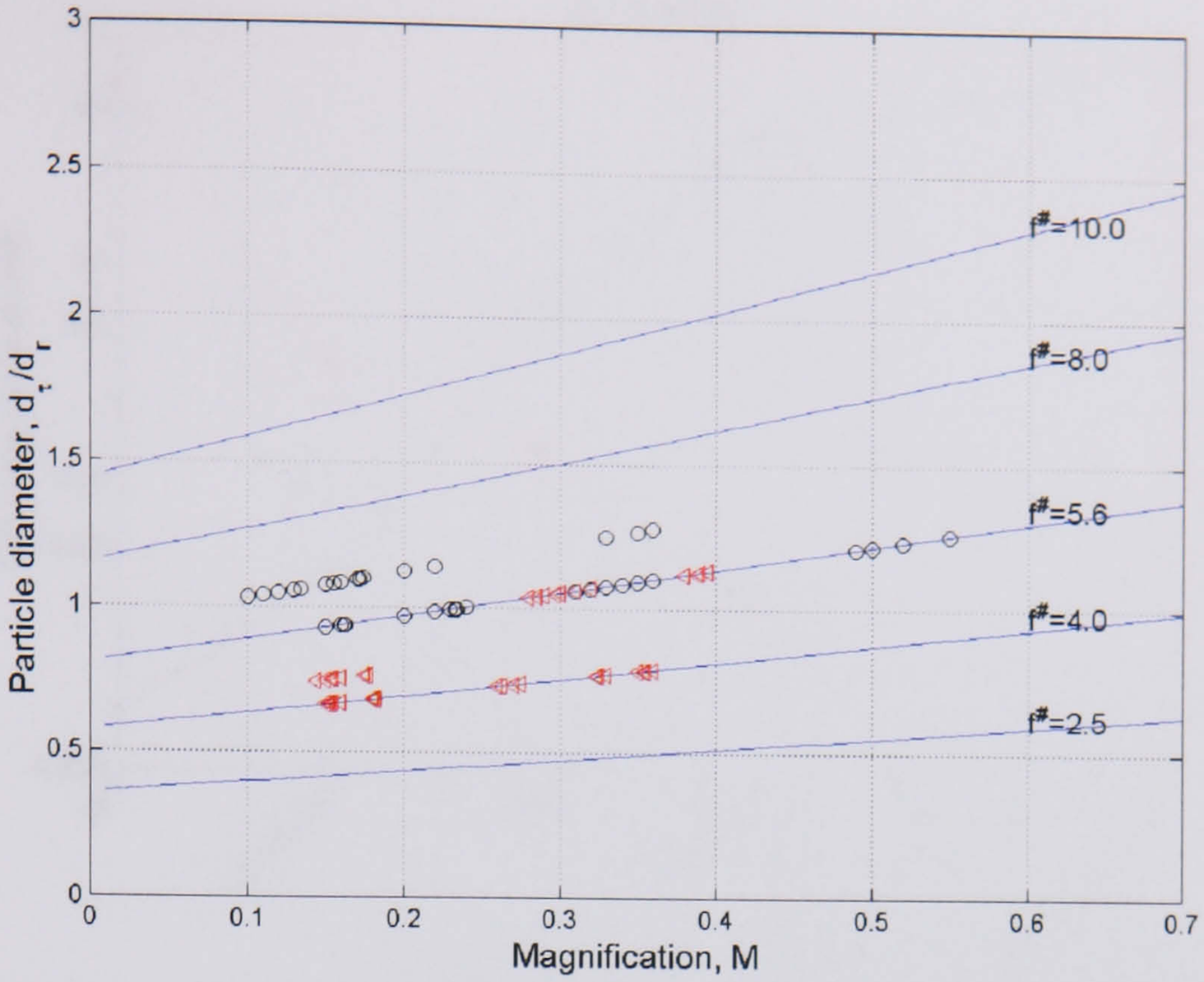

Figure 2.11. The effect of magnification on the projection of the particle diameter onto the CCD array. The symbols represent the various image capture set-ups used.

○ : Twin-camera, twin-laser set-up (single pulse)

◁ : Twin-camera, single-laser set-up (double pulse)

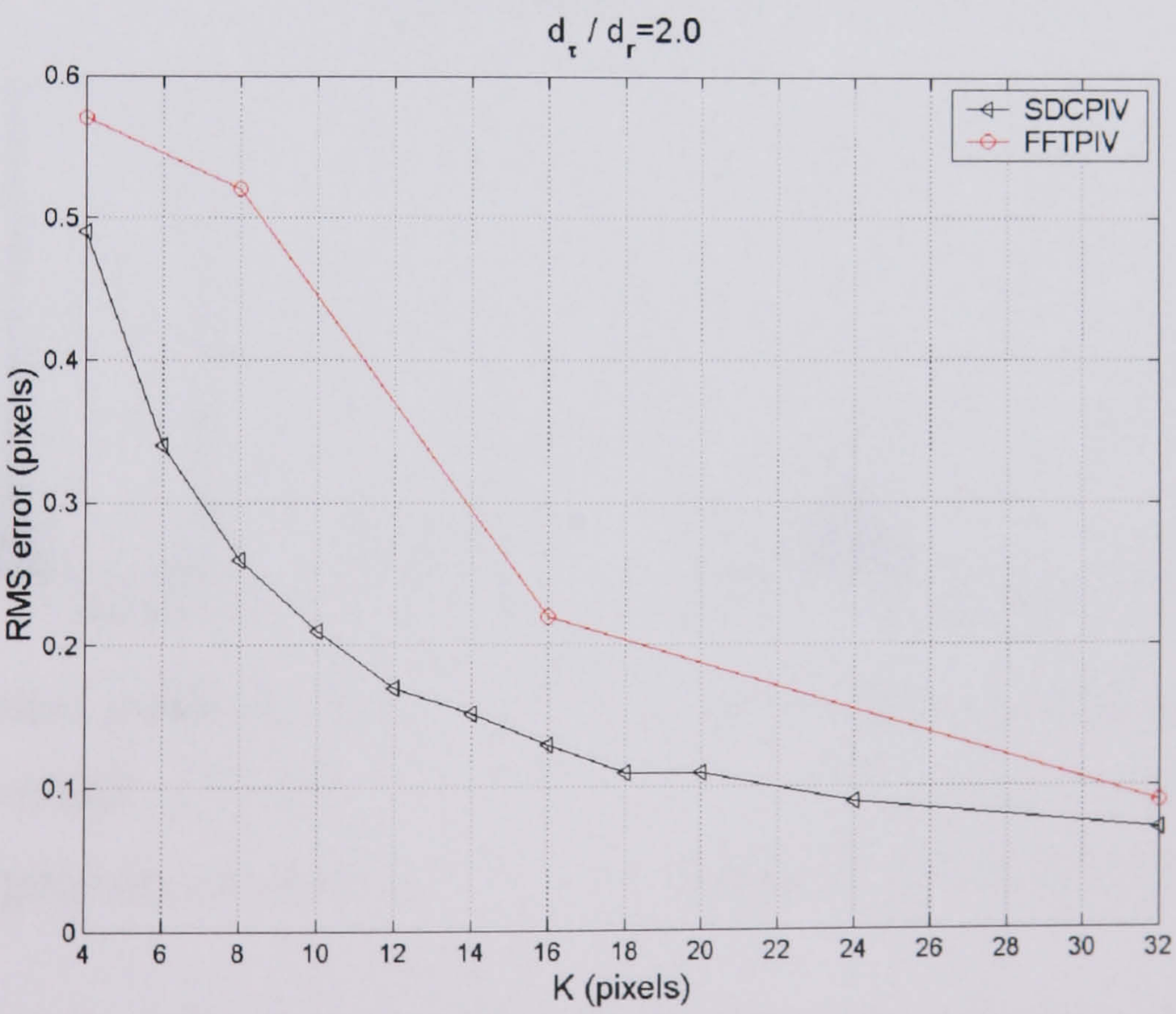

Figure 2.12. Comparison of the rms error incurred in comparison to the side length, K of the interrogation tile. The SDCPIV suppresses the bias error.

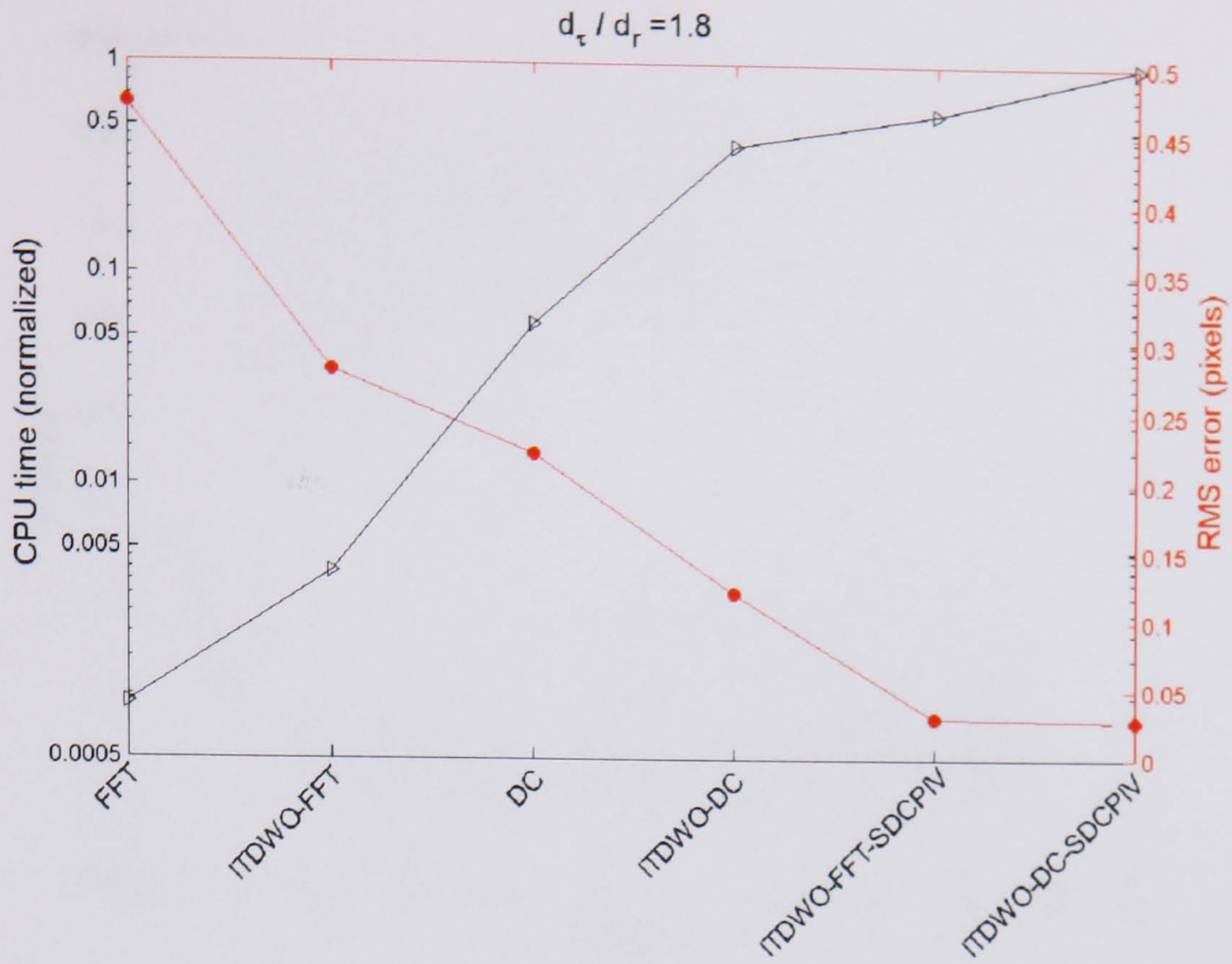

Figure 2.13. Comparison of some of the possible methodologies that yield a spatial resolution of 16 pixels against the number of computational operations required and accuracy obtained. Results are taken from a synthetic Oseen vortex with no noise. It appears beneficial to introduce DC only at the latter stages of calculation, which is when performing SDCPIV.

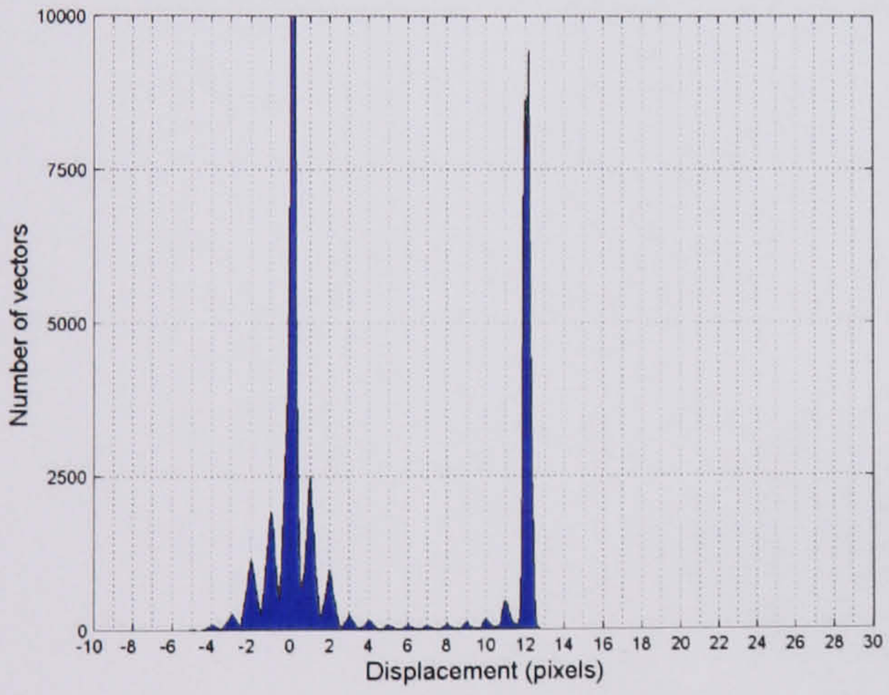

a. Single-camera, single-laser set-up. $M_I = 0.045,\ f^{\#} = 2.5$ Standard 48 pixel tile correlation.

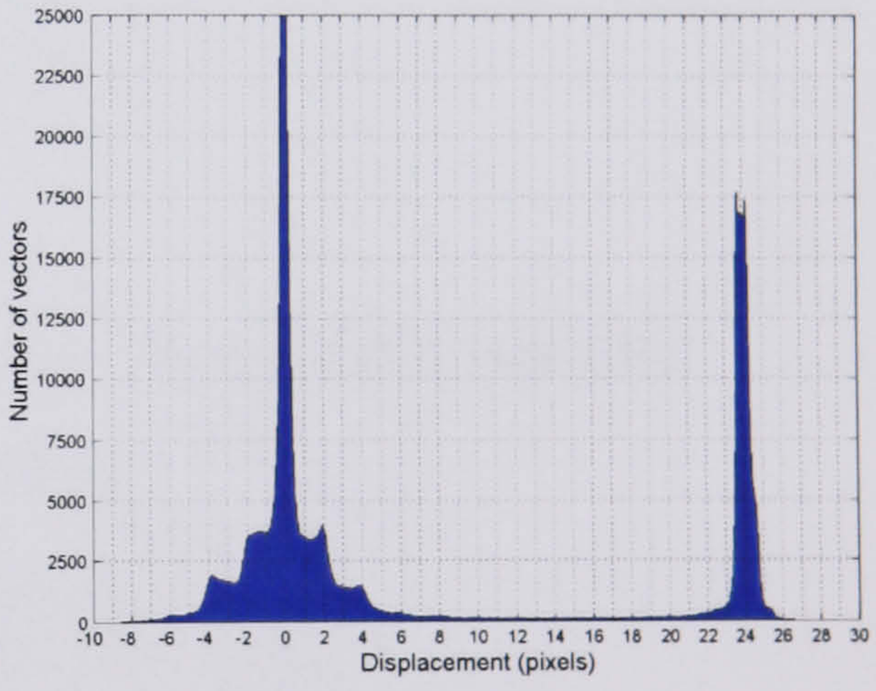

b. Twin-camera, twin-laser set-up. $M_I = 0.1,\ f^{\#} = 5.6$ ITDWO-DC-SDCPIV (16 pixel).

Figure 2.14. Histograms of the velocity component presented by two different DPIV set-ups for the case of flow over a cavity $L/D = 2.0$. For the standard/non-optimised experiment (a) the effects of peak locking (bias error) are discernible as peaks around integer pixel displacements.

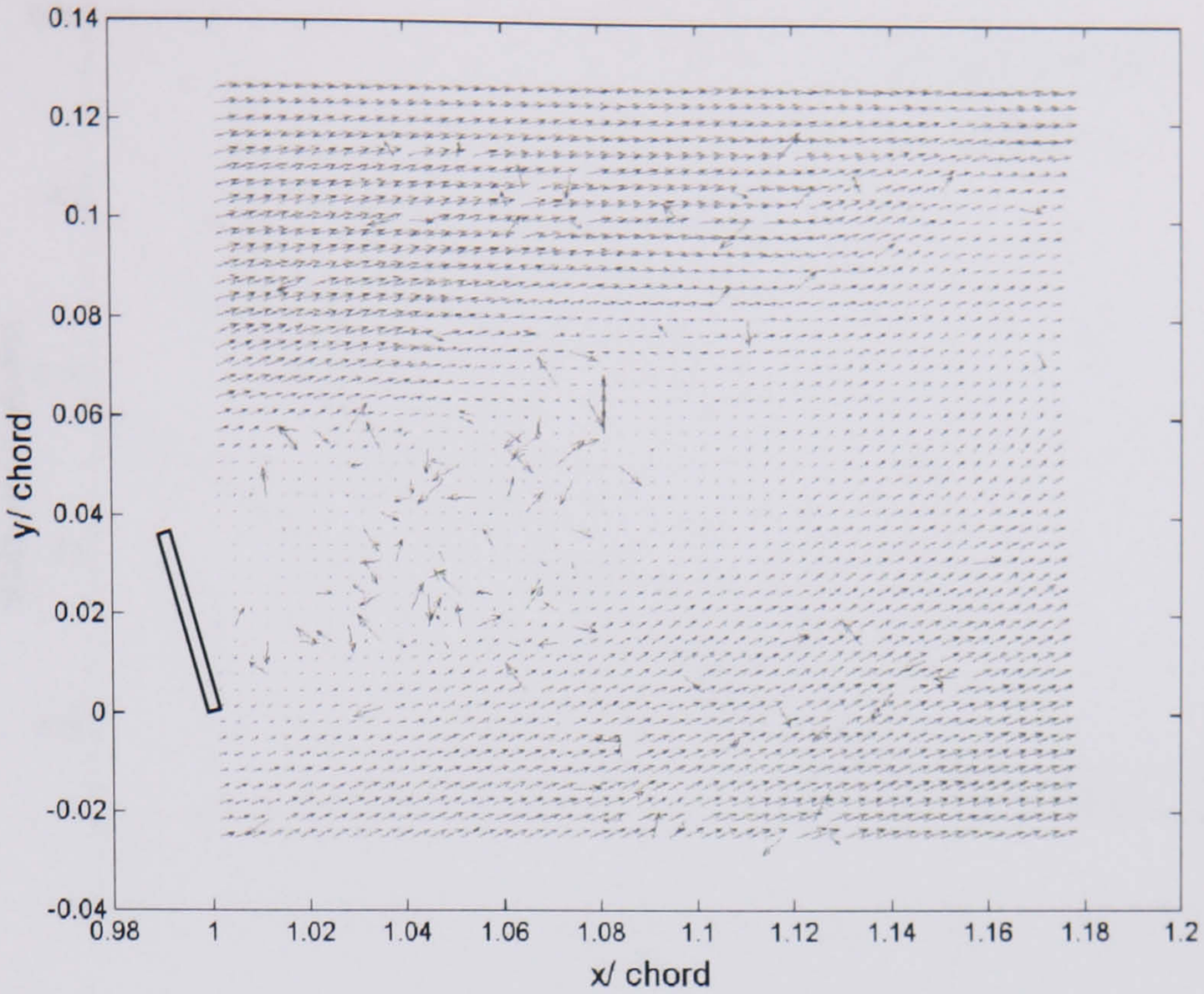

Figure 2.15. PIV measurement of flow downstream of a NACA 23015 section with 4% gurney flap (shown to the left of the picture) and angle of attack 12.0 deg $\mathrm{Re}_{chord} = 1.2 \times 10^5$, the flow is from left to right. In this example 6% of the measurement (143 vectors) were deemed to be bad vectors. These spurious vectors tend to cluster in regions of poor seeding, such as the flow immediately aft of the gurney flap.

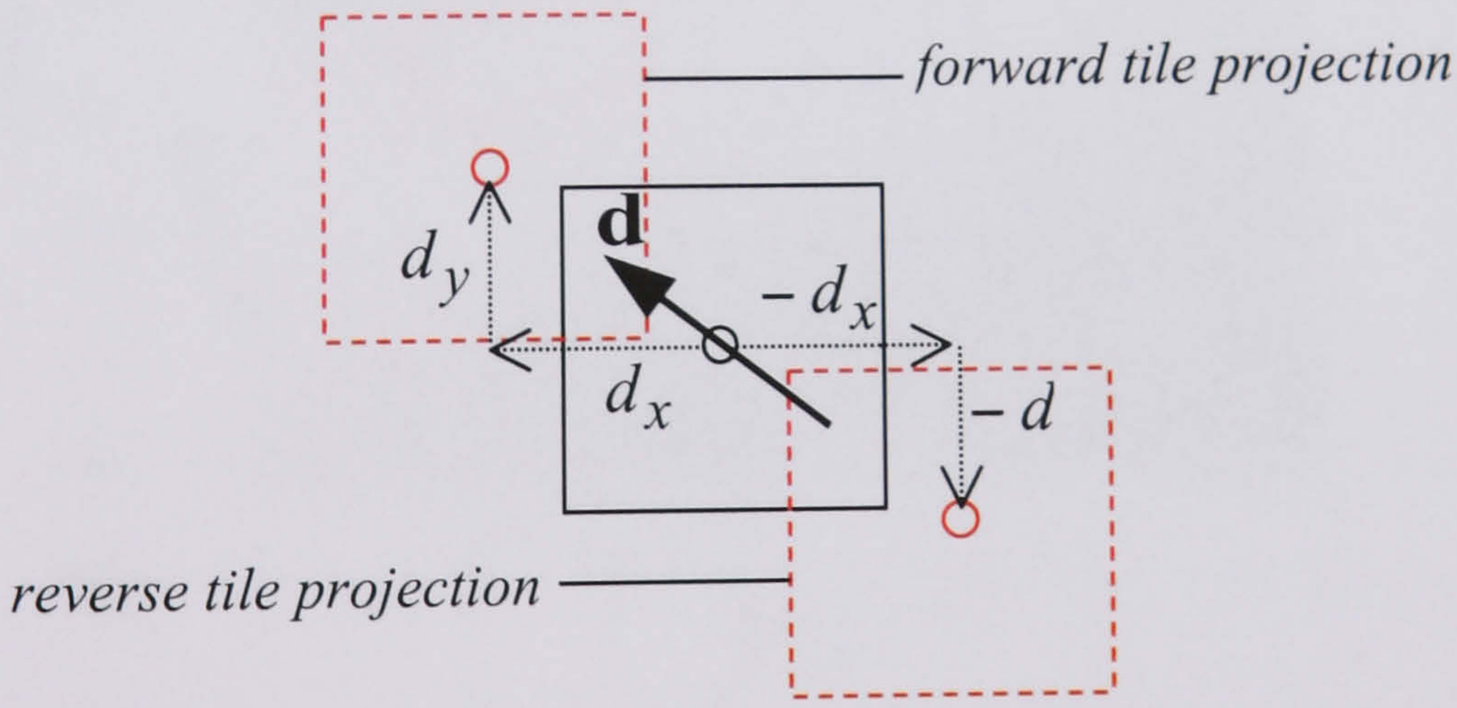

Figure 2.16. Tile shifting notation. The forward projected tile is shifted relative to the central tile by the displacement $\mathbf{d}$ ($\mathbf{d} = d_{x\mathbf{i}} + d_{y\mathbf{j}}$) of the central vector. The reverse projected tile is moved in the opposite sense.

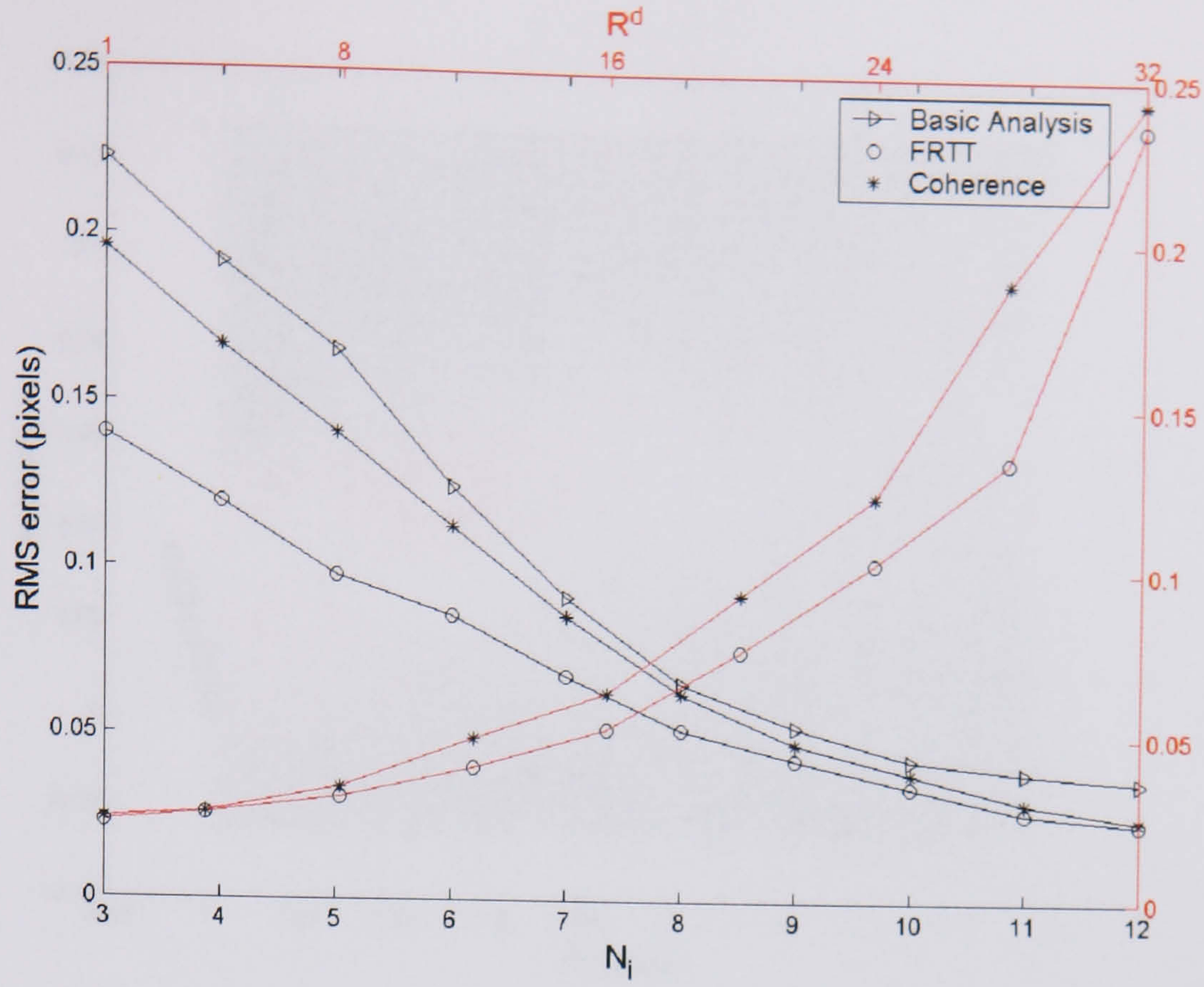

Figure 2.17. The effect of changing the seeding density (when $R^d = 16$) and the flow displacement range (when $N_i = 8$), on the rms error.

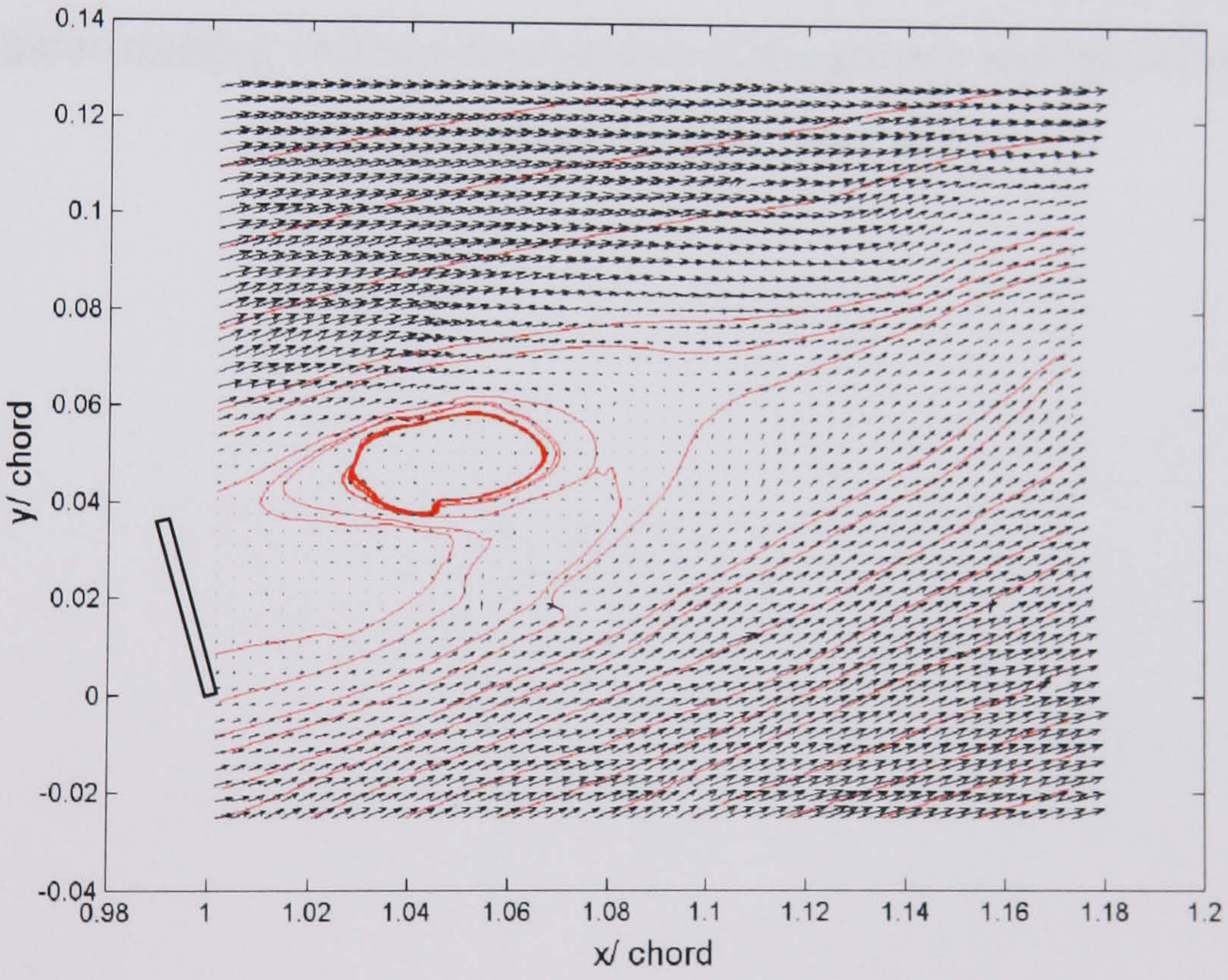

Figure 2.18. Application of the coherence algorithm to the flowfield shown in figure 2.15 (with streamlines). In this instance there was very little change in the response of the technique over $T\% \in (20\%, 35\%)$ and $NV \in (5\%, 20\%)$. In the best case 140 of the vectors previously judged to be spurious have been identified, although the replacement routine in the clusters has caused distortion to the streamlines.

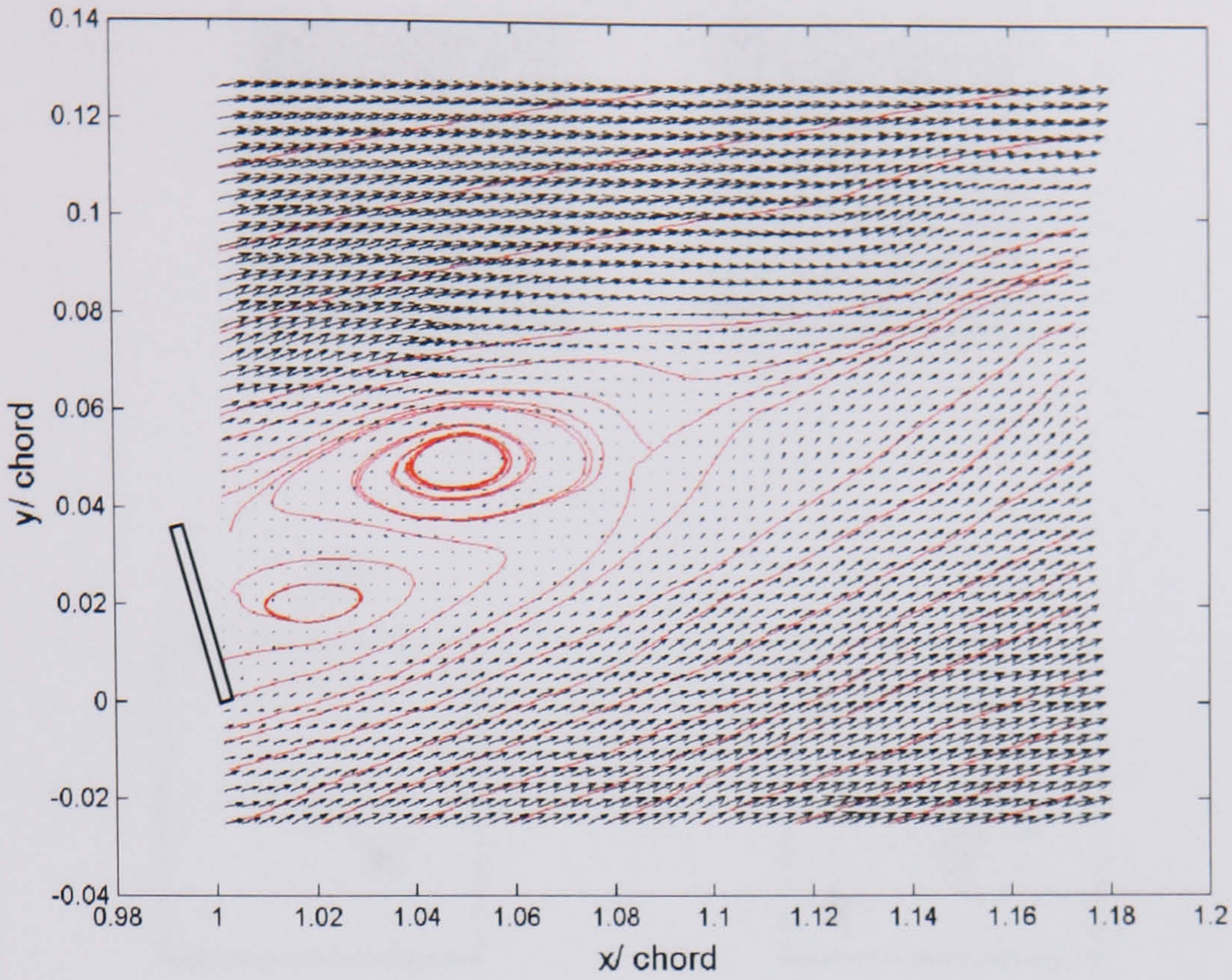

Figure 2.19. Application of the FRTT algorithm to the flowfield shown in figure 2.15 (with streamlines). All vectors deemed to be spurious from figure 2.15 have been identified and replaced. Here the replacement strategy has been able to preserve the distinct counter-rotating vortices downstream of the gurney and the off surface saddle point that defines the near wake region.

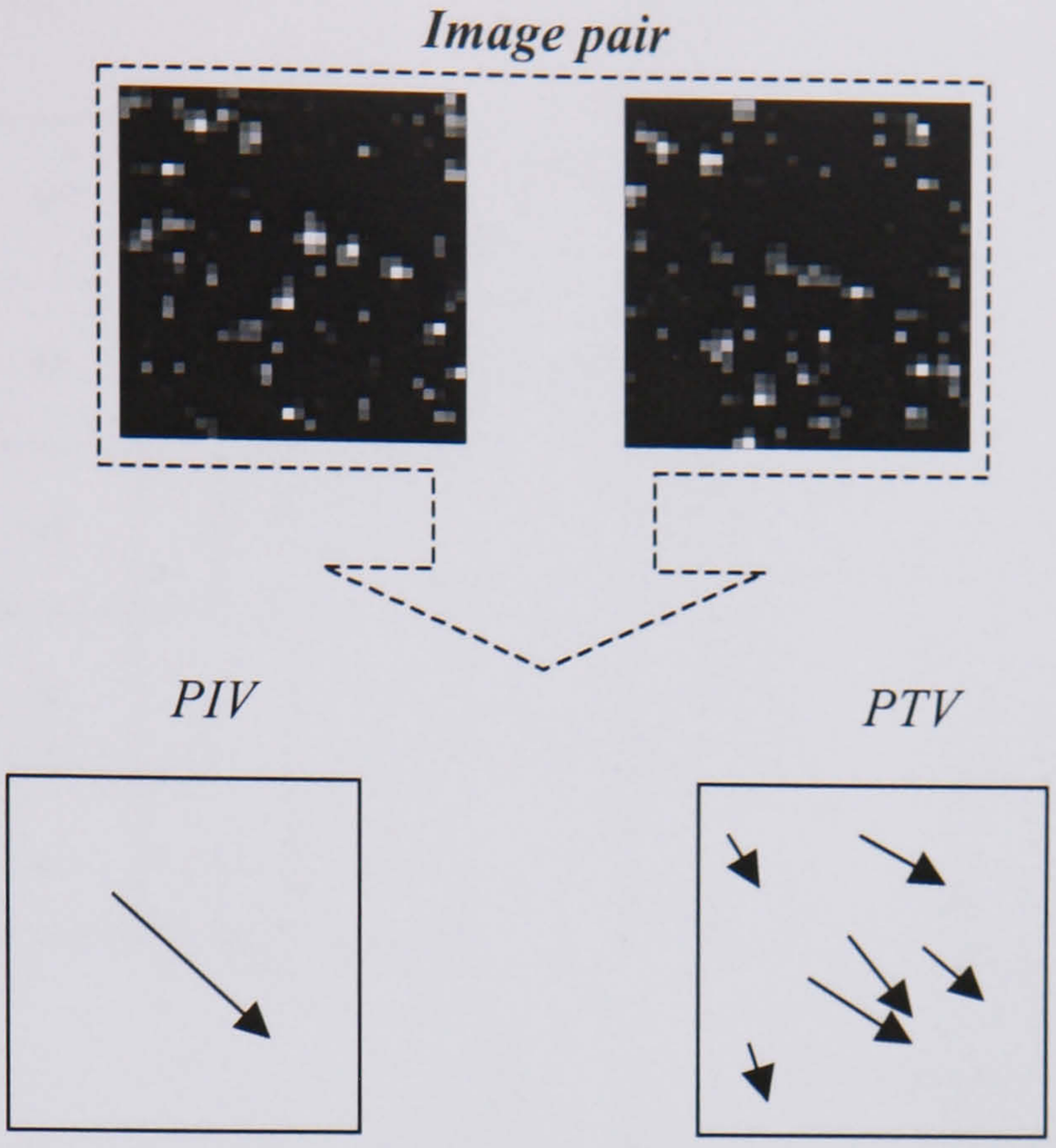

Figure 2.20. The principle of the hybrid approach to particle velocimetry. Whereas PIV returns a reliable measurement averaged over a single interrogation tile, PTV has the potential to increase the spatial resolution of velocity vectors by measuring the individual particle traces.

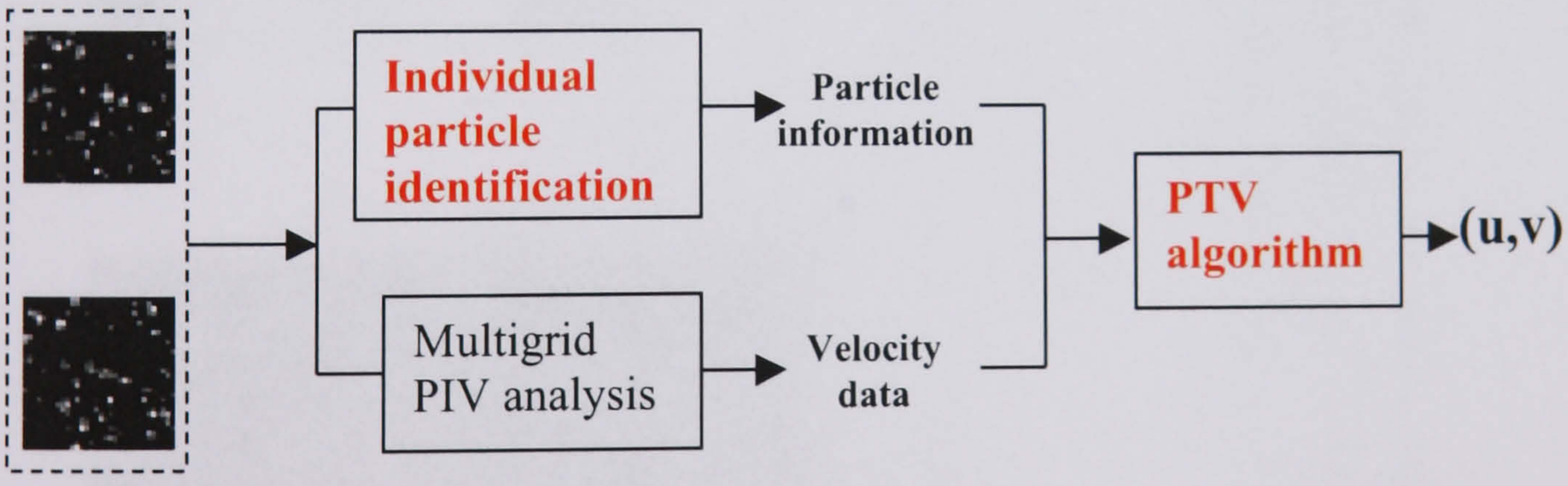

Figure 2.21. Procedure for a hybrid PIV-PTV system using the multigrid analysis presented in section 2.2.5.

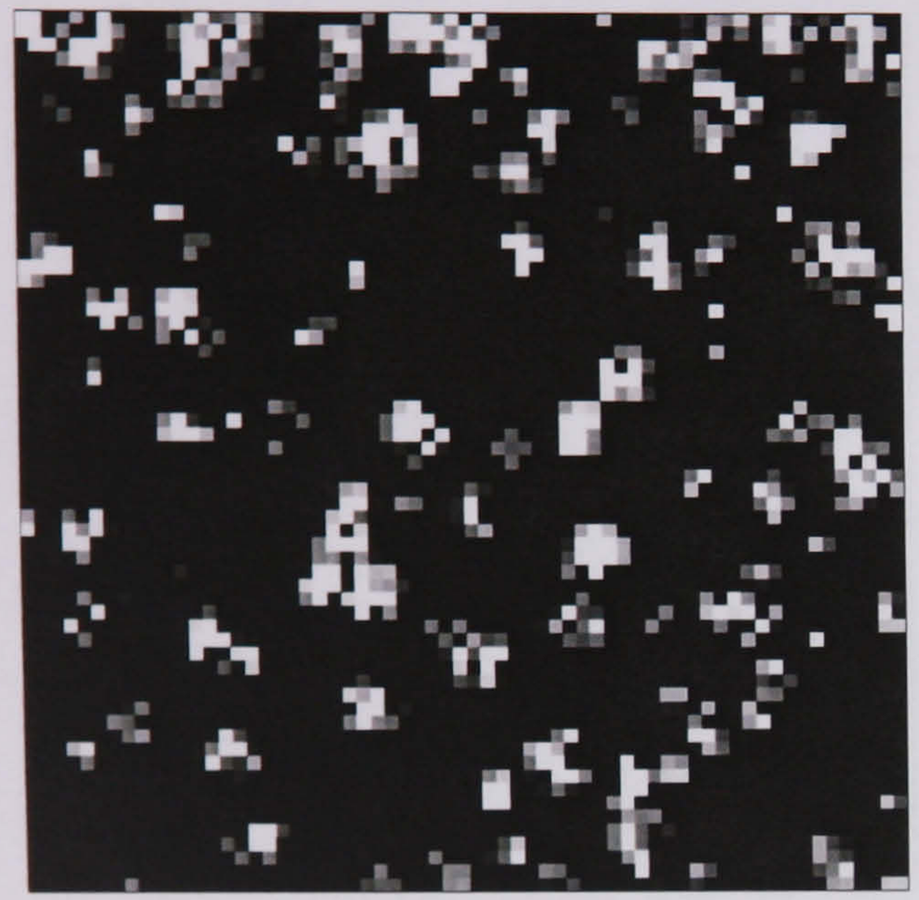

a. A composite image for an arbitrary image pair.

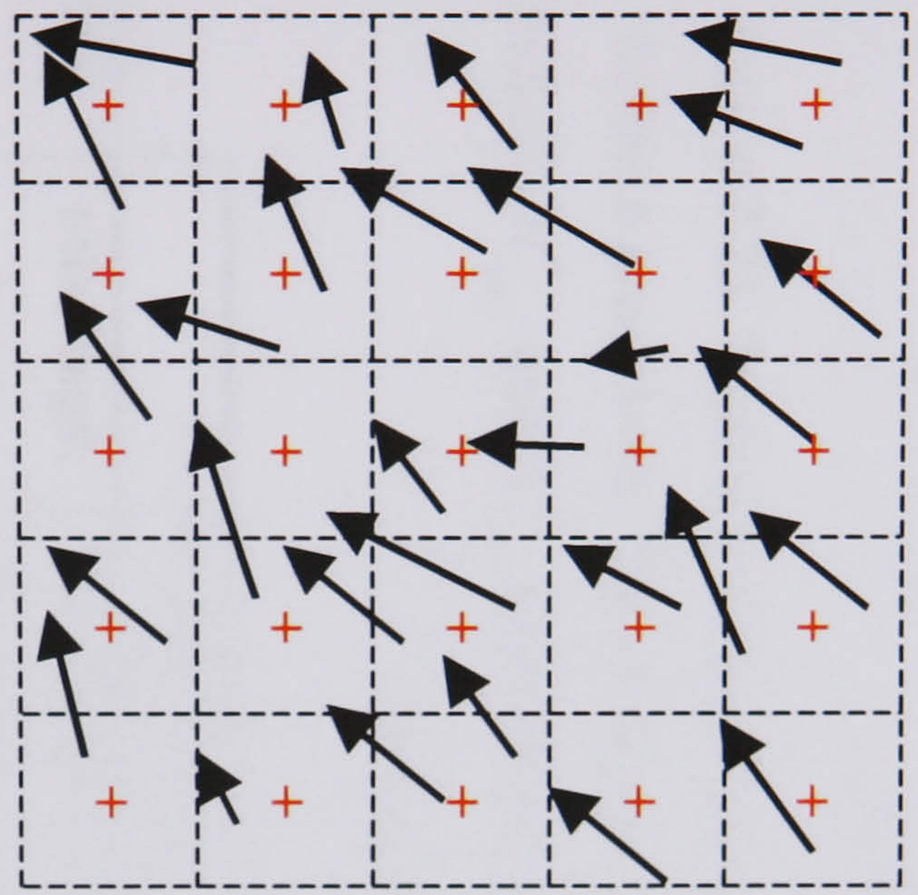

b. The measured velocity field output from the hybrid PIV-PTV system.

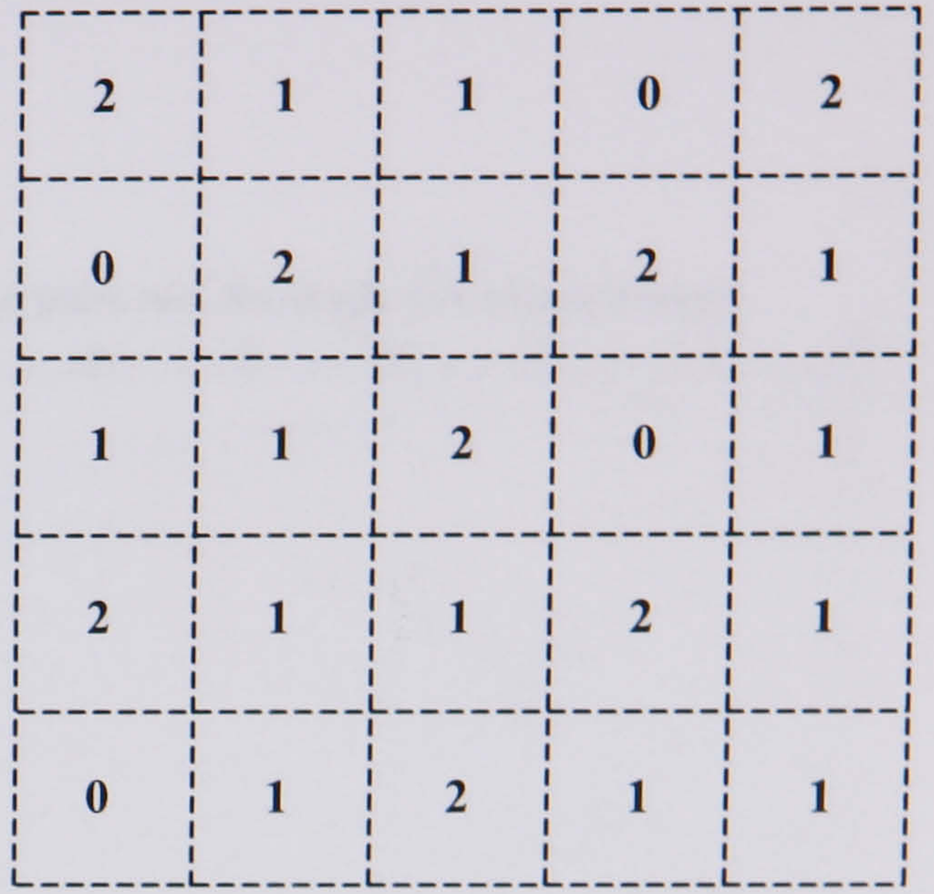

c. Using the t-tile procedure the numbers of velocity measurements made within that grid box are counted.

Figure 2.22. The t-tile procedure. Using typical PIV images the hybrid PIV-PTV calculation is performed, which yield results irregularly spaced on the pixel plane. A grid structure is then imposed with abscissa only a few pixels apart, the local measurements are 'binned' to the centre of the tile. A relocation of only a few pixels preserves the accuracy of the measurement and also permits statistical measurement to be made over a predetermined sample width.

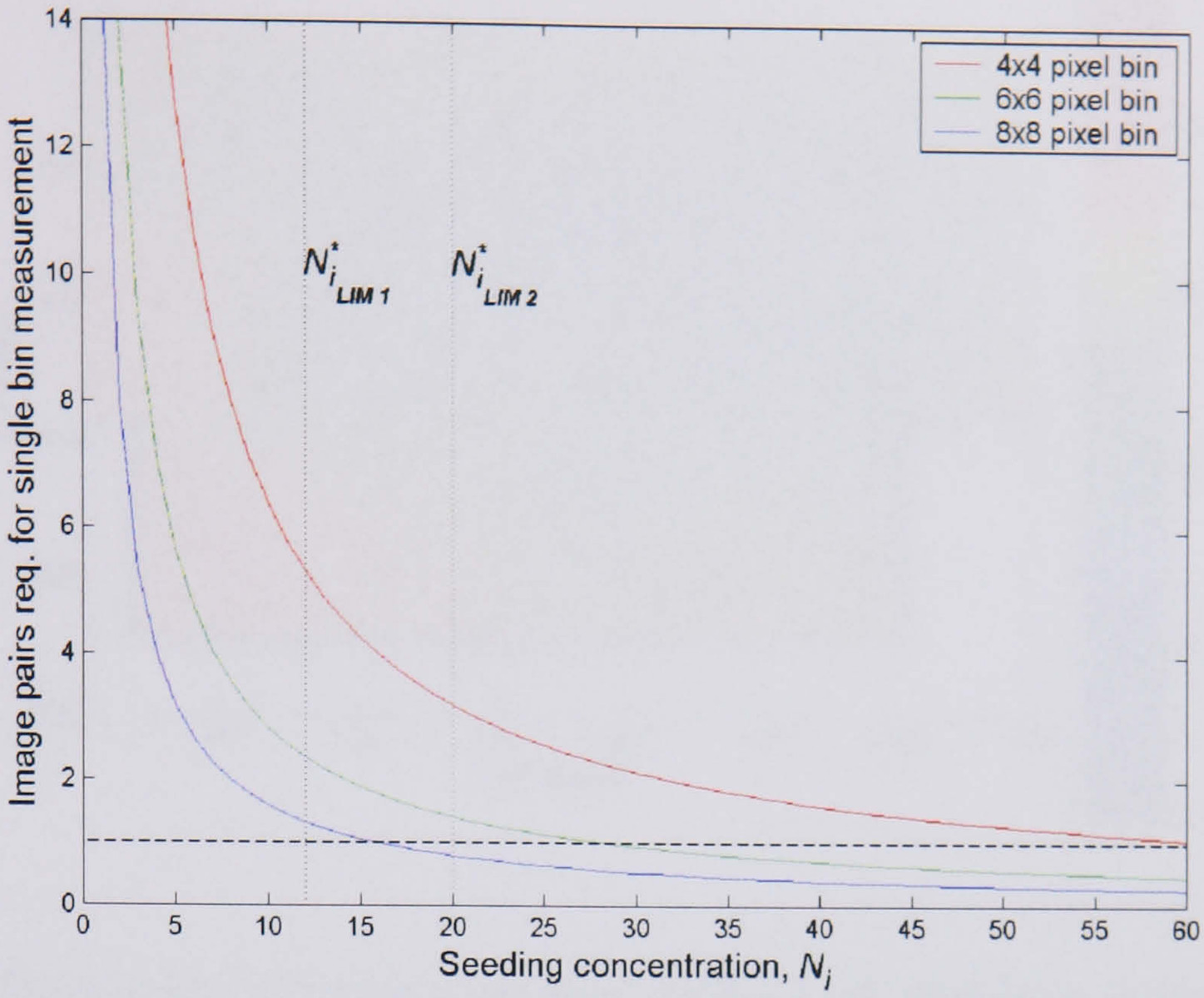

Figure 2.23. Typical number of image pairs required before a tracked particle falls within a given t-tile. The results are based on homogeneous seeding for any given flowfield. $N^*_{i_{LIM\,1}}$ and $N^*_{i_{LIM\,2}}$ represent the minimum seeding requirements for standard and multigrid PIV respectively.

	t – tile size $6 \times 6\ px$			*t – tile size* $0.3 \times 0.3 mm$		
L/D	t-tile length (mm)	Vectors per image pair	relocation error (mm)	t-tile length (px)	Vectors per image pair	relocation error (mm)
1.0	0.24	1.00	±0.12	25	1.37	±0.15
1.5	0.30	1.00	±0.15	20	0.87	±0.15
2.0	0.38	1.00	±0.19	16	0.56	±0.15
2.5	0.43	1.00	±0.22	14	0.43	±0.15
3.0	0.5	1.00	±0.25	12	0.31	±0.15

Table 2.1. For a realistic seeding density of $N_i = 25$ the number of measurement per t-tile dimension is shown. The t-tile dimension required to return one measurement per image is shown on the left and the images required for a single measurement for a t-tile of set physical size is shown on the right.

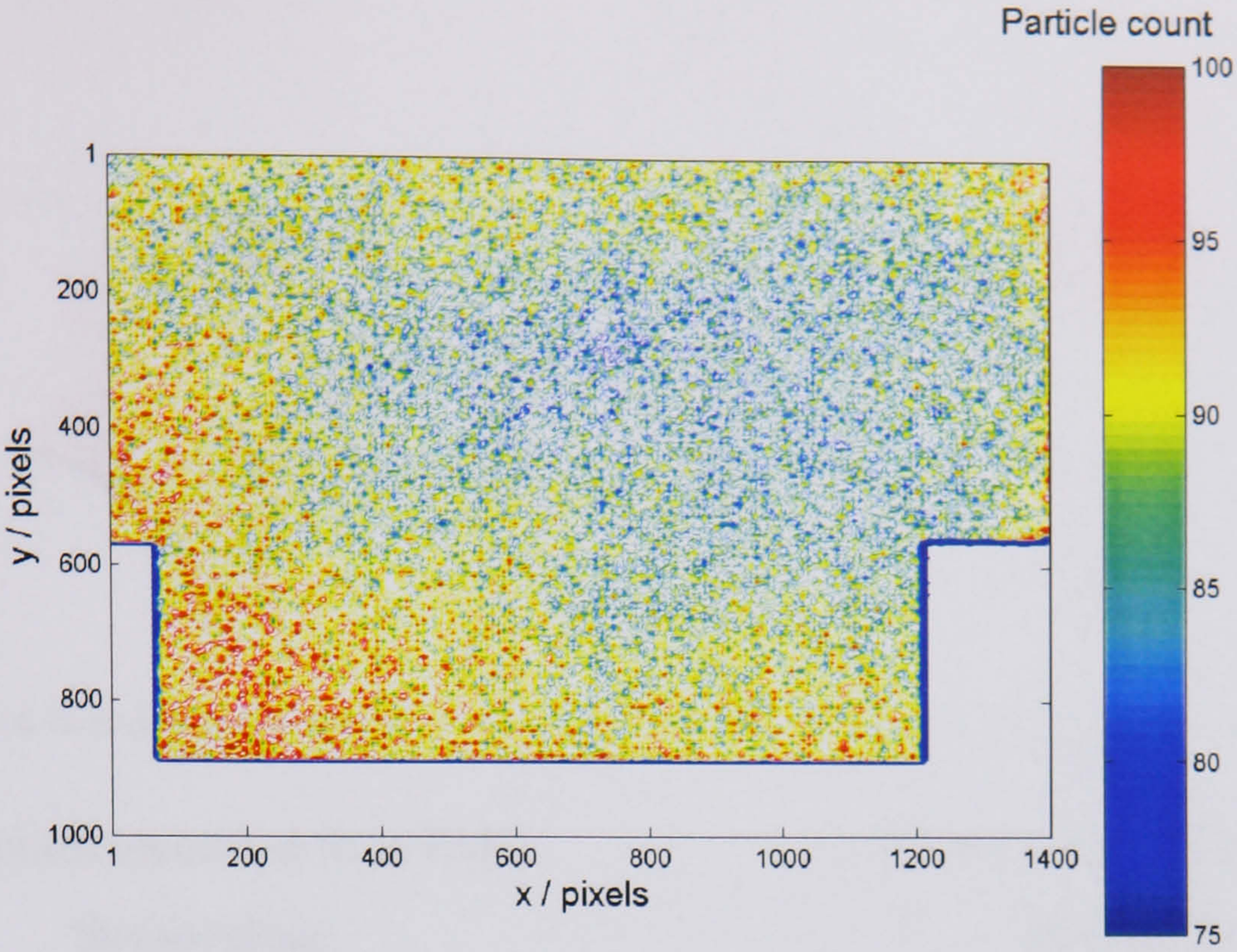

Figure 2.24. The number of particles counted within each t-tile for a series of first frame images. The sample size is 110 images with t-tile size $6 \times 6\,px$ for cavity size $L/D = 3.0$. Surprisingly there is reasonably uniform seeding inside the cavity itself; the largest seeding inhomogeneities are in the downstream freestream area and at shear layer impingement on the downstream corner.

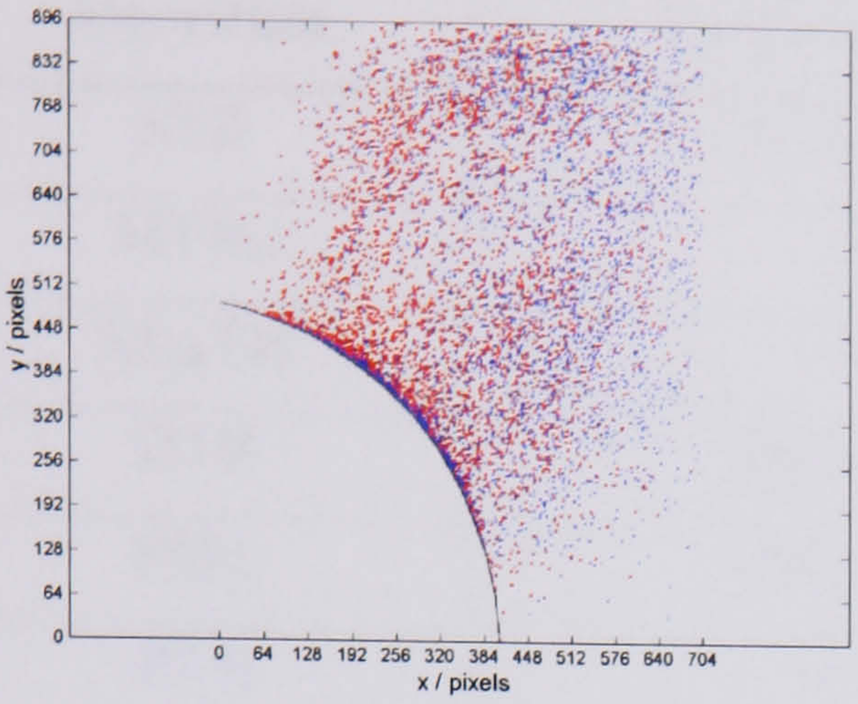

a. Particles identified from PMC thresholding.

particles identified in image 1:4987

particles identified in image 2: 4460

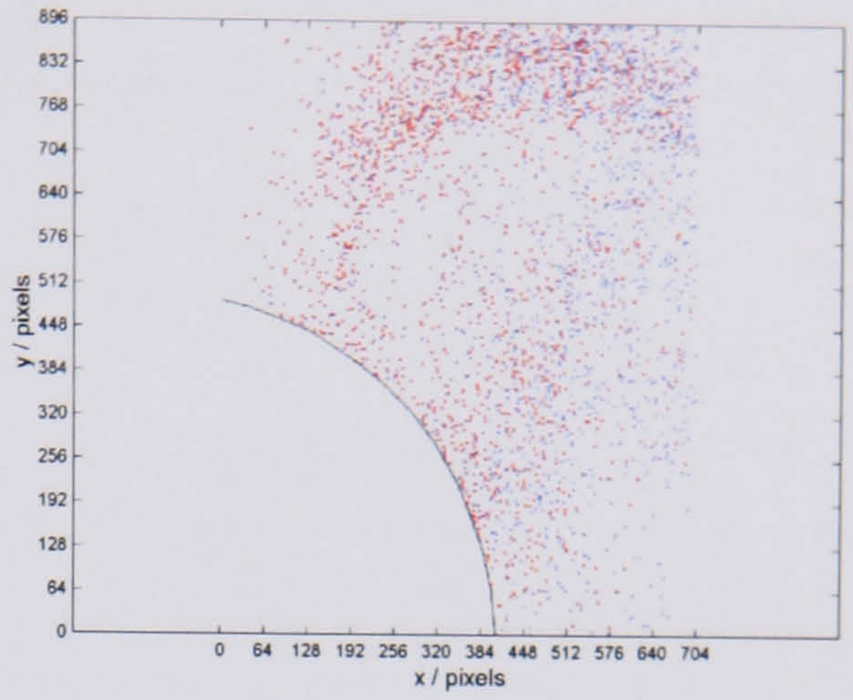

b. Particles identified from RTB thresholding.

particles identified in image 1: 1344

particles identified in image 2: 1563

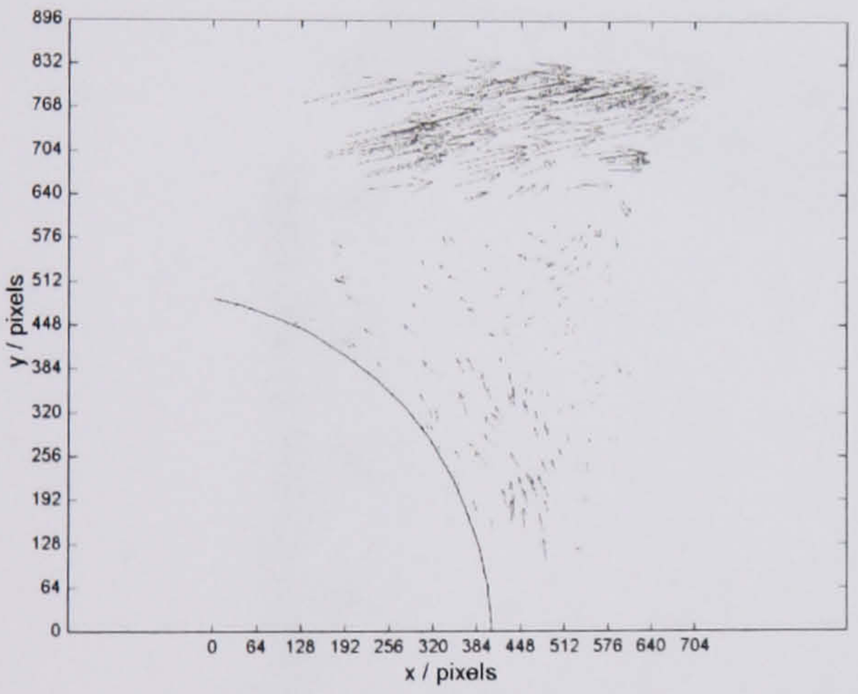

c. PTV applied to particle set in a.

Number of tracked particles: 508

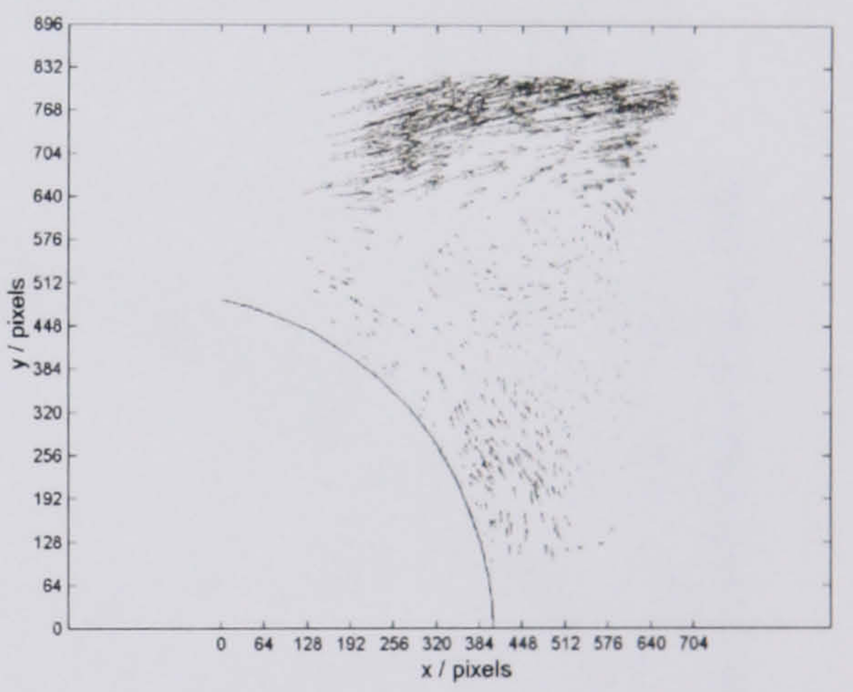

d. PTV applied to particle set in b.

Number of tracked particles:1005

Figure 2.25. Flow in the near wake of a circular cylinder. The red dots indicate particles picked up in image 1 with the blue dots indicating particles picked up in image 2. Distortion in the camera lenses is causing poor particle recognition at the periphery of the image. The results indicate that a system identifying a high population of particles is not necessarily a successful particle identification scheme.

	Standard image database image reference		
	piv01_1	*CM2-2874*	
Algorithm	**Particles counted**	**CPP (%)**	**IPP (%)**
STB	1178 (*1160*)	56	21
MTB_M	1503	64	19
$M_{OR}TB$	1996	87	5
DTB	2348 (*2338*)	93	1
PMC	2391 (*1134*)	92	7
RTB	2415	95	3

Table 2.2. The results of the various threshold operators being applied to standard images. The red italic text represents the results published by Ohmi et al. 1999. Image *CM2-2873* has a particle diameter range $1.0 \leq d\tau/d_r \leq 2.0$ with $N_i = 25$.

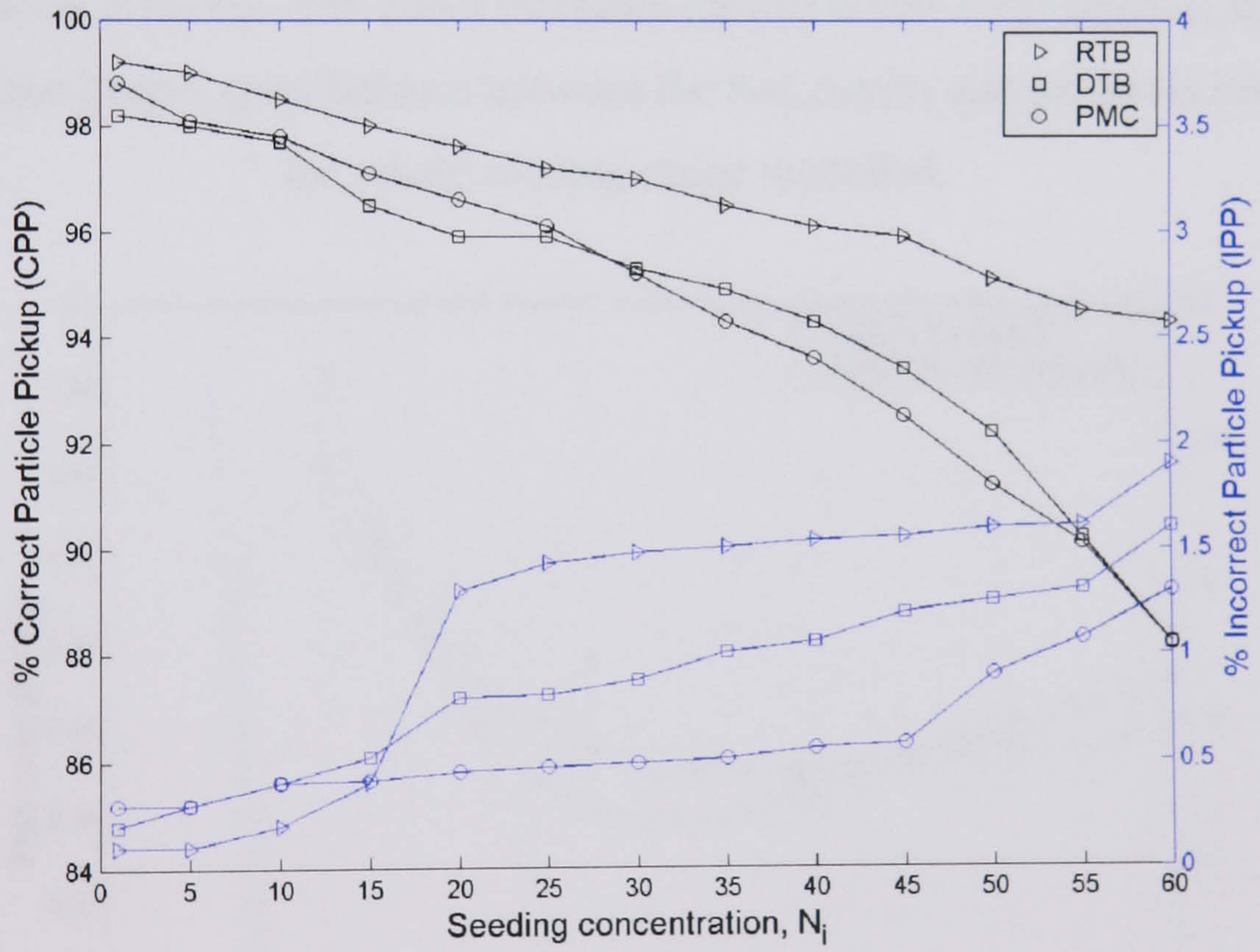

Figure 2.26. For a simulated diameter range of $1.0 \leq d\tau/d_r \leq 2.0$ the performance of each particle identification technique is worsened in comparison to the optimal range (typically $1.3 \leq d\tau/d_r \leq 2.3$). *IPP* is generally unaffected through the range of seeding concentrations although *CPP* for PMC and DTB is much reduced.

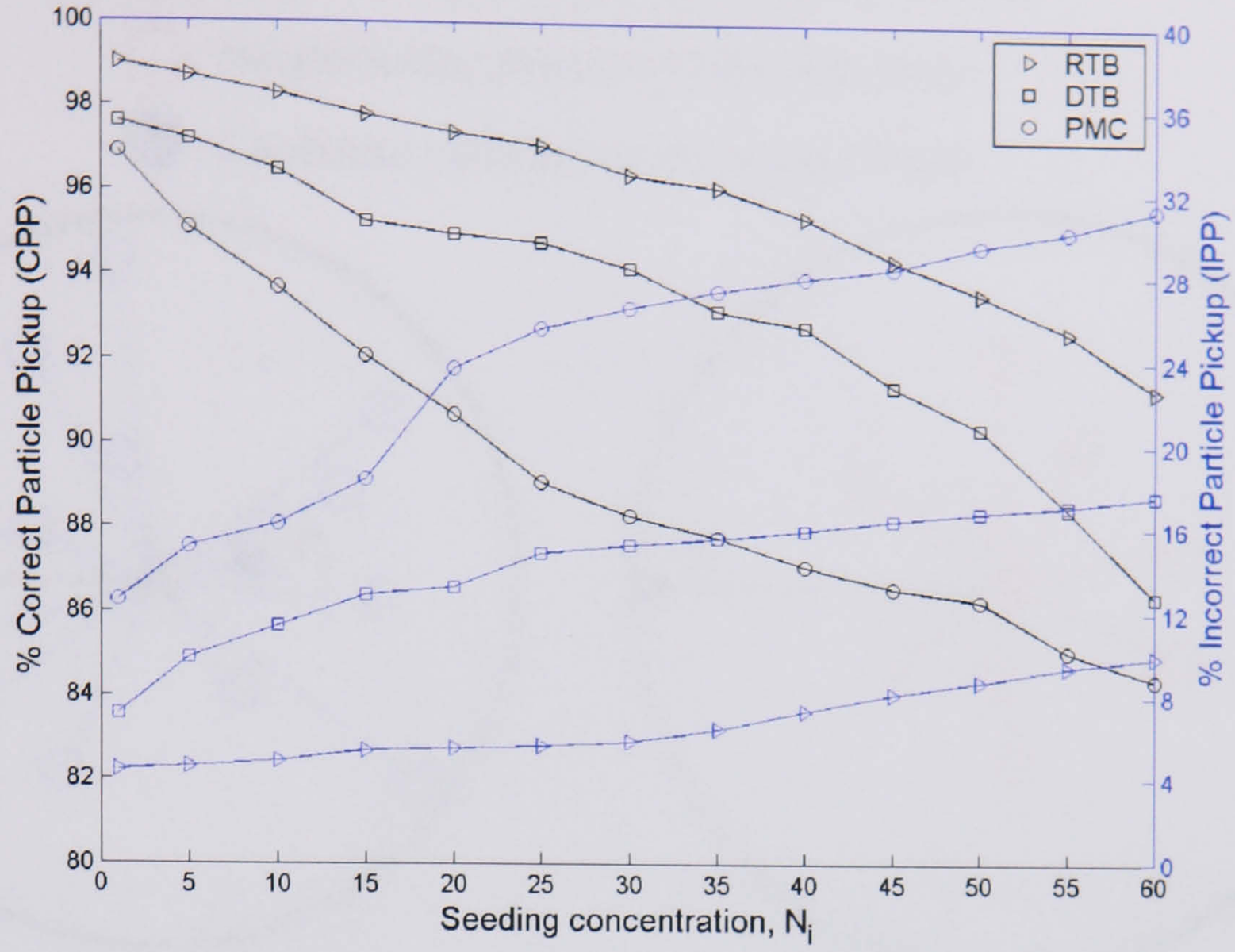

Figure 2.27. Using a particle diameter range of $1.0 \leq d\tau/d_r \leq 2.0$ and introducing a simulated noise level the *IPP* count increases rapidly while *CPP* remains stable. The RTB technique keep a good balance between the two counts and performs best through the whole seeding range modelled.

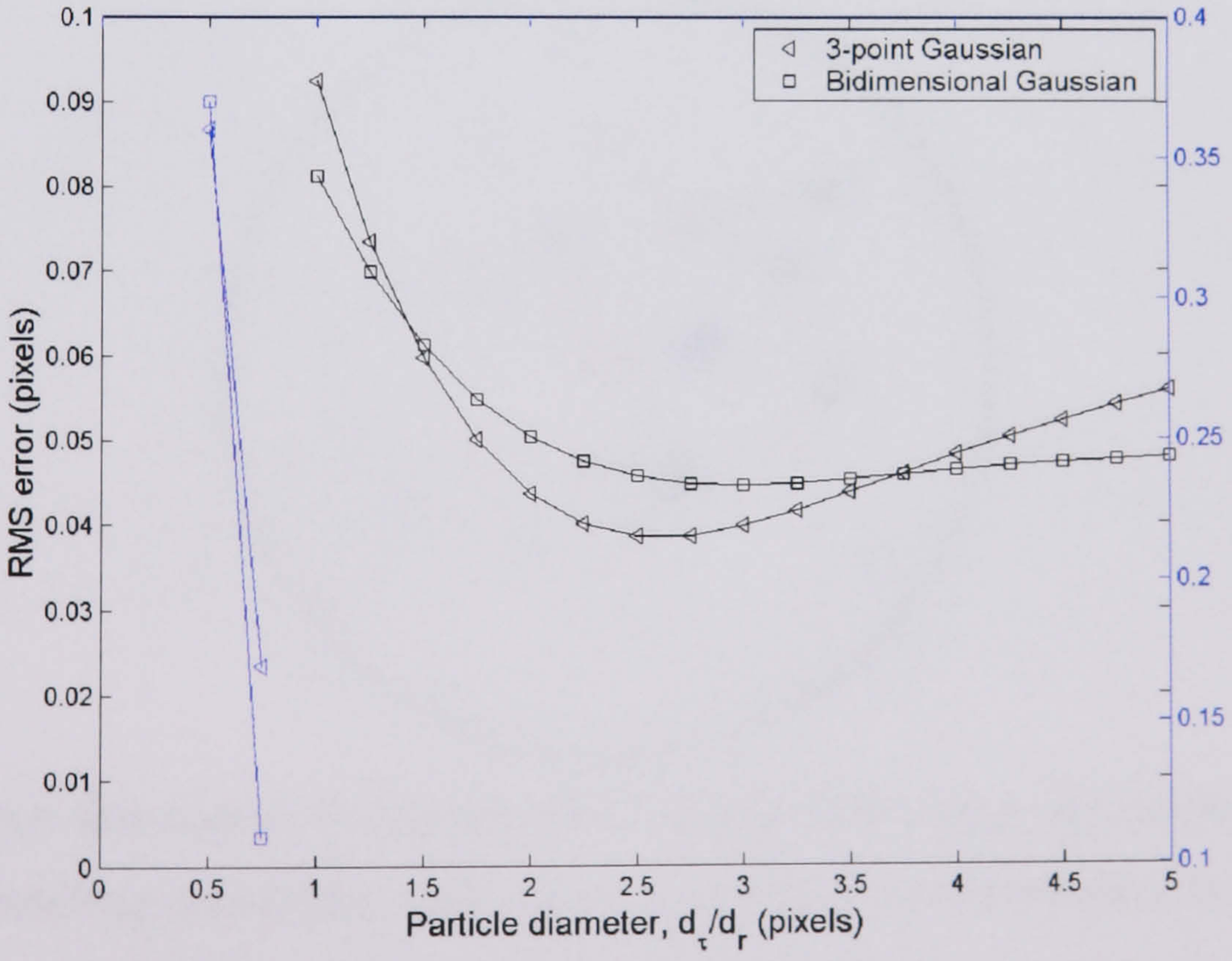

Figure 2.28. The behaviour of two sub-pixel estimation schemes. The particles were displaced through a 3% shear and $N_i = 12$. Higher RMS errors are expected as the Nyquist sampling criterion breaks down (shown in blue here).

: Primary particle i in first frame

: Neighbouring particles in the second frame

: Neighbouring particles in the first frame

: Candidate particle j in the second frame

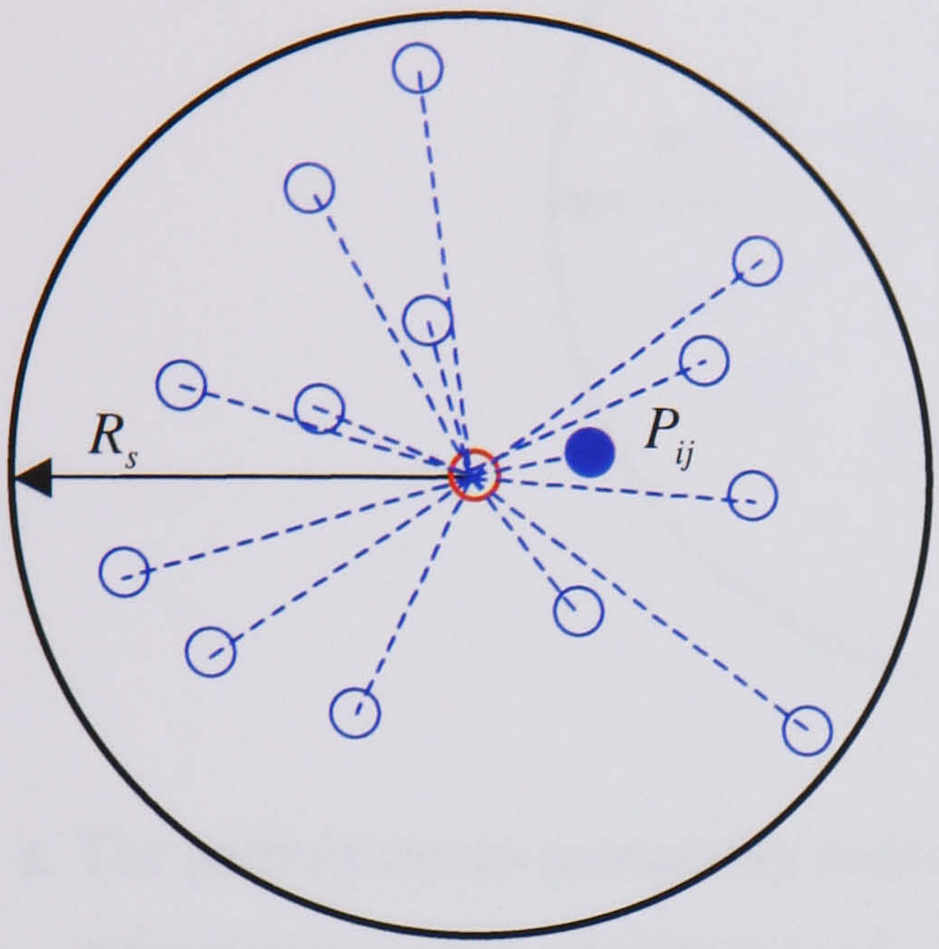

a. The primary particle selects particles of interest from the second frame using a radius threshold, R_s.

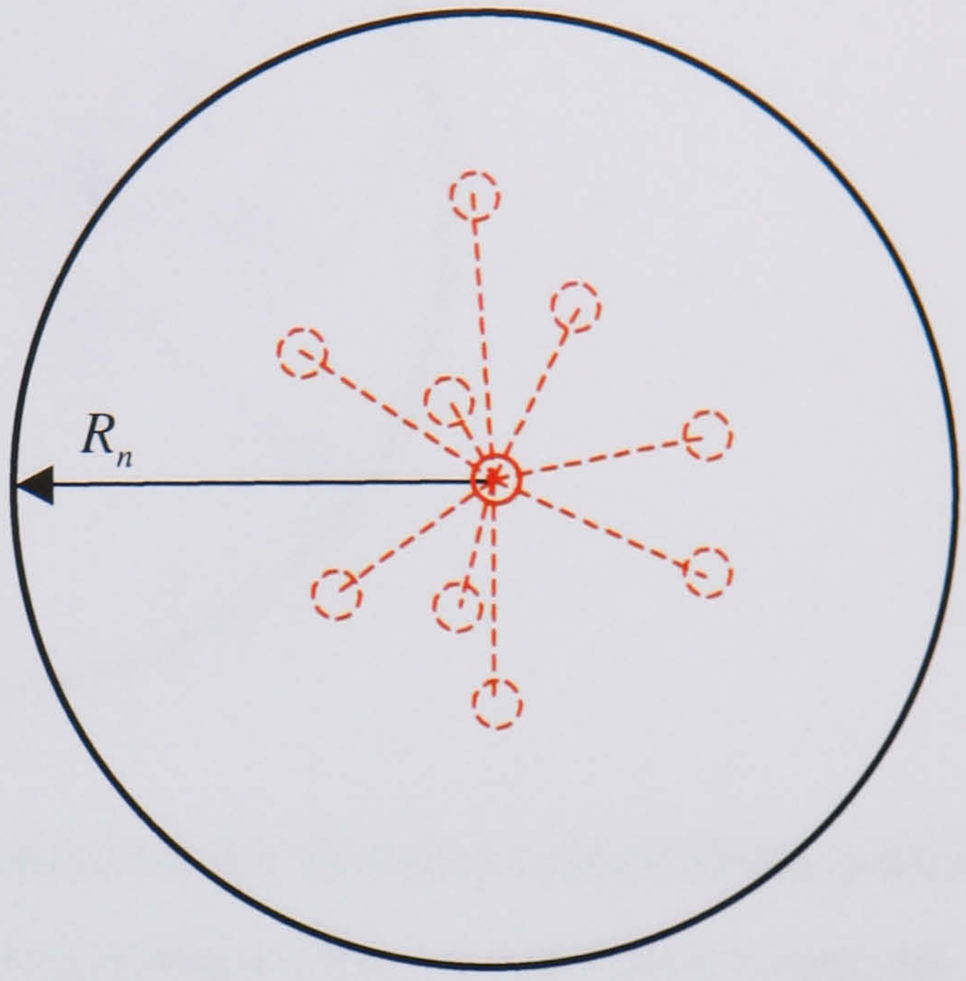

b. Particles within R_n are expected to preserve the general flow nature of the particle in the first frame.

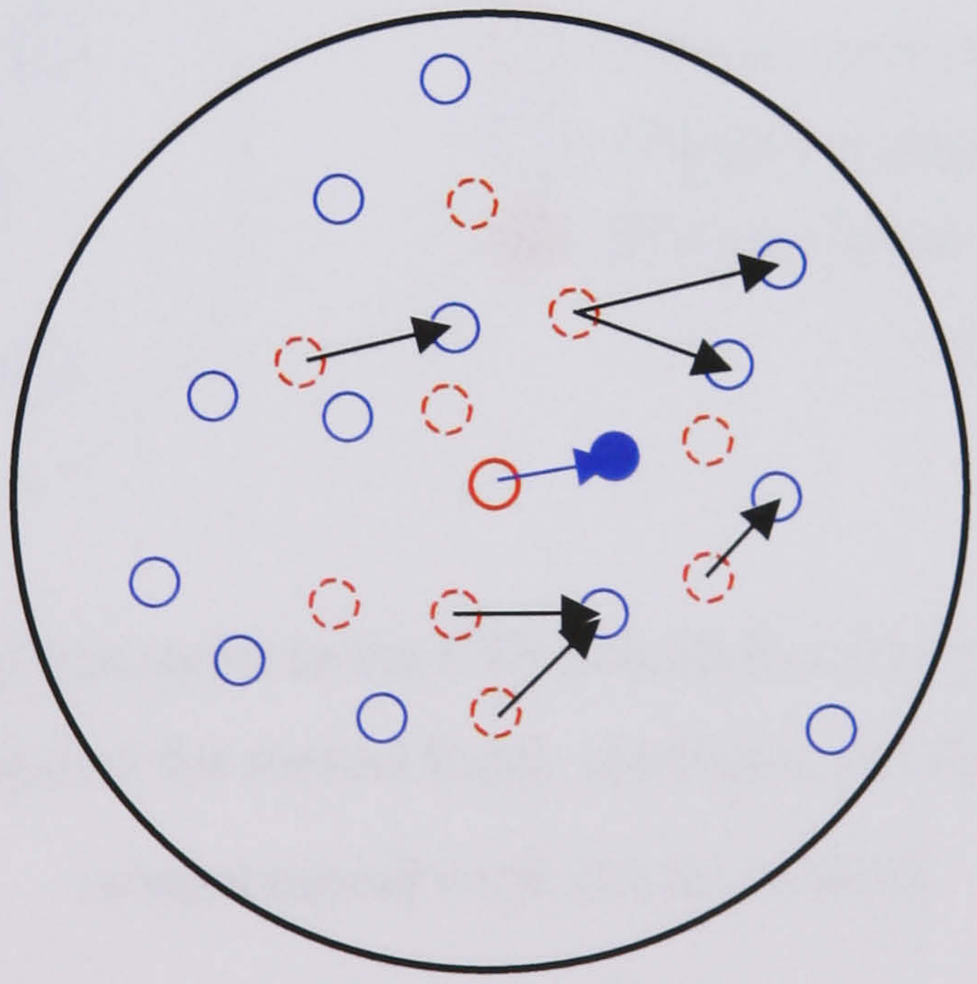

c. Any motion that repeats the primary flow motion (blue vector) is used to update the particle matching probability. Relaxation R_c is afforded between particles k and l illustrated with a black vector such that the motion is quasi-parallel.

Figure 2.29. Construction of the probability matrix using the radius criterion.

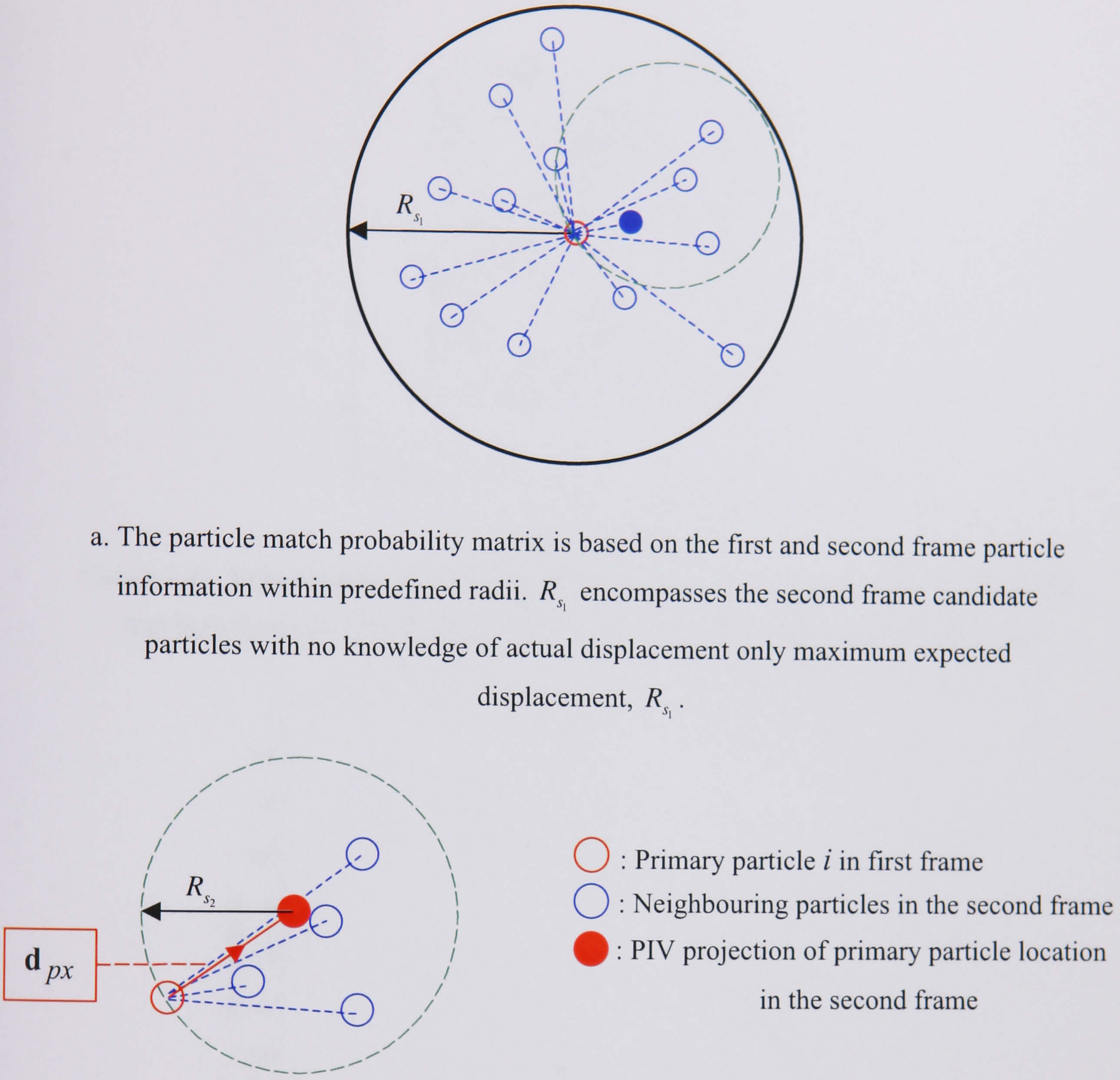

a. The particle match probability matrix is based on the first and second frame particle information within predefined radii. R_{s_1} encompasses the second frame candidate particles with no knowledge of actual displacement only maximum expected displacement, R_{s_1}.

b. By using a multigrid pass prior to the PTV calculation it is possible to both shift and reduce the search window for second frame candidate particles to R_{s_2} such that the computational work can be reduced.

Figure 2.30. Using the hybrid approach to the Barnard and Thompson tracking allows a much-reduced R_s value to be applied for similar tracking success.

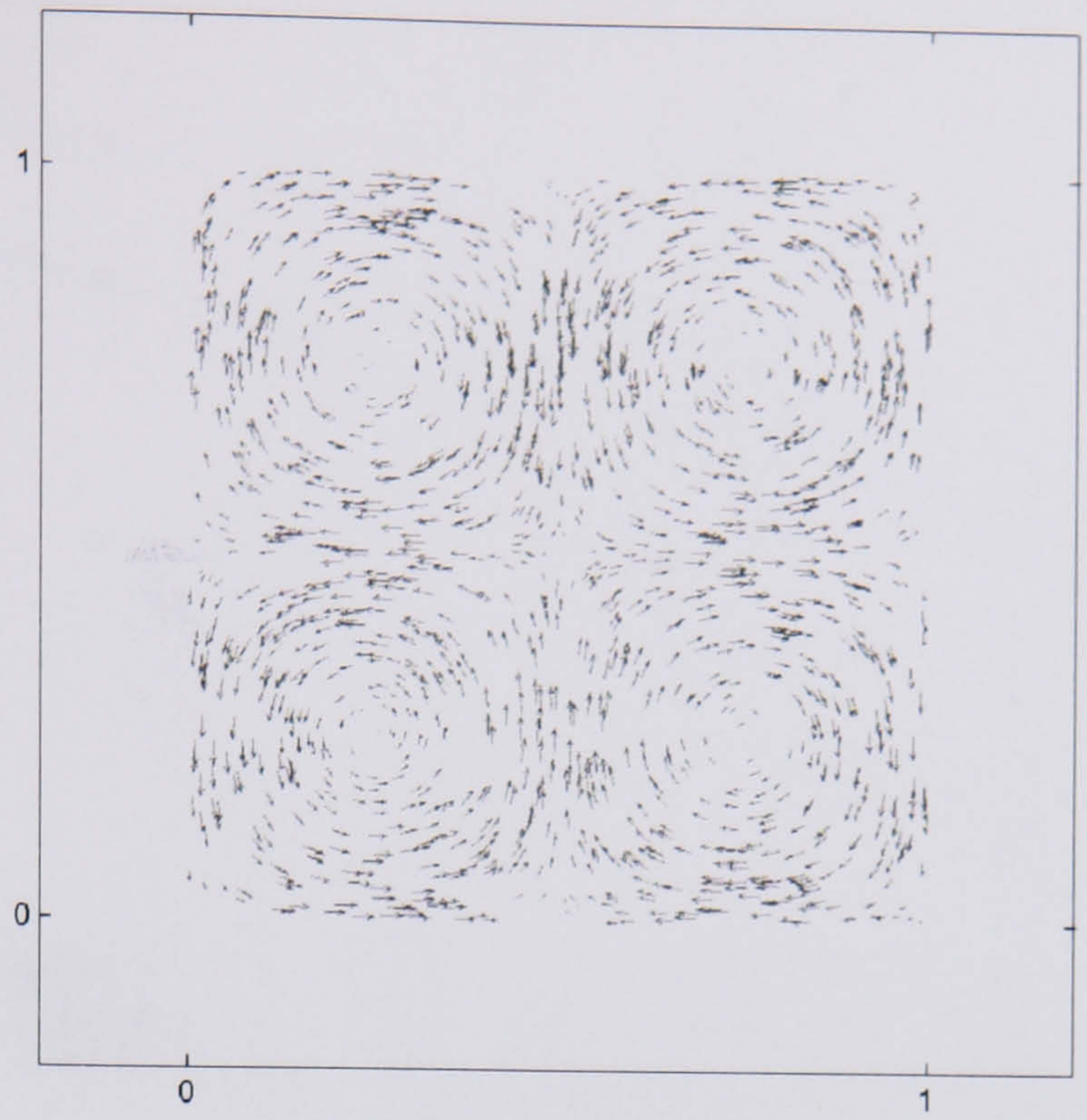

Figure 2.31. Velocity map of the Taylor-Green vortex interaction, $k = 1.0$. It can be seen that high dynamic velocity ranges are possible with pertinent vortex interactions.

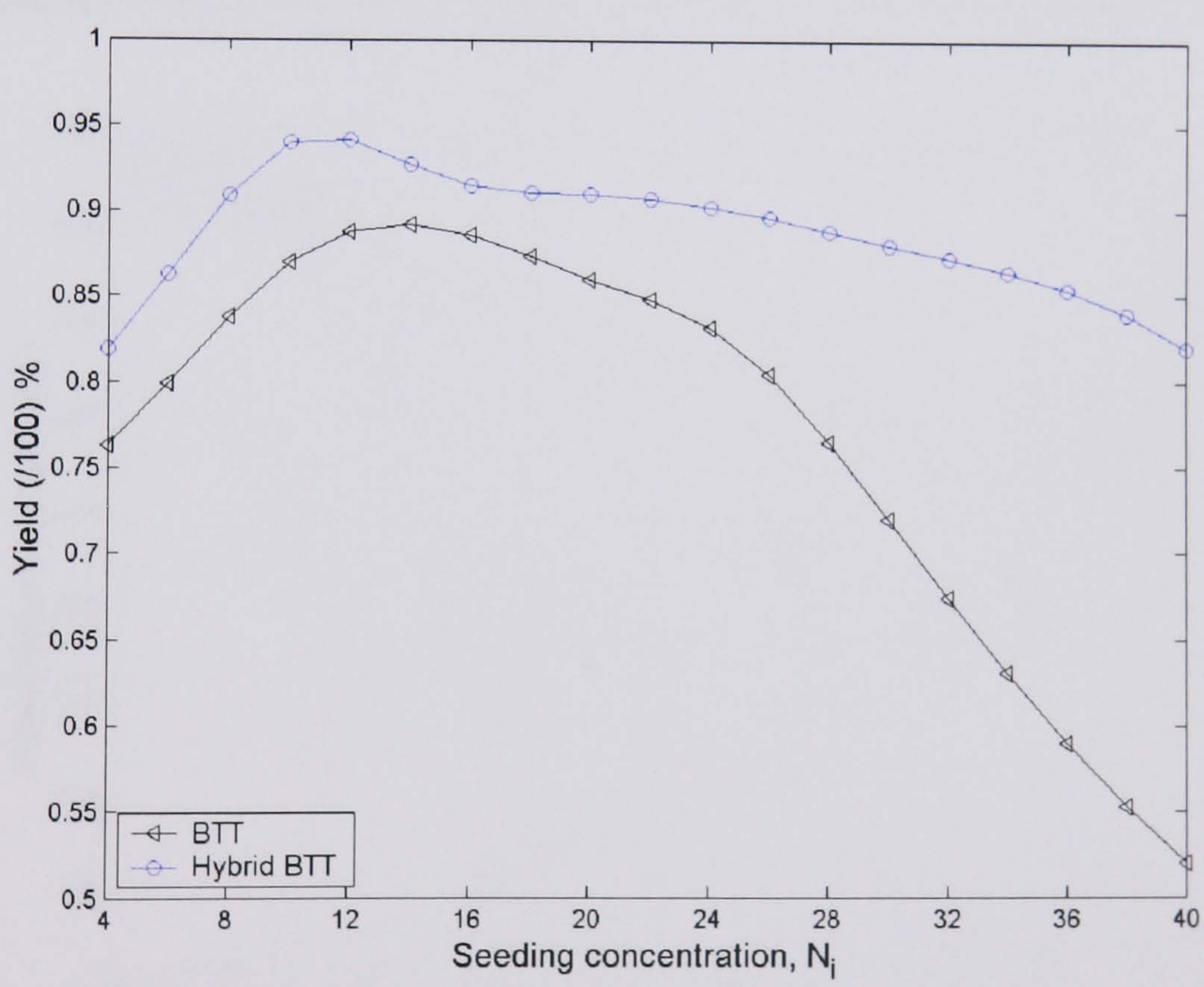

Figure 2.32. Test carried out on the Taylor-Green vortex, $k = 1.0$ showing the relationship between yield and seeding concentration, N_i. The R^d is 16 pixels. Values for the BTT algorithm were $R_s = 16$, $R_n = 20$ and $R_s = 4$.

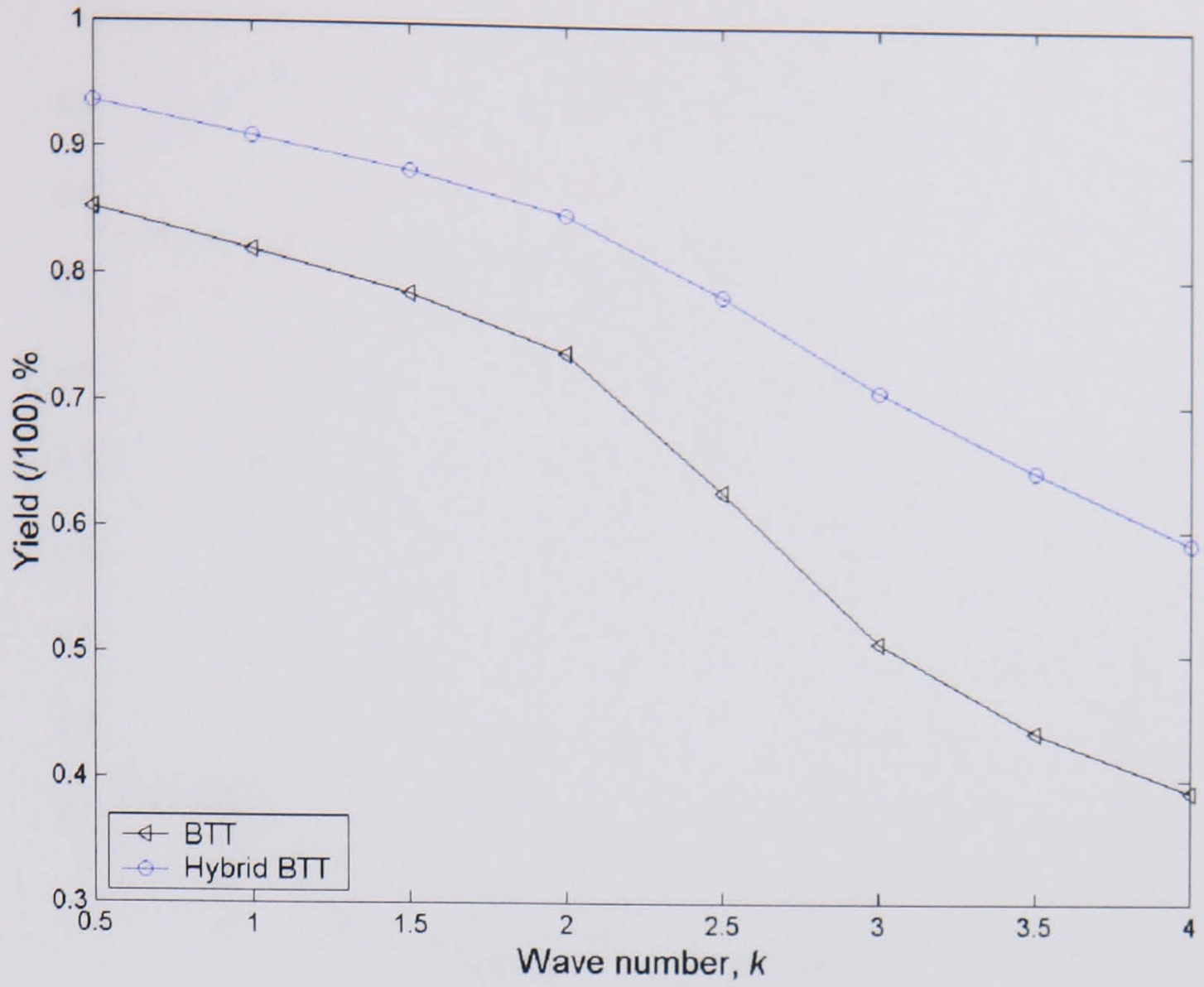

Figure 2.33. Test carried out on the Taylor-Green vortex, $N_i = 25$ showing the relationship between yield and wave number, k. The displacement range and values for the BTT algorithm are the same for those described in figure 2.32.

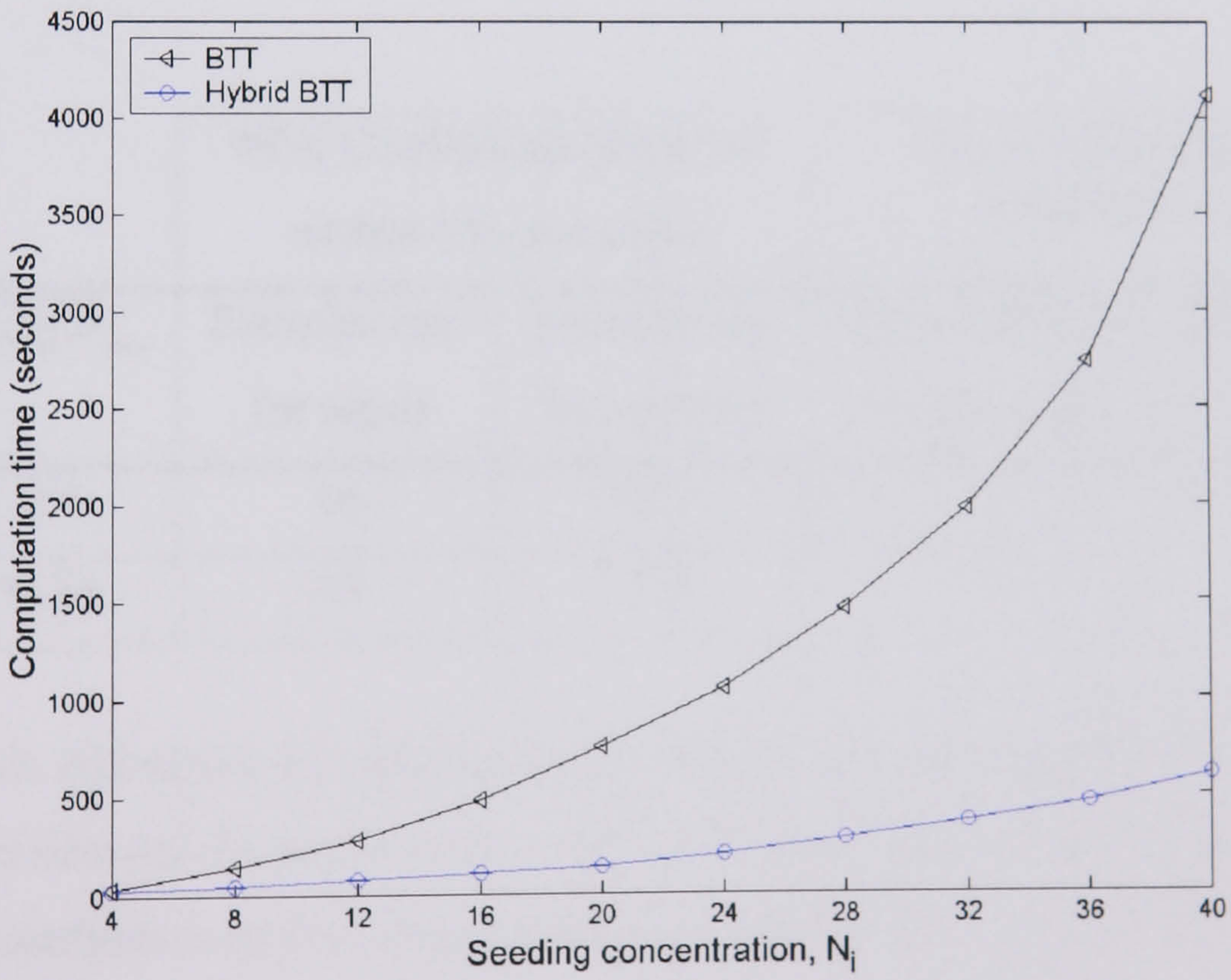

Figure 2.34. Test carried out on the Taylor-Green vortex, $k = 1.0$ showing the relationship between computational time (P4 1GHz PC) and seeding concentration, N_i. As expected the arbitrary radii decisions made for standard BTT cause the computational times to rapidly increase with particle population.

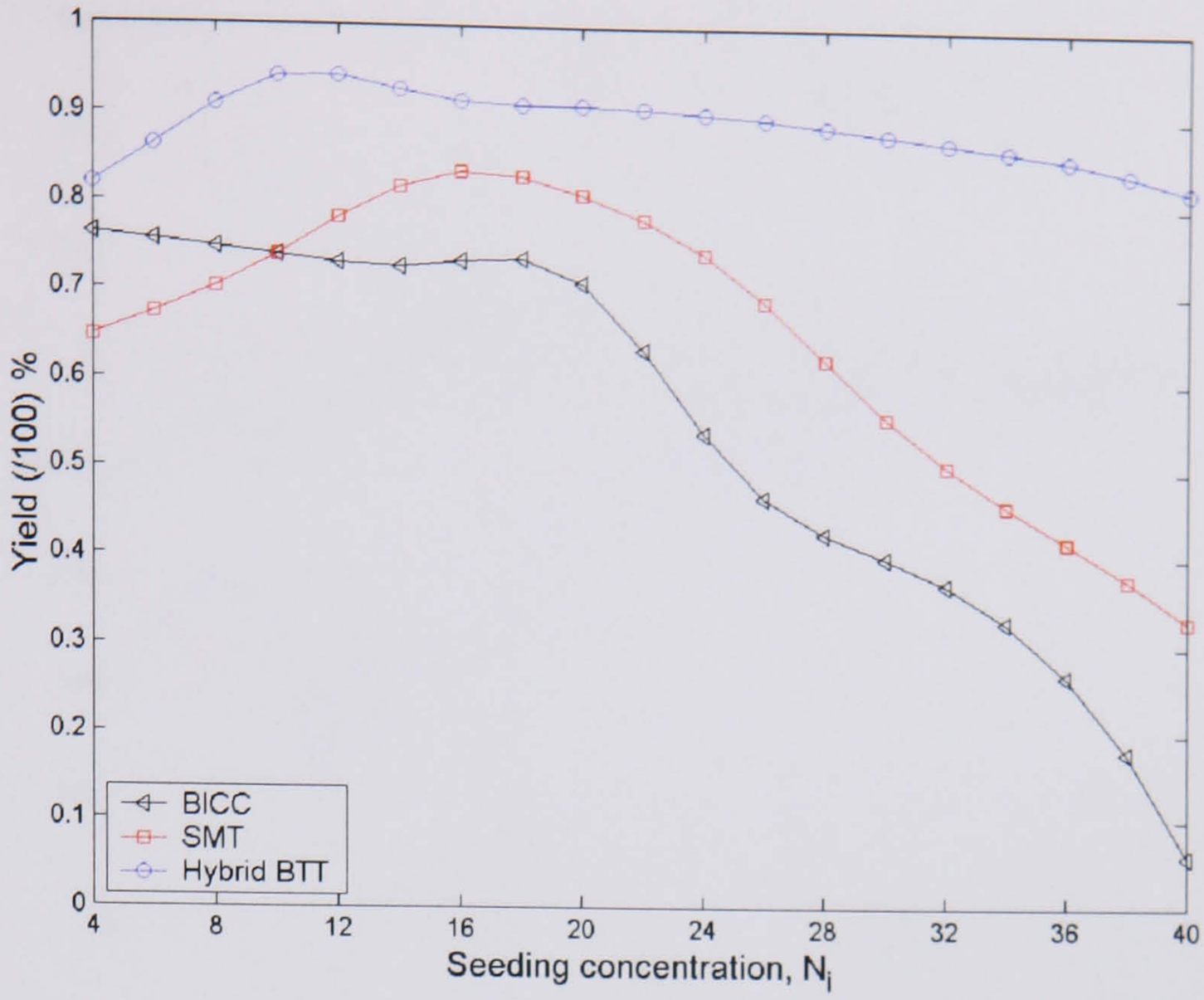

Figure 2.35. Test carried out on the Taylor-Green vortex, $k = 1.0$ showing the relationship between yield and seeding concentration, N_i.

For BICC, interrogation window length=16pixels and the search radius=16pixels.

		95% Confidence limit for within 5% accuracy		95% Confidence limit for sample size of 250	
x/L	σ_{pop}/μ_{pop}	Samples req. for mean	Samples req. for variance	Expected error in mean (%)	Expected error in variance (%)
0.1	0.1	16	801	<1	<10%
0.8	0.24	89	773	<1	<10%

Table 2.3. All values are calculated such that the estimations fall within the 95% confidence interval. To accommodate the fixed sample size of $N = 250$ and maintain confidence in the measurement the expected error was increased.

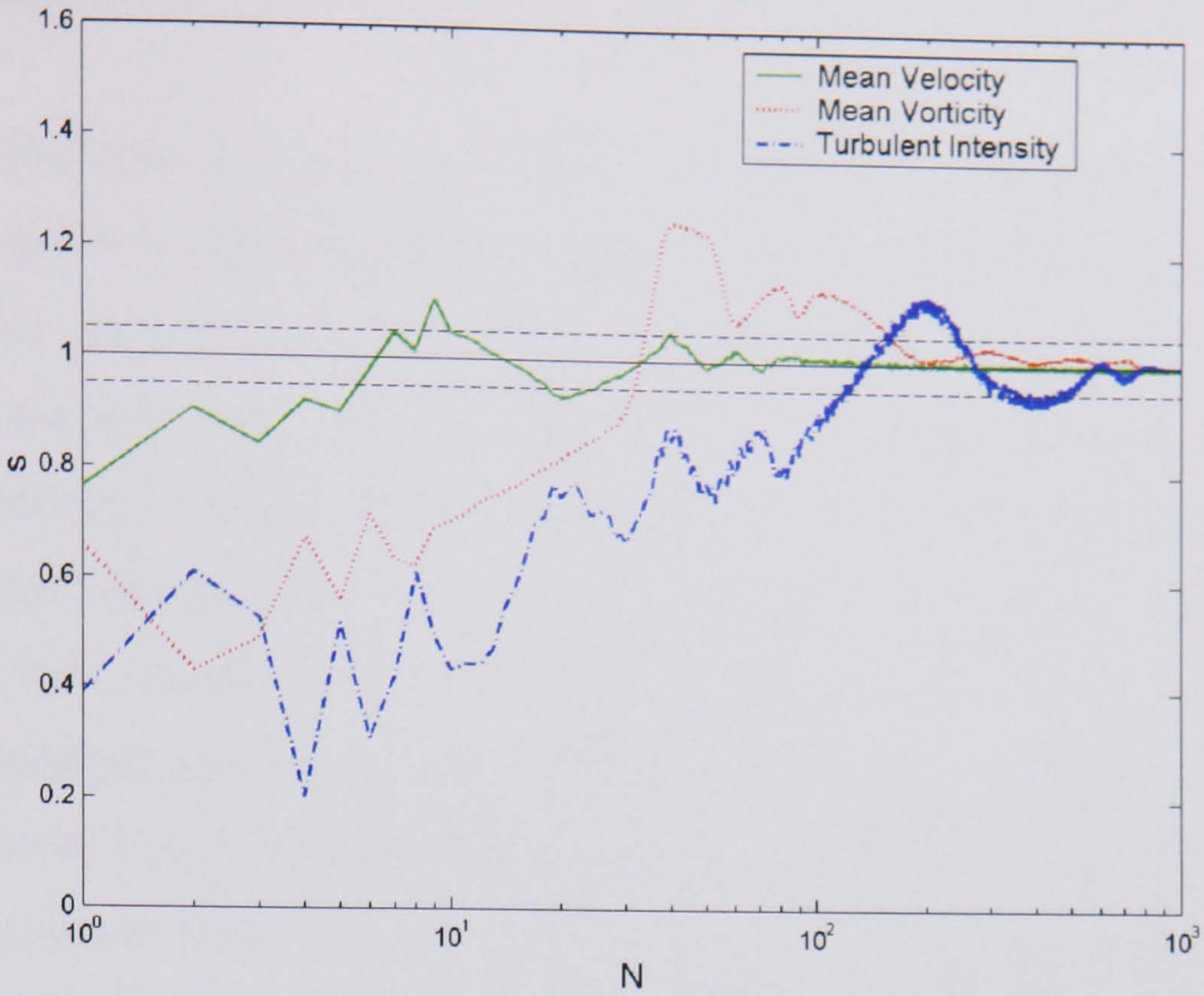

Figure 2.36. The convergence of various flow measurement over a range of sample widths at $x/L = 0.8$. Both the mean velocity and mean vorticity appear to be converging rapidly enough to be well measured in this study.

x/L	l_δ (m)	Δ_{IJ}/l	$\varepsilon_u(\%)$	$\varepsilon_{\omega_{bias}}(\%)$	λ_ω	$\varepsilon_{\omega_{rand}}(\%)$
0.1	0.0015	0.8	1.0	48.3	0.56	0.56
0.8	0.015	0.08	1.3	0.53	5.59	7.27

Table 2.4. Error estimation for two different stations along the cavity shear layer. The length of the structures, l_δ present at $x/L = 0.1$ was not measured in the current study and as such the boundary layer displacement thickness (at $x/L = 0$) was used.

Scheme	Accuracy at the 95% confidence level
ITDWO-FFT	0.17±0.05
ITDWO-DC	0.15±0.05
ITDWO-FFT-SDCPIV	0.14±0.05
Hybrid BTT	0.11±0.05

Table 2.5. Results are based on the average uncertainty over a $R^d = 16$ pixels. The particles are subject to translation in the u and v direction independently. This benchmark is adopted from Soria et al. 1996.

CHAPTER 3: MODEL DESIGN AND INSTRUMENTATION

This chapter describes the design and build of a simple cavity model required to deliver both surface and flowfield information. The range of cavity geometries that may be included in this study is then dictated by this design criterion and by the wind-tunnel facilities that are to be used. A brief description of the pressure measurement system is also included along with other pertinent experimental issues. The Glasgow University 2.13x1.61 metre 'Handley Page' tunnel (***HPT***) was used for the measurement of static pressure data both longitudinally and spanwise along the cavity model. Limited use of surface-mounted pressure-transducers was also made to provide a modal description of the internal cavity flowfield. The Glasgow University 1.15x0.85 metre 'Anatomy' tunnel (***AT***) was used for PIV measurements, while skin friction data was obtained downstream of the cavity using a Preston tube set-up. Measurement of the boundary layer both upstream and downstream of the cavity section was conducted using a specially constructed rake probe.

3.0 Model description

A simple symmetric wing-section with flap assembly was chosen as the parent body for a rectangular, three-dimensional cavity. The appropriate dimensional definitions are included in figure 3.1. The cavity model would have to be of sufficient width/span such that any inboard three-dimensional wing effects are suppressed, while the cut-out must be located in such a fashion that it is optically accessible for the PIV system. The physical cavity dimensions were ultimately dictated by the solid blockage and the expected wake blockage in the smaller of the two wind tunnels (***AT***).

The primary requirement of the model design are that the boundary layer profile immediately upstream of the cavity leading edge should be turbulent, stable and have a good repeatability in shape factor. Therefore the model nose section geometry was designed such that the pressure gradient in this region was minimal and the local pressure coefficient was as small as the solid blockage would allow. To ensure this behaviour for the proposed model nose two fluid simulations were undertaken. First the SPARV_V9.0 panel method, BAE 1997 was used to determine the optimal nose profile, then the PMB2D_V3.0 RANS flow solver, Badcock et al. 1998 was used for

comparison using a grid independence study. The results from these simulations are shown in figure 3.2 and indicate good agreement for the chosen elliptic profile of 1:4 (major axis : minor axis) with only a slight pressure gradient predicted at the cavity leading edge. These simulations included the proximity of the wind-tunnel walls.

Using this nose section profile the remainder of the model dimensions were determined by blockage and mounting considerations. The width of the model was fixed at 840mm so that it was possible to install the model both horizontally and vertically in the ***AT***, while this also improved the two-dimensional flow behaviour along the centreline section of the model. When fixed horizontally the model was supported in the centre of the test-section using four legs of which the front two were faired to reduce tare drag (and wake blockage). The model chord line was set approximately equal to the test-section vertical centreline (rather than below it) thus reducing the flap angle required to balance the model when testing (and minimize wake blockage). The model thickness was set to 60mm, which imposed a total solid blockage value of 5.2% and complies with good experimental procedures for closed return type wind tunnels, Barlow et al. 1999 (the solid blockage for the ***HPT*** was less than 2% including leg sections). Based on the smallest test section length and the hardware capabilities of the PIV system the maximum cavity length was estimated to be 150mm ($L/D = 3.0$). A flat plate section downstream of the cavity was necessary for measuring the state of the flow after it had encountered the cavity section and to shift the flap section (attached via the boat tail) away from the region of interest. This distributed the wake blockage sufficiently far enough downstream to ensure better flow quality in the region of interest. The final model designs for pressure and PIV measurement are shown in figures 3.3 and 3.4 respectively.

The base of the cavity and the model legs were constructed from aluminium and anodised black to reduce laser reflection. The nose section was constructed from mahogany while the main body of the model was made from marine ply and was hollow in construction to facilitate easier instrumentation. Each wooden section was painted matt black and rubbed smooth with a cloth.

A boundary-layer transition strip was applied to the leading edge of the nose section to ensure that the flow entering the cavity was fully turbulent for all test conditions. In order to preserve repeatability between test runs it was decided that a thin strip of sandpaper would be used instead of applying grit to wet adhesive. Based on the reports by Braslow et al. 1958 and 1966 a 4mm strip of No. 36 grit was required for a good three-dimensional trip at 3.5% chord ($x = -195mm$). It was found that this corresponded to P1200A silicon carbide paper (English Abrasive and Chemical Ltd.). Although the P600A product represents the closest nominal roughness to No.36 grit an oil flow study[1] immediately downstream of this strip indicated that this transition was two-dimensional in nature. The P1200A product was also more resilient to the oil saturation expected during the PIV tests.

It was predicted that the minimum boundary layer height at the cavity leading edge would be 9mm and that the flap area required for balancing the maximum cavity volume was roughly $0.24m^2$ for a flap angle of 12 degrees.

3.1 Test conditions

The tests were conducted at an angle of attack of 0° and a yaw angle of 0°. The wind-tunnel freestream speed was set to $28m/s$, which corresponds to a unit Reynolds number of $1.9x10^6/m$. Five test cases were chosen in this study that varied between $L/D = 1.0$ to $L/D = 3.0$, the physical dimensions of the cavity are shown in table 3.1 and the Reynolds number based on cavity length is included in table 3.2 for reference. A qualitative assessment of the flow around the model was completed using surface-flow visualization. It was observed that there were no separated regions upstream of the cavity section on the parent wing and there was no unexpected flow behaviour downstream of the cutout for each of the test cases. Using this technique it was also possible to determine the correct height of the end plate required to suppress three-dimensional effects at the outboard sections of the model. Some results from this particular study are included in figure 3.5 and show the elimination of a corner vortex in the x-z plane by using a larger endplate section. By reducing such effects a better

---

[1] For these studies a mixture of motor oil and fluorescent dye was carefully painted onto the model surface, illuminated using a UV lamp and photographed using TMAX 35mm film (ISO2400) with a skylight filter.

repeatability in the experimental process is assured. The endplate section actually used is shown in figure 3.6f. The ***AT*** was configured such that the freestream turbulent intensity was approximately 0.23%, while the ***HPT*** was expected to be ~0.6% at the freestream speed indicated, Rae et al. 1984; see appendix A for more details.

3.2 Pressure measurement

Both static and dynamic pressure measurements were recorded in this study. The instrumentation required is now described and the physical locations of the surface mounted probes are included in appendix C for reference.

3.2.1 Surface static pressure

The parent cavity model was instrumented with 85 permanent static-pressure orifices arranged into four distinct measurement locations, as shown in figure 3.3. Each area of measurement is now briefly described. In order to balance the model correctly using the flap assembly a series of 9 static pressure orifices were required around the nose section (in the x-y plane, ***NSXY***), these locations are listed in table C1 (appendix C). For the measurement of upstream spanwise effects 11 pressure measurements were recorded along the entire nose section (in the x-z plane, ***NSXZ***), these locations are listed in table C2. To measure any three-dimensional effects on the cavity floor 28 static pressure measurements were made spanwise through the entire cavity section (in the x-z plane, ***CAVXZ***), these locations are listed in table C3. Finally, 37 longitudinal pressure measurements were taken through the cavity section, (in the x-y plane, ***CAVXY***), these locations are listed in table C4. The blue text in the table indicates pressure orifices located on the front and rear bulkheads of the cavity. In order to measure the static pressure profile for cavities of $L/D = 2.5, 2.0, 1.5$ and 1.0, instrumented aluminium blocks were inserted to the back of the original cavity, thus changing the effective cavity length. The static pressure orifice locations for each individual cavity length are listed in tables C5 to C8; the red text indicates measurements taken from the aluminium insert. Figure 3.6a and 3.6b show the model set-up in the Handley-Page tunnel (looking downstream) and a spanwise view of an aluminium insert respectively.

Each static pressure orifice was flush mounted onto the surface of the model with a diameter of 1.0 mm and was connected to a scanivalve assembly through a 2 metre

length of nylon tubing. A Scanivalve Corp. model PDCR24 differential pressure transducer was used with a model 48S solenoid stepper drive. A model CTLR2 solenoid controller was used for both units and the gains were optimised for the expected measurement range. The scanivalve assembly, shown connected in figure 3.6c was located under the tunnel and comprised of two individual pressure transducers mounted on two separate units. Each unit has 48 input lines for measurement making it possible to scan 96 channels sequentially each referenced to the tunnel static pressure.

The scanivalves were controlled through a NI NAQCard-700 using a Toshiba 110 (Pentium 1) series laptop. A LabVIEW interface was constructed that could fully control the scanivalve environment and also had the functionality for individual transducer calibration against a Druck DPI 610 pressure calibrator. This configuration was specific to the current study. With careful attention to the travelling volume and length of nylon tubing used it was found that a scan rate of approximately 10 pressures per second was possible for 99.9% stability (although this discounts actual channel sampling time). The transducer has a quoted accuracy of ±0.12% **F.S**. (±0.5mmH_2O), which translates to ΔCp±0.002. Plentovich 1990 and Dix 1987 among others have reported unsteadiness in the unaveraged static pressure for open cavity flow. A quick study for each of the cavity configurations indicated that a 3 second sampling period with greater than a 30Hz-sampling rate was sufficient to ensure repeatable results. A Matlab (C) program handled the raw data produced.

3.2.2 Unsteady pressure

The model was instrumented with 2 miniature Sensym SCCOSGSMT pressure transducers at the locations shown in figure 3.3 (***PTL***) and listed in table C9. These transducers have a frequency response of 10kHz. The transducers were connected to a surface orifice of 1.0mm diameter and connected to the transducer through a small length of plastic tubing (approximately 3mm in length). It was calculated that the tubing would cause no attenuation or phase shift, uncertainty in the pressure coefficients is expected to be 0.5%. The second transducer was mounted on an aluminium insert that could be changed in length such that measurements could be taken for every configuration listed in table 3.1. The transducers were controlled using the LabVIEW interface (as described above) while a Matlab program performed the required signal analysis.

3.3 PIV measurement

The model designed for pressure measurement was adapted for PIV tests using some simple modifications. The flat plate section immediately aft of the cavity itself was replaced with a clean flat wooden section that could be translated in the x-direction. The rear bulkhead of the cavity was attached to this moving part, which then enabled the effective length of the cavity section to be changed without the need for inserts; these moving parts are outlined with blue in figure 3.4. The space created beside the boat-tail section was covered with an aluminium sheet. A 160 x 240mm rectangle was cut from the floor of the cavity centred on a spanwise ordinate of -130mm. A similarly sized section was cut from the moveable flat plate section behind the cavity. During the PIV tests these regions were fitted with 6mm thick glass sections, part of the rear bulkhead was replaced with a glass section also.

As described in chapter 2 the illumination power of the laser may at best facilitate an f-number of 5.6. However, such a large aperture diameter causes considerable saturation of the images at any solid boundaries and renders the local velocity measurement invalid (affecting over 16,000 pixels in the image). Although these effects may be alleviated by the use of a polarizing filter it is still the case that regions of highly localized spurious vectors tend to occur in salient parts of the flowfield. The perspective of the camera may also compound the effects of glare. By introducing removable glass sections the laser strike is able to pass through the solid boundary and minimise solid reflections. Figure 3.7 illustrates the difference these glass sections make for automatic edge detection and particle identification. For this example the edges are automatically detected using a Sobel algorithm, Henk 1998 (with some additional structured element filtering procedures) and the particles are detected using MTB.

The roof of the wind tunnel was replaced with a 7mm thick circular Perspex™ GS100 window. This laser window reduces laser refraction and transmission losses. By mounting the optics onto an assembly of runners and sliders it was possible to have optical access to all regions of the test-section. An interchangeable glass section on the wind-tunnel door allowed camera access into the test section. Replacing the starboard endplate on the model with a 6mm glass section then allowed camera access into the cavity section, as shown in figure 3.6f.

3.4 Skin friction measurement

Making further use of the interchangeable slots constructed for the PIV tests, the glass inserts were replaced with smooth aluminium sections instrumented for pressure measurement. Using a Preston tube, Preston 1954 this allowed a complete set of surface friction measurements to be extracted from a seamless flat plate section downstream of the cavity.

The first aluminium section was instrumented with 50 static pressure orifices that were flush mounted onto the surface of the model. These had a diameter of 1.0mm and their locations are included in table C10 (longitudinal positions) and table C11 (spanwise positions). Each channel is connected to a multiplexor unit through a 2metre length of nylon tubing. A moveable pitot probe was then attached to the aluminium section and differential measurements are taken between the local static measurement and the corresponding total pressure measurement. Correct operation of the Preston tube requires the validity of the logarithmic law of a turbulent flow above a wall. For flows with pressure gradients this region becomes smaller and as such the probe diameter must be carefully considered, Bechert 1996. Based on observations by Chue 1975 the internal-to-external diameter ratio of the probe used was 0.6 and the physical probe diameter was 2.0mm (round). The output pressures were then sequentially measured by a factory calibrated Furness Control manometer (model FC012). The transducer has a quoted accuracy of ±0.5% **F.S.** (±1.0mmH_2O).

Calibration of the Preston tube is traditionally done using the three definitive empirical equations listed by Patel 1965 (corresponding to the wall law regions). For this work the interpretation of Head and Ram 1971 is preferred since it removes implicitness and yields a calibration accuracy of ±1%. By defining an inner pressure gradient parameter Patel 1965 was able to identify limits on the prescribed accuracy of the Preston tube in adverse (and favourable) pressure gradients. Considering pressure gradient effects in isolation a maximum error of 6% is expected downstream of the cavity section.

3.5 Boundary layer measurement

A rake probe was constructed to measure the total pressure inside the boundary layer both upstream and downstream of the cavity section. The probe was designed with reference to specifications listed in Pankhurst et al. 1971. The probe constructed is

shown in figure 3.8 and shown mounted in figure 3.6g. For this boundary layer study a correction for wall proximity effects was included in the reading for square ended probes and a correction for the total pressure (based on internal probe diameter) has also been used. These corrections were adopted from Chue 1975 (from Young and Maas 1936 also). There is approximately a ±15° yaw tolerance for this probe (given a 99% dynamic pressure accuracy).

Each channel was recorded in the same fashion as the Preston tube measurements while downstream of the cavity the probe position was controlled using a traverse positioned to the starboard (under-) side of the model. Solid blockage was increased by 1% in this scenario. The traverse was controlled using a pre-programmed Macintosh computer running LabVIEW with an RS232 connection. Downstream measurements were made on a clean aluminium insert, as shown in figure 3.6h. The cantilever arm used for probe movement was faired using a shroud sleeve and the arm root was positioned downstream relative to the measurement plane to reduce interference.

The boundary layer thickness was estimated by using the traditional definition whereby the edge of the boundary layer is defined to be the height above the surface at which $u/U_\infty = 0.99$. The boundary layer displacement thickness, δ^* the momentum thickness, θ and the shape factor (or form parameter), H are then calculated as described in Kuethe and Chow 1998.

3.6 Preliminary results

Each of the quantities mentioned above were measured regularly throughout the wind tunnel tests and their average values are included in table 3.3. For the ***HPT*** the shape factor was seen to vary in the range $H = 1.18 \pm 0.18$, and for the ***AT*** it was $H = 0.88 \pm 0.11$. The normalized centreline velocity profiles experienced in each of the wind tunnels are included in figure 3.9. Measuring at different spanwise locations within ±300mm ($z/W = \pm 0.36$) of the model centreline it was seen that the upstream boundary layer profile had a 93% similarity and 96% similarity for the ***HPT*** and ***AT*** respectively. These spanwise profile differences appear to originate from the pressure gradient experienced along the nose of the model, as shown in figure 3.10. The error bars included in the figure represent the deviation from the average pressure profile

experienced from all of the experiments and as such is a good measure of experimental repeatability.

Figure 3.11 shows the measured static pressures around the model nose section for each cavity length after the flap assembly balances the model[2]. It can be seen that in each case the suction pressure around the nose is sufficiently far upstream to allow a pressure plateau to persist just in front of the cavity. There is good agreement between these results and those of the simulation performed in section 3.1 (figure 3.2), which vindicates the use of a flap to rebalance a wing with cut out.

[2] A symmetric wing profile with a cavity on the upper surface will produce lift

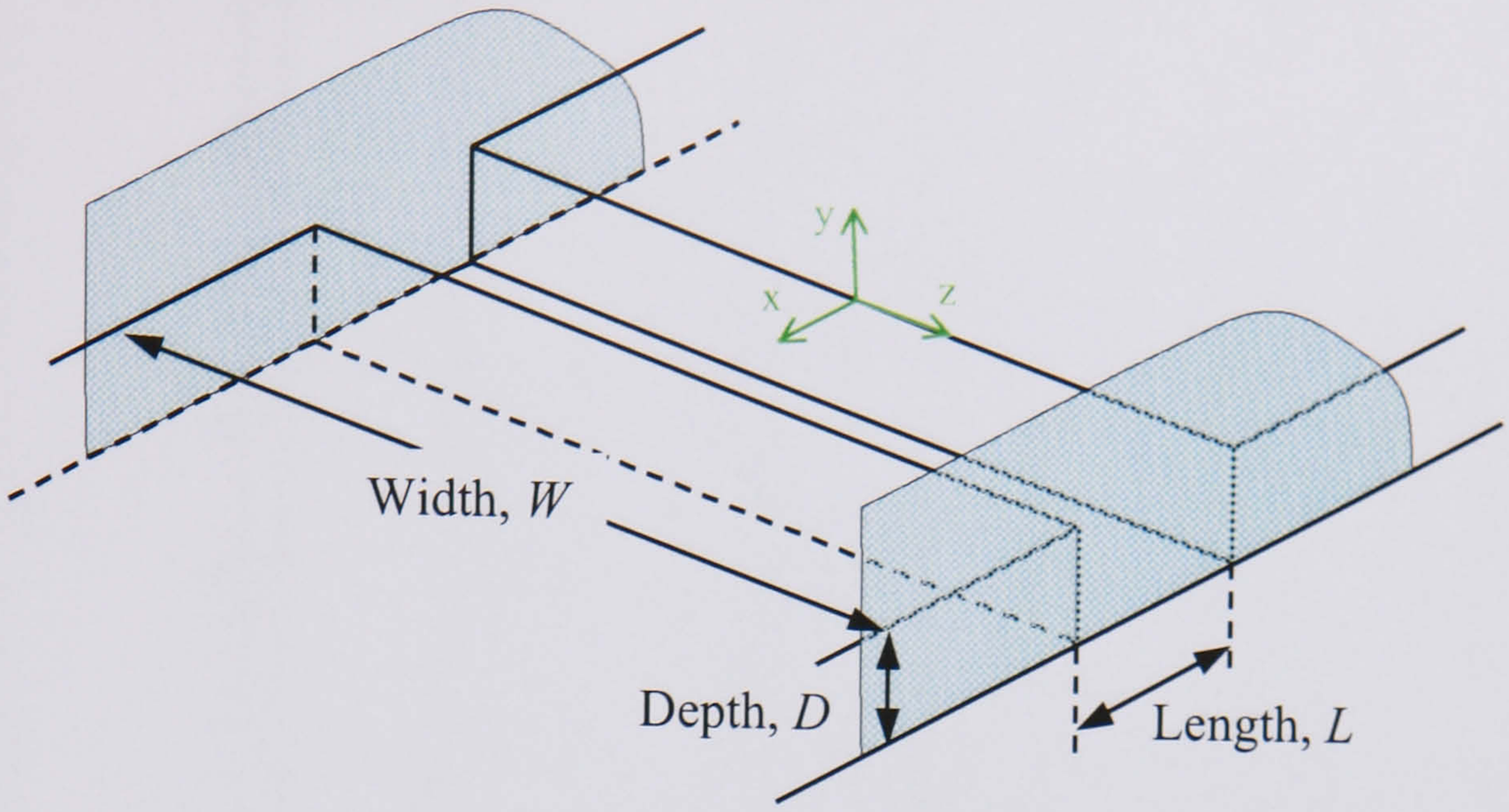

Figure 3.1. Definition of the cavity dimensions. The endplates are indicated in light blue with the origin of the axes system indicated in green.

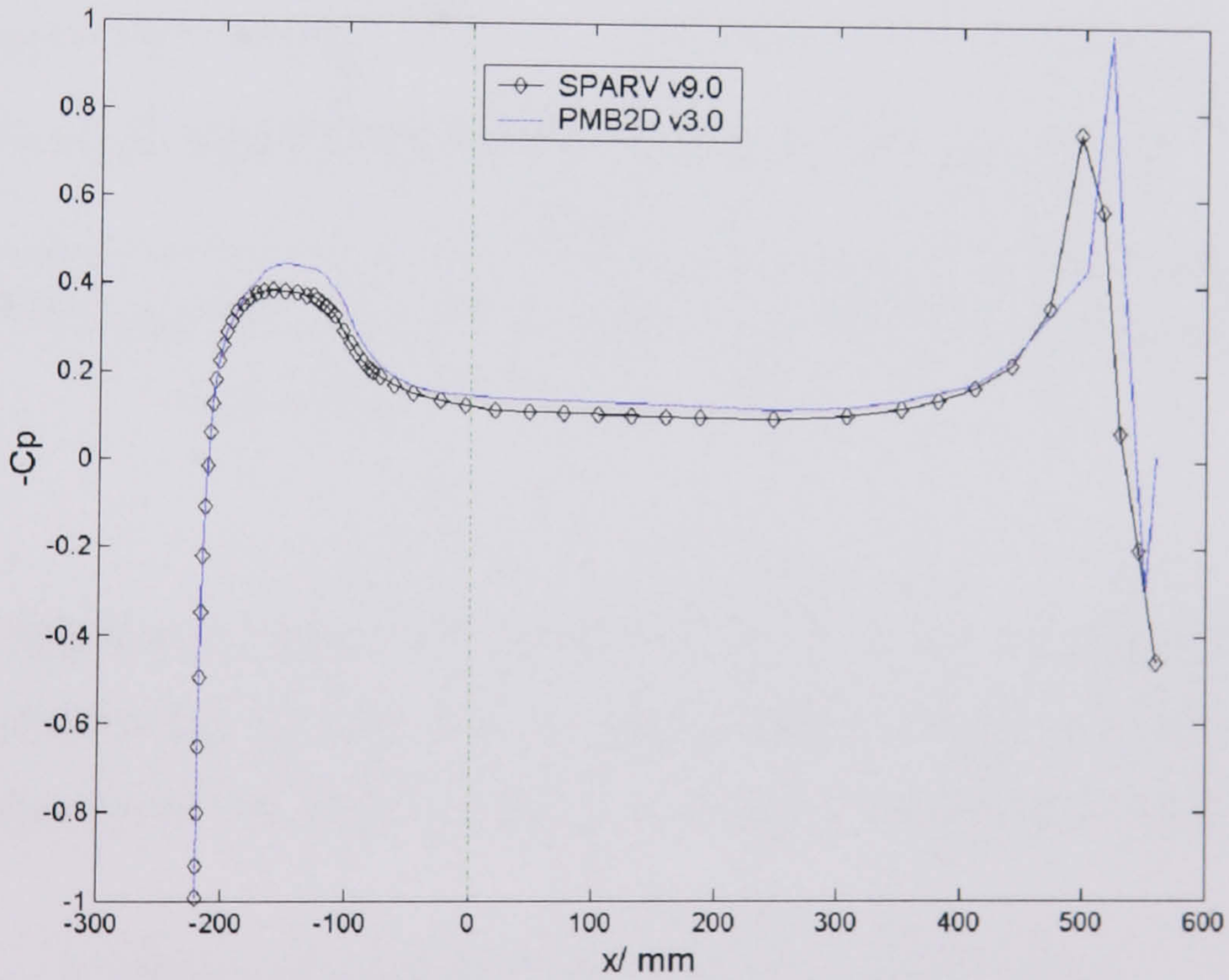

Figure 3.2. The pressures distribution around the proposed parent body for the cavity flow study. The SPARV panel method was used to quickly determine a suitable nose profile, PMB2D was then used for further verification. Both results indicate a slight pressure gradient immediately upstream of the cavity leading edge ($x = 0mm$).

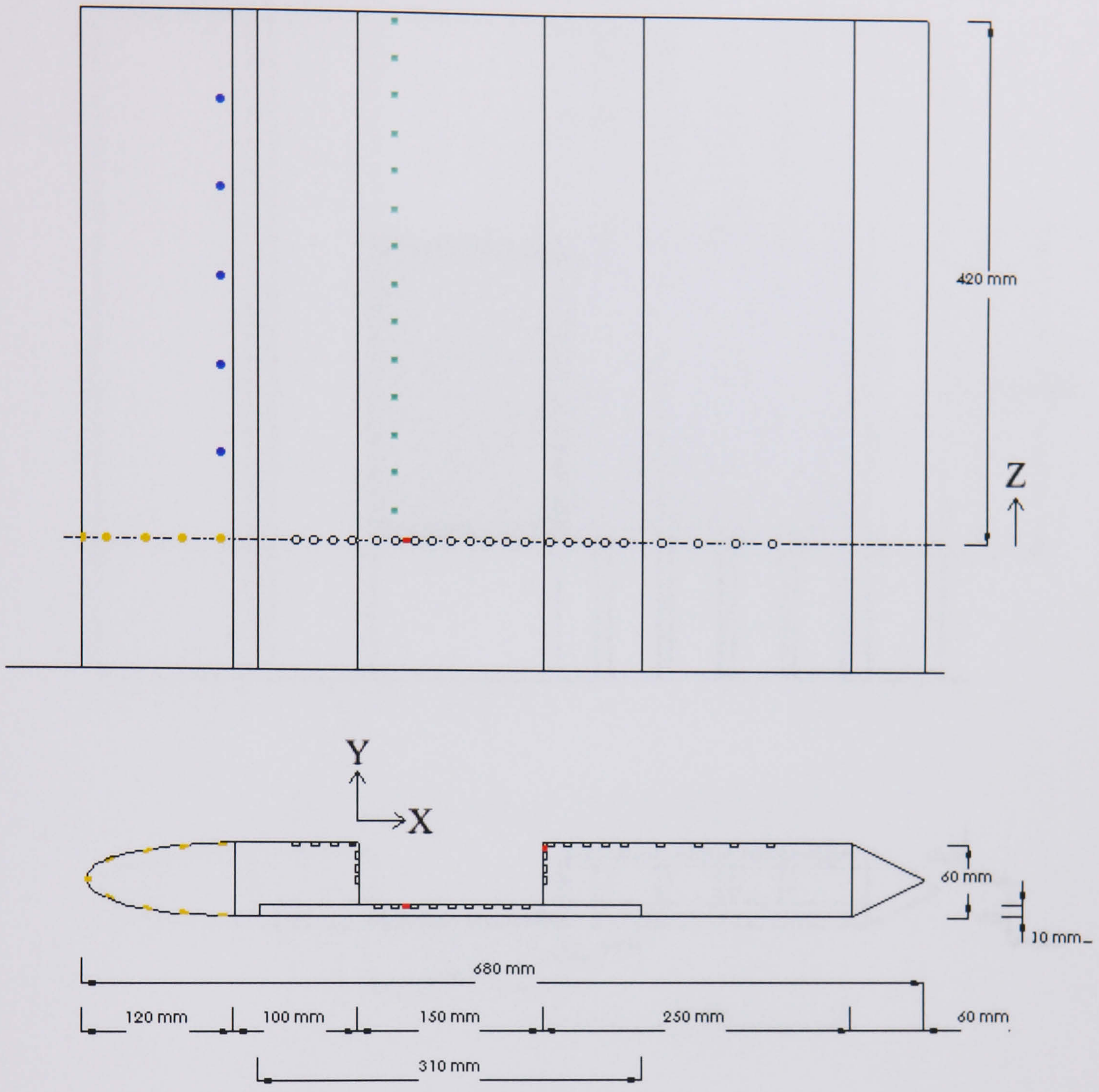

Figure 3.3 Schematic diagram of wind-tunnel cavity model showing dimensions and positions of static and dynamic pressure measurement. A plan view of model the is shown at the top and the elevation is shown to the bottom. Scale 1:6.

- : Static tappings along cavity section (CAVXY)
- : Spanwise static tappings on nose section (NSXZ)
- : Static tappings around nose section (NSXY)
- : Spanwise static tappings on cavity floor (CAVXZ)
- : Pressure transducer locations (PTL)

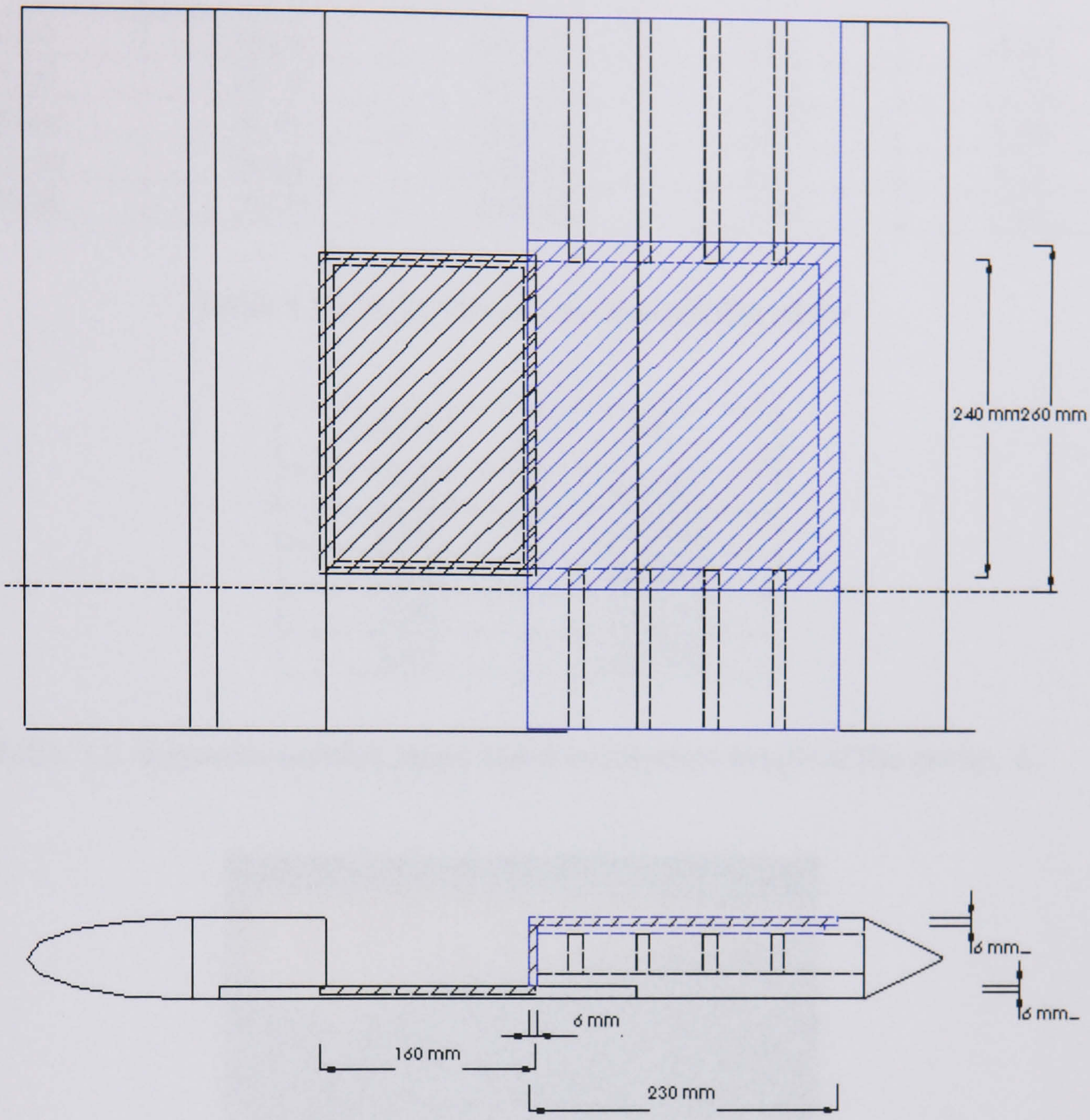

Figure 3.4. Schematic diagram of wind-tunnel cavity model used for PIV measurement. Shaded regions indicate interchangeable sections (glass or aluminium) while the blue regions indicate the moving part of the model used to modify the effective cavity length. A plan view of model is shown at the top and the elevation is shown to the bottom. Scale 1:6.

L (mm)	D (mm)	W (mm)	L/D	W/L
50.00	50.00	840.00	1.00	16.80
75.00	50.00	840.00	1.50	11.20
100.00	50.00	840.00	2.00	8.40
125.00	50.00	840.00	2.50	6.72
150.00	50.00	840.00	3.00	5.60

Table 3.1. Cavity dimensions used in this study

L/D	Re_L
1.00	94500
1.50	141800
2.00	189000
2.50	236275
3.00	283500

Table 3.2. Reynolds number range based on physical length of the cavity, L.

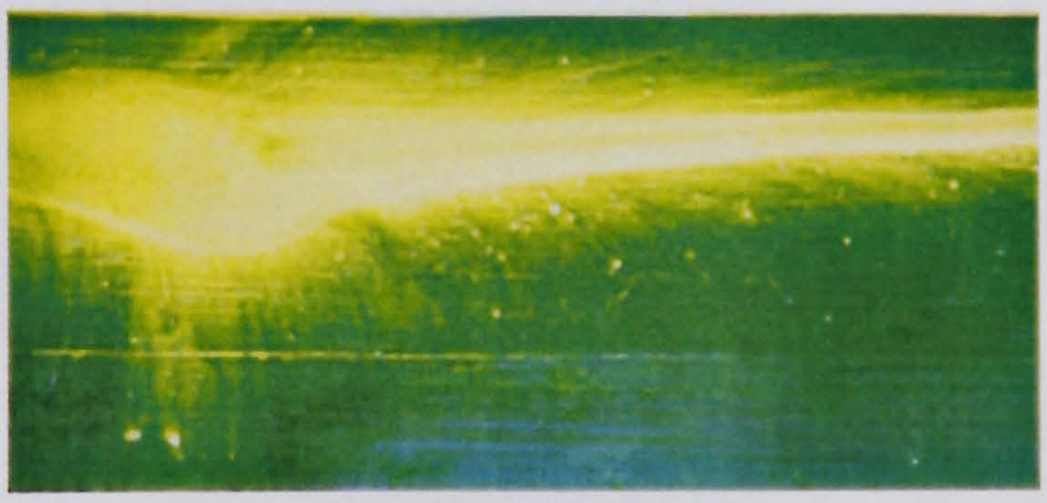

a. No endplates.

b. Endplates (300mm x 200mm).

Figure 3.5. Surface flow visualization of the cavity floor taken at the port side of the cut out. The bottom left hand (physical) coordinates of the pictures are $(-420,-150,-50)\,mm$, the flow direction is from top to bottom. (a) indicates a region of strong recirculation in the x-z plane caused by the model edge effects, (b) demonstrates better two-dimensionality by using larger endplates (shown in figure 3.6f).

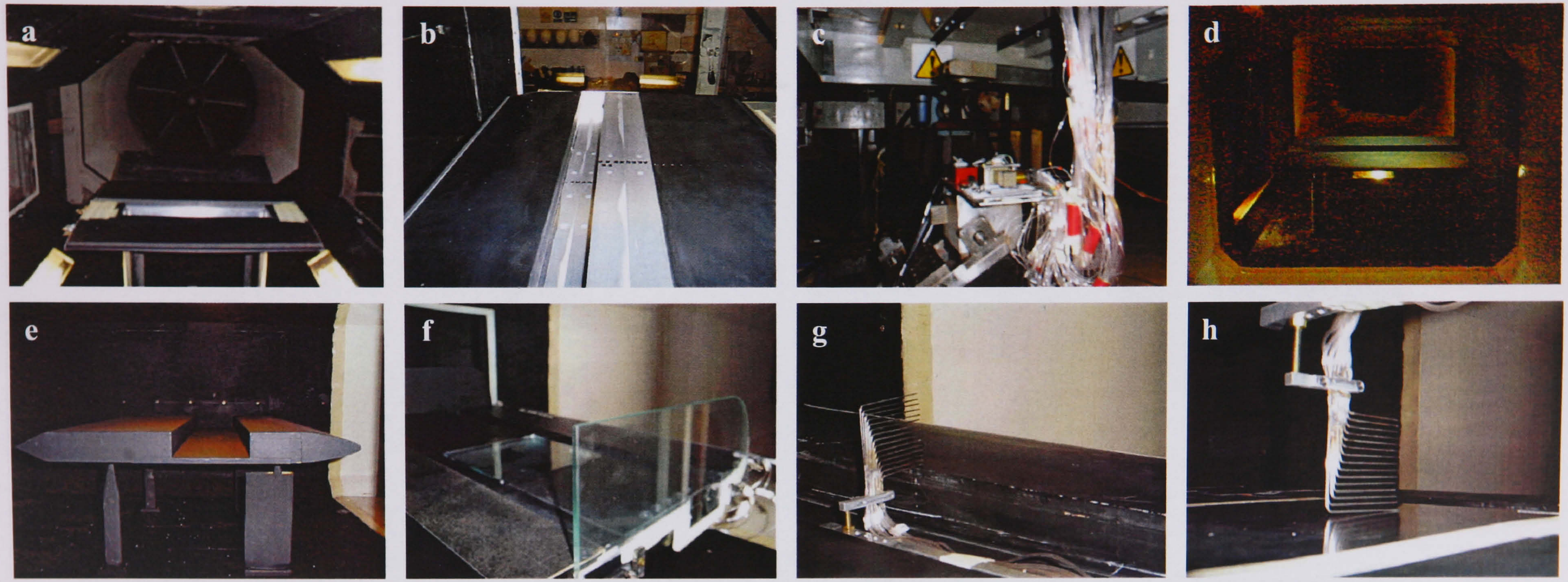

Figure 3.6. Photographs from the pressure measurement and PIV tests taken in the Handley–Page tunnel (a, b and c) and the Anatomy tunnel (d, e, f, g and h) respectively.

a. Model set-up showing typical flap angle. b. Aluminium insert required for pressure measurement tests. The transition strip along the wing nose may also be seen. c. Twin scanivalve assembly mounted under the tunnel working section recording 85 pressure signals. d. Frontal view of model set-up for PIV measurement. e. Elevation of model set-up. f. Glass endplate and glass insert required for PIV tests (looking upstream). g. Positioning of rake for boundary layer measurement (looking upstream). h. Similar measurement taken downstream on the interchangeable aluminium insert.

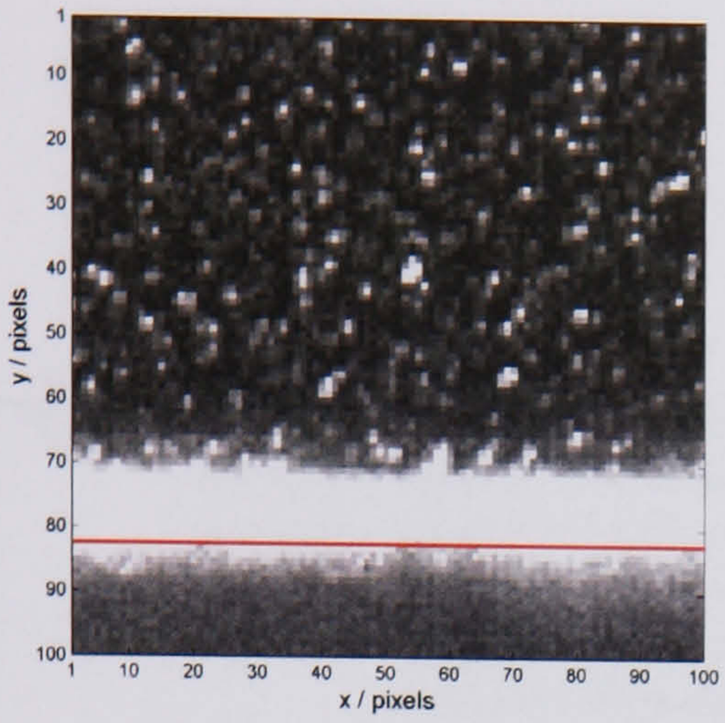

a. Region of seeded flow close to a solid (wood) boundary.

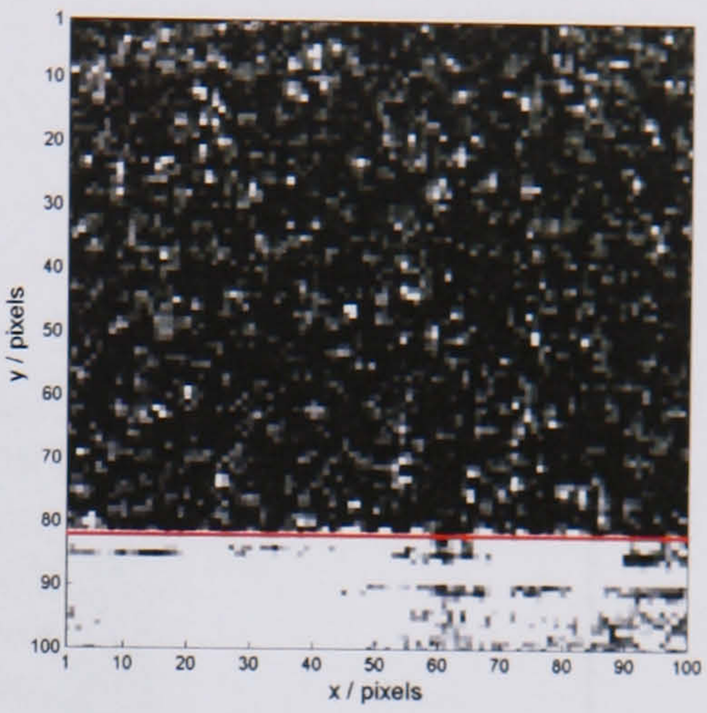

b. Exact region as in (a) with a glass boundary used. Red line indicates real boundary location.

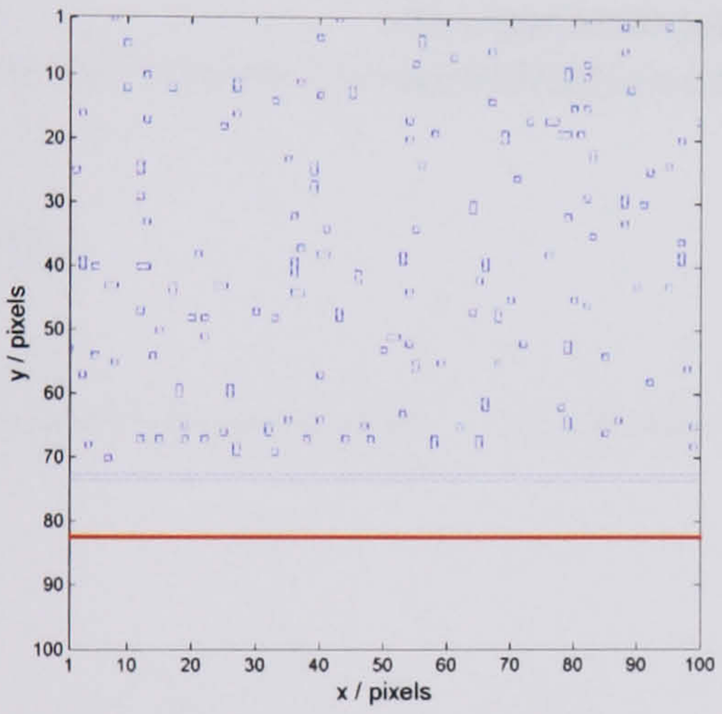

c. Edge detection and particle identification for (a).

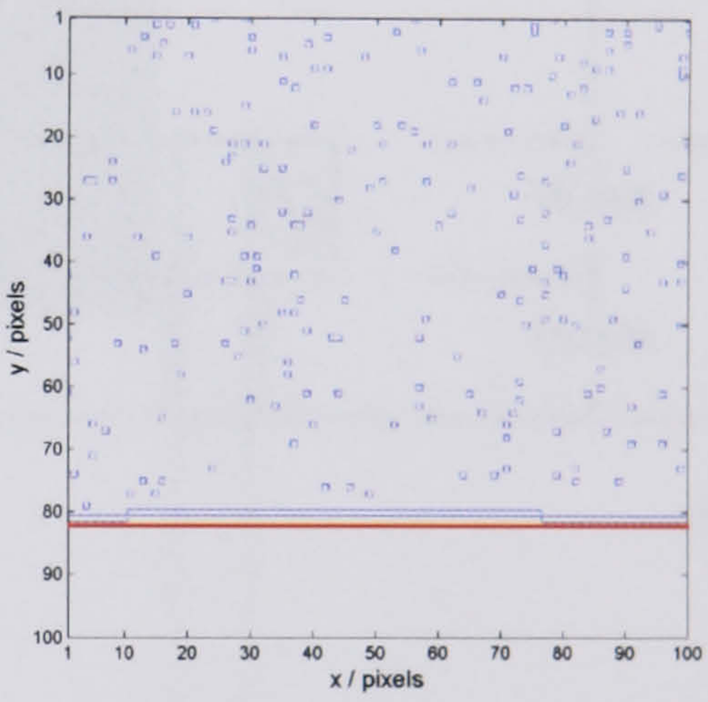

d. Edge detection and particle identification for (b).

Figure 3.7. A comparison of images captured using wood and glass for the walls of the cavity model. The location of the boundary and local particle identification is clearer when the laser reflection is reduced at the wall. Although these regions of glare may only equate from 1 to 5mm in height their presence will impose biased measurements and/or clusters of spurious data that are difficult to fix.

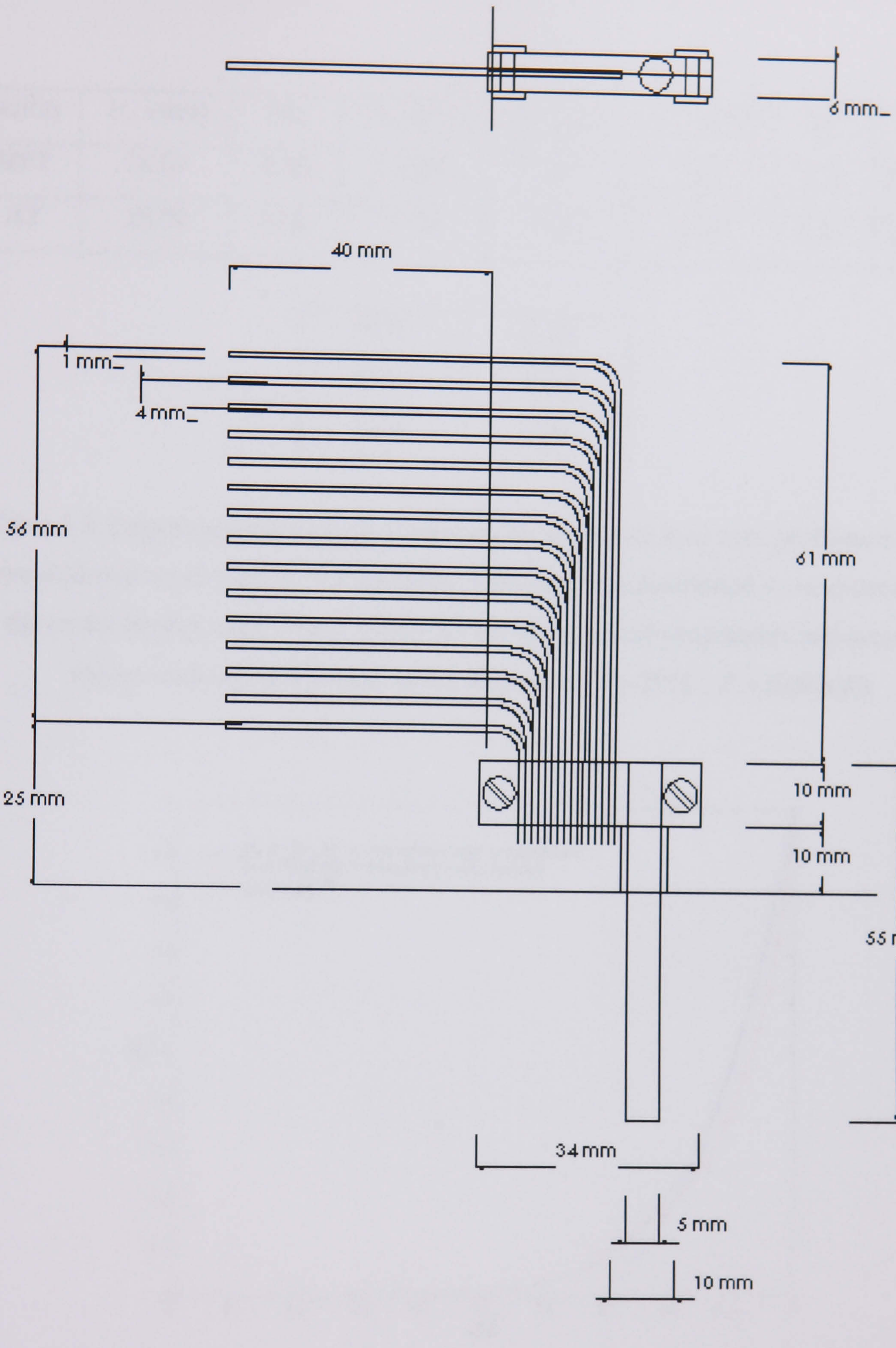

Figure 3.8. Design of a total-head probe used for measuring the upstream boundary layer profile and downstream of the cavity section. The orifice diameter (not shown) was $0.6mm$. Scale 1:1.

Facility	U_∞ (m/s)	M_∞	δ_o (mm)	δ_o^* (mm)	θ_o (mm)	H	Re_θ
HPT	28.00	0.08	13.00	1.27	1.08	1.18	2390.00
AT	28.00	0.08	11.00	1.10	0.88	1.25	1664.00

D/θ_o	δ_o^*/D
46.30	0.03
56.82	0.02

Table 3.3. Experimental boundary conditions for the cavity flow tests performed in the two different wind tunnels. The boundary layer rake was positioned 5mm upstream of the cavity leading edge. These values are based on typical temperature and pressure values recorded in the wind tunnel laboratory ($T = 20^\circ C$, $P = 1020\,mB$).

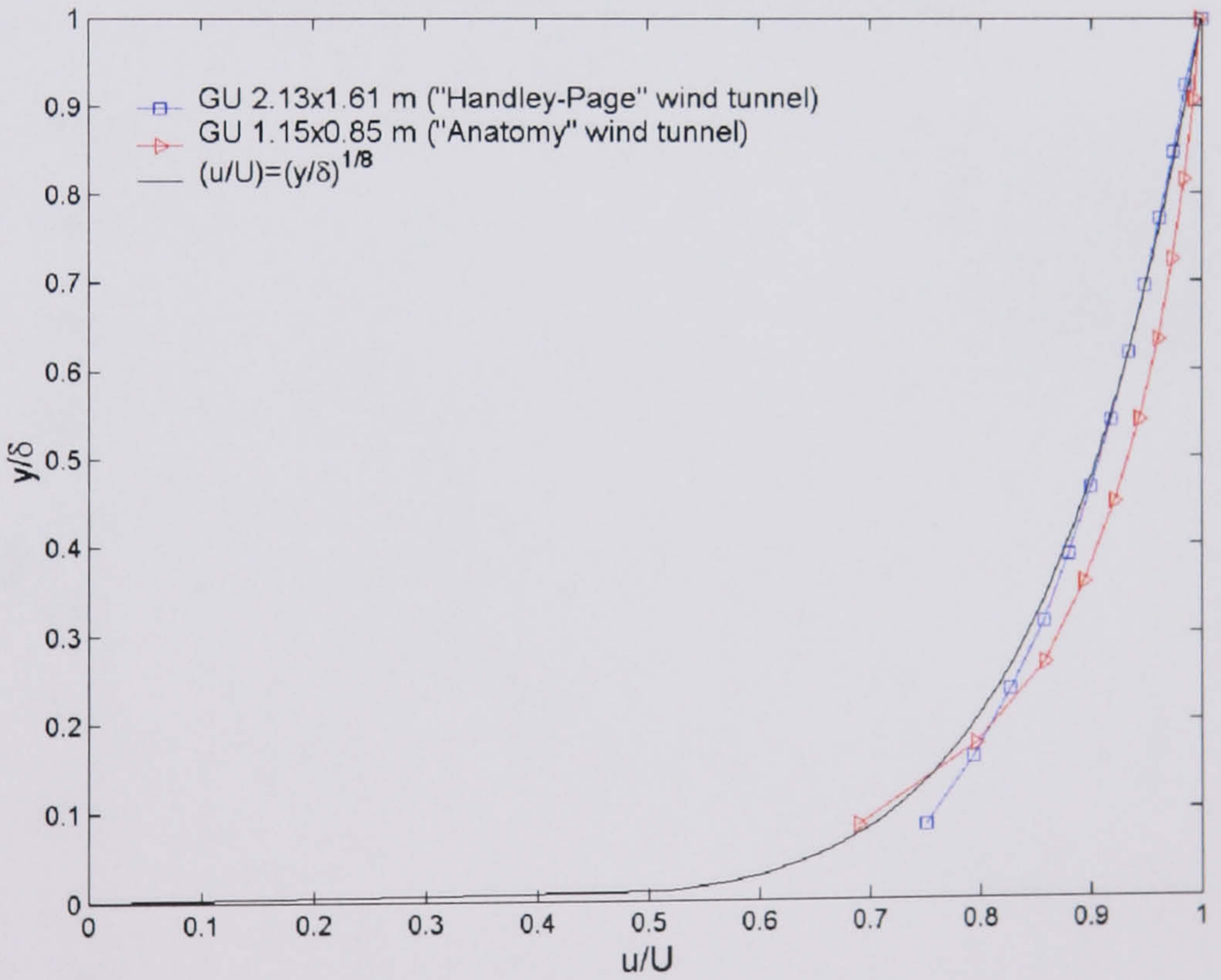

Figure 3.9. Normalized velocity profile measured 5mm upstream of the cavity leading edge. There are differences in the two boundary layer measurements although there was good repeatability for each profile.

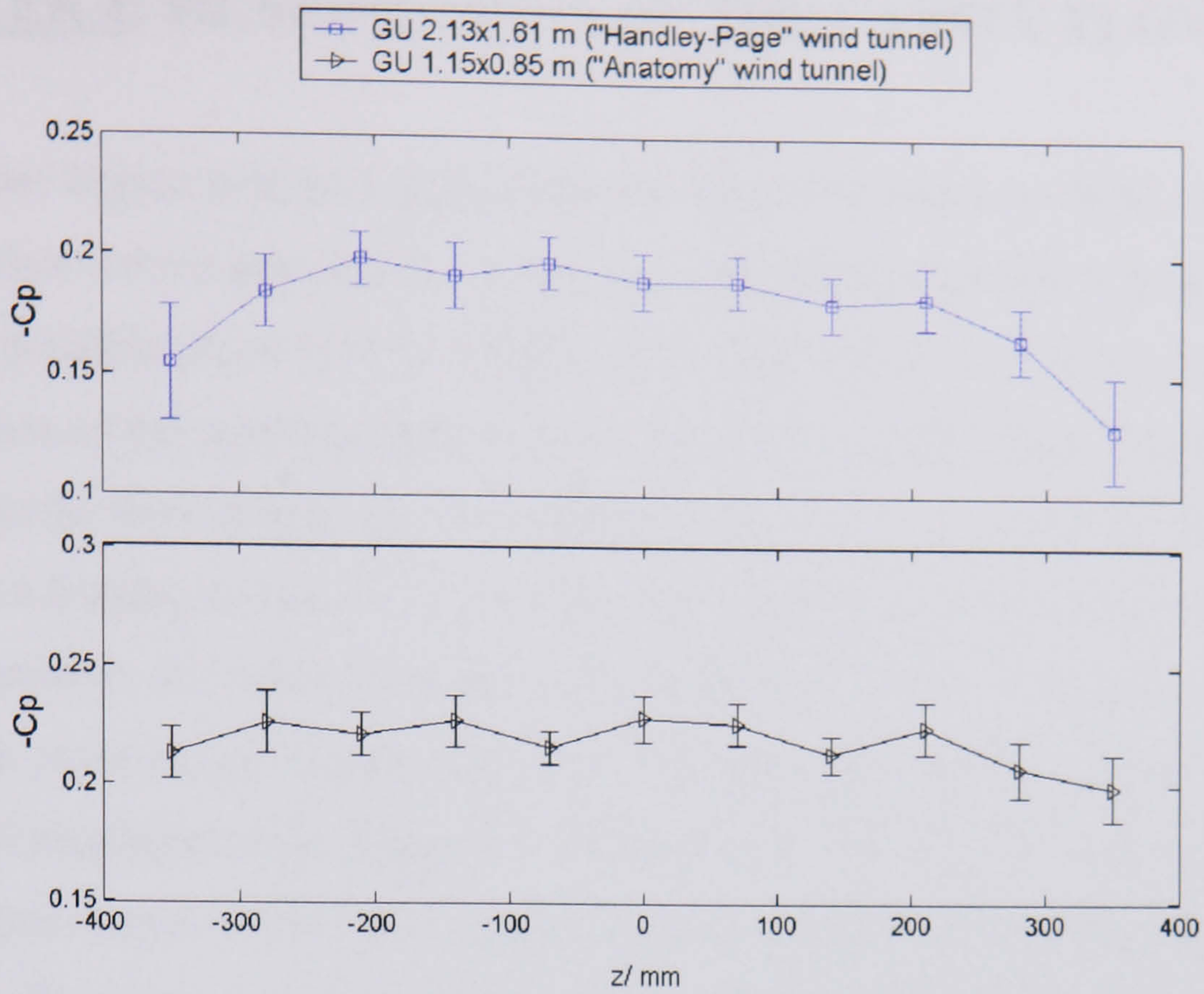

Figure 3.10. The pressure coefficient profile measured upstream and parallel to the cavity section. For both tunnel facilities the spanwise pressure gradient was acceptably two-dimensional within the region of interest (that is ±300mm). The error bars represent the deviation from the average condition.

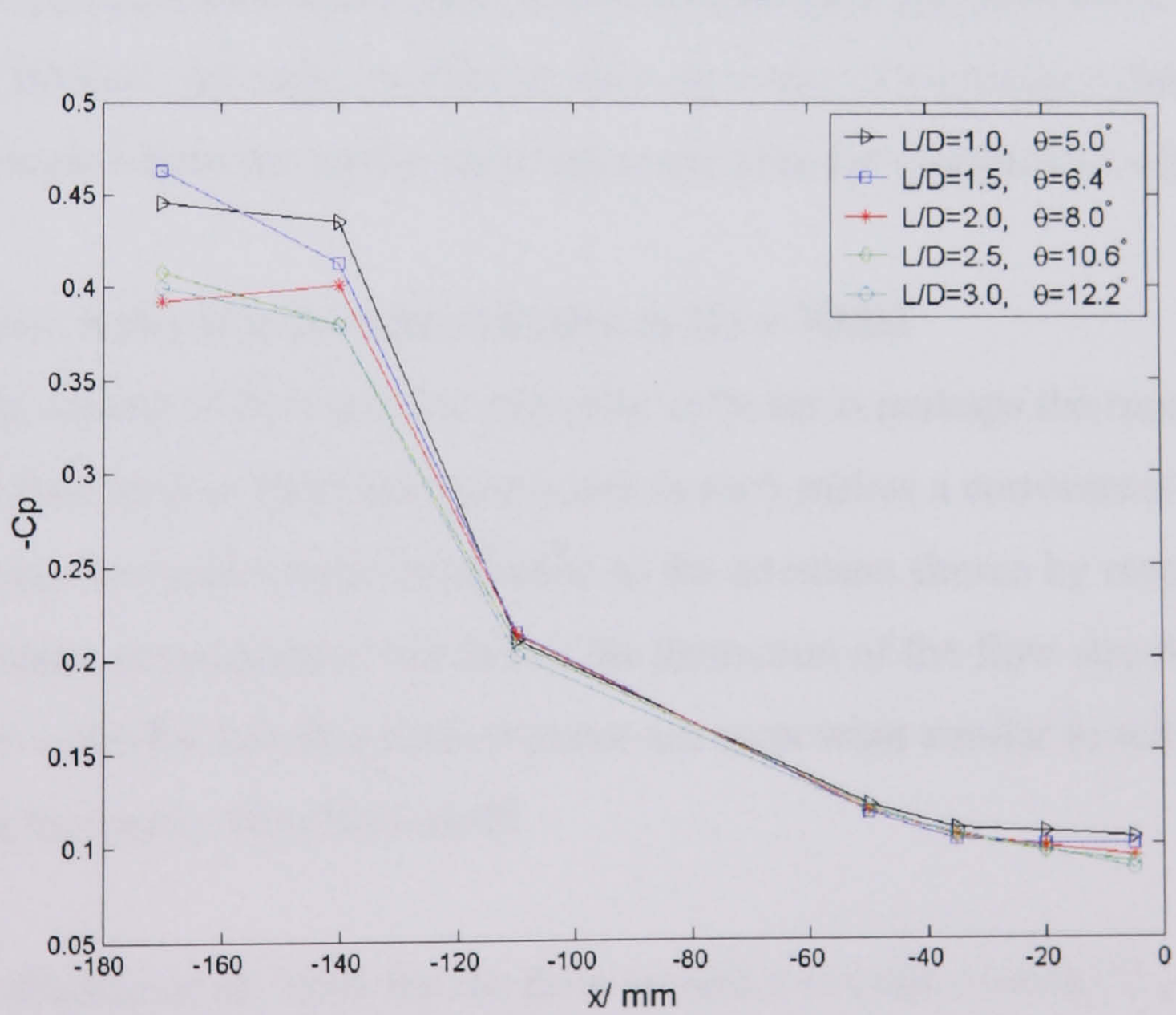

Figure 3.11. The pressure coefficient profile measured upstream of the cavity section for each cavity geometry. It may be seen that the pressure gradient upstream of the cavity section is reasonably weak and similar for each case. Slight movement of the suction peak profile over the wing nose section is noted.

CHAPTER 4: MEASUREMENT OF THE CAVITY FLOWFIELD

This chapter begins with two appropriate test cases that seek to validate the accuracy and usefulness of the correlation and tracking algorithms developed in chapter 2. The effects of possible phase biasing are also given mention at this juncture. An investigation of the spanwise effects inside the cavity is then pursued that helps to reconstruct the three-dimensional behaviour of the flow in the cavity itself. This chapter ends with a lengthy discussion of the data accumulated for the flowfield sampled in and around a number of cavities with different lengths. Of particular interest is the interaction of the cavity internal structures with the shear layer spanning the open face. In order to supplement the observations made by the PIV system both static and unsteady pressure measurements have been recorded inside the cavity. For the relevant figures the freestream velocity direction is from left to right unless stated otherwise.

4.0 Test case

The criterion required for a test case in these circumstances is that it should be a popular and well-documented flow interaction, and it should share characteristics with the main flowfield of interest. As such, the flow in the near wake of a circular cylinder and point-wise data sampled from the cavity shear layer are used for comparison with PIV data.

4.0.1 The near wake of a circular cylinder at Re = 70000

The unsteady separated flow around a circular cylinder is perhaps the most widely investigated flowfield in fluid mechanics and as such makes a convenient test for the PIV algorithms developed here. In addition to the attention shown by researchers that will allow proper measurement validation the formation of the flow structures in the cylinder near wake for this Reynolds number are somewhat similar in scale to those found within the cavity flowfield itself.

As noted by Roshko et al. 1969 for the flow around a circular cylinder it is possible for the transition from laminar to turbulent flow to occur in the wake, the shear layer or the boundary layer and is dependent on Reynolds number. For the case investigated here (that is for $\mathrm{Re} = 70000$ based on cylinder diameter, d_c) the transition occurs in the free shear layer and is more specifically termed the upper subcritical regime, Bloor and

Gerrard 1966, Hanson and Richardson 1968 and Zdravkovich 1997. An immediate transition of turbulence close to the cylinder and a short eddy formation region that produces a wide near wake characterizes this state, which immediately precedes the precritical transition in the boundary layer. There are no transition eddies in the free shear layers and it should be expected that the transition to turbulence is reduced to a spot of sudden burst in the free shear layer close to the cylinder. This will take place at approximately $0.02 < x/d_c < 0.29$, from Bloor 1964 where x is measured from the cylinder centre.

A simple illustration of the model set-up and nomenclature used is shown in figure 4.1. The cylinder was positioned horizontally and in the centre of the wind-tunnel test-section (***AT***) and was constructed from a smooth Perspex tube with diameter 80mm and width 400mm, thus $W_c/d_c = 5$ with the freestream speed set to 13m/s. The cylinder was held on a cantilever (with no endplates) away from the main supports to reduce glare and optical obstruction while flowfield measurement were taken in the spanwise centreline plane. The turbulence intensity in the tunnel was estimated to be 0.34% for this test and the blockage was low (<4%). 250 image pairs of the near wake were captured in the downstream range $0.25 < x/d_c < 0.75$ such that quantitative and qualitative measurement validation could be sought from Maekawa and Mizuno 1967, Hanson and Richardson 1965, 1968 and Toebes 1967, 1969. It is expected that there will be two well defined regions in the near wake, a turbulent region (extending to approximately $1.5d_c$) and an intermittent free shear layer bounded within a predefined region.

Figure 4.2 indicates a typical instantaneous measurement obtained from the study. In this instance it can be seen that the thin shear layer (with high initial vorticity) is oscillating laterally in the rhythm of eddy shedding (indicated from the superimposed vectors). Rapid dissipation of the free shear eddies are also observed which is caused by the freestream entrainment into the progressively thicker shear layer. The mean characteristics of the near field region are in qualitative agreement to that presented by Hanson and Richardson 1968. The rms of the image set is calculated and the results are shown in figure 4.3. The expected boundary of the intermittent shear layer as calculated by Maekawa and Mizuno 1967 is included in the plot and it can be seen that this

contains the maximum amplitude rms values for the current study. Further qualitative agreement with the rms values from Hanson and Richardson 1968 is also found. The high rms values at $x/d_c \approx 0.3$ and $y/d_c \approx 0.5$ may indicate the burst to turbulence as described by Bloor 1964 although measurements taken further upstream indicate that this area of high rms extends between $0 < x/d_c < 0.3$ (for the same y-station). This long smeared region of unsteadiness is characteristic of transition. The high rms values indicated to the far right hand side of the plot are caused by the increased unsteadiness in the v-component of velocity eventually culminating in the (steady-state) closure of the near wake prior to $1.5d_c$.

From the study of Toebes 1967 and 1969 ($\mathrm{Re} = 68000$ and further data from Hanson and Richardson 1965) a comparison between the accumulated statistics from PIV data (correlation and tracking) and hot-wire data was made. The position of simultaneous hot-wire measurement made by Toebes 1969 are indicated as white filled dots in figure 4.2. It may be seen from figure 4.4 that there is good agreement between the two sets of results and the amplitude of fluctuation is particularly well measured by the PIV system. A small deviation from the peak rms values between the point probe and PIV data is shown in the plot and cannot be fully accounted for. One possible explanation is that the upper subcritical regime is seen to be much more three-dimensional than the preceding regimes and as such spanwise variation in the burst to turbulence is possible and perhaps even random, Werlé 1974 and Yokoi et al. 1993. Toebes 1969 used a cylinder with $W_c/d_c = 12$ and as such the spanwise behaviour at the cylinder centreline may differ slightly between the two experiments, causing a slight shift of the peak rms values.

Because the hybrid BTT tracking method is dependent on local seeding concentrations and correct tracking the increase in spatial resolution it offers typically reduces the number of useful samples it yields. For the current case it was possible to accumulate 170 samples from the 250 image pairs captured and as such demonstrates that a close inspection of statistical confidence must be maintained. In this instance it appears that the increase in spatial resolution provided by the hybrid BTT scheme has reduced the bias error inherent in the typical correlation (ITDWO-FFT-SDCPIV) resulting in a better-defined rms peak and augmented amplitude.

4.0.2 The random sampling assumption

The normal efficient mode of operation for the image capture phase of the PIV system is best described as intermittent-cinematic. Essentially this means that the image pair accumulation is not truly random in process but is comprised of a series of random capture bursts of 30 image pairs taken at 10Hz (laser flash lamp signal). The issue then exists that phase biasing of the accumulated image pairs is possible and further investigation should be pursued.

It was found that the best procedure to dispel the issue of phase biasing was to procure two individual sets of data each of which 250 samples in length, one of which is truly randomly sampled (camera and laser triggered at an arbitrary time) and the other sampled in the more convenient manner described above. A direct comparison of the statistical and ensemble-averaged properties of this data should be a sufficient indicator on the degree of convergence between the two. In the case of the near wake of a circular cylinder figure 4.3 represents the rms for an intermittent-cinematic capture and figure 4.5 represents the difference in measured rms between that data and the measured rms using a truly random capture criterion. The predicted Strouhal number for the upper subcritical regime of a circular cylinder is roughly 0.21, which yields a frequency of instability of approximately 32 Hz (this puts the time spacing of images acquired for the intermittent-cinematic series, 0.1s, close to a multiple of shedding). However in this case at least the comparison between the two data ensembles does not seem to deviate in a fashion that represents phase biasing (the local levels of rms are very similar with no localized reductions). The maximum rms difference between the two data sets is approximately 0.04, which falls well within the error limits for the confidence interval stated, as discussed in section 2.7.

For the case of flow over a cavity the instability frequency in the shear layer is much higher than that of the circular cylinder, while the frequency of oscillation inside the cavity is much lower. So although in principle it appears that phase biasing is unintentionally very difficult to maintain another comparison above was made for $L/D = 2.0$. This is included in section 4.3.

4.0.3 Point-probe measurement of the cavity shear layer

A point-probe measurement of the shear layer developing across a cavity for $L/D = 2.5$ was made and compared to the statistical PIV data obtained for the same case, using 250 instantaneous image pairs. Two stations in the shear layer were chosen at $x/L = 0.16$ and $x/L = 0.4$ and a hot-wire probe was passed from the freestream into the cavity through 21 positions (with 2mm increments), as shown in figure 4.6. The data was taken at the centreline of the model ($z = 0\,mm$) and the probe was mounted onto a traverse by two holes drilled in the cavity floor. The hot-wire recorded 2 blocks of 4096 samples for each point, which is an order of magnitude greater than the PIV sample size. The PIV image data used for comparison was captured using a magnification of 0.12, an f-number of 5.6 and was correlated in the normal fashion (ITDWO-FFT-SDCPIV) and as such it is typical of all the cavity flowfield data presented herein. The Reynolds shear stress $\langle u'v' \rangle$ is used for comparison (the sample average is indicated by the brackets $\langle\ \rangle$).

At the first location measured ($x/L = 0.16$) it can be expected that the Kelvin-Helmholtz instability waves will be evolving into a periodic array of compact streamwise vortices moving at some proportion of the freestream velocity. This means that the Reynolds shear stress profile through the shear layer will measure a local peak at the mean position of the stagnation streamline where the vortex roll-up is occurring (typically the height of the leading edge corner). Figure 4.7a presents the measurement comparison for this position where it can be seen that this is the case (normalized with respect to the freestream speed). In comparing the two data sets it appears that the PIV system has overestimated the point of maximum Reynolds stress. This is perhaps expected since the shear layer roll-up is so thin and as such not sufficiently (spatially) measured leading to bias error in the correlated result, as briefly discussed in section 2.7. At the second position of point measurement ($x/L = 0.4$) the length scales of the flow will be approximately doubled (from the general similarity property) and a better-sampled profile from the PIV system is expected. From figure 4.7b it can be seen that the PIV data does match the hot-wire data much more closely while the amplification and growth in the shear layer is represented by the increase in Reynolds stress. The degree of similarity between the two data sets does indicate that it is possible to obtain very accurate statistical information using a carefully set-up PIV system of limited

sample depth. The movement of the captive vortex in the cavity itself causes the shear stress profile discernable below the shear layer.

It would appear from this representative case that proper measurement of the developing free shear layer will not be completely possible in this study. Instead, what will be found is good statistical measurement after the initial separation region of the boundary layer, estimated to be $x > 20mm$. The entrainment of the shear downstream of this point will provide larger scales and thus better measurement.

4.1 Observations of the spanwise structure in the cavity

From the observations of Maull and East 1963 and Rockwell 1980 it seems possible that there will be a transverse instability wave present within some of the cavity configurations included in this study. It has not yet been fully investigated whether or not a fully turbulent shear layer at separation can give rise to organized transverse waves in the cavity, Wyganshi et al. 1979 and Rockwell 1983. If they do exist these spanwise effects have important consequences for structural loading and heat transfer, while it is important to quantify the encroachment of such effects onto the x-y plane data that is presented in the remaining sections.

4.1.1 Oil flow and pressure measurement

The cavity model was mounted in the wind tunnel (***AT***) in the normal fashion, as shown in figure 3.6 d and e. From initial oil flow investigations it was immediately apparent that for some cases the flow was not two-dimensional in the cavity but was instead of a regular three-dimensional nature. Figure 4.8 shows some oil-flow visualization taken on the cavity floor with $U_\infty = 28\,m/s$ and various L/D and W/L ratios (width reduced by inserting pairs of wooden blocks into the cavity with periphery sealed). In every case a collection of oil has pooled at the location of separation of the primary vortex from the cavity floor and it can be seen that this line is wavy, indicating a spanwise variation in separation position. It is also apparent from these pictures that the spanwise wavelength is approximately equal to the cavity length (as indicated).

The oil flow patterns recorded were in qualitative agreement with the measured spanwise pressure profiles, which was taken in both wind tunnel facilities and good

repeatability was found. Pressure data alone was then collected to estimate the spanwise behaviour in the flow. Some of the data collected is included in figure 4.9 and 4.24 for a cavity with $L/D = 1.5$ and variable width and it can be seen that the transverse wavelength may still be well-estimated using static pressures. The lengthwise pressure data is obviously affected by the spanwise cellular gradient. For the five cases of interest here (L/D from 1.0 to 3.0) the pressure transducer on the cavity floor indicated a pressure coefficient of low frequency and large amplitude that could correspond to the movement of the transverse structure. In contrast there was no discernable movement in the separation line using the oil flow visualisation, the static Cp profiles are shown in figure 4.10. The amplitude of these pressure coefficient values appear small since they are normalized using the tunnel static pressure, although their influence on the primary vortex structure may be considerable. It was noted that for two of the cavity configurations ($L/D = 1.5$ and $L/D = 2.0$) the transverse wavelength is present and approximately equal to the cavity length. A higher-pressure location in the wave is indicative of compression to the primary vortex, while a lower pressure indicates an expanded primary vortex. A schematic diagram is included in figure 4.11 for illustration. It appears from the results that the occurrence of three-dimensional behaviour is in agreement with the observation of Maull and East 1963 (where the Reynolds number is comparable), in which transverse waves are observed within the range $1.2 < L/D < 2.2$. It should be noted that these results were repeatable in both wind-tunnel facilities (***HPT*** and ***AT***) over a period of several months and the presence of the static pressure orifices along the nose section was not seen to affect the spanwise development.

4.1.2 The transverse instability

It appears that the most likely origin of this spanwise cellular behaviour is from some organisation and/or amplification of instabilities from the shear layer. The spanwise extent of large scale features (that is streamwise vorticity) for an initially laminar mixing layer have been investigated on a number of occasions, see for instance Brown and Roshko 1974, Browand et al. 1980 and Huang and Ho 1990. It appears that the fluid entrained in the turbulent mixing layer by the large two-dimensional (spanwise) structures actually causes very little mixing. Konrad 1976 and Breidenthal 1980 observed that the level of mixing increases drastically as the onset of three-dimensional

activity begins in the shear layer. In accordance with this Miksad 1972 reported that for a free shear layer the onset of spanwise activity coincided with a noticeable decay in fundamental mode energy, thus indicating a spanwise redistribution of energy at the instance of nonlinear disturbance growth. From this it appears that shear layers exist as complex three-dimensional structures. Using a three-dimensional model for a transitional free-shear layer Jimenez et al. 1985 proposed that both spanwise and streamwise vortical structures can co-exist, and some experimental agreement was found by Daily et al. 1984. The origin and the evolution of the streamwise vorticity remains the topic of further research.

In a study of three-dimensional free shear layers Lasheras et al. 1986 used Laser Induced Fluorescence (LIF) to record the qualitative spanwise profiles of the mixing layer. From this he was able to determine that in the braids of the primary spanwise shear layer roll-up (see figure 4.11), well-organized counter-rotating pairs of streamwise vortices of approximately similar strengths existed. Numerical calculations by Corcos 1979 indicated that this streamwise vorticity would evolve into concentrated round vortices for certain values of strain. Additional numerical modelling by Corcos and Lin 1984 identified the concentration of streamwise vorticity as the main contributor to the mixing transition phase of the shear layer, which appeared to be in agreement with experimental observations of Jimenez et al. 1979 and Bernal 1981. It seems therefore that in order to elucidate on the cellular structures that exist spanwise along the cavity some quantitative measurement of the flowfield streamwise vortical structures must be made.

4.1.3 PIV measurement of the spanwise plane

A rudimentary PIV test was performed to measure the flow velocities across a number of spanwise planes within the $L/D = 1.5$ cavity. For this test only the cavity model was mounted from floor to roof in the wind tunnel such that the laser light sheet could illuminate the x-z plane while being able to traverse through a number of y-elevations, as shown in figure 4.12. Spanwise pressure measurements indicated that the cellular structures were maintained for this model orientation. The laser light sheet was thickened to 3mm and the inter-pulse delay on the laser head was suitably reduced such that any out-of-plane motions were minimized. From the initial results in figure 4.13 it

appears that the spanwise pressure oscillations are caused by a channelling of a high-velocity core being re-circulated back across the cavity floor after interaction with the cavity rear-bulkhead. Calculation of these average velocities was performed at each spatial coordinate by considering the average of the two particular instantaneous velocities for that plane, that is:

$$\langle u \rangle = \frac{1}{N}\sum_{i=1}^{N} u_i(x,y) \ , \ \langle v \rangle = \frac{1}{N}\sum_{i=1}^{N} v_i(x,y) \ , \ \langle w \rangle = \frac{1}{N}\sum_{i=1}^{N} w_i(x,z) \qquad [4.1]$$

where this ensemble average is taken over a number of samples, N. This jet edge type of interaction with the cavity rear wall is later seen to instigate and modulate the primary recirculation in the x-y plane. It appears that this interaction at the rear wall is transmitting instability from the shear layer into the transverse direction of the cavity.

Measuring a number of other y-planes in the cavity reaffirms this observation, as shown in figure 4.14. A progressive cutting of the cavity from the floor to the shear layer indicates that pairs of counter-rotating vortices are formed in the mid-plane of the cavity ($y/D = -0.5$) from vorticity that is cast into the cavity from the shear layer itself. The dashed line drawn across each plot highlights the line of symmetry for this contra-rotating vortex pair and it seems to correspond to the position of deflection symmetry in the shear layer ($y/D = -0.1$). Further investigation indicated that these pairs of counter-rotating vortices were repeated along the cavity width as expected and in each case their vorticity was equal and opposite in strength. Each vortex in the pair corresponds to a positive or negative strain from the shear layer created by the spanwise vortices. For a typical free shear layer the spanwise non-uniformities decay in the downstream direction because the cores are continually rotating as they are being convected. In this instance the interaction with the cavity rear face instigates a pattern whereby the shear layer streamwise vorticity is being fed into the cavity structure, as shown in figure 4.15. With this organized periodic mass-flux into the cavity a steady cellular structure may exist, as opposed to the more erratic nature observed for free-shear layers; see Ashurst and Meiburg 1988 for instance. Unsteady pressure measurement on the cavity floor indicates that these vortex structures exhibit a second frequency that is similar to that measured in the shear layer spanning the cavity face, thus giving credibility to its proposed origin.

Metcalfe et al. 1987 showed that spanwise instability modes that are triggered by upstream non-uniformities in the spanwise vorticity are convected with the flow and grow at similar rates as the two-dimensional modes. In addition to this Lasheras et al. 1986 noted that even though the location of the first manifestation of the streamwise vortices varied, they were always found on the braids between spanwise vortices. Recalling the feedback loop described by Rockwell et al. 1978 an interaction of vorticity concentration at the downstream corner causes shear layer fluctuation at the upstream corner. Therefore the braid portion of the shear layer is fixed as the cavity length/mode number, and with similar amplification rates in both planes the transverse wavelength will then adopt a similar wavelength disturbance. This also suggests the shear layer interaction at the impingement edge will vary in the spanwise direction, which affects the feedback. Spanwise differences in the x-y plane measurements are then expected.

Figure 4.16 presents the calculation of the Reynolds shear stress (as defined in equation 4.2) for the mid-plane of the shear layer spanning the cavity face ($y/L = 0$). From this it appears that at the rear cavity face the small-scale spanwise velocity correlation is organized around the symmetry point for each contra-rotating vortex pair. This type of fluctuation localization was observed spanwise across the cavity face for each of these corresponding saddle positions. This is in agreement with the observations of Bernal et al. 1981, Bernal and Roshko 1986 and Jimenez 1983 who realized a time-averaged velocity 'corrugation' across the free shear layer. The Reynolds stress for $y/L = 0$ and $y/L = -0.8$ were found to be of a similar magnitude and localization, while the planes measured in-between these was much lower ($\left(\langle u'v' \rangle / U_\infty^2\right)_{\max} \approx 0.001$). Aided with the knowledge of the mean flow behaviour it appears that the rear wall interaction with the shear layer is transmitting fluctuation directly down, onto and across the cavity floor. The instability is then being propagated (weaker) back up into the cavity by the motion of the primary recirculation structure.

$$\langle u'v' \rangle = \frac{1}{N}\sum_{i=1}^{N}\left[u_i(x,y) - \langle u(x,y) \rangle\right]\left[v_i(x,y) - \langle v(x,y) \rangle\right] \qquad [4.2]$$

It was also found that placing a small vortex generator upstream along the nose section could change the origin of these vortex pairs. Although this is not to say that upstream non-uniformities are responsible for the generation of streamwise vorticity. The origin

of the instability mode is still the topic of further research although an intrinsic instability in the shear layer vortices appears to be the most commonly accepted origin, Nygaard and Glezer 1990 and 1991 and references therein.

Some irregular transverse oscillation is measured for $L/D = 1.0$, as noted from figure 4.10. In this instance it is probably the case that the cavity length is not sufficiently long to facilitate the level of strain required in the shear layer braid to develop a strong three-dimensional motion, Corcos'mechanism 1979. This is not the case when $L/D > 2.2$ where it appears that the transverse instability disappears, and a more two-dimensional pressure profile is measured on the cavity floor. Huang and Ho 1990 have shown in their study that the shear layer vortex merging process is seen to suppress the activity of the streamwise vortices since this causes a marked reduction in the positive and negative straining rates between the (spanwise) vortex cores. These results have also been numerically verified by Corcos and Lin 1984 and Metcalfe et al. 1987. This may then indicate that the strength of the cavity feedback loop is attenuated for these longer cavities. This seems possible since an increase in Reynolds number to $\mathrm{Re}_\theta = 3841$ during testing was seen to re-establish the cellular pattern on the cavity floor for $L/D > 2.5$. Another possibility is that the distance between the spanwise vortices is such that the streamwise vorticity is imported into spanwise cores themselves, Lasheras et al. 1986. If this were the case then the transverse instability would be more weakened by a vortex escape at the cavity trailing edge. Further investigation is required to vindicate these points. It is the case however that such three-dimensional instability is inviscid, Benney and Lin 1960, but the actual formation of the spanwise cellular structures may be Reynolds number dependent.

4.1.4 Effect on the x-y plane data

The remaining issue is to determine the effects this three-dimensional flow structure will have on the x-y plane data to be looked at in this study. It appears that for $L/D = 1.0, 2.5$ and 3.0 at the Reynolds number of interest, the flow is typically two-dimensional and any plane close to the mid-span of the model would suffice for proper measurement. For the remaining two scenarios ($L/D = 1.5$ and 2.0) evidence suggests that the through plane component of velocity (w) for the x-y plane data will be dependent on the z-station of the laser light sheet. For instance figure 4.17 shows two

ensemble averaged spanwise vorticity results in the cavity at two different z-locations for $L/D = 1.5$. These correspond to primary vortex expansion (4.17a) and compression (4.17b). The ensemble average vorticity is calculated according to equation 4.3.

$$\langle \omega \rangle = \frac{1}{N} \sum_{i=1}^{N} \omega_i(x, y) \qquad [4.3]$$

In figure 4.17 the contours are chosen in a manner such that the shear layer vorticity does not dominate the colour mapping. It remains evident that there is a spanwise distortion in the shear layer spanning the cavity face (as expected). For the case of primary vortex expansion (4.17a) the captive recirculation fills the majority of the cavity, which will have a prominent effect on the amplification growth of the shear layer. For the case of primary vortex compression (4.17b) a stronger jet-like flow into the cavity at the trailing edge is observed and it carries with it more vorticity. This transported vorticity has a more pronounced effect over the cavity floor and along the cavity front wall, which confines the primary vortex to a smaller area of recirculation making the primary vorticity region stronger. For experimental convenience it was decided that $z = 40mm$ would be taken as the location for x-y plane data for all cases. This location corresponded closely to the average spanwise pressure coefficient values for all cases, including those that demonstrated steady cellular behaviour.

It is not satisfactory to try and explain the three-dimensionalities present in the cavity flowfield using a two-component PIV measurement that is orientated in planes both perpendicular and parallel to the freestream direction. For a more thorough investigation a stereoscopic PIV system is required. This allows simultaneous viewing with two cameras to reconstruct all three components in the planar region; see Prasad 2000 for instance. A more rigorous interpretation of the results can then be made without the inference that follows two-component measurement and would impart some information about the orientation of these vortex pairs inside the cavity. For instance figure 4.14 ($y/D = -0.5$) demonstrates a re-reversal of the flow at $x/L = 0$ for the next vortex pair, which suggest a pairing formation similar to that shown in figure 4.18. Obviously more investigation is required to be sure of this hypothesis. More investigation is also required for various W/L ratios since it appears from the oil-flow visualization that the transverse instability is sometimes not steady. That is to say that in some instances the cellular structure undergoes a transition to another transverse

wavelength, which is maintained for a period and then changes to another, thus exhibiting the behaviour of a chaotic attractor. The most frequently observed scenario is that the wavelength of the cellular structure modulate between the cavity length and twice the cavity length, see for instance figure 4.9 for $W/L = 8.53$.

4.2 The cavity case

Over recent years a number of numerical investigations have addressed the issue of the possibility that coexisting structures within the cavity couple together to form complicated hydrodynamic quasi-periodic flow phenomena. Most recently Lin and Rockwell 2001 added an experimental investigation that sought to complement some of the observations of these simulations and vindicate previous qualitative work on shear layer-edge interactions, Ziada and Rockwell 1982a and 1982b. What is clear from these results is that a fully turbulent inflow boundary layer at nearly zero Mach number may still give rise to organized oscillations within the cavity, although the exact formation and progression of eddy structures below the shear layer is still not really understood. For experimentalists it appears that any further work should escape from point-wise measurement and instead try to resolve the cycle-to-cycle variations that persist in this flow. The 'clipping' phenomenon discussed in section 1.2.5 is of particular interest here since the coupling of different flow scales is a possible cause. At this test Mach number the current investigation is typically devoid of elements that seek to organise the cavity interactions, that is Mach wave reflections, elastic effects and strong acoustic resonance.

In reiteration, it is known from the work of Sarohia 1977 and Rockwell 1979 that when a critical value of the Reynolds number is exceeded self-sustained oscillations are expected in the shear layer, generated by the selective amplification of extraneous disturbances. In addition to these oscillations, a feedback mechanism exists whereby vortical structures impinge on the downstream cavity corner causing the propagation of pressure waves upstream, thus sustaining the oscillation. An explanation of the full dynamical system is sought in this section that takes into account the small scales of the shear layer and the larger scales of the recirculating cavity eddy. The central case of $L/D = 2.0$ is used for this purpose, with other cases mentioned when necessary. To the author's knowledge the common literature contains no prior wind tunnel investigations that detail the whole flowfield in and around the cavity at any Reynolds number.

For each of the cavity geometries considered in this study it can be expected that the characteristics of the flow structure classify these as shallow and open (as defined in section 1.1). That is, even though these tests are conducted in a wind tunnel the ratio between the cavity length and acoustic wavelength of standing waves is still small therefore generating 'pseudo-sound', Knisely and Rockwell 1982a. In addition it can be expected that the dividing streamline at any time will not impinge on the cavity floor. These cavity oscillations are also categorised as 'fluid dynamic', which may incorporate shear layer mode or wake mode. The model was orientated in the tunnel as shown in figure 4.19 with the laser light sheet being directed down into the cavity section. The mean flow vectors and streamlines, measured within and above the cavity for $L/D = 2.0$ are shown in figure 4.20. From this it is apparent that the mean flow in the cavity is characterised by a large recirculation zone that fills the entire cavity. Closer inspection of the velocity magnitudes indicate that flow close to the rear cavity wall experiences a mean flow velocity of approximately 25% of freestream speed, while there still appears to be a strong flow movement along the floor and a weakened core directed up the front face of the cavity. An exact centre of the recirculation zone cannot be easily determined and as such it is possible that there is significant modulation of the internal cavity structure during the shear layer oscillation mode.

The mean pressure coefficient on the lower cavity wall is shown in figure 4.21 and is included with other acquisition runs for repeatability testing, while in figure 4.22 it is shown with the other cavity configurations tested. Pressure data over the front, aft and floor of the cavity is included in these plots. At these Reynolds numbers the pressure profile imposed on the cavity wall fits into the categorization of an open cavity flow (as discussed previously in section 1.1). Even though there is clearly a well-defined pressure distribution on the cavity floor it would be considered a uniform distribution with regard to the small values of suction actually generated. However one point of interest is that there is no pressure plateau evident prior to the stronger recirculating motion, which is indicated by a concave pressure region on the cavity floor. At these Reynolds numbers it appears that the entire extent of the cavity is affected by a recirculation within the cavity; that is there are no apparent zones of sedentary flow. For each L/D the strongest effects of the cavity recirculation zone are localized within $0.4 < x/L < 0.9$. Figure 4.23 includes an approximate calculation of the normalized

circulation for the internal cavity recirculation structure. The integration path for the calculation of circulation was defined in each case by a streamline released at $(x,y)=(L/2,D)$. As the cavity length is seen to increase the centre of rotation moves aft, while the average recirculation strengthens. As expected the pressure is seen to increase close to the rear cavity face as the flow stagnates. The pressure measured along the aft wall indicates that there is a strong vertical inflow into the cavity, as already suggested by the mean velocity vectors. In general the peak-measured pressure on the aft wall occurs at the pressure orifice nearest the cavity trailing edge corner. This indicates a proximity to the dividing streamline for the open cavity flow regime, already defined by Plentovich 1993 and there is no evidence of a wake mode oscillation. Each test was conducted at the W/L as mentioned in table 3.1. It is known that a reduction in this parameter will increase the suction profile on the cavity floor, thus increasing the strength of the steady state circulation inside the cavity, as demonstrated by figure 4.23.

The pressure data indicates that the centre of the recirculation zone remains stationary relative to the cavity rear face as the cavity length increases (approximately at a distance $D/2$ from the wall). Even though this is consistent with other pressure measurement studies the flowfield velocity data in figure 4.20 indicates that the recirculation core is actually much further forward at approximately $(x/L,y/L)=(0.35,-0.25)$ denoting a discrepancy between the two sets of data, which is borne out for each L/D greater than unity. Since these observations are based on sample-averaged data only a better analysis of the problem is now sought with unsteady and instantaneous measurement.

4.2.1 Shear layer mode

Looking at the spectral distributions of fluctuations using unsteady pressure measurement at the shear layer impingement on the rear cavity face Rockwell 1977 was able to determine the existence of different modes of oscillation. These modes of oscillation are important in determining the fluctuation behaviour of the cavity itself. In this experiment the unsteady pressure data was acquired in two runs of 32000 samples at a frequency of 10kHz. The data was Fourier analysed with a Hanning window and the resulting spectral densities were averaged. For comparison with the work mentioned earlier by Block et al. 1976 the results are plotted with Mach number and Strouhal number based on cavity length in figure 4.25 (for this plot only), for the transducer

mounted on the cavity aft wall. The evidence from this plot suggests that this semi-empirical relationship used to predict the Strouhal number of fluid-resonant oscillations is adequate enough to predict the Strouhal number for fluid-dynamic oscillations also. For $M_\infty = 0.08$ the predominant mode of oscillation is in the second mode (in agreement with other hot-wire data taken) and it is a number of modes that is present for each cavity configuration. For the second mode ($m = 2$) the system is usually denoted a two-eddy system and is characterized by the presence of two eddies evolving simultaneously within the impingement length. The Kelvin-Helmholtz instability is responsible for this roll-up inside the shear layer.

It is the case that there are two modes present at any one time, with $L/D < 2.0$ oscillating in the first and second modes and $L/D > 2.0$ oscillating in the second and third modes. One caveat to these observations is for $L/D = 1.5$, which does not have a dominant mode at a Strouhal number of approximately unity and the preferred (primary) state of oscillation is at $St_L \approx 0.6$ (corresponding to $m = 1$). This is indicative of a single eddy roll-up occurring in the shear layer. From the plot this mode switch does not appear to be caused by a depthwise resonance effect since the oscillation would then adopt a much higher (rather than lower) oscillation frequency. It can also be seen that this behaviour does not persist as the Mach number increases (at $M_\infty = 0.13$ the fundamental mode is at $m = 2$). Figure 4.26 presents the modal data with the more expected reference to momentum thickness and Reynolds number; the blue numbering indicates the SPL (sound pressure level) for that particular mode calculated using equation 4.1.

$$SPL = 20\log_{10}\left(\frac{P_{rms}}{2\times10^{-5}}\right) \qquad [4.1]$$

From figure 4.26 it appears as if the both modes present have a similar strength (in fact less that 0.5dB of a difference) and it was deemed that the blade passing frequency of the wind-tunnel fan was sufficiently distant enough from the shear layer oscillation frequency (and harmonics) to affect their measurement. From the studies of Knisely and Rockwell 1982a and Cattafesta et al. 1998 the capture of data over long time intervals was able to expose the possibility of mode switching. In these studies the data was subjected to a bicoherence analysis and other sophisticated signal processing techniques to reveal the recurrence of mode switching. Indeed this may be the case here, although

the signal durations taken in this instance are too short to make any proper judgement and is an issue for further work. What is established here is that the hydrodynamic instability of the separated shear layer causes more than one mode to be generated. Of particular interest here is how these modes interact with the modulation of the internal cavity structures and how these modes may be related to changes in concentration of vorticity (e.g. distension) at the impingement corner.

From the pressure transducer on the cavity floor it appears as though there is a very persistent low-frequency component that is stronger than the main shear layer mode (even though the SPL's are lower) as shown on the sub-axis of figure 4.26. As the cavity length is increased the Strouhal number and oscillation strength appear to decrease. This low frequency oscillation is not apparent from the transducer on the rear wall, although this alone is not sufficient to discount it as a structural vibration (proper accelerometer measurements are needed for this). The resonant acoustic frequencies of the working section were approximated from an expression more typical to that of ducts and enclosures and as expected it was found that the frequencies detected are much lower than those possible from an acoustic response of the test-section.

It is hypothesised here that the three-dimensional movement in the cavity itself, already mentioned in the previous section, is at least in part responsible for these oscillations. The decrease in Strouhal number as the cavity length increases coincides with a typical fluid dynamic oscillation, while there is a severe reduction in strength as the L/D increases beyond 2.0; the limit at which the static spanwise cellular structure is seen to collapse. At an increased Reynolds number (tests conducted at $M_\infty = 0.13$) the SPL of this low frequency component did not undergo any severe reductions after this limit, again coinciding with the observations from the static pressure measurements. Consequently it seems reasonable to attribute this energy to this fluid movement.

4.2.2 Self-sustained low-frequency components

While the fundamental component of the shear layer is seen to exist there are a number of other lower-frequency components present in the upstream and downstream travelling waves, as shown in figure 4.27 for $L/D = 1.5$. This plot is indicative of all the other cavity geometries in that there are three sub-harmonic components of the first

shear layer mode with another intermittent frequency between the first and second shear layer modes. The first shear layer mode is seen to be the strongest on the cavity floor and as such predicates the motion of a one-eddy system in this region. The other low-frequency components conform to $\beta/4, \beta/2$ and $3\beta/4$ (indicated with an arrow and circle in figure 4.27) where β is the strongest shear layer mode detected (or $m = 1$). The magnitudes are similar for each L/D also, with $\beta/4$ being slightly less than the magnitude of the fundamental; the remaining components are taken to be sub-harmonics. Knisely and Rockwell 1982a have already observed such behaviour and interpreted their results with the aid of linearized, inviscid stability theory (applicable to laminar flow only). However their work was concerned only with laminar inflow boundary conditions and it is interesting to note that this behaviour persists for a turbulent inflow condition with a much higher Reynolds number than previously used. In the configurations tested here these well-defined low-frequency components suggest that there is a particular mechanism generating these sub-harmonics. Knisely and Rockwell 1982a were able to ascertain that these low-frequency components may interact with the shear layer mode to either reinforce itself or to produce an additional (weaker) low-frequency component. Therefore they are perhaps the result of a self-selection process whereby a cyclic displacement of the shear layer at impingement gives rise to a low-frequency component whose overall phase difference is compatible with the cavity length. It is known from previous investigations, for instance Woolley and Karamcheti 1974, that these oscillations have a similar phase as the fundamental and that there is the possibility for strong non-linear coupling also. In this study these modulations are also recorded by the transducer at the rear cavity corner, which seems to indicate that these frequencies correspond to an oscillation in the whole cavity that imposed vorticity fluctuations at the rear cavity face. The part that these low-frequency components may play on the manifestation of one of the three possible impingement events at the cavity trailing (that is compete clipping, partial clipping or complete escape as previously discussed) will be pursued later.

It can then be hypothesised that the shear layer oscillation will act to selectively amplify low-frequency components within the cavity such that they may travel downstream with the travelling wave. It has also been noted that these sub-harmonics are evident by the transducer on the cavity floor affirming their presence around the whole cavity,

indicating that the growth of these components is not localized simply to the neighbourhood of the shear layer. The extent to which these sub-harmonics modulate the internal structure of the cavity is now investigated using a dual-laser/camera PIV system. This dual system PIV mode is briefly mentioned.

The maximum PIV image capture rate from one laser and one camera is controlled by the maximum flash lamp frequency on the laser head itself, which is set by the manufacturer at 10Hz in this case. Recording higher frequency oscillations is possible with a dual laser/camera system whereby two lasers are set-up to be coplanar (using a beam combiner) and two cameras are positioned to capture the same field of view, as shown in figure 4.28a. In this way a data ensemble can be gathered at any number of pre-defined time delays (or Δt_2 from figure 4.28c). This system may then allow the capture of sequential image pairs at a time-delay corresponding to any of the frequencies of interest described by figure 4.27, for instance the $\beta/4$ subharmonic. Therefore if $\Delta t_2 = 4/\beta$ and the flowfield beneath the shear layer is isolated and dominated by this mode (as expected) this data pair should approximate a phase-locked result. Each sequential data pair captured in this way should yield the same result similarity, thus allowing a data ensemble (of typically 100 image pairs) to be collated at one particular time-delay. Figure 4.29 illustrates the capture at this frequency for $L/D = 1.5$ (that is $\Delta t_2 = 0.014$ seconds) with rows one and three (labelled 'RAW') of interest here. It can be seen that in both instances the flow within the cavity is dominated by a single recirculation structure that appears to be in a similar state of maturity and location; it appears there is good 'matching' between the two velocity fields.

The level of 'matching' observed between two results captured at a specific time-delay is indeed subjective and a more rigorous parameter is sought here. It was found that the individual (normalized) correlation of each component of velocity between the two results, sample averaged and multiplied together provided an adequate 'matching' parameter between two velocity fields (represented as $\langle R_{II_u} \rangle \langle R_{II_v} \rangle$). In other efforts the velocity magnitude and velocity derivatives were deemed either to have insufficient information or too noisy to provide a clearly defined correlation peak. Additionally, it is not possible to use data windowing procedures since it biases the final result. As in

every correlation the offset information of the correlation peak is important and is recorded here as the product of the displacement of the individual correlations normalized by the cavity length (represented as $|d_u - d_v|/L$).

By accumulating a series of images at a number of different time-delays (Δt_2) it is possible to build up a profile of temporal events inside the cavity for comparison. Figure 4.30 presents the data obtained from such a study in a three-dimensional plot showing time-delay with correlation strength and the correlation displacement, while figure 4.33 presents a slice of this data using only time-delay and correlation strength (once again for $L/D = 1.5$). The triangular filled markers indicate information that is extracted from the base 10Hz frequency (that is corresponding to $\Delta t_2 = 0.1,0.2,0.3,...$etc). If there is a large-scale coherent oscillation inside the cavity it will be characterised by a point that indicates high 'matching' at a small measured shift (similar to phase locking). Closer inspection of the data yields four points that fit these criteria and are emphasised using circular filled markers with stems. The best match is observed when $\Delta t_2 = 0.015$ seconds, which closely corresponds to the $\beta/4$ sub-harmonic component previously measured by the pressure transducer. Although the correlation value is not particularly strong it still indicates that the internal velocity field structure of the cavity is dominated by a pervasive coherent structure of low-frequency oscillation. The low-level of correlation is expected since it is known there are a number of other possibly non-linear interactions present within the cavity oscillation, causing some cycle-to-cycle variation.

It is possible to retain only the most energetic large-scale features of the flow by using the technique of proper orthogonal decomposition (POD), also known as Karhunen-Loève expansion. In this way it is possible to filter out the small-scale features present within a typical oscillation and improve the 'matching' quality between velocity vector fields that previously exhibited decent levels of similarity. Specific details of the snapshot POD method will not be covered here although Holmes et al. 1996 provides a comprehensive review, while application to numerical simulation and experimental data is provided by Gillies 1998 and Cipolla et al. 1998 respectively. In this method the coherent velocity structures can be extracted from the flowfield from which the resulting eigenfunctions are capable of reconstructing the original flow in an optimal way. Thus a low-order model may be presented since it is possible to retain only the

most energetic eigenfunctions. In developing this low-dimensional system it is important to keep as few modes as possible, although enough modes should be retained in the expansion to maintain an accurate dynamical representation of the flow system. Even though the reconstruction error decreases as the number of modes retained increases, using too many snapshots will reduce the performance of the technique due to the inevitable noise present in the calculated higher eigenmodes (projection of the velocity data on the eigenfunctions or expansion coefficients). The main plot in figure 4.31a illustrates this point for 20, 30 and 40 snapshots. Using this data it was decided that 30 snapshots (that is 30 instantaneous PIV pictures) was sufficient, of which the first fifteen modes capture approximately 85% of the total fluctuation energy. The expansion coefficients for the two most energetic modes are included in the subplot of this figure and the representative eigenfunctions are included in figures 4.31b and c.

Using the technique described the velocity fields previously mentioned in figure 4.29 (labelled 'RAW') are reconstructed (using the first fifteen modes) and included in the intermediate figure rows (labelled 'POD'). The changes to the velocity field are quite apparent and the level of matching between each pair appears to be better. By then repeating the more rigorous correlation methodology it can be seen from figure 4.32 that there has been an improvement in the performance of this technique. Once again the points displaying the best correlation strength with minimal displacement are shown using circular filled markers in this plot while a comparison between both data sets ('RAW' and 'POD') are included in figure 4.33. The reconstructed data reaffirms the observations already made whereby the point closest to the $\beta/4$ subharmonic ($\Delta t_2 = 0.015$ seconds) shows the highest level of correlation, while the harmonics of this component all show an improvement in matching (on average a 3-fold increase in strength).

There is then a clear indication that the low-frequency subharmonic component of interest does correspond to a large-scale coherent fluid fluctuation beneath the shear layer. There has also been a reasonable amount of validation given to the performance of the spatial correlation technique in identifying temporal modes of the cavity oscillation using velocity data only. Knowing that one particular type of oscillation

dominates the internal cavity fluctuation aids the interpretation of the instantaneous PIV results discussed in the following section.

4.2.3 Internal cavity structure

Structures that are formed by the shear layer impingement at the cavity rear wall and floor are forced back into the shear layer by the mechanism of fluid entrainment, demanded by the oscillating shear layer itself. The envelopment of such structures into the shear layer will modify the disturbance arriving at the downstream corner and thus affect the next oscillation cycle amplitude through feedback. This will subject any shear layer spanning a cavity to a certain amount of (non-linear) amplitude modulation. In a study by Ziada and Rockwell 1982 a shear layer was seen to impinge upon a wedge (and as such no cavity was formed underneath). The presence of this impingement edge organized the shear layer oscillation through the feedback mechanism as expected and there was a repeatable vortical interaction at the downstream wedge (although some 'jitter' effects were always present). This is because there was no opportunity for other structures to be entrained below the shear region. In order to understand the amplitude-modulated nature of the shear layer spanning a cavity, the structures that form and persist beneath the shear layer itself must first be understood. Therefore this section on the observations of the internal cavity structure precedes a discussion about the behaviour of the shear layer itself.

Both the pressure data and the velocity correlation procedure has given credibility to the concept that the internal structure of the cavity is dominated by large-scale coherent oscillations that appear to be driven by the shear layer mode, selected to correspond to the phase characteristics of the oscillating shear layer. Figure 4.34 shows the average vorticity calculated for the central case. From this figure it is apparent that the mean flow within the cavity is dominated by a jet-like flow along the rear and bottom walls of the cavity as revealed by the zone of negative vorticity (as indicated). This jet-edge effect is present in all the cases investigated in this study and has a different level of upstream propagation depending on the specific cavity L/D. Figures 4.35 and 4.36 include the average vorticity for $L/D = 1.5$ and $L/D = 3.0$ where these effects are particularly evident. The importance of this particular interaction will be reiterated later in the section since it is crucial to the internal flow oscillation.

The highest values of vorticity are generated immediately downstream of the front corner and at the downstream corner, where there is impingement of the shear layer. Positive vorticity extends along each of the cavity walls with a lip of negative vorticity extending well upstream along the cavity floor. Lin et al. 2001 discovered a similar flow pattern in which it is described as a wall jet, having a boundary layer on one side and a free separated layer on the other. In this instance the discontinuity of the jet-like flow into the cavity is starker making the perimeter of the jet more discernable, which encapsulates a single clockwise rotating structure in the right hand side of the cavity. The flow rate associated with this jet-like flow into the cavity must satisfy the entrainment demands of the shear layer that spans the cavity (which will be discussed in the next section). From inspection of the instantaneous vector plots the momentum of this wall-jet is strong enough to travel the complete length of the cavity floor and turn upwards as it meets the cavity front wall. It then has a direct effect on the initial development of the shear layer. It seems therefore that there are perhaps a number of effects present that will modulate the development of the shear layer. The first type is the feedback mechanism in addition to the expected Biot-Savart induction, the next is that caused by pockets of vorticity cast from this wall-jet colliding with the underside of the shear layer and finally by a more direct jet impingement back into the underside of the shear layer in proximity to the separation location. The latter two interactions are primarily the reason that self-similar free turbulent jets have constant maximum shear stress while those formed over a cavity do not, even thought the shear layer thickness still increases linearly with distance. As opposed to the feedback mechanism these latter two effects cause an upstream influence only after a certain time-delay, these effects are now discussed.

4.2.3.1 The cavity oscillation

A complete oscillation of the internal cavity structures is described with the aid of figures 4.37 to figure 4.44 using the dual PIV system described in section 4.3.2. Although the feedback mechanism described in section 1.2.3 is not disputed a new explanation of the low-frequency oscillatory motion is given. In contrast to the mean flow vectors already shown there is no stationary vortex present within the cavity at any time. As previously discussed the shear layer interaction with the cavity trailing edge causes mass addition and mass removal from the cavity itself. During mass addition the stagnation streamline is deflected into the cavity and a jet-edge is formed along the rear

cavity wall that will continue to convect along the cavity floor. By the time this vorticity interacts with the cavity front wall a vortex is formed that will be further strengthened by a successive incoming jet edge (mass addition stroke) and the upward entrainment demanded by the region of exponential (or even linear) growth at the shear layer separation (figure 4.37). A large recirculation region is formed in proximity to the cavity front wall (figure 4.38), although the vorticity levels are relatively low. At this time this primary recirculation extends from the cavity floor to the separated shear layer and as such is being strongly influenced by the fundamental shear layer oscillation. This structure will move forward through the cavity (figure 4.39) at an instance corresponding with phase agreement of the shear layer and at the same convective velocity. Over these latter two stages it is possible that further vortices are cast along the cavity wall and coalesce with this recirculation region. At this time the internal cavity structure and the shear layer oscillation are coupled. Evidence that coupling indeed occurs is presented in section 4.3.4.

As this primary recirculation region is convected downstream the shear layer is drawn upward by the incoming rotation at the rear corner (figure 4.40) and there is large-scale mass expulsion from the cavity (figure 4.41). This goes some way to reaffirming the predicted coupling between the shear layer and the internal motion since the entire extent of the shear layer is deflected upward and the volume underneath undergoes a common motion of mass expulsion (forming a large-scale clockwise rotation) from the cavity. After the structure has encountered the rear cavity corner the modulation of the internal structure may take on any one of two possible scenarios. The type of vortex-edge interaction that has preceded it dictates each specific scenario.

The first possibility is that the vortex-edge interaction has facilitated a complete vortex escape and as such there are no discernable small-scale structures left in the cavity as a new jet edge forms along the cavity floor for the next mass addition stroke (figure 4.42 and figure 4.43). As can be seen more clearly in figure 4.43 this is typically associated with a strong discontinuous jet-edge forming once again along the cavity floor. The second possibility is that the approaching vortex experiences some degree of distension or severing by the rear edge and as such some artefacts from that vorticity cluster remains in proximity to the corner even after the large scale mass expulsion of figure 4.41. Thereafter (figure 4.44) the vorticity clusters of the 'clipped' vortex will either

amalgamate with the incoming shear layer to be eventually cast downstream with it or will be swept back into the cavity by virtue of the jet-edge formed during mass addition to the cavity. Figure 4.45 illustrates the 'clipped' interaction with the rear corner whereby the vorticity cast downstream can be seen at the periphery of the image while packets of vorticity persist (forming a fully rolled-up coherent vortex) at the edge of the cavity. In figure 4.46a and 4.46b the same structure is shown, as it is being distorted and swept back down along the cavity rear wall.

Because the flow in the cavity is then obviously not quiescent 'roll-out' behaviour of the internal cavity structures will account for the well-documented low frequency flapping of the shear layer. The details of the internal periodic flow recirculation is different to the findings of low Reynolds number computational studies, in particular Pereira and Sousa 1993 and Najm and Ghoniem 1991. In some instances the cavity oscillation shows a better similarity to findings from transonic and supersonic cavity studies, as in Takakura 1996 for instance (this is pursued further by Lin et al. 2001). What is congruent between these studies and the work presented here is that the recirculation zone takes the form of a large-scale eddy that migrates downstream while temporarily dominating the motion of the smaller-scale vortices.

4.2.3.2 Perturbation of the shear layer via jet impingement

The interpretation of a perturbed shear layer is taken to describe some interaction that the shear layer encounters out-with that of normal fluid entrainment. For instance the typical interaction seen here is shown in figure 4.47 and figure 4.48 whereby the mass addition stroke has such momentum that the jet-edge is able to travel the total internal perimeter of the cavity and osculate the shear layer itself. The unsteadiness imposed on the shear layer in this region will significantly contribute to the modulation and amplification of the shear layer as it progresses downstream, and is a point for further discussion in section 4.3.4. This impingement appears to be periodic where a similar interaction is shown to be repeatable through the sample set taken at a time delay corresponding to $\beta/4$.

The nature of the internal oscillation already given for the central case is generally noted in the other cavity geometries studied, although it is this disruption caused by the wall

jet-impingement back onto the underside of the newly separated shear layer that disseminates the precise internal modulation observed. It is judged that as the cavity length decreases (say $L/D < 2.0$) the effect of the jet-edge with the separated shear layer becomes a more dominant interaction, while for longer cavities (say $L/D \geq 2.0$) the described internal interactions are more prevalent to the articulation of the shear layer. Figure 4.49 illustrates the 'roll-out' interaction where the internal recirculation structure locks onto the shear layer convection and effectively 'empties' the cavity of the primary recirculation and any satellite vortices (operating at the $\beta/4$ frequency in each case). As it can be seen in each case the motion of this 'roll-out' adopts a similar interplay with the surrounding fluid. The wall-jet already formed along the cavity floor is enveloped into the shear layer and thus forms a nearly discontinuous (vertical) edge within the cavity. Thus, as the cavity effectively 'empties' it leaves near stagnant flow upstream of this edge. In each case A, B and C indicate the centre of this roll-up shown in figure 4.49.

As the length of the cavity increases the backflow range of the jet-edge along the cavity floor decreases and there is much less impact with the cavity front wall. Instead the backflow motion is more immediately entrained into the shear layer, thus balancing the larger amplitude mass stroke with the higher entrainment demands of the longer shear layer. Looking at the Reynolds stress calculated for each of the individual cavities will serve to show the magnitude of these effects on the formation of the flow in and around the cavity. These contour plots are shown in figures 4.50 to 4.54, note that the colour bar limits float to accommodate each measured Reynolds stress.

For the shortest of cavities ($L/D = 1.0$ and figure 4.50) the measured negative stresses are at their lowest. In this and every other case the level of stress in the shear layer is much higher than anywhere else in the cavity with their dominance characterized by a number of high-stress small-scale segments along the span of the shear layer. This is consistent with the recognized dynamics of the separated shear layer, which is known to roll-up into small vortical structures. Already mentioned a number of times is the formation of a jet edge along the vertical and bottom walls of the cavity and it can be seen from each plot that this jet-edge carries with it a substantial amount of positive momentum fluctuation. One important point is that the value of positive velocity

correlation along the rear wall does not seem to change appreciably with respect to the cavity length although the Reynolds stresses at impingement are seen to nearly triple in magnitude between $L/D = 1.0$ to $L/D = 3.0$. However, this does not necessarily intimate that the unsteady loading of the rear face is similar in every instance, since the mass addition and removal is much more violent (inducing more momentum into the cavity) for the longer cavities. A longer shear layer amplifies disturbances more, so the final amplitude of oscillation is larger, thus increasing the Reynolds stress. As shown for the limiting cases in figure 4.55 there is a stronger (mean) jet flow along the rear face as the cavity length increases.

In each instance of the presented Reynolds stress there is a discernable lip of high fluctuation that forms from the cavity floor back up into the shear layer, and represents a typical recirculation of the internal flow. For the smallest cavity case there is very little velocity correlation in this lip (or elsewhere internally) because the vortex neatly fills the whole cavity (known as a captive vortex) and the agitation of the flow is minimized, although the low frequency component is maintained. As the length of the cavity increases the distortion of this recirculation lip increases until the momentum transport of the jet is drawn back into the shear layer after smaller upstream propagations, which is in agreement with the vorticity and vector plots already shown. For instance in figure 4.52 the jet-edge is displaced from the cavity floor at approximately $x/L = 0.5$ and travels further upstream to eventually encroach onto to the underside of the shear layer at the same location. With reference to figure 4.34 it can be seen that the loci of maximum Reynolds stress in figure 4.52 corresponds to the location of the jet-edge. This is expected since this edge is seen to convect small vortical structures directly from the shear layer that increase the velocity fluctuation at these locations, this is consistent with the observations of Fiedler et al. 1981 for a number of different fluid interactions. It can be seen that there are similar observations for the remaining cavity cases. As already noted, this leaves an increasing proportion of the cavity at the front wall with very low velocity fluctuations causing less modulation to the incipient shear layer region. A fuller discussion of the shear layer will be presented in the next section.

As already expressed in section 4.1.2 some quantification of the chosen acquisition procedure must be mentioned at this stage. Figure 4.56 includes the two methods of

image acquisition for acquiring statistical data, that being by random image capture and that using a base 10Hz frequency (with $L/D = 2/0$). It is shown in the calculation of the RMS that there is remarkably little difference between the two methods described, thus vindicating the use of the more convenient 10Hz-sampling rate used in this study. In figure 4.56c the PTV 't-tiling' methodology is presented using the RMS calculation and it is apparent that there is good similarity between this and the other data although there is some reduction in the RMS levels in the vicinity of the shear layer. Any discrepancies between the RMS levels of the correlated and tracked data are caused by the inclusion of bias error in the (correlated) results. In this instance the bias error entices the correlated RMS results to be elevated especially in areas of excessive velocity gradient.

4.2.4 The separated shear layer

The large-scale instability of the shear layer along the cavity is a convective instability of the entire separating turbulent boundary layer. Since energy can travel upstream to form a self- excited oscillation this type of parallel flow is better described as being globally unstable. Even though it is well known that the inclusion of an impingement edge can change the measured pressure signal in the shear layer from a non-stationary /convectively unstable process (Dimotakis and Brown 1976) to a deterministic/globally unstable process (Knisely and Rockwell 1982a) there is still the need for further research. It is how the shear layer coexists with a recirculation zone spanning its entire length that is the topic of this section.

4.2.4.1 The shear layer state

The single most striking feature that is apparent from the instantaneous PIV results is that the shear layer may take on either of two possible states. In the first state the parallel flow reaches the upstream corner of the cavity and begins to continually generate vorticity and it is then the presence of the Kelvin-Helmholtz instability that causes small-scale vorticity pockets to roll-up and amalgamate together encouraging larger clusters of vorticity to progress downstream, see figure 4.57a for example. A region of weaker vorticity is seen to envelope the entire extent of the shear layer and depending on the shear layer mode of oscillation, any other large scale clusters of vorticity. It is the impingement of these vorticity clusters with the downstream corner that provides the actual feedback signal. Further, it is the roll-up of the shear layer that

causes it to undulate and amplify as it progresses downstream, while the wavelength is strongly related to the cavity length. In the second state the wavelength of the shear layer is substantially smaller than the length of the cavity, sometimes even an order of magnitude so. This type of shear layer structure, shown in figure 4.57b does not appear to organize itself in a fashion corresponding to a globally unstable parallel flow. In fact the apparent loss of feedback in the shear layer spanning the cavity makes it appear more similar to a free shear layer. Lin et al. 2001 encountered similar small-scale structures in their study and identified hairpin vortices in the upstream boundary layer as a possible source. In this study the pressure transducer at the rear cavity corner has already identified the shear layer modes and movement of the larger internal cavity structures. This leaves one unidentified oscillatory component in the spectrum at $St_\theta = 0.028 \pm 0.005$ and is curious in that the frequency has very little variation over the complete range of cavity L/D. If this component were in some way linked to the shear layer mode the Strouhal number would be expected to decrease as the cavity length increases. So it appears then that this frequency is probably related to movement in the upstream boundary layer and is able to persist within the shear layer along the length of the cavity when the feedback signal is attenuated. These two states of the shear layer are encountered in every case; figure 4.58 includes the case for $L/D = 1.0$ where the shear layer second mode is extremely close to this component, but remains very distinct.

From observations with the dual-PIV set-up there is one particular stage in the oscillation that is concomitant with the existence of this second state of the shear layer. Once again the behaviour of the shear layer is intrinsically linked with the recirculation structure beneath it and is now explained. In figures 4.57a and 4.58a and b the first state of the shear layer is present when the recirculation region is forming from the mass addition to the cavity. The rim of the recirculation region caused by this jet-edge interaction is clearly distinguishable in figure 4.57a as a rim of negative vorticity (at $x/L = 0.25$) that partitions a zone of positive vorticity upstream of it. For figures 4.58a and b this is congruent with a centred (nearly rigid) vortex structure in the cavity, noted by the presence of a negative vorticity region at $(x/L, y/L) = (0.25, 0.25)$ and positive vorticity established at the upstream cavity face (lower quadrant). As can be seen in figures 4.57b and 4.58c and d the second state of the shear layer is characterised either by a lack of any coherent vortical flow beneath it or by some marginal inflow along the

cavity rear corner, noted by a layer of negative vorticity in proximity to the rear wall abutting a layer of positive vorticity. It appears then that the global mass expulsion from the cavity (figure 4.41) immediately precedes the small-scale instability in the shear layer. This seems reasonable since the feedback signal would be attenuated when the stronger vorticity in the shear layer is lifted away from the rear cavity corner. This is also in accord with Knisely and Rockwell 1979 who found that an upward (or downward) displacement of $6\theta_0$ of the shear layer at the impingement corner was enough to reduce the transverse fluctuation by half. In fact the vorticity strength of the exiting recirculating structure is seen to be less than half of that in the shear layer (where, $\omega_z\theta_0/U_\infty \approx 0.025$), thus dramatically affecting the transmitted upstream agitation. A more concise measurement would be of the circulation in the exiting recirculation, although this is complicated by the cavity geometry and straining of the structure.

4.2.4.2 The potential for vortex coalescence

When the feedback signal is attenuated and the shear layer is in the second state its behaviour is more akin to that of a free shear layer. In this instance there is the possibility for neighbouring shear layer vortices to coalesce as they travel downstream, which would otherwise be impossible for any other forced shear layer. If this coalescence were present there would be expected changes both in the loading of the downstream corner and in acoustic propagation. Vortex coalescence is the classical process that governs the growth of a free shear layer and using linear stability theory the instability frequency that this occurs at is approximately $St_\theta \approx 0.017$ (for laminar inflow conditions). Lin et al. 2001 indicated in their study that their measured small-scale instability corresponded to a Strouhal number an order of magnitude higher, which is clearly not the case here (where, $St_\theta = 0.028$). It is important therefore to gauge the potential for vortex coalescence being present in the shear layer.

In an effort to corroborate the complexity that these two shear layer states bring to the cavity oscillation some results from the hybrid BTT technique are presented here. It is expected that these results are not from the common mode of oscillation, but are taken from the non-linear type interactions that are present. In figure 4.59a the instant at which global mass expulsion has just occurred is shown with a portion of the freestream

velocity removed for clarity. Using trial and error it was found that the best reference frame to interpret individual shear layer roll-up is at a frame moving at $0.25U_\infty$. The argument for a suitable reference frame rests with the distinction between streaklines and timelines and as such a moving frame should yield additional information about the flowfield, see for instance Gursul et al. 1990. The criterion set here was for each cluster of vorticity to correspond to individual swirls in the velocity vectors. Figure 4.59b presents the same result as shown in figure 4.59a with the frame moving. It can be seen that there is large-scale vortical motion in the shear layer even after global mass expulsion (not noted in figure 4.42 for example) insinuating the presence of vortex coalescence. In figure 4.60 the presence of small-scale vortices upstream in the shear layer and larger vortices in the downstream region again alludes to the fact that vortex coalescence is perhaps present. What is clear from this study is that the proximity of the cavity corner does not facilitate the use of the normal means to identify vortex agglomeration, that is vortex nutation and sign changes in Reynolds stress, Ho and Huerre 1984. While this particular issue requires further investigation, it is certain is that this second state of the shear layer is not the dominant state.

One final note is with regard to the modulation of the shear layer and processes that exist beneath it. For the spatial correlation calculation (where $L/D = 1.5$) a decent amount of structure similarity was present during the oscillation of the cavity and this was reaffirmed by the POD analysis. However, as the cavity length increases the shear layer is subjected to larger amplitudes of oscillation and thus exposed to longer periods in the two states of the shear layer. It is probable that this effect contributes to the cycle-to-cycle variation of the flow pattern and possibly to the clipping fate at the rear face. In figure 4.61 structures with a wavelength similar to those observed in the second state of the shear layer (labelled A, B, C and D) are seen to convect back upstream into the recirculation region of the cavity. This is dissimilar to the feedback mechanism previously mentioned and would impose some cycle-to-cycle variation.

4.2.4.3 The interaction with the shear layer on roll-out

It has already been mentioned that there is phase agreement between the exiting internal recirculation and the vortices in the shear layer itself. Some evidence is now included to satisfy this conjecture. When the large recirculation region inside the cavity migrates

downstream it does so at the same speed as the vortices in the shear layer. Figure 4.62 is a repeatable observation and indicates that the recirculation region (indicated by 'C' on the figure) is drawn into the braid region of the shear layer, which is the thin vorticity layers that are positively strained and transmit mass addition to the shear layer vortices (indicated by 'A' and 'B' on the figure). As this vortex evolves downstream (as it rolls-out of the cavity) it entrains the vorticity of the recirculation eddy-region and as such develops into a much larger and stronger structure than a typical vortex progression would have. In contrast vortices that are following this larger vortex e.g. vortex 'A' may only entrain typical non-vortical fluid and as such are much weaker than normal.

Using the dual-PIV system two sequential sets of results are used in figure 4.63 to illustrate a low frequency flapping of the shear layer. It can be seen that as the vortex of interest is convected downstream (indicated with the prefix 'A') it entrains by mutual induction the large recirculation region underneath, while the next vortex is much smaller and weaker by comparison. In summary, roll-up 'B1' is a typical shear layer structure that precedes the roll-up 'A*'. Roll-up 'A*' coincides with the entrainment cycle while the roll-up 'C*' succeeds the large-scale interactions of 'A'. This type of feeding mechanism between the shear layer and the internal cavity fluid is typical of part of the bluff-body vortex shedding mechanism, more commonly visible downstream of a circular cylinder, Gerrard 1966. Figure 4.64 compares a normal shear layer roll-up and an entrained roll-up at the same physical position along the cavity. As expected the roll-up that entrains the internal recirculation is causing much higher rates of positive strain across the open face of the cavity than that of the normal roll-up. It is interesting to note that these effects are not localised to the adjoining braid but instead affects the entire extent of the cavity at this time. These high rates of positive strain persist until there is a global mass expulsion from the cavity.

4.2.4.4 The shear layer oscillation with respect to $\langle uv \rangle$

With regards to the jet-edge interaction with the shear layer at the upstream separation corner some further points can be made. Using the hybrid BTT t-tiling scheme the distribution of $\langle uv \rangle / U_\infty^2$ is calculated along the open face of the cavity (at $y/L = 0$) and shown in figure 4.65. In general each cavity modulation is characterised by a region of inflow along the initial portion of the shear layer that is balanced by a region of outflow

in proximity to the downstream corner. The integration of the mean momentum transfer along this line will always be negative, since it makes a positive contribution to the drag. There is a good degree of similarity between these profiles for $L/D \geq 2.0$ where there is a broad region of outflow along approximately the first 75% of the cavity length. As expected there is an increasing level of inflow at the downstream corner as the cavity length increases, caused by the maturation in the shear layer roll-up. In the remaining cases (in particular $L/D = 1.5$) there is a much higher and localised level of outflow at the upstream corner of the cavity that is caused by the jet-edge impingement on the underside of the shear layer. It is interesting to note the repercussions that this has on the development of the shear layer since an augmented region of inflow must then balance this. In fact most of the outflow occurs very close to the upstream corner rather than over a broader region of the cavity face and there is a disproportionate amount of inflow at the downstream corner for the actual cavity case. In the captive vortex case ($L/D = 1.0$) the internal structure is better described as a vortex since the recirculation region neatly fills the entire cavity and there is negative vorticity present in and around the structure. This causes the jet-edge formed over the cavity rear wall to be more easily induced into the established steady-state recirculation and reduces the effect of jet-edge impingement at the front corner. This is conformed by the Reynolds stress calculated in figure 4.50 that shows very little fluctuation along the upstream wall. For $L/D = 1.5$ the cavity oscillation mechanism is much stronger causing a stronger outflow over the first 10% of the cavity face.

In the pursuit of shear layer amplification attenuation it is seen that the internal modulation of the cavity must be controlled in order to have any steady-state improvements on the state of the shear layer. Any actual improvements are characterised by the vortex-edge interaction at the cavity trailing edge and the conversion of these disturbances at the sensitive region of the shear layer. In the final chapter passive control techniques are used on cavity cases to reduce velocity fluctuation inside the cavity itself and to reduce mass expulsion from the cavity. These suppressions are pertinent to the case of aircraft stores and the inter-car gap on trains respectively.

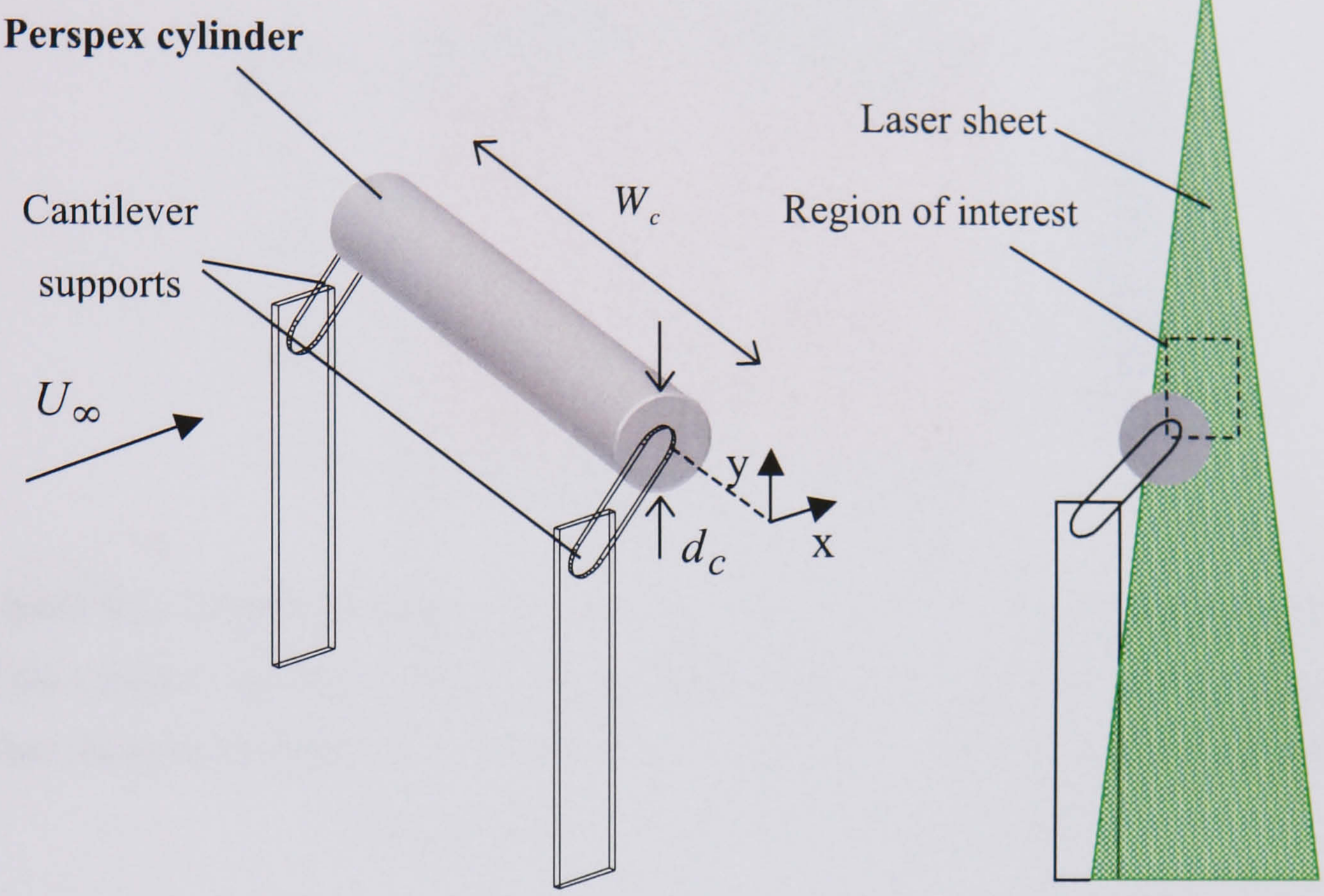

a. Isometric view of model used for flow around a circular cylinder. Although not indicated, shrouds were placed around the model struts.

b. Elevation indicating position of laser light sheet and region measured.

Figure 4.1. Experimental set-up used for the PIV measurement of the near wake of a circular cylinder.

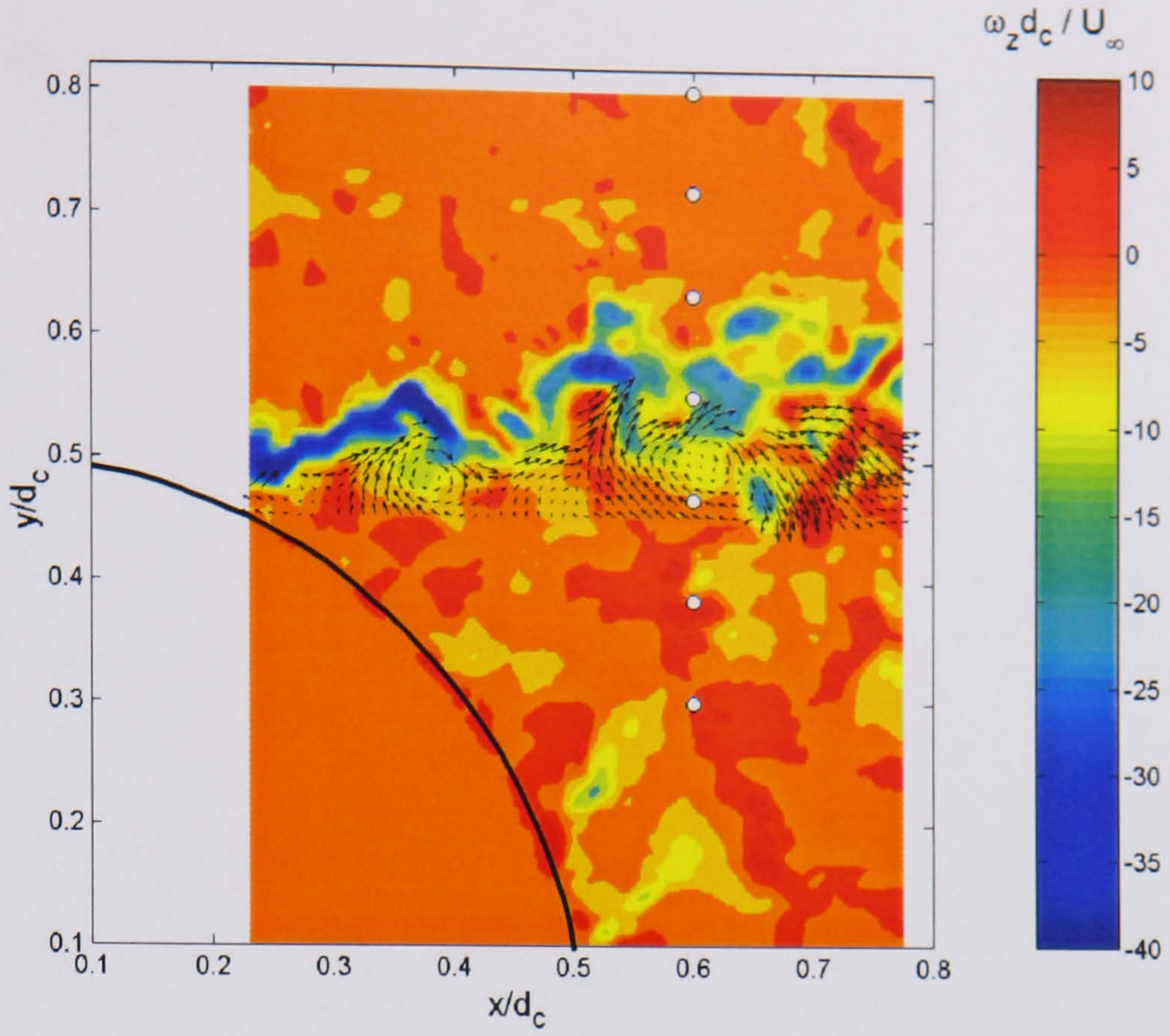

Figure 4.2. A typical instantaneous normalized vorticity measurement in the near wake of the circular cylinder. Velocity vectors are superimposed to indicate the position of the free shear layer eddies. The white dots indicate hot-wire measurement positions from Toebes 1969 used for comparison in figure 4.4.

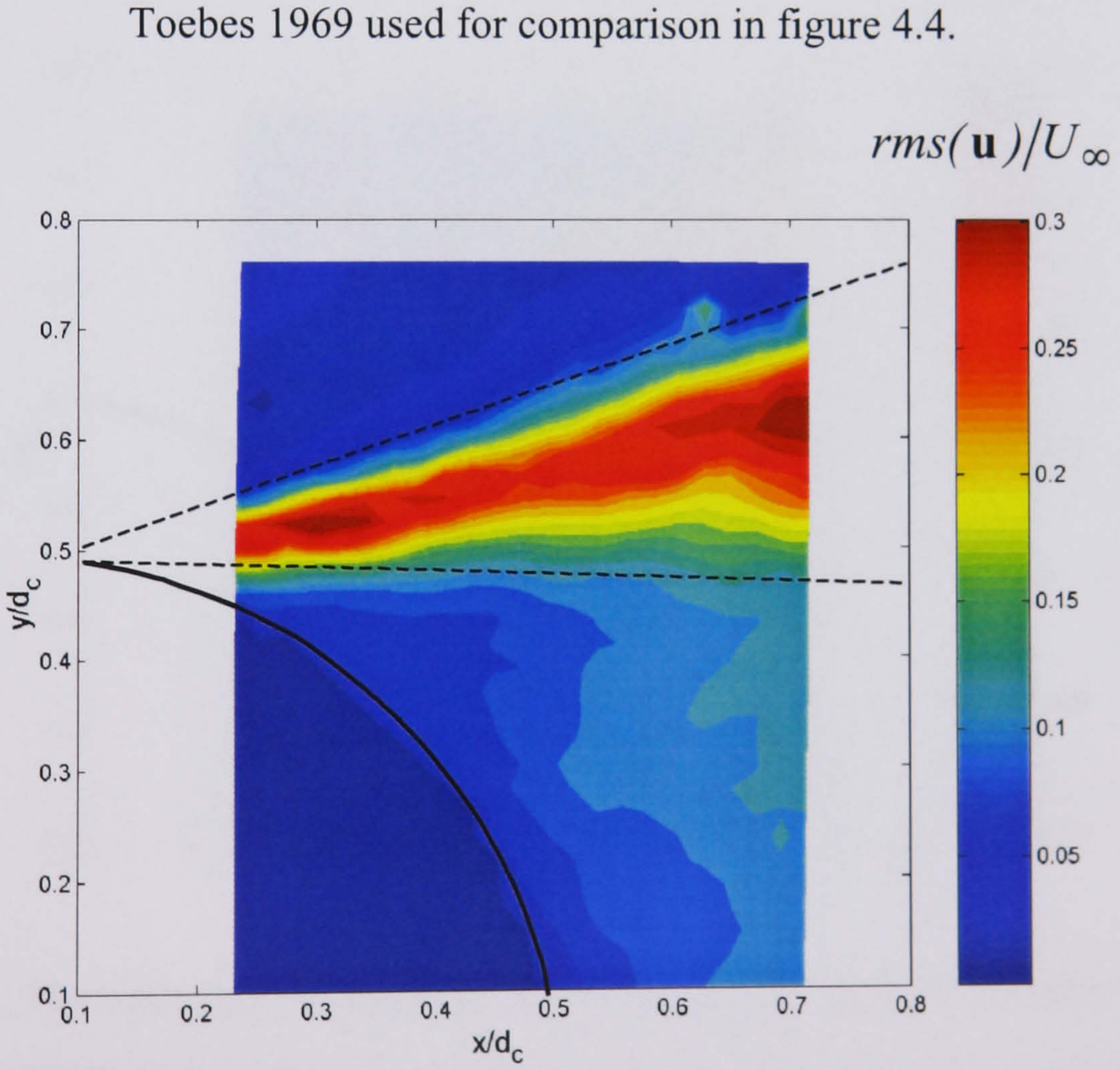

Figure 4.3. Rms calculation of the near wake normalized using the freestream speed. The dotted lines indicate the approximate position of the typical wave form region as defined by Maekawa and Mizuno 1967.

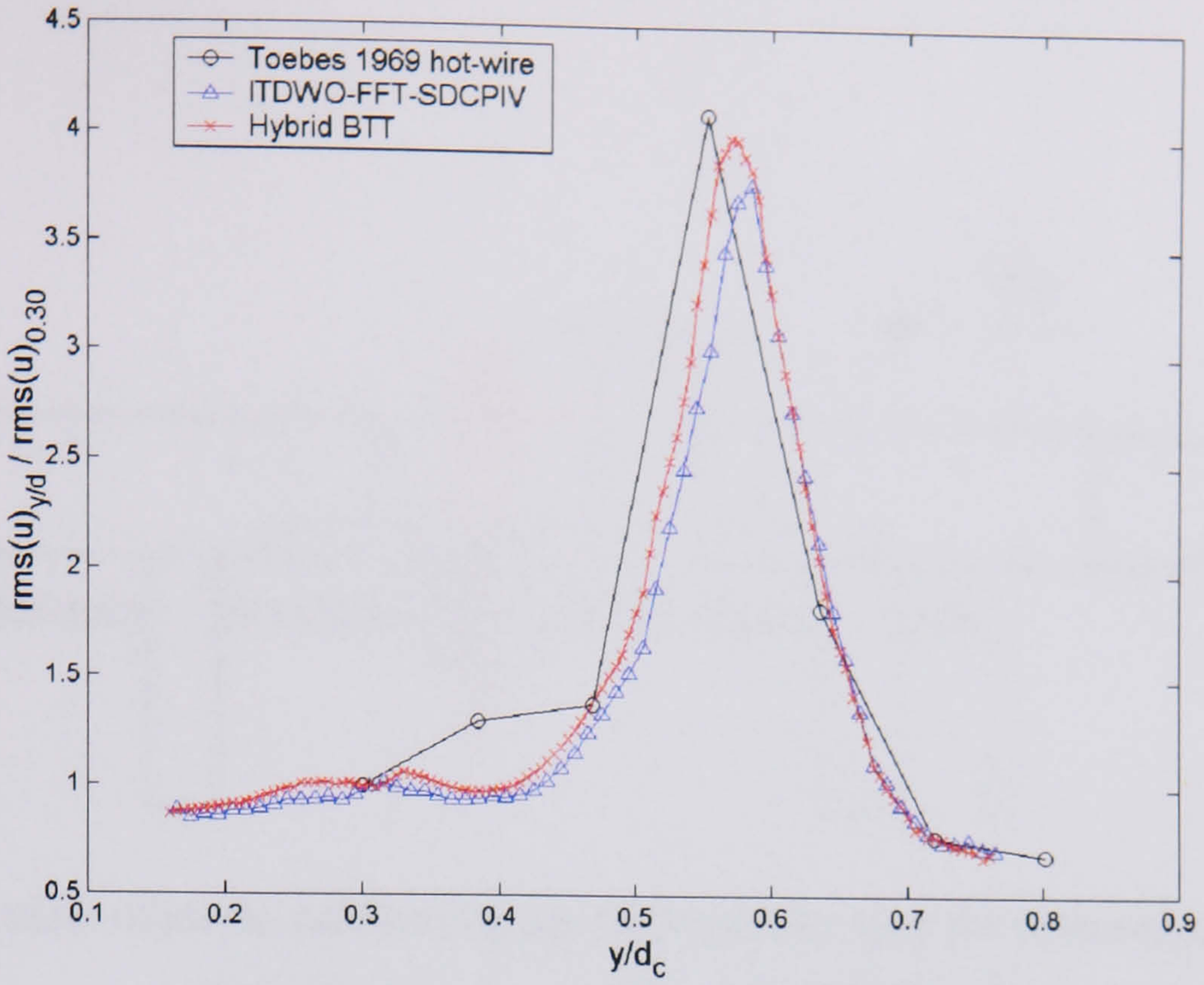

Figure 4.4. Comparison of the normalized rms values for $x/d_c = 0.6$. The hot-wire signal is normalized rather than calibrated.

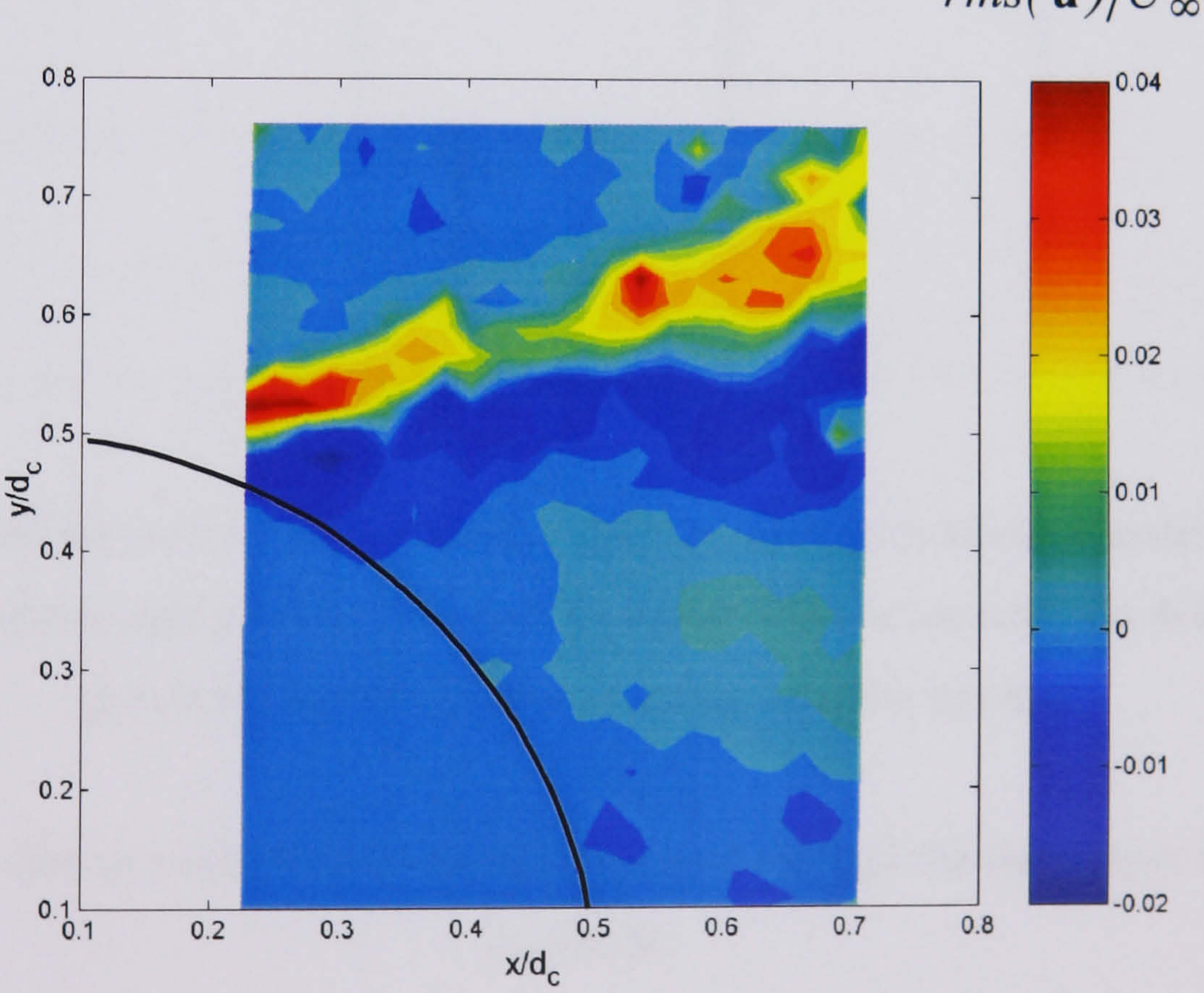

Figure 4.5. The difference in measured rms for the near wake of a circular cylinder between an intermittent-cinematic capture ensemble (figure 4.3) and a truly randomly captured image ensemble. The interval between each image pair was greater than 10 seconds (total capture time 45 minutes).

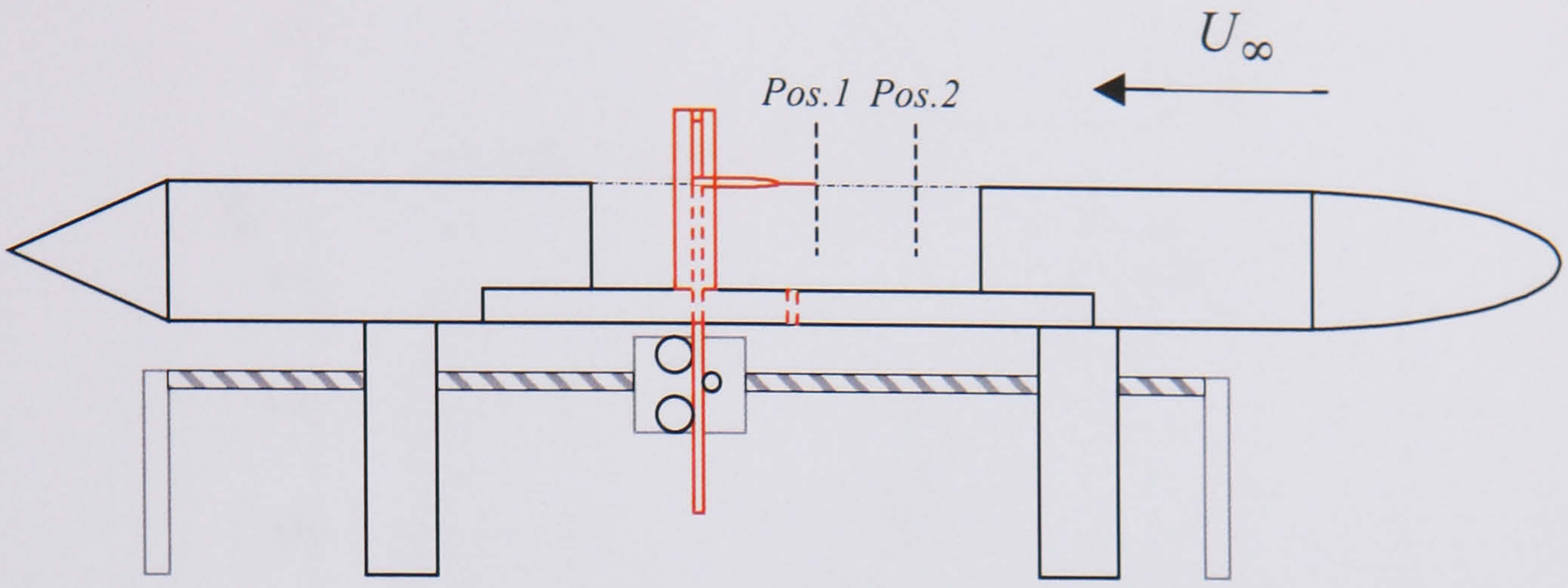

a. Elevation view of probe positioning and movement using the traverse assembly. The hot-wire components are indicated in red.

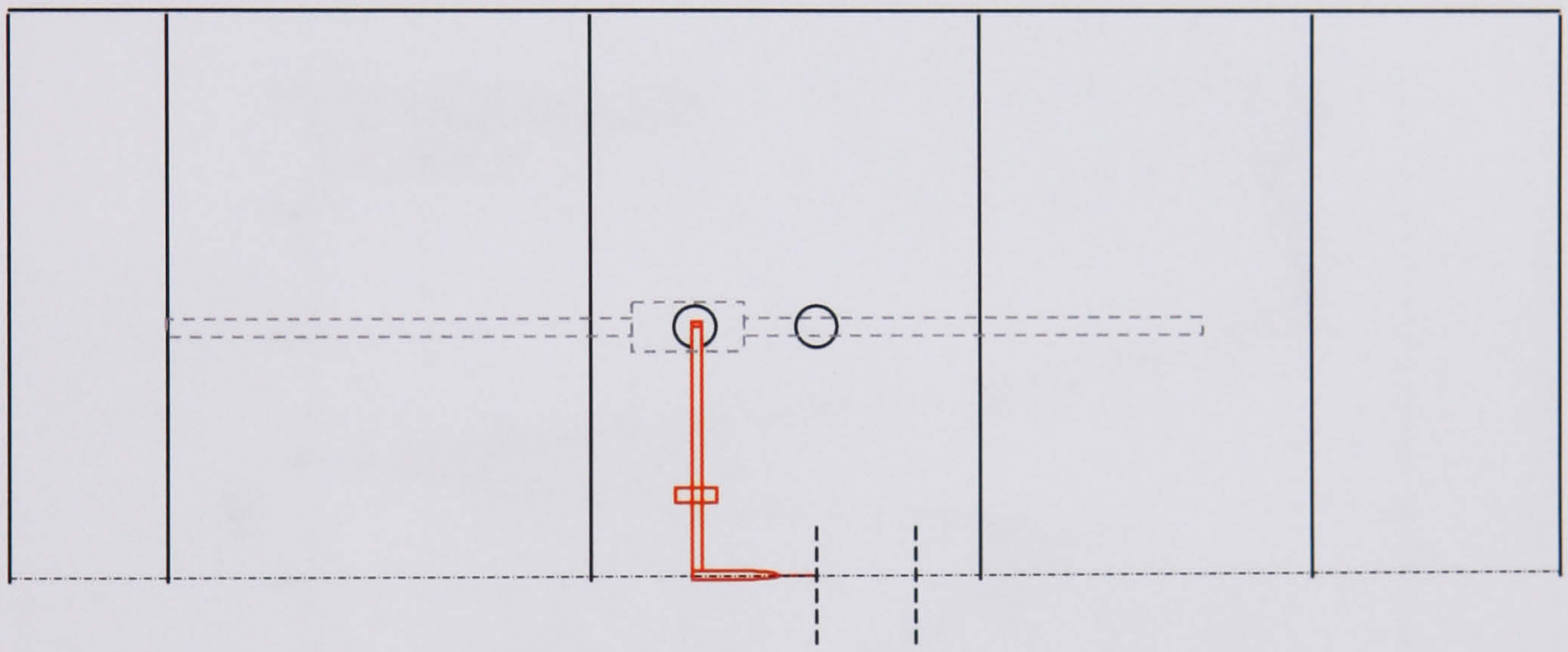

b. Plan view of the port side of the model. The traverse was positioned under the model and added approximately 1% to the tunnel blockage. Two holes were cut in the floor of the cavity to allow probe mounting onto the traverse.

Figure 4.6. Set-up used for hot-wire measurement through the shear layer at two x-positions.

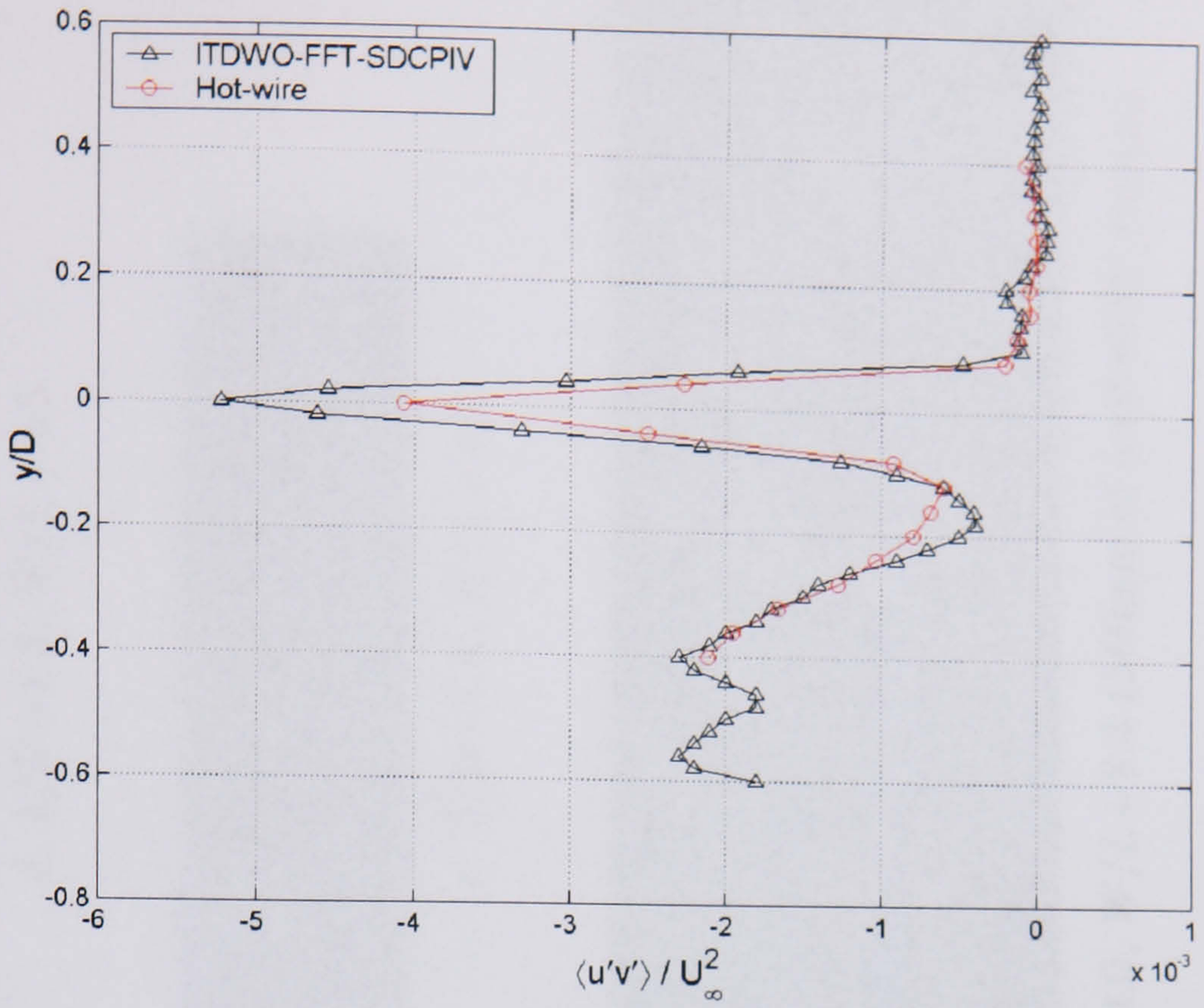

a. Measurement of the Reynolds stress at $x/L = 0.16$.

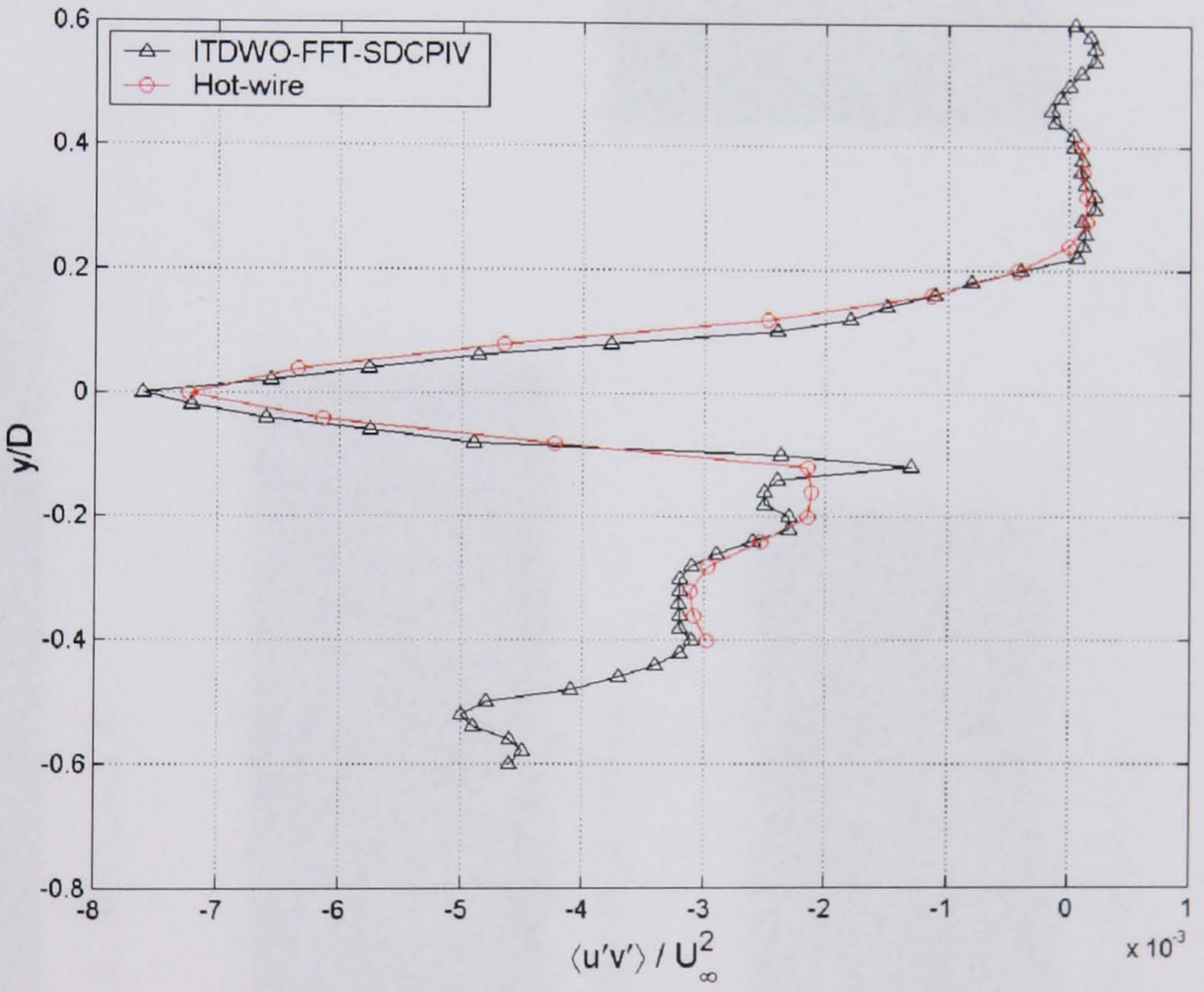

b. Measurement of the Reynolds stress at $x/L = 0.4$.

Figure 4.7. Turbulent measurements at two different locations along the cavity shear layer for $L/D = 2.5$.

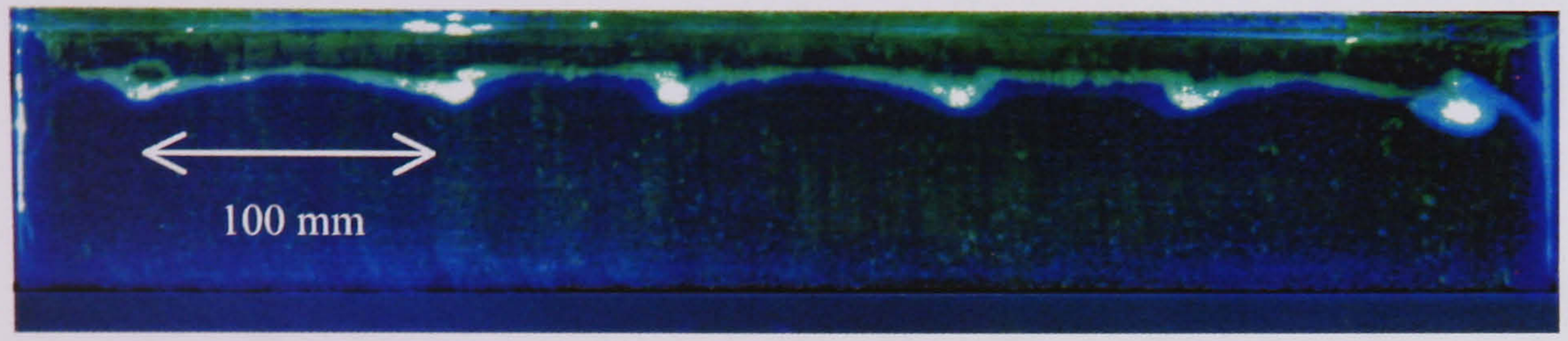

a. $L/D = 2.0$, $W/L = 5.4$

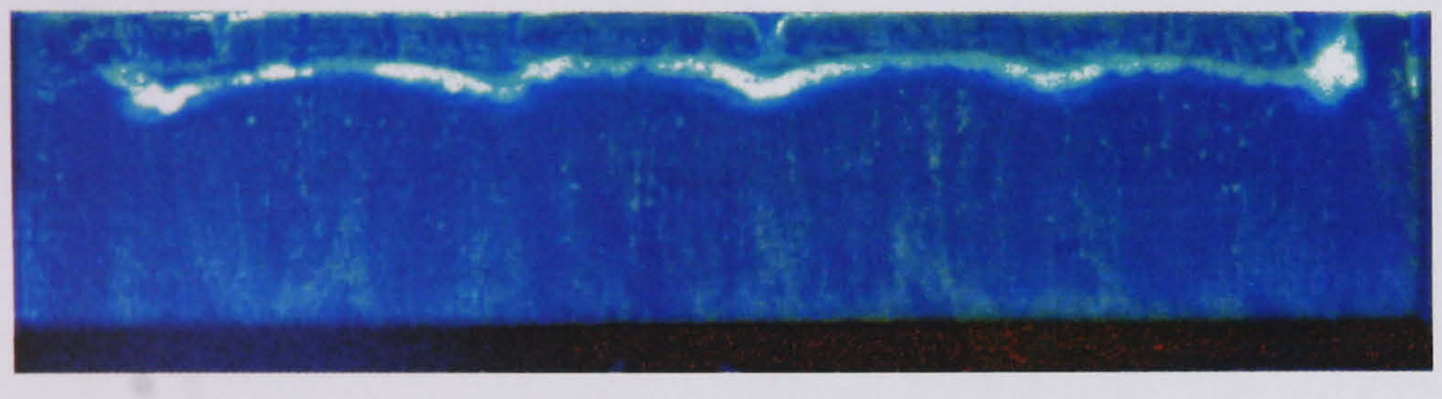

b. $L/D = 2.0$, $W/L = 4.4$

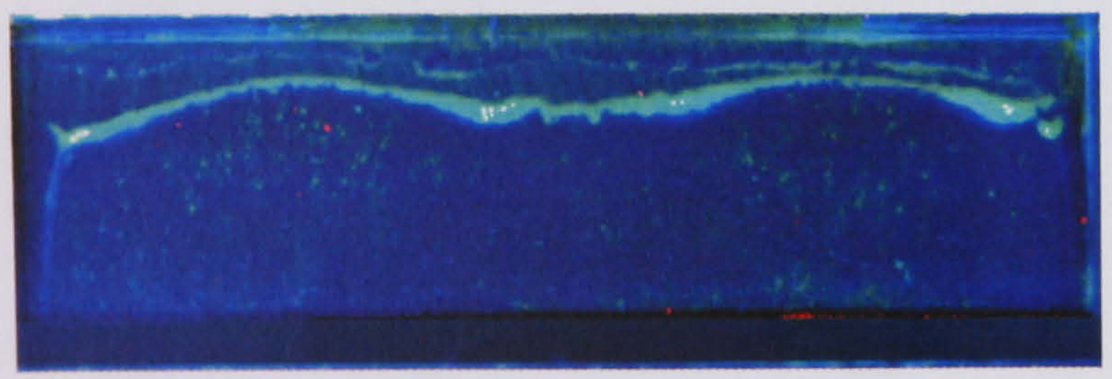

c. $L/D = 2.0$, $W/L = 3.4$

d. $L/D = 1.5$, $W/L = 4.5$

e. $L/D = 1.5$, $W/L = 4.0$

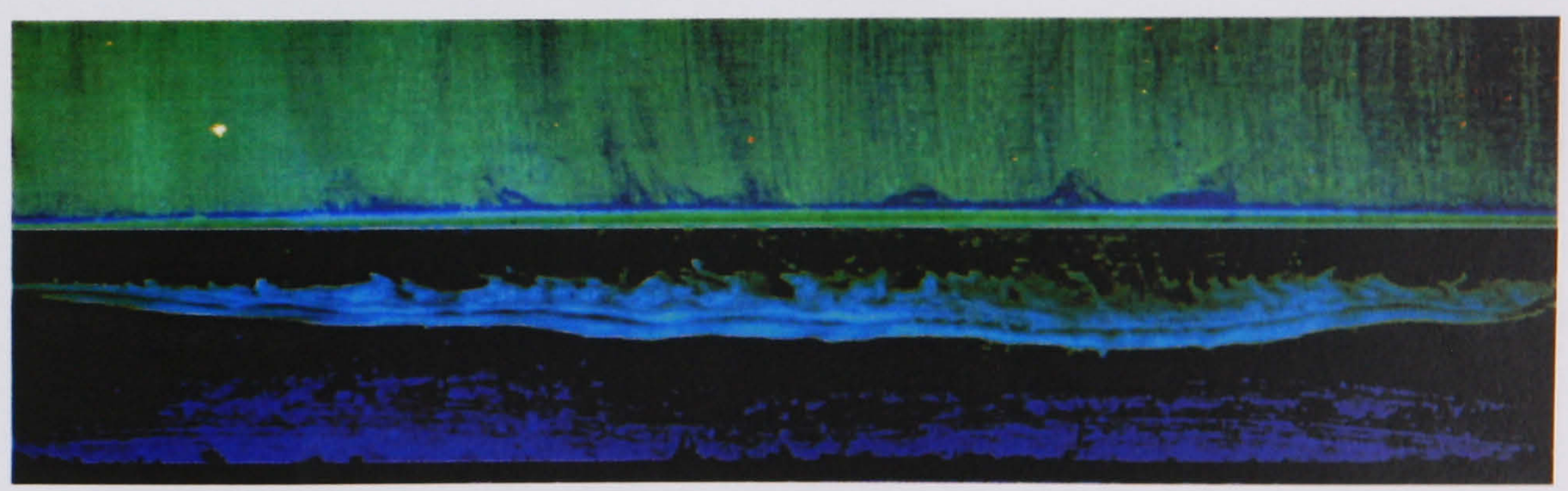

f. $L/D = 4.0$, $W/L = 8.4$ (560mm of total width shown)

Figure 4.8. Some examples of oil-flow visualisation used to determine transverse wavelength of instability. Freestream direction from top to bottom of page. Scale 1:4.4.

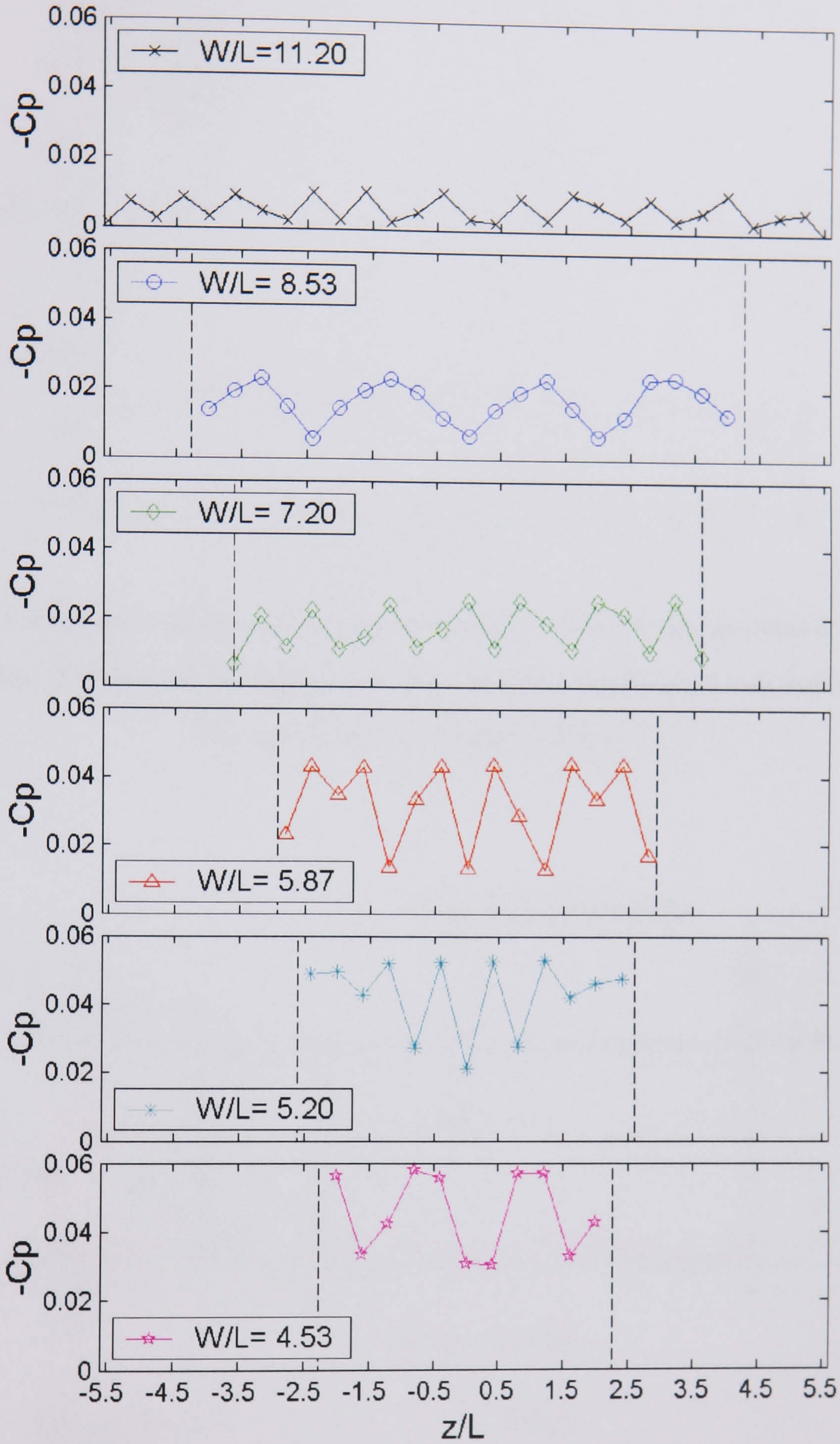

Figure 4.9. The coefficient of pressure measured for $L/D = 1.5$ as the cavity width is decreased (from top). Apart from $W/L = 8.53$ the transverse wavelength is consistently well approximated by the length of the cavity.

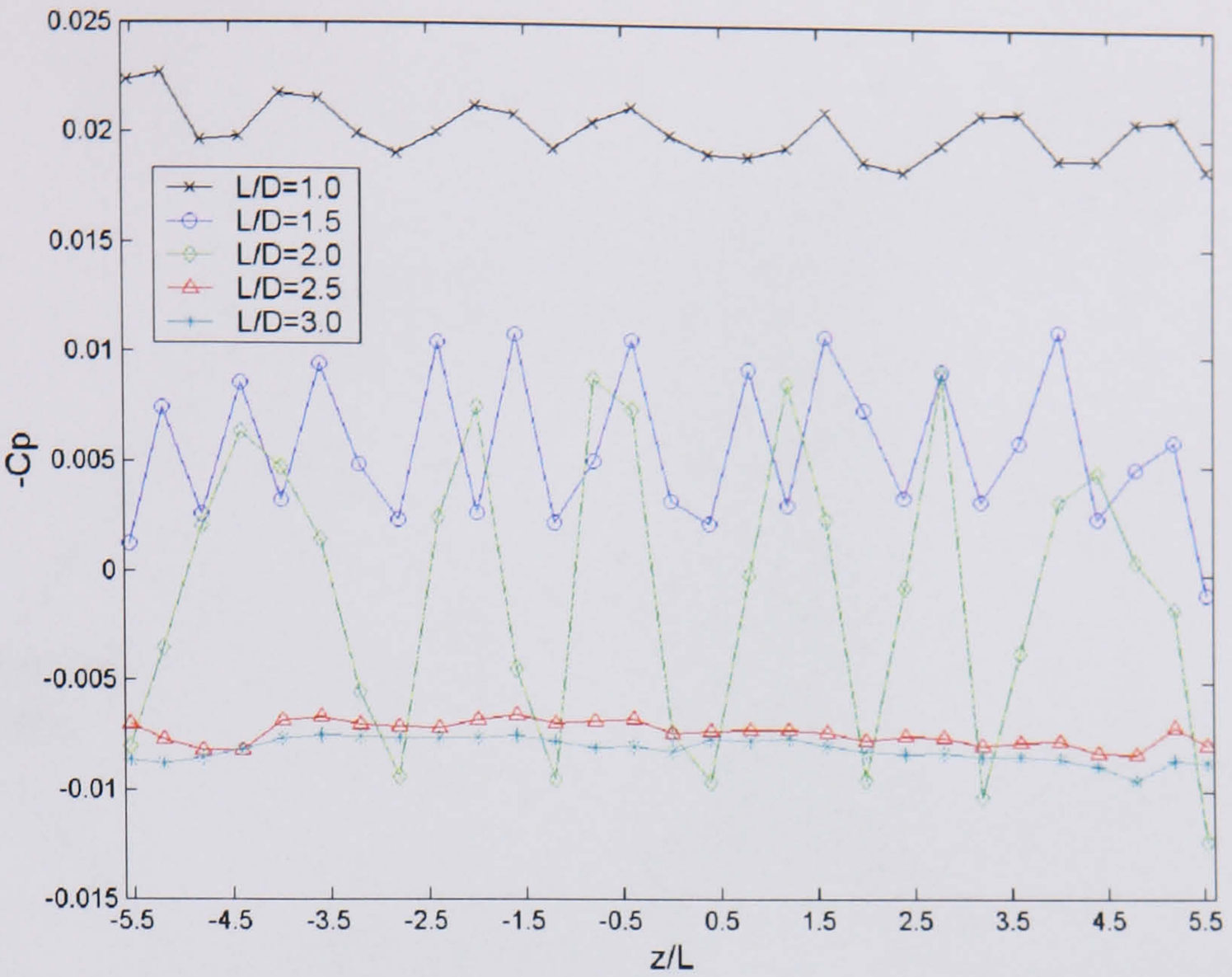

Figure 4.10. Pressure coefficient measured for each of the cavity geometries of interest in this study. Steady cellular behaviour was observed spanwise along the cavity floor for cases $L/D = 1.5$ and $L/D = 2.0$.

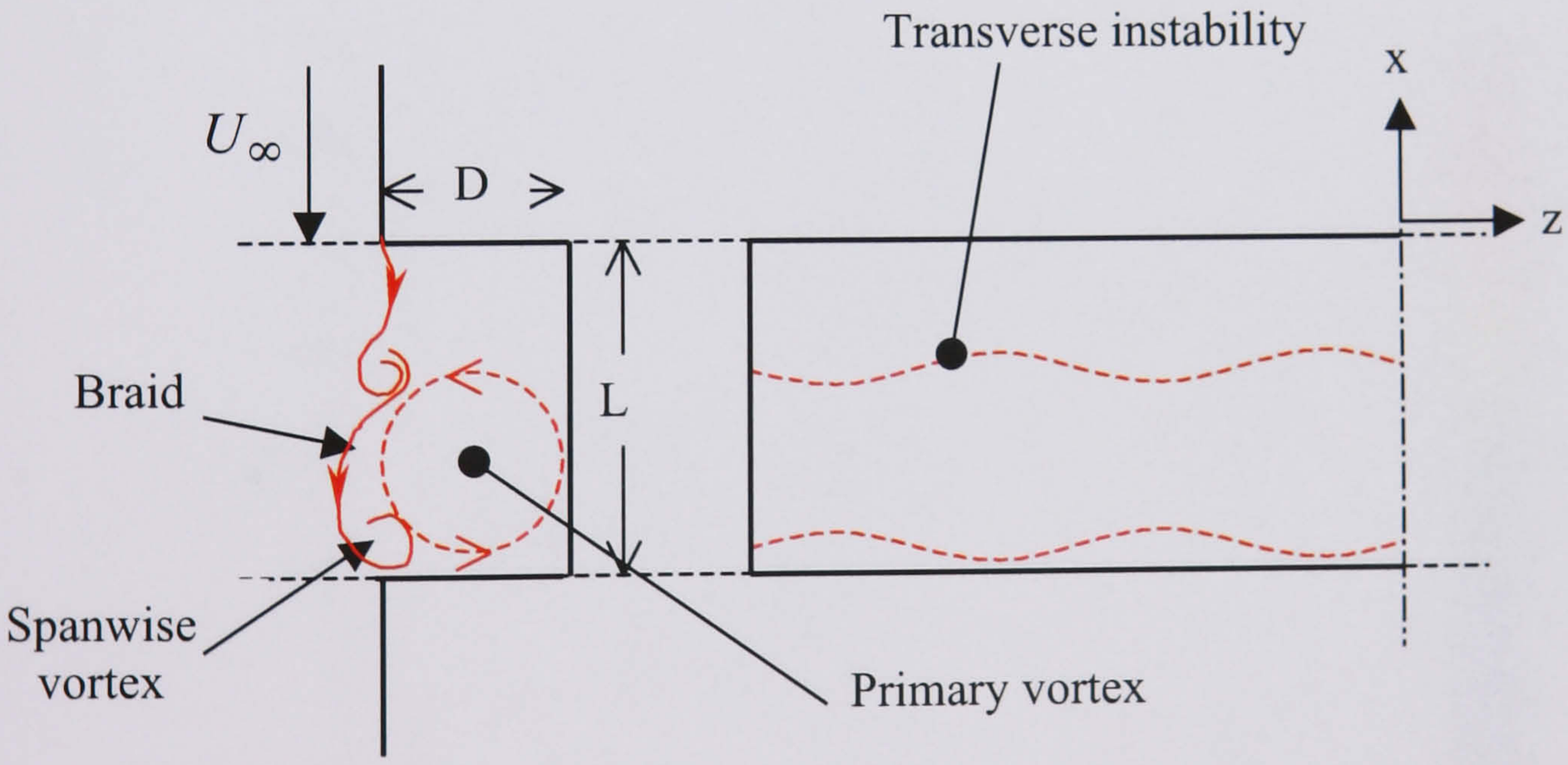

Figure 4.11. Schematic diagram showing the transverse wave instability and its effect on the primary vortex shape.

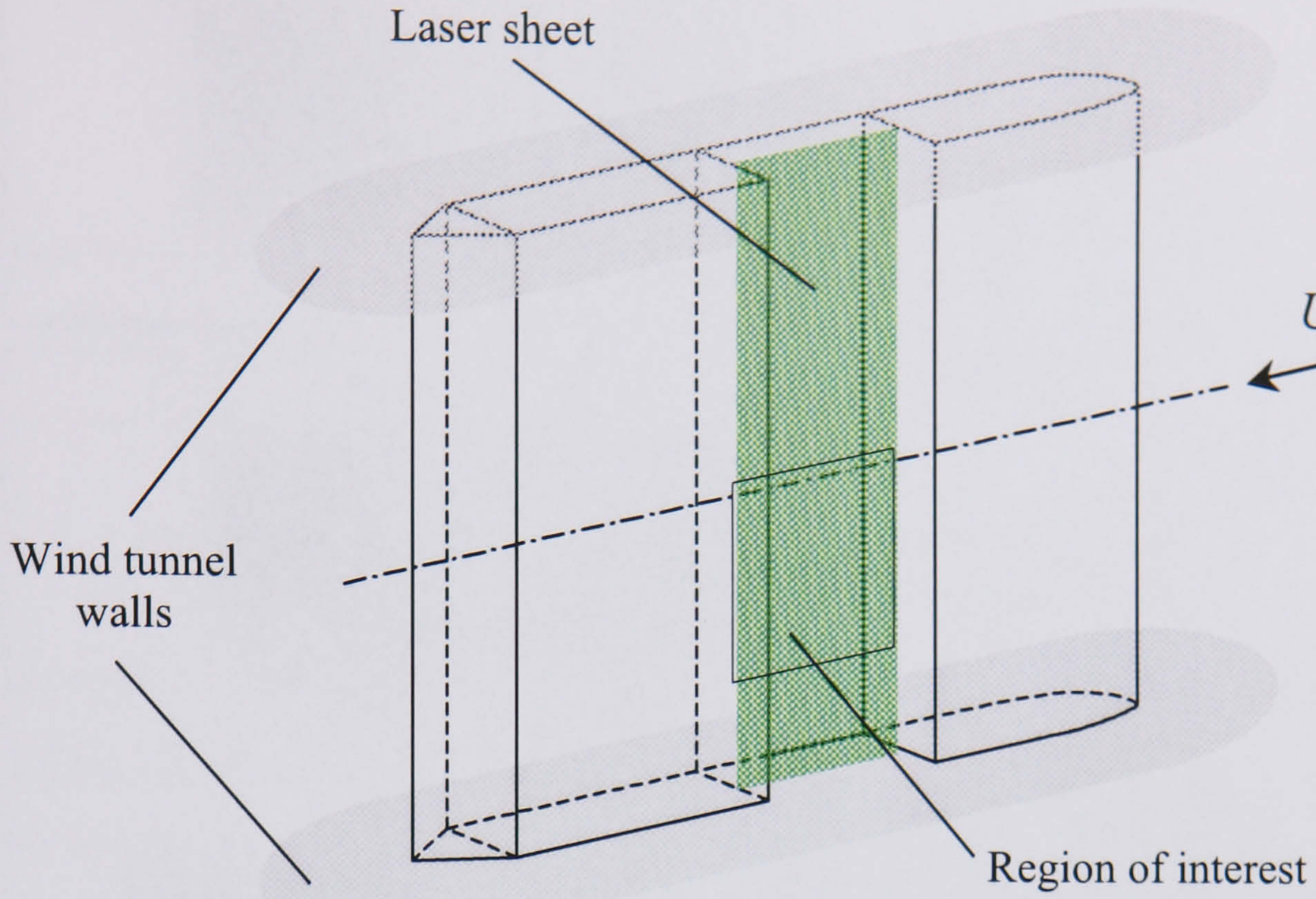

Figure 4.12. Diagram representing the installation orientation of the model in the test-section of the wind tunnel. The laser light sheet is directed in a plane parallel to the floor of the cavity.

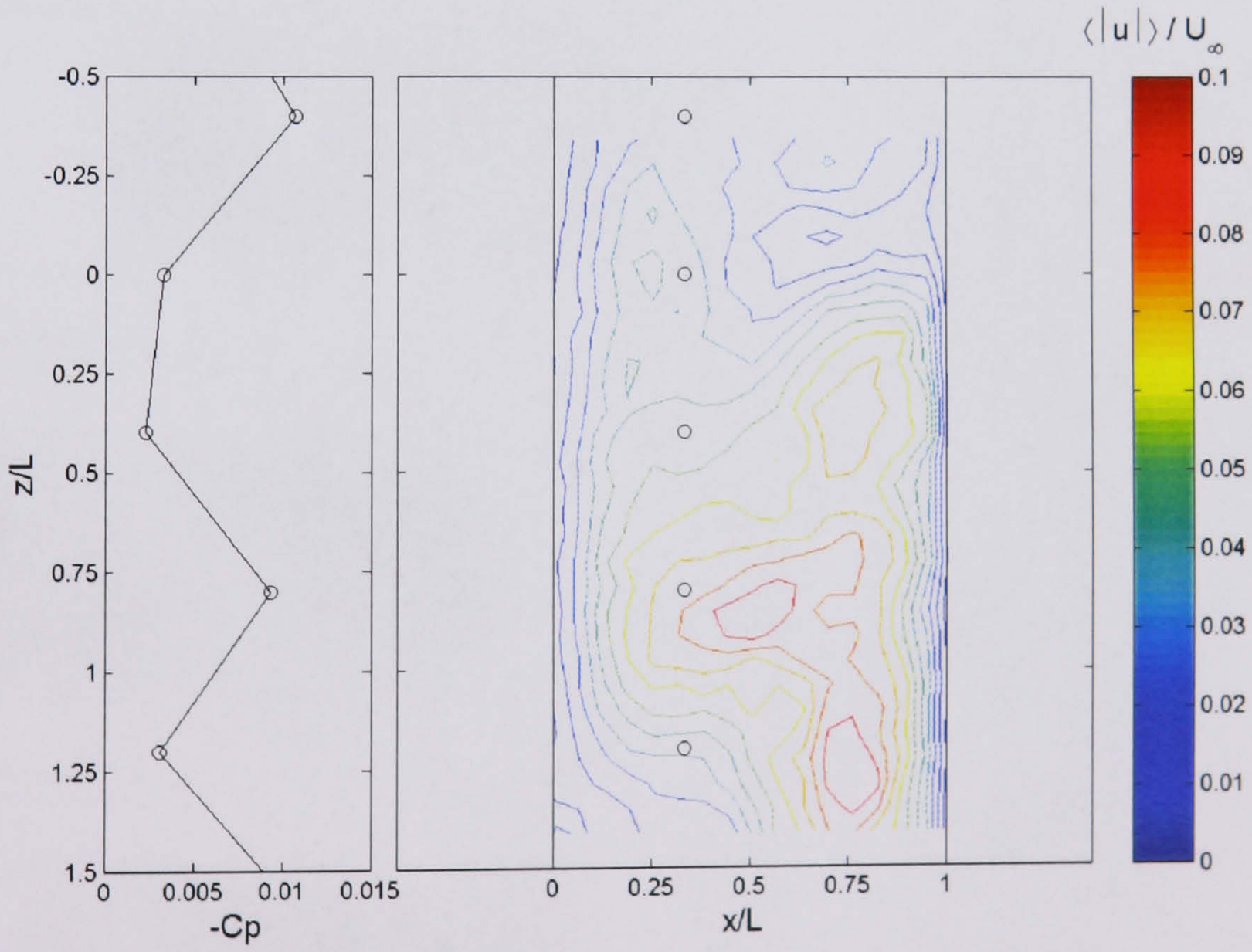

Figure 4.13. Static pressure measurement compared with the captured flowfield information showing average velocity magnitude at $y/D = -0.8$ for $L/D = 1.5$. The black dots indicate the position of the static pressure ports on the cavity floor.

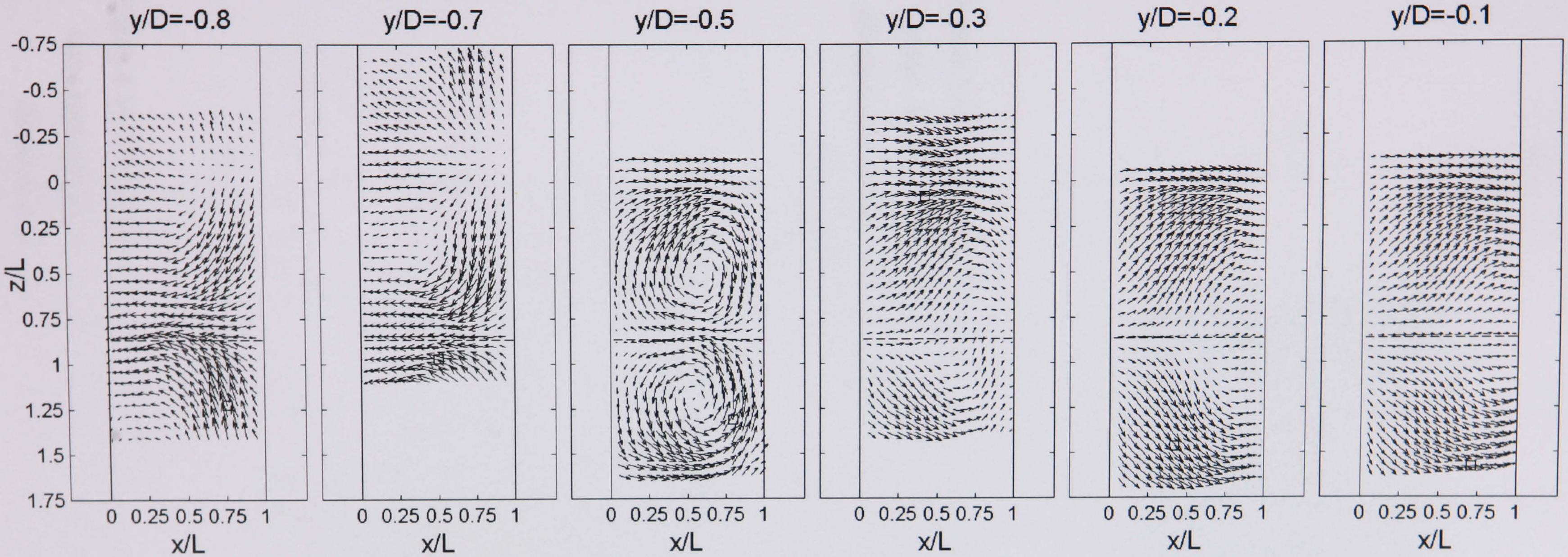

Figure 4.14. The velocity measurement of several spanwise planes within the cavity itself for $L/D = 1.5$. The box indicates the position of maximum velocity, while the dashed line indicates the position of the re-circulating core identified in figure 4.13. One quarter of the velocity vectors are shown unless stated otherwise. Maximum velocity from left to right are $\mathbf{u}_{max}/U_\infty = 0.095, 0.099, 0.113, 0.097, 0.167, 0.238$.

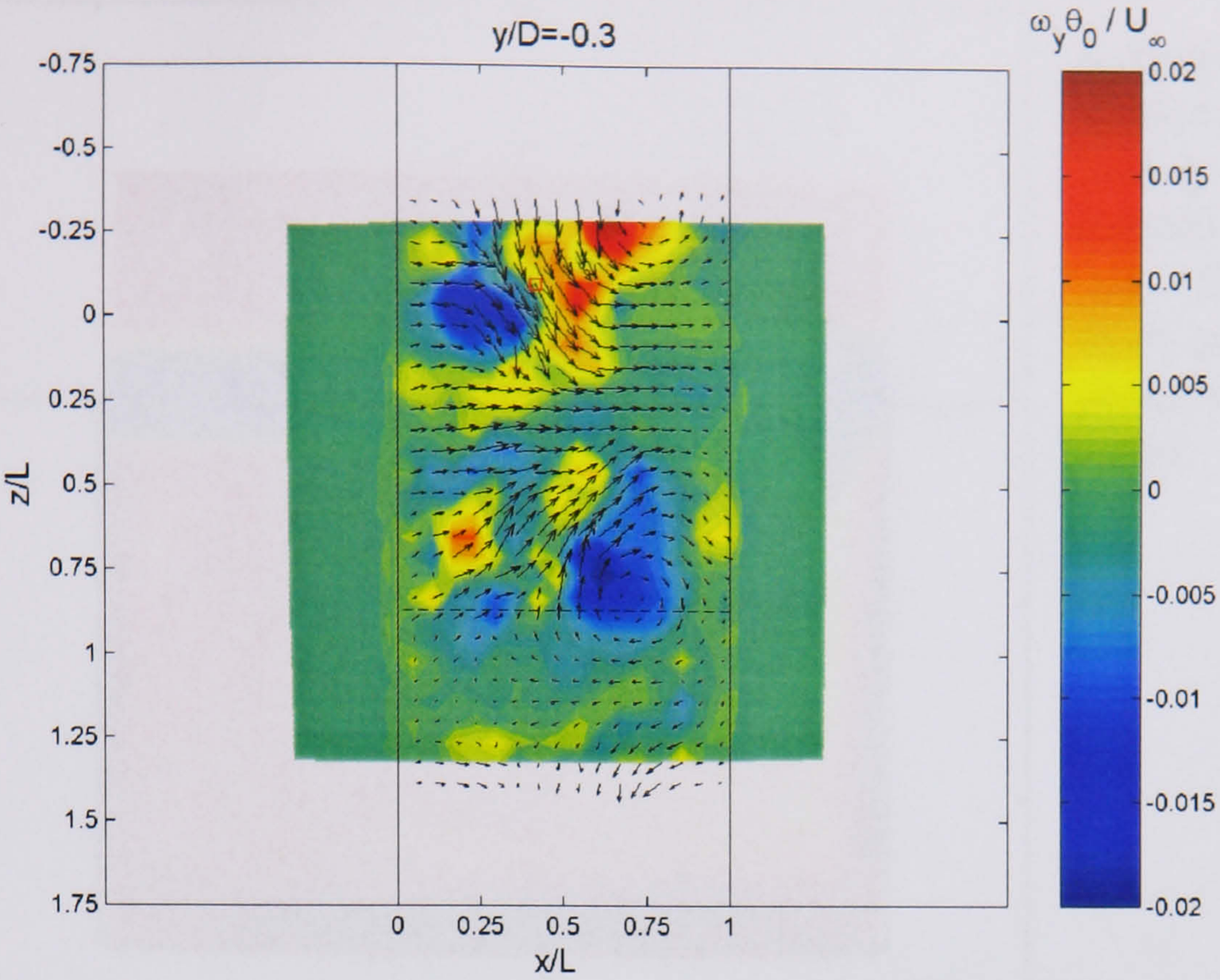

Figure 4.15. The instantaneous measurement of the velocity and vorticity in a spanwise plane. At this elevation the pockets of vorticity are much smaller and stronger and propagate up into the cavity. There is considerable streamwise meander of vorticity at this height, smearing the data of figure 4.14. $\mathbf{u}_{\max}/U_\infty = 0.22$.

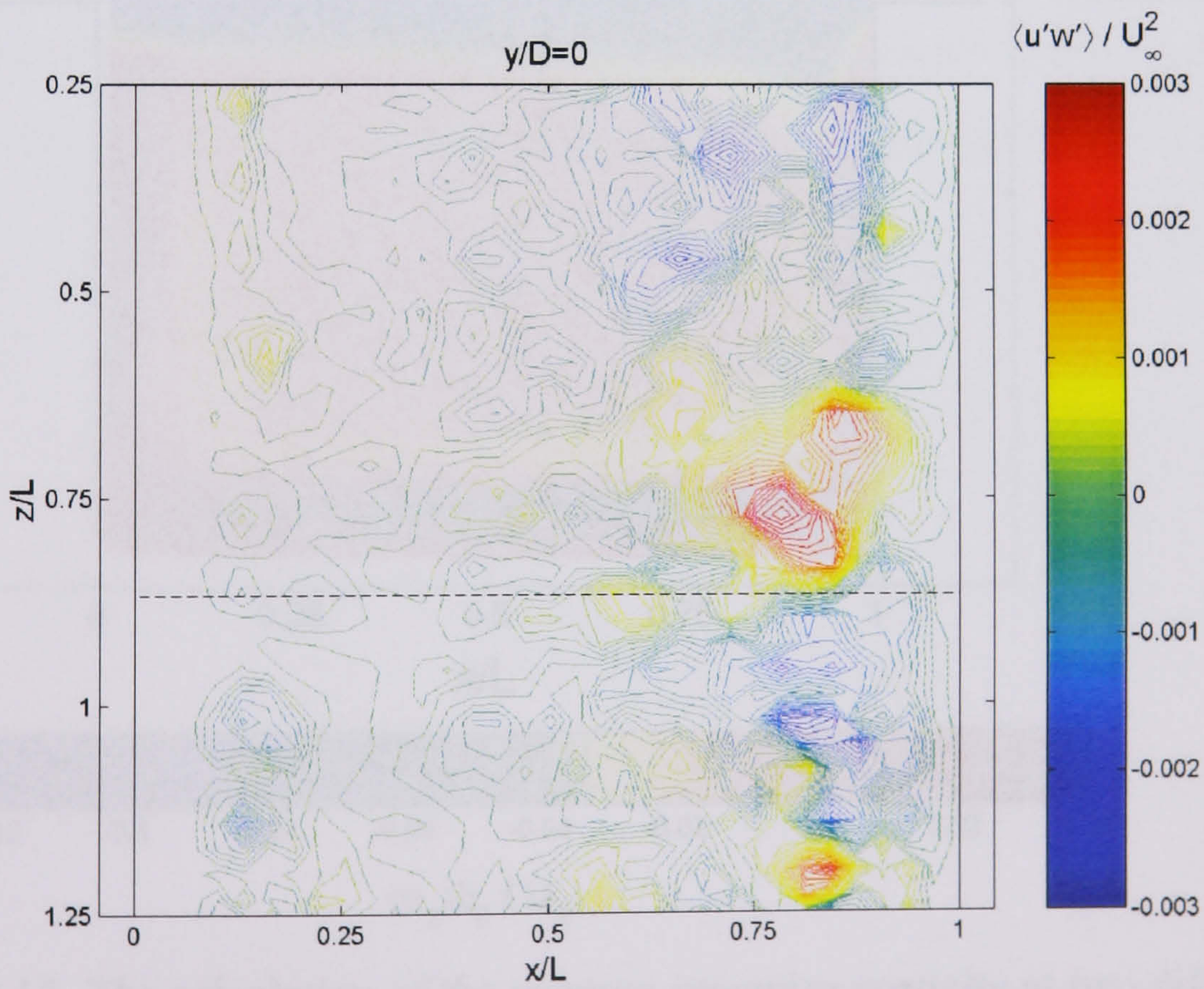

Figure 4.16. Calculation of the Reynolds shear stress through the mid-plane of the shear layer spanning the cavity face for $L/D = 1.5$. Two localized regions of energy are developed on either side of the dashed line, as plotted in figure 4.14.

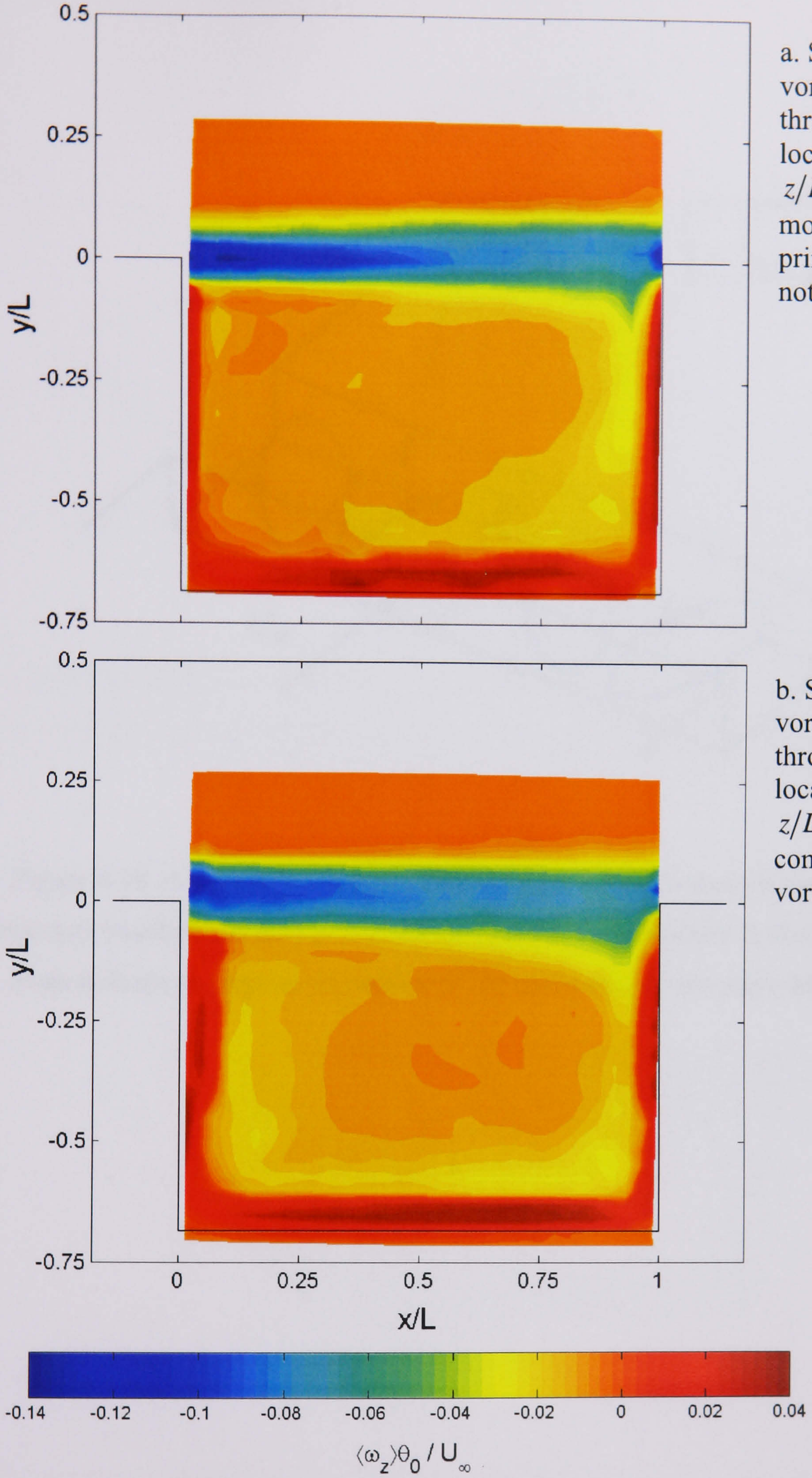

a. Spanwise vorticity measured through the plane located at $z/L = 0.072$. A more expanded primary vortex is noted.

b. Spanwise vorticity measured through the plane located at $z/L = 0.286$. Slight compression to the vortex is seen.

Figure 4.17. The calculation of the average spanwise vorticity at two different z-positions along the cavity model for $L/D = 1.5$. The limits of the colourbar have been set to make the structures inside the cavity more visible.

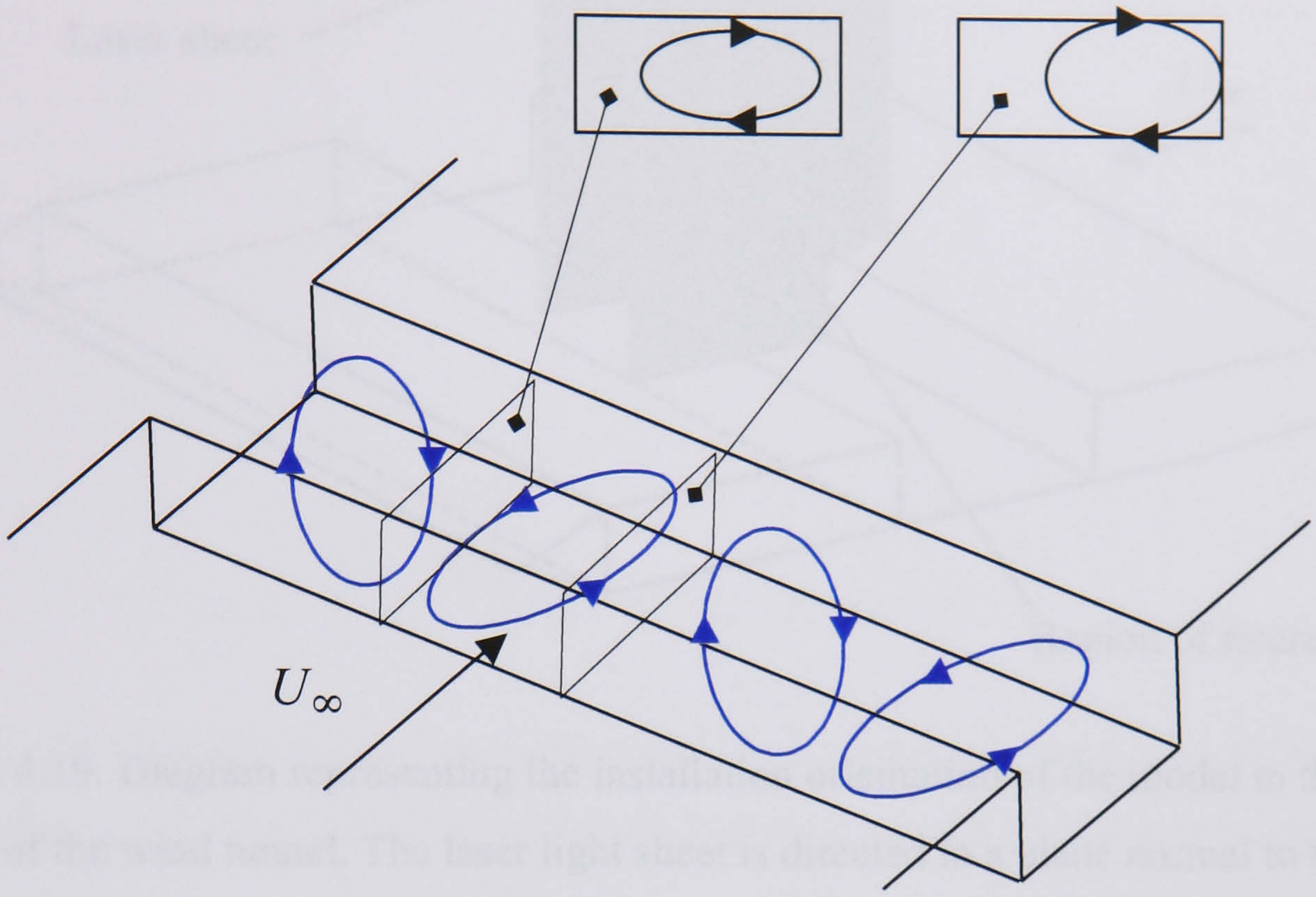

Figure 4.18. A schematic diagram indicating the probable three-dimensional cavity structure based on the strictly two-component data accumulated in this study. The blue ovals indicate the typical orientation of the transverse vortex pairs inside the cavity.

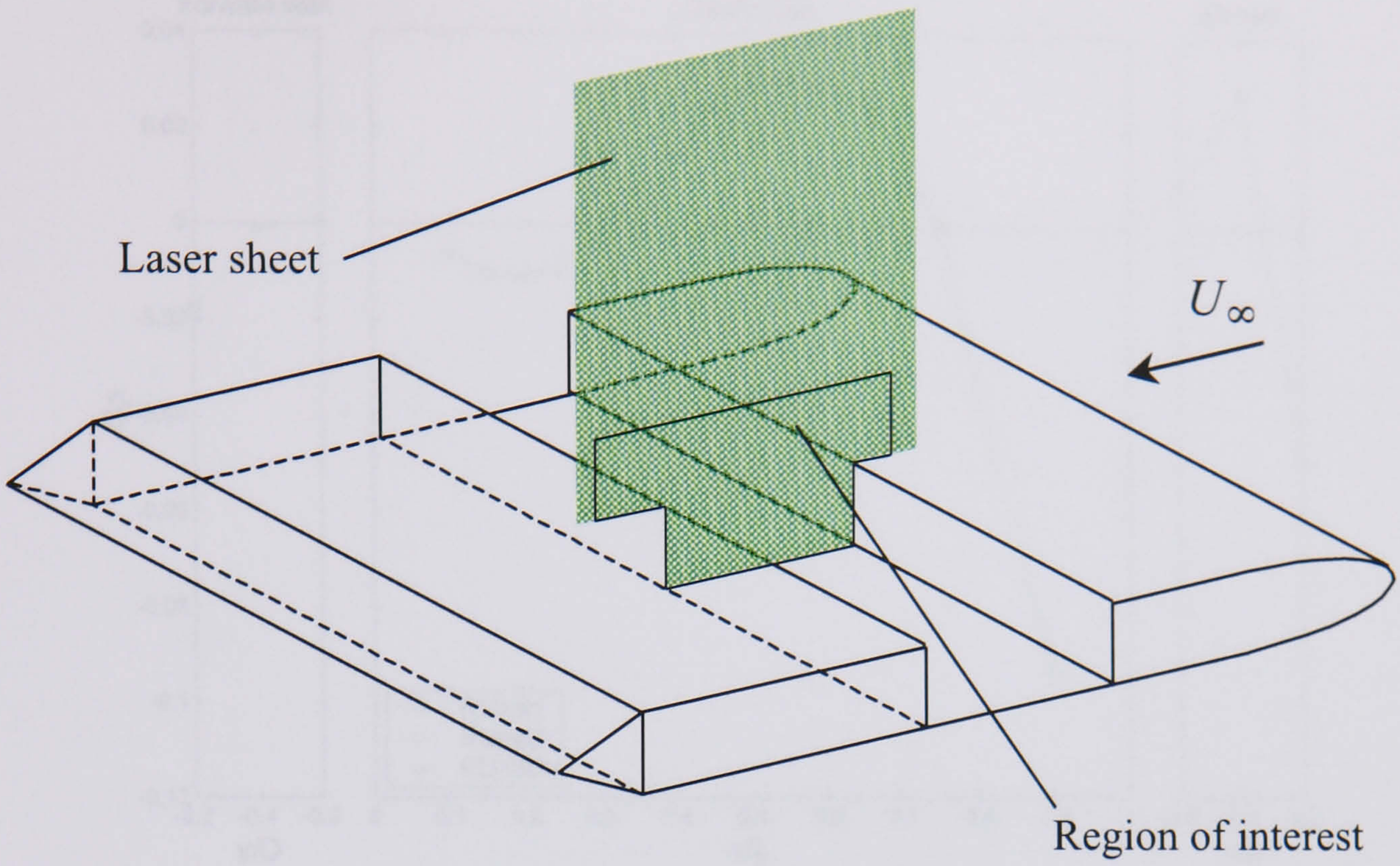

Figure 4.19. Diagram representing the installation orientation of the model in the test-section of the wind tunnel. The laser light sheet is directed in a plane normal to the floor of the cavity.

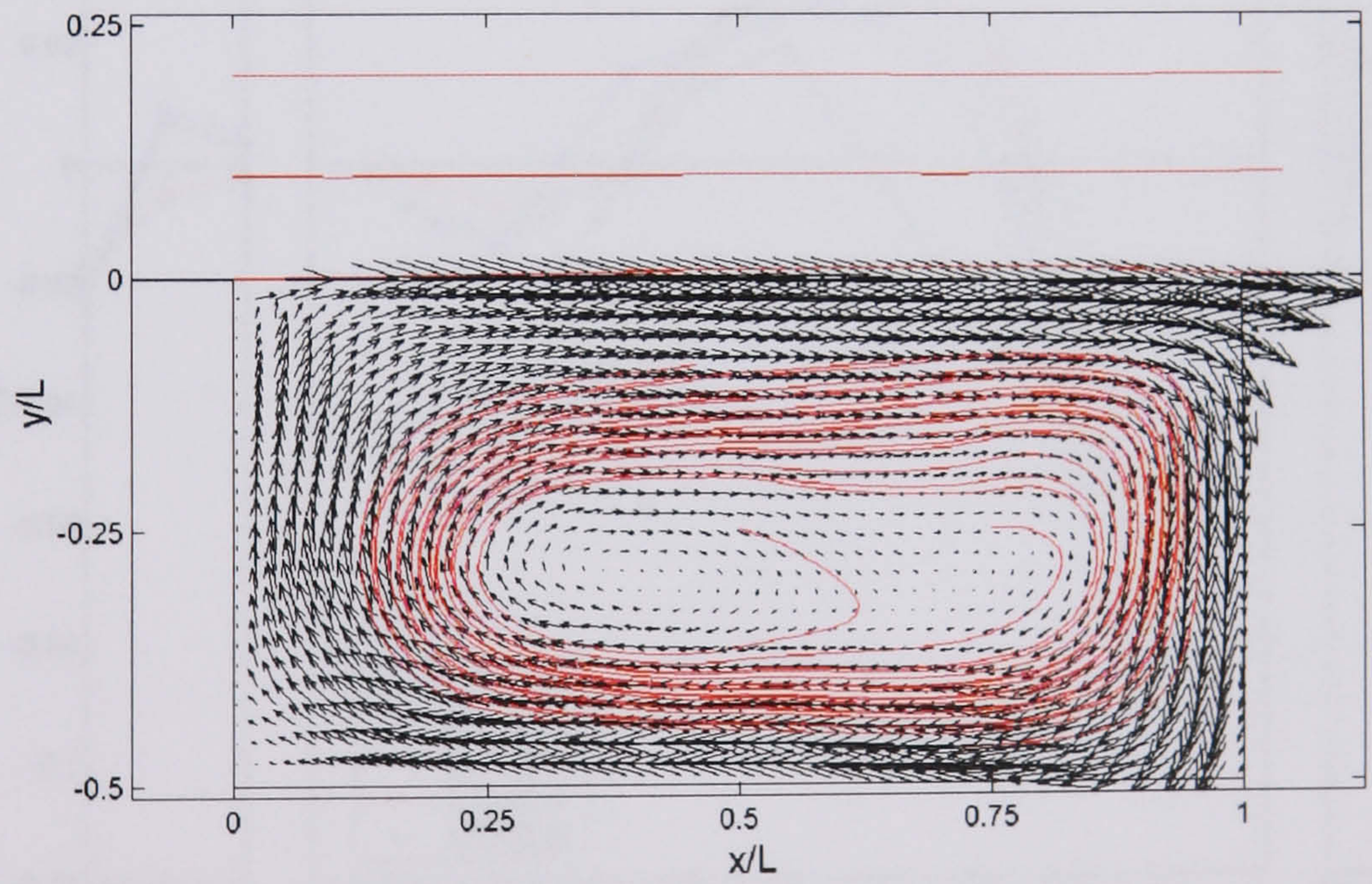

Figure 4.20. Mean flow properties in the cavity for $L/D = 2.0$. Streamlines are shown with velocity vectors superimposed in the cavity itself (flow is from left to right). The average internal cavity flow is characterised by a stagnant zone surrounded by a much stronger recirculation flow along walls and the open face.

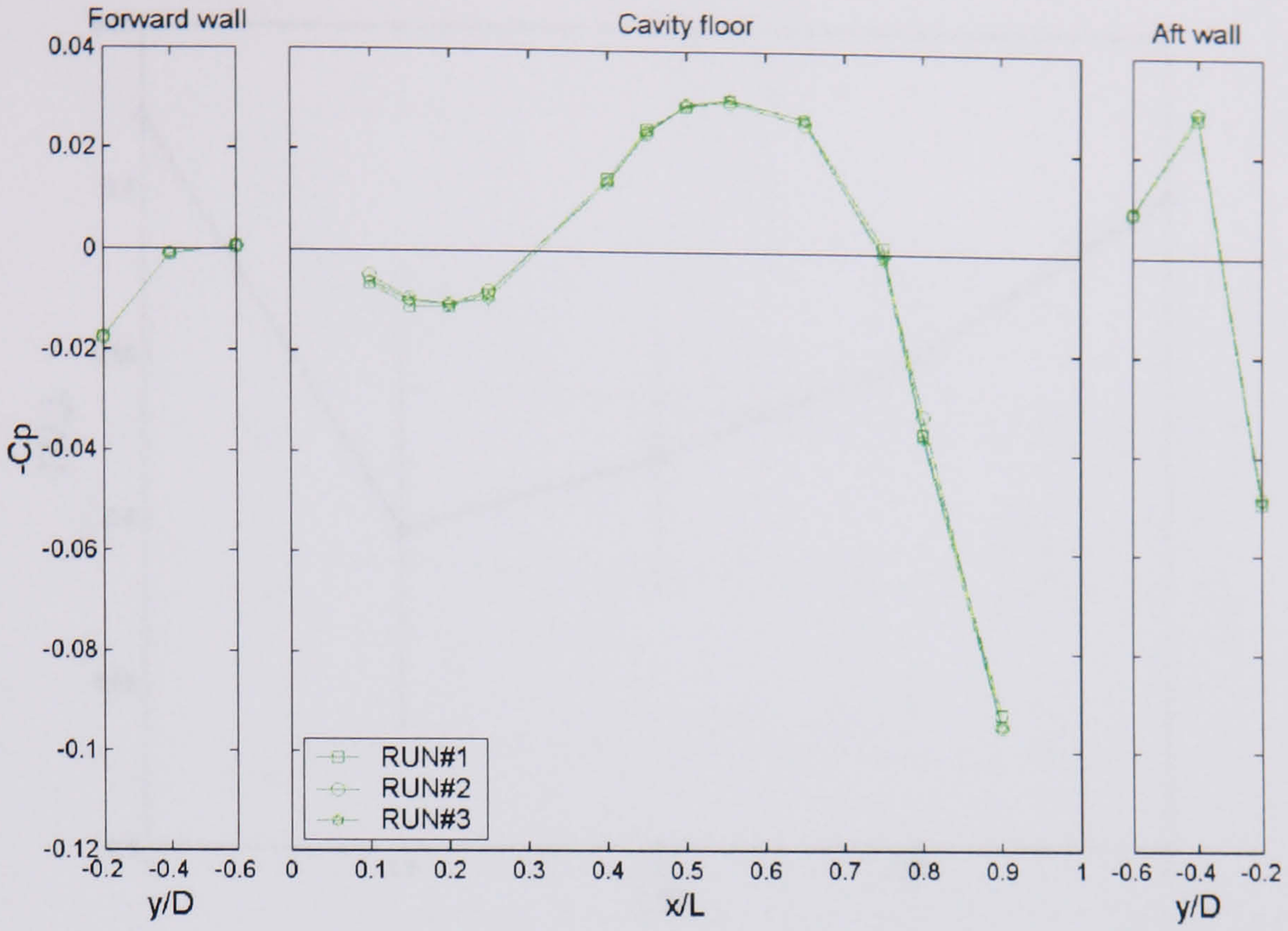

Figure 4.21. Pressure coefficient measured along the cavity forward wall, aft wall and cavity floor for $L/D = 2.0$. As a test for acquisition repeatability three runs are shown. There appears to be very little measured difference between each set.

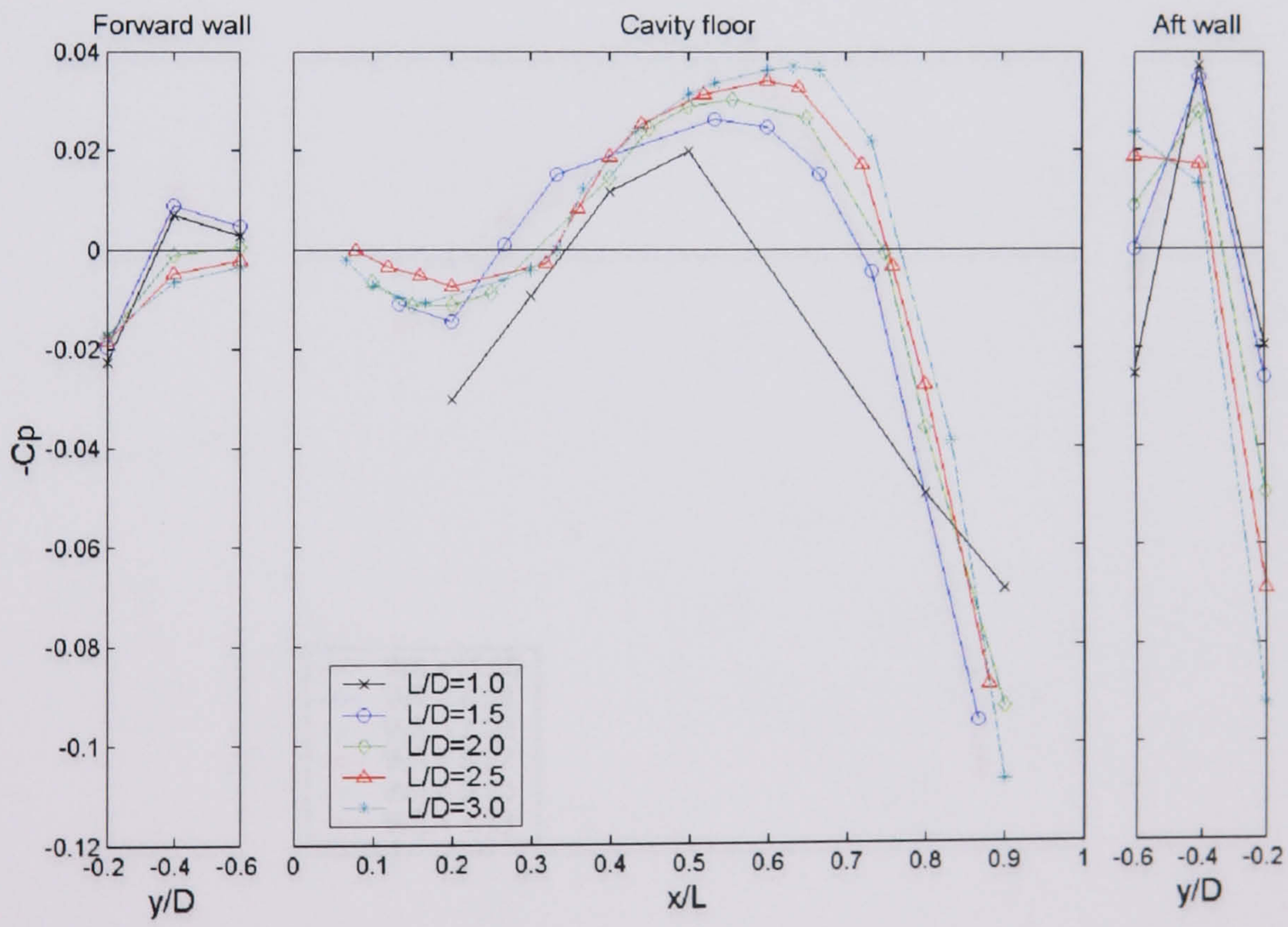

Figure 4.22. Pressure coefficient measured in the same manner already mentioned. Each cavity L/D included in this study is shown in the graph.

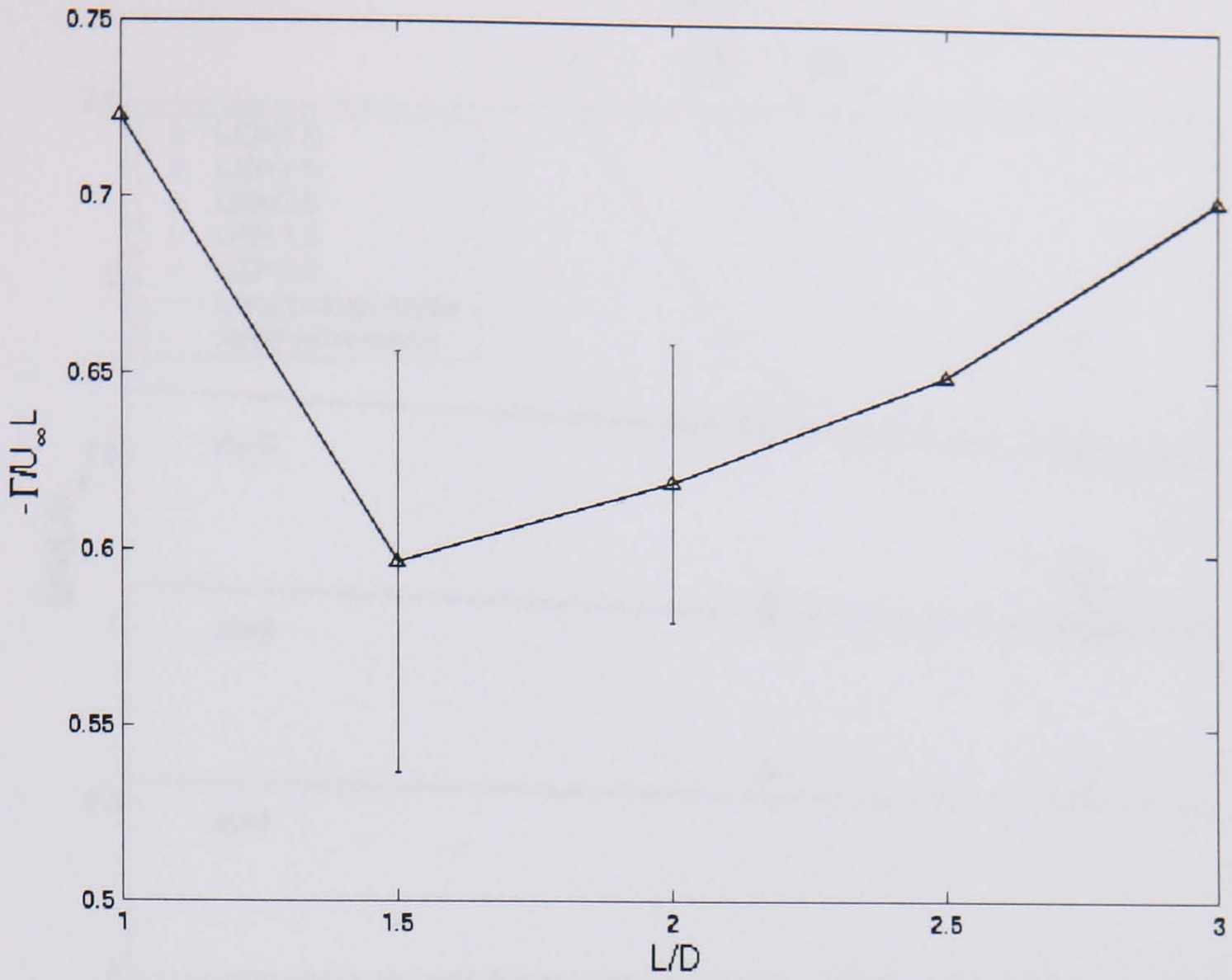

Figure 4.23. Circulation plotted against L/D. The integration was performed around a path implied from the streamline calculation and as such is approximate. Error bars indicate the spanwise variation in circulation strength,

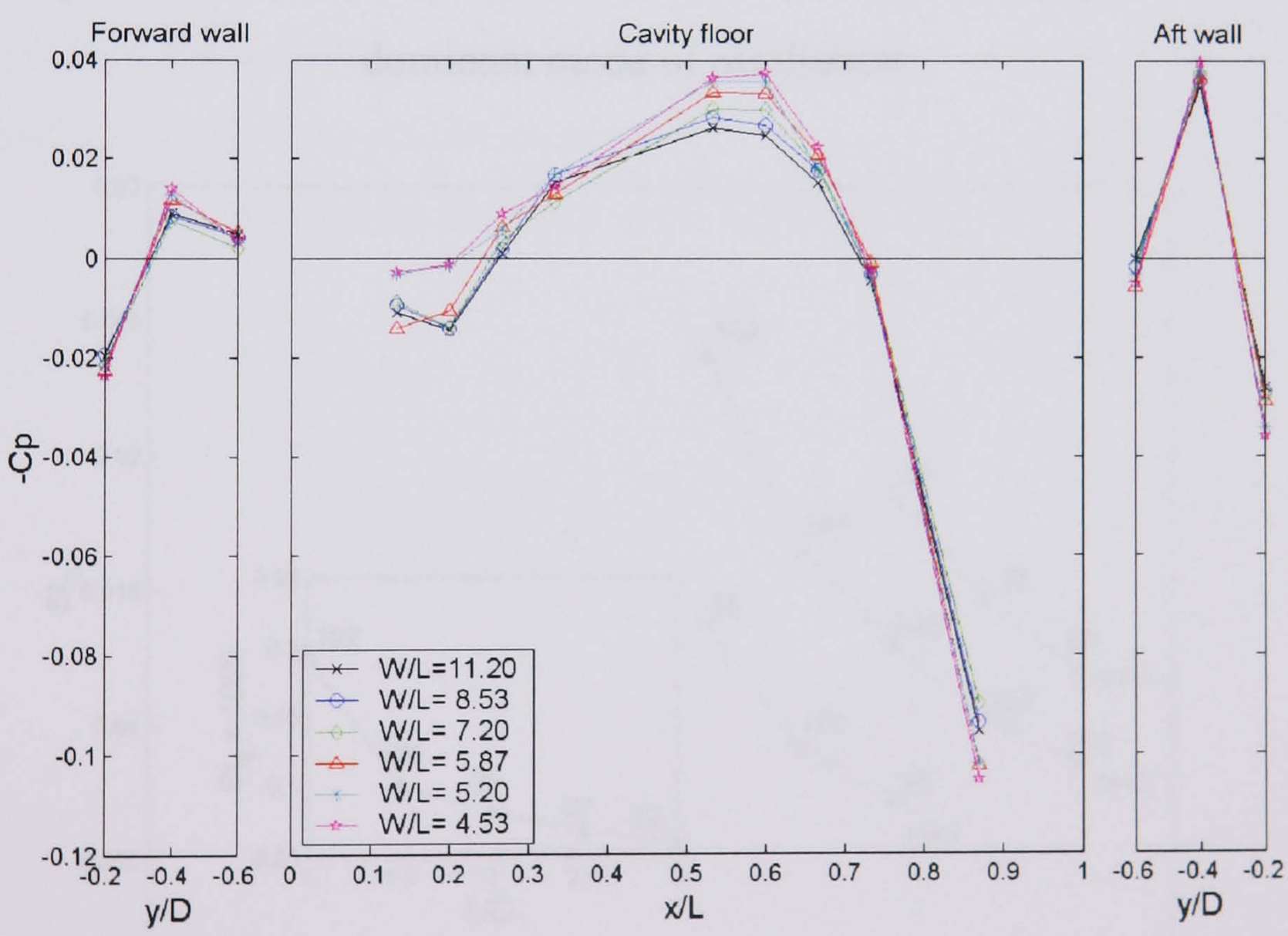

Figure 4.24. Pressure coefficient measured along the cavity forward wall, aft wall and cavity floor for $L/D = 1.5$ using a number of W/L ratios.

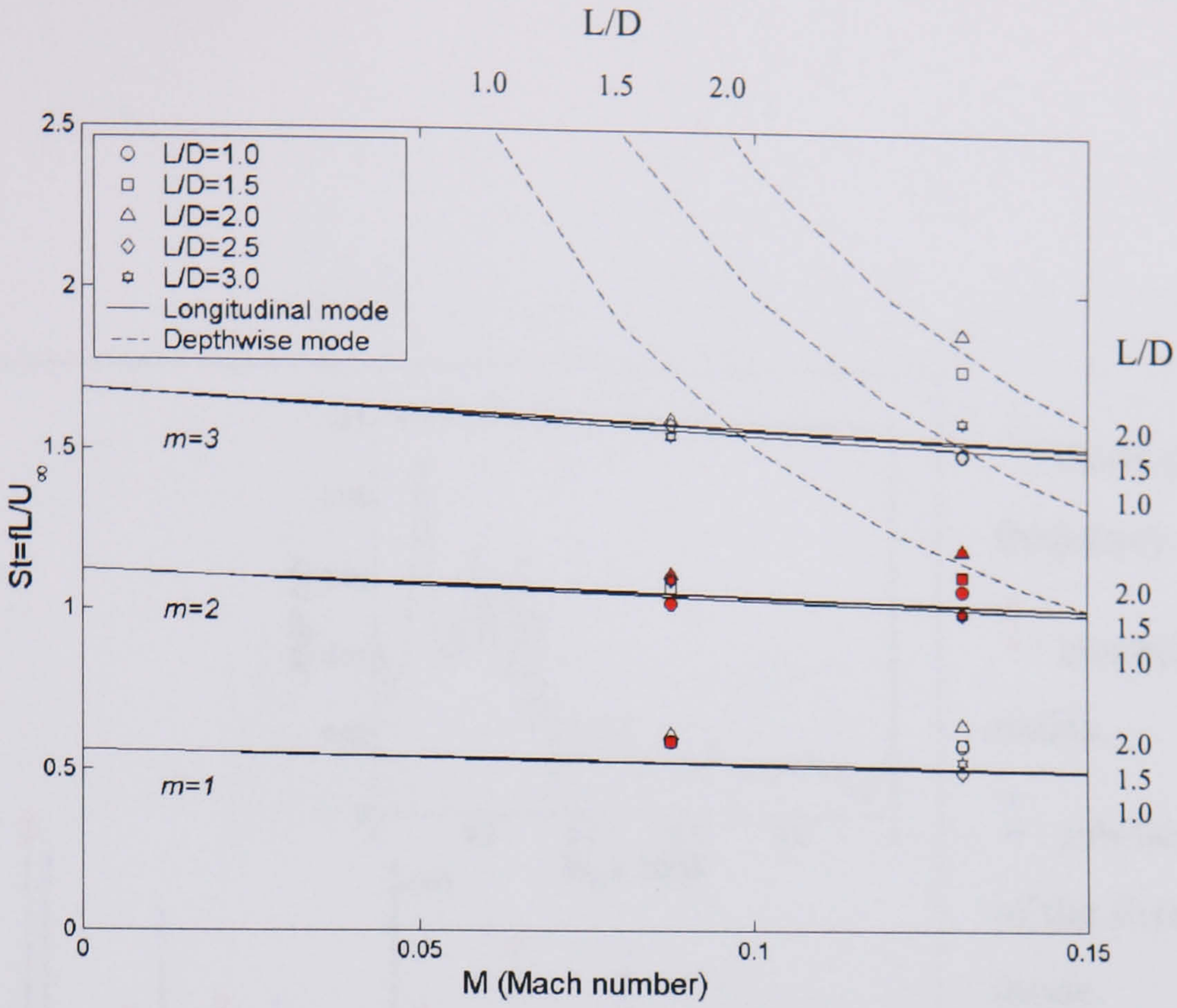

Figure 4.25. Strouhal numbers calculated from the tests with predicted Strouhal numbers from Block et al. 1976. Note that two sets of Mach number have been included in the experimental data, $M_\infty = 0.08$ and $M_\infty = 0.13$. Filled markers indicate the dominant mode of oscillation.

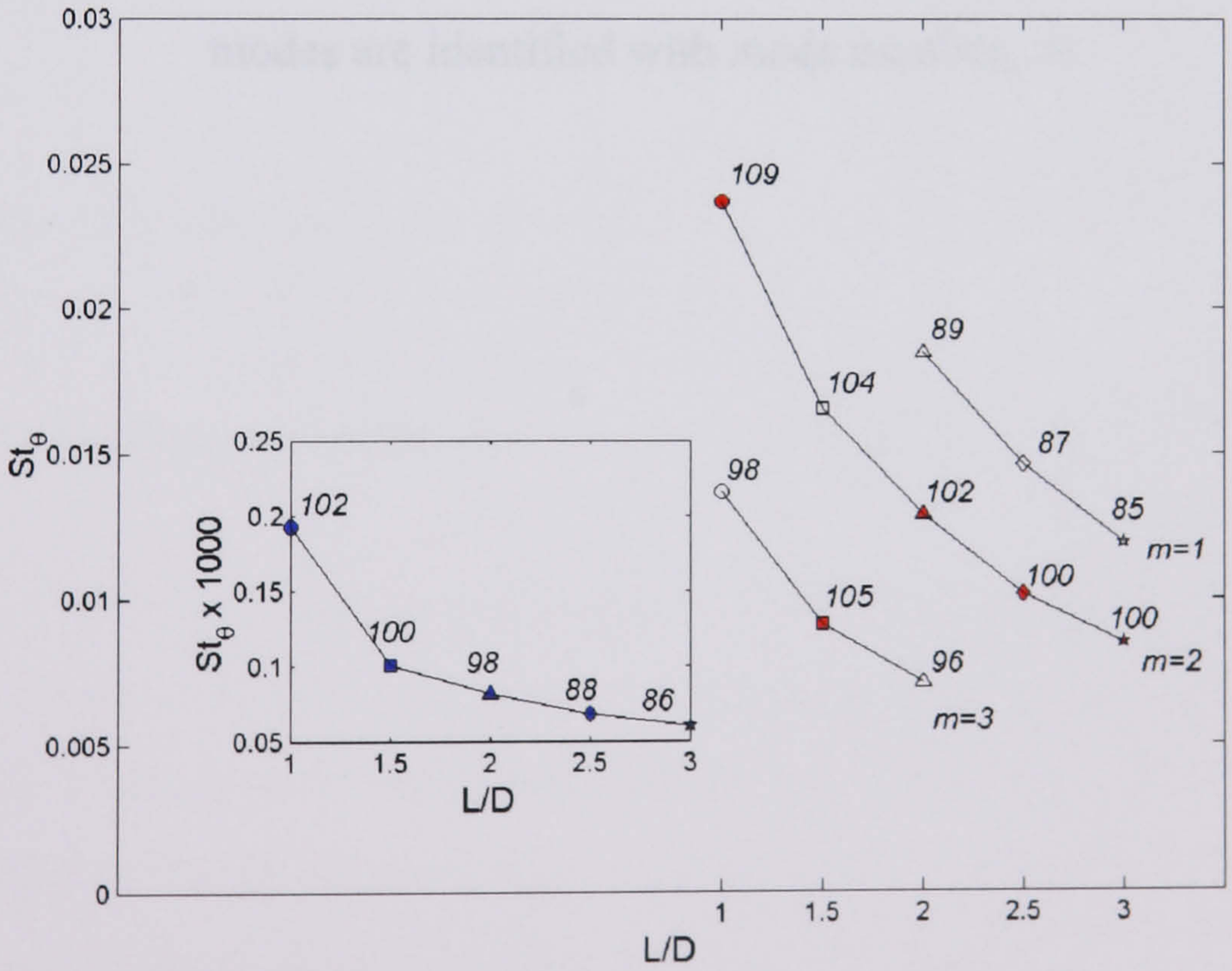

Figure 4.26. Data for test matrix only showing cavity L/D against St_θ. As expected the Strouhal number decreases as the L/D increases. The numbers next to each data point indicate the measured SPL for that particular oscillation.

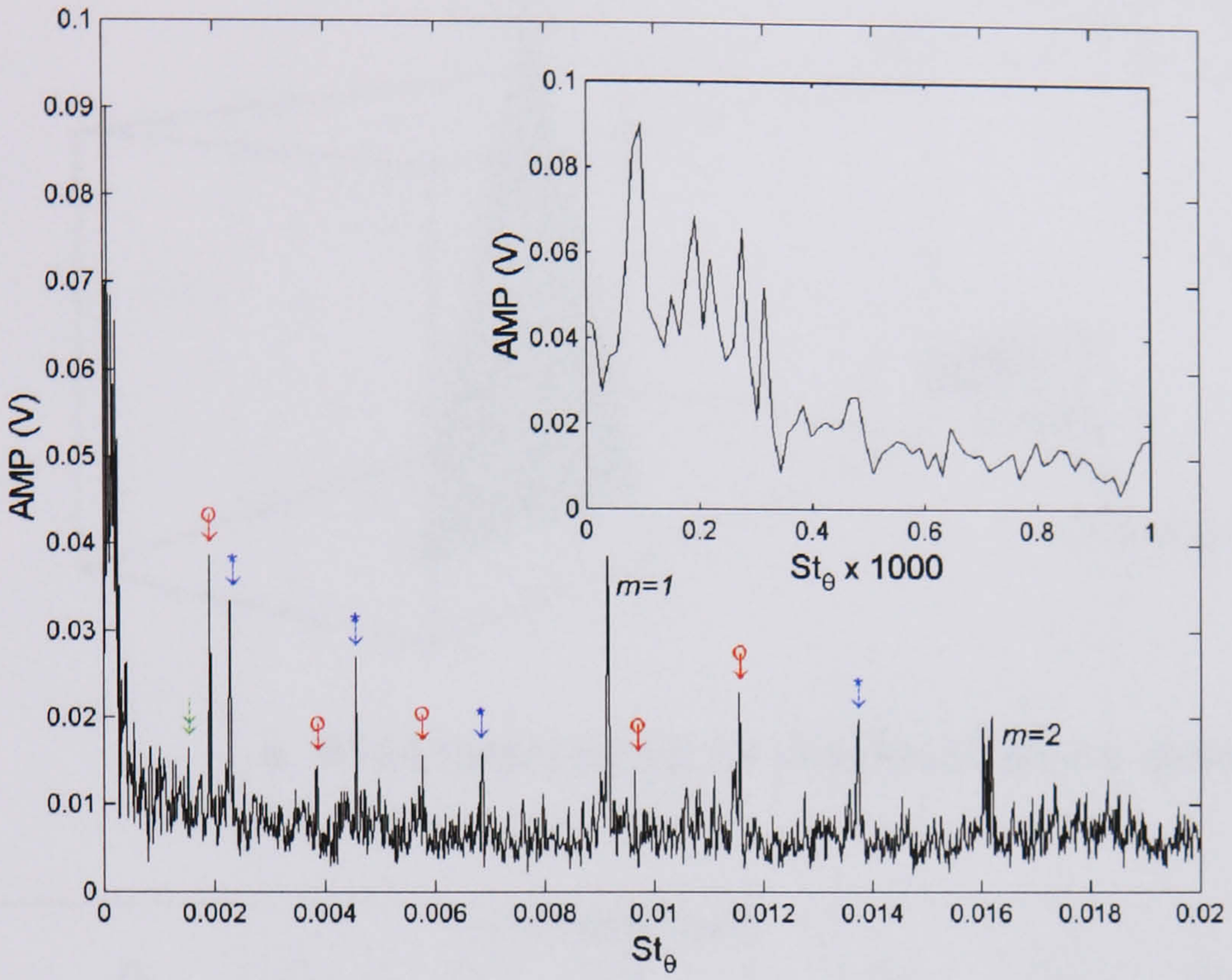

: blade passing frequency.

: electricity mains.

: sub-harmonics of the shear layer mode.

Figure 4.27. Raw data of the unsteady pressure measurement from the cavity floor. The top right hand axes illustrate a zoomed in portion of the main axes while the shear layer modes are identified with mode number, m.

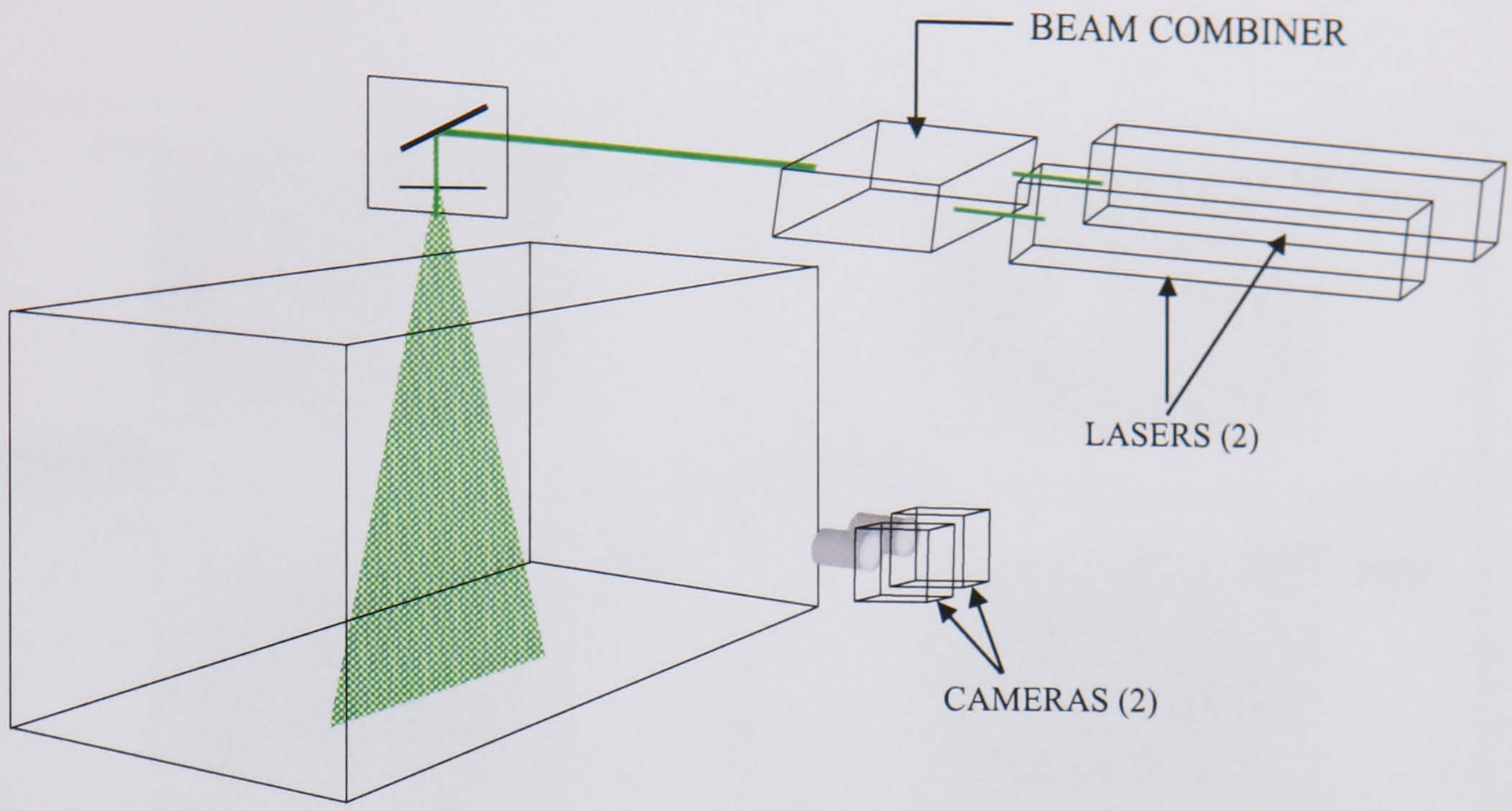

a. Wind-tunnel set-up for dual laser/camera operation.

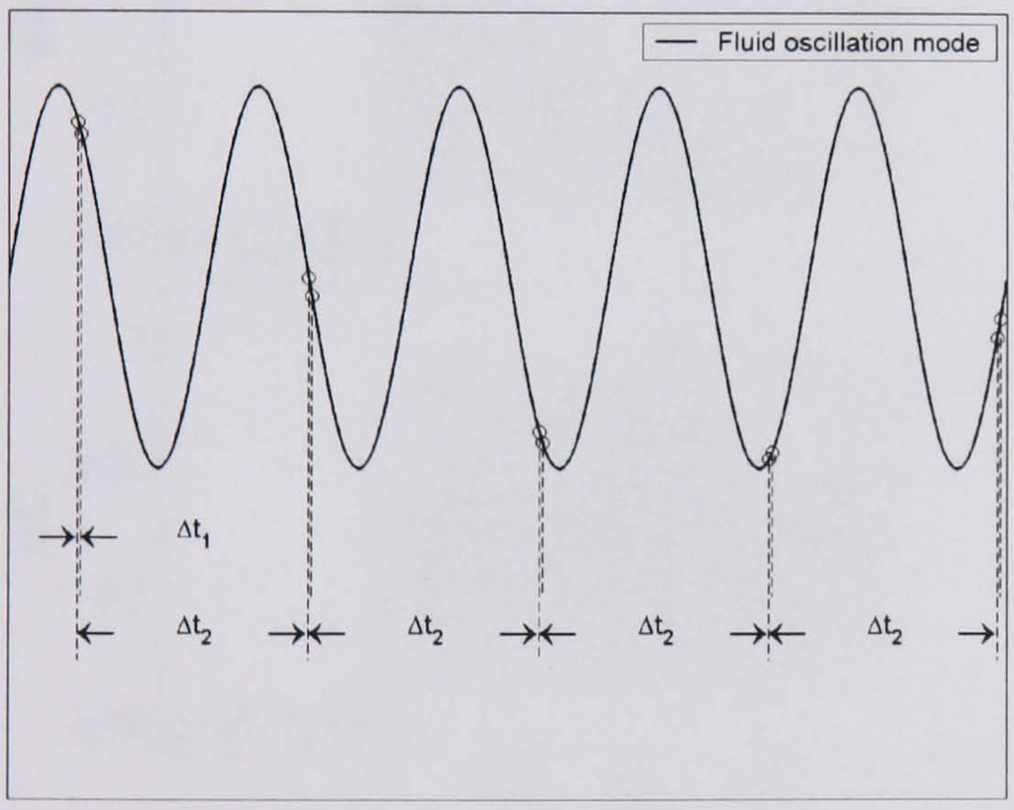

b. Single laser/camera operation.

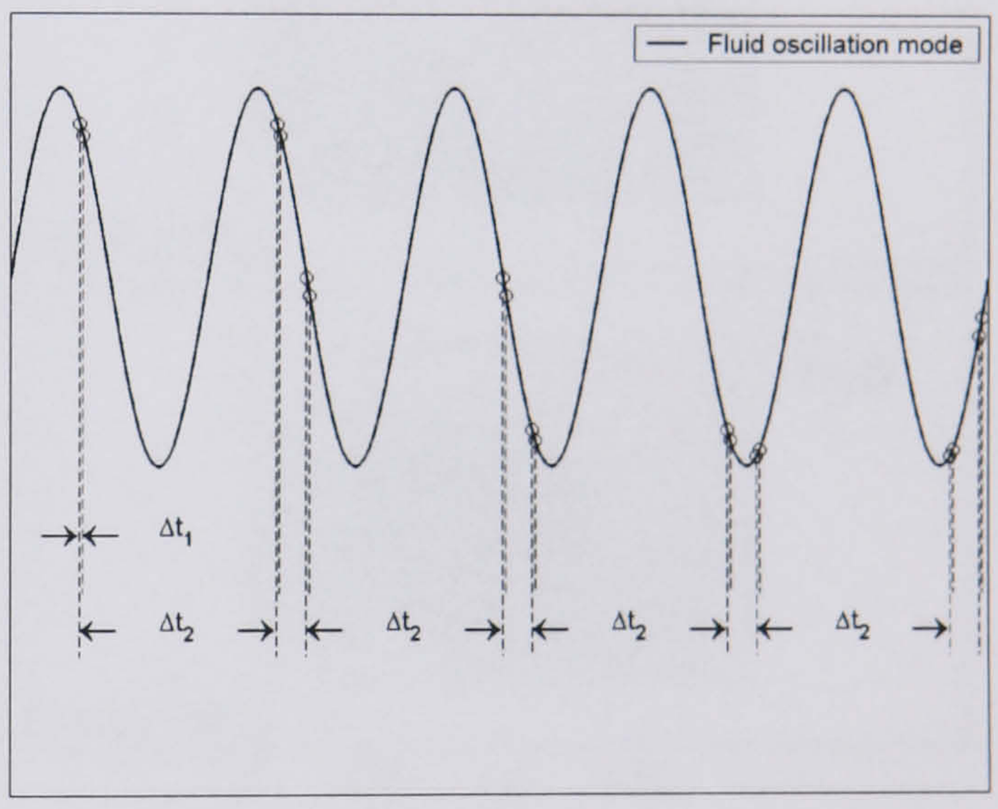

c. Dual laser/camera operation.

Figure 4.28. Two laser beams are channelled into one plane using the beam combiner as shown in (a). Parts (b) and (c) illustrate the sampling procedure for an idealized fluid oscillation. For the normal laser/camera operation (b) the inter-pulse delay (Δt_1) is dictated by the velocity dynamic range (section 2.3.4), while the second time delay (Δt_2) is imposed by the laser flash lamp. In the dual set-up (c) it is possible to control the second time delay although the fundamental capture frequency is still dictated by the flash lamp delay.

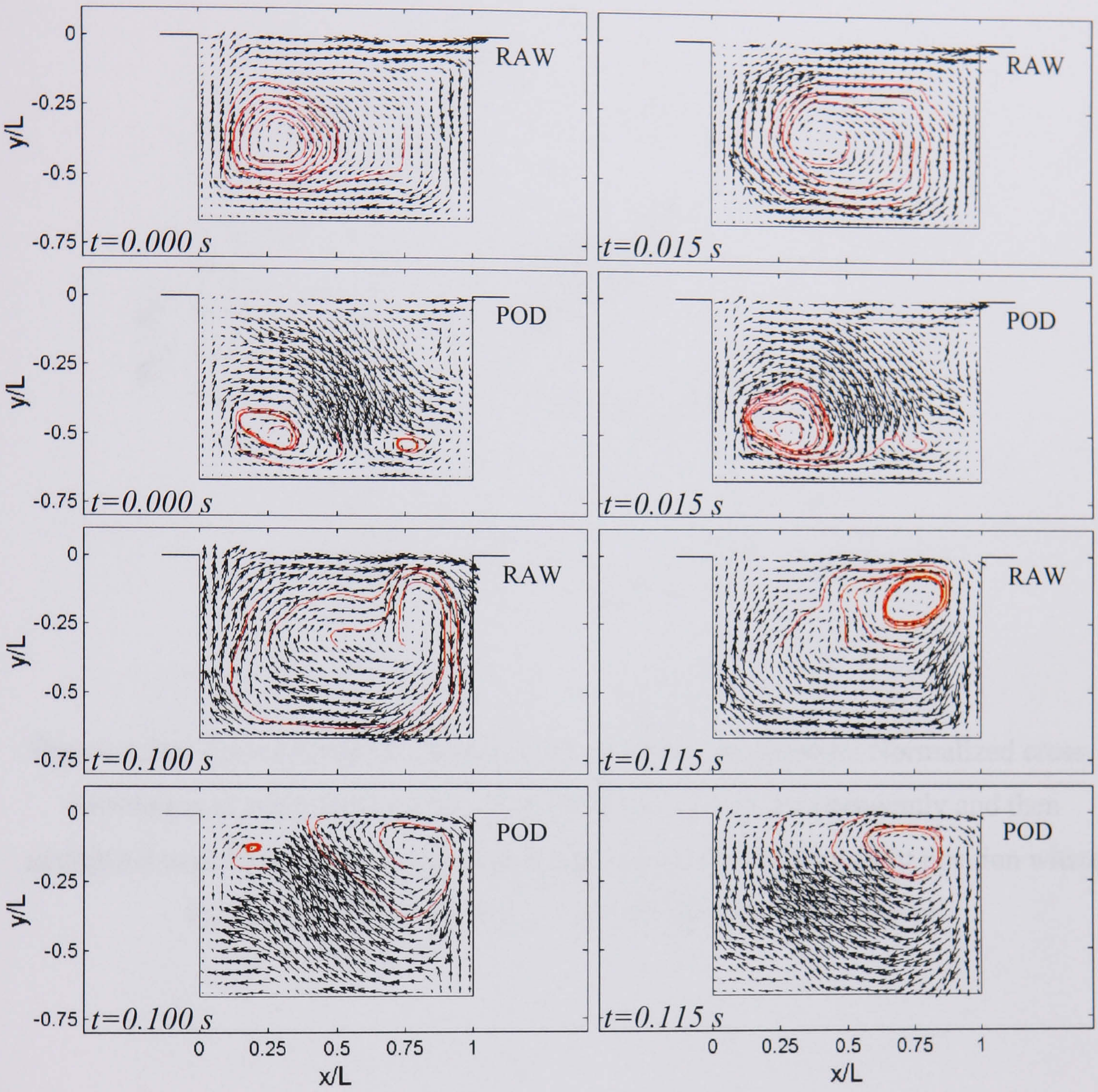

Figure 4.29. A sequence of results captured using the dual laser/camera set-up. $\Delta t_2 = 0.015$ seconds, which corresponds approximately to the $\beta/4$ subharmonic frequency of the fundamental shear layer oscillation ($St_\theta = 0.0023$). 'RAW' and 'POD' indicate whether the results are obtained directly from a typical correlation or reconstructed using Proper Orthogonal Decomposition. Streamline positions are seeded at $(x/L, y/L) = (0.25,-0.33;0.5,-0.33;0.75,-0.33)$ for the 'RAW' data.

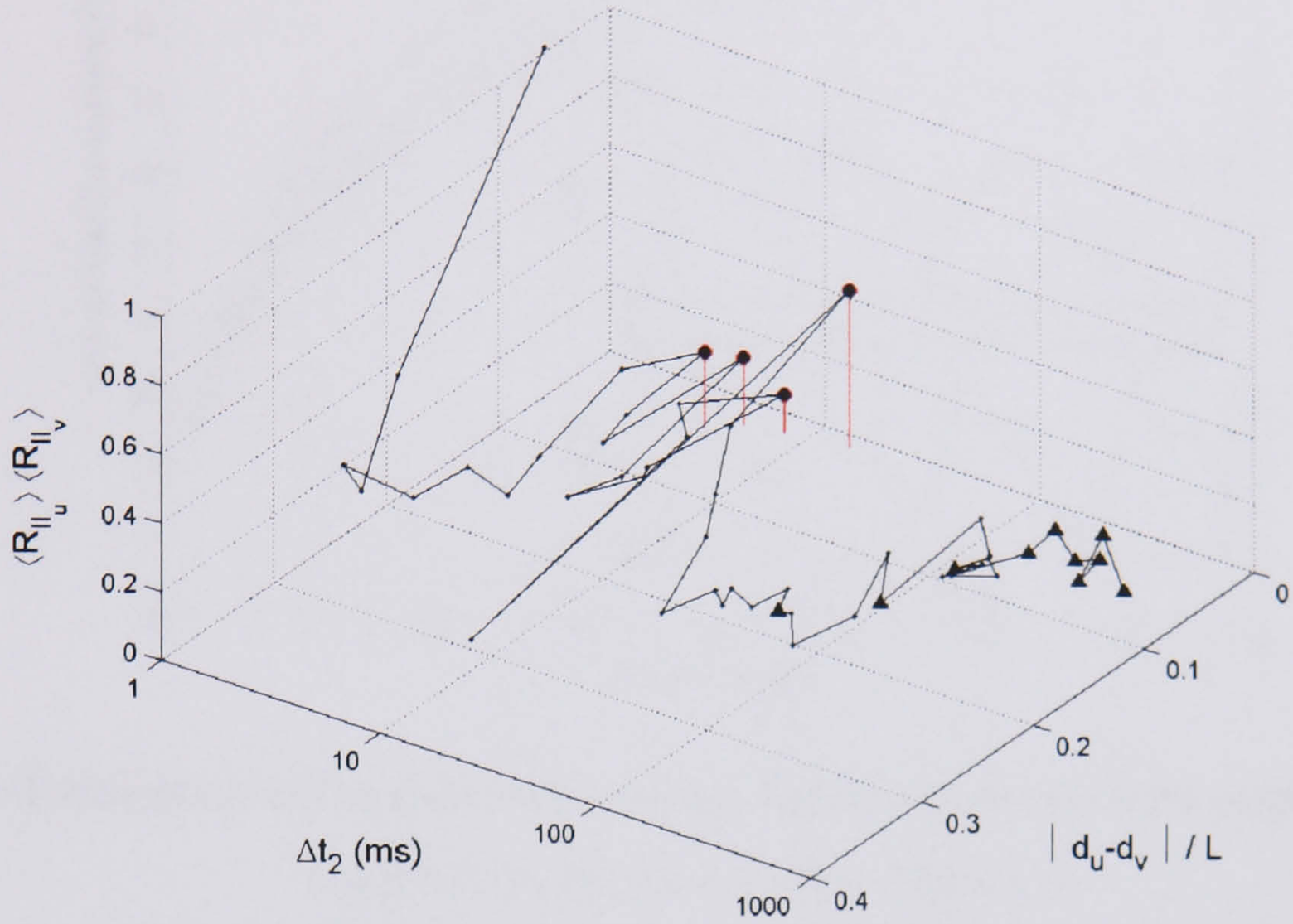

Figure 4.30. Velocity data at a number of time-delays is acquired. Normalized cross-correlation is performed on the components of velocity independently and then multiplied together to provide the 'matching' factor. The displacement position where the best match is found ($|d_u - d_v|/L$) is included in the plot.

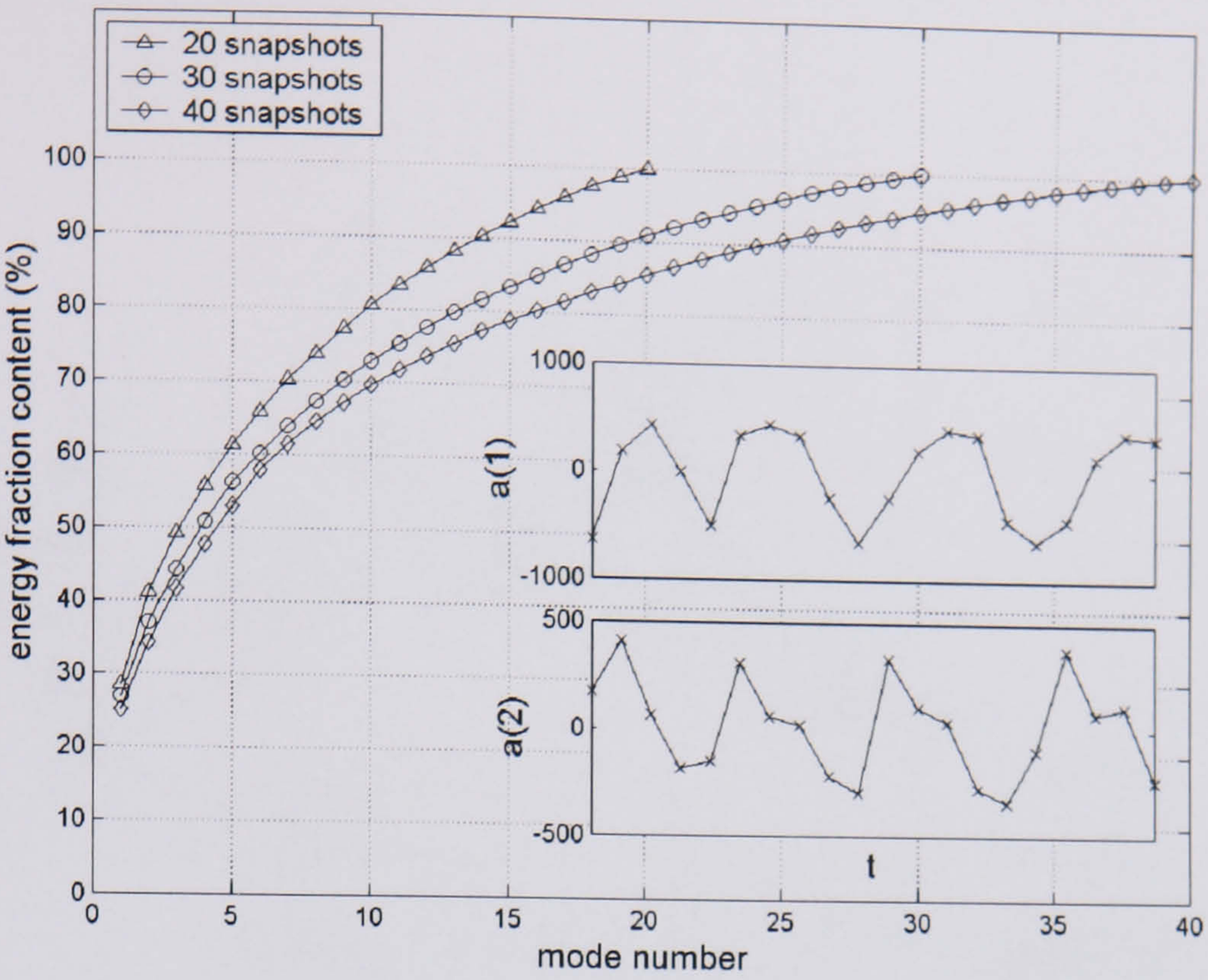

a. The distribution of the eigenvalue energy fraction is shown with amplitude data included on the sub-axis for $L/D = 1.5$

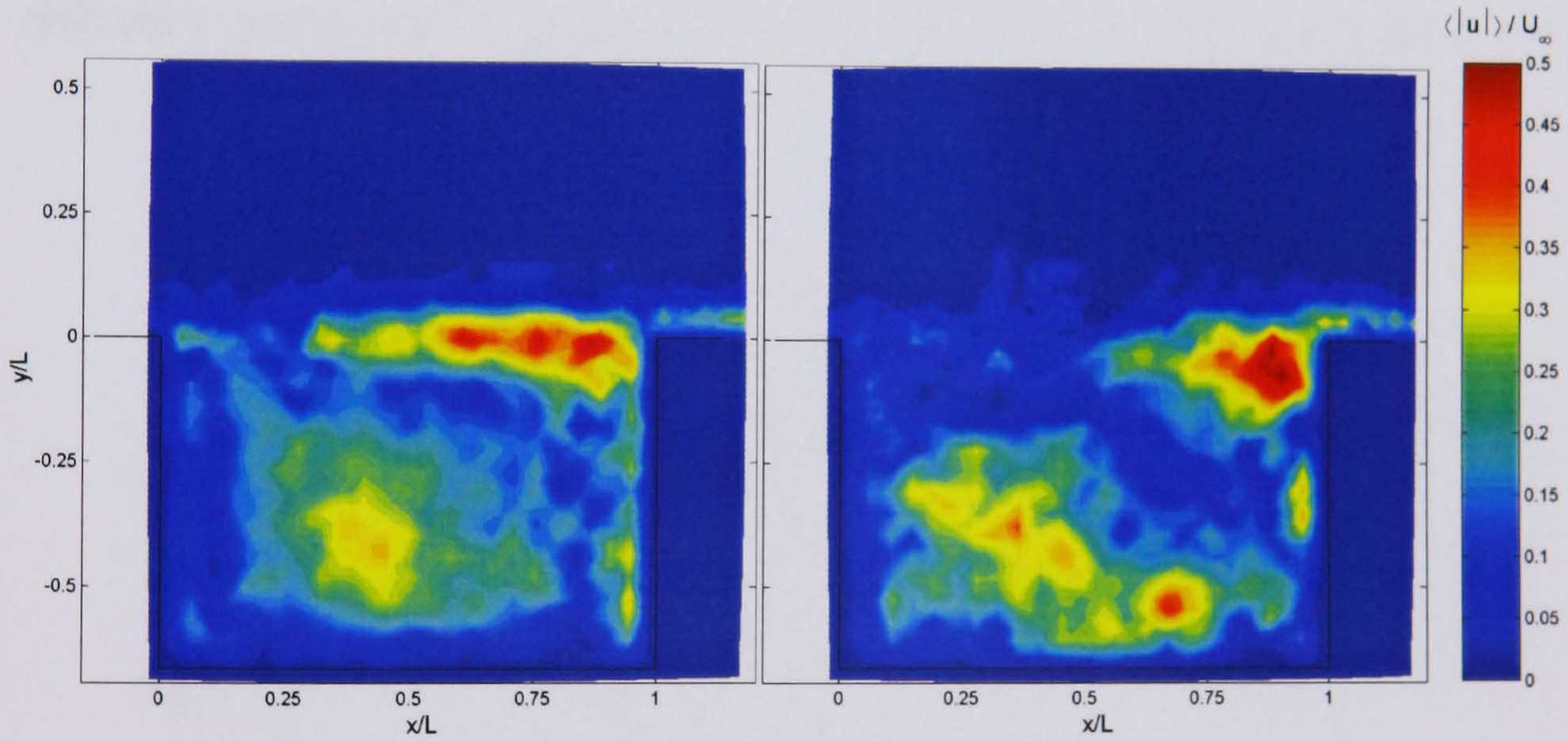

b. Velocity magnitude eigenfuction of the first POD-mode.

c. Velocity magnitude eigenfuction of the second POD-mode.

Figure 4.31. The main plot (a) indicates the change in the distribution of modal energy observed using a variable number of snapshots. The expansion coefficient data for the two most energetic modes of the projection using 30-snapshots is included to the bottom right of this plot (a) with the corresponding eigenfunctions included in (b) and (c) for reference.

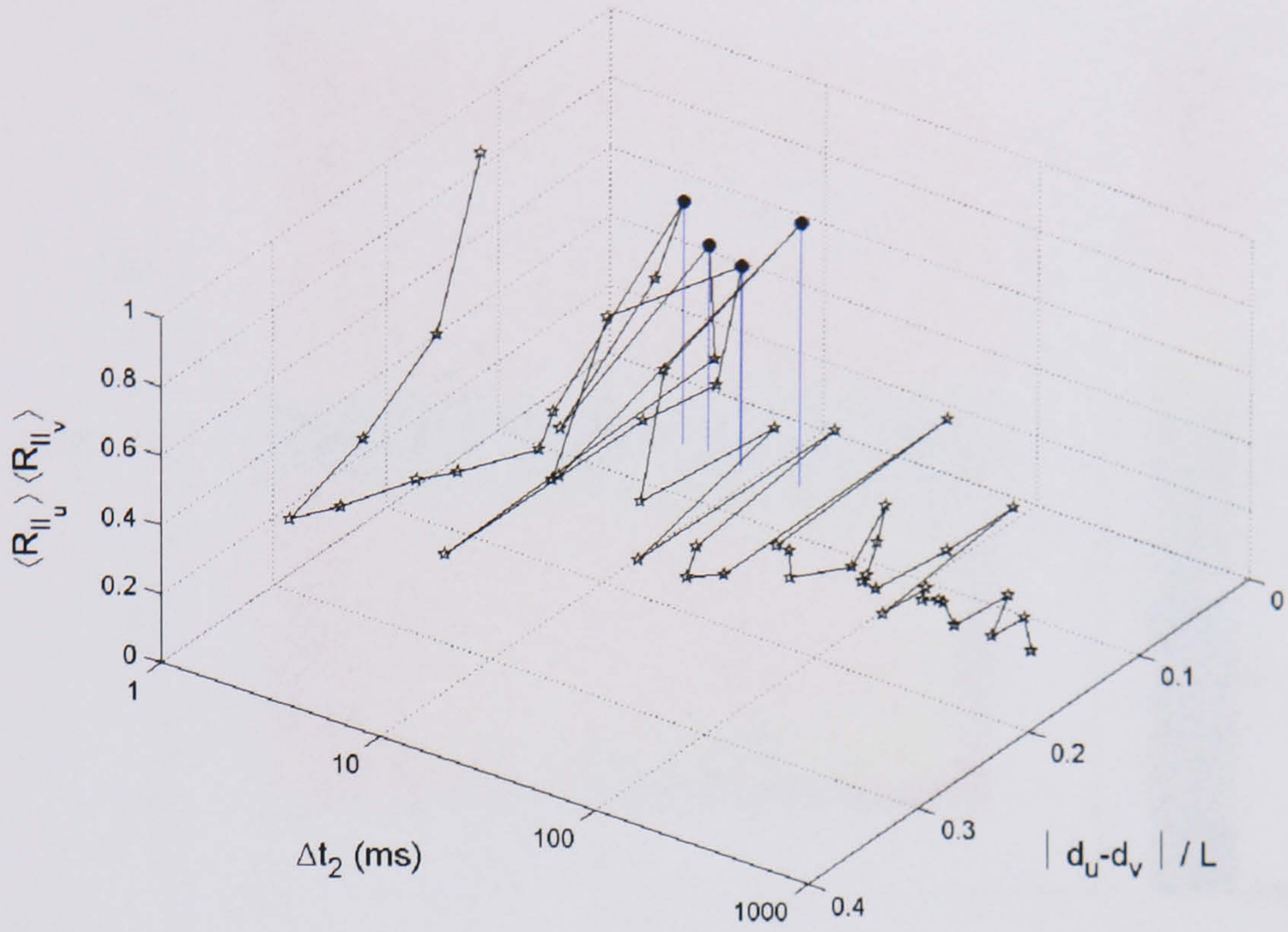

Figure 4.32. Normalized cross-correlation of reconstructed POD data. The positions that indicate a 'phase lock' are the same as those shown in figure 4.30 although in this instance the correlation is much stronger.

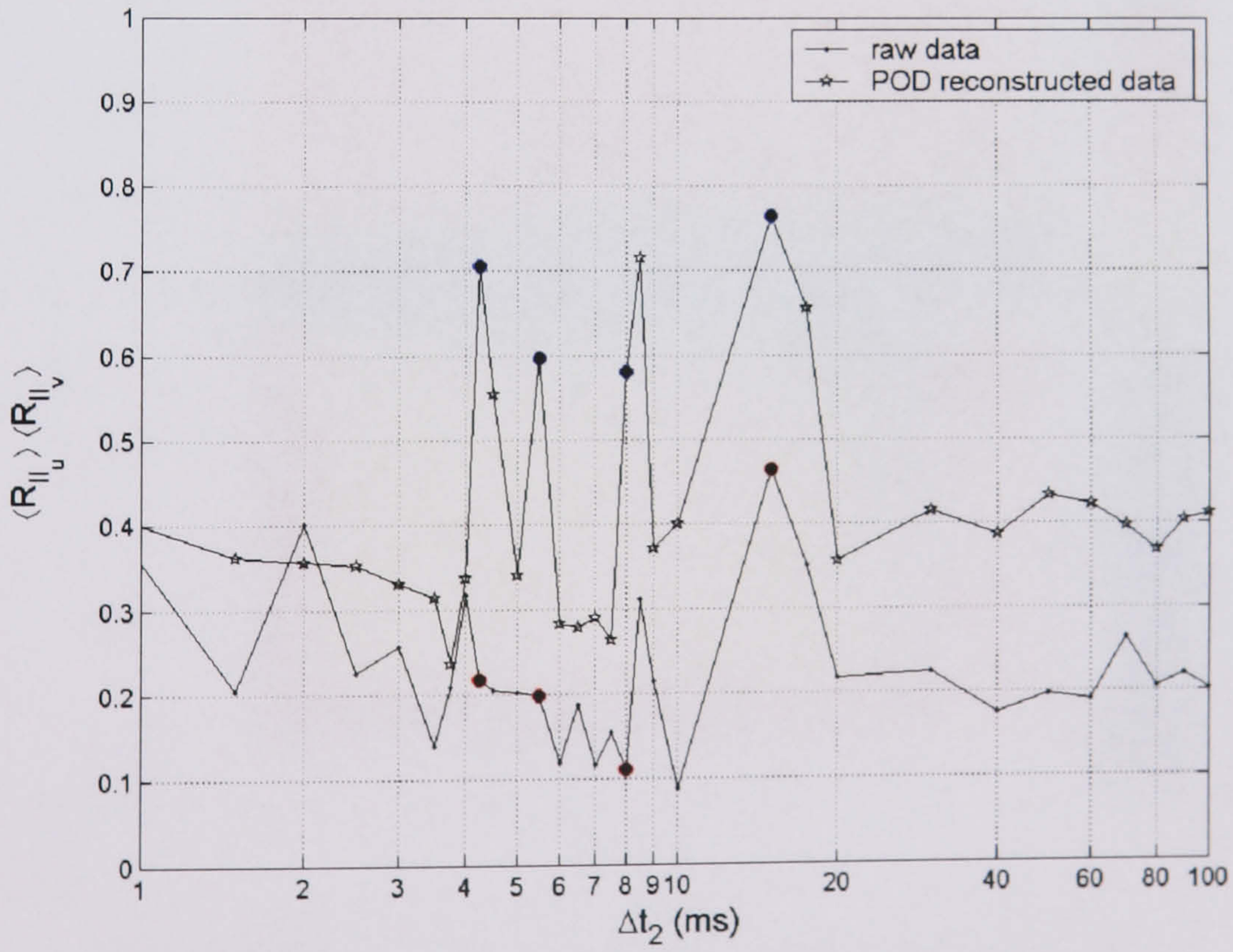

Figure 4.33. 2D slice of the data plotted in figure 4.30 and figure 4.32. The filled markers indicate the position where the offset was closest to zero.

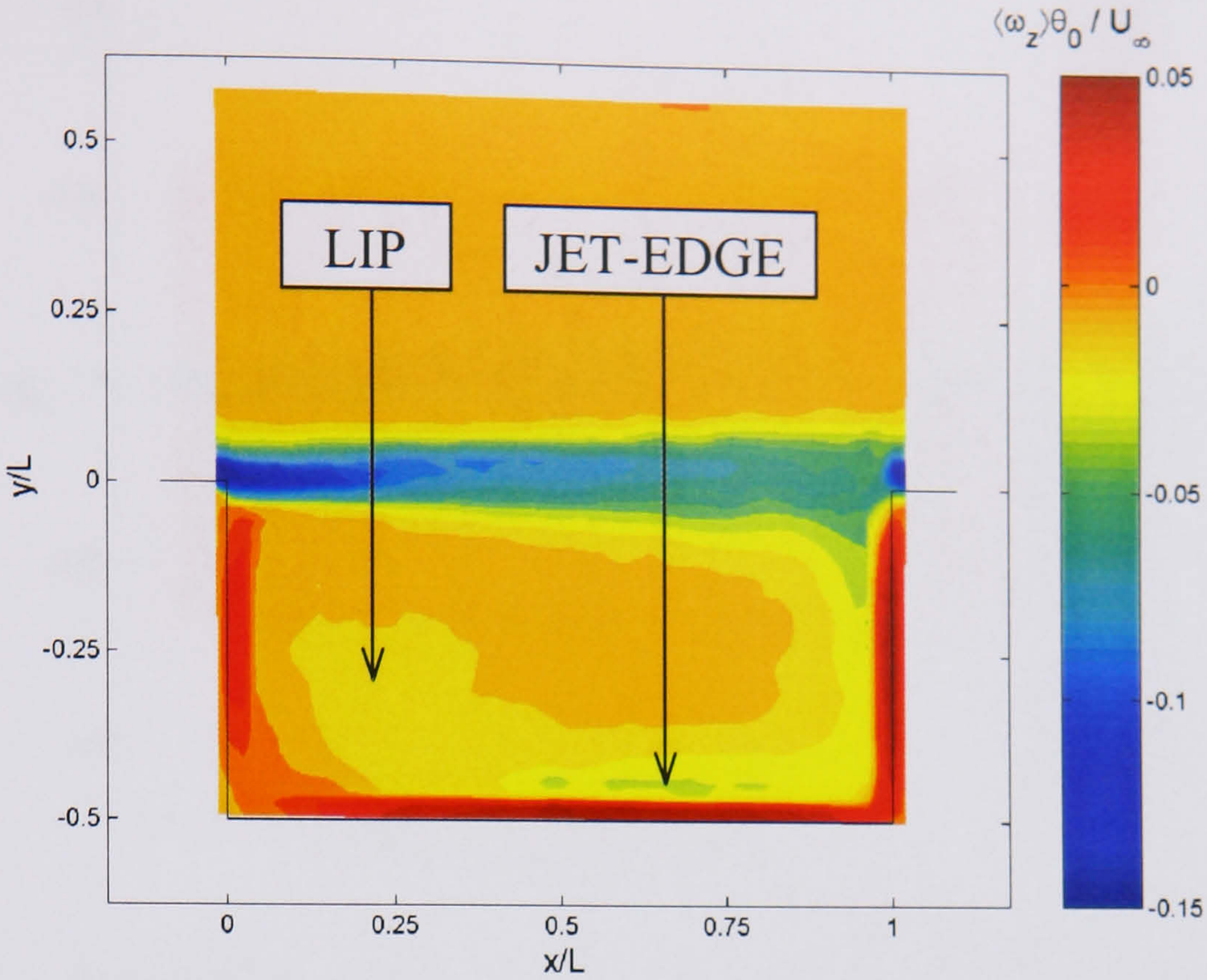

Figure 4.34. Average normalized vorticity for the central case ($L/D = 2.0$). The cavity is dominated by a jet-like flow along the rear and bottom walls of the cavity.

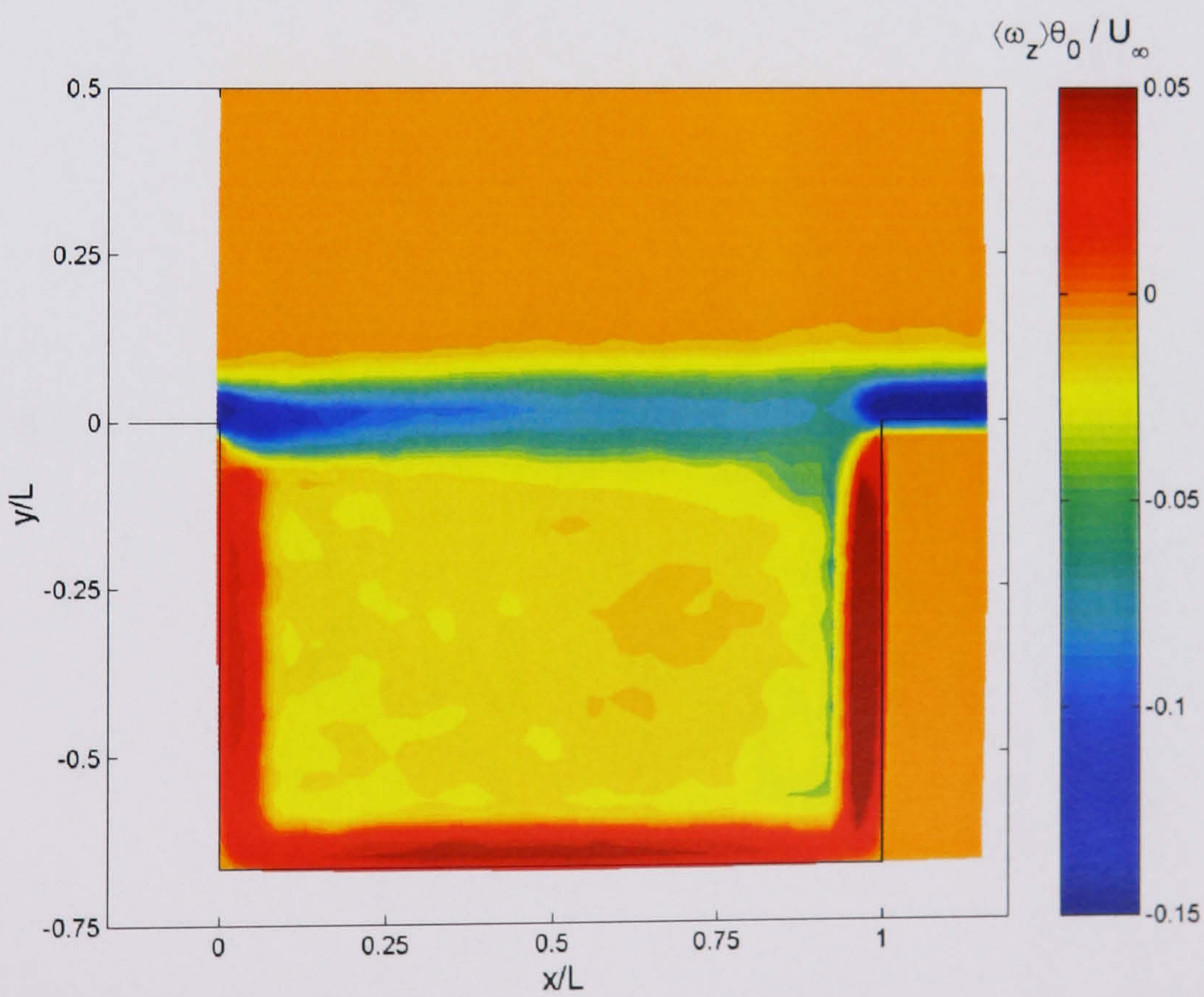

Figure 4.35. Average normalized vorticity for $L/D = 1.5$.

The same contour limits and contour levels are used as in figure 4.34.

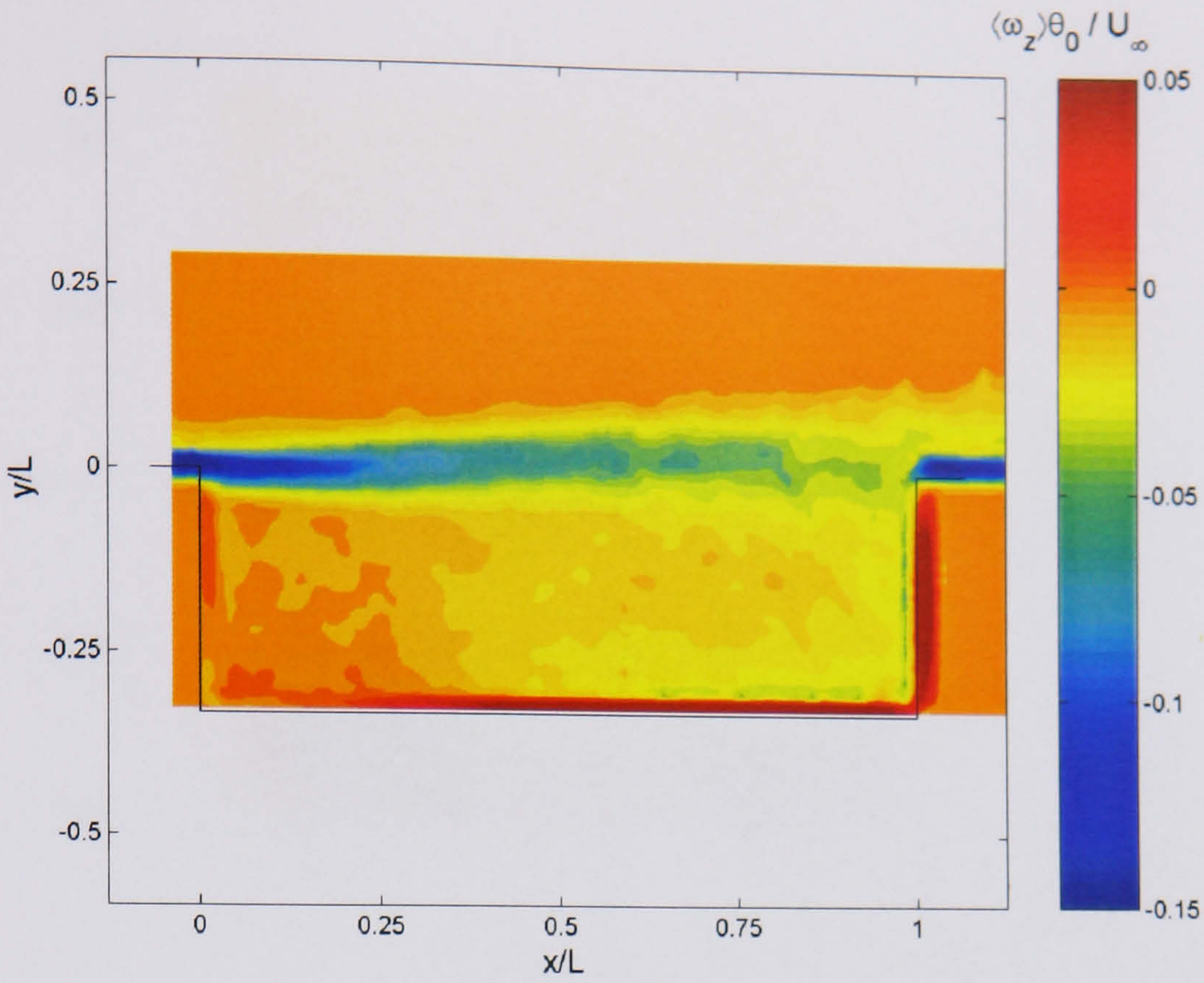

Figure 4.36. Average normalized vorticity for $L/D = 3.0$.

The same contour limits and contour levels are used as in figure 4.34.

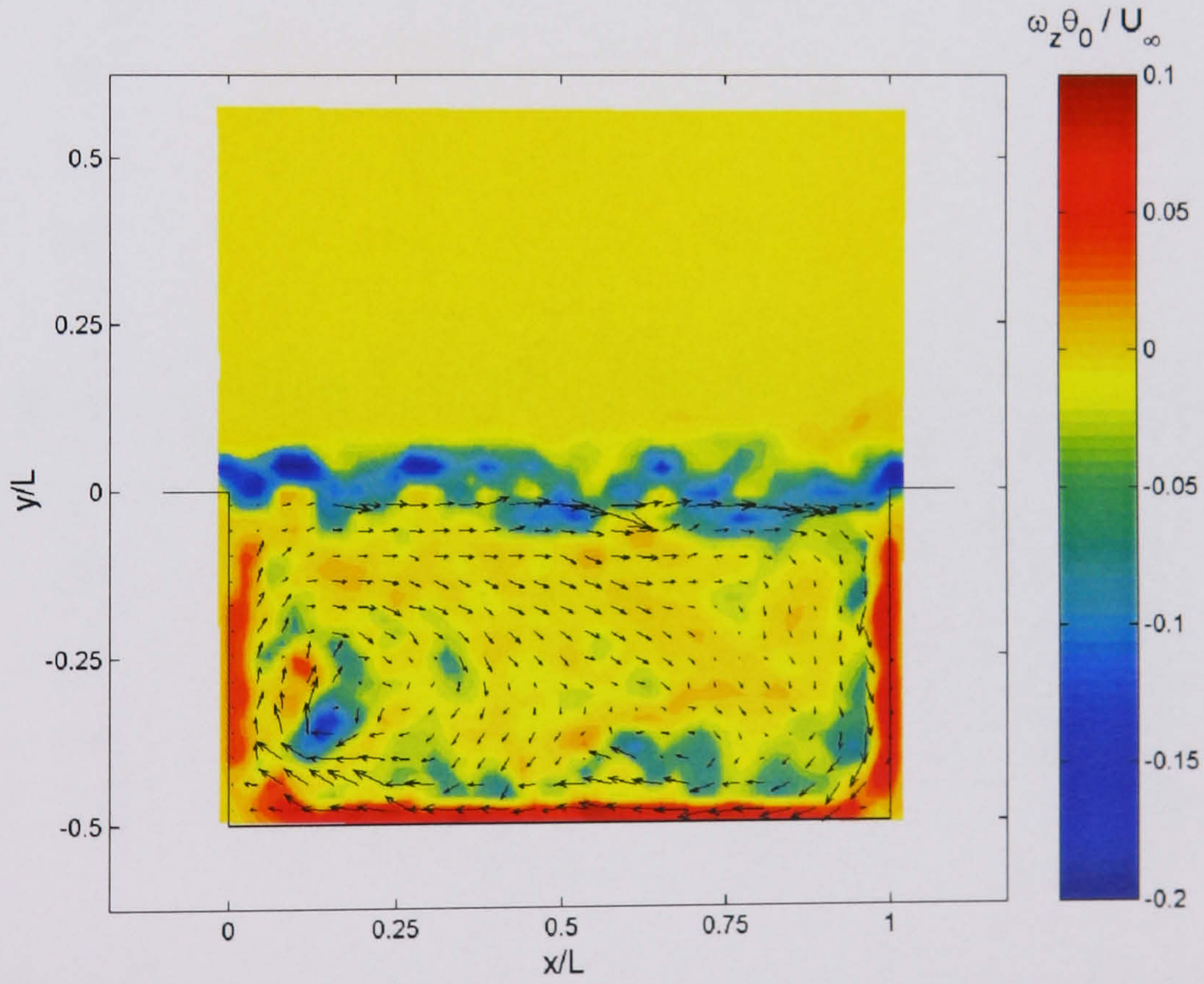

Figure 4.37. Instantaneous velocity and vorticity for $L/D = 2.0$. The initial stages of the internal oscillation show a vortex forming at the front wall of the cavity. 1/16th of the total vectors are shown.

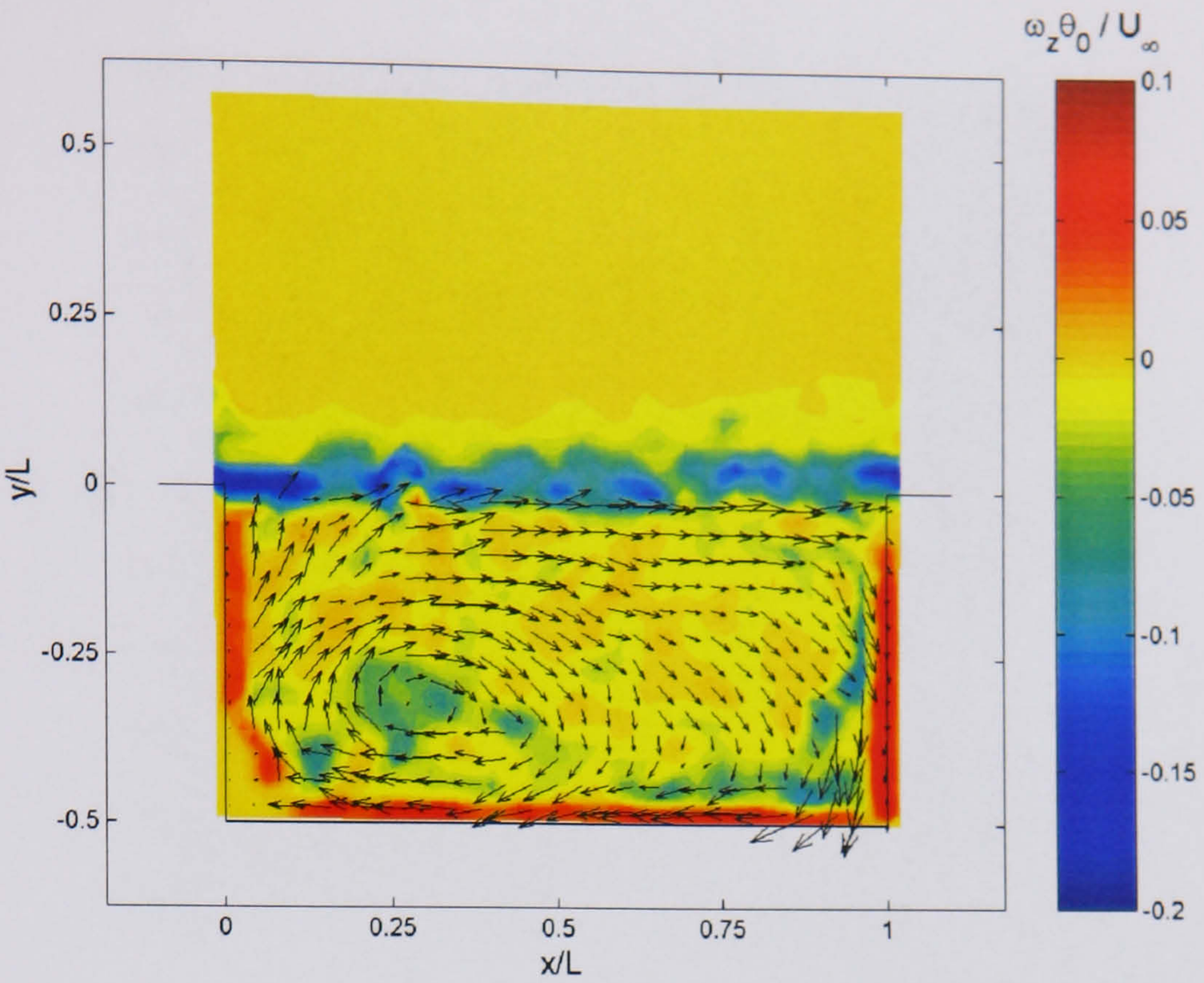

Figure 4.38. Instantaneous velocity and vorticity for $L/D = 2.0$. Packets of vorticity cast into the cavity from the trailing edge shear interaction coalesce at the front wall.

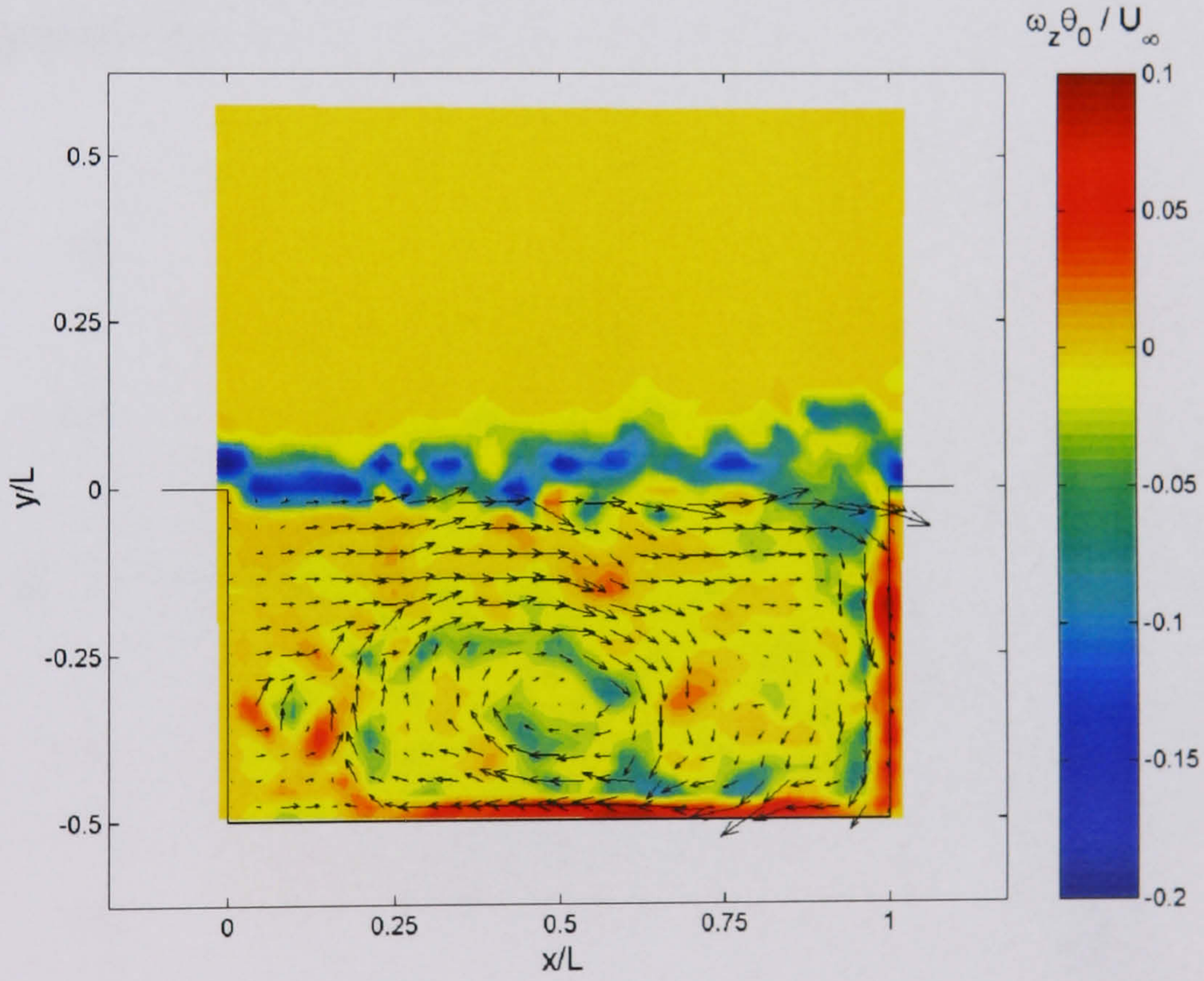

Figure 4.39. Instantaneous velocity and vorticity for $L/D = 2.0$. When the primary cavity vortex has gained sufficient strength and size it rolls forward through the cavity (having locked phase with the shear layer).

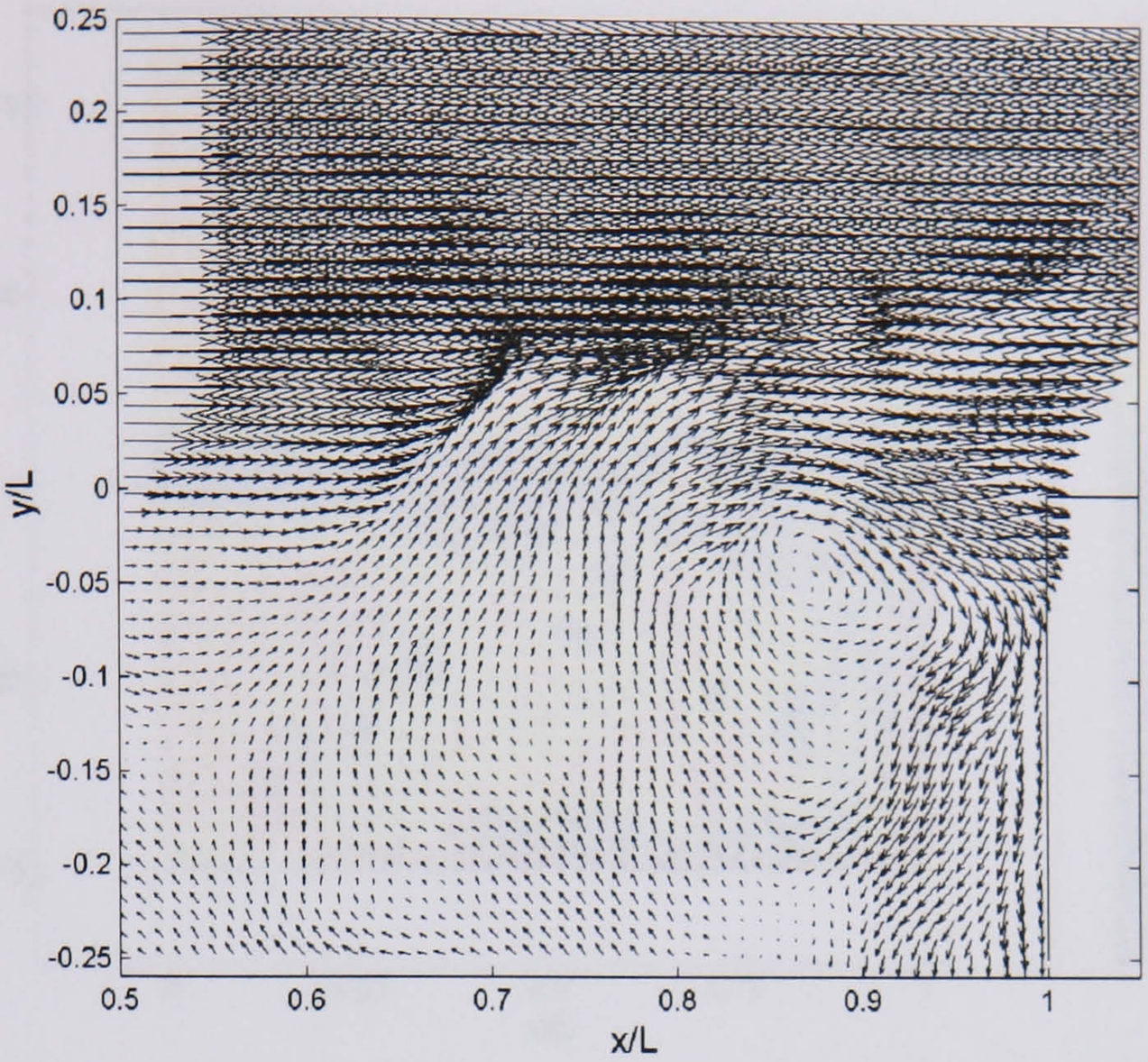

Figure 4.40. Instantaneous velocity vectors for $L/D = 2.0$. (zoomed in portion of the trailing edge). Immediately prior to a violent mass expulsion cycle the primary vortex progresses toward the rear corner as the shear layer is deflected upward.

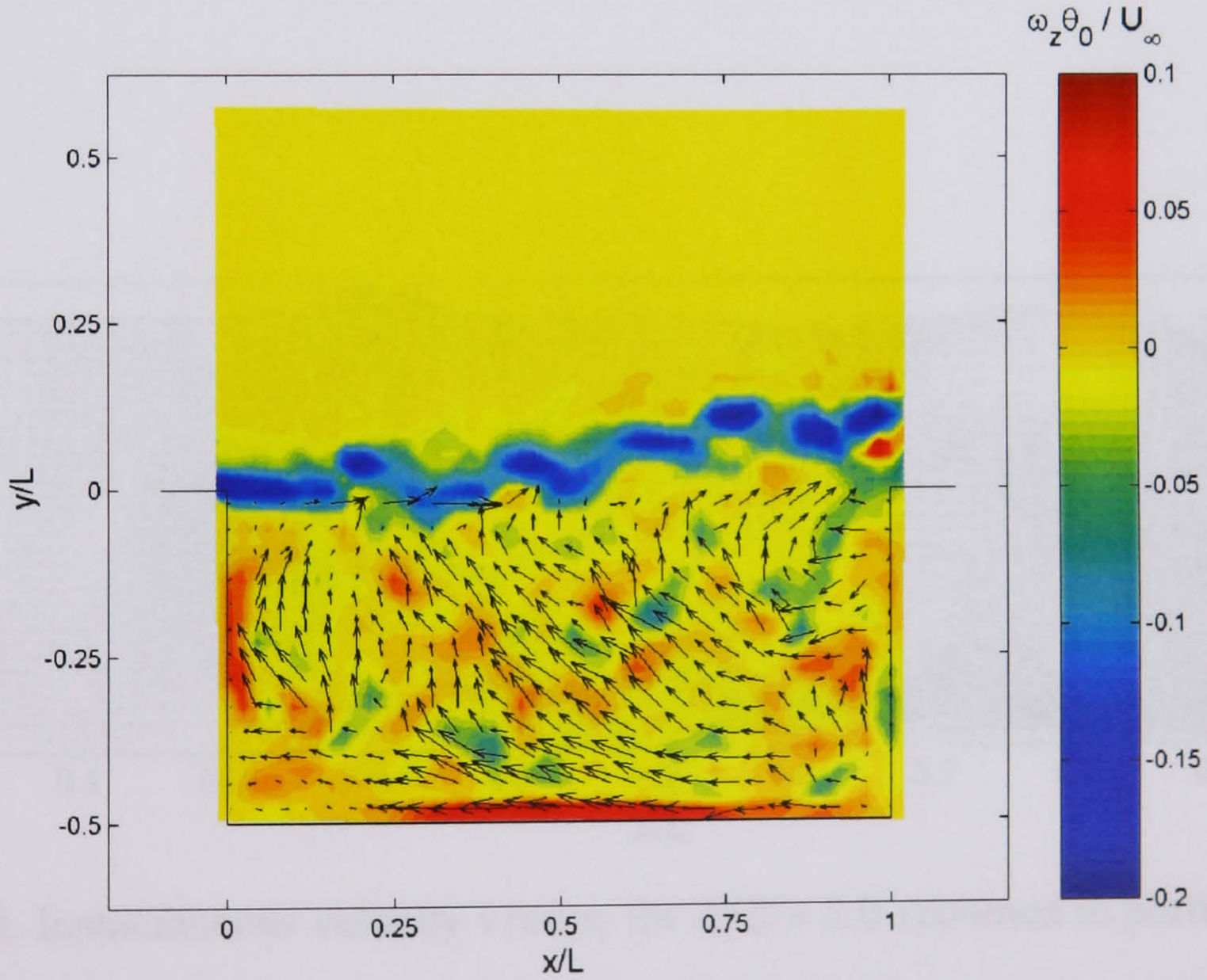

Figure 4.41. Instantaneous velocity and vorticity for $L/D = 2.0$. The primary recirculation region escapes from the cavity after an interaction with the trailing edge.

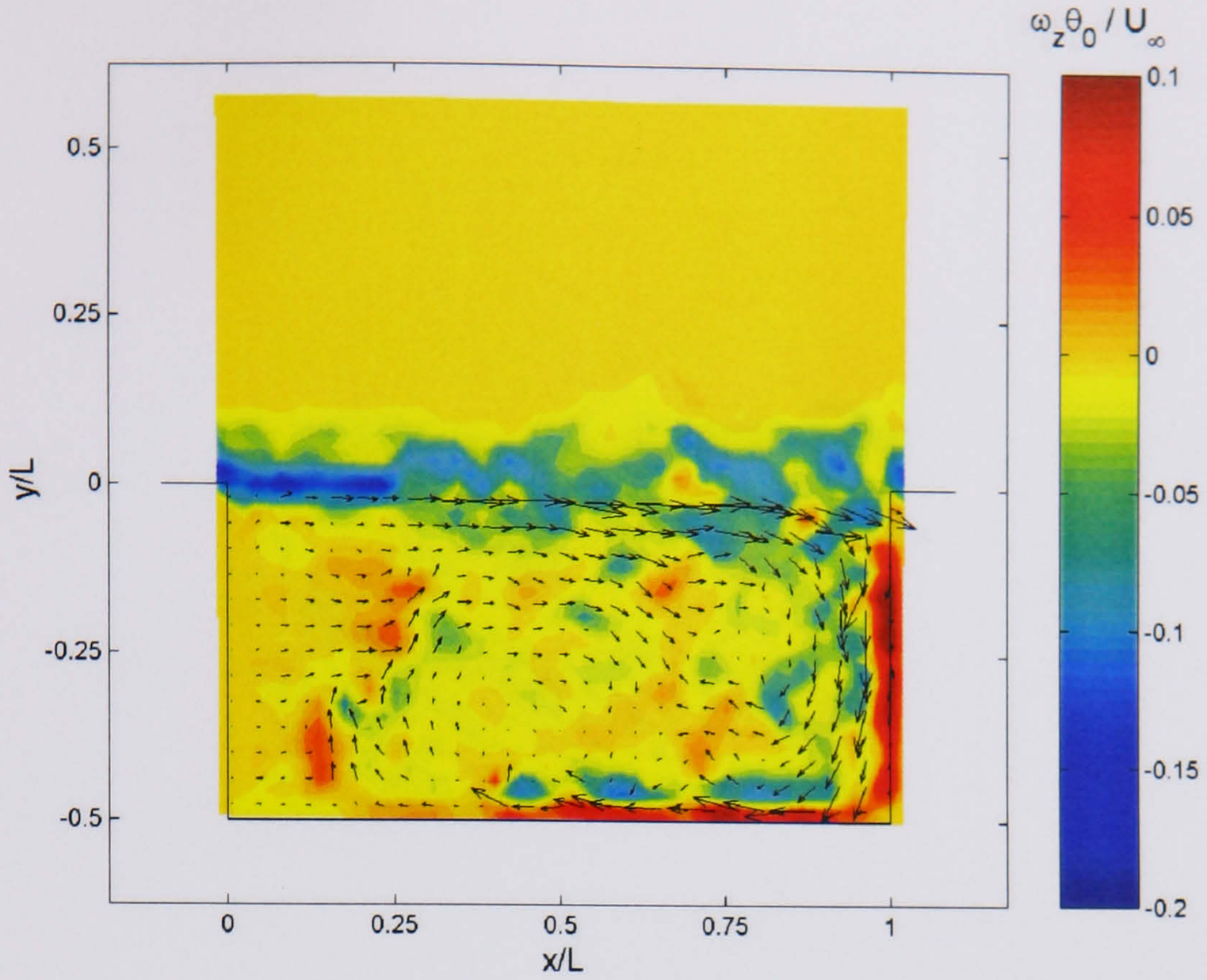

Figure 4.42. Instantaneous velocity and vorticity for $L/D = 2.0$. After the complete primary recirculation is expelled from the cavity the mass addition to the cavity will convect along the cavity floor to reform a vortex at the front wall.

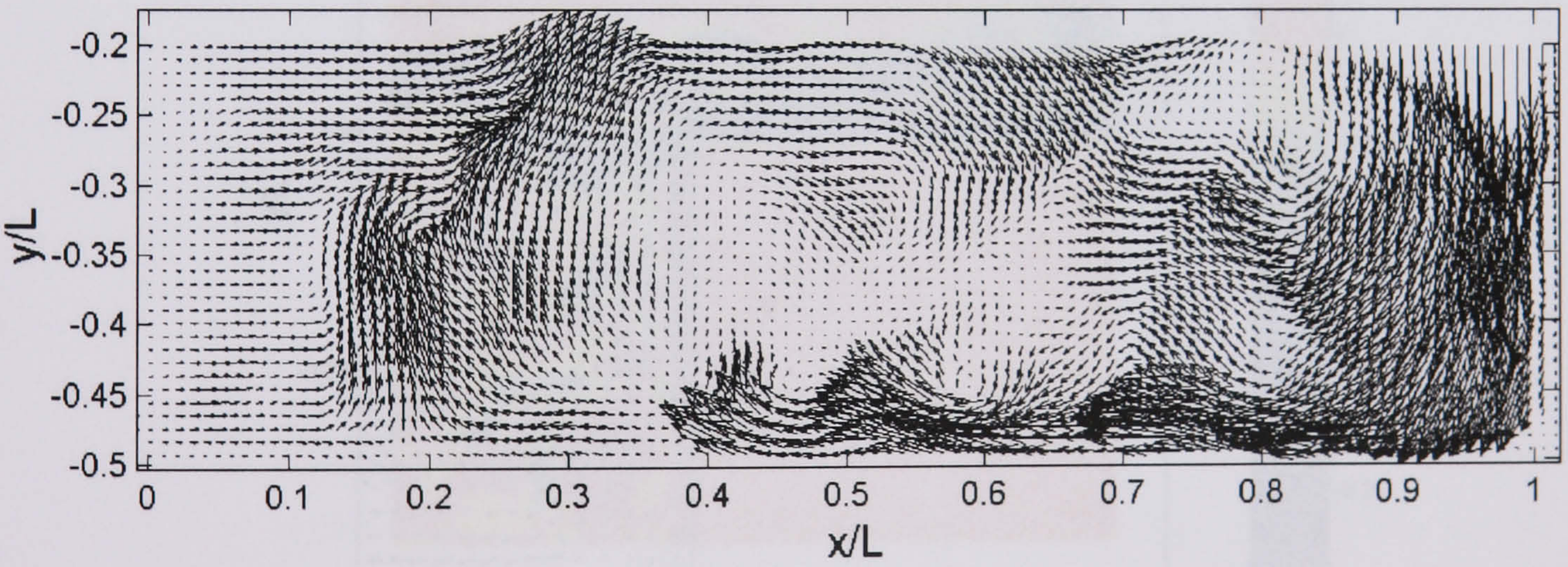

Figure 4.43. Instantaneous velocity vectors for $L/D = 2.0$ (zoomed in portion of figure 4.42). A strong jet edge along the cavity floor is conducive to a prior complete escape from the cavity. All correlated vectors are shown.

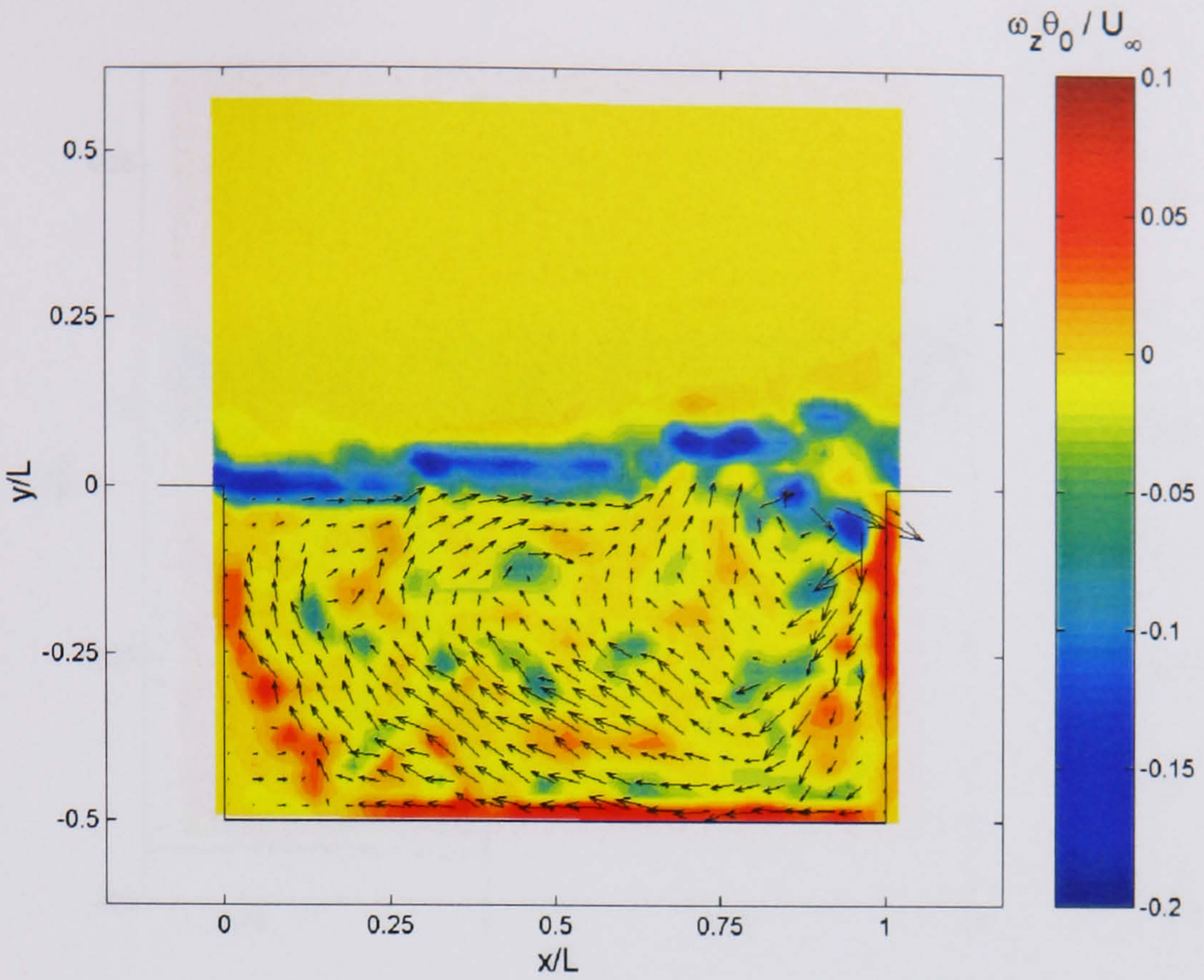

Figure 4.44. Instantaneous velocity and vorticity for $L/D = 2.0$. If complete escape of the primary vortex from the cavity is not successful then artefacts from the prior oscillation will persist at the trailing edge.

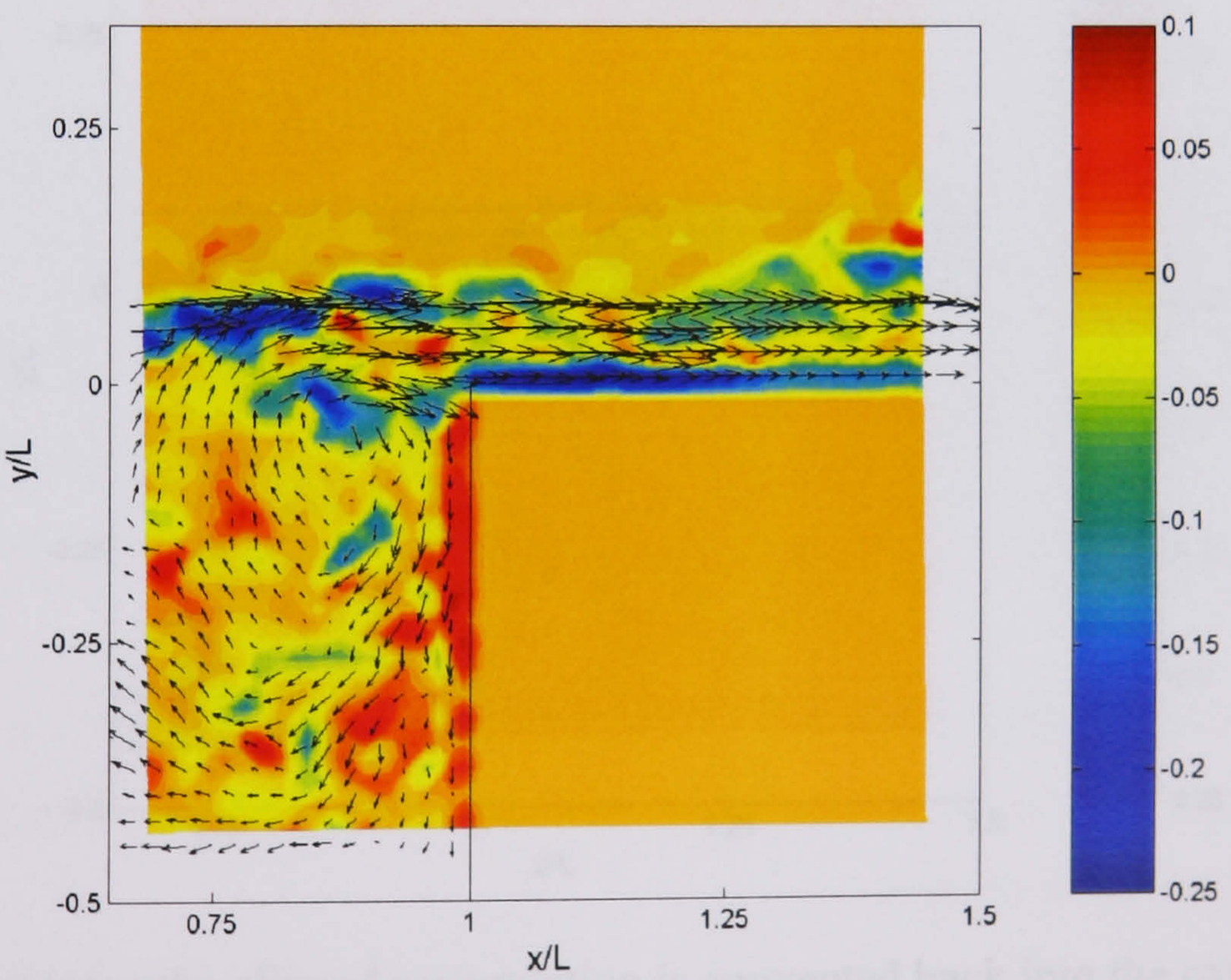

Figure 4.45. Instantaneous velocity and vorticity for $L/D = 2.0$ (zoomed in portion of figure 4.44). Mass from the partial escape of the primary vortex can be seen leaving the field of view, while other structures are held at the cavity trailing edge.

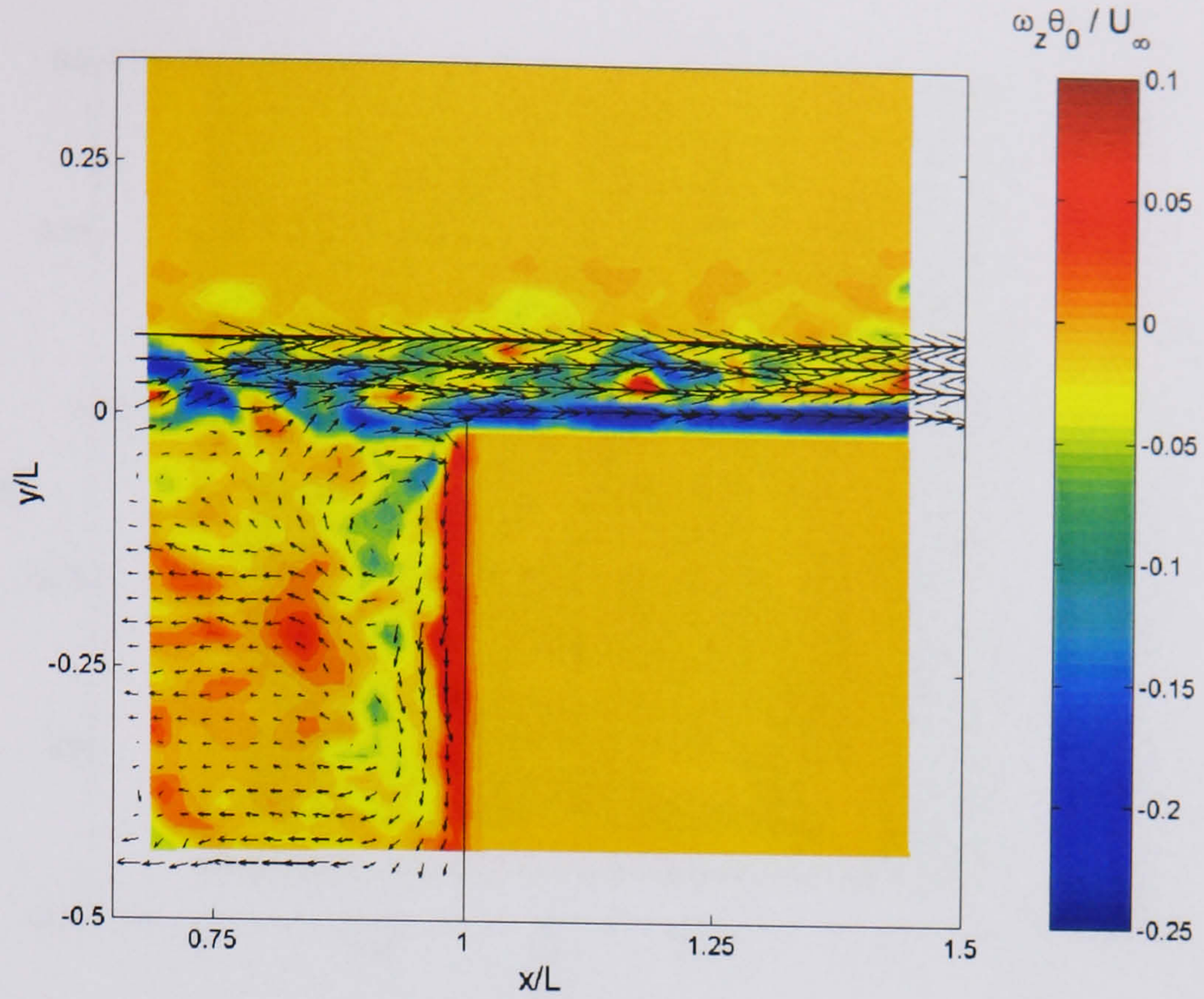

a. In some instances it is possible that not all the vorticity is cast from the cavity during the low-frequency flapping of the shear layer.

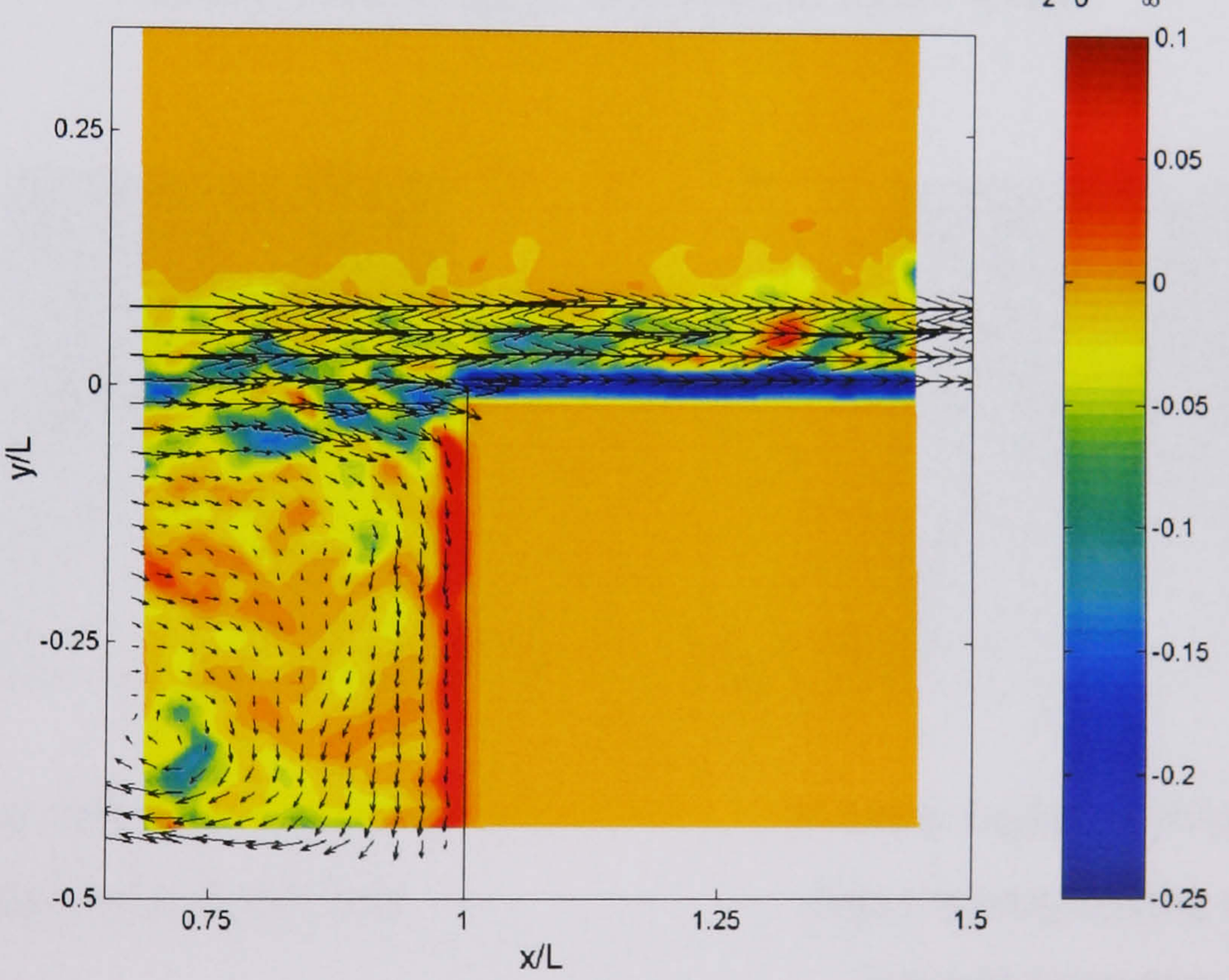

b. In some instances the clipped recirculation is convected back into the cavity itself to coalesce with the upstream recirculation. Time-delay is 0.004 seconds.

Figure 4.46. Instantaneous velocity and vorticity for $L/D = 2.0$. It is interactions such as this that cause the cycle-to-cycle variation in the low-frequency oscillation of the cavity.

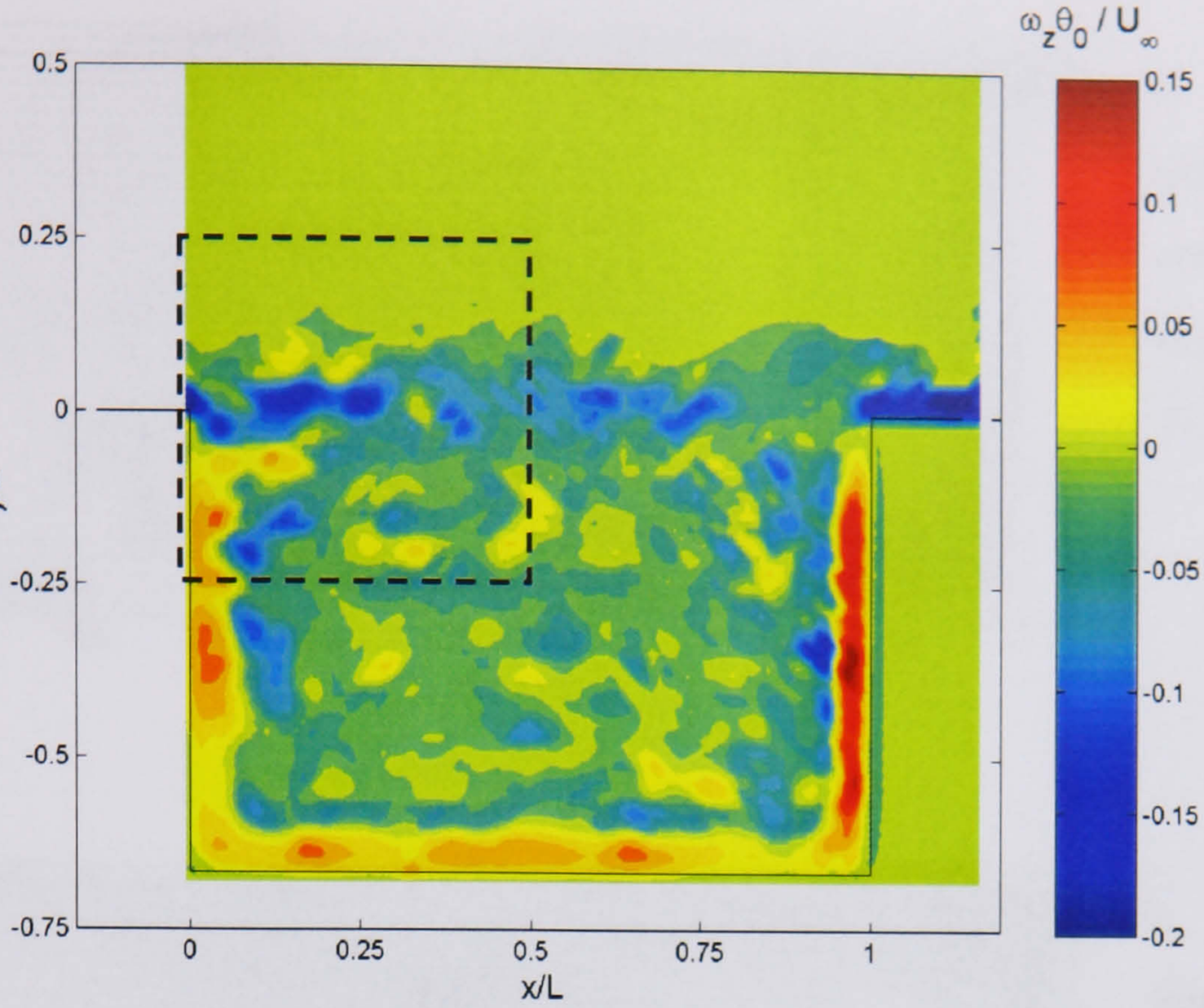

Figure 4.47. The instantaneous vorticity for $L/D = 1.5$. The dashed box indicates the velocity vector region displayed in figure 4.48a.

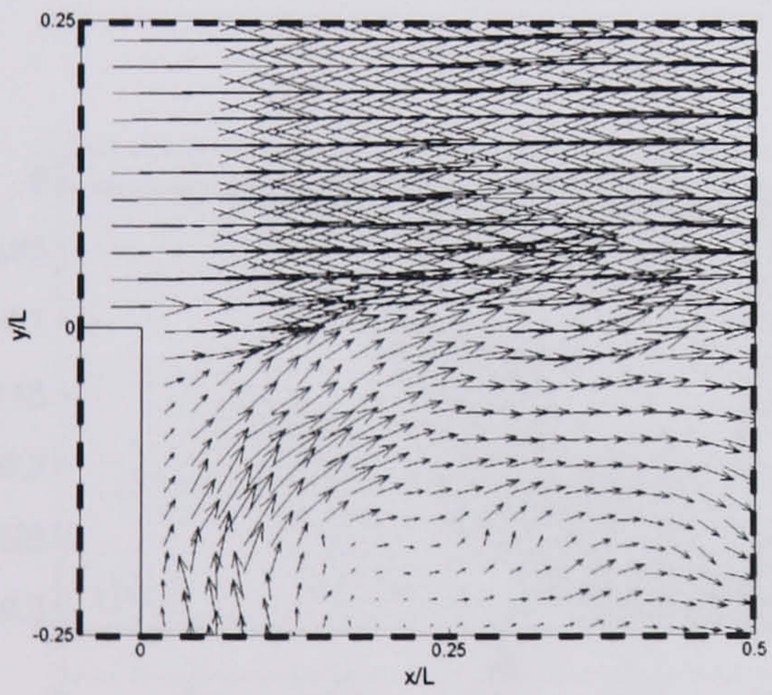

a. Vector plot for the portion highlighted in figure 4.47.

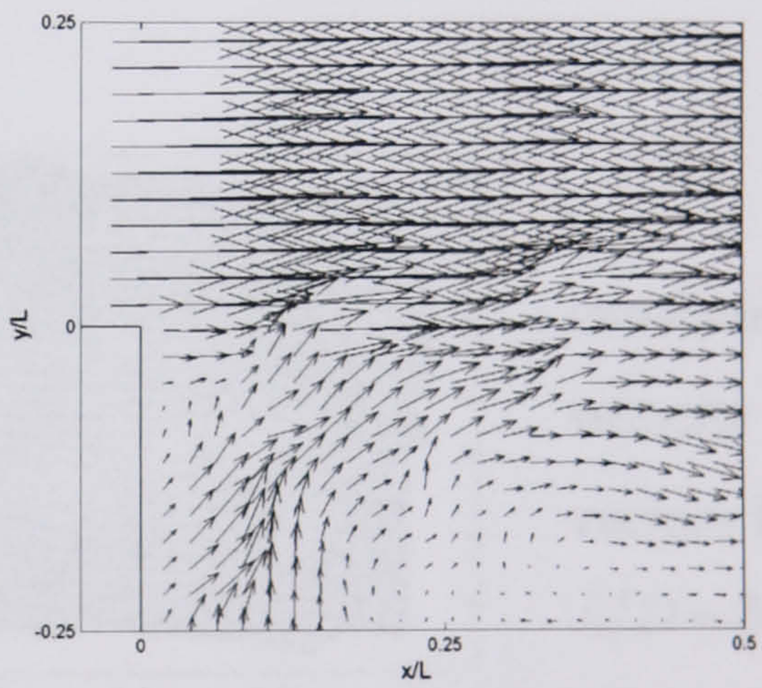

b. Same region as in (a) at a time elapse corresponding to the main internal frequency ($\beta/4$).

Figure 4.48. A closer look at the cavity leading edge for $L/D = 1.5$ shows that the wall edge jet directly impinges onto the initial development region of the shear layer.

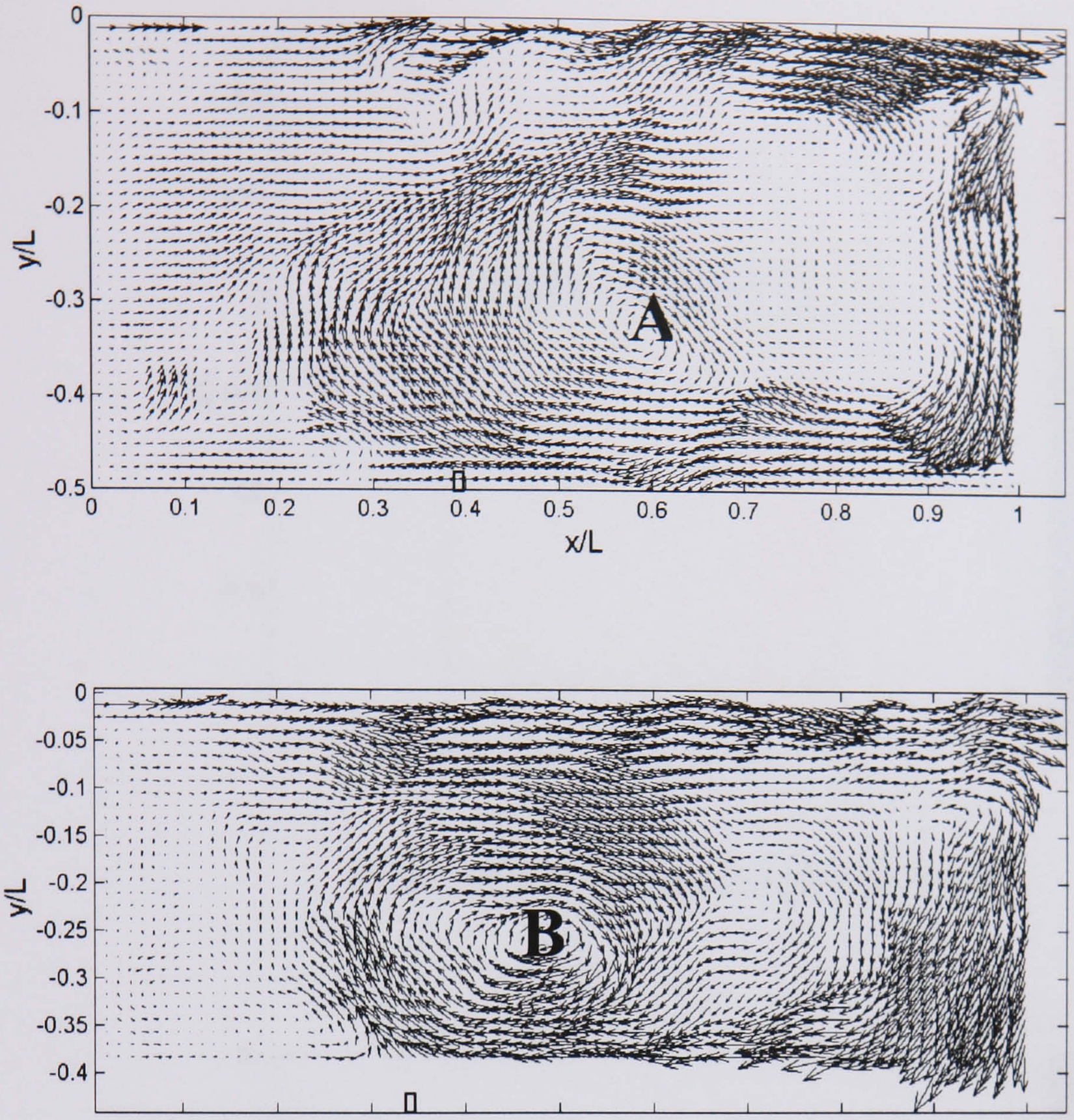

a. Instantaneous velocity vectors for $L/D = 2.0$

b. Instantaneous velocity vectors for $L/D = 2.5$

c. Instantaneous velocity vectors for $L/D = 3.0$

Figure 4.49. Each picture in the series corresponds to the 'roll-out' of the primary vortex for various L/D ratios. The approximate centre for this 'roll-out' is indicated A, B and C in each figure respectively. The effective backflow into the cavity is reduced for the longer cavities. The hollow black rectangle indicates the position of the pressure transducer.

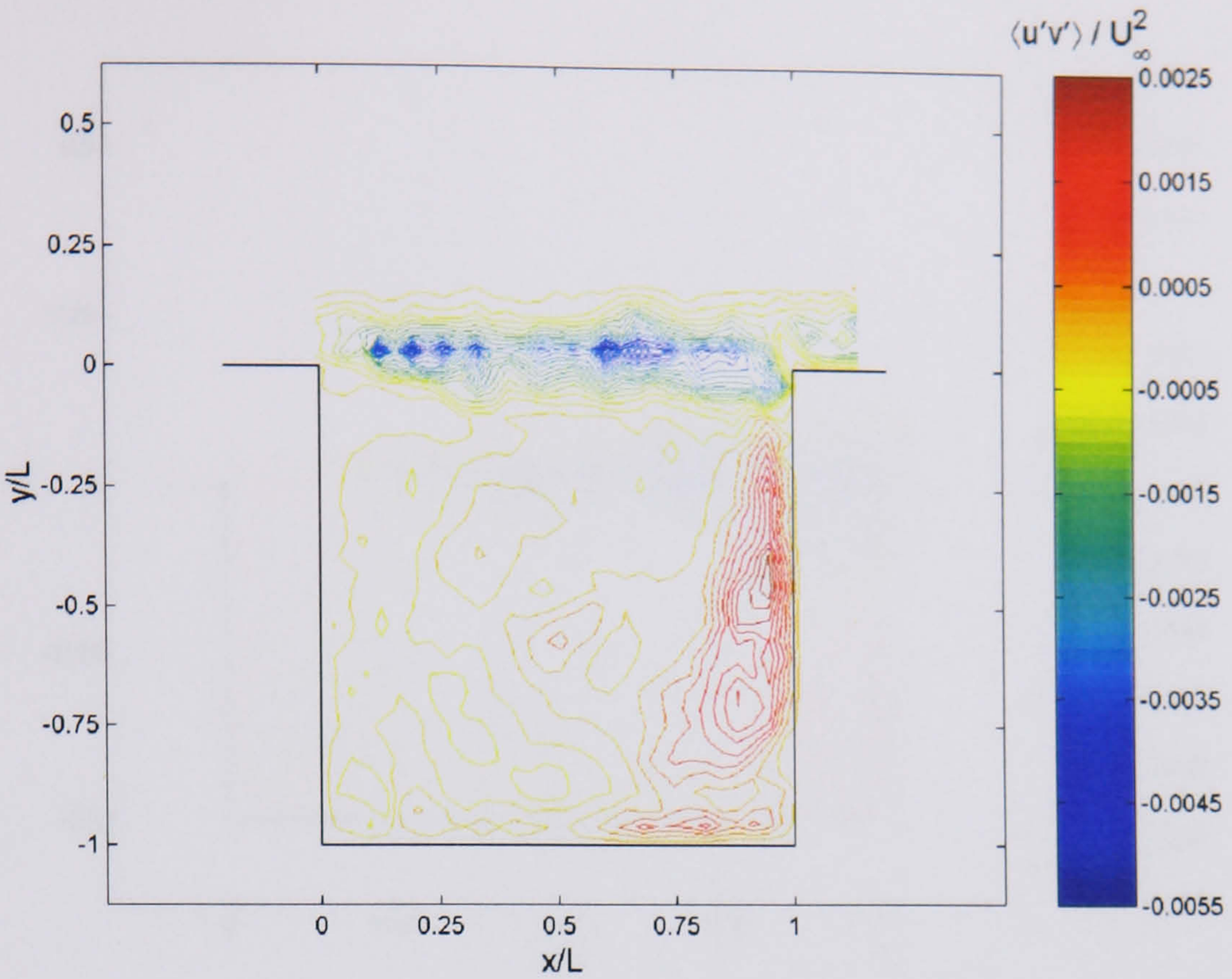

Figure 4.50. Reynolds stress for $L/D = 1.0$.

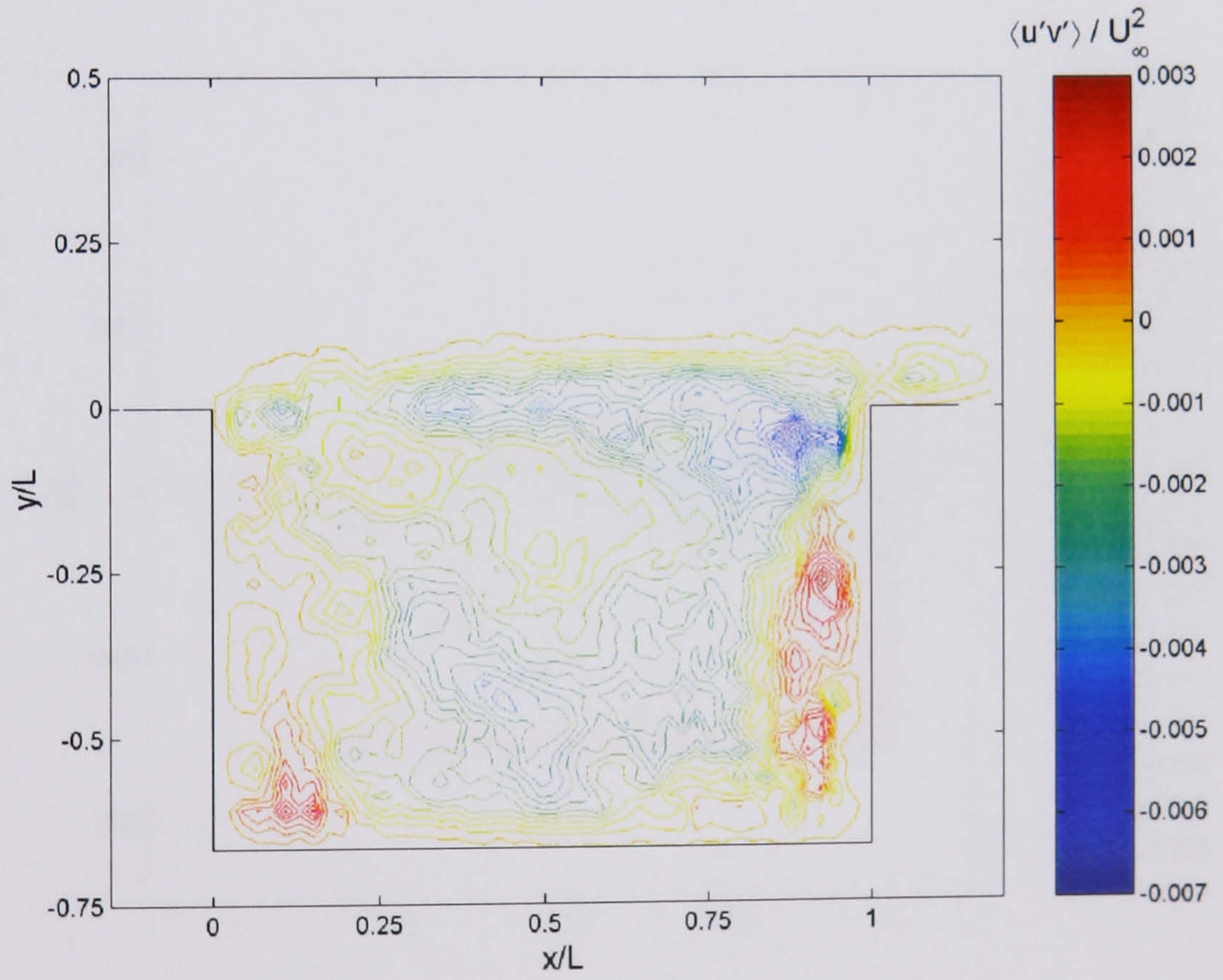

Figure 4.51. Reynolds stress for $L/D = 1.5$.

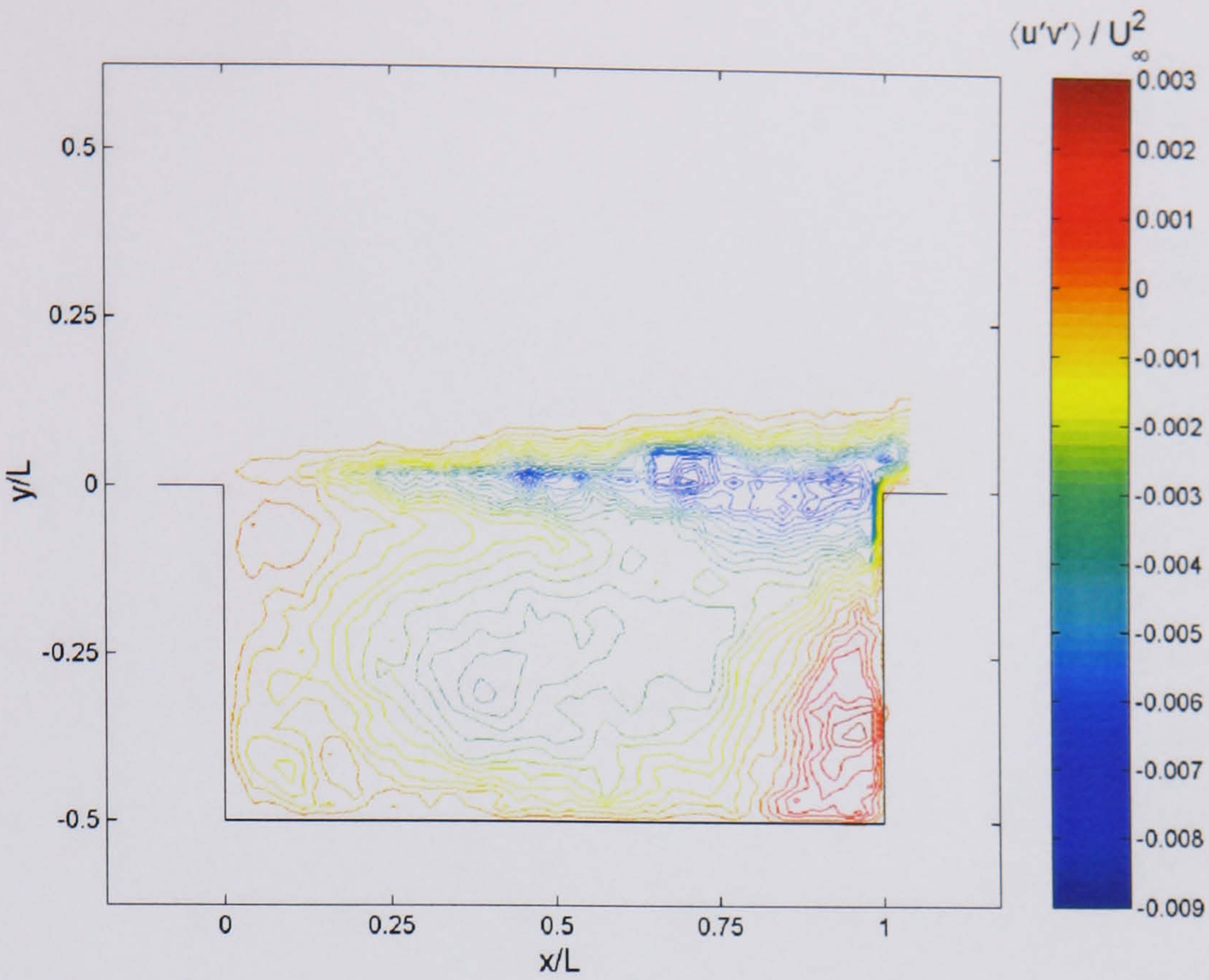

Figure 4.52. Reynolds stress for $L/D = 2.0$.

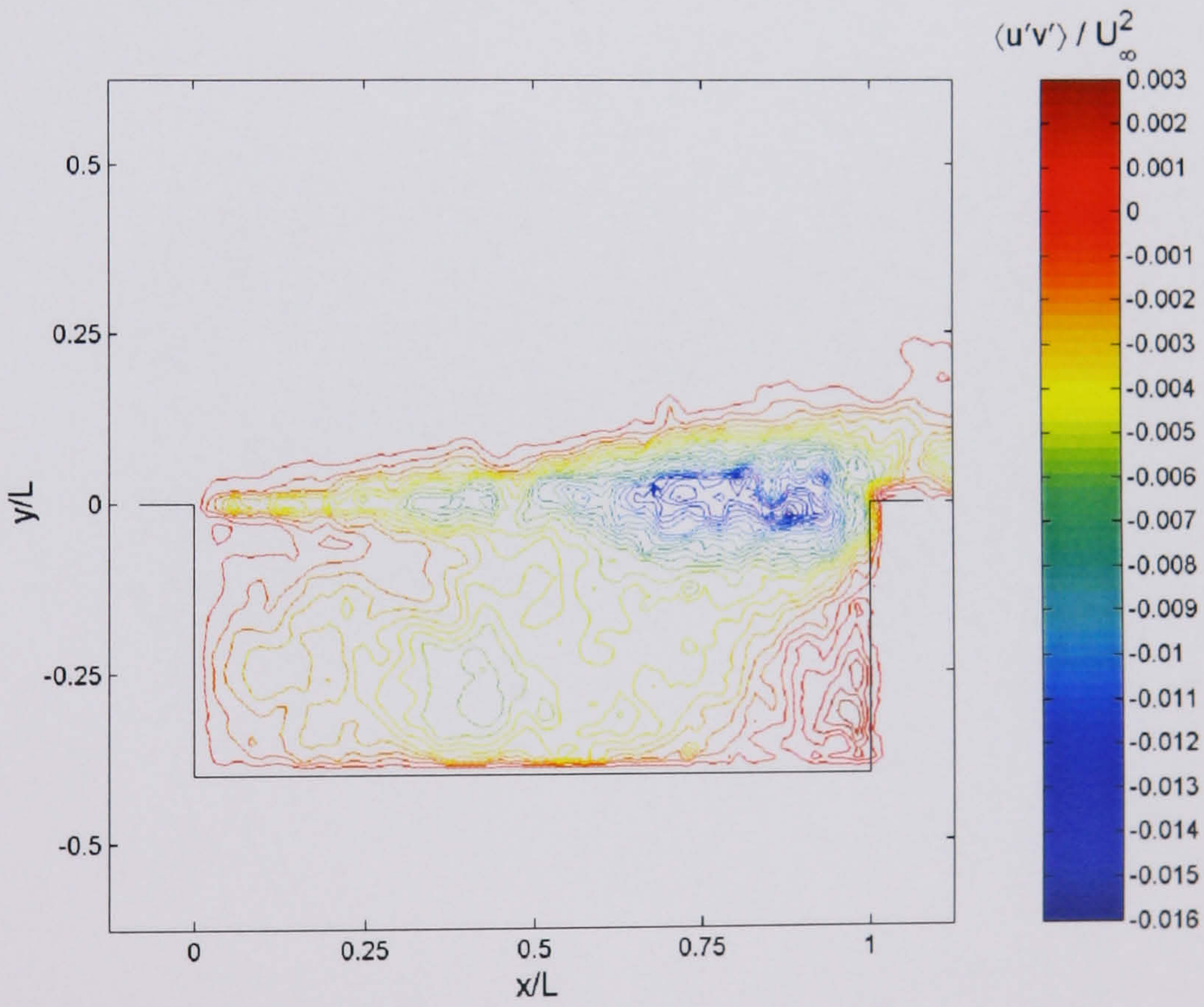

Figure 4.53. Reynolds stress for $L/D = 2.5$.

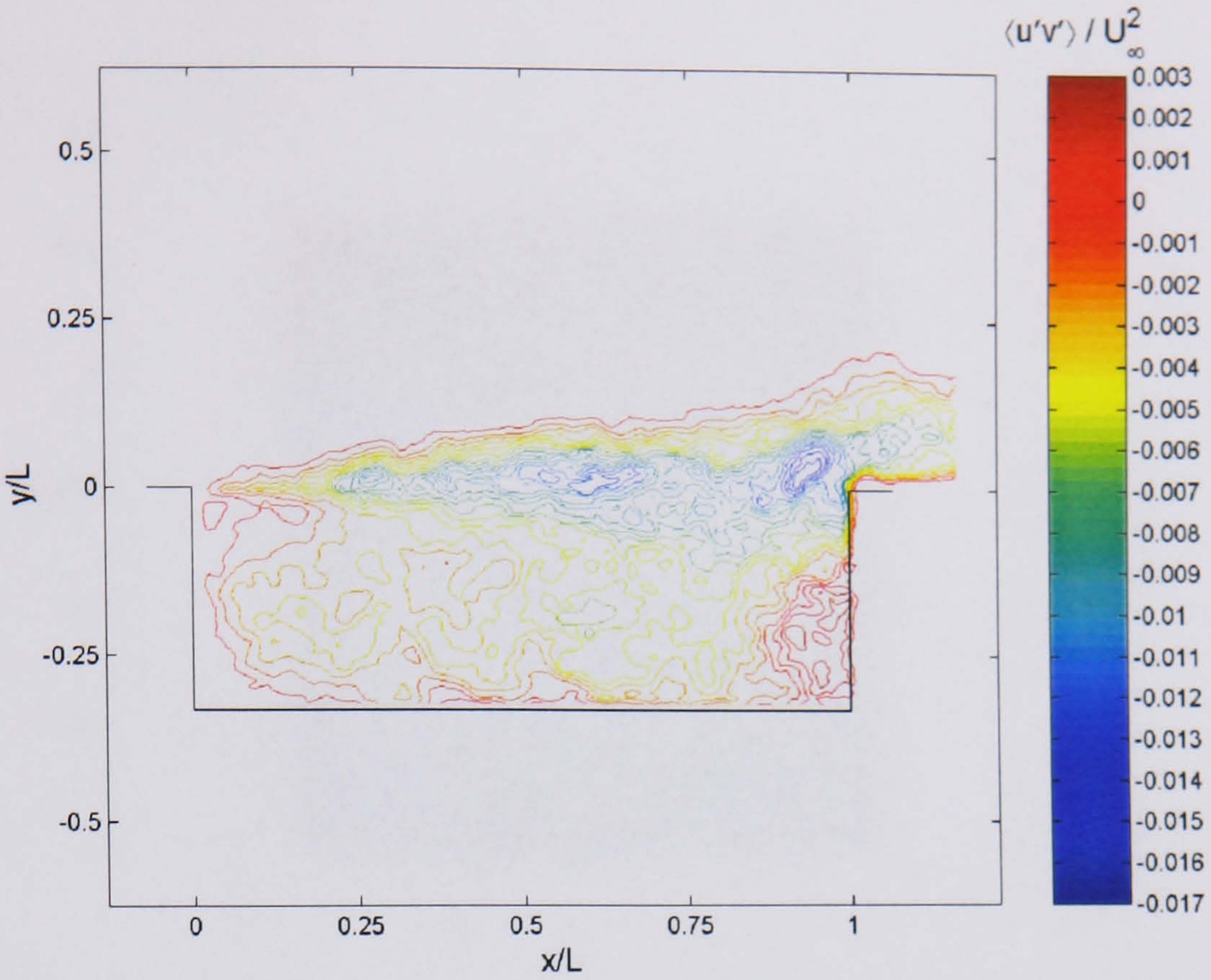

Figure 4.54. Reynolds stress for $L/D = 3.0$.

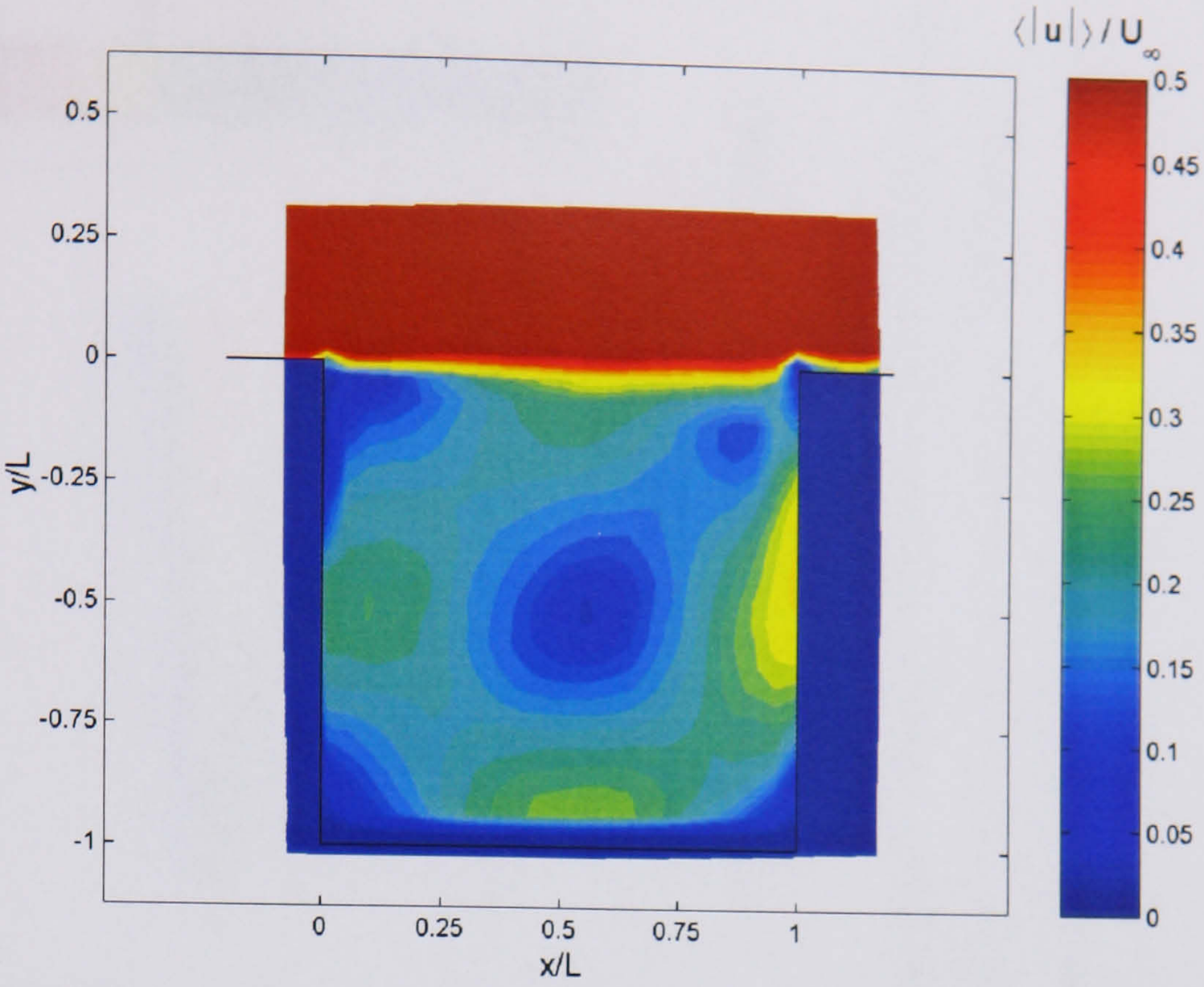

a. Velocity magnitude for $L/D = 1.0$. Colour bar limits are preset.

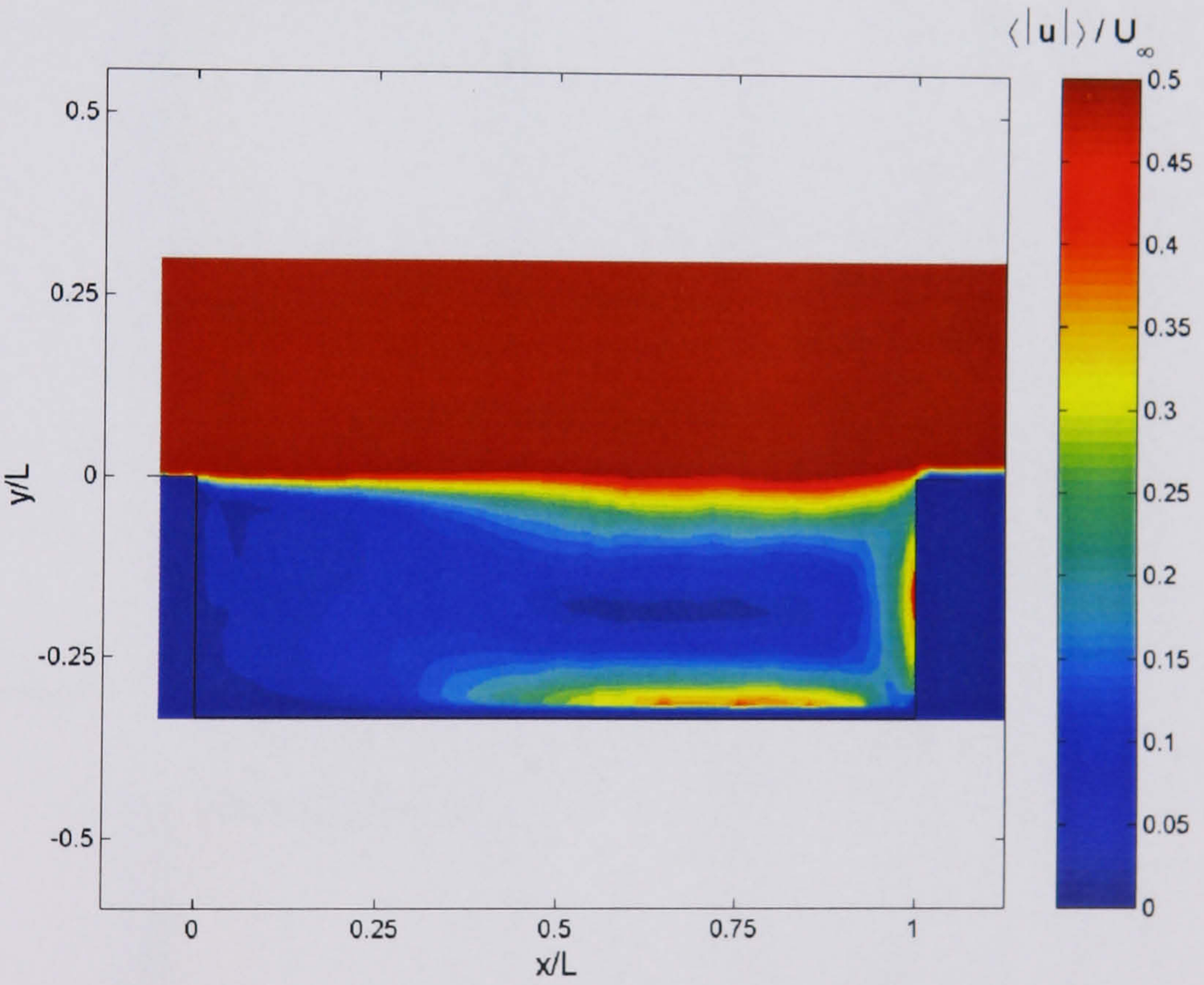

b. Velocity magnitude for $L/D = 3.0$. Colour bar limits are preset.

Figure 4.55. The mean velocity magnitude plots show that the jet edge and core along the rear and bottom walls becomes stronger as the cavity length increases. This accounts for the increase in drag experienced by the longer cavities. The colourbar limits are chosen to delineate the main features of interest.

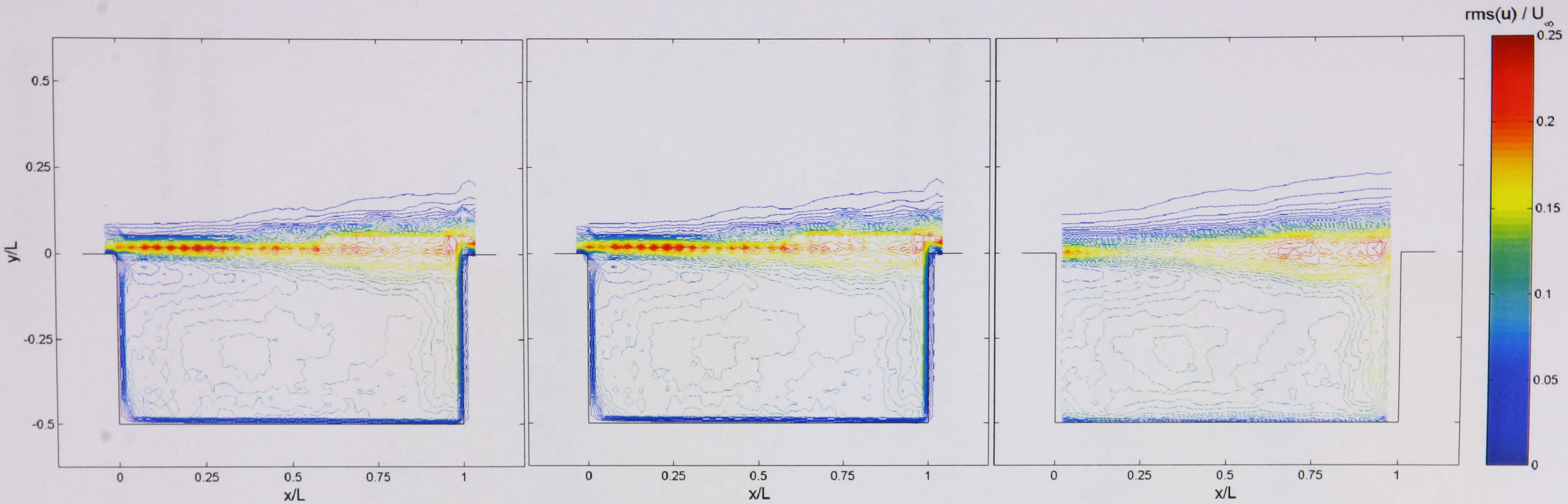

a. Sample set accumulated at 10Hz. b. Sample set randomly accumulated. c. Sample set as in (a), using PTV 't-tiling'.

Figure 4.56. Comparison of the RMS calculation for data acquired at 10Hz and that acquired randomly. There is marginal difference between the first two plots although there are more significant differences when the PTV algorithm is used to interrogate the image data. The 't-tiling' technique may reproduce more accurately the vector field although the cost is a reduced sample size. From the 250 samples captured in (a) only 160 are useful in this RMS calculation for (c).

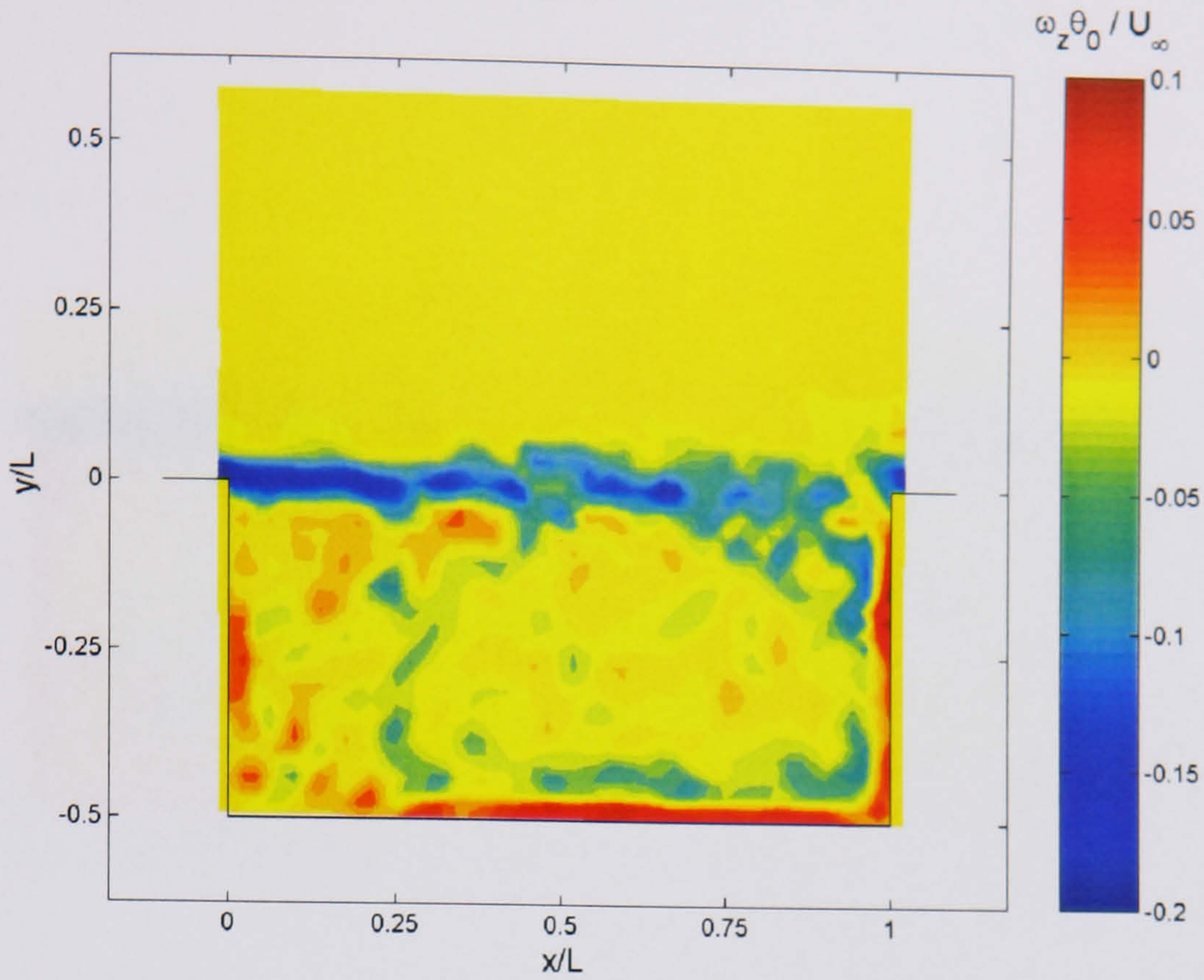

a. Vorticity is continually being generated at the cavity leading edge while the Kelvin-Helmholtz instability noticeably acts to roll-up the shear layer after some progression downstream.

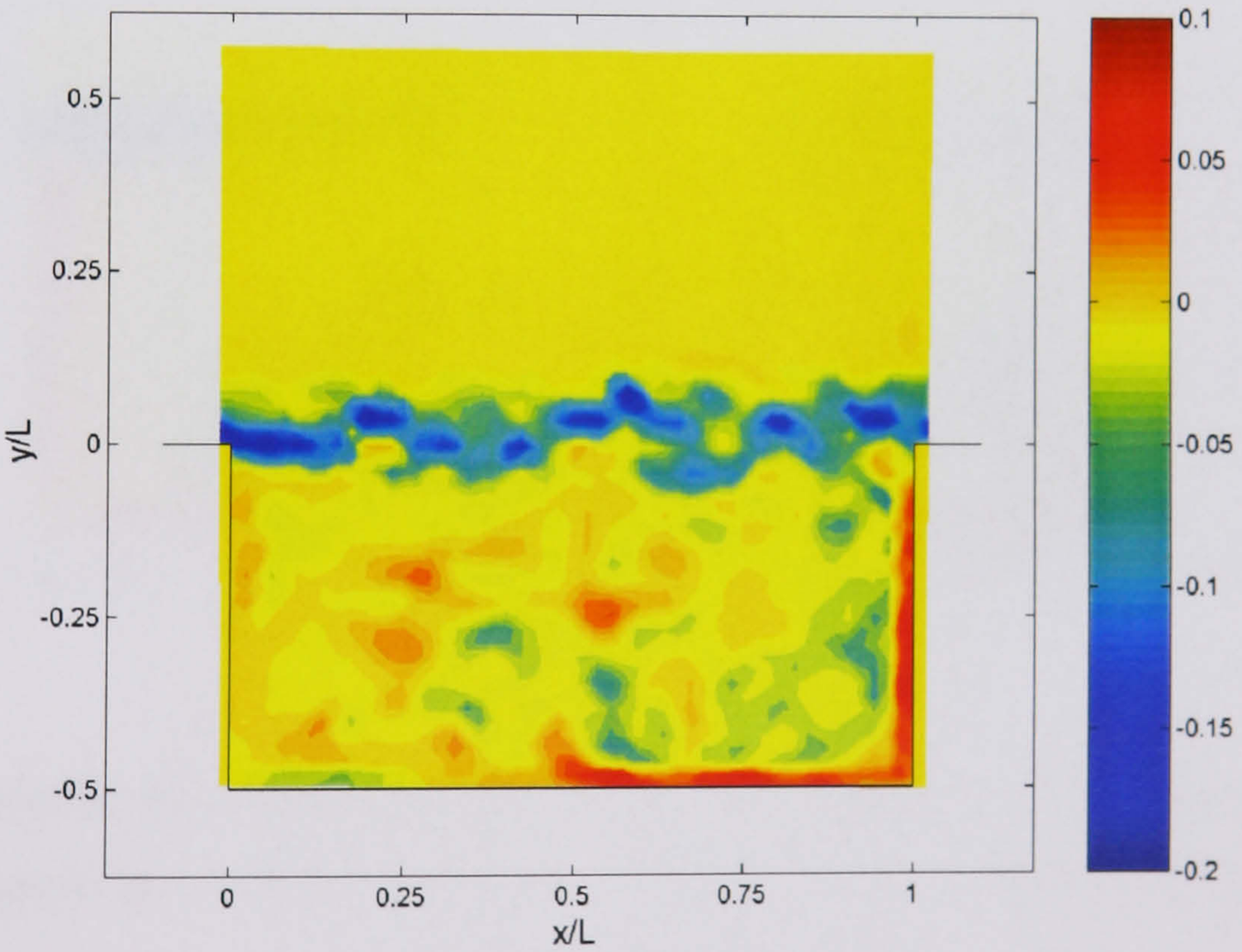

b. In a different type of shedding the shear layer is punctuated with small-scale high vorticity segments. This effectively illustrates the change in shedding frequency after actual separation.

Figure 4.57. Instantaneous vorticity for $L/D = 2.0$. The colour bar limits are set.

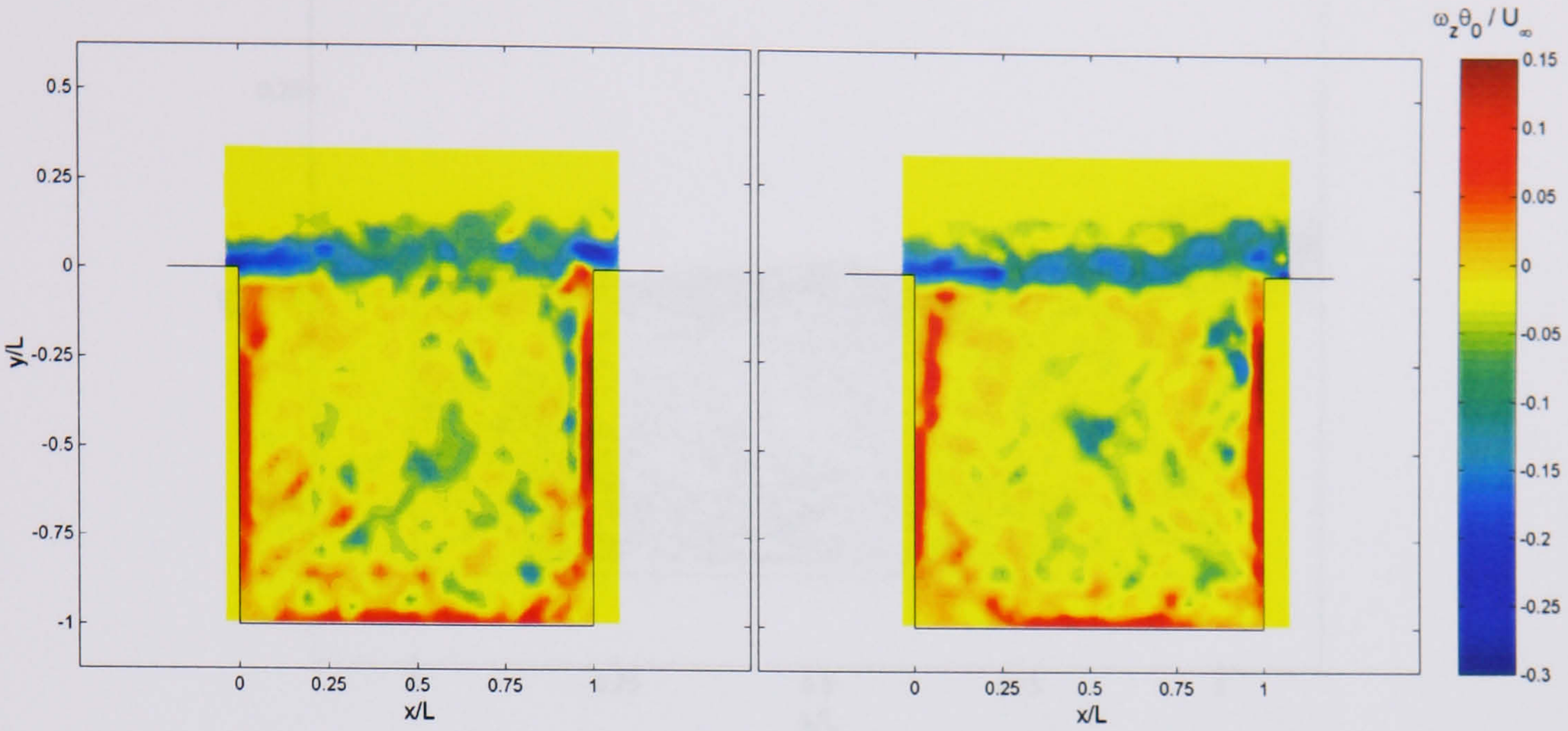

a. b.

In this case the freshly separated shear layer displays lip of similar strength vorticity that begins the process of entrainment and roll-up.

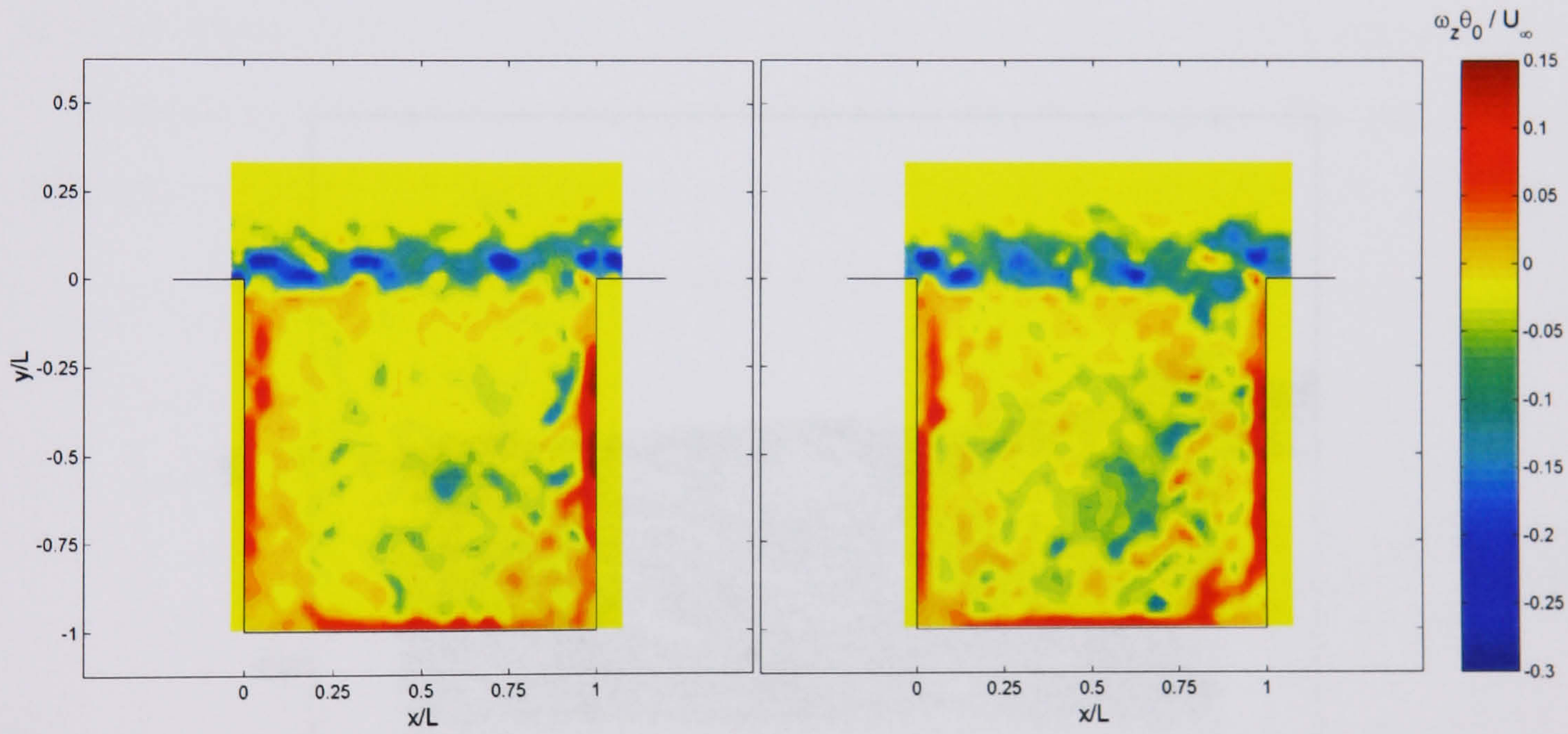

c. d.

It is also possible that immediately after separation the shear layer displays a tendency to break apart into small-scale pockets of strong vorticity. This does not facilitate a large-scale roll-up process.

Figure 4.58. Instantaneous vorticity for $L/D = 1.0$. The colour bar limits are set.

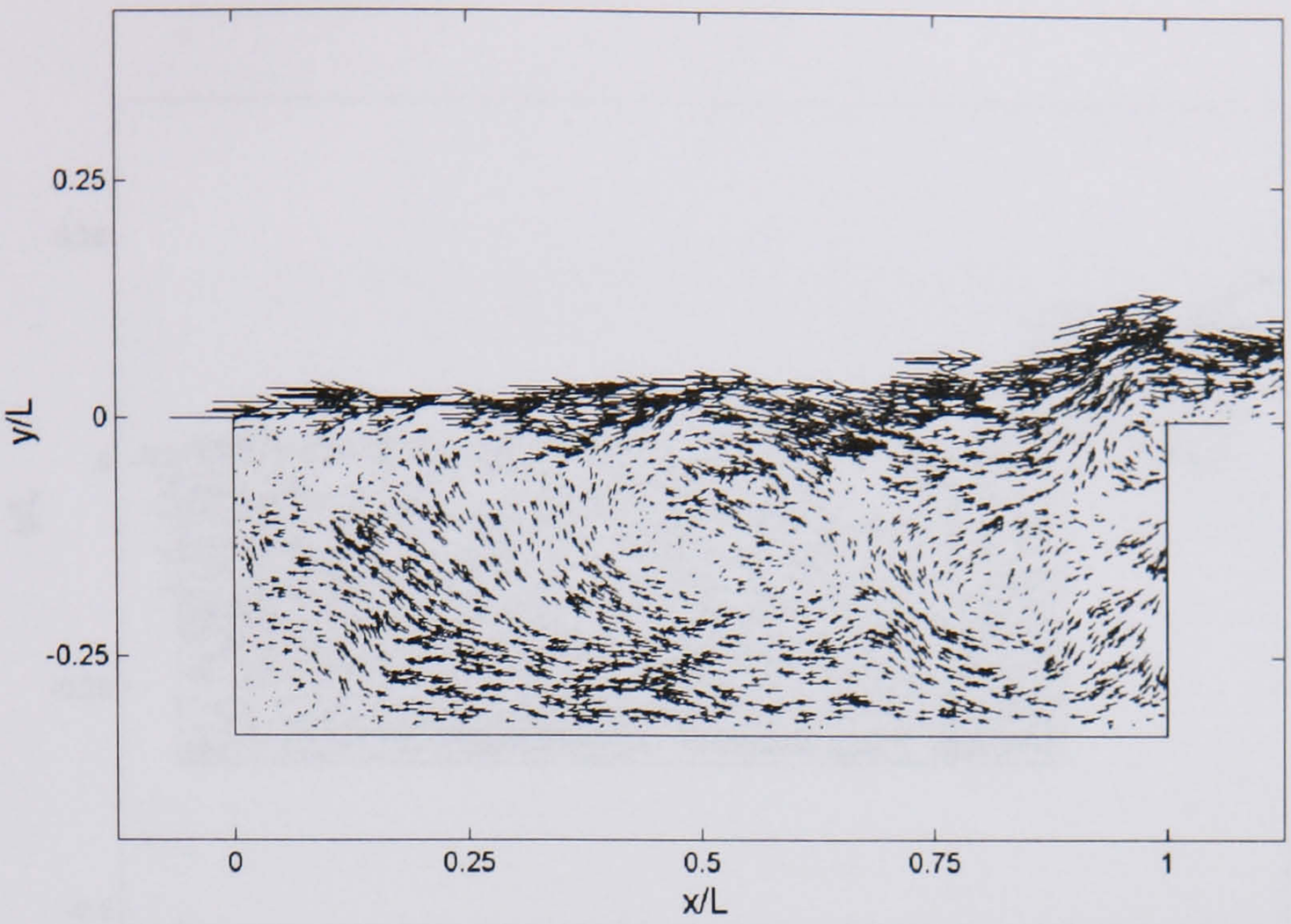

a. Immediately after global mass expulsion from the cavity the shear layer returns to the downstream corner.

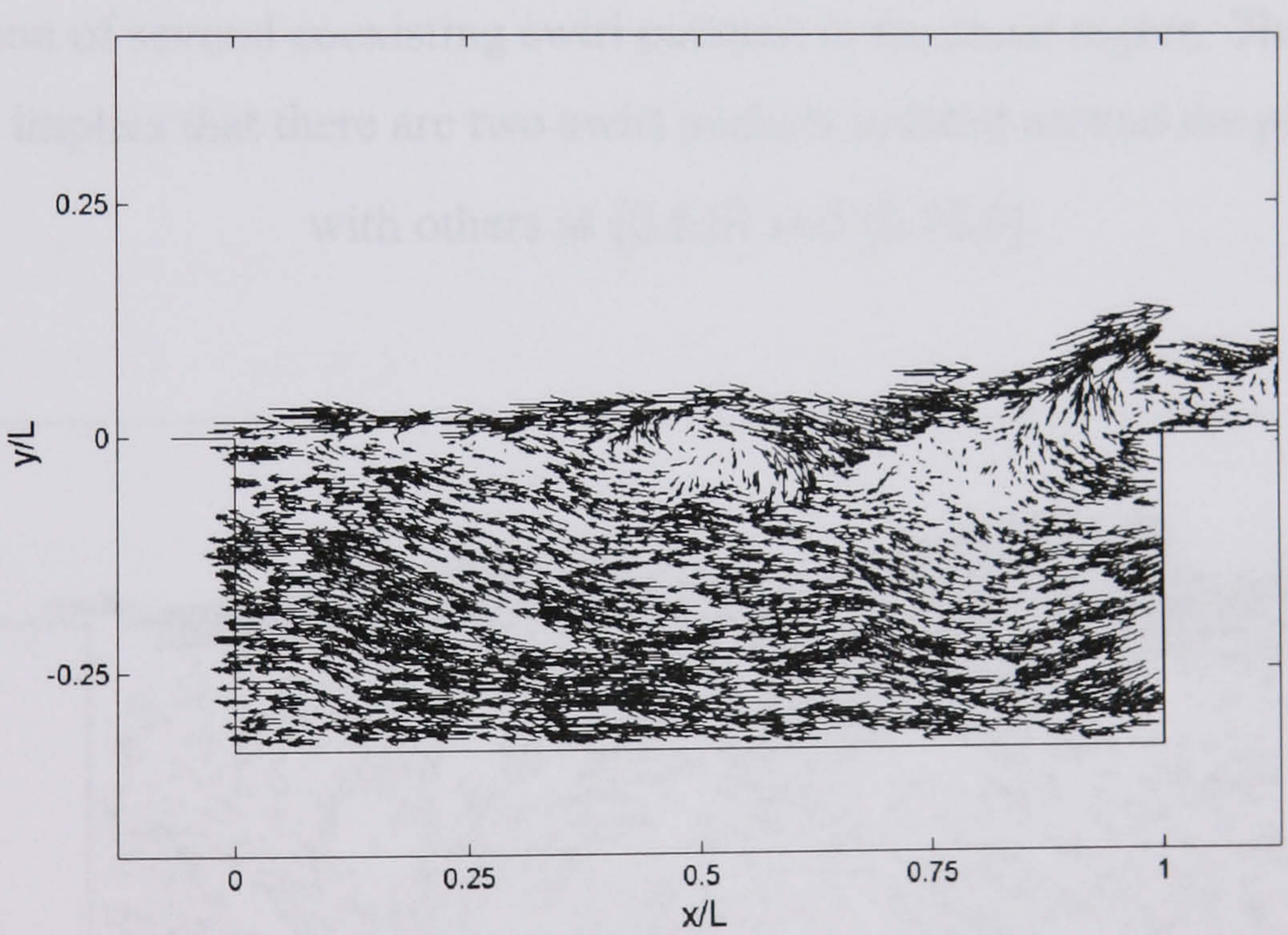

b. With the frame moving at $0.25U_\infty$ it is easier to spot the presence of individual structures in the shear layer, these are at $(0.2,0)$, $(0.5,0)$ and $(1.0,0)$.

Figure 4.59. Instantaneous velocity vectors for $L/D = 3.0$ using the hybrid BTT scheme.

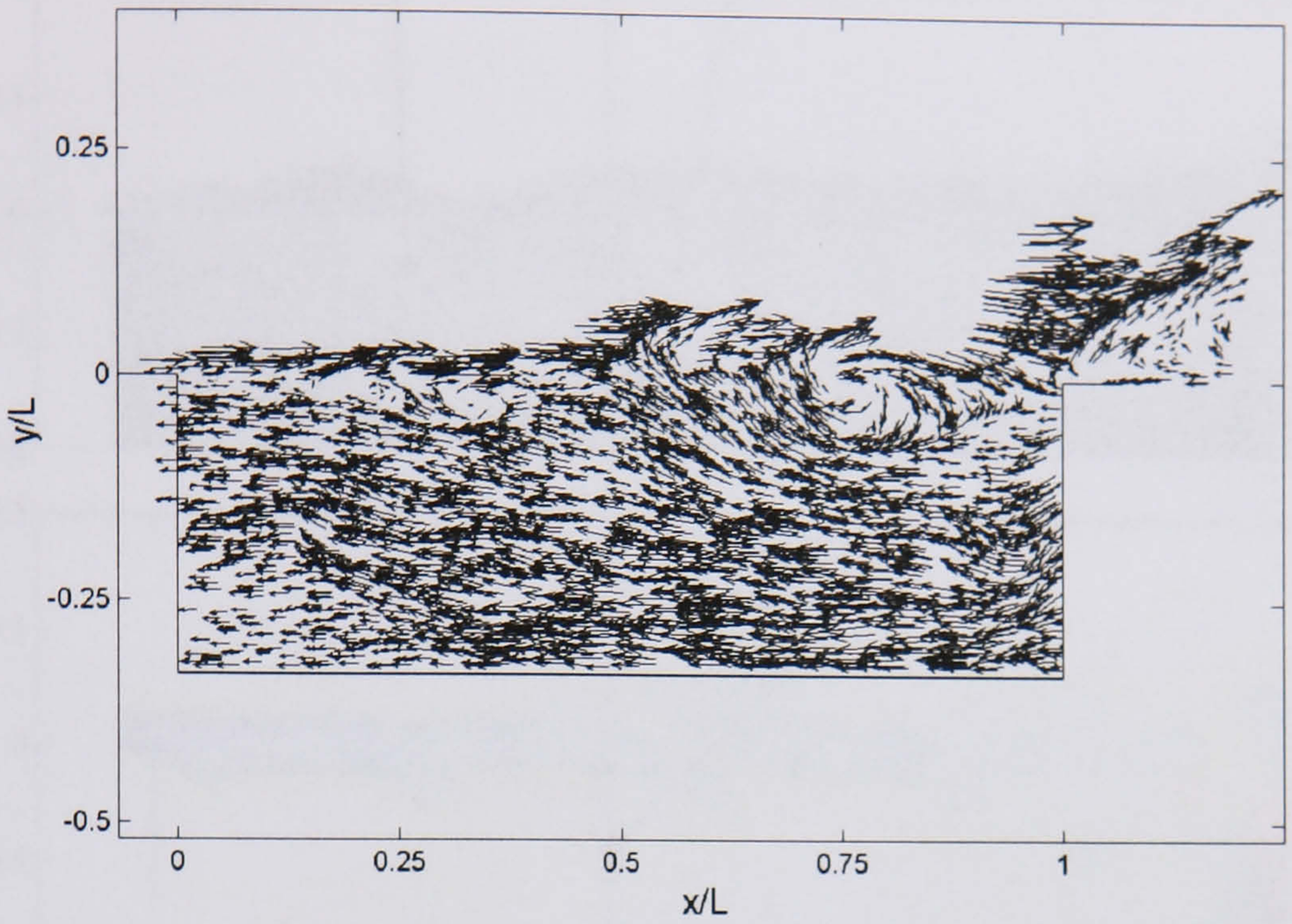

Figure 4.60. Instantaneous velocity vectors for $L/D = 3.0$ using the hybrid BTT scheme with the frame moving at $0.25U_\infty$. Once again the mass expulsion cycle succeeds the formation of several coexisting swirl patterns in the shear region. The tracking algorithm implies that there are two swirl pockets saddled around the point $(0.25,0)$ with others at $(0.6,0)$ and $(0.75,0)$.

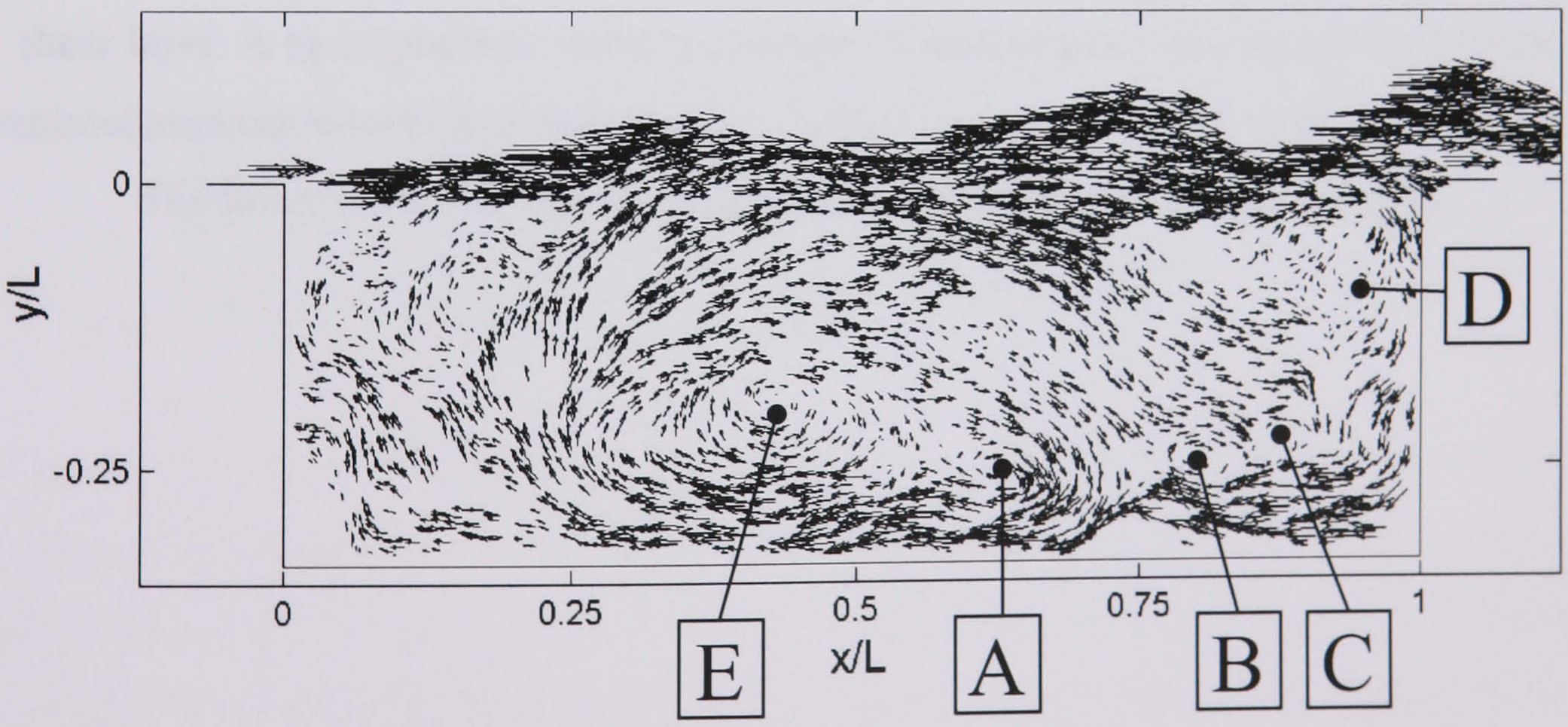

Figure 4.61. Instantaneous velocity vectors for $L/D = 3.0$ using the hybrid BTT scheme. The features A, B, C and D indicate the centre of small satellite vortices cast into the cavity during a mass addition stroke to the cavity when the shear layer is still in the second state. The primary roll-up is indicated by feature E.

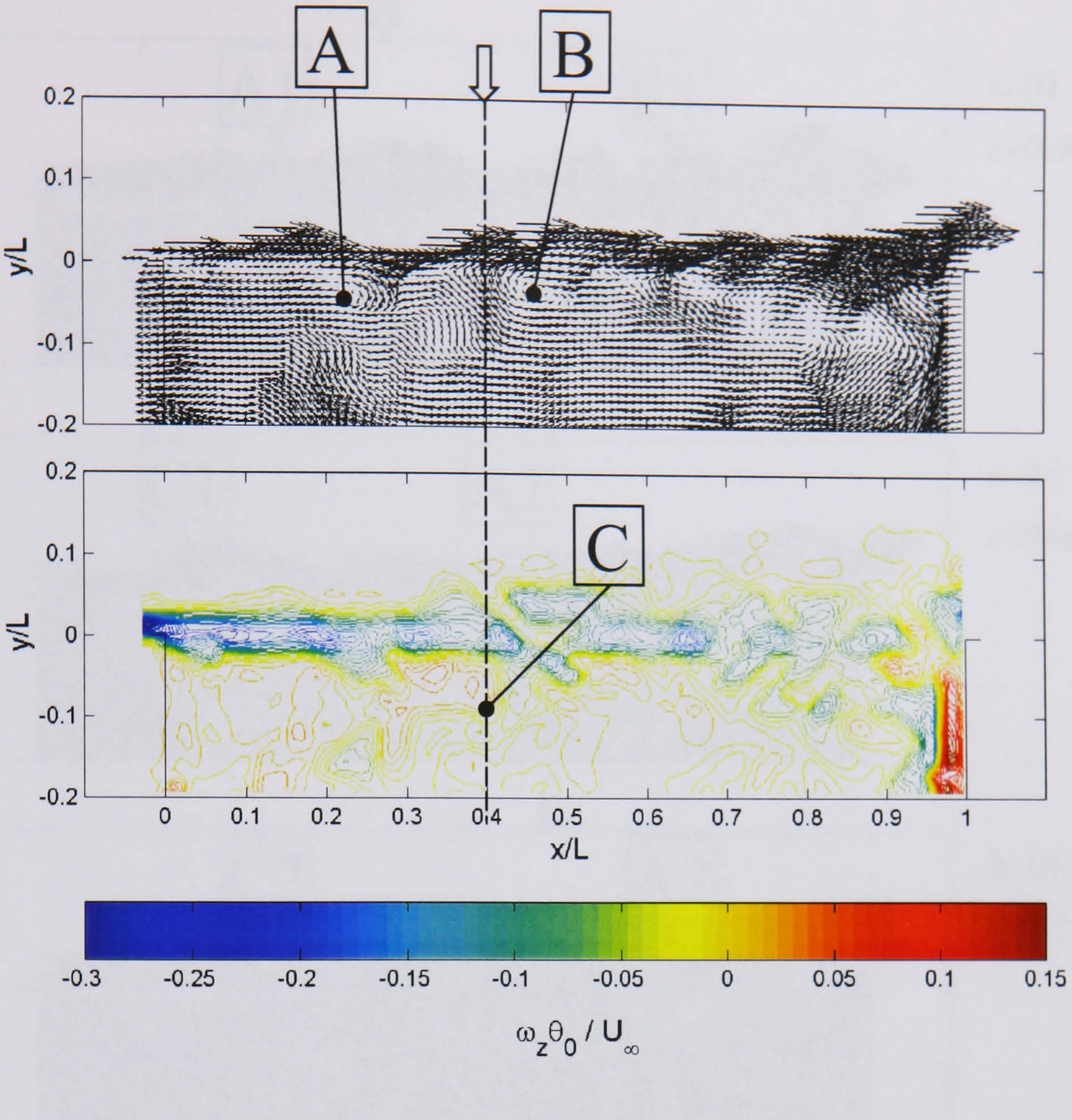

Figure 4.62. Instantaneous velocity vectors and vorticity for $L/D = 2.0$ with the frame moving at $0.25U_\infty$. Features A and B indicate two separate regions of roll-up in the shear layer. A lip of positive vorticity (feature C) indicates the relative position of the recirculation wavefront (also indicated by a hollow arrowhead in the vector plot above). The lower portion of the figure is included in its entirety in figure 4.57a.

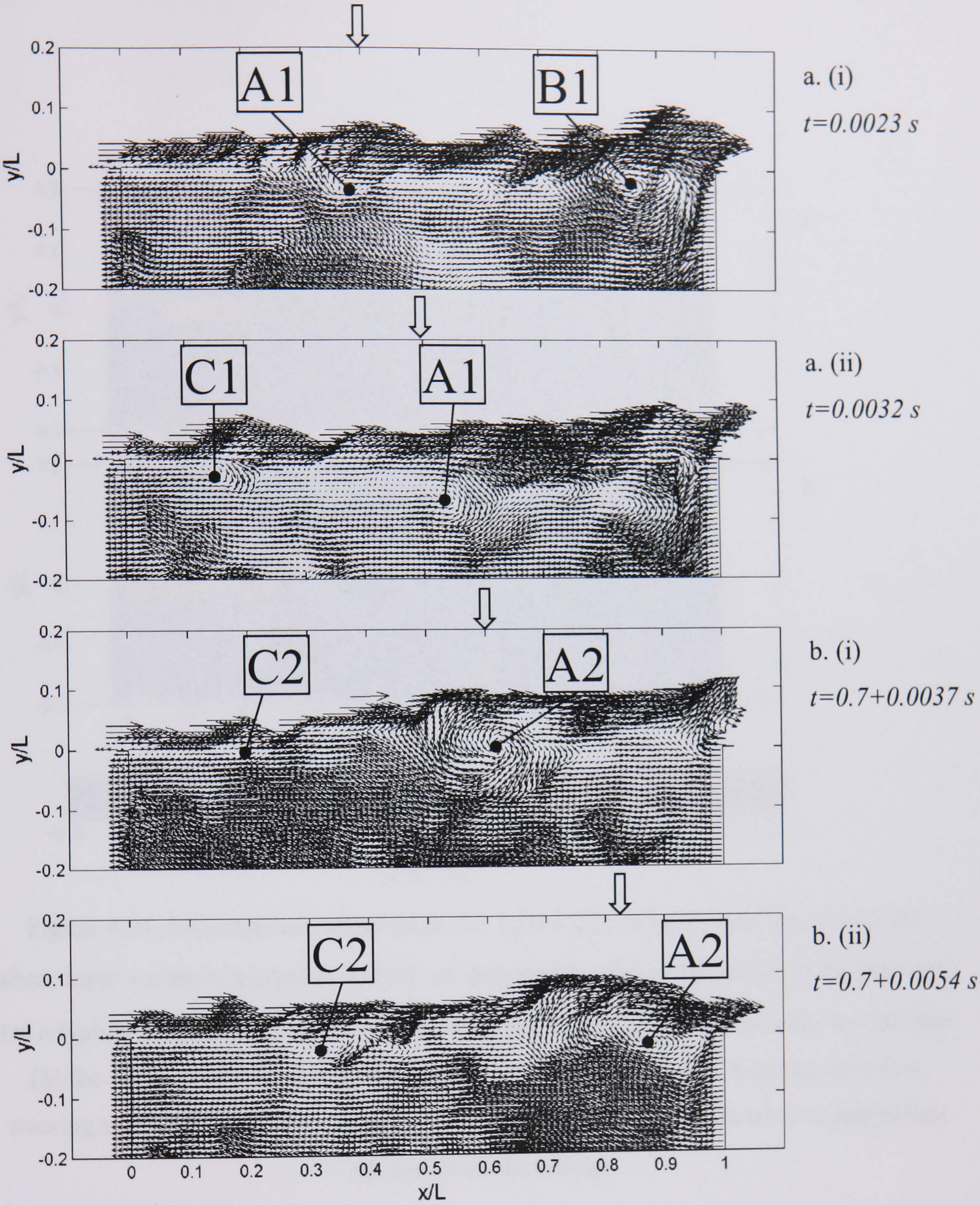

a. (i)

t=0.0023 s

a. (ii)

t=0.0032 s

b. (i)

t=0.7+0.0037 s

b. (ii)

t=0.7+0.0054 s

Figure 4.63. Instantaneous velocity vectors for $L/D = 2.0$. The series is made up of two sets of sequentially acquired data used to illustrate a typical interaction between the shear layer and the internal cavity recirculation zone. A1 and A2 indicates the roll-up of interest in the shear layer, while the arrow designates the approximate position of the recirculation wave front. The roll-up region that is 'locked-on' experiences increased entrainment and as such grows much larger.

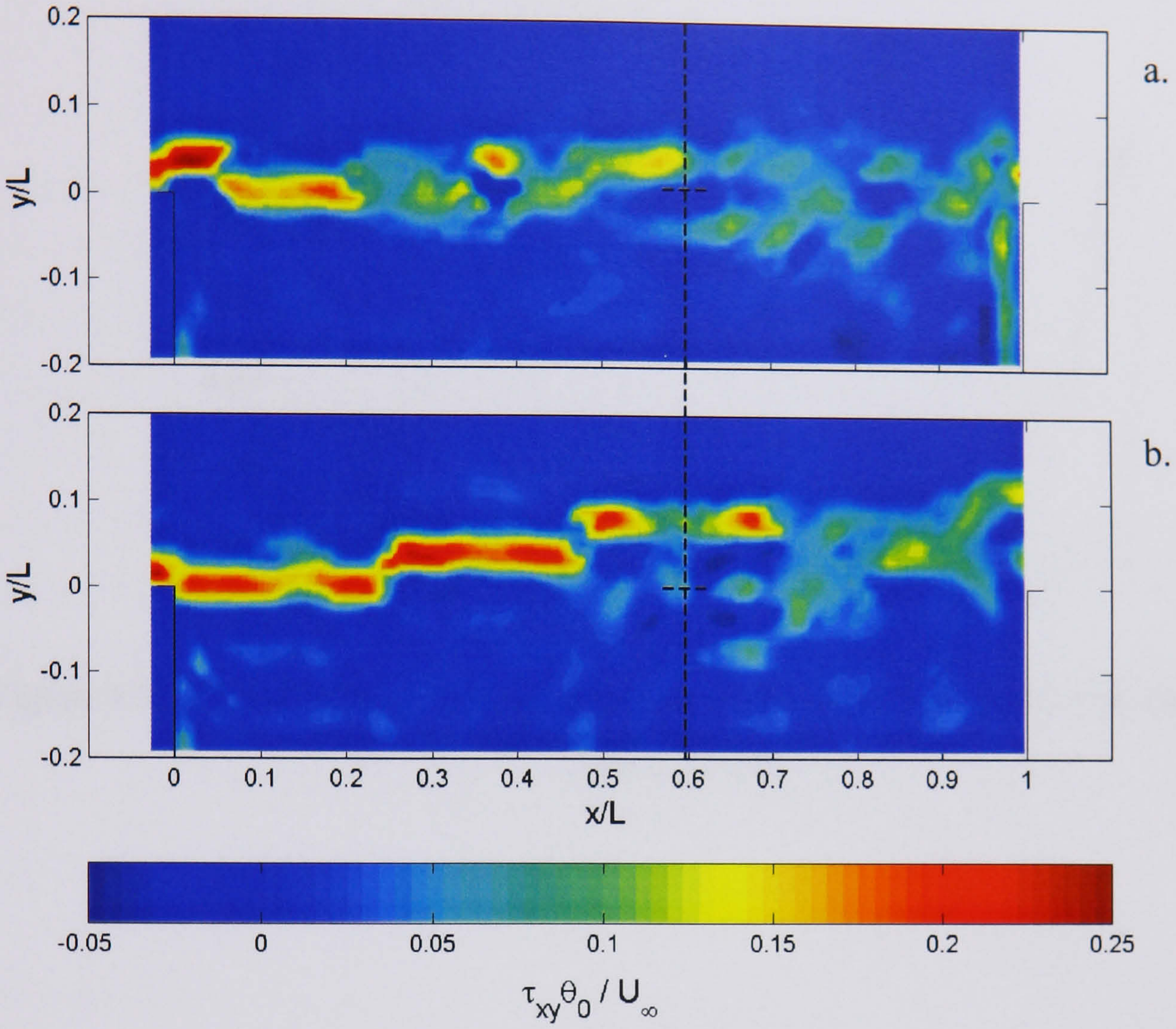

Figure 4.64. Instantaneous shear strain for $L/D = 2.0$. In both cases the roll-up of a shear layer vortex is located at $(0.6,0)$, as indicated by the dashed line. For the first case (a) a typical Kelvin-Helmholtz shear layer vortex is rolling-up, while in the second case (b) the entire cavity flow is being entrained into the roll-up of a shear layer vortex, causing much higher rates of positive strain from the separation location to just before the centre of the roll-up.

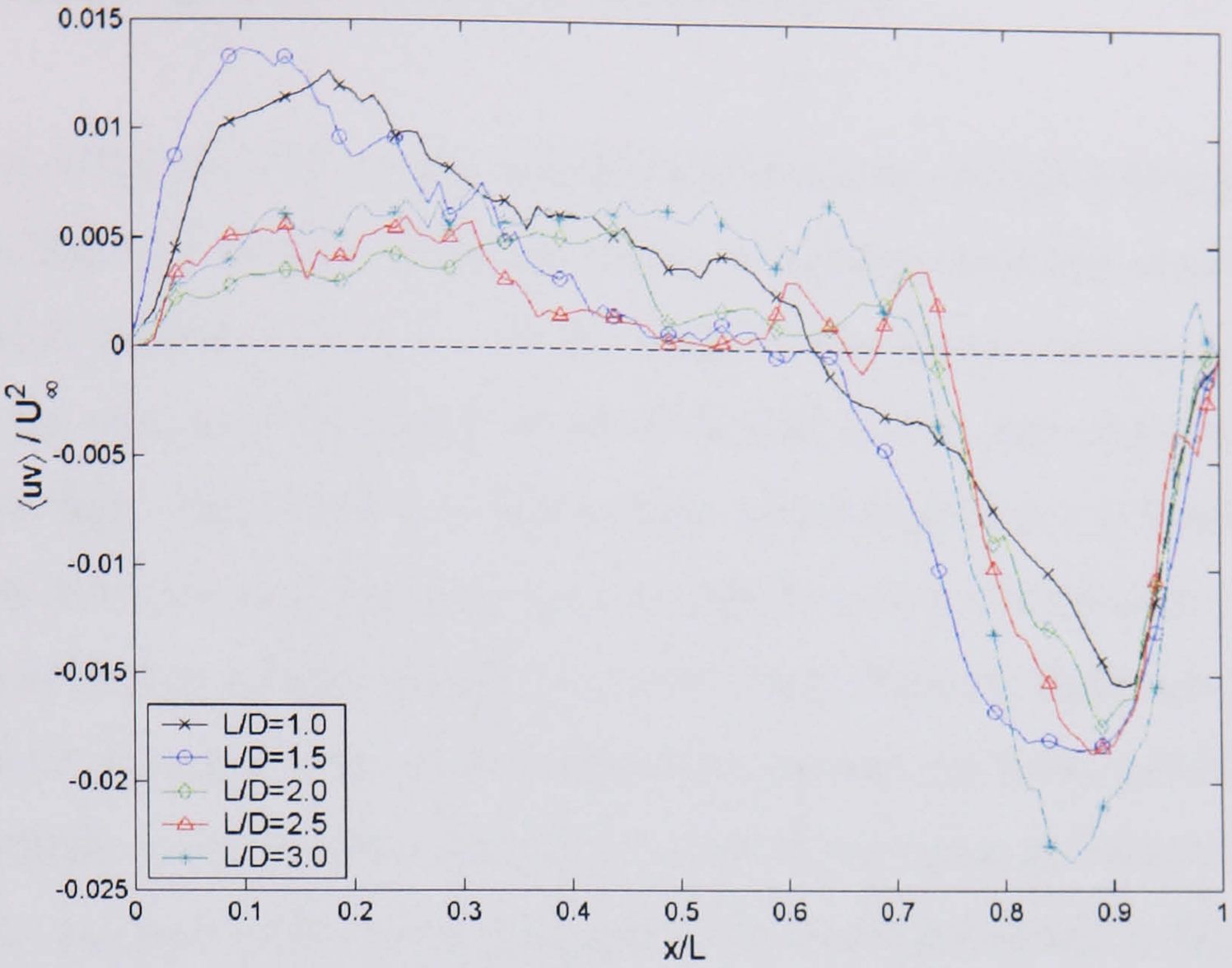

Figure 4.65. Distribution of the mean momentum transfer for each cavity case along the line $y/L = 0$.

CHAPTER 5: AERODYNAMICS OF THE INTER-CAR GAP AND SOME PASSIVE CONTROL STRATEGIES

A derivative of the flowfield experienced in and around a normal (rectangular) cavity geometry is that of the inter-car gap on a train. A small geometrical modification to the cavity walls of chapter 4 (now termed the 'clean' cavity cases) can impose distinct changes to the measured fluctuation of the flowfield, and as such merits a brief investigation here. This problem is particularly interesting since it is beneficial to reduce skin-friction downstream of an inter-car gap, which does not necessarily demand diminution of flow fluctuation inside the cavity itself. Velocity field data for a number of standard cavity geometries are recorded and proposals for better performance are made. In addition some mainstream passive control strategies are tested for the central clean cavity case and observations are made. The results presented in this section are not supplemented by pressure data while the statistical data is produced with the hybrid 't-tiling' scheme using the required amount of image pairs to generate a 250-sample size set. The physical 't-tile' dimension was preset to that indicated in the right hand side of table 2.1.

5.0 The inter-car gap

According to simple flat plate theory the immediate downstream vicinity of an inter-car gap on a train will result in a local increase of skin friction. In fact using the logarithmic theory of Von Karman it is predicted that approximately 14% of the total skin friction imposed by a typical carriage of a Pendolino S220 train will be generated within a single cavity length downstream of the inter-car gap (for typical operating conditions). At first it appears that design modifications to the gap may improve the skin friction drag in this vicinity and have a noticeable improvement in the overall drag. However, the boundary layer grows quickly, after approximately three carriages downstream the boundary layer is taller than the inter-car gap itself, and the skin friction is much reduced anyway. Therefore, the drag improvements obtained from design modifications to the cavity will diminish downstream and for a common 12-car assembly the reduction of skin-friction drag should only be very slight (perhaps 1% or less). Nevertheless, it may be the case that distinct reductions in skin-friction are possible courtesy of a subtler mechanism associated with cavity flow unsteadiness.

With the prerequisite of cavity oscillations being detected once the shear layer has reattached to the downstream wall the distribution of Reynolds stress through the zone close to the wall is changed in comparison to a typical boundary layer. That is the organisation and growth of the shear layer structures encourage an elevation in Reynolds stress very close to the wall, which has been seen to increase the local value of skin friction. It is well known from past research, Bechert et al. 1997 and references therein that this type of momentum transfer (in particular the tangential Reynolds stress) close to the wall is responsible for approximately 80% of skin friction generated in wall bounded shear flow. In fact almost all skin friction reduction devices work by actually impeding the fluctuating velocity at the wall and thus reducing the low speed streak generation, ejection and bursting in the boundary layer, Kerho 2002. It is also pertinent to mention that a majority of train manufacturers use riblets as a passive skin friction reducing technique and the optimal performance of these devices is only assured when the approaching flow is wall bounded and steady. In essence, there may be benefits to designing an inter-car gap that minimizes the transmitted fluctuation from the shear layer into the downstream flat plate regions. In addition to this the suppression of vortex escape from the cavity itself is beneficial in reducing the overall radiated noise from an inter-car gap / pantograph assembly.

5.0.1 Modelling the inter-car gap

There appears to be three common types of inter-car gap configuration used by current train manufacturers, Johnston 2001. In all instances the modifications made to the internal geometry of the cavity is symmetrical about the vertical centreline such that bidirectional efficiency is preserved. For the first type the front and rear bulkheads are slanted in opposite directions, which is common for inter-car gaps within the range $1.0 \leq L/D \leq 2.0$. In the second case the floor of the cavity is slanted inward and downward, which is common to an inter-car gap of $L/D = 2.0$. The third common design concept is typically observed when $L/D < 1.5$, where a portion of the cavity floor is elevated to accommodate passenger movement between cars (sometimes termed the 'concertina' section).

5.0.1.1 Configuration 1: Slanted front and rear bulkheads

The effect of chamfered/slanted rear faces has been seen to attenuate the oscillation amplitude from cavities in gate slots, Ethembabaoglu 1973 to supersonic resonating cavity flow, Heller and Bliss 1975. In each instance amplitude attenuation is encouraged by manipulating similar aspects of the fluid nature, that is a reduction of the feedback strength from the rear corner. For the case of gate slots additional attenuation is encouraged by reducing the effective roll-up length of the hydrodynamic instability.

For the purpose of simple classification the L/D of the investigated cavity types are determined by the exposed length of the cavity floor. Therefore a cavity geometry of $L/D = 2.0$ in configuration 1 will actually have an effective shear layer length equivalent to $L/D = 2.8$, while for $L/D = 1.5$ the exposed shear layer length is actually $L/D = 2.1$. The average vorticity and Reynolds stresses are calculated for these particular cases and are included in figures 5.1 and 5.2. With added reference to figures 4.51 and 4.52 and table 5.1 it is observed that in comparison to the clean configuration the average circulation within the cavity increases (based on the mean case) and the centre of the internal recirculation region is positioned further downstream. The average vorticity indicates that the formation of a jet-edge along the cavity rear wall and floor persists for this configuration, while the shear layer impingement is distributed over the slanted rear face. Simple oil flow visualization was repeated, this indicated a very weak cellular behaviour that was barely discernable when $L/D = 2.0$. The most apparent change is the increase of maximum agitation experienced by the shear layer spanning the open face of the cavity. The reason for this is that the entrainment demands of the longer shear layer require a larger mass exchange at the rear face since the cavity volume has only been moderately increased. It should be noted if the Reynolds stresses of these cavities are compared to the clean cavity cases of a comparable shear layer length (that is compared to figures 4.52 and 4.53 where $L/D = 2.0$ and $L/D = 2.5$ respectively) the unsteadiness of the shear layer is actually reduced. However as already stipulated the cavity dimensions are defined using the exposed floor length.

As mentioned in chapter 1 a clean cavity shear layer vortex may experience one of three possible events at the downstream corner, complete clipping, partial clipping and escape. When the rear face is slanted the stagnation streamline is exposed to a surface

area that facilitates a normal impingement for the inflectional shear layer profile and inherently reduces the oscillation amplitude (best indicated in figure 5.4a). The most infrequent event then becomes partial clipping since there are no sharp corners to sever the impinging vortical structures. In the absence of point-probe measurement the frequency of particular clipping events are difficult to confirm even though the hypothesis seems logical. For the purposes of this study a simple filter was applied to the instantaneous velocity data that would seek out regions of velocity swirl, and measure them accordingly (based upon vector topology and swirl age). These results were then confirmed through visual inspection of each instantaneous velocity record, these results are presented in figure 5.5. It can be seen in the clean cavity case that small pockets of swirl velocity are noted along the shear layer, down into the cavity, across the cavity floor and then within a particular upstream zone of the cavity. The larger swirl scales are seen to be present within this zone also and then almost exclusively at the downstream corner region of the cavity. This progression of scales is concurrent with the shear layer interaction with the internal cavity motion, as already mentioned in chapter 4. For configuration 1 the location of swirl pockets in and around the cavity are similar to those of the clean case although in this occasion there are more instances whereby the smaller scales of the shear layer are convected back into the cavity along the slanted bulkhead. This is suggested by the Reynolds stress calculations presented in figure 5.1 and 5.2, in which the distributions of Reynolds stress are not self-similar between configuration 1 and the clean case. In fact for configuration 1 there is a notable reduction in shear layer agitation for $x/L > 0.9$.

It is plausible that by biasing the clipping fate of the shear layer vortices in this way will increase the mean inflow into the cavity, as indicated by figure 5.3 (and illustrated in figure 5.4b) where even in comparison to $L/D = 3.0$ the average inflow at the trailing edge is markedly increased. This subsequently increases the (average) internal circulation (indicated in table 5.1) and implies[1] an increase in pressure drag imposed by the cavity. In addition, the slanted front face increases the effective length of the shear layer and as such the maturity of the vortical roll-up is greater at any given location in comparison to the clean case. Since the low-frequency modulation is observed to persist (exclusively from instantaneous velocity data using the dual-PIV set-up) a stronger

internal recirculation structure (figure 5.4c) will roll-out of the cavity in phase with a more mature shear layer vortex. Therefore the escape event associated with the low-frequency modulation of the cavity increases in amplitude, as shown in figure 5.4b. From an inspection of the instantaneous velocity results for configuration 1 it is apparent that the instability growth in the shear layer is less amplified than for the clean case of a comparable shear layer length, see for instance figure 4.53 and 5.2d. This is caused by a change in the amplitude-modulated fluctuations that are induced into the sensitive region near separation (or 'pseudo-sound') caused by the slanting of the bulkheads. Most studies concerned with disturbance generation and growth are approached using unsteady pressure measurement since it is the induced forcing that is of principal importance, see for instance Ziada and Rockwell 1982a and 1982b. Although the usefulness of solitary flowfield measurements is limited, the dual laser-camera set-up positioned at the front and rear corners of the cavity may crudely observe the disturbance conversion phenomenon that is required for feedback. Using a camera time-delay of $\Delta t_1 = 70ms$ between the vortical interaction event at the rear face and the separation corner capture the induction of the fluctuation into the sensitive region near separation will have grown sufficiently to be measured adequately by the PIV system. These results are included in figure 5.6. The clean cavity shear layer interaction of figure 5.6b demonstrates a lower instantaneous velocity fluctuation at the trailing edge than in the case of configuration 1 (figure 5.6d) although the (delayed) upstream fluctuation is similar in strength. These results are entirely repeatable[2] and agree with the results of Morkovin and Paranjape 1971 (included in the review of Rockwell 1983) that stated the conversion of disturbance incident upon an edge becomes more efficient as the edge becomes sharper. On an additional note, it is not possible to imply the induced force at the rear cavity face using only fluctuating velocity data.

There is evidence to suggest that the low-frequency modulation of the cavity may facilitate the propagation of intact and relatively undistorted vortices from the cavity that will impose modified induced loading, vibration and sound generation[3]. From the work by Howe 1995 it is actually possible to relate the unsteady loading to the

---

[1] No static pressure measurements were made in this configuration and the skin friction on the cavity floor is unknown.
[2] If the events of direct jet impingement are neglected (covered in section 4.2.3.2).

distortion of the incident vortical structures in incompressible viscous flow, although this is a topic for further research. The issue of sound generation will be mentioned later.

Figure 5.10 and 5.11 illustrates the first three POD modes and energy data for the clean case and configurations 1 and 2 for $L/D = 2.0$. Previous POD studies of cavity flow, Rowely et al. 2000 and forced shear layer oscillations, Rajaee et al. 1994 have shown that the phenomena can be characterised with relatively few POD modes. For the results presented here it appears that the cavity oscillations still exhibit phenomena characteristic of a low-dimensional nonlinear dynamical system although the energy distribution is more similar to that of a jet-flow where both large and small scales in the flowfield play an equally important role, as in Bernero et al. 2000 for instance. This is borne out in the energy distribution plot of figure 5.11 where it can be seen that over 30 modes are needed to reconstruct 75% of the total fluctuation energy. The distribution of POD mode energy is similar for each case (figure 5.11). The first mode represents the interaction of the shear layer with the downstream corner and the primary recirculation within the cavity itself. The modes following this are then concerned with the next largest scale, for instance the upstream corner and other impingement events at the downstream corner. As the modes progress the areas of fluctuation move further upstream along the shear layer. In the case of configuration 2 it can be seen that the first three POD modes are with the rear bulkhead indicating a change in the impingement scenario.

Using a Preston tube the skin friction was measured downstream of the cavity for each configuration and compared to the clean cavity cases. Any parasitic effects are removed by inserting a smooth aluminium plate aft of the cavity section (shown in figure 3.6h), while the same plate was used in each instance to remove parasitic porosity effects. It was found that the quality of the shear stress measurements on the plate deteriorated as the Preston tube was traversed upstream (the prerequisite of wall-bounded flow breaks down), although the geometrical constraints of the model and a strengthening adverse pressure gradient meant a compromise had to be made. Therefore for each case no data

---

[3] The surface loading will predominately be a function of vortex circulation and weakly dependent on the actual vorticity distribution.

is presented within the first 50mm downstream of the cavity. In the case of configuration 1 it is apparent from figure 5.12 that as the cavity length increases there is more skin friction generated downstream of the gap. It is also significant to mention that the skin friction gradient (dC_f/dx) experienced in each case is comparable. For configuration 2 the skin friction distribution generated downstream is greater than that for the clean cavity case. This is perhaps caused by a more mature roll-up in the shear layer transmitting larger fluctuations (tangential Reynolds stress) across the flat plate section. One pertinent observation is that configuration 2 (with an effective shear layer length of $L/D = 2.8$) invokes a smaller skin friction distribution than a clean cavity with $L/D = 2.5$.

5.0.1.2 Configuration 2: Slanted cavity floor

With reference to the linear (spatial) instability theory of Michalke 1965 any disturbances just downstream of the cavity leading edge are amplified first exponentially with streamwise distance and then by finite-amplitude effects. Therefore if the amplification of the unsteadiness in the shear layer is attenuated then it is probable that one or both of these effects have been subdued. Configuration 2 illustrates the point that the suppression of one type of mechanism can intensify another, causing an overall increase in unsteadiness. The floor of configuration 2 is slanted into the clean geometry (reducing cavity volume), which causes a small reduction in perpendicular impingement area that will incur some diminution to the feedback signal generated. From inspection of figure 5.7a and b it can be seen that this sloped floor is promoting the tongue of vorticity formed by the jet-edge along the cavity floor to extend essentially further upstream and closer to the separation position. Thus there is an increase in the influence that the internal structures impart on the growth of the shear layer. This is indicated in figure 5.3 for configuration 2 where the positive mean momentum transfer is amplified over the initial 20% of the open face of the cavity (indicated by a distinct plateau region). With reference to figure 5.7c and d it appears as though the distribution of Reynolds stress within the shear layer for the clean and sloped floor cavity are in fact very different (the clean case is 0.002 lower in maximum stress).

A crucial benefit in this type of cavity geometry is the attenuation of the low-frequency oscillation inside the cavity that lead to the 'roll-out' and global mass expulsion

phenomena noted for the clean cavity case. In figure 5.7d there are small-scale regions of high velocity correlations along the two-sloped surfaces actually increasing in amplitude (and changing sign) as it progresses upstream. The average circulation of the internal recirculation zone is also much smaller than for the clean case (see table 5.1) since the sloped bottom geometry inhibits both growth and movement of structures equivalent to the cavity depth. Figure 5.7b shows this recirculation zone being perched on the adverse pressure gradient side of the slope. Using the dual-PIV system it is apparent that the high Reynolds stress along the internal perimeter correspond to vorticity being cast into the cavity at the trailing edge (during the mass addition stroke) which then travels unhindered upstream. These are indicated in figure 5.8a as regions **A**, **B**, **C** and **D** and appear as velocity swirl patterns. When region **D** arrives underneath the separation position of the shear layer it may be entrained immediately into a convecting shear layer instability or there will be a short delay, depending upon phase compatibility of the two structures (similar to the discussion of section 4.2.4.3). This typical oscillation is the reason why there is a strong dissimilarity between the velocity correlation of the shear layers for configuration 2 and the clean cavity case.

If it were possible to measure the unsteady pressure on the cavity floor in this configuration then a sub-harmonic of the shear layer oscillations would still be expected. The reason for this is illustrated in figures 5.8b and c where previously agglomerated regions of vorticity (regions **E** and **F**) in the shear layer are clipped back into the cavity for another internal cycle (the same regions are followed between figures). This type of interaction is carefully noted to only occur with pairs of vortices and it disrupts the entire process of upstream shear layer entrainment described in the previous paragraph[4]. The first three POD modes for this configuration are shown in figure 5.10. These are in agreement with the predicted oscillation where the downstream corner is responsible for the majority of the fluctuation energy (mode 1) and the progression of small scales along the sloped cavity floor become more dominant (mode 3), indicated by a loci of maximum velocity magnitude along the cavity floor.

It is thought by reducing (by half) the height of the vertical face in this cavity configuration will considerably reduce the unsteadiness in the shear layer. The cost is

---

[4] Repeatable in over 25 (10%) of the samples taken.

that the deleterious effects of shear layer osculation will be amplified since the internal perimeter of the cavity is reduced. Not only will the feedback strength be attenuated but also the internal oscillation of the recirculation structures will be more confined to the upstream wall since the pressure gradient is stronger. From the calculation of Reynolds stress shown in figure 5.9a there does appear to be a small reduction in velocity correlation across the shear layer and a smaller fluctuation inside the cavity itself. In addition to this the comparison of figures 5.9b and c indicate that the unsteadiness convected downstream of the cavity section is considerably reduced (presented as tangential Reynolds stress). Inspection of figure 5.12 signifies very little discrepancy between the skin friction encountered for the clean cavity case and that for configuration 2. For the modified case configuration 2 shown in figure 5.13 there is a reduction in skin friction, albeit small. It was found through the course of this study that the measurement of the Reynolds stresses reflected the magnitude of the skin friction generated downstream of the cavity. This relationship between the inhomogeneous Reynolds stress contribution and skin friction is well known (see Fukagata et al. 2002 for example) although the flowfield PIV data can only imply a tendency in skin friction unless the entire boundary layer shape is well sampled.

The amount of skin friction drag generated by configuration 2 is comparable to the clean cavity case, although the low-frequency roll-out and global mass expulsion has been suppressed. Any acoustic effects caused by the expulsion of such structures have therefore been inhibited, thus improving the acoustic profile of this configuration.

5.0.1.3 Configuration 3: Modified cavity floor

The third and final cavity configuration is for the clean cavity of $L/D = 1.0$ with the inclusion of a concertina section on the cavity floor. In most cases this floor block section will stand no greater than 30% of the total clean cavity depth (or $d_c/D \leq 0.3$). For the purposes of this study three scenarios of configuration 3 will be included for comparison; these are $d_c/D = 0.1$, 0.2 and 0.3, or $L/(D-d_c) = 1.11$, 1.25 and 1.43. The effect of increasing the concertina height is to reduce the size of the mean recirculation zone beneath the shear layer (to $D-d_c$) as illustrated in figure 5.14. This increase in height will then sequentially weaken the primary recirculation strength as indicated in table 5.1. For the average cases there are small vortices located in the lower corners of

the cavity that grow stronger as the side cavities deepen. The instantaneous velocity data imply that these eddies appear cyclically and that those formed in the downstream section are stronger than those formed at the upstream corner.

Throughout these cases there are no significant changes to the level of velocity correlation within the shear layer itself, although there appears to be a difference in the distribution of the Reynolds stress across the open face, as shown in figure 5.15. Additionally there is no evidence from figure 5.14 that there is a strong (discontinuous) jet-edge being formed over the internal cavity walls. This is expected since the physical length of the shear layer is shorter thus reducing the oscillation and fluid entrainment required. The mass-addition cycle for the clean case remains discernable from the velocity correlation of figure 5.15a. It can be seen that negative vorticity small-scale structures are continually ingested into the stronger (more steady) negative vorticity captive vortex structure that is formed within the cavity walls. For the central case of $d_c/D = 0.2$ it can be seen in figure 5.15c that the jet-edge (indicated by the maximum fluctuation loci) impinges onto the downstream edge of the elevated floor section, which causes a contra-rotating vortex to be formed in the corner. With energy extracted from the jet-edge the Reynolds stresses are now reduced and there is a much weaker unsteadiness transmitted upstream over the cavity floor and upstream wall.

There are distinct changes to the oscillation of the internal vortex structure. By locating the regions of swirl within the cases of interest the interaction of the small and large scales may be better understood, as shown in figure 5.16. For the clean case (figure 5.16a) there are no small-scale regions of roll-up indicated within the cavity and the primary eddy is centred in the cavity. As the floor section increases in height the movement of the primary eddy increases and there are more instances of small-scale vortices at the cavity corners and around the primary eddy. For the case $d_c/D = 0.3$ (figure 5.16d) there is an obvious progression of the central recirculation area to the downstream corner, although the roll-up oscillation and global mass expulsion noted in chapter 4 does not appear to be present. Using the dual-PIV system it can be seen that the periodic mass-inflow to the cavity causes the downstream corner vortex to increase in strength (dependent upon d_c/D) as seen in figure 5.17a. It is then reintroduced into the primary recirculation zone (figure 5.17b). This entrainment of positive vorticity

causes distortion and weakening to the primary eddy, which is forced down into the cavity. When this smaller eddy is forced upstream by another inflow-cycle the flow sometimes bifurcates at the upstream wall, causing a second contra-rotating vortex to be formed at the upstream corner. The impedance caused by the two corner regions maintains the clean case level of Reynolds stress within the shear layer, since it not only reduces the strength of the primary eddy but it diminishes the formation of a jet-edge along the floor and front wall. From the POD modes shown in figure 5.18 mode 2 and mode 3 (in configuration 2) the same spatial structures are characterized by a phase shift of approximately one half-wavelength, that is when one mode reaches its maximum energy state the other reaches its minimum energy state. This then describes a cyclic process of the jet-edge forming along the rear wall that is temporally constrained by the downstream corner, which is then re-injected into the main recirculation zone. This is indicative of all the cases in this configuration. The cumulative energy in the fluctuations shown in figure 5.19 indicates there are only slight changes to the energy accounted for a particular POD mode. The sub-plot of figure 5.19 represents the actual energy fraction for a particular mode and shows that modes 2 and 3 share an equal amount of energy, which increases in fraction as the volume between the concertina section increases.

A sequential increase in floor section height is seen to systematically increase the level of skin friction measured along the downstream flat plate section, as shown in figure 5.20. In this configuration the vortical structures cast-off from the shear layer impingement at the rear corner maintains their integrity for a short duration downstream. These structures are observed as waves of positive vorticity (shown for example in figure 5.21) and are thought to persist because of the relatively incipient state of the instability for this L/D. The vorticity strength of these waves increases as the concertina height increases.

5.0.1.4 The potential generation of acoustic power

For the purposes of this study it is too specific a problem to deal with one particular train model at one particular operating speed, and it is useful to impose some generalities. Therefore, if it is accepted that the typical inter-car gap range will be $1.0 < L/D < 2.0$ and the train will operate in the range $0.1 < M_\infty < 0.25$ then with

reference to figure 1.5 there appears to be several potential instances where reinforced high amplitude tones are expected (coupling of the lengthwise vortical shedding and duct resonance mode). This interaction represents the maximum amplitude response of the cavity and as such should be offset or weakened using geometrical changes to the cavity itself e.g. slanting the bulkheads. This range of cavity L/D and Mach number is interesting because of the presence of both length-wise and depth-wise propagating waves within the cavity. According to the results of Tam and Block 1978 there is a smooth transition between the normal mode resonance and the lengthwise tones (neglecting coupling) as the cavity changes from deep to shallow. This presents an opportunity for interpreting the contribution that the hydrodynamic velocity and vorticity bring to the acoustic propagation.

If it is assumed that the instantaneous hydrodynamic velocity and vorticity fields already measured in the study would exist within a resonant acoustic field with only slight modification, a sense of the hydrodynamic acoustic contribution may be predicted[5]. These instantaneous measurements have already been shown to play a central role in determining the acoustic power generation in situations where the resonant acoustic mode is present at the instance of vortex impingement at the rear cavity bulkhead, Lin et al. 2001. Using the formulation of Howe 1975 and 1980 (equation [5.1]) it is possible to gain a sense of the hydrodynamic contribution without specific details of the vector acoustic velocity, $\mathbf{u_a}$,

$$P = -\rho \int \left(\omega_z \times \mathbf{U}\right) \cdot \mathbf{u_a} \, \mathrm{d}V \qquad [5.1]$$

where P is the instantaneous acoustic power generated in a volume V, ω_z is the vorticity through the z-plane, $\mathbf{U}$ is the instantaneous full-field velocity determined by the PIV system.

For the clean cavity case with $L/D = 2.0$ it is shown in figure 5.22 that the contribution of the $\omega_z \times \mathbf{U}$ term produces vectors predominately orientated in the negative vertical direction along the extent of the shear layer. This type of behaviour is consistent with all the cavity configurations investigated here. The magnitude of the cross-product term is indicated by the contour levels and has an increment of 0.01. Additionally it is seen that

[5] Compressibility effects are required in the feedback mode

during the mass addition stroke to the cavity there are elevated levels of the $\omega_z \times \mathbf{U}$ term along the downstream wall of the cavity. It is predicted that if this cavity were resonating it would do so in the horizontal direction and this would then contribute to the overall acoustic power provided there is phase agreement (since the value of the dot product is maximum). This method of acoustic radiation has already been noted by Bilanin and Covert 1973, while by comparison the acoustic response of the large-scale recirculation structures does not seem to be strong in figure 5.22. Figure 5.23 indicates that the magnitude of the cross-product term for a clean cavity with $L/D = 1.0$ is much reduced around the vicinity of the cavity although normal mode resonance is expected (vertical acoustic velocity vector). Therefore, irrespective of any phase agreement the shear layer and the sink like pattern of the internal recirculation will consistently contribute to the acoustic power making this geometry particularly efficient at acoustic radiation.

Energy is extracted from the acoustic field when vorticity is generated and it is possible to take advantage of this to attenuate the acoustic field, as demonstrated by Howe 1978. As shown in figure 5.24 the geometry of the first cavity configuration facilitates the production of small-scale concentrations of vorticity with large contributions to the acoustic power. These sinks are then able to roll-off the rear-slanted bulkhead into the mean flow where they would no longer interact with the acoustic field and the kinetic energy would be dissipated as heat. This is ideal for reducing the acoustic power of the cavity so long as the vorticity cast from the shear layer does not impinge onto another surface where the acoustic field will be modified (such as a pantograph).

5.1 Concepts for reducing cavity unsteadiness

In this final section two common concepts for internal cavity oscillation suppression are investigated using exclusively the PIV system for $L/D = 2.0$. These cases model the inclusion of a fence on the floor of the cavity (configurations 4, 5 and 6) and a nose section added to the rear cavity wall (cases 7 and 8). The suppression of the internal cavity flowfield is of primary importance and as such there is no skin friction data presented.

5.1.1 Configurations 4, 5 and 6: Cavity floor fence

Following the study of Kuo et al. 2001 (where $\mathrm{Re}_\theta = 194$) it appears that a significant reduction in the level of fluctuation within the cavity can be achieved with the inclusion of small fence on the cavity floor. In this case the study focuses on fences orientated at 90°, 45° and –45° (configuration 4, 5 and 6 respectively) positioned at $x/L = 0.5$; the fence height is $d_c/D = 0.2$. From an inspection of the vorticity and streamlines of figure 5.25 it is apparent that the inclusion of this device separates the internal cavity flowfield into two distinct regions, now termed zone 1 (approximately $0 \le x/L < 0.5$) and zone 2 (approximately $0.5 \le x/L \le 1.0$). In each of these configurations there are two well-defined regions of fluid rotation experienced within the cavity, with counter-clockwise rotation in zone 1 and clockwise rotation in zone 2. From table 5.2 it can be seen that the strongest zone 2 circulation (invariably the strongest zone) is encountered by configuration 6 (fence -45°) since the fence orientation does not directly inhibit the progression of the jet-edge. With reference to the Reynolds stress of figure 5.26 there are perceptible reductions in flow fluctuation within the cavity for each configuration (with configuration 5 being the best), although there are dramatic increases in the velocity correlation of the shear layer (with configuration 6 showing the largest increase). This partitioning of the internal flow causes zone 2 to be much more unsteady than zone 1, which will be effective at nullifying the roll-out cycle of this cavity. However, the increase in shear layer unsteadiness is a direct result of the re-orientation of the jet-edge along the cavity floor.

In contrast to the low Reynolds number study of Kao et al. 2001 the inclusion of a vertical fence on the floor of the cavity imposes an enlarged oscillating amplitude on the shear layer. The reason for this is simple, Reynolds number effects are important since this dictates the scale and amplification of the shear layer at the downstream corner and thus the level of fluid entrained into the cavity. With a large mass addition cycle at the trailing edge the momentum of the jet-edge formed over the rear wall is considerably increased allowing it to be more resistive to entrainment with permeation further into the cavity zones. The mean momentum transfer shown in figure 5.27 indicates significantly modified profiles across the open face with distinct inflections in mean momentum at $x/L = 0.67$, 0.7 and 0.6 for configuration 4, 5 and 6 respectively. It is clear from the instantaneous velocity fields of figure 5.28 and the POD modes of the v-

velocity in figure 5.29 that these mean momentum maxima indicate the position of jet-edge impingement underneath the shear layer. For configuration 4 the vertical fence redirects the jet-edge to perturb the shear layer slightly downstream of the fence (convected by the shear layer velocity). It is evident from figure 5.28a that this scenario is entirely unsteady, and this discontinuous vortical edge may proceed upstream and contribute to the circulation of zone 1. The positive inclination of the fence (configuration 5) shifts the mean impingement location of the edge downstream, while the negative inclination (configuration 6) redirects it further upstream. The Reynolds stress indicates that there is very little fluctuation in zone 1 and, in fact, the lip of velocity correlation extending from the fence edge in each case describes the typical interaction to be one of entrainment into the shear layer (shown for instance in 5.28a(ii), 5.28b(iii) and 5.28c(ii)). As the size of the recirculation in zone 2 gets smaller (configuration 6 to 4 to 5) the extent of the positive vorticity tongue increases in length (from figure 5.25), signifying a reduction in the shear layer fluctuation over these regions (as clarified by the Reynolds stress). This is accord with Kuo et al. 2001 and vindicates the point that fence orientation will determine the scale and upstream movement of the recirculating flow.

Using the data from the first four POD modes (figure 5.29) it is possible to add clarification to these points. For the clean case it is obvious that the most energetic structures in the flowfield belong to the large scale recirculation roll-ups beneath the shear layer. The dark red regions represent the maximum positive value, upward flow and the dark blue regions represent the maximum negative value, downward flow. There is a contribution to this scale from each of the 4 modes shown, with the first POD mode being responsible for 29% of the total fluctuation energy. For configuration 4 and 5 the first 3 POD modes are entirely made up of contributions from the energy in the shear layer (indicating little movement within the cavity) and show a marked similarly. For these two cases the maxima of mode 1 represents the approximate location of jet-edge impingement into the shear layer. Modes 2 and 3 for these cases describe an energy exchange process whereby one mode is in its maximum energy state as the other is in its minimum energy state, thus propagating the flow pattern. One significant difference is with the first POD mode of configuration 6 where a 20.1% of the energy fluctuation has a contribution from the coherent structures within the cavity. This indicates a return of the low-frequency oscillation of the internal structures (that is

global mass expulsion). As evidenced by figures 5.28c(ii) and (iii) the jet-edge is able to find phase compatibility with a convecting instability in the shear layer that entrains the edge and rolls-out a portion of the recirculation in zone 2.

With decent pointwise measurement in the shear layer for a two-dimensional flowfield it is possible to approximate the steady drag coefficient of the cavity by calculating the momentum flux out of the cavity, as shown in equation [5.2].

$$C_D = \frac{2}{L}\int_0^L \left(-\frac{\langle uv \rangle}{U_\infty^2} - \frac{\langle u'v' \rangle}{U_\infty^2} + \upsilon \frac{\partial \langle u \rangle}{\partial y} \right) dx \qquad [5.2]$$

The viscous stress term can be neglected in this case leaving the drag coefficient as the sum of the mean momentum flux and Reynolds stresses across the open cavity face. In this case the integral has been performed using 1000 image pairs with ITDWO-FFT-SDCPIV with a spatial resolution of 1 vector per mm. The accuracy of the integral is obviously an issue even though the spanwise effects of the clean case have been quantified using errorbars; the results are presented in figure 5.30. From this data it can be seen that there is a tremendous increase in drag coefficient for the fence configurations investigated. For the clean case the drag contribution from the mean and correlated fluctuation part are approximately equivalent although for the fence configuration the entire contribution is made up from Reynolds stress alone (the mean part is approximately zero). Therefore in all cases the cost of a reduction in internal oscillation amplitude is an increase in drag coefficient.

5.1.2 Configurations 7 and 8: Trailing edge nose section

The usefulness of a trailing edge nose section is to modify the clipping fate of the shear layer vortex such that the feedback signal is attenuated and the disturbance growth can be reduced. In this study the nose geometries are formed from a 1:2 and 1:4 ellipse shape (configuration 7 and 8 respectively). From inspection of figure 5.32 where $L/D = 2.0$ the average vorticity and streamlines specify the existence of two zones, one underneath the open face of the cavity and one beneath the nose section itself (once again denoted zone 1 and 2). The results indicate that the jet-edge is formed into the cavity as with the clean case with negative vorticity contained in zone 1 and positive vorticity in zone 2. As the nose section increases in length the circulation of zone 1 reduces as zone 2 becomes both larger and stronger (for $L/D = 2.0$). In a lower

Reynolds number study of cavity flow ($Re_D = 3360$) Pereira et al. 1994 found that a nose shape geometry (circular section) produced decreased circulation within the cavity (thus implied a decrease in drag).

The Reynolds stress for these configurations is included in figure 5.33 and is in direct contrast to those of the previous section. In this instance the velocity correlation across the entire span of the shear region has decreased below that of the clean cavity case. It is obvious the feedback signal has been attenuated since these Reynolds stresses are lower than for a shorter shear layer span (see $L/D = 1.5$ for example, figure 4.51). The internal oscillation is also markedly reduced, through inspection of the instantaneous vector fields it appears that the two zones of flow are steady and persistent. The fate of a downstream travelling vortex is between complete clipping and complete escape, while the global mass expulsion cycle is completely suppressed. As the nose section increases in length the shear layer instability has less time to mature and the Reynolds stress are sequentially reduced. In addition the jet-edge is formed further from the rear wall and during the mass addition cycle to the cavity the jet bifurcates on the cavity floor, thus sectioning the two zones. The mean momentum transfer across the open face of the cavity is shown in figure 5.31. The mean momentum transfer across configurations 7 and 8 is greater than that for the clean cavity case, with the latter being comparable to the mean mass transfer for $L/D = 3.0$ (clean). This cause of this will be related to the modified clipping fate experienced by the shear layer vortices at the trailing edge. In contrast to the fence configuration the majority of the drag experienced in this case originates from the mean momentum transfer term and not the Reynolds stresses. In figure 5.30 it can be seen that these geometrical changes to the cavity have once again significantly increased the drag coefficient. In the range $2.0 \leq L/D \leq 3.0$ the shorter nose section imposed less drag on the cavity and maintained a significant reduction in Reynolds stress in and around the cavity.

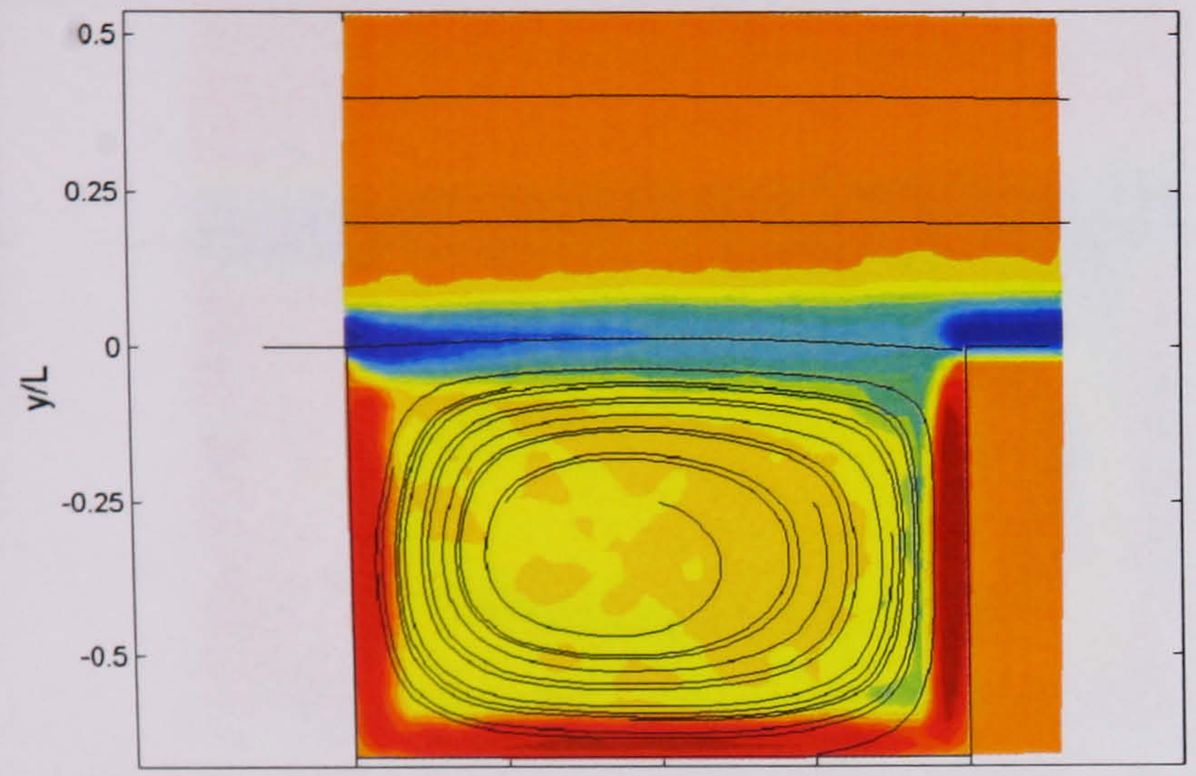

a.

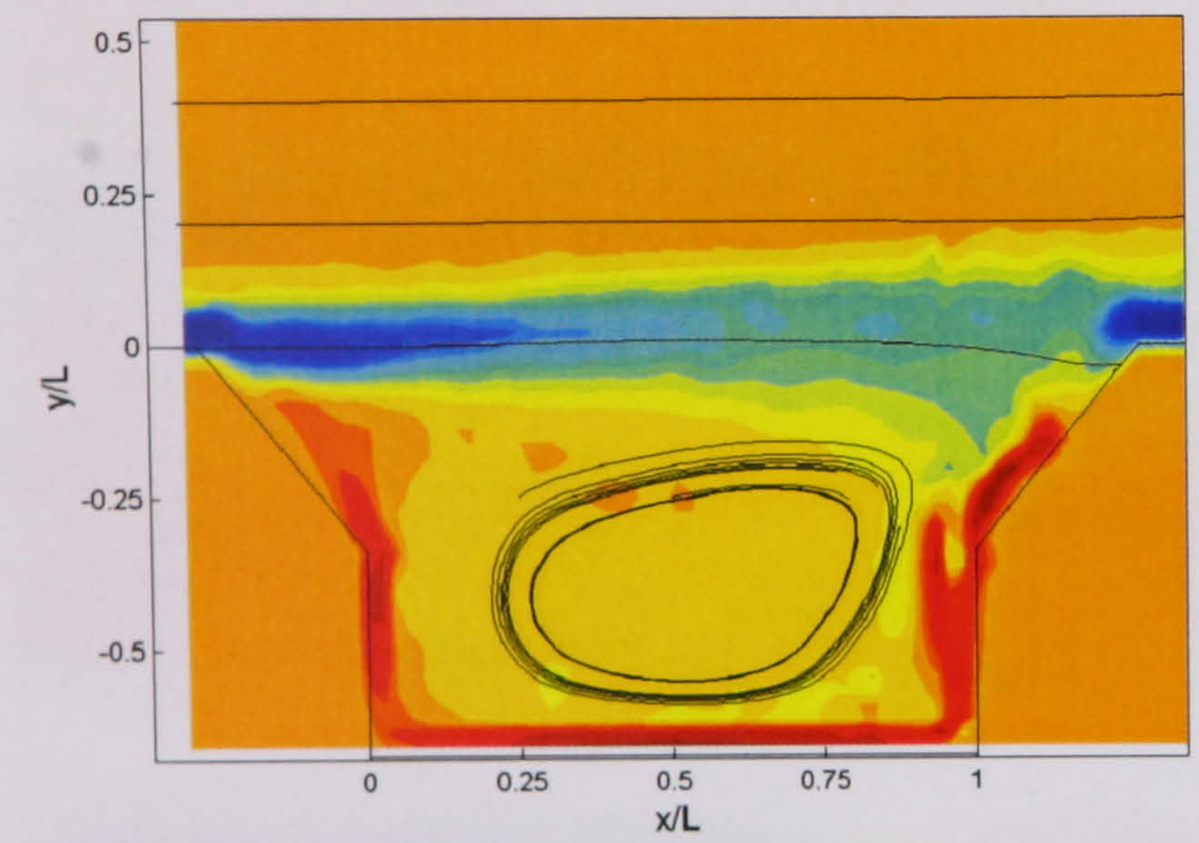

b.

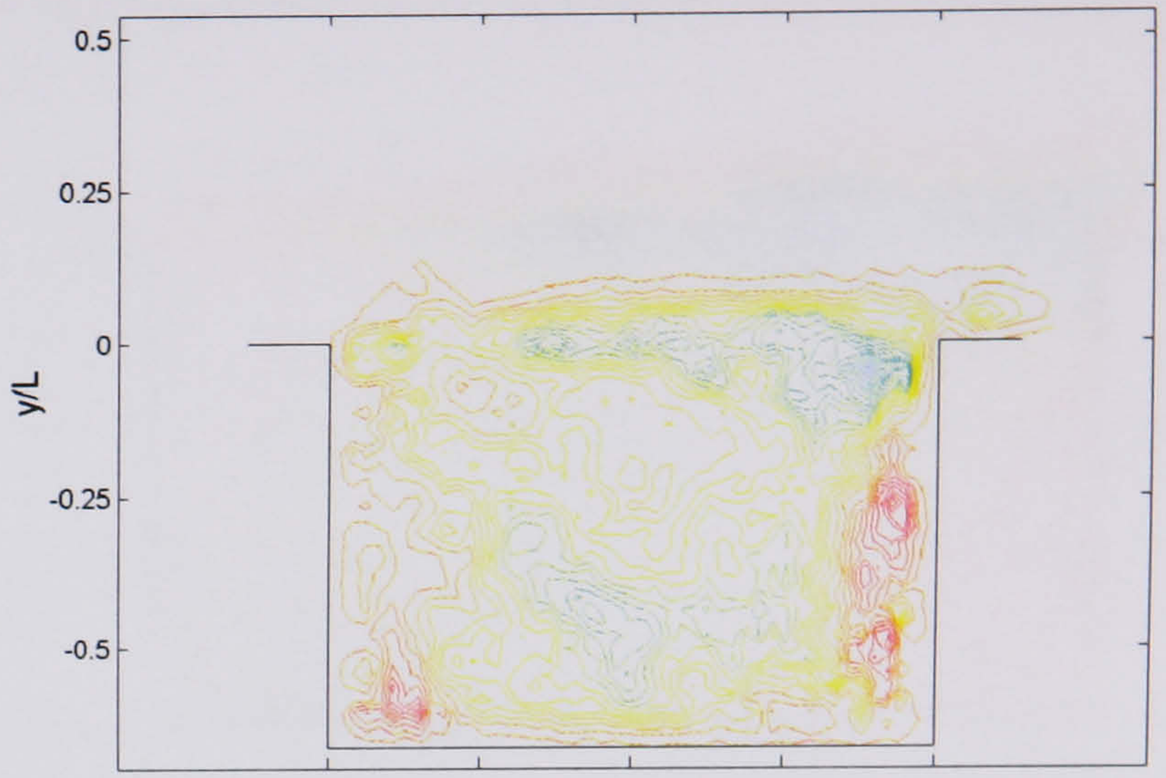

c.

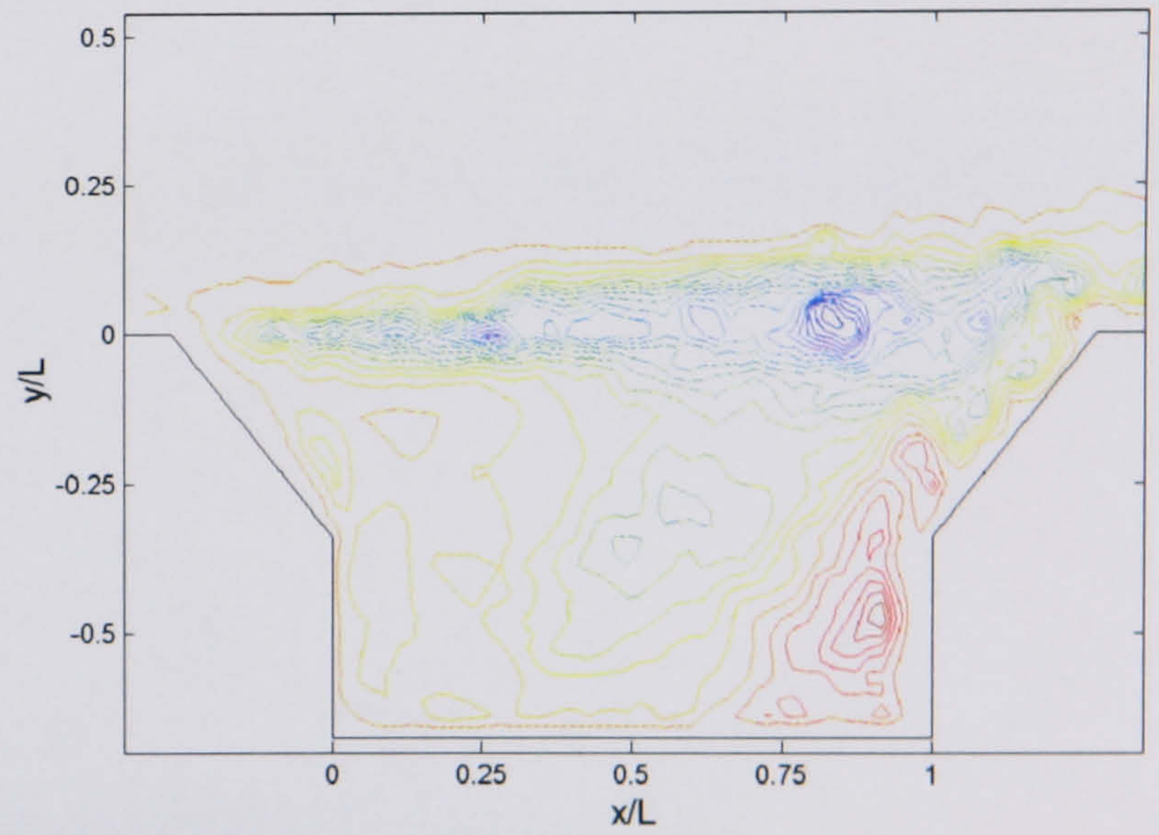

d.

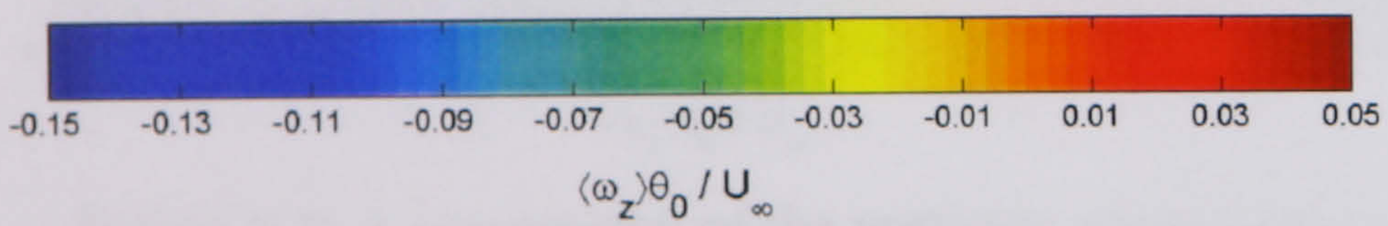

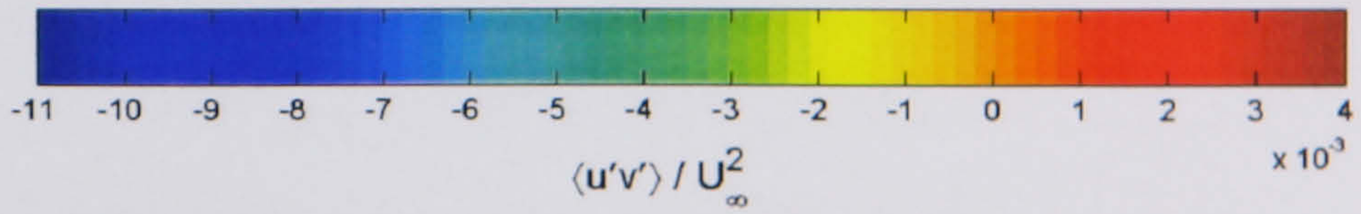

Figure 5.1. A comparison of the vorticity, streamlines and Reynolds stress for the clean case and configuration 1 for $L/D = 1.5$.

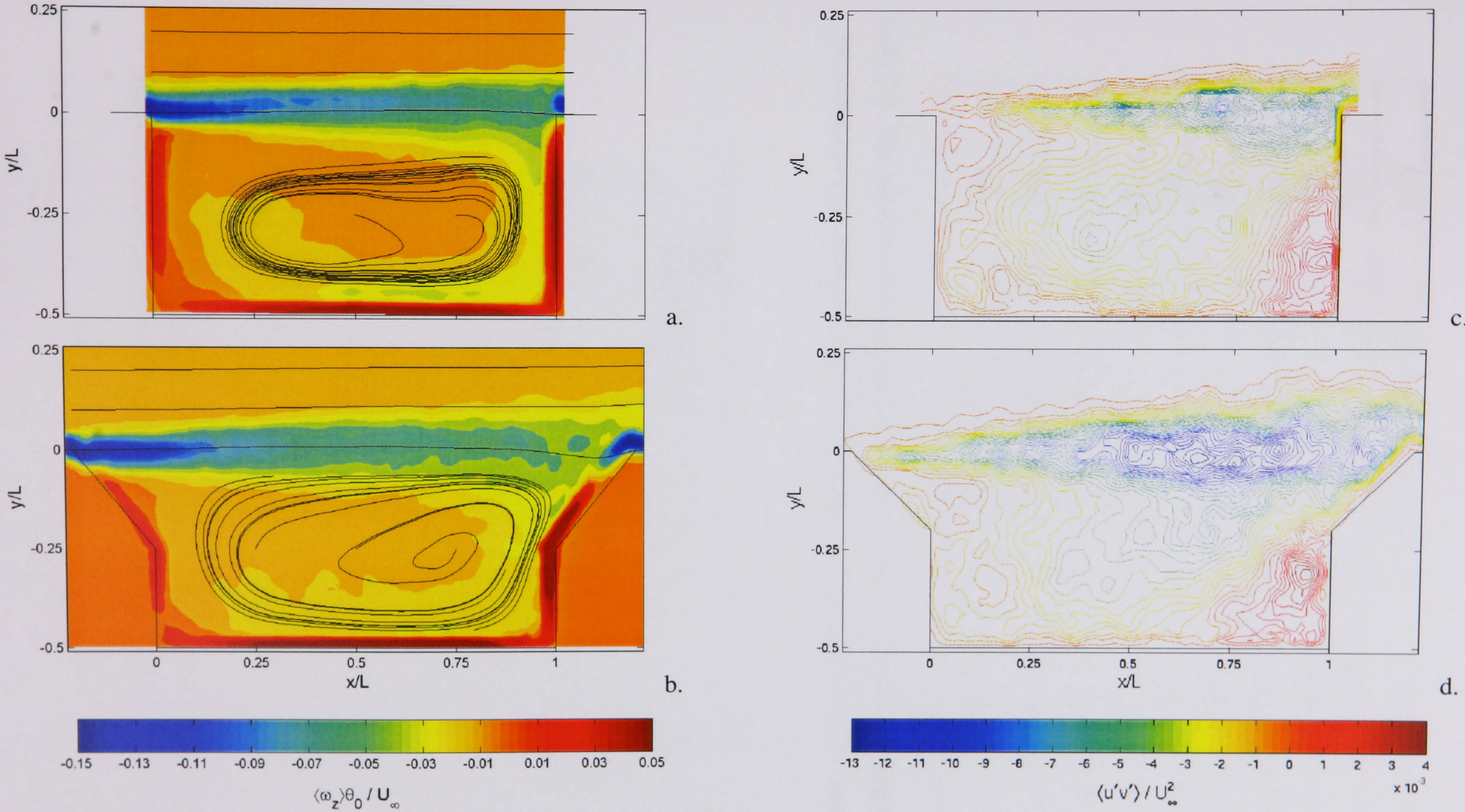

Figure 5.2. A comparison of the vorticity, streamlines and Reynolds stress for the clean case and configuration 1 for $L/D = 2.0$.

L/D	CONFIGURATION	$-\Gamma/U_\infty L$
2.0	CLEAN	-0.6194±0.04
2.0	1	-0.7091
1.5	CLEAN	-0.5966±0.06
1.5	1	-0.6271
2.0	2	-0.4612
1.0	CLEAN	-0.7226
1.0	3 $(d_c/D = 0.1)$	-0.6882
1.0	3 $(d_c/D = 0.2)$	-0.6139
1.0	3 $(d_c/D = 0.3)$	-0.5352

Table 5.1. The normalized average internal recirculation strength present with the cavity for various cavity configurations. The clean data has been pre-plotted in figure 4.23.

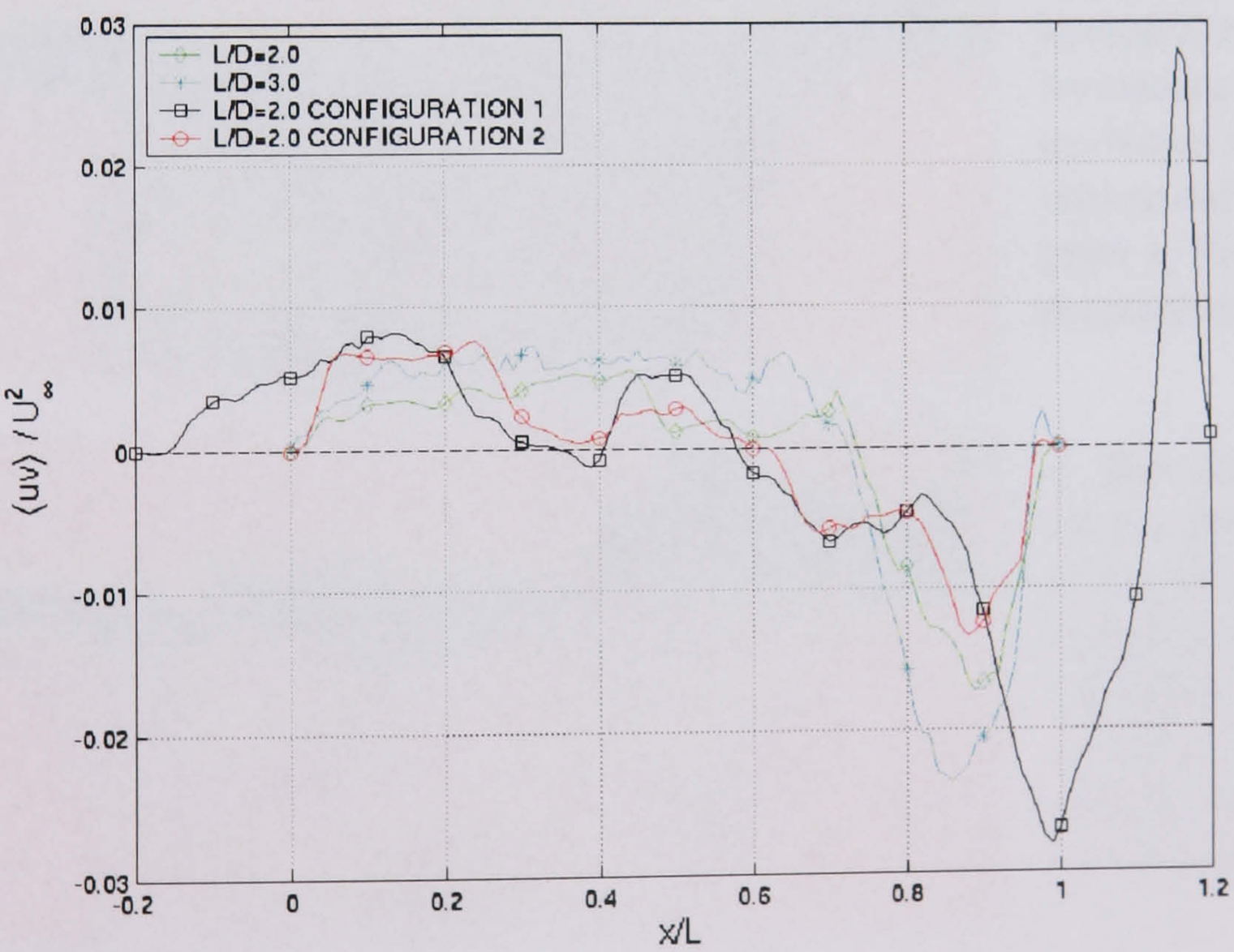

Figure 5.3. Distribution of the mean momentum transfer for clean cavity cases $L/D = 2.0$ and $L/D = 3.0$ and configurations 1 and 2 along the line $y/L = 0$.

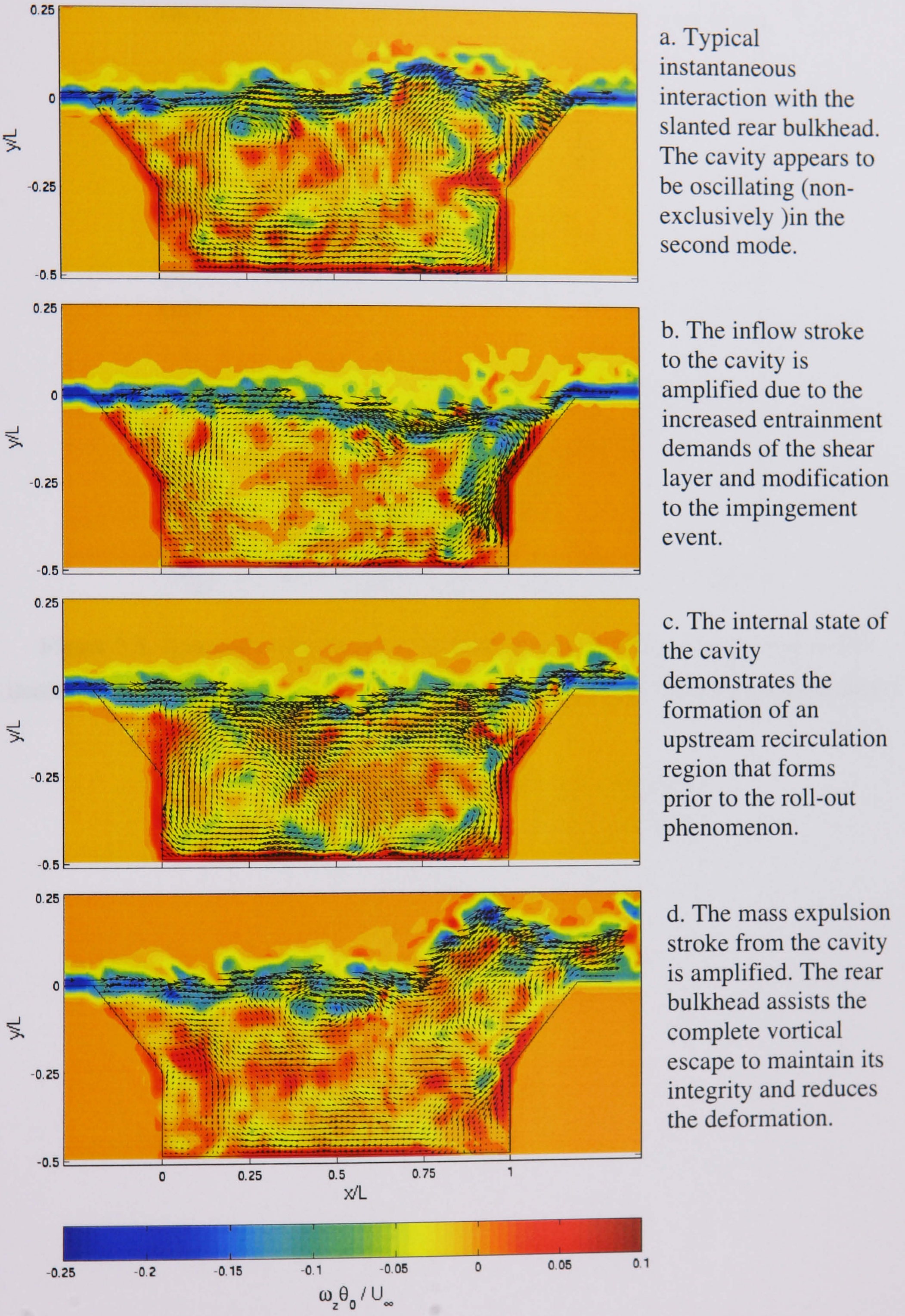

a. Typical instantaneous interaction with the slanted rear bulkhead. The cavity appears to be oscillating (non-exclusively)in the second mode.

b. The inflow stroke to the cavity is amplified due to the increased entrainment demands of the shear layer and modification to the impingement event.

c. The internal state of the cavity demonstrates the formation of an upstream recirculation region that forms prior to the roll-out phenomenon.

d. The mass expulsion stroke from the cavity is amplified. The rear bulkhead assists the complete vortical escape to maintain its integrity and reduces the deformation.

Figure 5.4. Instantaneous vorticity and velocity for $L/D = 2.0$ in configuration 1.

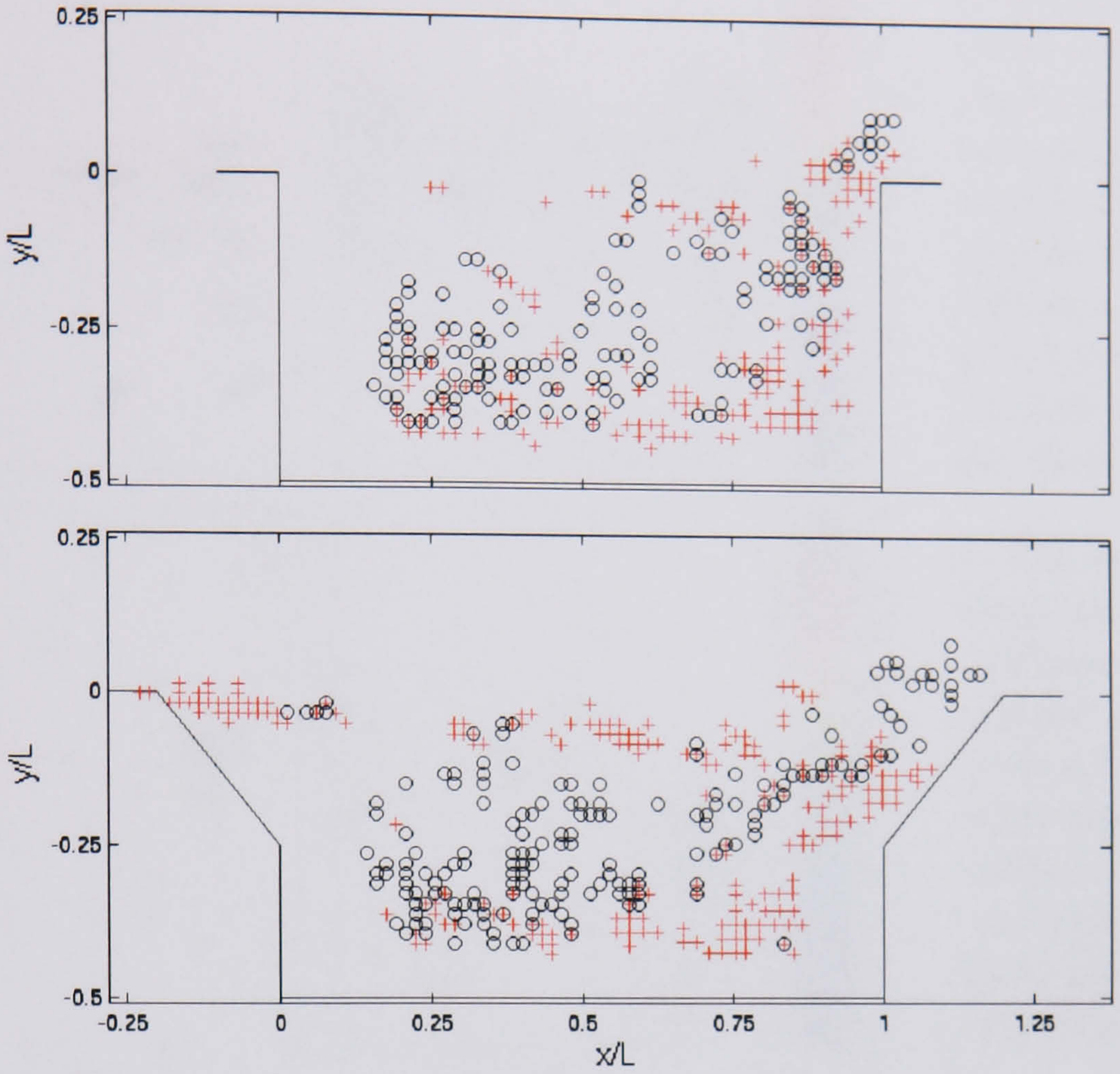

Figure 5.5. A record of the locations of swirl observed within a sample set of 150 instantaneous velocity records for $L/D = 2.0$ in the clean case (top) and configuration 1 (bottom).

+ : Swirl region approximately smaller than $D/2$.

◯ : Swirl region approximately greater than $D/2$.

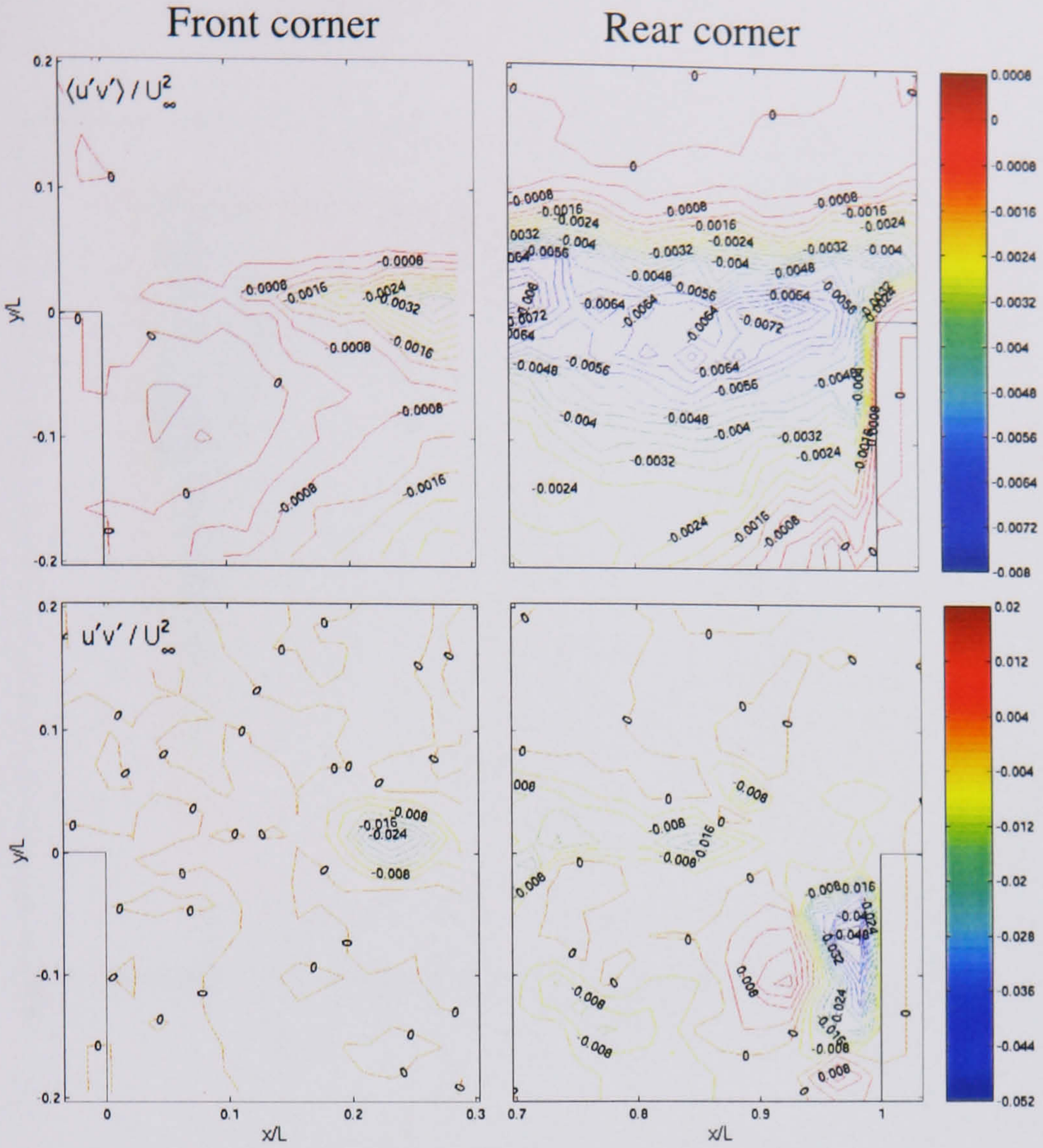

a. Average Reynolds stress for the clean cavity case. The contour incremental level is 0.0004. The stresses imply a coherent development of vortical structures in the shear layer.

b. The instantaneous Reynolds stress for configuration 1. The contour incremental level is 0.004. The shear layer interaction at the rear face induces fluctuation into the upstream part.

c. The average Reynolds stress for the clean cavity case. The contour incremental level is 0.0008. The longer effective shear causes significant increases in the downstream region.

d. The instantaneous Reynolds stress for configuration 1. The contour incremental level is 0.008. For a stronger downstream interaction there is a weaker fluctuation imposed upstream.

Figure 5.6. Instantaneous and average Reynolds stress for $L/D = 2.0$ for the clean case and in configuration 1.

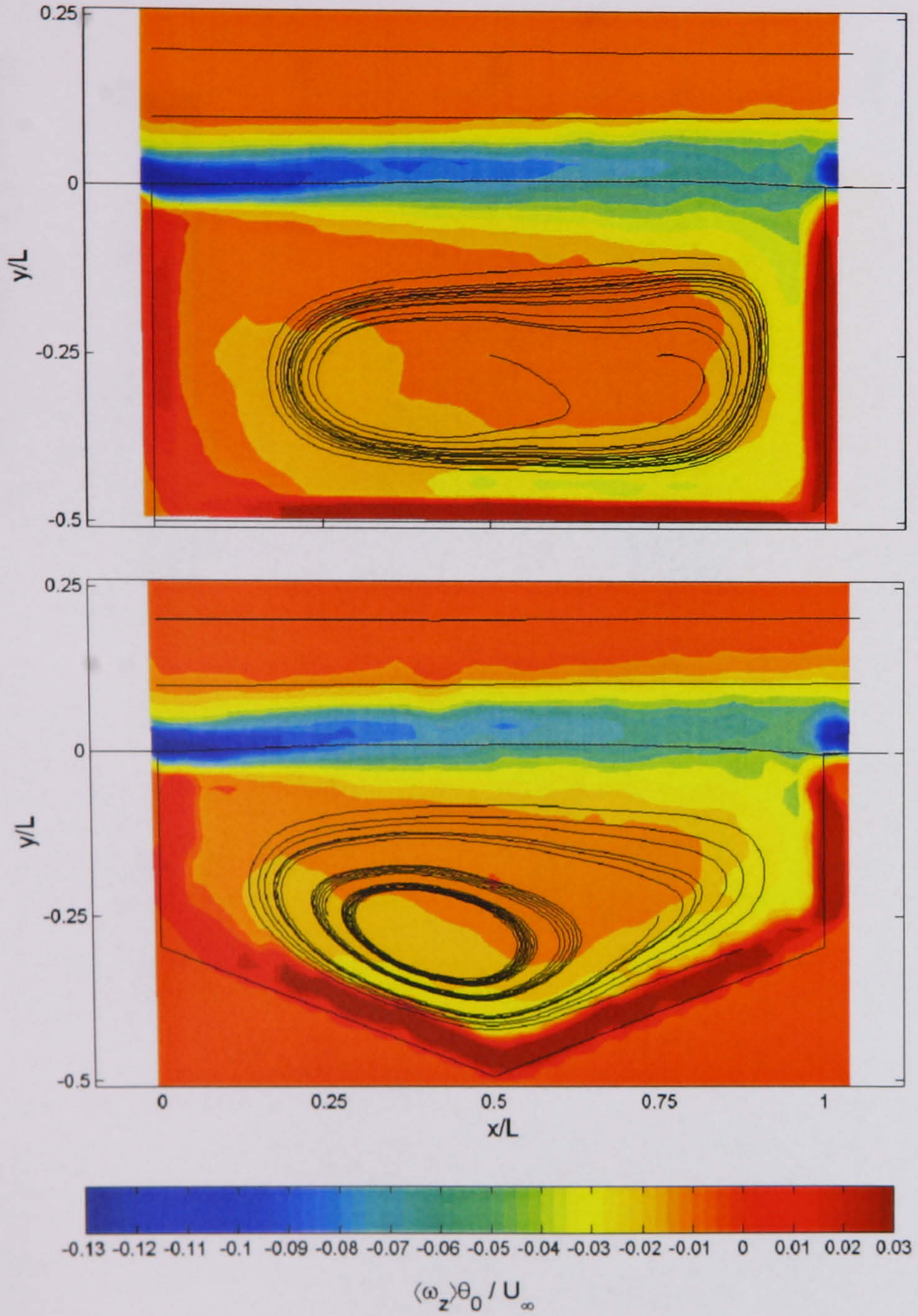

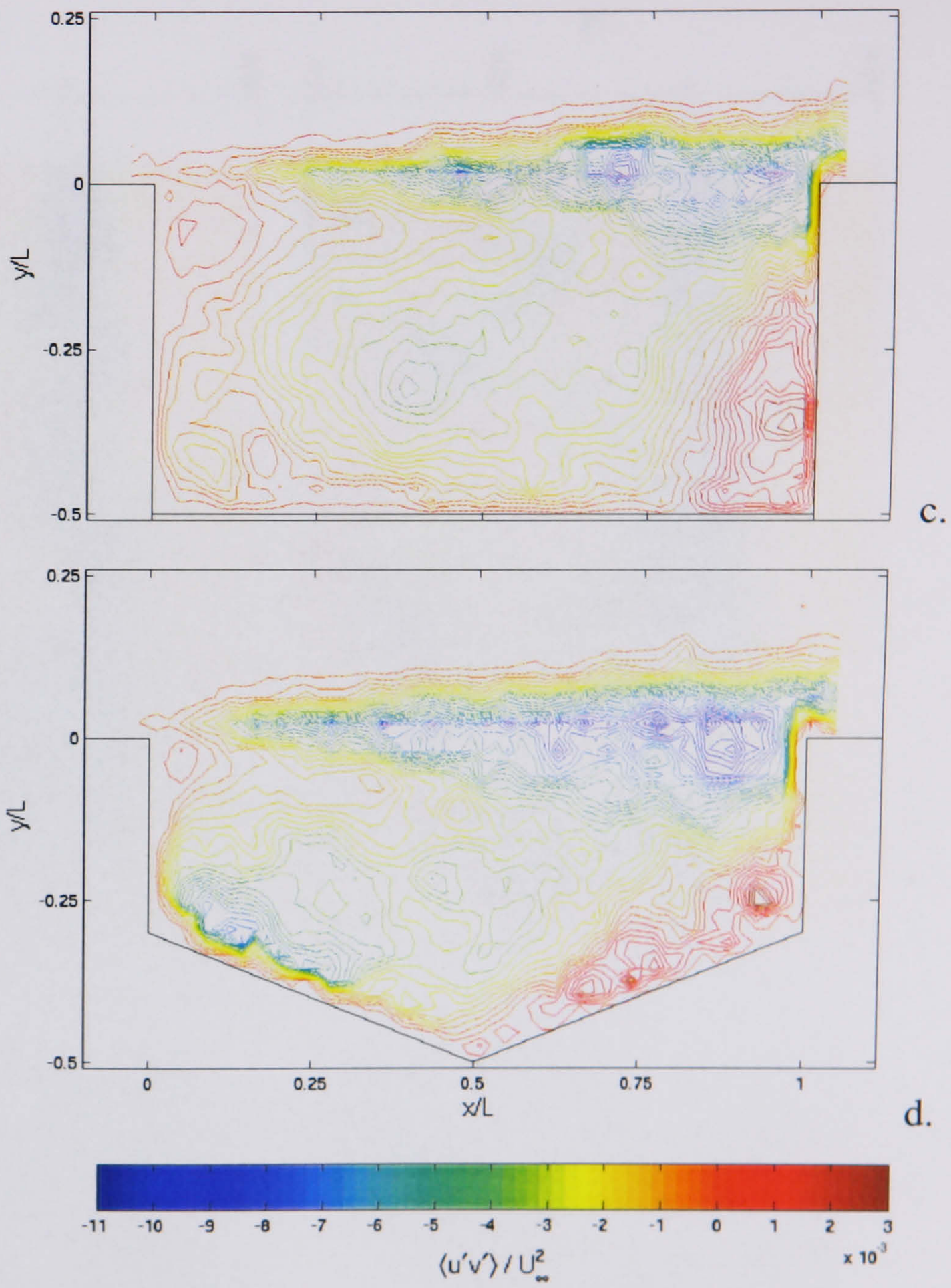

Figure 5.7. A comparison of the vorticity, streamlines and Reynolds stress for the clean case and configuration 2 for $L/D = 2.0$.

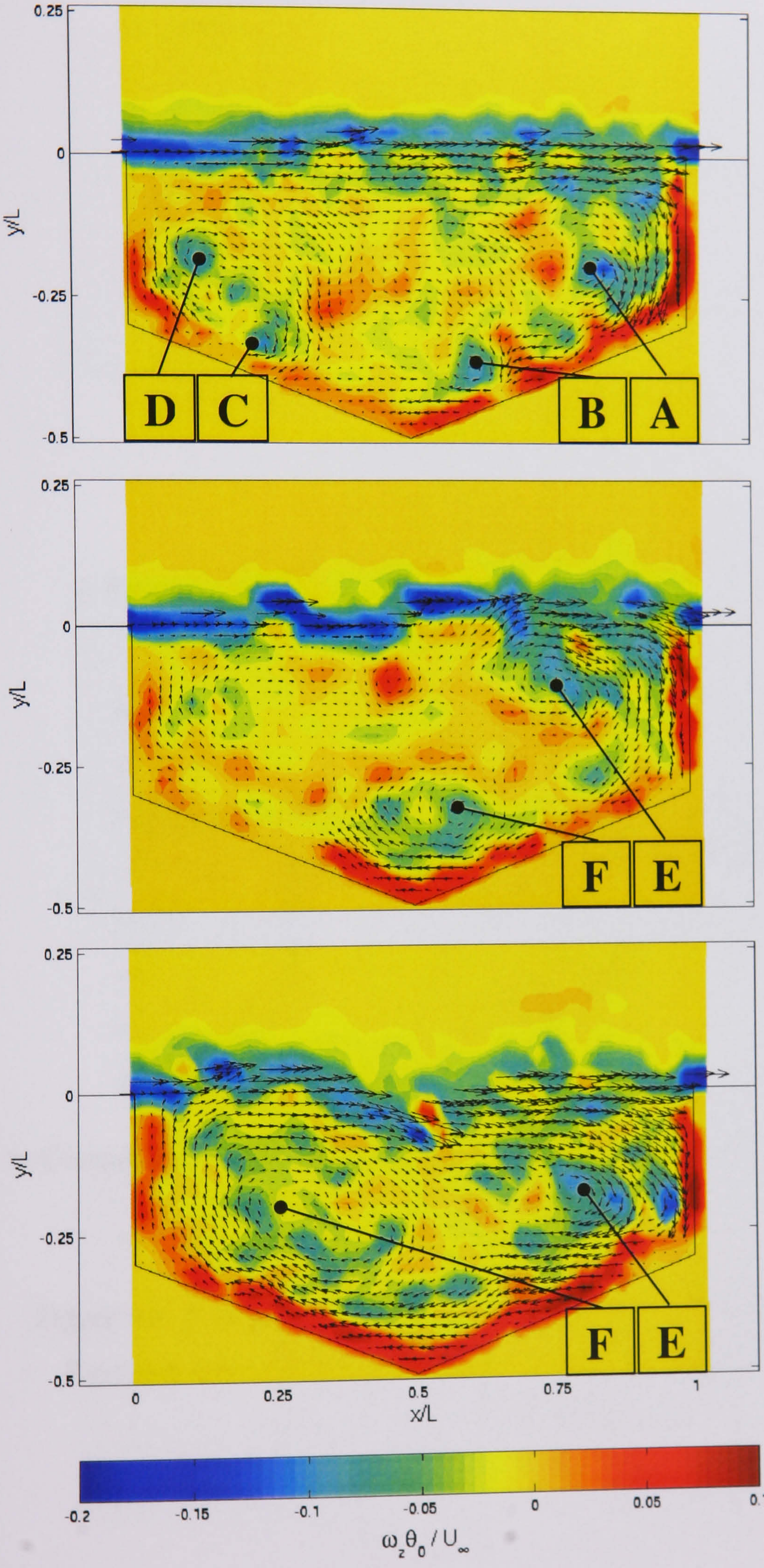

a. The impingement of vortical structures at the trailing edge casts discrete regions of negative vorticity into the cavity, where they are seen to roll-up into more distinct swirl patterns as they move along the sloped floor.

b. If there is phase agreement with the shear layer when the packet of vorticity is in proximity to the front cavity corner the vorticity is entrained into the instability growth and it is carried across the open face.

c. There are several instances whereby the structures entrained into the shear layer (b) are clipped back into the cavity and are re-ingested once again into the shear layer at the upstream station. Time delay between (b) and (c) is $\Delta t_1 = 6ms$

Figure 5.8. Instantaneous vorticity and velocity for $L/D = 2.0$ in configuration 2.

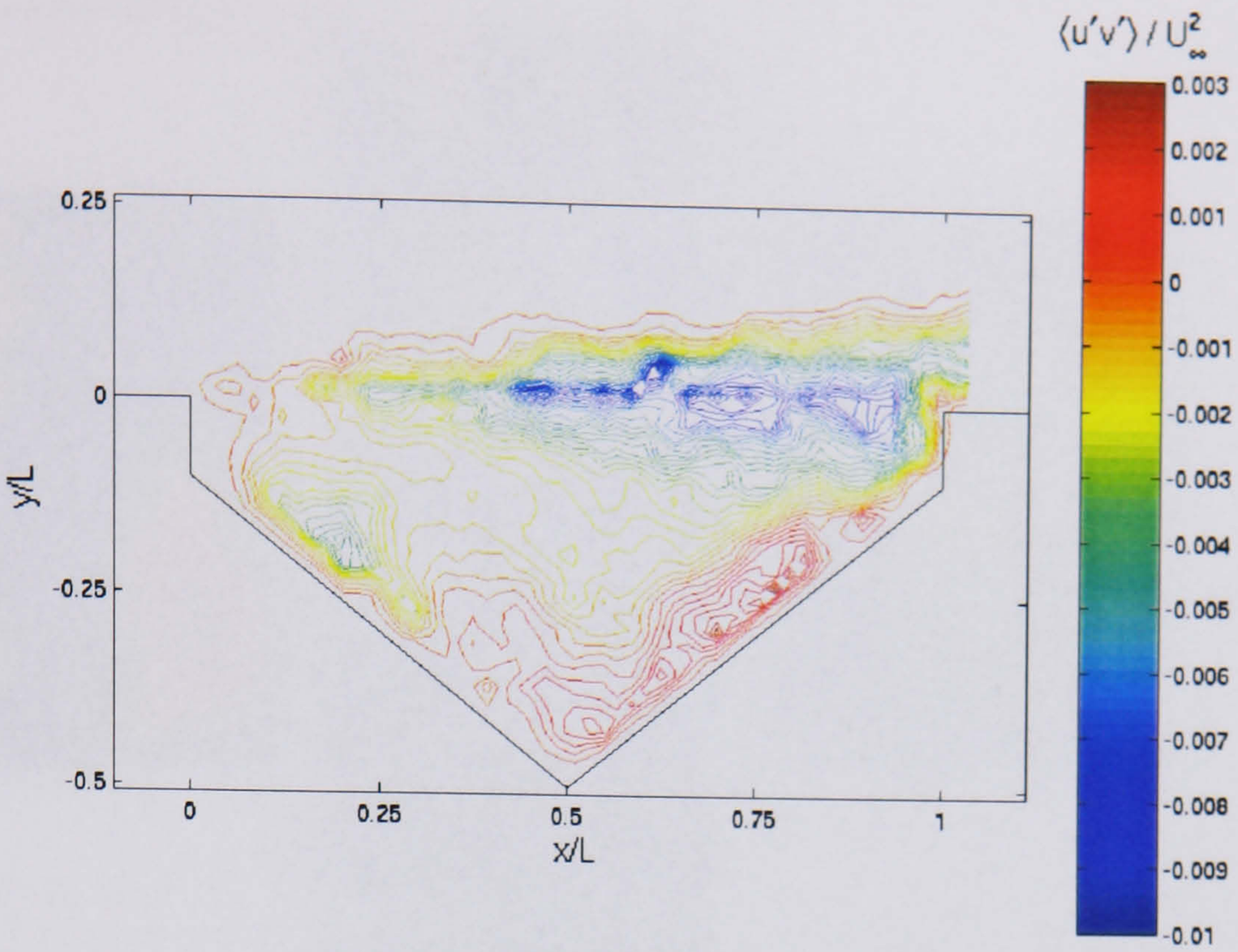

a. Reynolds stress for configuration 2 with modified slant on the cavity floor, $L/D = 2.0$.

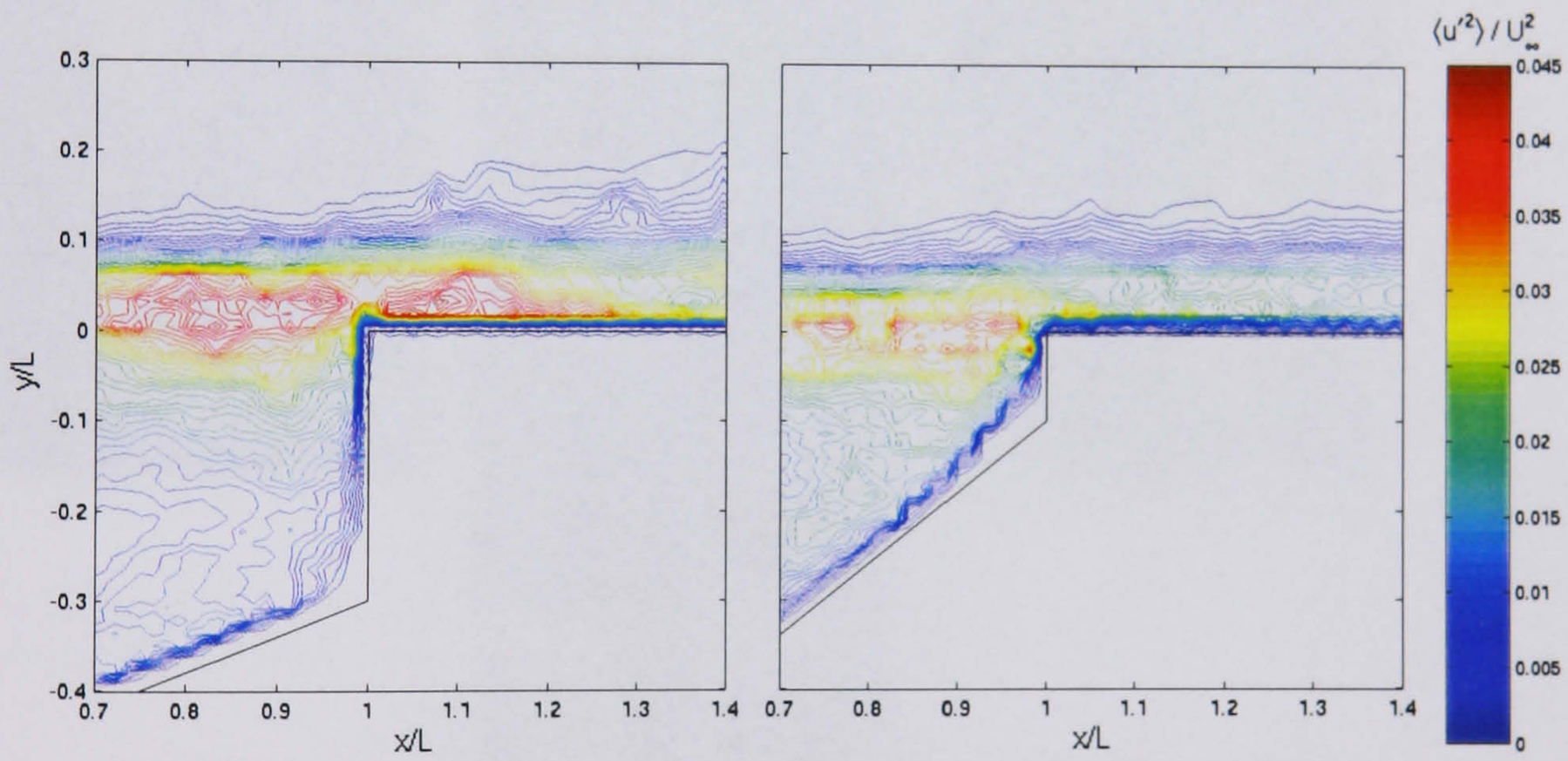

b. Comparison of the Reynolds normal stress for configuration 2 (left) and configuration 2 modified (right).

Figure 5.9. A modification to the floor slope angle of configuration 2 can reduce the Reynolds stress within the shear layer and reduce the transmission of instability downstream of the gap.

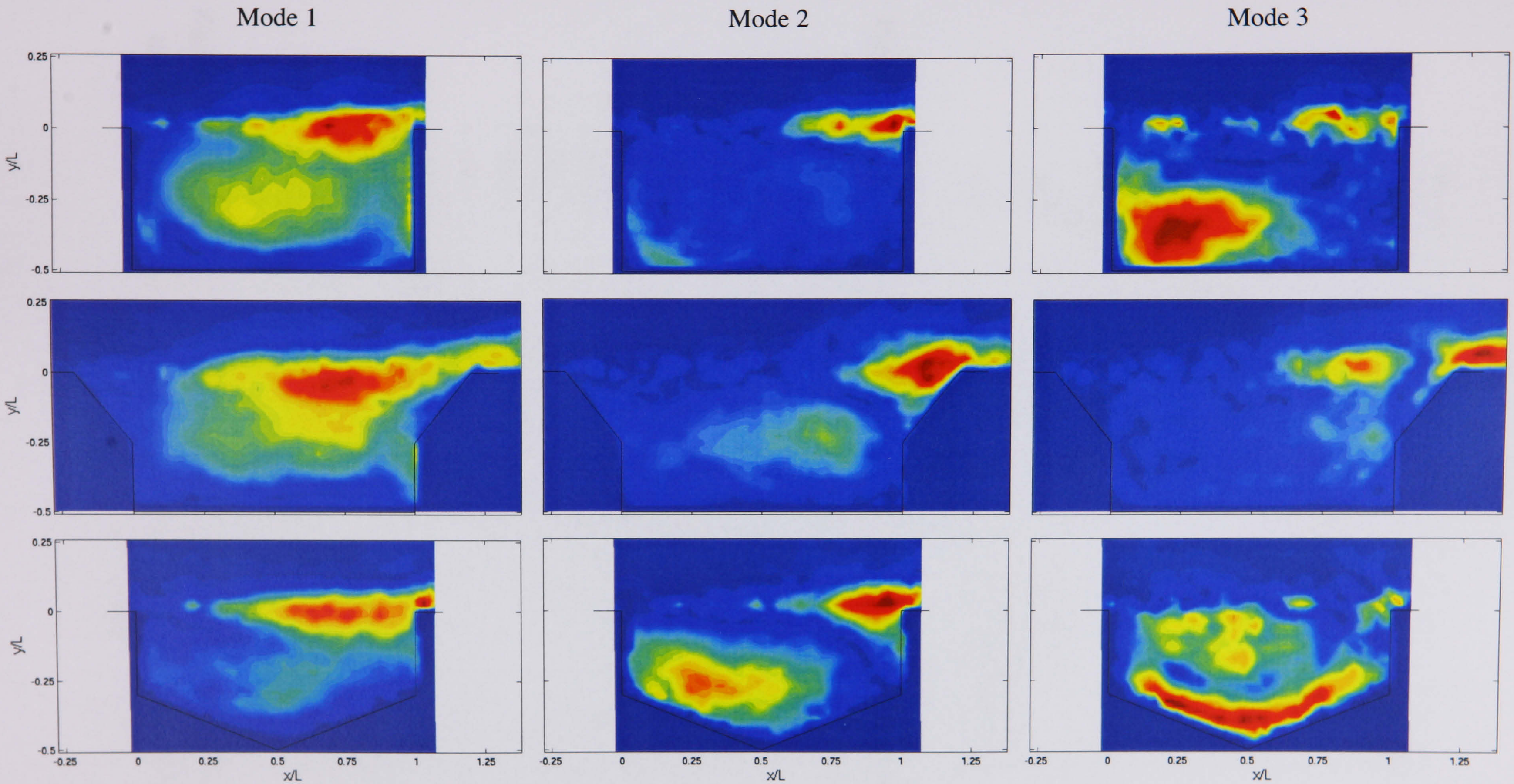

Figure 5.10. First three POD modes with $L/D = 2.0$ for the clean cavity case (top row), configuration 1 (middle row) and configuration 2 (bottom row). Figures indicate normalised velocity magnitude.

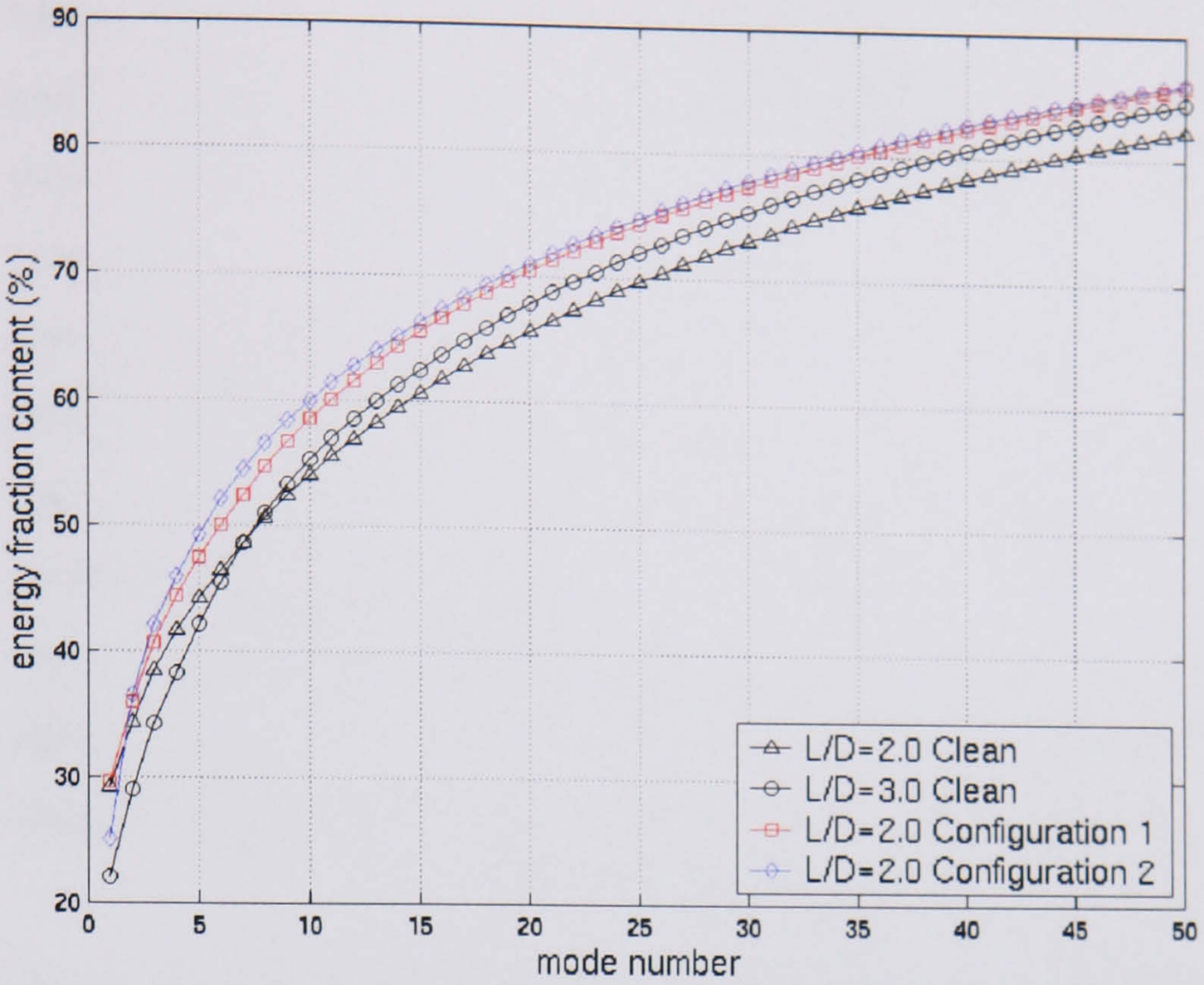

Figure 5.11. Cumulative percent energy in the fluctuation captured by POD modes for some clean cavity configurations and for configuration 1 and 2 ($L/D = 2.0$).

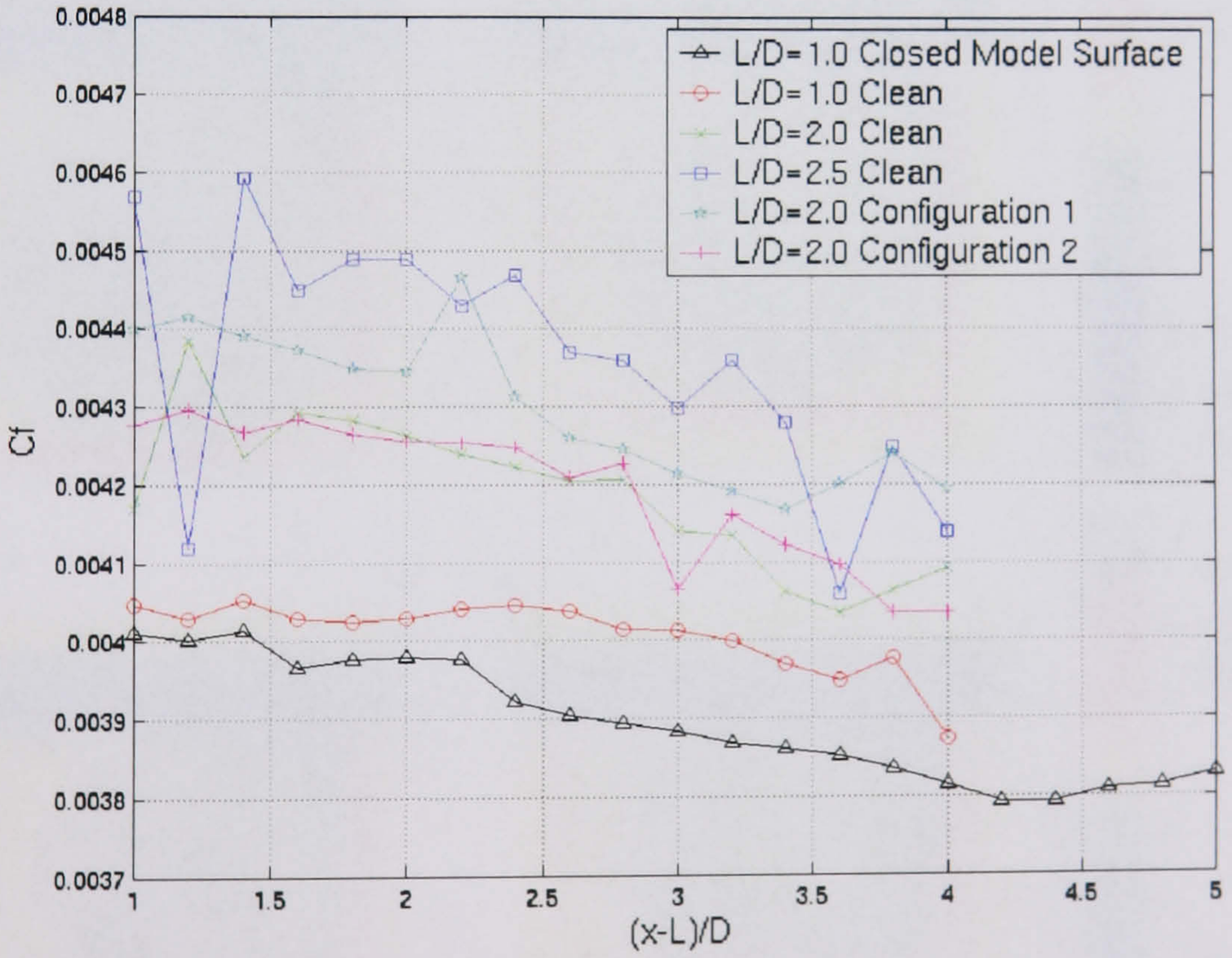

Figure 5.12. Measurement of the skin friction downstream of the cavity for a number of different configurations. The 'closed model surface' indicates measurements made when the cavity section is filled.

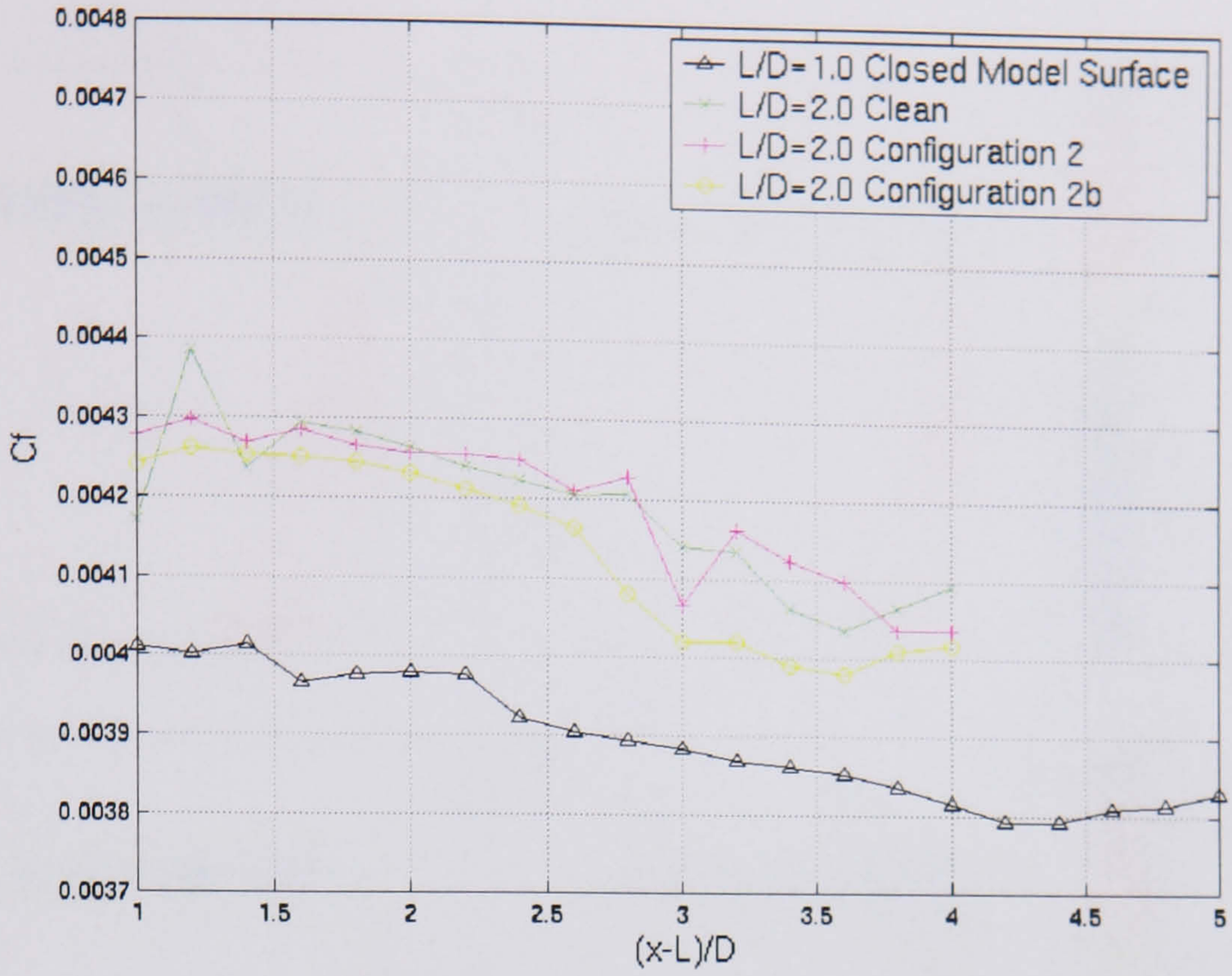

Figure 5.13. Measurement of the skin friction downstream of the cavity for $L/D = 2.0$. Two variants of configuration 2 are included for comparison.

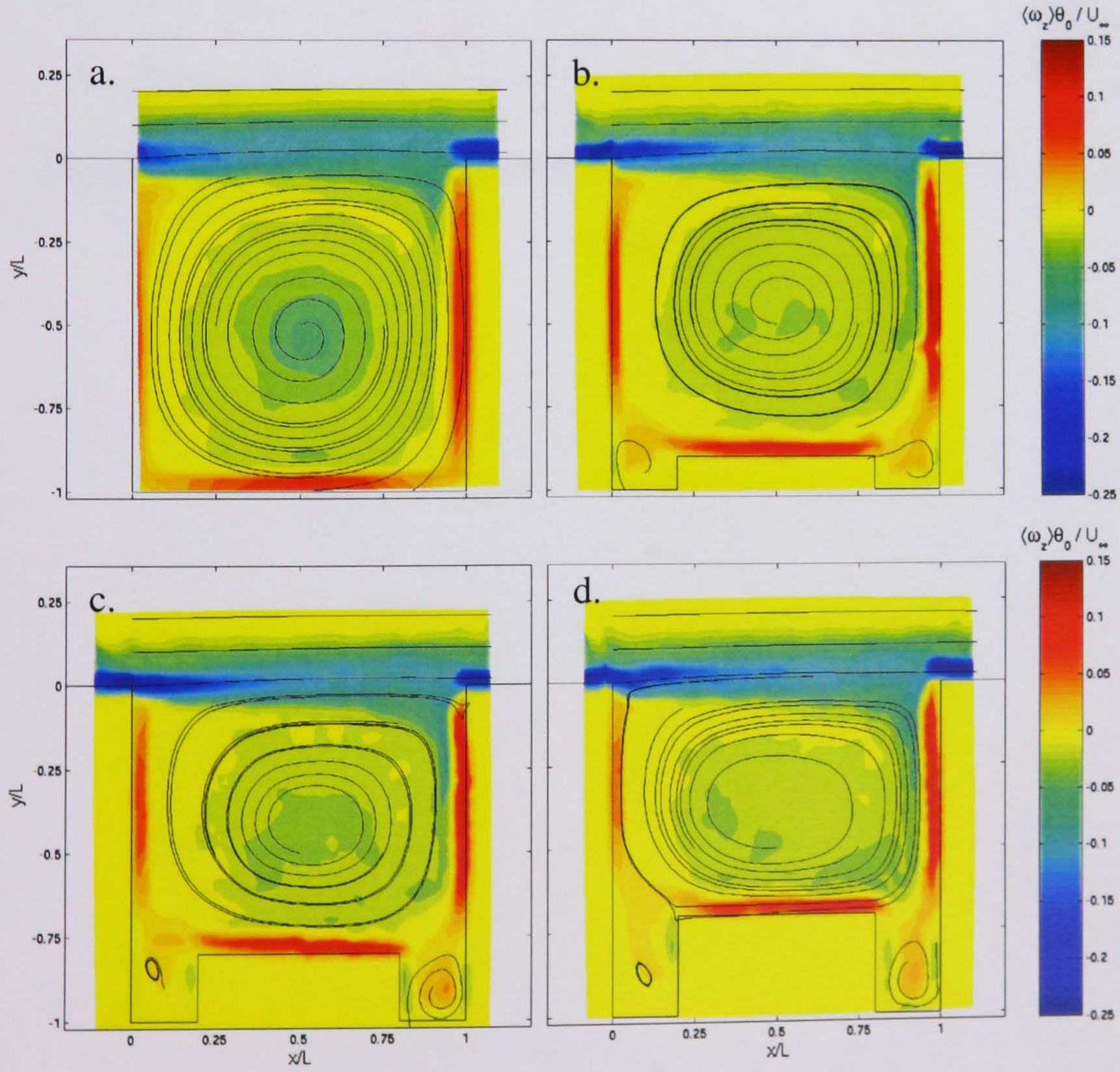

a. Clean cavity case $L/D = 1.0$.

b. $L/D = 1.0$ in configuration 3 for $d_c/D = 0.1$.

c. $L/D = 1.0$ in configuration 3 for $d_c/D = 0.2$.

d. $L/D = 1.0$ in configuration 3 for $d_c/D = 0.3$.

Figure 5.14. Vorticity and streamlines for the clean case and configuration 3 for $L/D = 1.0$ for $0.1 \le d_c/D \le 0.3$.

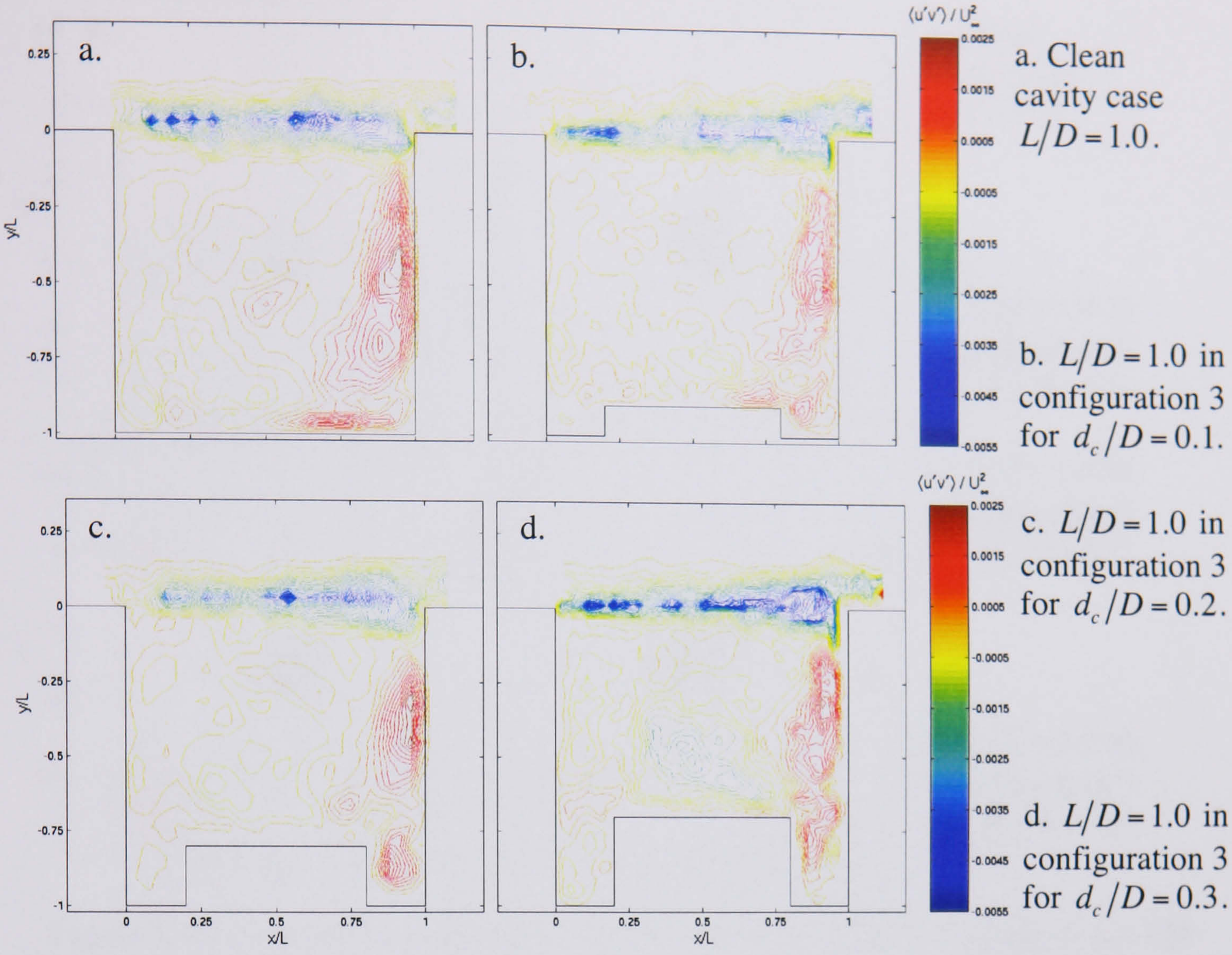

Figure 5.15. Reynolds stress for the clean case and configuration 3 for $L/D = 1.0$ for $0.1 \leq d_c/D \leq 0.3$.

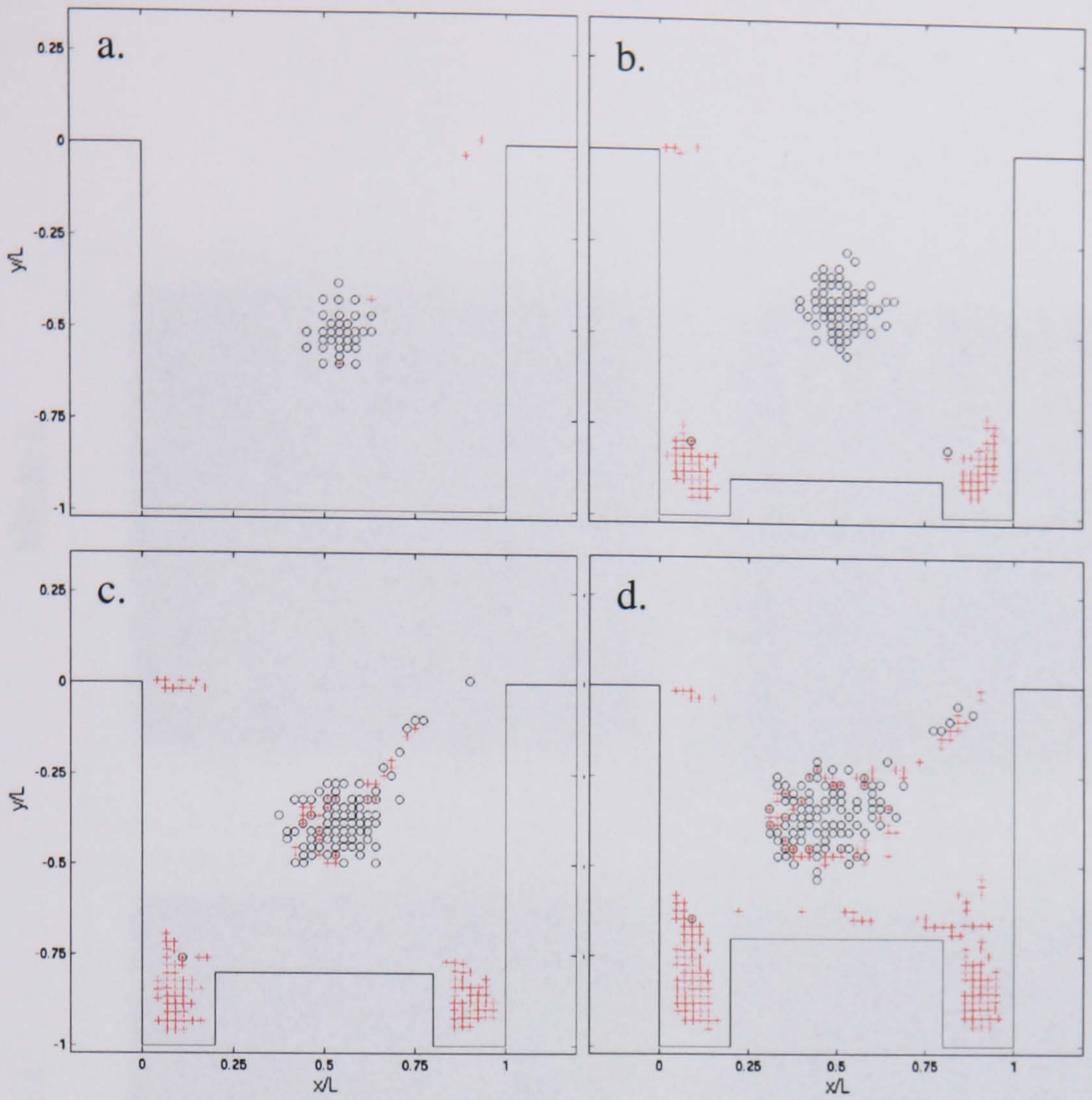

a. Clean cavity case $L/D = 1.0$

b. $L/D = 1.0$ in configuration 3 for $d_c/D = 0.1$.

c. $L/D = 1.0$ in configuration 3 for $d_c/D = 0.2$.

d. $L/D = 1.0$ in configuration 3 for $d_c/D = 0.3$.

Figure 5.16. A record of the locations of swirl observed within a sample set of 150 instantaneous velocity records for $L/D = 1.0$ for $0.1 \le d_c/D \le 0.3$. The swirl limits are set as for figure 5.5.

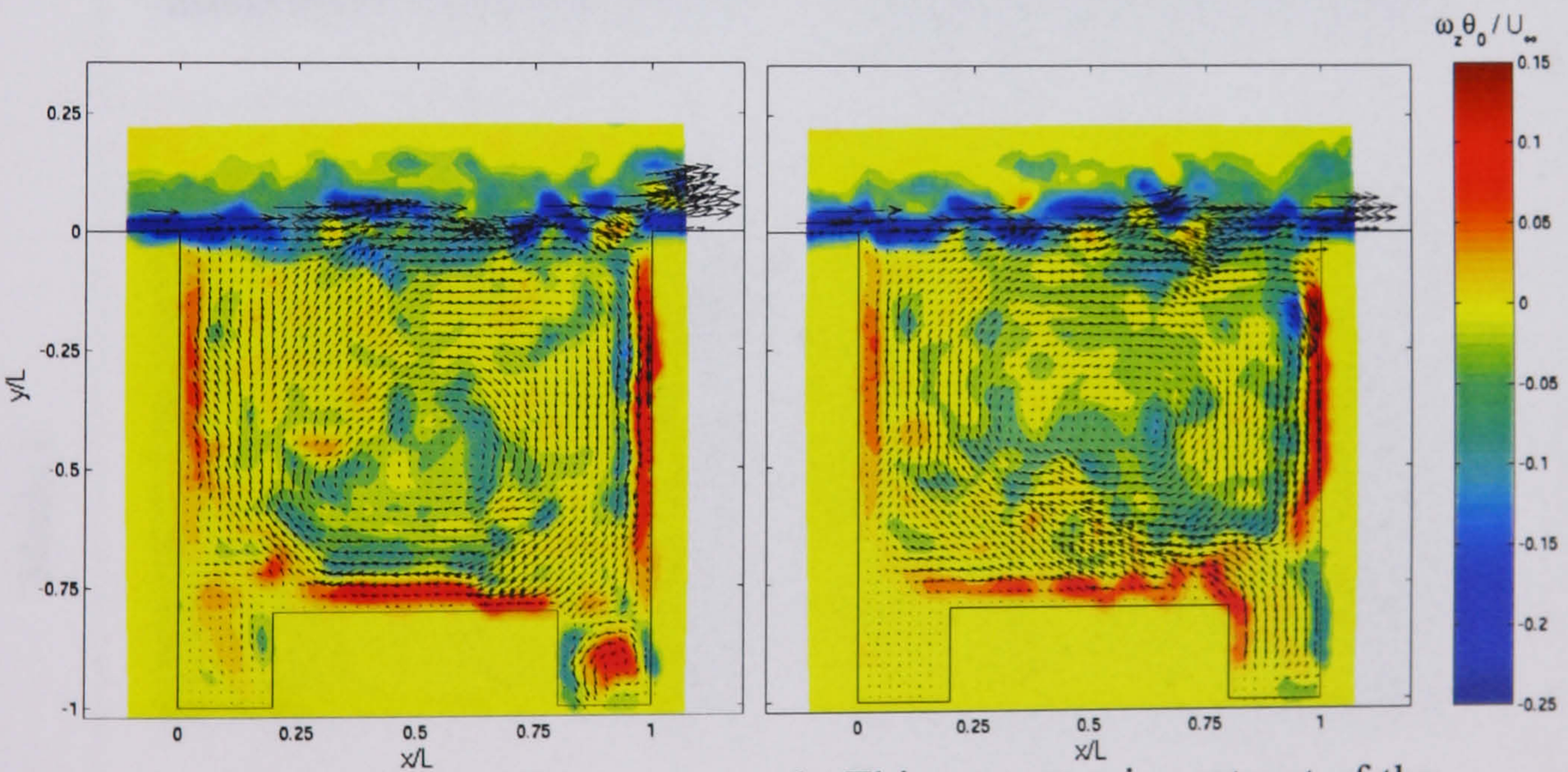

a. A nascent vortex at the downstream cavity corner is formed during the mass in stroke.

b. This structure is cast out of the corner cavity a short time later and distorts the primary eddy.

Figure 5.17. Instantaneous vorticity and velocity for $L/D = 1.0$ in configuration 3 ($d_c/D = 0.2$).

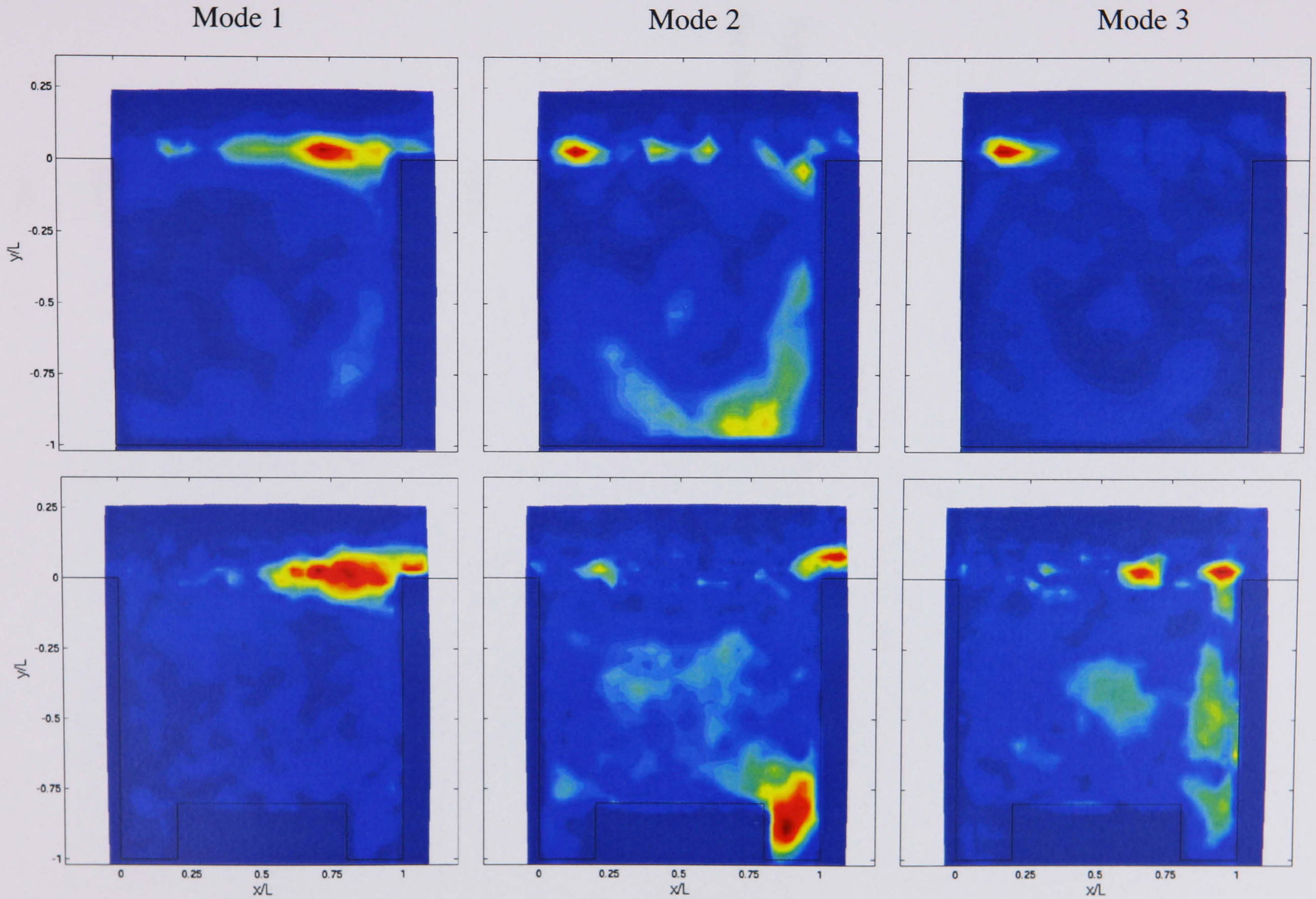

Figure 5.18. First three POD modes with $L/D = 1.0$ for the clean cavity case (top row) and configuration 3, $d_c/D = 0.2$ (bottom row).

Figures indicate normalised velocity magnitude.

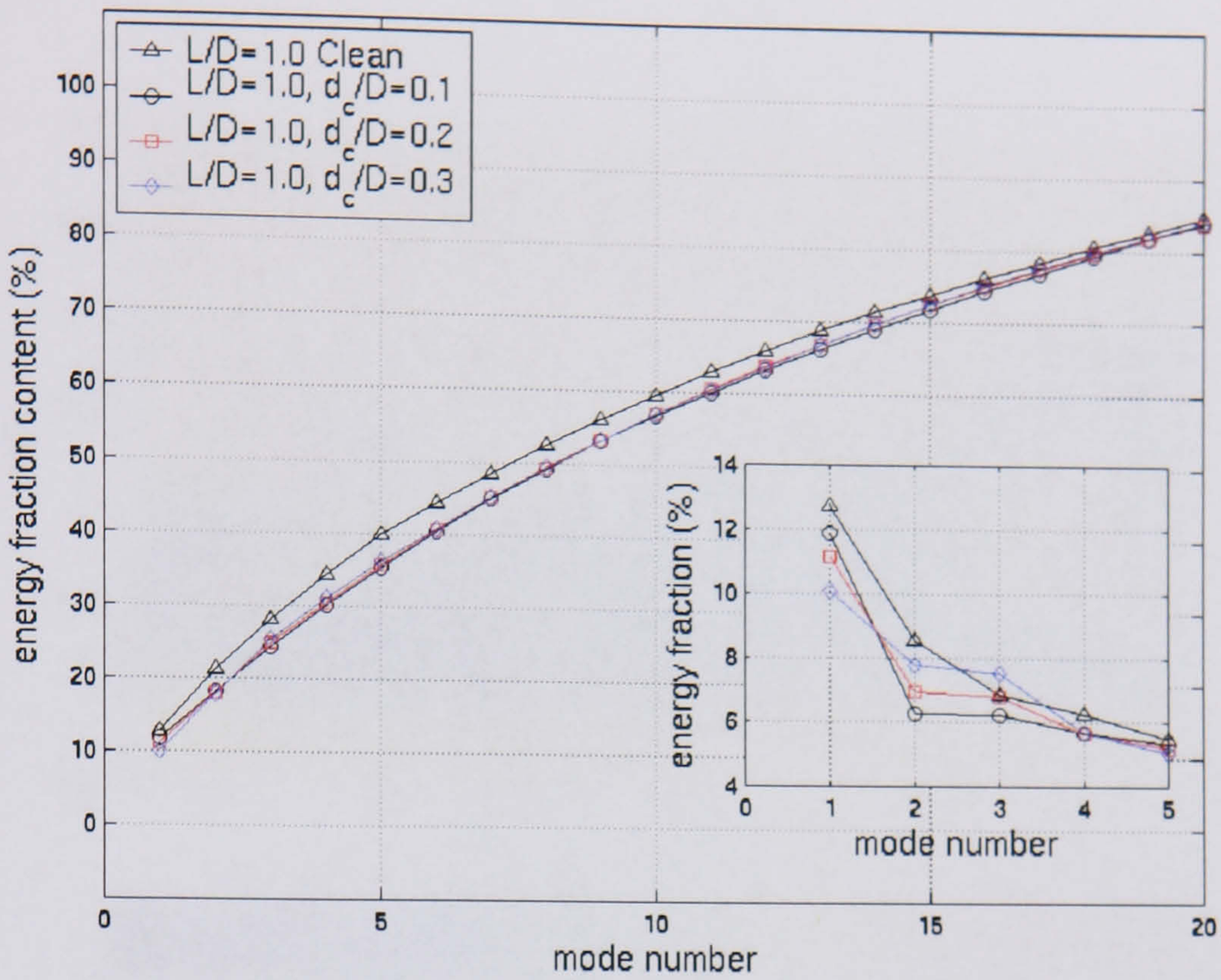

Figure 5.19. Cumulative percent energy in the fluctuation captured by POD modes for the cases of configuration 3 ($L/D = 1.0$). Shown to the bottom right of the main axis is the simple percent energy contribution for each individual POD mode.

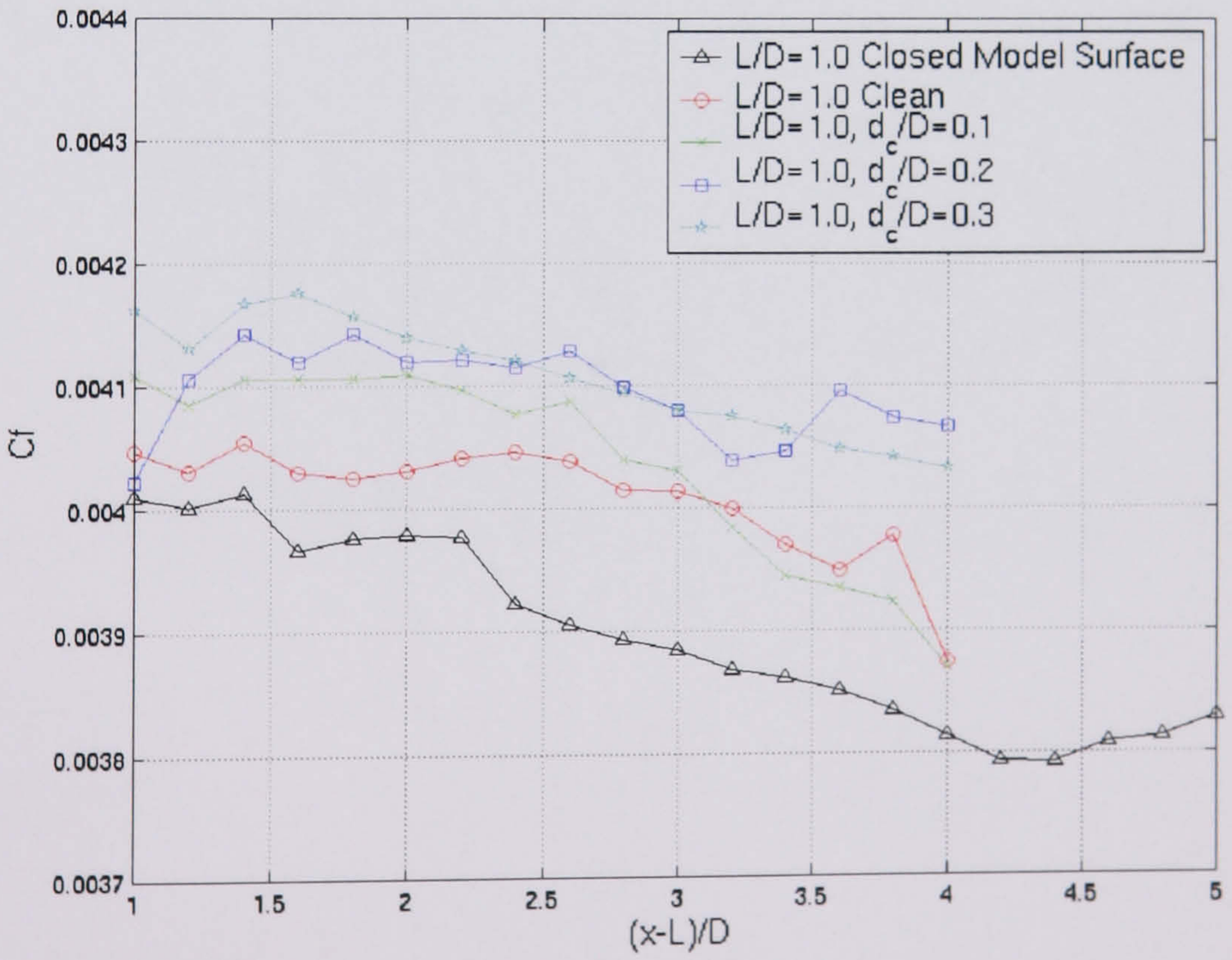

Figure 5.20. Measurement of the skin friction downstream of the cavity for $L/D = 1.0$. Each case of configuration 3 is included and indicates a self-similar behaviour in shear stress.

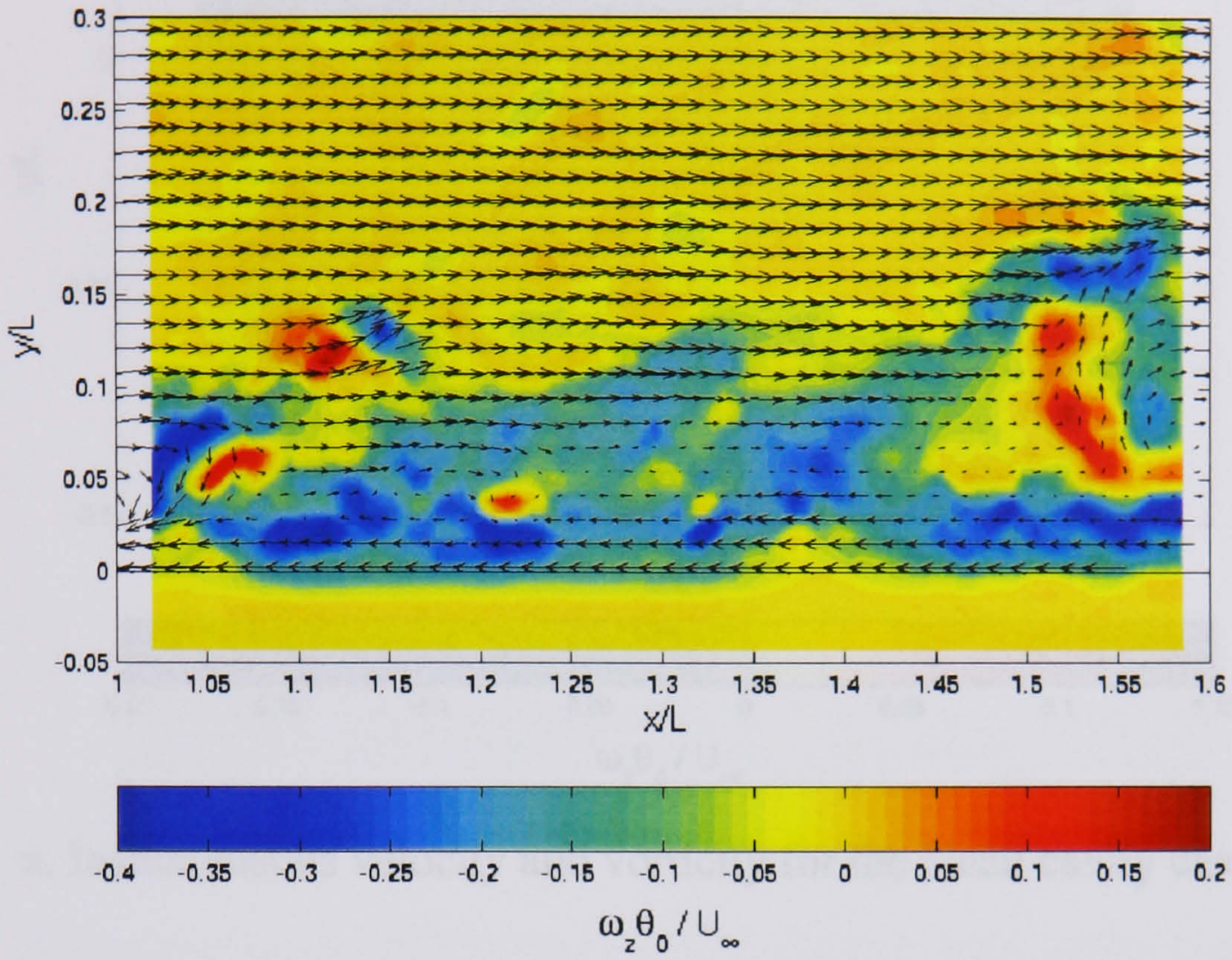

Figure 5.21. Instantaneous velocity and vorticity of the region downstream of the cavity for $L/D = 1.0$ and $d_c/D = 0.3$. For the vectors the coordinate system is moving at U_∞ to indicate the extent and structure of the cast-off shear layer in terms of vortex structures

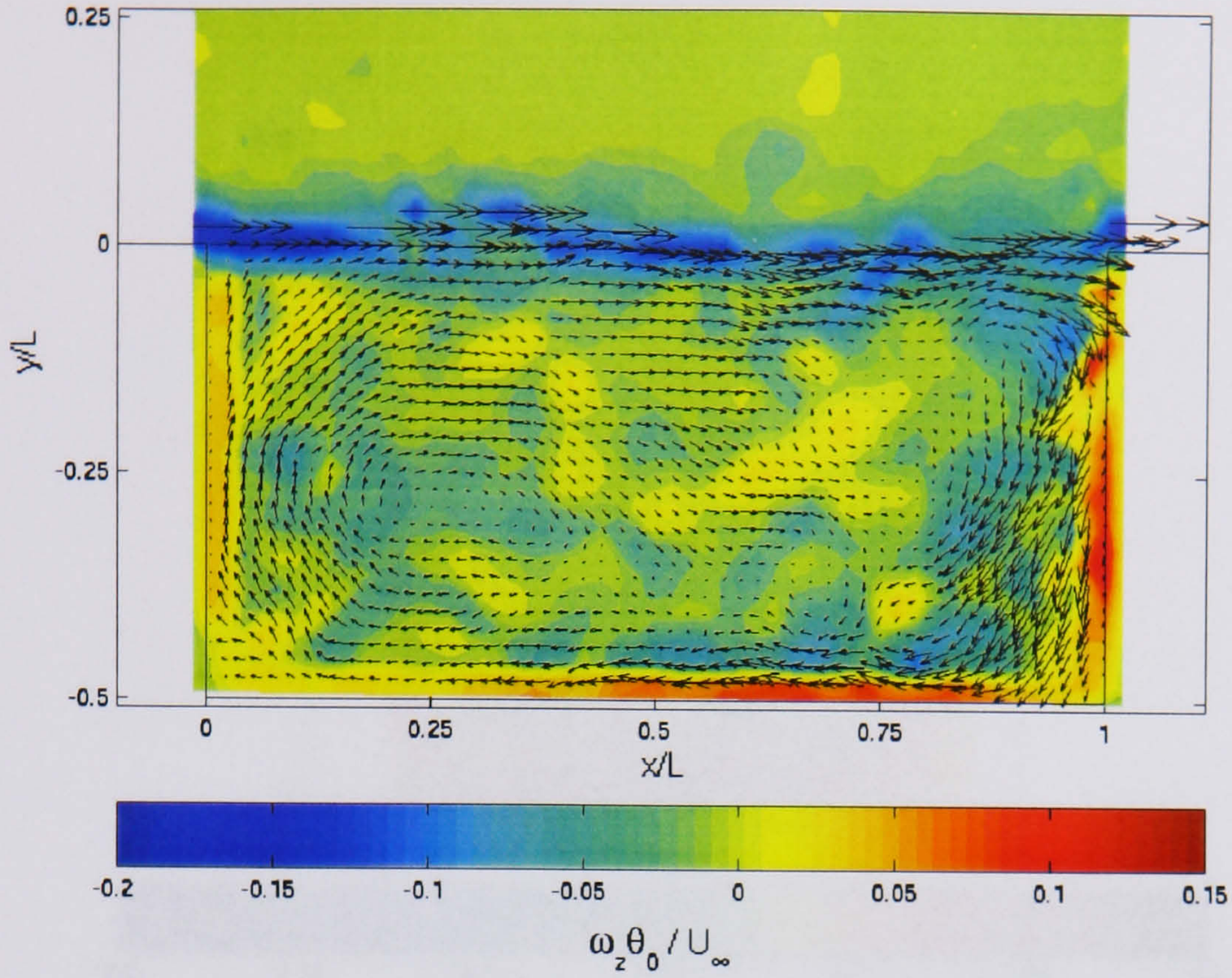

a. Instantaneous velocity and vorticity for the clean cavity case.

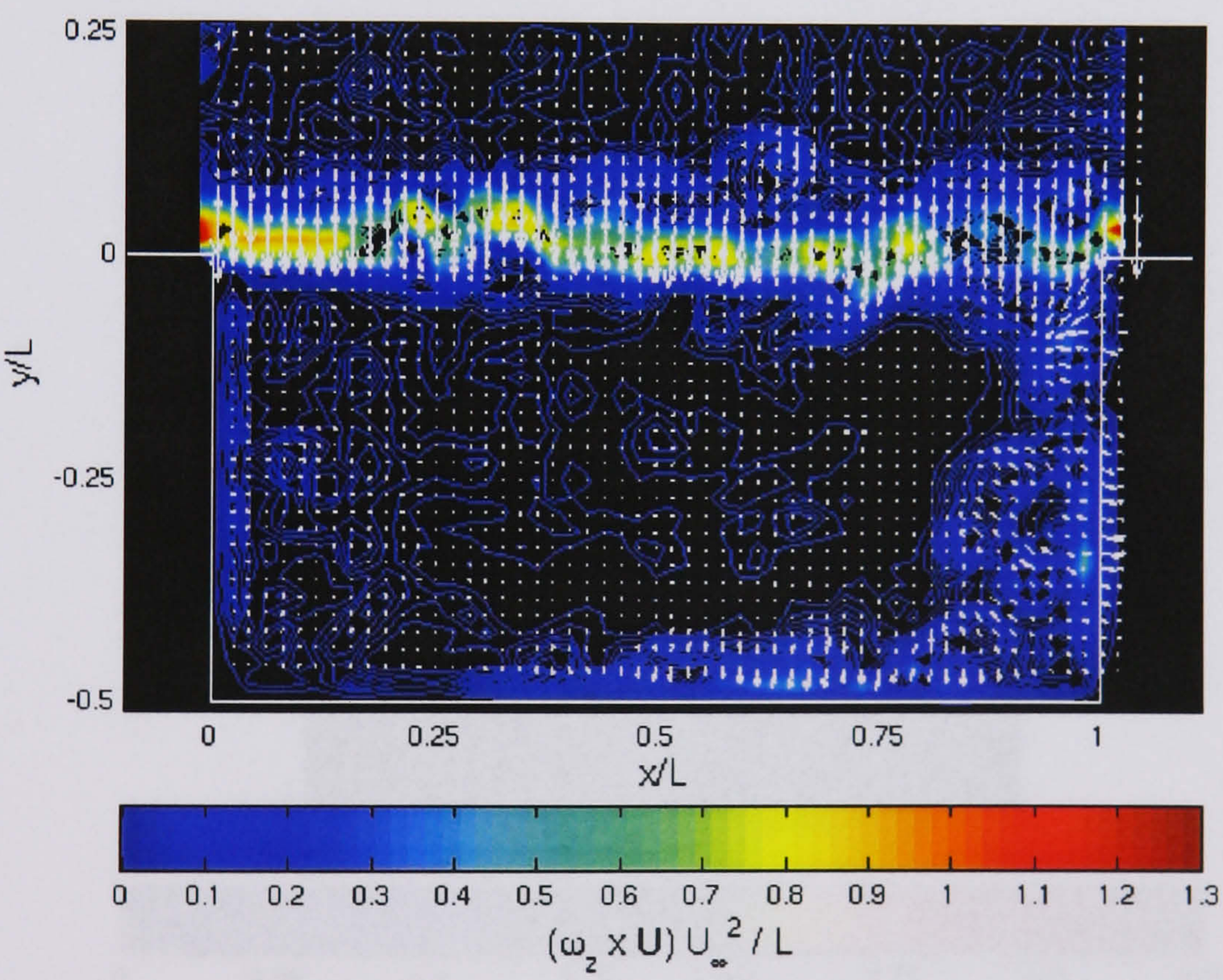

b. Contribution of the hydrodynamic effects to the acoustic response of the cavity for the flowfield shown in (a). Increments between the contours are 0.01.

Figure 5.22. A prediction of the acoustic properties of the clean cavity case for $L/D = 2.0$.

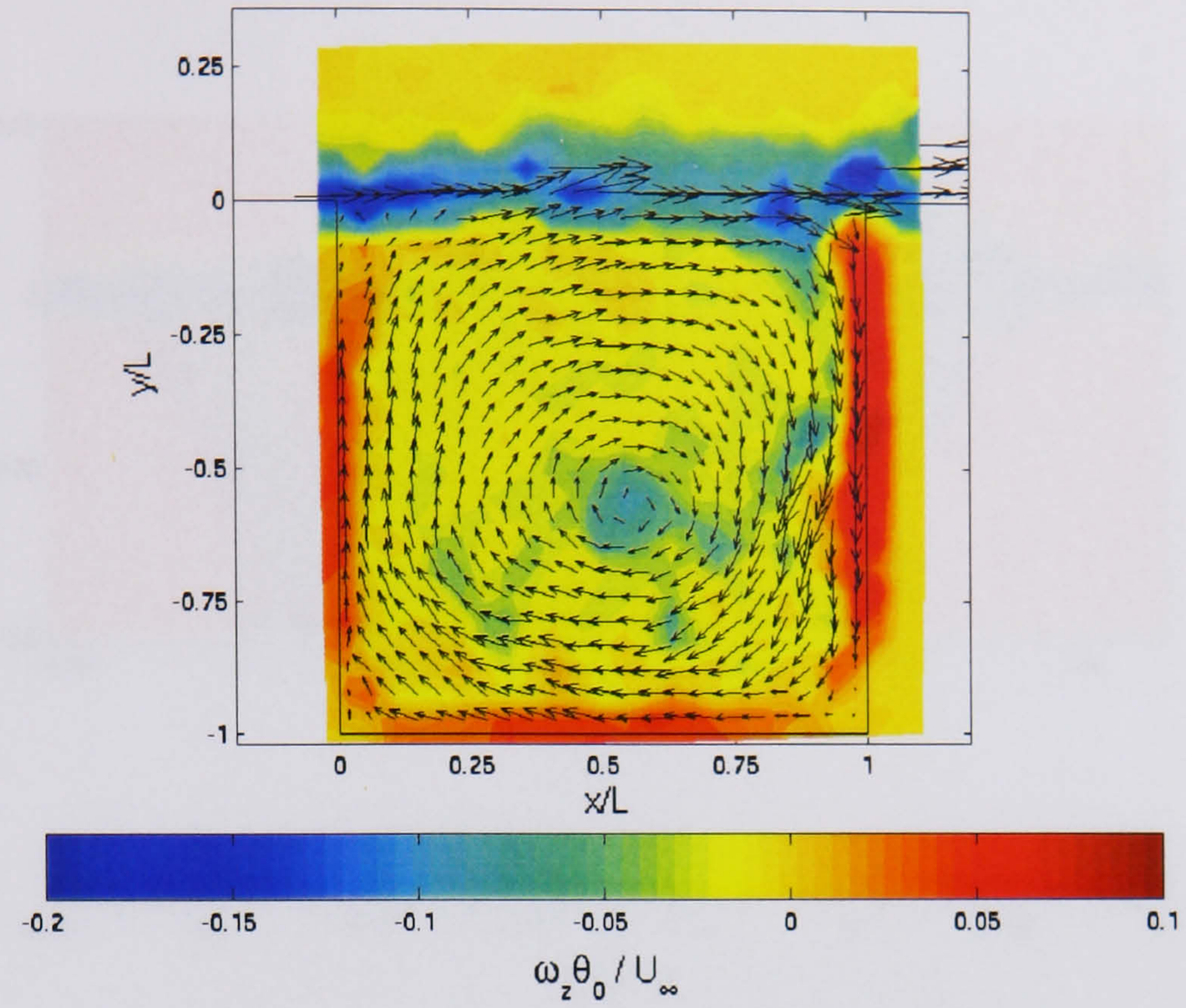

a. Instantaneous velocity and vorticity for the clean cavity case.

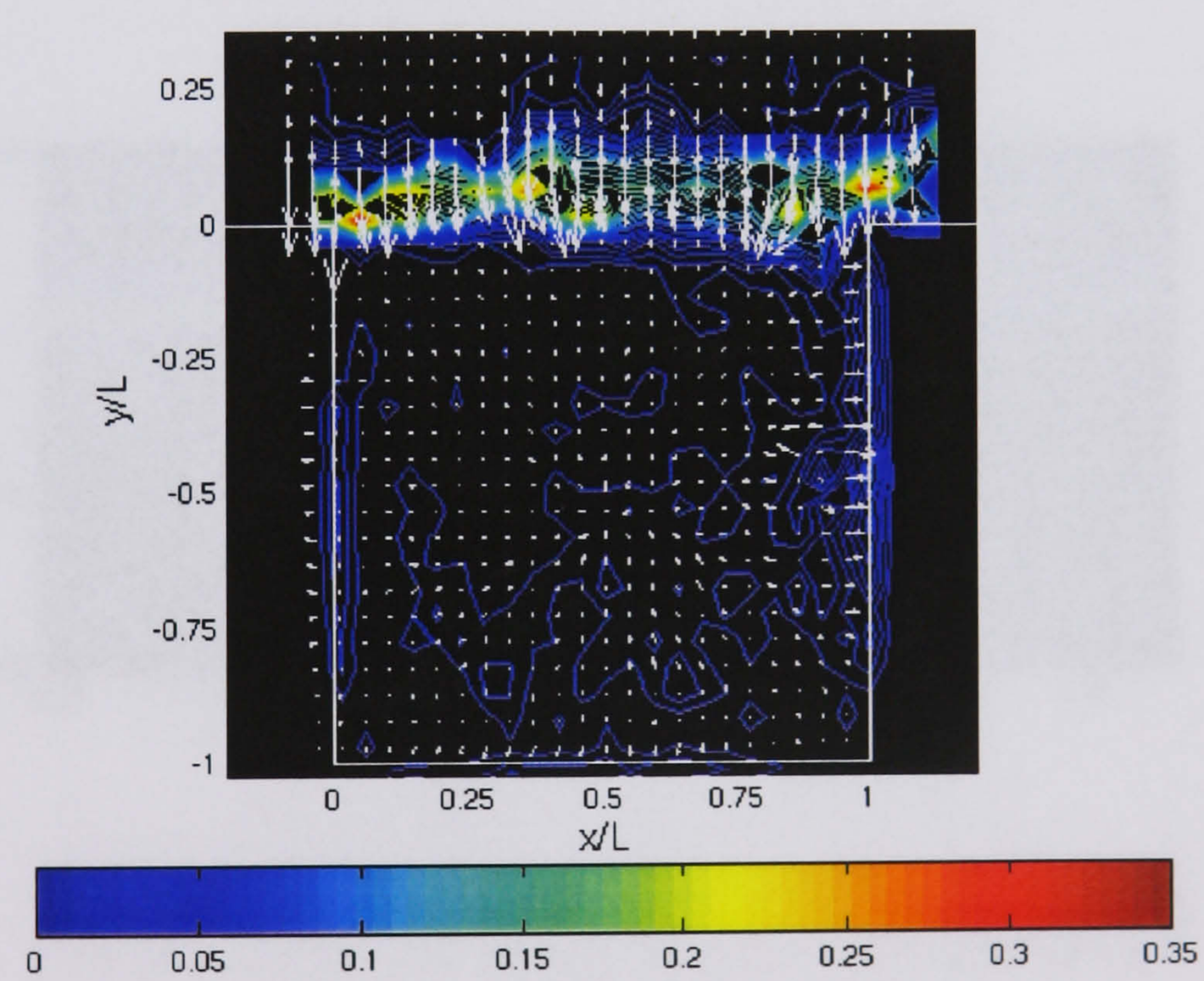

b. Contribution of the hydrodynamic effects to the acoustic response of the cavity for the flowfield shown in (a). Increments between the contours are 0.01.

Figure 5.23. A prediction of the acoustic properties of the clean cavity case for $L/D = 1.0$.

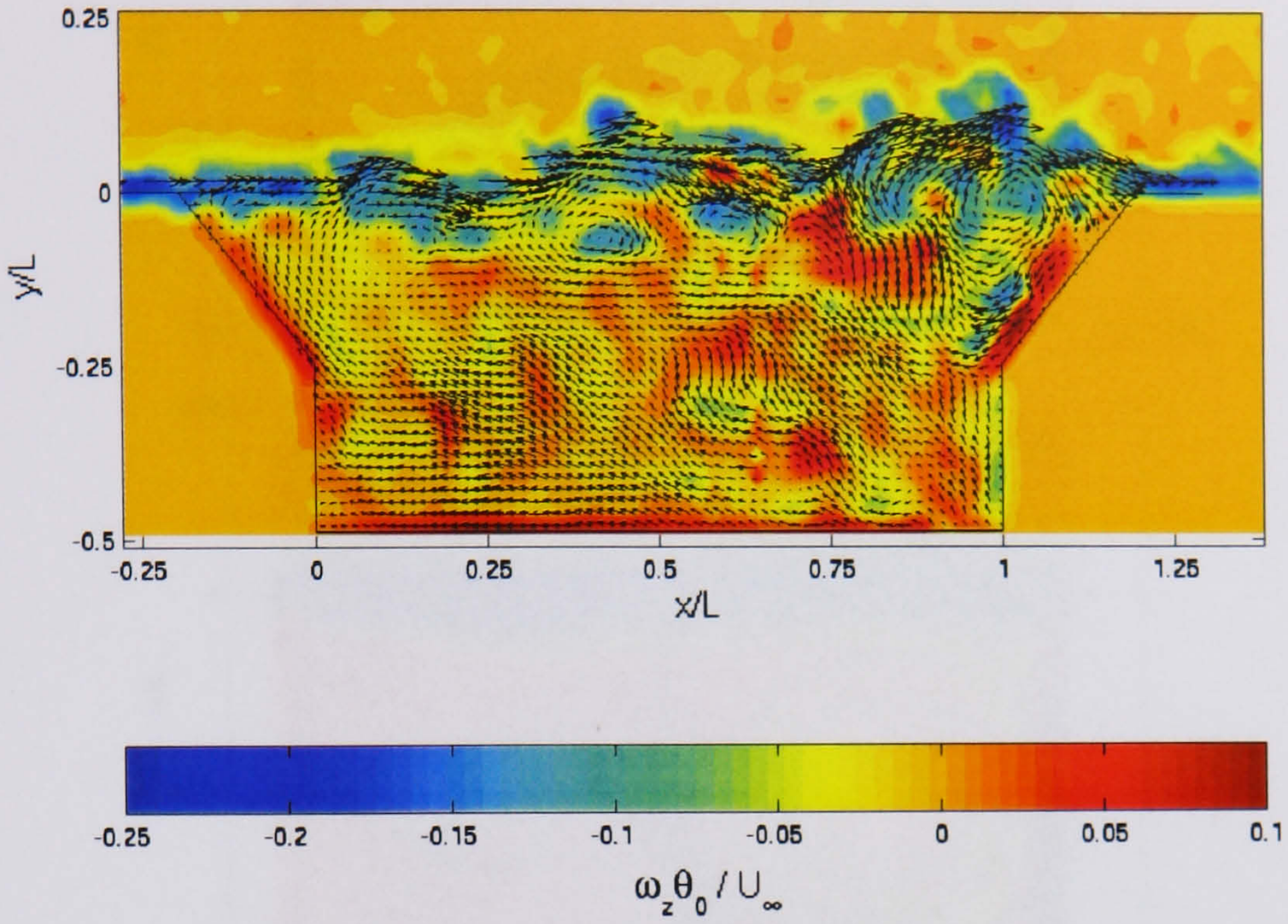

a. Instantaneous velocity and vorticity for configuration 2.

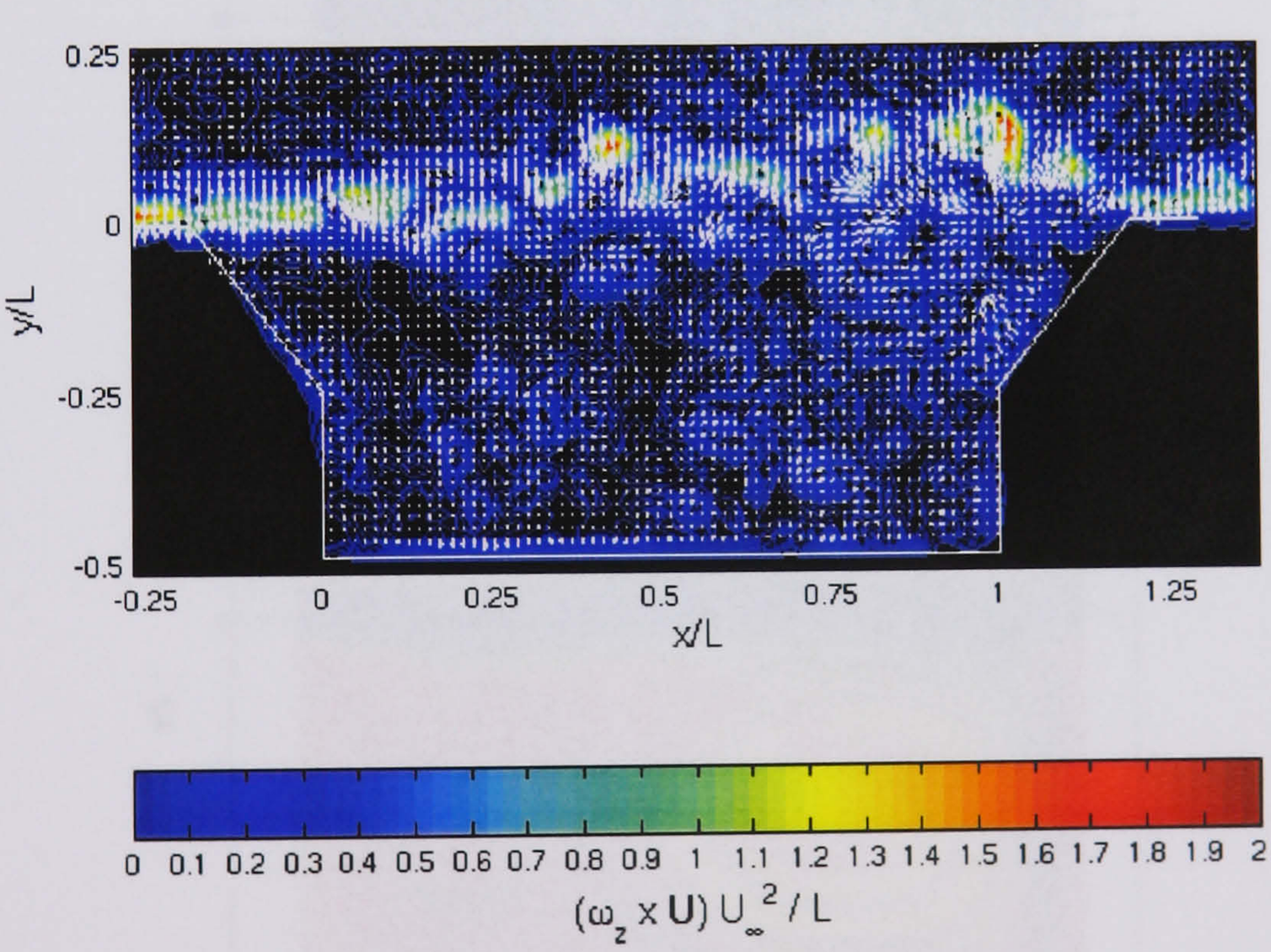

b. Contribution of the hydrodynamic effects to the acoustic response of the cavity for the flowfield shown in (a). Increments between the contours are 0.01.

Figure 5.24. A prediction of the acoustic properties of the clean cavity case for $L/D = 2.0$

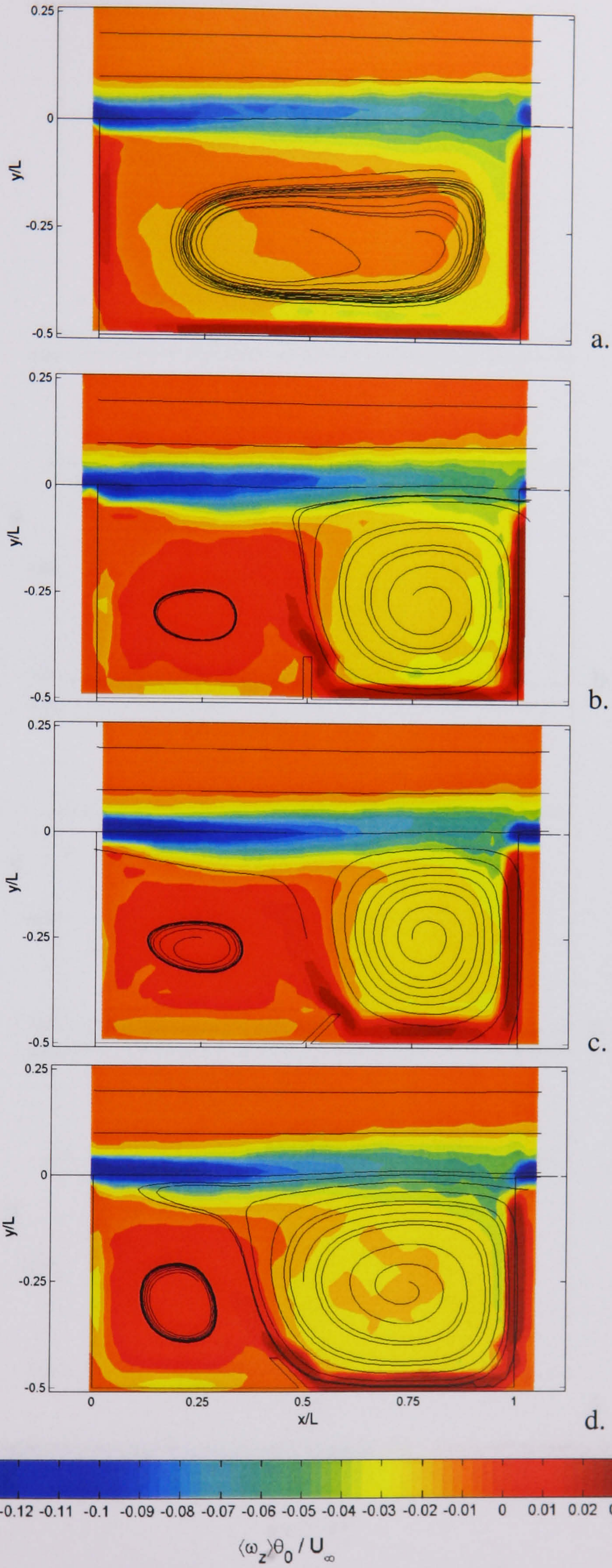

Figure 5.25. A comparison of the vorticity and streamlines for the clean and fence configurations (4, 5 and 6) for $L/D = 2.0$.

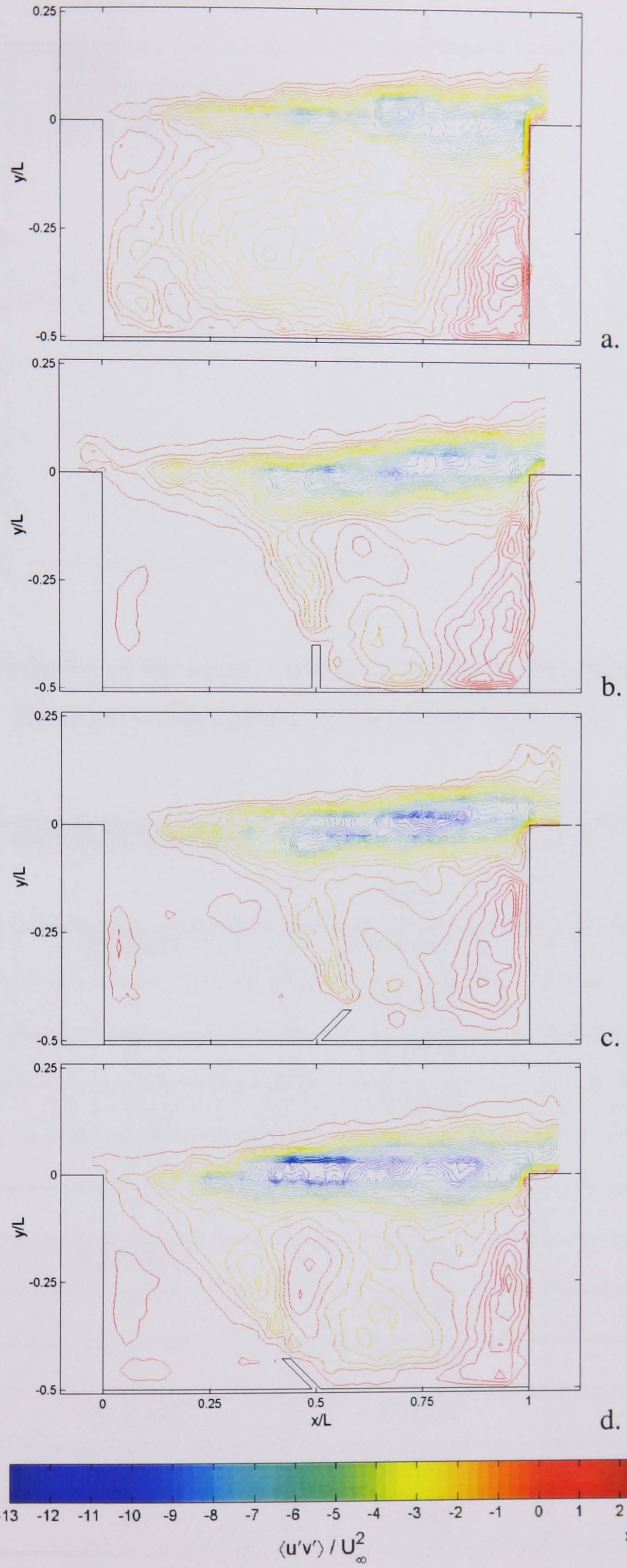

Figure 5.26. A comparison of the Reynolds stress for the clean and fence configurations (4, 5 and 6) for $L/D = 2.0$.

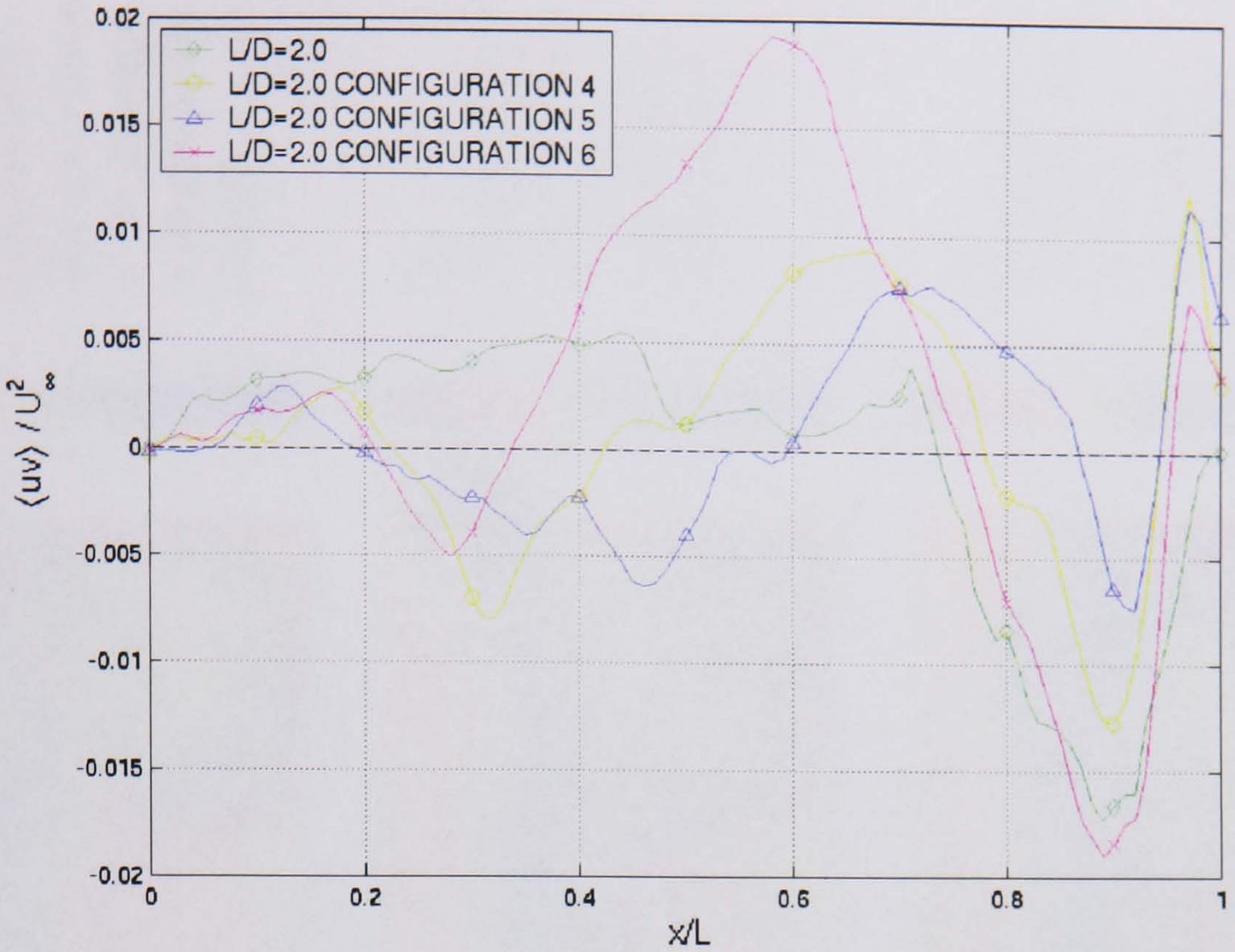

Figure 5.27. Distribution of the mean momentum transfer for the clean cavity case and the fence configurations (4, 5 and 6) for $L/D = 2.0$.

L/D	CONFIGURATION	$-\Gamma/U_\infty L$	
		Zone 1	Zone 2
2.0	CLEAN	0.6194±0.04	--
2.0	4	-0.1063	0.4010
2.0	5	-0.0960	0.2911
2.0	6	-0.1010	0.4821
2.0	7	0.5436	-0.0055
2.0	8	0.3406	-0.051
2.5	CLEAN	0.6504	--
2.5	7	0.5225	-0.0032
2.5	8	0.4294	-0.0335
3.0	CLEAN	0.7014	--
3.0	7	0.4831	--
3.0	8	0.4038	-0.0180

Table 5.2. The normalized average internal recirculation strength present with the cavity for various cavity configurations. The clean data has been pre-plotted in figure 4.23.

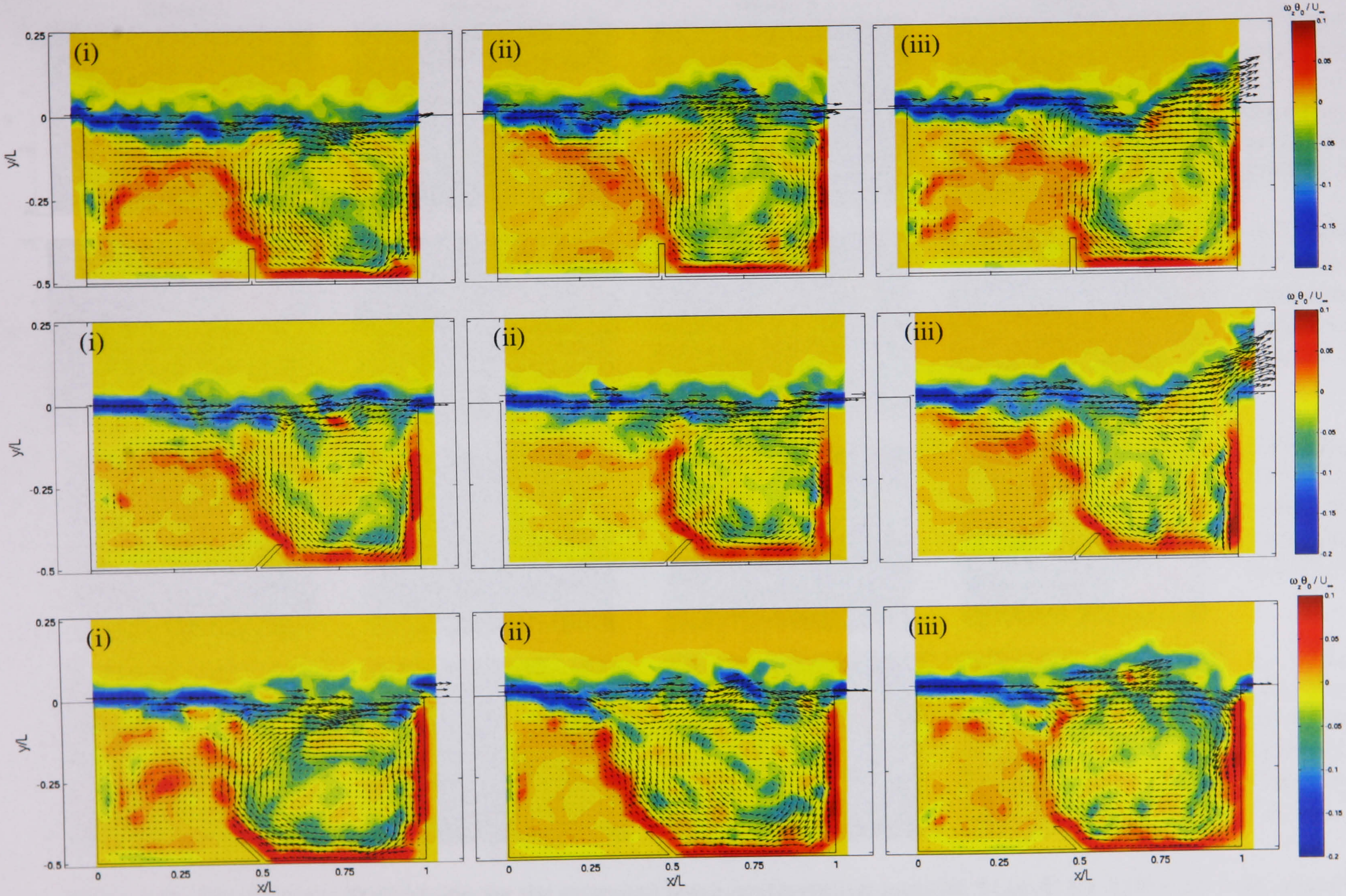

a. Configuration 4 (fence 90°). The orientation of the jet-edge is dramatically altered.

b. Configuration 5 (fence 45°). Zone 2 is more steady than zone 1.

c. Configuration 6 (fence -45°). A low-frequency modulation returns to the internal cycle.

Figure 5.28. Instantaneous velocity and vorticity for $L/D = 2.0$ for the fence configurations (4, 5 and 6).

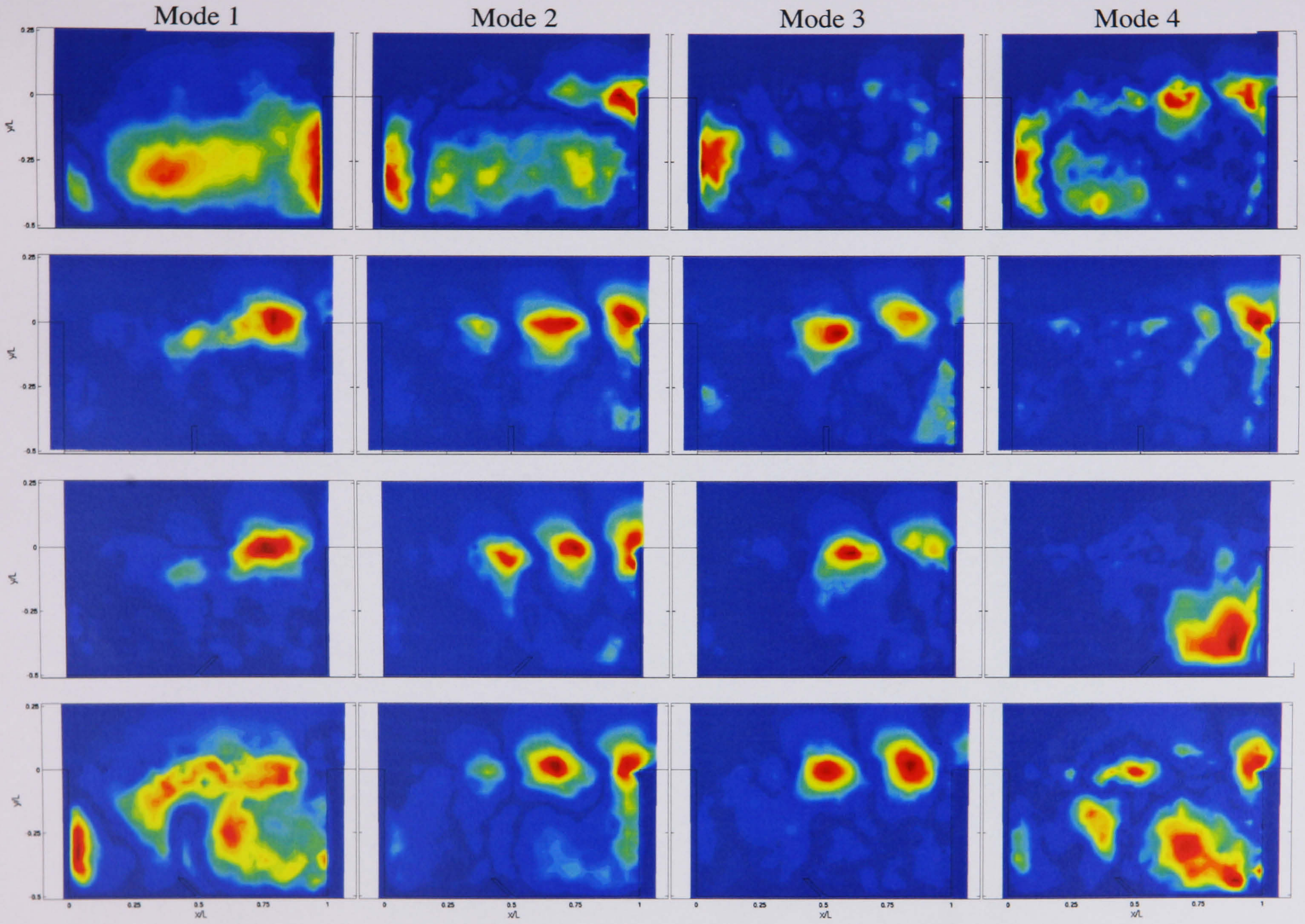

a. Clean case. The POD decomposition yields energy v-fluctuation within the cavity and downstream in the shear layer. [29.0%, 6.1%, 4.2%,3.9%]

b. Configuration 4 (fence 90°). The shear layer is punctuated with discrete maxima of v-fluctuation. [10.2%, 7.4%, 7.1%, 5.3%]

c. Configuration 5 (fence 45°). The distribution of energy shows a close resemblance to b. [12.2%, 9.0%, 8.6%, 4.4%]

d. Configuration 6 (fence -45°). The first POD mode has changed significantly although both 2 and 3 remain similar to b and c. [20.1%, 7.0%, 6.0%, 4.9%]

Figure 5.29. The first four POD Modes for the clean and fence configuration cases (4, 5 and 6) for $L/D = 2.0$ with normalized v-velocity.

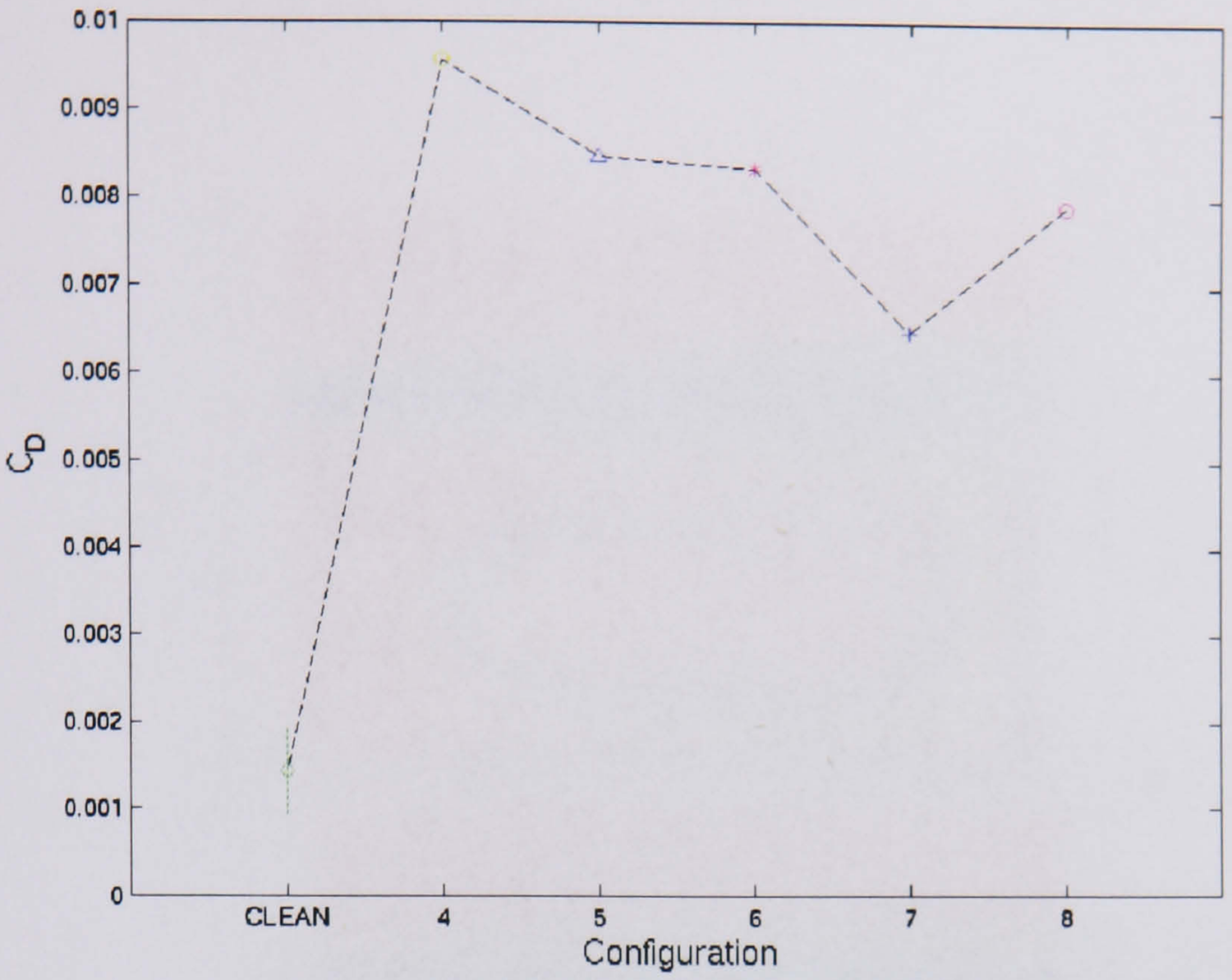

Figure 5.30. The drag coefficient for the clean, fence configurations (4, 5 and 6) and nose section configurations (7 and 8) for $L/D = 2.0$. The drag is calculated from the momentum flux out of the cavity.

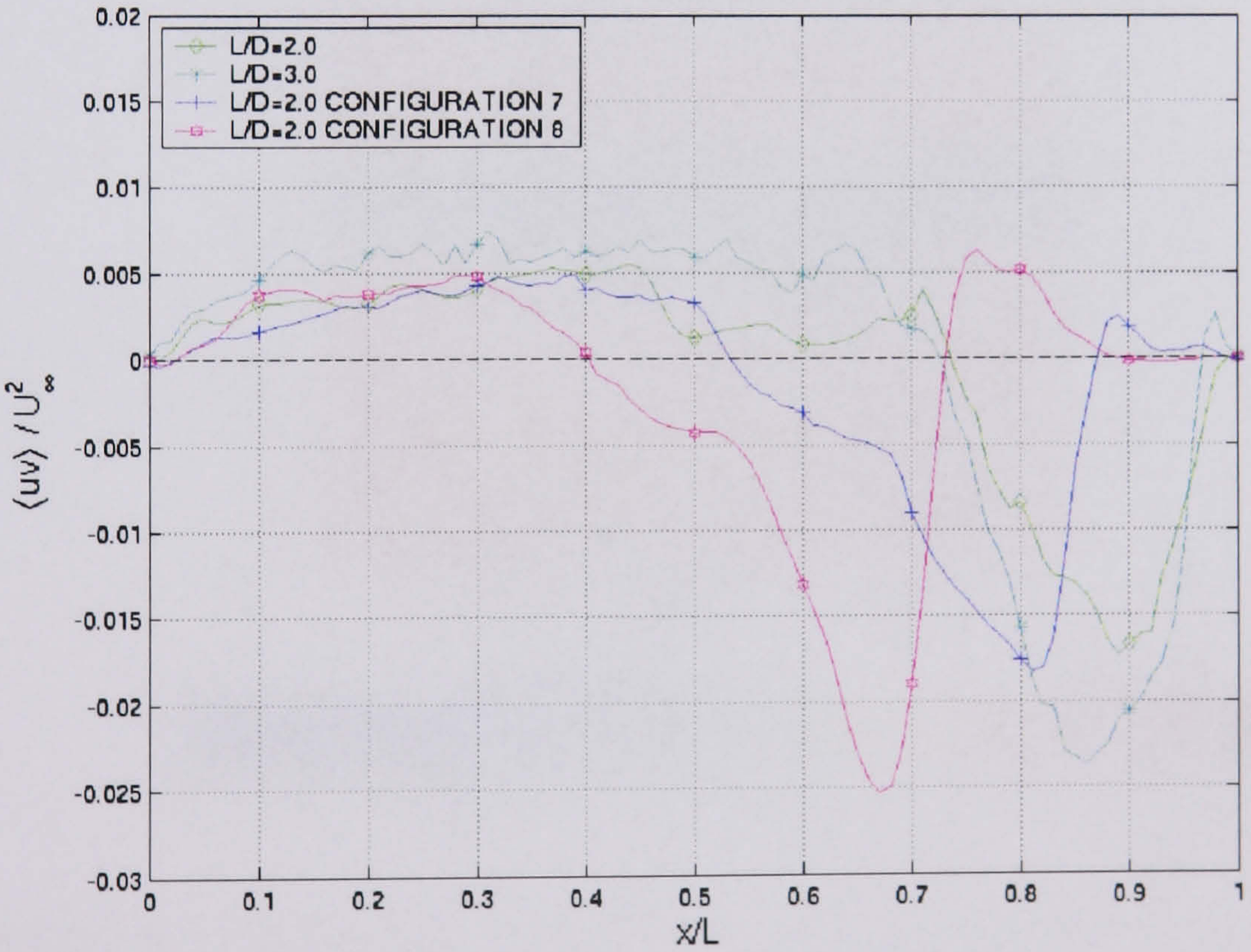

Figure 5.31. Distribution of the mean momentum transfer for the clean cavity case and the nose configurations (7 and 8) for $L/D = 2.0$.

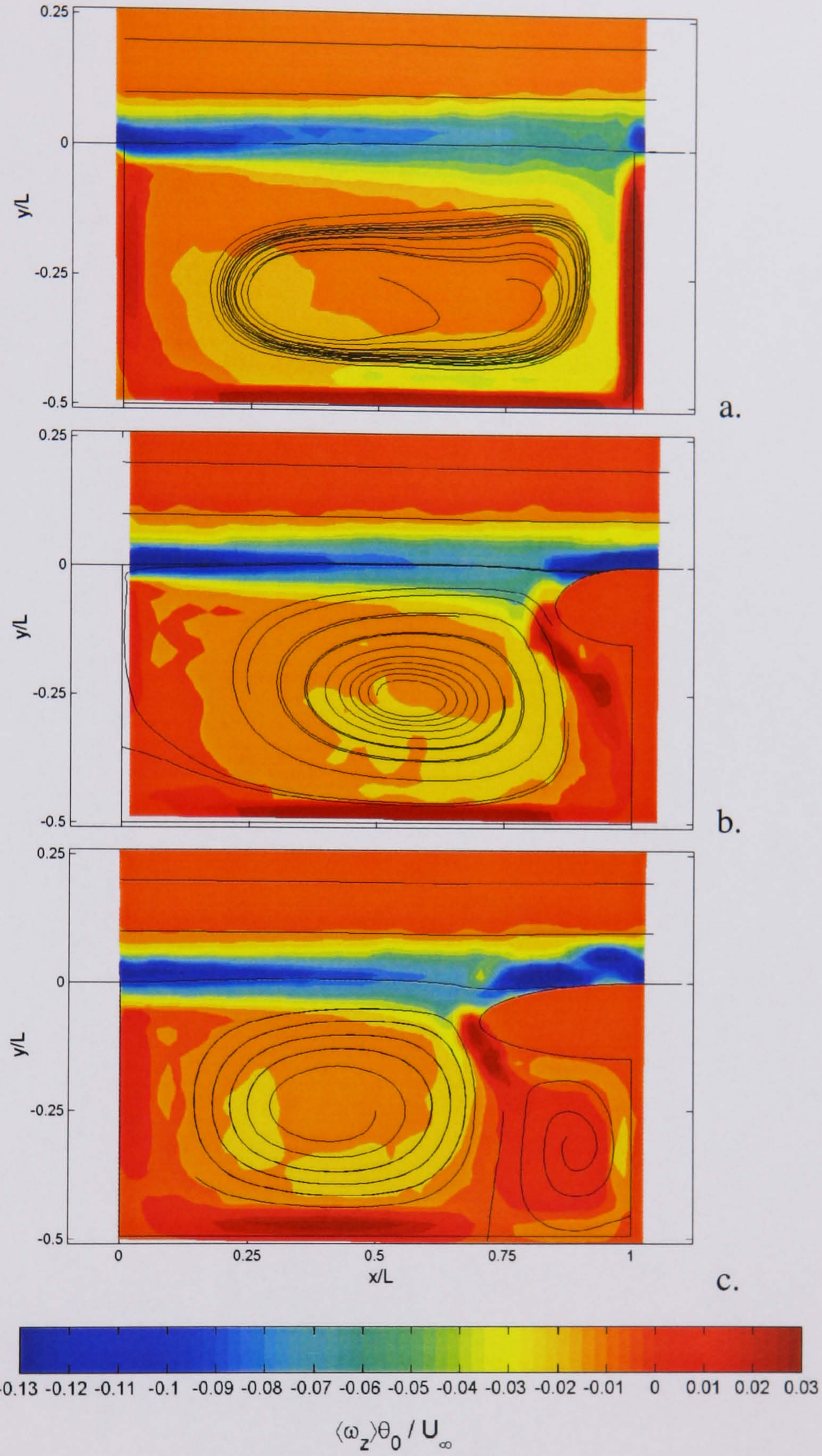

Figure 5.32. A comparison of the vorticity and streamlines for the clean and nose configurations (7 and 8) for $L/D = 2.0$.

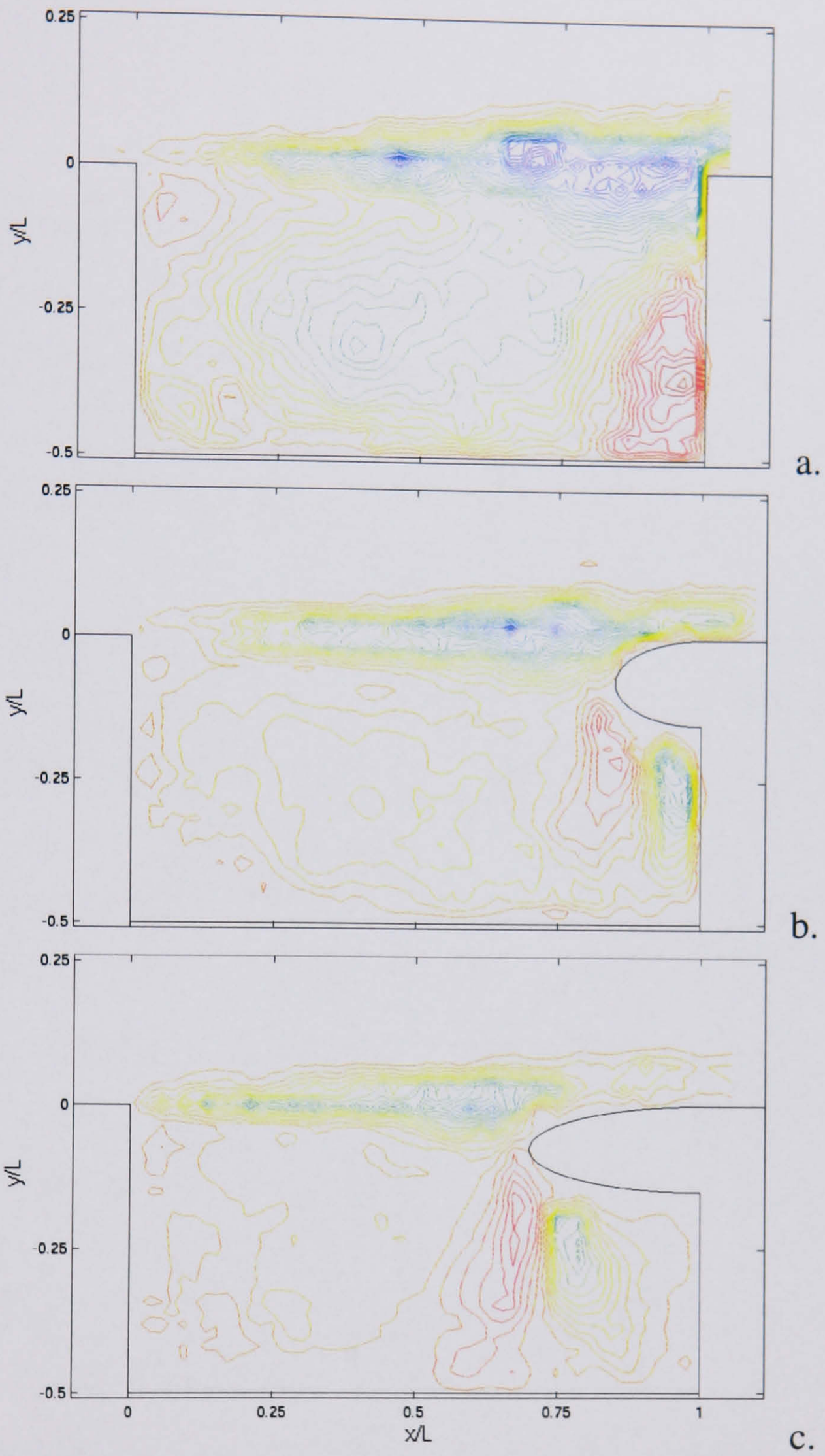

Figure 5.33. A comparison of the Reynolds stress for the clean and nose configurations (7 and 8) for $L/D = 2.0$.

CHAPTER 6: CONCLUSIONS AND FURTHER WORK

The current experimental investigation of cavity flow has raised a number of issues concerning aspects of the measurement procedure, data interpretation and the central findings from the wind-tunnel tests. These will be dealt with in chronological order.

It is well known from previous research that the behaviour of the cavity flowfield is complicated, not only by the various interactions that take place, but through the large amount of cycle-to-cycle variation possible within a number of fluid oscillations. Therefore, within such an investigation it is essential to accumulate an ensemble of data that is substantial enough to encapsulate each oscillation permutation. Using a DPIV system to capture the cavity flowfield is beneficial and progressive since it can present a collection of full-field instantaneous velocity data. However, this convenience comes at the price of reduced measurement accuracy in comparison to wet-film PIV and LDA from a pointwise sense. Therefore at the initial stages of this work a concentrated effort was made to construct a post-processing module that sought to maximise the accuracy and fidelity of the digital system and deliver an adequate dynamic range metric that could encapsulate the essential characteristics of the flowfield. With careful attention to both the bias and random error components using synthetic imaging it is possible to optimise the image capture and correlation algorithms to improve upon velocity accuracy and increase the spatial resolution, which ultimately increases this metric. Application of a tile-skewing procedure is seen to be essential in maintaining the correlation signal quality as a finer velocity (spatial) resolution is converged upon. The measurement fidelity is enhanced with application of the FRTT scheme that is superior to other schemes at adapting to regions of poor particle seeding density, which are commonplace within a eddy populated flowfield such as this. It has been possible to design an apposite post-processing module because details of the flowfield of interest have been measured, estimated and simulated.

With the persistent of peak locking errors and random errors in the correlation and imaging set-up the estimation of total error is included for the new calculation scheme. This is complemented by a confidence estimate in the measurements aided by a hot-wire traverse of the shear layer. This estimate is an extremely important verification of

the improved system accuracy and benchmarks the confidence, a requisite for the proper interpretation of results. This also draws attention to sampling inadequacies at the incipient region of the shear layer where the light sheet thickness is very large compared to the length scale at which the gradients vary.

The use of PTV has long been dedicated to low Reynolds number investigations where the velocity dynamic range is low and all particle matching is implied using simple robust algorithm sets. A hybrid PIV-PTV scheme where the imaging conditions are optimised for super-resolution PIV is presented. Application of the Barnard and Thompson probability-tracking algorithm has found success in these conditions only after careful and faithful identification of the particles on the image plane. A tracking algorithm is a useful tool since it combines the strengths of improved spatial resolution with the elimination of gradient bias errors from correlation assessment. Experimental validation of the tracking is fundamentally important, albeit difficult, and the simulated data results afford the scheme an over-predicted accuracy than actually expected. Any divergence of the scheme is hindered by the correlation scheme precursor, which reselects and hones the pertinent particle neighbourhood localized between the frame pair. In contrast to the principle correlation scheme the calculation time is an issue for PTV, and dramatic improvements have been made using the developed algorithms. When there is excessive out-of-plane loss of particle pairs (three-dimensional nature of the flow is increased, e.g. $L/D = 1.5$) the tracking scheme is stalled by excessive loss of particle data between frame pairs. This is difficult to counter since the dynamic velocity range of the flowfield demands a large inter-pulse delay between frames. As opposed to interpolation onto a regular grid for statistical processing a 't-tiling' procedure was constructed to take full advantage of irregularly spaced data with a good yield and reliability that encounters only systematic errors in subpixel estimation. It was found that for inhomogeneous seeding conditions to achieve the required statistical bin length of 250 samples a larger number of image pairs had to be acquired. This compounded testing exigencies although the outcome was a compendium of Reynolds stress data with improved accuracy. The Glasgow University PIV system has since been upgraded to accommodate vast amounts of image data.

During a series of separate wind-tunnel runs both static and dynamic pressure data was accumulated in and around the cavity. The static data was essential for proper classification and repeatability of the cavity flowfield and gave an insight into the mean flow behaviour of the cavity. The unsteady pressure measurement was restricted to 2 pressure transducers, one on the rear cavity bulkhead and one on the cavity floor. It was found that these pressure signals exhibited both amplitude- and frequency-modulated features, although the frequency of formation of large-scale structures was well predicted by common semi-empirical formulae. A lower frequency mode was observed to coexist with the separating shear layer mode (as a sub-harmonic $\beta/4$) and some clarification as to its behaviour was necessary. Since this internal oscillation occurred more frequently that the laser-pulse repetition a dual-laser/camera PIV system was utilised, this was capable of capturing two complete sets of velocity data in rapid succession. At the $\beta/4$ oscillation frequency ($\Delta t_2 = 4/\beta$) this technique proved successful at consistently matching vortical structures at similar positions within the cavity zone. With a sequential increase in the time delay between lasers (Δt_2), it was possible to track the movement of the larger structures and gain an understanding of the $\beta/4$ cycle. As an automated procedure this technique has some merit since it has been shown that the matching of velocity data sets has a maxima at this sample period. Using the method of POD to optimally reconstruct a fraction of the energy in the velocity data a better matching quality can be achieved, although careful extraction of the shear layer from the data is essential.

The central findings of the present study are as follows:

1. At the Reynolds number tested with this model design the cavity has a fully turbulent inflow, which evolves through the presence of a Kelvin-Helmholtz instability into a pattern of well-organized vortical structures. With the exception of $L/D = 1.5$ each clean cavity case investigated oscillated in the second mode where the SPL is highest, corresponding to two-eddies existing simultaneously within L. With the exception of $L/D = 1.0$ the normalized circulation within the cavity walls is seen to increase with L/D, and corresponds to a stronger suction profile imposed on the cavity floor. The internal flowfield of the cavity is not quiescent and is dominated by the periodic formation of a jet-edge along the rear bulkhead that travels upstream along the cavity

floor. The edge of this jet is discontinuous and with negative vorticity, formed during the mass addition cycle to the cavity. The upstream convection of this jet is related to the impingement scenario at the downstream corner (which is in turn related back to the feedback strength).

2. A transverse wave instability is present across the span of the cavity for cases $L/D = 1.5$ and 2.0. Using quantitative and qualitative flow visualization with static and dynamic pressure data it was found that the transverse wavelength is approximately equal to the cavity length and most likely oscillates at a Strouhal number where $St_\theta < 0.0001$. PIV data from the x-z plane shows this instability to form into well-defined pairs of contra-rotating velocity swirl (most pronounced at $y/D = 0.5$) that fills the entire cavity length. During the mass addition stroke to the cavity the instability from the shear layer is transmitted along the rear wall and cavity floor (verified by unsteady pressure measurement). It is therefore probable that the spanwise instabilities, which grow at a similar rate as the lengthwise instabilities are also being convected into the cavity during this stroke. These exist between the braids of the spanwise vortices and form into pairs of streamwise vortices, thus the transverse wavelength is unrelated to the shear layer mode number. Consequently the transverse wavelengths of $L/D = 1.5$ and $L/D = 2.0$ are the same even though their dominant modes are different. Cellular variations in velocity and Reynolds stress across the shear layer itself ($y/D = 0$) supports these clams as to its origin and also indicates that there will be spanwise variations in signal feedback. These effects manifest themselves as a spanwise variation in shear layer growth and recirculation eddy morphology within the cavity.

3. As the L/D of the cavity increases a lower frequency mode of $\beta/4$ is seen to coexist with the separating shear layer mode. It was found that this component is responsible for the oscillation of the recirculation zone and consequently the low-frequency flapping of the shear layer. From the PIV data an explanation of this oscillatory component was presented. During the mass addition cycle the shear layer dips into the cavity, causing the formation of a jet-edge over the rear bulkhead. This region of positive vorticity convects the extent of the cavity floor and a recirculation region is formed at the upstream corner. The strength and size of this zone may be consequently strengthened by the coalescence of further vorticity, courtesy of sequential mass addition strokes. As

the shear layer grows it entrains this coherent vortical fluid through the braid, and with phase agreement convects the entire structure across the cavity (or roll-out). At the downstream corner the shear layer is drawn upward by the clockwise rotation and there is large-scale (global) mass expulsion from the cavity (complete-escape scenario). This development becomes more violent as the L/D increases. As described this coupling more closely resembles the behaviour of transonic and supersonic cavity flow rather than that of low Reynolds number studies.

4. A coexisting low-frequency oscillation explains some of the cycle-to-cycle variation observed in the cavity flow phenomenon. It is apparent that the shear layer entrains typically vortical fluid that modifies the growth of the shear layer eddy and subsequently the clipping fate at the downstream corner. Osculation at the incipient region of the shear layer from the jet-edge is also prevalent; this is seen to amplify the shear layer disturbance.

The frequency of formation of the large organized vortical structures in the shear layer are well approximated by inviscid stability theory, which is in agreement with previous studies. The shear layer is seen to take another state whereby the organized vortical structures are shed at a much higher frequency causing small pocket of vorticity to be cast downstream where their persistence is variable. This state of the shear layer emerges after the feedback signal has been attenuated during the global mass expulsion stroke.

5. The common inter-car gap for a train was summarized into three basic configurations. (i) For the first configuration (slanted front and rear bulkheads) the common oscillation of the clean cavity persisted. A modification to the clipping fate at the downstream corner is noted and a reduction in velocity perturbation at the upstream corner via feedback is observed. The low-frequency flapping of the shear layer is amplified allowing relatively undistorted eddies to be cast off downstream. The skin-friction generated downstream is increased and there is an increased likelihood of generated sound.

(ii) In the second configuration (slanted cavity floor) there is a suppression of the coexisting recirculation zone oscillation noted for the clean case. An increase to the

Reynolds stress in the shear layer is attributed to an increase in shear layer osculation from jet impingement. The internal zone is steadier and the feedback signal is attenuated, the skin friction generated is comparable to the clean case.

(iii) For configuration three (modified cavity floor) the increase in height of the concertina section is seen to increase the downstream skin-friction value. The progression of the jet-edge is hindered and the primary eddy is weakened through the cyclic expulsion of fluid from the downstream corner section. The primary eddy is no longer captive and an internal oscillation is re-established.

6. The addition of a fence on the cavity floor at $x/L = 0.5$ is seen to reduce the unsteadiness within the internal cavity volume and increase the fluctuation within the shear layer. Using fence configurations 4 and 5 it is possible to suppress the low-frequency modulation of the cavity. In each case the reorientation of the jet-edge is significant and perturbs the shear layer causing significant changes to the mean momentum transfer across the open face of the cavity. With an increased unsteadiness in the shear layer the drag contribution from Reynolds stress is markedly increased, each controlled cavity produces significantly more drag that the clean case. Use of a downstream nose section is observed to increase the partial and complete clipping vortex scenario at the downstream edge. The cavity flowfield is distinctly steady although an increase of the mean momentum transfer to the cavity zone increases the drag produced.

Substantial progression of the current work may be achieved with little expense.
It is recommended that a synchronous pressure-PIV study will yield significantly more information regarding the shear layer interaction at the rear cavity corner. The simultaneous measurement of pressure and velocity at the downstream edge can provide information on the loading at the rear corner with respect to the impinging vortical structure. In addition it has been shown that the dual-PIV system is capable of capturing the conduction of the feedback signal into a velocity perturbation at the cavity leading edge. There is then the opportunity to extensively research feedback attenuation concepts. Use of parallel pressure-velocity measurement also releases the burden of individual inspection of velocity data.

The application of a stereoscopic PIV system would also be beneficial. These systems use simultaneous viewing with two cameras to reconstruct all three components of the velocity in a planar cross section of the observed flow. Initial wind-tunnel tests have been completed on an in-house system[1] and the required software updates are complete. With a careful optical arrangement it will be possible to interrogate planes though the cavity and gain a better understanding of the full three-dimensional behaviour. It has been shown that the hydrodynamic contribution to the acoustic field is useful in the case of cavity flow. If a more detailed study is required then it is possible to use a finite element model to simulate the acoustic particle velocity within the cavity, which can then be included with the velocity data to provide the acoustic power. Scrutinising the persistence of vortices downstream of the cavity may give some insight into the sound generated by a pantograph assembly for a train. CFD simulations can provide this information also.

Improvements to the 2D post-processing module should not be required. However, in the pursuit of bias error suppression a camera that can provide a reduction in pixel size with an increase in CCD chip size will be beneficial to future work (increases d_τ/d_r).

The dual-PIV system used here is capable of taking two frame pairs over a preset time-delay, while new generation PIV systems are capable of capturing a sequence of images over similar time-delays. However, their operation comes at a cost of camera image quality (baud limit) and reduction in the field of view (imposed by reduced laser power). For example, to sample the shear layer second mode 10 times over a single oscillation can be done with a region of interest of 0.5 mega-pixels for a field of view of 15x15mm. Improved skin friction measurement is also essential. Measurements taken with the Preston tube are quick and easy although the assumption of wall-bounded flow can significantly reduce the accuracy of the data, while the limitations of pressure gradient are also prohibitive. The use of a flush mounted film probe can provide reliable time-resolved comparative friction data, while liquid crystal measurement can provide data over an entire surface. A more inexpensive route would be in the use of oil-film interferometry, which is easy to apply and is capable of measuring positions downstream of re-attachment and reversed flow.

---

[1] Using the angular method (Scheimpflug condition)

REFERENCES

Adrian, R.J. 1984 Scattering particle characteristics and their effect on pulsed laser measurements of fluid flow: speckle velocimetry vs. particle image velocimetry. Appl. Opt. 26, p3855-3858.

Adrian, R.J. 1986 An image shifting technique to resolve directional ambiguity in double-pulsed velocimetry. Appl. Opt., 25, p3855-3888.

Adrian, R.J 1988 Statistical properties of particle image velocimetry measurement in turbulent flow. Laser anemometry in fluid mechanics, Lisbon, p115-129.

Adrian, R.J. 1991 Particle-imaging techniques for experimental fluid mechanics. Ann. Rev. Fluid Mech., 23, p261-304.

Adrian, R.J. 1997 Dynamic ranges of velocity and spatial resolution of particle image velocimetry. Meas. Sci. Technol., 8, p1393-1398.

Agüí, J.C., Jiménez, J. 1987 On the performance of particle tracking. J. Fluid Mech., 185, p447-468.

Ahuja, K.K., Mendoza, J. 1995 Effects of cavity dimensions, boundary layer, and temperature on cavity noise with emphasis on benchmark data to validate computational aeroacoustic codes. NASA CR-4653.

Ashurst, W.T., Meiburg, E. 1988 Three-dimensional shear layers via vortex dynamics. J. Fluid Mech., 189, p87-116.

Badcock, K., Cantariti, F., Gribben, B. 1998 Theory guide to PMB2D version 3.0. Aerospace Engineering Report, Glasgow University.

Baek, S.J., Lee, S.J. 1996 A new two-frame particle tracking algorithm using match probability. Exp. Fluids, 22, p23-32.

Baker, C.J. 1986 Review of train resistance data. Rail Research UK.

Barker, D.B., and Fourney, M.E., 1977 Measuring fluid velocities with speckle patterns. Optics Lett., 1977, 1, p135-137.

Barlow, J.B., Rae, W.H., Pope, A. 1999 Low-speed wind tunnel testing. Wiley-Interscience. Third Edition.

Barnard, S.T., Thompson, W.B. 1980 Disparity analysis of images. IEEE Trans. Pattern Analysis Machine Intelligence, 2, p333-340.

Batchelor, G.K. 1967 An introduction to fluid dynamics. Cambridge University Press.

Bechert, D.W. 1996 Calibration of Preston tubes. AIAA J., 34, p205-206.

Bechert, D.W., Bruse, M., Hage, W., Van Der Hoeven, J.G.T, Hoppe, G. 1997 Experiments on drag-reducing surfaces and their optimization with an adjustable geometry. J. Fluid Mech., 338, p59-87.

Bendat, J.S. 1958 Principles and applications of random noise theory. Wiley.

Benney, D.J., Lin, C.C. 1960 On the secondary motion induced by oscillations in a shear flow. Phys. Fluids, 3, p656-657.

Bernal, L.P., Breidenthal, R., Brown, G.L., Konrad, J.H., Roshko, A. 1981 On the development of three-dimensional small scales in turbulent mixing layers. Proc. 2nd Symp. Turbulent Shear Flows.

Bernal, L.P., Roshko, A. 1986 Streamwise vortex structure in plane mixing layers. J. Fluid Mech., 170, p499-525.

Bernero, S., Fiedler, H.E. 2000 Application of particle image velocimetry and proper orthogonal decomposition to the study of a jet in a counterflow. Exp. Fluids, 29, p274-281.

Betchov, R., Criminale, W.O. 1967 Stability of parallel flows. Academic press.

Bilanin, A.J., Covert, E.E. 1973 Estimation of possible excitation frequencies for shallow rectangular cavities, AIAA J., 11, p347-351.

Bliss, D.B., Hayden, R.E. 1976 Landing gear and cavity noise prediction. NASA CR-2714.

Block, P.J.W. 1976 Noise response of cavities of varying dimensions at subsonic speeds. NASA TN-D-8351.

Bloor, S.M. 1964 The transition to turbulence in the wake of a circular cylinder. J. Fluid Mech., 19, p290-309.

Bloor, S.M., Gerrard, J.H. 1966 Measurements on turbulent vortices in a cylinder wake. Proc. Royal Society, A299, p319-342.

Brandesis, J. 1982 Flow separation in shear-layer-driven cavities. AIAA J., 18, p892-898.

Braslow, A.L., Knox, E.C. 1958 Simplified method for determination of critical height of distributed roughness particles for boundary-layer transition at Mach numbers from 0 to 5. NASA TN-4363.

Braslow, A.L., Hicks, R.M., Harris, R.V. 1966 Use of grit type boundary layer transition trips on wind tunnel models. NASA TN D-3579.

Breidenthal, R. 1979 Chemically reacting, turbulent shear layer. AIAA J., 17, p310-311.

Breidenthal, R. 1980 Response of plane shear layers and wakes to strong three-dimensional disturbances. Phys. Fluids, 23, p1929-1934.

Brigham, E.O. 1974 The fast Fourier transform. Prentice-Hall.

British Aerospace PLC, 1997 SPARV v9.0 users manual, Issue 1.

Browand, F.K., Latigo, B.O. 1979 The growth of the two-dimensional mixing layer from a turbulent and non-turbulent boundary layer. Phys. Fluids, 92, p1011-1019.

Browand, F.K., Troutt, T.R. 1980 A note on the spanwise structure in the two-dimensional mixing layer. J. Fluid Mech., 97, p771-781.

Browand, F.K., Plocher, D.A. 1985 Image processing for sediment transport. Proceedings, 21st IAHR Congress.

Brown, G., Roshko, A. 1974 On density effects and large structures in turbulent mixing layers. J. Fluid Mech., 83, p641-671.

Burch, J.M., Tokarski, J.M. 1968 Production of multiple beam fringes from photographic scatters. Opt, Acta., 15, p101.

Cattafesta, III.L.N., Garg, S., Kegerise, M.S., Jones, G.S. 1998 Experiments on compressible flow-induced cavity oscillations. AIAA 1998-2912.

Cho, Y.C. 1989 Digital image velocimetry. Appl. Opt., 28, p740-748.

Chue, S.H. 1975 Pressure probes for fluid measurement. Prog. Aerospace Sci., 16, p147-223.

Cipolla, K.M., Liakopoulos, A., Rockwell, D.O. 1998 Quantitative imaging in proper orthogonal decomposition of flow past a delta wing. J. AIAA, 36, p1247-1255.

Corcos, G.M. 1979 The mixing layer: deterministic models of a turbulent flow. U.C. Berkely, Mech. Eng. Rep. FM-79-2.

Corcos, G.M., Lin, S.J. 1984 The mixing layer: deterministic models of a turbulent flow. Part 2. The origin of the three-dimensional motion. J. Fluid Mech., 139, p67-95.

Courtney, B.B., Stinebring, D.R. 1994 Cavity flow tones in water. J. Acoust. Soc. Am.. 953, p1256-1263.

Covert, E.E. 1970 An approximate calculation for the onset of cavity oscillations. AIAA J., 8, p2189-2194.

Cowen, E.A., Monismith, S.G. 1997 A hybrid digital particle tracking velocimetry technique. Exp. Fluids, 22, p199-211.

Daily, J.W., Lundquist, W.J. 1984 The three dimensional structure in a turbulent mixing layer. 20th Symp. on Combustion, The Combustion Institute Ed.

Dimotakis, P.E., Brown, G.L. 1976 The mixing layer at high Reynolds number. Large-structure dynamics and entrainment. J. Fluid Mech., 78, p535-560.

Disimile, P.J., Toy, N., Savory, E. 1998 Pressure oscillations in a subsonic cavity at yaw. AIAA J., 36, p1141-1148.

Disimile, P.J., Toy, N., Savory, E. 2000 Effect of planform aspect ratio on flow oscillations in rectangular cavities. Trans. ASME, 122, p32-38.

Dix, R.E. 1987 On simulation techniques for the separation of stores from internal installations. SAE Tech. Paper Series 871799.

East, L.F. 1966 Aerodynamically induced resonance in rectangular cavities. J. Sound Vib., 33, p277-287.

Eckert, W.T., Mort, K.W., Jope, J. 1976 Aerodynamic design guidelines and computer program for estimation of subsonic wind tunnel performance. NASA TN D-8243.

Elder, S.A. 1978 Self-excited depth-mode resonance for a wall mounted cavity in turbulent flow. J. Acoust. Soc. Am., 64, p877-890.

Ethembabaoglu, S. 1973 On the fluctuating flow characteristics in the vicinity of gate slots. Ph.D. Thesis, Div. Of Hydraulics Eng., Univ. of Trondheim, Norwegian Inst. of Technology, Norway.

Etoh, T., Takehara, K. 1998 The particle mask correlation method. Proc. 8th Int. Symp. on flow visualisation, Seattle, USA, Sept. 11-14.

Fiedler, H.E., Dziomba, B., Mensing, P., Rösgen, T. 1981 Initiation, evolution and global consequences of coherent structures in turbulent shear flows. Role for coherent structures in modelling turbulence and mixing. Ed. J.Jimenez, Lecture notes in physics. 136, p219-251, Springer-Verlag.

Fincham, A.M., Spedding, G.R. 1997 Low cost, high resolution DPIV measurement of turbulent fluid flow. Exp. Fluids, 23, p449-462.

Fincham, A.M., Delerce, G. 1999 Advanced optimisation of correlation imaging velocimetry algorithms. Proc. 3rd Intl. Workshop on PIV, Santa Barbara, USA, Sept. 16-18 Sept.

Florio, D.Di., Felice, F.Di., Romano, G.P. 2002 Windowing, re-shaping and re-orientation interrogation windows in particle image velocimetry for the investigation of shear flows. Meas. Sci. Technol., 13, p953-962.

Foucaut, J.M., Stanislas, M. 2002 Some considerations on the accuracy and frequency response of some derivative filters applied to particle image velocimetry vector fields. Meas. Sci. Technol., 13, p1058-1071.

Fouras A., Soria, J. 1998 Accuracy of out-of-plane vorticity measurements derived from in–plane velocity field data. Exp. Fluids 25 p409-430.

Franke, M.E., Carr, D.L. 1975 Effect of geometry on open cavity flow-induced pressure oscillations. AIAA 1975-492, Proc. of 2nd AIAA Aeroacoustics Conference.

Frémion, N., Vincent, N., Jacob, M., Robert, G., Louisot, A., Guerrand, S. 2000 Aerodynamic noise radiated by the intercoach spacing and the bogie of a high-speed train. J. Sound Vib., 231, p577-593.

Friesing, H. 1971 Measurement of the drag associated with recessed surfaces: cut-outs of rectangular and elliptical planform. Z.W.B.F.B., 628. (RAE Lib. Trans. 1614 1971).

Fujita, I., Kaizu, T. 1995 Correction method of erroneous vectors in PIV. J. Flow Visualization Image Process., 2, p173-185.

Fukagata, K., Iwamoto, K., Kasagi, N. 2002 Contribution of Reynolds stress distribution to the skin friction in wall-bounded flows. Phys. Fluids, 14, p73-76.

Fung, J.C.H., Hunt, J.C.R., Malik, N.A., Perkins, R.J. 1992 Kinematic simulation of homogeneous turbulence by unsteady random Fourier modes. J. Fluid. Mech., 236, p281-318.

Gaudet, L., Winter, K.G. 1973 Measurements of the drag of some characteristic aircraft excrescences immersed in turbulent boundary layers. RAE Tech. Memo. Aero., 1538. (Also AGARD CP124).

Gawthorpe, R.G. 1978 Aerodynamics in railway engineering. 1-Aerodynamics of trains in the open air. Proc. World Congr. Inst. Mech. Eng. Railway Eng. Int., p7-12.

Gawthorpe, R.G. 1983 Train drag reduction from simple design changes. In Impact of Aerodynamics on Vehicle Design. Ed. Dorgham, p308-341. Inderscience.

Gaylard, A.P., Howlett, A.B. 1994 Assessing drag reduction measures for high-speed trains. Rail Research UK.

Gerrard, J.H., 1966 The mechanics of the formation region of vortices behind bluff bodies. J. Fluid Mech., 25, p401-413.

Ghadder, N.K., Korezak, K.Z., Mikic, B.B., Patera, A.T. 1986 Numerical investigation of incompressible flow in grooved channels. Part 1. Stability and self-sustained oscillations, J. Fluid Mech., 163, p99-127.

Gharib, M., Roshko, A. 1987 The effect of flow oscillations on cavity drag. J. Fluid Mech., 177, p501-530.

Gillies, E.A. 1998 Low-dimensional control of the circular cylinder wake. J. Fluid Mech., 371, p157-178.

Goldman, R.L., Morkovin, M.V., Schumacher, R.N. 1968 Unsteady control surface loads of lifting re-entry vehicles at very high speeds, AIAA J., 6, p44-50.

Goodman, J.W. 1968 Introduction to Fourier Optics. McGraw-Hill.

Grant, I., Owens, E. 1990 Confidence interval estimates in PIV measurements of turbulent flows. Appl. Opt., 29, p1400-1402.

Grant, I. 1994 Selected Papers on PIV; SPIE Milestone Volume MS99, Society of Photo-Optical Instrumentation Engineers, Bellingham, Washington.

Grant, I. 1997 Particle image velocimetry: A review. Proc. Inst. Mech. Engrs., 211 Part C.

Green, R.B., Doolan, C.J., Cannon, R.M. 2000 Measurements of the orthogonal blade-vortex interaction using a particle image velocimetry technique. Exp. Fluids, 29, p369-379.

Guezennec, Y.G., Nagib, H.M. 1985 Documentation of mechanisms leading to net drag reduction in manipulated turbulent boundary layers. AIAA 1985-0519.

Guezennec, Y.G., Kiritsis, N. 1990 Statistical investigation of errors in particle image velocimetry. Exp. Fluids, 10, p138-146.

Gui, L., Merzkirch, W. 1998 Generating arbitrarily sized interrogation windows for correlation-based analysis of particle image velocimetry recordings. Exp. Fluids, 24. p66-69.

Gui, L., Merzkirch, W. 2000 A comparative study of the MQD method and several correlation-based PIV evaluation algorithms. Exp. Fluids, 28, p36-44.

Gursul, I., Lusseyran, D., Rockwell, D. 1990 On interpretation of flow visualization of unsteady shear flows. Exp. Fluids, 9, p257-266.

Hankey, W.L., Shang, J.S. 1980 Analysis of pressure oscillations in an open cavity. AIAA J., 18, p892-898.

Hanson, F.B., Richardson, P.D. 1965 Hot wire measurements in the near wake of a circular cylinder. Brown University Department, W742. (Available from www.brown.edu).

Hanson, F.B., Richardson, P.D. 1968 The near-wake of a circular cylinder in cross flow. J. Basic Eng., 90, p476-483.

Hardin, J.C., Pope, D.S. 1993 Sound generation by flow over a two-dimensional cavity. AIAA 1993-4327.

Hart, D.P. 1999 Super-resolution PIV by recursive local-correlation. VSJ-SPIE International Conference on optical technology and image processing in fluid, thermal, and combustion flow. 1998 Yokohama, Japan, Dec. 6-10.

Hassan, Y.A., Canaan, R.E. 1991 Full-field bubbly flow velocity measurements using a multiframe particle tracking technique. Exp. Fluids, 12, p49-60.

Head, M.R., Ram, V.V. 1971 Simplified presentation of Preston tube calibration. Aeronautical. Quart., 22, p295-300.

Heller, H.H., Holmes, D.G., Covert, E.E. 1971 Flow-induced pressure oscillations in shallow cavities. J. Sound Vib., 184 p545-553.

Heller, H.H., Bliss, D.B. 1975 Aerodynamically induced pressure oscillations in cavities – Physical mechanisms and suppression concepts. AFFDL-TR-74-133.

Heller, H., Delfs, J. 1996 Cavity pressure oscillations: The generating mechanism visualised. J. Sound Vib., 1962, p248-252.

Henderson, J., Badcock, K.J., Richards, B.E. 2001 Understanding subsonic and transonic cavity flows. Aeronautical J., 105, p77-84.

Henk, J.A.M. 1998 Mathematical morphology and its applications to image and signal processing (computational imaging and vision). Kluwer academic.

Hesselink, L. 1988 Digital image processing in flow visualization. Ann. Rev. Fluid Mech., 20, p421-485.

Ho, C.M., Huerre, P. 1984 Perturbed free shear layers. Ann. Rev. Fluid Mech., 16, p365-424.

Höcker, R., Kompenhans,J. 1990 Application of particle image velocimetry to transonic flows. Application of laser techniques to fluid mechanics. Eds., Adrian, R.J., Durao, D.F.G., Durst, F., Maeda, M., Whitelaw, J.H., p415-435. Springer-Verlag.

Holmes, P., Lumley, J., Berkooz, G. 1996 Turbulence, coherent structures, dynamical systems and symmetry. Cambridge University Press.

Howe, M.S. 1975 Contributions to the theory of aerodynamic sound, with application to excess jet noise and the theory of the flute. J. Fluid Mech., 71, p625-673.

Howe, M.S. 1978 A review of the theory of trailing edge noise. J. Sound Vib., 61, p437-465.

Howe, M.S. 1980 The dissipation of sound at an edge. J. Sound Vib.. 70, p407-411.

Howe, M.S. 1995 On the force and moment exerted on a body in an incompressible fluid, with application to rigid bodies and bubbles at high and low Reynolds numbers. Q. J. Mech. Appl. Math., 48, p401-426.

Howe, M.S. 1997 Edge, cavity, and aperture tones at very low Mach number. J. Fluid Mech., 330, p61-84.

Huang, L.S., Ho, C.M. 1990 Small-scale transition in a plane mixing layer. J. Fluid Mech., 210, p475-500.

Huang, H.T., Feidler, H.E., Wang, J.J 1993a Limitation and improvement of PIV. Part I: Limitation of conventional techniques due to deformation of particle image patterns. Exp. Fluids 15, p168-174.

Huang, H.T., Fielder, H.E., Wang, J.J. 1993b Limitation and improvement of PIV Part II: Particle image distortion, a novel technique. Exp. Fluids, 15, p263-273.

Huang, H., Dabiri, D., Gharib, M. 1997 On errors of digital particle image velocimetry. Meas. Sci. Technol., 8, p1427-1440.

Hunt, J.C.R., Abell, C.J., Peterka, J.A., Woo, H. 1978 Kinematical studies of the flows around free or surface mounted obstacles applying topology to flow visualisation. J. Fluid Mech., 86, p620-632.

Hussain, A.K.M.F., Clark, A.R. 1977 Upstream influence on the near field plane of a plane turbulent jet. Phys. Fluids, 20, p1416-1426.

Inagaki, M., Murata, O., Kondoh, T. 2002 Numerical prediction of fluid-resonant oscillation at low mach number. AIAA J., 40, p1822-1829.

Ishikawa, M., Yamamoto, F., Murai, Y., Iguchi, M., Wada, A. 1997 A novel PIV algorithm using velocity gradient tensor. Proc. 2nd Int. Workshop on PIV, Fukui, Japan. July 8-11.

Ishikawa, M., Murai, Y., Wada, A., Iguchi, M., Okamoto, K., Yamamoto, F. 2000 A novel algorithm for particle tracking velocimetry using the velocity gradient tensor. Exp. Fluids, 29, p519-531.

Jacobs, J.H. 1990 Quantifying the effects of suppression devices on acoustic levels within open cavities. AIAA 1990-4017.

Jambunathan, K., Ju, X.Y., Dobbins, B.N., Ashforth-Frost, S. 1995 An improved cross correlation technique for particle image velocimetry. Meas. Sci. Technol., 6, p507-514.

Jimenez, J., Martinez-Val, R., Rebollo, M. 1979 On the origin and evolution of three-dimensional effects in the mixing layer. DA-ERO 79-G-079. Universidad Politecnica de Madrid. AD-A096007.

Jimenez, J. 1983 A spanwise structure in the plane shear layer. J. Fluid Mech., 132, p319-336.

Jimenez, J., Cogollos, M., Bernal, L.P. 1985 A perspective view of the plane mixing layer. J. Fluid Mech., 152, p125-143.

Johnston, T. 2001 Private communication. AEA Technology Rail.

Kaufman, L.G., Maciulaitis, A., Clark, R.L. 1983 Mach 0.6 to 3.0 flows over rectangular cavities. Air Force Wright Aero Lab. Report, AFWAL-TR-82-3112.

Keane, R., Adrian, R. 1990 Optimization of particle image velocimeters. Part I: Double pulsed systems. Meas. Sci, Technol., 1, p1202-1220.

Keane, R.D., Adrian, R.J. 1991 Optimization of particle image velocimeters: II. Multiple pulsed systems. Meas. Sci. Technol., 2, p963-974.

Keane, R.D., Adrian, R.J. 1992 Theory of cross-correlation analysis of PIV images. J. Appl. Sci. Res., 49, p191-215.

Keane, R.D., Adrian, R.J. 1993 Theory of cross-correlation of PIV images. Nieuwstadt FTM. Flow visualization and image analysis, p1-25. Dordrecht: Kluwer Academic.

Keane, R.D., Adrian, R.J., Zhang, Y. 1995 Super-resolution particle image velocimetry. Meas. Sci. Technol., 6, p754-768.

Kegerise, M.A., Spina, E.F., Cattafesta, L.N. 1999 An experimental investigation of flow-induced cavity oscillations. AIAA 1999-3705.

Kegerise, M.A., Cattafesta, L.N., Ha, C. 2002 Adaptive identification and control of flow-induced cavity oscillations. AIAA 2002-3158.

Kerho, M. 2002 Active reduction of skin friction drag using low-speed streak control. AIAA 2002-0271, 40th Aerospace Sciences Meeting & Exhibit, 14-17 Jan, Reno.

King, J.L., Boyle, P., Ogle, J.B. 1958 Instability in slotted wall tunnels. J. Fluid Mech., p283-305.

Knisely, C., Rockwell, D.O. 1979 The organized nature of flow impingement upon a corner. J. Fluid Mech., 93, p413-432.

Knisely, C., Rockwell, D.O. 1982 Self-sustained low-frequency components in an impinging shear layer. J. Fluid Mech., 116, p157-186.

Kobayashi, T., Saga, T., Segawa, S. 1989 Multipoint velocity measurement for unsteady flow field by digital image processing. Flow Visualization, Ed. R.Reznieck, p197-202. Hemisphere.

Komerath, N.M., Ahuja, K.K., Chambers, F.W. 1987 Prediction and measurement of flows over cavities – A survey. AIAA 1987-0166, 25th Aerospace Sciences Meeting, Reno, Jan 12-15.

Konrad, J.H. 1976 An experimental investigation of mixing in two-dimensional turbulent shear flows with application to diffusion limited chemical reactions. Tech. Rep., CIT-8-PU.

Kook, H., Mongeau, L., Zorea, S.I., Brown, D.V. 1997 Analysis of the interior pressure oscillations induced by flow over vehicle openings. Noise Control Eng. Journal, 45, p223-234.

Kook, H., Mongeau, L. 2002 Analysis of the periodic pressure fluctuations induced by flow over a cavity. J. Sound Vib., 251, p823-846.

Kriesels, P.C., Peters, M.C.A.M., Hirschberg, A., Wijnands, A.P.J., Iafrati, A., Riccardi, G., Piva, R., and Bruggeman, J.C. 1995 High amplitude vortex induced pulsations in gas transport systems. J. Sound Vib., 184, p343-368.

Krishnamurty, K. 1955 Sound Radiation From Rectangular Cutouts. NACA TN 3487.

Kuethe, A.M., Chow, C.Y. 1998 Foundations of aerodynamics. Bases of aerodynamic design. Wiley. Fifth Edition.

Kuo, G.H., Huang, S.H. 2001 Influence of flow path modification on oscillation of cavity shear layer. Exp. Fluids, 31, p162-178.

Labonté, G. 1999 A new neural network for particle-tracking velocimetry. Exp. Fluids, 26, p340-346.

Lasheras, J.C., Cho, J.S., Maxworthy, T. 1986 On the origin and evolution of streamwise vortical structures in a plane, free shear layer. J. Fluid Mech., 172, p231-258.

Lecordier, B., Lecordier, J.C., Trinite, M. 1999 Iterative sub-pixel algorithm for the cross-correlation PIV measurement. Proc. 3rd Int. Conf. on PIV, Santa Barbara, USA, Sept. 16-18 Sept.

Lecuona, A., Nogueira, J.I., Rodriguez, P.A. 1997 Flowfield vorticity calculation using PIV data. Proc. 2nd Int. Workshop on PIV, Fukui, Japan, July 8-11.

Lele, S.K. 1997 Computational aeroacoustics: A review. AIAA 1997-0018.

Lepicovsky, J., Ahuja, K.K. 1985 Experimental results on edge-tone oscillations in high-speed subsonic jets. AIAA J., 23, p1463-1468.

Liu, L.C., Landreth, C.C., Adrian, R. J., Hanratty, T. J. 1991 High resolution measurement of turbulent structure in a channel with particle image velocimetry. Exp. Fluids 10, p301-312.

Lin, J.C., Rockwell, D. 2001 Organised oscillations of initially turbulent flow past a cavity. AIAA J., 39, p1139-1151.

Lin, J.C., Rockwell, D. 2001 Oscillations of a turbulent jet incident upon an edge. J. Fluids and Structures, 15, p751-829.

Lourenco, L., Krothapalli, A. 1995 On the accuracy of velocity and vorticity measurements with PIV. Exp. Fluids, 27 p107-116.

Maas, H.G., Gruen, A., Papantoniou, D. 1993 Particle tracking velocimetry in three-dimensional flows – part 1. Photogrammetric determination of particle coordinates. Exp. Fluids, 15, p133-146.

Mabey, D.G. 1970 Flow unsteadiness and model vibration in wind tunnels at subsonic and transonic speeds. Royal Aircraft Establishment Technical Report RAE TR 70184.

Maekawa, T., Mizuno, S. 1967 Flow around the separation point and in the near-wake of a circular cylinder. Phy. Fluids, 10, p5184-5186.

Martin, W.W., Naudascher, E.N., Padmanabhon, M. 1975 Fluid-dynamic excitation involving flow instability. Proc. ASCE, J. Hydraulics Div., HY6, p681-698.

Maruta, Y., Matsuo, J. 2000 Sources of self excited tone radiated by flows around semi-cylindrical cavity. AIAA 2000-1902, Proc. of 6th AIAA/CEAS Aeroacoustics Conference.

Maull, D.J., East, L.F. 1963 Three-dimensional flow in cavities. J. Fluid Mech., 16, p620-632.

Maurer, O.F. 1976 Device to reduce flow-induced pressure oscillations in open cavities. U.S. Patent 3-934-846.

McGregor, O.W., White, R.A. 1970 Drag of rectangular cavities in supersonic and transonic flow including the effects of cavity resonance. AIAA J., 8, p1959-1964.

Melling, A. 1997 Tracer particles and seeding for particle image velocimetry. Meas. Sci. Technol., 8, p1406-1416.

Metcalfe, R.W., Orszag, S.A., Brachet, M.E., Menon, S., Riley, J.J. 1987 Secondary instability of a temporally growing mixing layer. J. Fluid Mech., 184, p207-243.

Meyers, J.F. 1991 Generation of particles and seeding. Von Karmen Institute for Fluid Dynamics Lecture Series, 1991-05.

Michalke, A. 1965 On spatially growing disturbances in an inviscid shear layer. J. Fluid Mech., 23, p521-544.

Miksad, R.W. 1972 Experiments on the nonlinear stages of free-shear-layer transition. J. Fluid Mech., 56, p695-719.

Moore, C.J. 1977 The role of shear-layer instability waves in jet exhaust noise. J. Fluid Mech., 80, p321-367.

Najm, H.N., Ghoniem, A.F. 1991 Numerical simulation of the convective instability in a dump combustor. AIAA J., 29, p911-919.

Nelder, J.A., Meade, R. 1965 A simplex method for function minimization. Computer Journal, 7, p308-313.

Nelson, P.A., Halliwell, N.A., Doak, P.E. 1983 Fluid Dynamics of a fluid excited resonance, Part II: Flow acoustic interaction. J Sound Vib., 91, p375-402.

Nishino, K., Kasagi, N., Hirata, M. 1989 Three-dimensional particle tracking velocimetry based on automated digital image processing. J. Fluid Eng., 111, p384-394.

Noger, C., Patrat, J.C., Peube, J., Peube, J.L. 2000 Aeroacoustical study of the TGV pantograph recess. J Sound Vib., 231, p563-575.

Nogueira, J., Lecuona, A., Rodriguez, P.A. 1997 Data validation, false vectors correction and derived magnitudes calculation on PIV data. Meas. Sci. Technol., 8, p1493-1501.

Nogueira, J., Lecuona, A., Rodriguez, P.A. 1999 Local field correction PIV, on the increase of accuracy of digital PIV systems. Exp. Fluids, 27, p107-116.

Nogueria, J., Lecuona, A., Rodriguez, P.A., 2001a Identification of a new source of peak locking, analysis and its removal in conventional and super-resolution PIV techniques. Exp. Fluids, 30, p309-316.

Nogueira, J., Lecuona, A., Rodriguez, P.A. 2001b Local field correction PIV, implemented by means of simple algorithms, and Multigrid versions. Meas. Sci. Technol., 12, p1911-1921.

Nussbaumer, H.J. 1982 Fast Fourier transform and convolution algorithms. Springer-Verlag.

Nygaard, K.J., Glezer, A. 1990 Core instability of the spanwise vortices in a plane mixing layer. Phys. Fluids, 2, p461-464.

Nygaard, K.J., Glezer, A. 1991 Evolution of streamwise vortices and generation of small-scale motion in a plane mixing layer. J. Fluid Mech., 231, p257-301.

Ohmi, K., Dao Hai Lam, 1998 New particle tracking PIV using an improved relaxation method. Proc. 8th Int. Symp. on flow visualisation, Seattle, USA, Sept. 11-14.

Ohmi, K., Li, H. 1999 Particle tracking velocimetry by combined use of the Moravec operator and the relaxation algorithm. Proc. 2nd Pacific Symp. on flow visualisation.

Ohmi, K., Hang-Yu, Li. 2000 Particle-tracking velocimetry with new algorithms. Meas. Sci. Technol., 11, p603-616.

Ohyama, R., Takagi, T., Tsukji, T., Nakanishi, S., Kaneko, K. 1993 Particle tracking technique and velocity measurement of visualized flow fields by means of genetic algorithm. J. Visualization Soc. Japan, 13, p35-38. (English translation).

Okamoto, K., Hassan, Y.A., Schmidl, W.D. 1995 New tracking algorithm for particle image velocimetry. Exp. Fluids, 19, p342-347.

Okamoto, K., Nishio, S., Saga, T., Kobayashi, T. 2000 Standard images for particle image velocimetry. Meas. Sci. Technol., 11, p685-691.

Pankhurst, D.W., Bryer, R.C. 1971 Pressure-probe methods for determining wind speed and flow direction. Her Majesty's Stationary Office, London.

Parmentier, E.M., Greenberg, R.A. 1973 Supersonic flow aerodynamic window. AIAA J., 17, p216-219.

Patel, V.C. 1965 Calibration of the Preston tube and limitations on its use in pressure gradients. J. Fluid Mech., 23, p185-208.

Pereira, J.C.F., Sousa, J.M.M. 1993 Finite volume calculations of self-sustained oscillations in a grooved channel. J. Comp. Physics, 106, p19-29.

Pereira, J.C.F., Sousa, J.M.M. 1994 influence of impingement edge geometry on cavity flow oscillations. AIAA J., 32, p1737-1740.

Pereira, J.C.F., Sousa, J.M.M. 1995 Experimental and numerical investigation of flow oscillations in a rectangular cavity. J. Fluids Eng., 117, p68-74.

Peters, J.L. 1983 Aerodynamics of very high speed trains and maglev vehicles: State of the art and future potential. Int. J. Vehicle Design, special publication.

Plentovich, E.B. 1990 Three-dimensional cavity flow fields at subsonic and transonic speeds. NASA TM-4209.

Plentovich, E.B., Stallings, R.L., Tracey, M.B. 1993 Experimental cavity pressure measurements at subsonic and transonic speeds, static-pressure results. NASA TP-3358.

Plumbee, H.E., Gibson, J.S., Lassiter, L.W. 1962 A theoretical and experimental investigation of the acoustic response of cavities in an aerodynamic flow. WADD-TR-61-75.

Powell, A. 1961 On the edgetone. J. Acous. Soc. Am., 33, p395.

Prandtl, L., Tietjens, O. 1934 Applied Hydro and Aerodynamcis. Dover.

Prasad, AK., Adrian, RJ., Landreth, CC., Offutt, PW. 1992 Effect of resolution on the speed and accuracy of particle image velocimetry interrogation. Exp. Fluids, 13, p105-116.

Prasad, A.K. 2000 Stereoscopic particle image velocimetry. Exp. Fluids, 29, p103-116.

Press, W.H., Flannery, B.P., Teukolsky, S.A., Vetterling, W.T. 1993 Numerical recipes in C. Cambridge University Press. Second Edition.

Preston, J.H. 1954 The determination of turbulent skin friction by means of pitot tubes. J. Roy. Aeronaut. Soc., 58, p109-121.

Pulliam, W.J., Marshakov, A., Tyll, J.S., Schetz, J.A., Marchman, J.F. 1996 Aerodynamics of the AMT Maglev train design. AIAA 1996-2476.

Rae, W.H., Pope, A. 1984 Low-speed wind tunnel testing. Wiley. Second Edition.

Raffel, M., Leitl, B., Kompenhans, J. 1992 Data validation for particle image velocimetry. Proc. 6th Int. Symp. on Appl. of Laser Techniques to Fluid Mechanics, Lisbon, Portugal, July 20-23.

Raffel, M., Kompenhans, J. 1996 Post processing: data validation. Von Karmen Institute for Fluid Dynamics Lecture Series, 1996-03.

Raffel, M., Willert, C., Kompenhans, J. 1998 Particle image velocimetry: A practical guide. p124-125. Springer.

Rajaee, M., Karlsson, K.F., Sirovich, L. 1994 Low-dimensional description of free-shear-flow coherent structures and their dynamical behaviour. J. Fluid Mech., 258, p1-28.

Rockwell, D. 1977 Prediction of oscillation frequencies for unstable flow past cavities. J. Fluids Eng., 99, p294-300.

Rockwell, D., Naudascher, E. 1978 Review – Self-sustaining oscillations of flow past cavities. J. Fluids Eng., 100, p152-165.

Rockwell, D.O., Naudascher, E. 1979 Self-sustained oscillations of impinging free shear layers. Ann. Rev. Fluid Mech., 11, p67-94.

Rockwell, D., Knisely, C. 1980 Observations of the three-dimensional nature of unstable flow past a cavity. Phys. Fluids, 23, p425-431.

Rockwell, D. 1983 Invited Lecture: Oscillations of impinging shear layers. AIAA J., 21, p645-664.

Rockwell, D. 1998 Vortex-body interactions. Ann. Rev. of Fluid Mech., 30, p199-229.

Roshko, A. 1955 Some measurements of flow in a rectangular cutout. NACA TN 3488.

Roshko, A., Fiszdon, W. 1969 On the persistence of transition in the near-wake. Problems in Hydrodynamics and Continuum Mechanics, Philadelphia, SIAM, p606-616.

Roshko, A. 1976 Structure of turbulent shear flows: A new look. AIAA J., 14, p1349-1357.

Rossiter, J.E. 1962 The effect of cavities on the buffeting of aircraft. Royal Aircraft Establishment Tech. Mem., 754.

Rossiter, J.E. 1964 Wind tunnel experiments on the flow over rectangular cavities at subsonic and transonic speeds. Royal Aircraft Establishment ARC R&M 3438.

Rossiter, J.E. 1966 Wind tunnel experiments on the flow over rectangular cavities at subsonic and transonic speeds. Royal Aircraft Establishment ARC R&M 3436.

Rowley, C.W., Colonius, T., Murray, R.M. 2000 POD based models of self-sustained oscillations in the flow past an open cavity. AIAA 2000-1969.

Sagawa, A., Ono, S., Hidetoshi, H. 1999 Aeroacoustic noise generated from high-speed trains in Japan. AIAA 1999-1894, Proc. of 5th AIAA/CEAS Aeroacoustics Conference.

Sarno, R.L., Franke, M.E. 1994 Suppression of flow-induced pressure oscillations in cavities. J. Aircraft, 31, p90-96.

Sarohia, V. 1977 Experimental investigations of oscillations in flows over shallow cavities. AIAA J., 7, p984-991.

Saunders, J.W., Watkins, S., Cassar, R.J. 1993 Vortex optimisation of slotted tops and cavities of two different open rail wagons. J. Wind Eng. Inst. Aero., 49, p421-430.

Savory, E., Toy, N., Disimile, P.J., DiMicco, R.G. 1993 The drag of three-dimensional rectangular cavities. J. Appl. Sci. Res., 50, p325-346.

Scarano, F., Riethmuller, M.L. 1999 Iterative multigrid approach in PIV image processing with discrete window offset. Exp. Fluids, 26, p513-523.

Scarano, F., Riethmuller, M.L. 2000 Advances in iterative multigrid PIV image processing. Exp. Fluids, 29, p51-60.

Schetz, J.A. 2001 Aerodynamics of high-speed trains. Ann. Rev. Fluid. Mech., 33, p371-414.

Shan, J., Gharib, M. 1998 Super-resolution particle tracking velocimetry. Proc. 8th Int. Symp. on flow visualisation, Seattle, USA, Sept. 11-14.

Shen, P. 1979 Supersonic flow over a deep cavity for a laser application. AIAA J., 17, p216-219.

Simpkins, P.G., Dudderar, T.D. 1978 Laser speckle measurement of transient Benard convection. J. Fluid Mech., 89, p665-671.

Sinha, S.N., Gupta, A.K., Oberai, M.M. 1982 Laminar separating flow over backsteps and cavities. Part II: Cavities. AIAA J., 20, p370-375.

Sinha, S., Kuhlman, P. 1992 Investigating the use of stereoscopic particle streak velocimetry for estimating the three-dimensional vorticity field. Exp. Fluids, 12, p377-384.

Sockel, H. 1996 The aerodynamics of trains. In the handbook of fluid dynamics and fluid machinery. Eds., Schetz, J.A., Fuhs, A.E., p1721-1741. Wiley.

Song, X.Q., Yamamoto, F., Iguchi, M., Murai, Y. 1999 A new tracking algorithm of PIV and removal of spurious vectors using Delaunay Tessellation. Exp. Fluids, 26, p371-380.

Soundhaus, C. 1894 Ann. Phys., 91, p214-240.

Soria, J. 1996 An investigation of the near wake of a circular cylinder using a video-based digital cross-correlation particle image velocimetry technique. Exp. Therm. Fluid Sci., 12, p221-233.

Soria, J. 2002 Private communication.

Sparrow, E.M., Vemuri, S.B., Kadle, D.S. 1983 Enhanced and local heat transfer, pressure drop, and flow visualisation for arrays of block like electronic components. Int. J. Heat and Mass Transfer, 26, p689-699.

Spedding, G., Rignot, E. 1993 Performance analysis and application of grid interpolation techniques for fluid flows. Exp. Fluids, 15, p417-430.

Spee, B.M. 1966 Wind tunnel experiments on unsteady cavity flows at high subsonic speeds. AGARD CP No.4, p947-974.

Srinivasan, G.R. 2000 Acoustics and unsteady flow of telescope cavity in an airplane. J. Aircraft, 37, p274-281.

Stanislas, M., Kompenhans, J., Westerweel, J. 1999 EUROPIV: A cooperative action to apply Particle Image Velocimetry to problems of industrial interest in preparation. Dordrecht: Kluwer.

Stanislas, M., Kompenhans, J., Westerweel, J. 2000 Particle image velocimetry: Progress towards industrial application (fluid mechanics and its applications). Kluwer Academic.

Stearns, S.D., Hush, D.R. 1990 Digital signal analysis. Prentice Hall.

Stitou, A., Rirthmuller, M.L. 2001a Extension of PIV to super resolution using PTV. Meas. Sci. Technol., 12, p1398-1403.

Stitou, A., Riethmuller, M.L. 2001b Assessment of a hybrid PIV-PTV method. Proc. 4th Int. Symp. on PIV, Göttingen, Germany, Sept. 17-19.

Sutton, G.W. 1969 Effect of turbulent fluctuations in an optically active fluid medium. AIAA J., 7, p1737-1743.

Takakura, Y., Higashino, F., Yoshizawa, T., Ogawa, S. 1996 Numerical study on unsteady supersonic cavity flows. AIAA 1996-2092.

Takaishi, T., Zenda, Y., Shimizu, Y. 1998 Study of the aeroacoustic noise from Shinkansen with mirror image models. Internal Report. Railway Technical Research Institute, Japan.

Tam, C.K.W. 1976 The acoustic modes of a two-dimensional rectangular cavity. J. Sound Vib., 49, p353-364.

Tam, C.K.W., Block, P.J.W. 1978 On the tones and pressure oscillations induced by flows over rectangular cavities. J. Fluid Mech., 89, p373-399.

Tam, C.K.W., Pastouchenko, N. 2001 Gap tones. AIAA J., 39, p1442-1448.

Tan, S., Hart, D.P. 2001 A novel ultra-fast and accurate particle displacement measurement technique using optical diffraction. Proc. 4th Int. Symp. on PIV, Göttingen, Germany, Sept. 17-19.

Tanner, C.S. 1984 Shuttle cargo bay vent noise and its effect on generic payload specifications and testing Methods. AIAA 1984-2352.

Toebes, G.H., Ramamurthy, A.S. 1967 Fluid elastic forces on circular cylinders. J. Eng. Mech., 93, p5627-5637.

Toebes, G.H. 1969 The unsteady flow and wake near an oscillating cylinder. J. Basic Eng., 91, p493-505.

Tracey, M.B., Plentovich, E.B. 1997 Cavity unsteady-pressure measurements at subsonic and transonic speeds. NASA TP-3669.

Udrea, D.D, Bryanston-Cross, P.J.,Lee, W.K., Funes-Gallanzi, M. 1996 Two sub-pixel processing algorithms for high accuracy particle centre estimation in low seeding density particle image velocimetry. Optics & Lasers Tech., 28, p389-396.

Uemura, T., Yamamoto, F., Ohmi, K. 1989 A high-speed algorithm of image analysis for real time measurement of a two-dimensional velocity distribution. Flow visualization, ASME FED-85, p129-134.

Utami, T., Blackwelder, R.F. 1991 A cross-correlation technique for velocity field extraction from particulate visualization. Exp. Fluids 10, p213-223.

Vakili, A.D., Cooper, G.C., Schatt, D.E. 1993 Effect of upstream mass injection on cavity flow aeroacoustics. Exp. Heat Transfer, Fluid Mech. Thermo., 1, p1157-1164.

Vakili, A.D., Gauthier, C. 1994 Control of cavity flow by upstream mass-injection. J. Aircraft, 31, p169-174.

Vogt, A., Reichel, F., Kompenhans, J. 1996 A compact and simple all optical evaluation method for PIV recordings, Developments in Laser techniques and applications to fluid mechanics. Ed. R.J. Adrian et al., p423-437. Springer Verlag.

Walpole, R., Meyers, R., Myers, S. 1998 Probability and statistics for engineers and scientists. Prentice Hall.

Werlé, H. 1972 Flow around a tube array. Revue Francaise de Mecanique, 41, p7-19. (results in English from Zdravkovich. 1997).

Wernet, M., Pline, A. 1993 Particle displacement tracking technique and Cramer-Rao lower bound error in centroid estimates from CCD imagery. Exp. Fluids, 15, p295-307.

Westerweel, J. 1993a Digital particle image velocimetry-theory and application. PhD Thesis University of Delft.

Westerweel, J. 1993b Analysis of PIV interrogation with low pixel resolution. p624-635 of: Cha, S.S., Trolinger, J.D. 1993 Optical diagnostics in fluid and thermal flow. Proc. SPIE-2005, San Diego USA, July.

Westerweel, J. 1994 Efficient detection of spurious vectors in particle image velocimetry data. Exp. Fluids 16, p236-247.

Westerweel, J. 1997a Fundamental of digital particle image velocimetry. Meas. Sci. Technol., 8, p1379-1392.

Westerweel, J., Dabiri, D., Gharib, M. 1997b The effect of discrete window offset on the accuracy of cross-correlation analysis of digital PIV recordings. Exp. Fluids, 23, p20-28.

Westerweel, 1999. Effect of Sensor Geometry on the Performance of PIV interrogation. Int. Sym. On Appl. Laser Tech.

Willert, C., Gharib, M. 1991 Digital particle image velocimetry. Exp. Fluids 10, p181-193.

Woolley, J.P., Karamcheti, K. 1974 Role of jet stability in edgetone generation. AIAA J., 12, p1457-1458.

Wygnanski, I., Oster, D., Fiedler, D., Dziomba, B. 1979 On the perseverance of a quasi two-dimensional eddy-structure in a turbulent mixing layer. J. Fluid Mech., 92, p1-16.

Yamamoto, F., Wada, A., Iguchi, M., Ishikawa, M. 1996 Discussion of the cross-correlation methods for PIV. J. Flow Visualization Image Process., 3, p65-78.

Yang, W.J., 2001 Handbook of flow visualization. Permagon

Yokoi, Y., Kamemoto, K. 1993 Initial stage of a three-dimensional vortex structure existing in a two-dimensional boundary layer separated flow. JSME Int. J.. B36, p201-207.

Young, A.D., Maas, J.N. 1936 The behaviour of a pitot tube in a transverse total pressure gradient. Brit. ARC, R&M 1770.

Young, A.D., Paterson, J.H. 1981 Aircraft excrescence drag. NATO AGARD-264, J.L. Jones Ed.

Zdravkovich, M.M. 1997 Flow around circular cylinders. Vol 1: Fundamentals. Oxford Science.

Zhang, X., Rona, A., Edwards, J.A. 1998 An observation of pressure waves around a shallow cavity. J. Sound Vib., 214, p771-778.

Zhang, X., Chen, X.X., Rona, A. 1999 Attenuation of cavity flow oscillation through leading edge flow control. J. Sound Vib., 221, p23-47.

Ziada, S., Rockwell, D. 1982a Vortex-leading edge interaction. J. Fluid Mech., 118, p79-107.

Ziada, S., Rockwell, D. 1982b Oscillations of an unstable mixing layer impinging upon a wedge. J. Fluid Mech., 124, p307-334.

Zimmer, L., Buchlin, J.M., Riethmuller, M.L. 1999 Particle tracking velocimetry and sizing: application to liquid sprays. Proc. 3rd Intl. Workshop on PIV, Santa Barbara, USA, Sept. 16-18 Sept.

APPENDIX A: A DESCRIPTION OF THE TEST FACILITIES.

This appendix includes a brief description of the 'Handley Page' wind tunnel (***HPT***) used to conduct the pressure tests recorded for this study. Also included is a description of the 'Anatomy Building' wind tunnel (***AT***), which was used for additional pressure measurement and extensive PIV measurement. Because of the locality and accessibility of the 'Anatomy building' wind tunnel it was possible to more rigorously determine the flow characteristics expected of this facility.

The Handley Page tunnel

The 'Handley-Page' low-speed wind tunnel is an atmospheric-pressure closed-return type with a 2.13 x 1.61 m octagonal working section that has a maximum operating speed of 61m/s. A plan view of this facility is shown in figure A1. Measurements included in Rae et al. 1984 indicate a turbulence intensity value of approximately 0.6% for the ***HPT***.

The tunnel speed was set using the difference in static pressure readings between the settling chamber and the working section. Thus factoring in the correction coefficient the tunnel velocity was to be found using equation A1.

$$U = \sqrt{\frac{\Delta hRTK}{(Pb \times 5.1)}} \qquad [A1]$$

where,

Δh: the difference in mmh_2O of the static measurements in the settling chamber and working section respectively.

R: the gas constant ($287m^2/s^2$ K for air).

T: temperature in K.

K: tunnel correction.

Pb: Barometric pressure measured in mB.

This equation uses the appropriate measuring devices accessible in the wind tunnel vicinity.

The Anatomy building tunnel

The 'Anatomy building' low-speed wind tunnel is an atmospheric-pressure closed-return type with a 1.15 x 0.85 m octagonal working section that has a maximum operating speed of 33m/s. A plan view of this facility is shown in figure A2.

For the purposes of this study it is appropriate to quantify the turbulence intensity present in the ***AT*** working section. This was conducted using a hot-wire probe, the turbulence sphere technique and the PIV system. Because the hot-wire system used here has been included in other comparative studies in this report it is now briefly mentioned.

The hot-wire measurements were made using a TSI IFA-300 constant temperature anemometer system using DANTEC P61 cross-wire probes. The probes used 5μm diameter plated tungsten wires with a length-to-diameter ratio of 250. The measuring volume of each probe was approximately 0.8mm in diameter and 0.5mm in height. The probe was calibrated in a special vertical flow wind tunnel dedicated to this purpose. During calibration, the probe was rotated in 3-degree increments through ±30 degrees in the plane of the sensor wires to determine yaw sensitivity.

Estimates from the turbulent sphere technique are taken to estimate the whole test-section. The hot-wire probe was mounted on a traverse and as such measurements were made over 18 different positions. In each instance the period of acquisition corresponded to four or five circuits of the tunnel. The PIV system accumulated volume averaged results over a number of samples (total sample length > 400*400). The spatially averaged results are presented at this time.

Using a number of screen configurations a profile of the test-section turbulence intensity was constructed, this data is shown in table A1. For completeness some results from the turbulence sphere are shown also in figure A3. The flow resistance of the wire screens used are proportional to the square of the local flow speed and as such the decision was made to limit the number of screens in any given arrangement to two. Using more and/or additional devices for guiding the flow would impose a static pressure loss that could not be balanced by an increase in motor power (for the freestream setting in this work). From the accumulated data it appears that the desired scenario is to use both screens 1 and 2 such that a turbulence intensity value of

approximately 0.22% is reached. To ensure good repeatability between tests runs each screen was tightened and cleaned regularly.

Using this configuration a study of the static pressure gradient in the test-section was made at several heights and locations. The definition of the X-Y-Z coordinate system used here is noted in figure A2. Figures A4 and A5 indicate the static pressure gradient associated with the flow through the test section for a particular Y elevation and figure A6 illustrates the gradient measured in the Y-Z plane at different X stations. In each instance the expected location of the cut-out on the wing model is indicated using dashed lines. It is typically not good practice to measure the static pressure through the test-section using wall mounted probes. However, these probes were inserted into the test-section wall for the purpose of this study and additional care was taken to smooth the wall on this side. These measurements are only included to complement the pressure measurements made using a pitot-static tube traversed through the test-section.

The static pressure gradient through the test-section shows nothing unexpected in either the X-Y or Y-Z planes. In the longitudinal direction (X-Y plane) it appears that the insert of corner fillets have been carefully used to control the horizontal buoyancy. It can therefore be expected that there will be a minimal interaction between the pressure gradient caused by the model and that of the clean test-section. Effects caused by the lateral boundaries are therefore minimized. The results in the Y-Z plane indicate that there is good flow uniformity in this direction also. There profile also indicates that there will be a uniform spanwise distribution of lift experienced on the flap assembly. The full data ensemble was made up of traverse readings taken at Y-heights (for the X-Y plane) of 250, 350, 450, 550,650 mm and X-ordinates (for the X-Z plane) of 500, 720, 870, 1000, 1230 and 1380mm. No abrupt changes in static pressure gradient were observed at these locations.

A measurement of the flow angularity in the X-Y and Y-Z planes into the test-section required careful orientation calibration of the hot-wire probe on the traverse. In this instance the error margin can only be expected to be $\pm 2^{\circ}$ although the results are mentioned here for completeness. Using screens 1 and 2 with a freestream speed of 28m/s the flow angle in the X-Y plane (for Z=0mm) was measured at 0.0°, which indicates good parallel flow. In the Y-Z plane (at X=720mm) the flow angle measured

89.5°, once again indicating flow parallel to the solid boundaries. Rotating the probe head 90° and resampling the flowfield yielded the final value of 0.6° for the X-Z plane. The period of acquisition corresponded to five tunnel circuits while the maximum standard deviation equated to less than 1.0°.

A measurement of the static pressure through the first diffuser and the first corner turning vanes indicate that both the length and the angle of the diffuser are not ideal for freestream speeds greater than 20m/s. The solution to this problem is to replace the constant area second leg with another diffuser section and/or to realign the angle of the turning vanes through the first corner for more efficient turning, Eckert et al. 1976. There was no possibility of amending these problems for the current study. The problems associated with this part of the tunnel will manifest themselves as an increase power demand on the fan motor and slight degradation of the tunnel flow quality. This explains why using no screens in the configuration of the tunnel incurs a turbulence intensity of approximately 0.45%, while the Y-Z and X-Z flow angles into the test-section are 89.5°±2° and 0.6°±2° respectively.

The tunnel speed was set using the difference in static pressure readings between the settling chamber and the working section (appropriate for the solid blockage present), as already shown in shown in equation A1. For the screen configuration used $K = 1.12$.

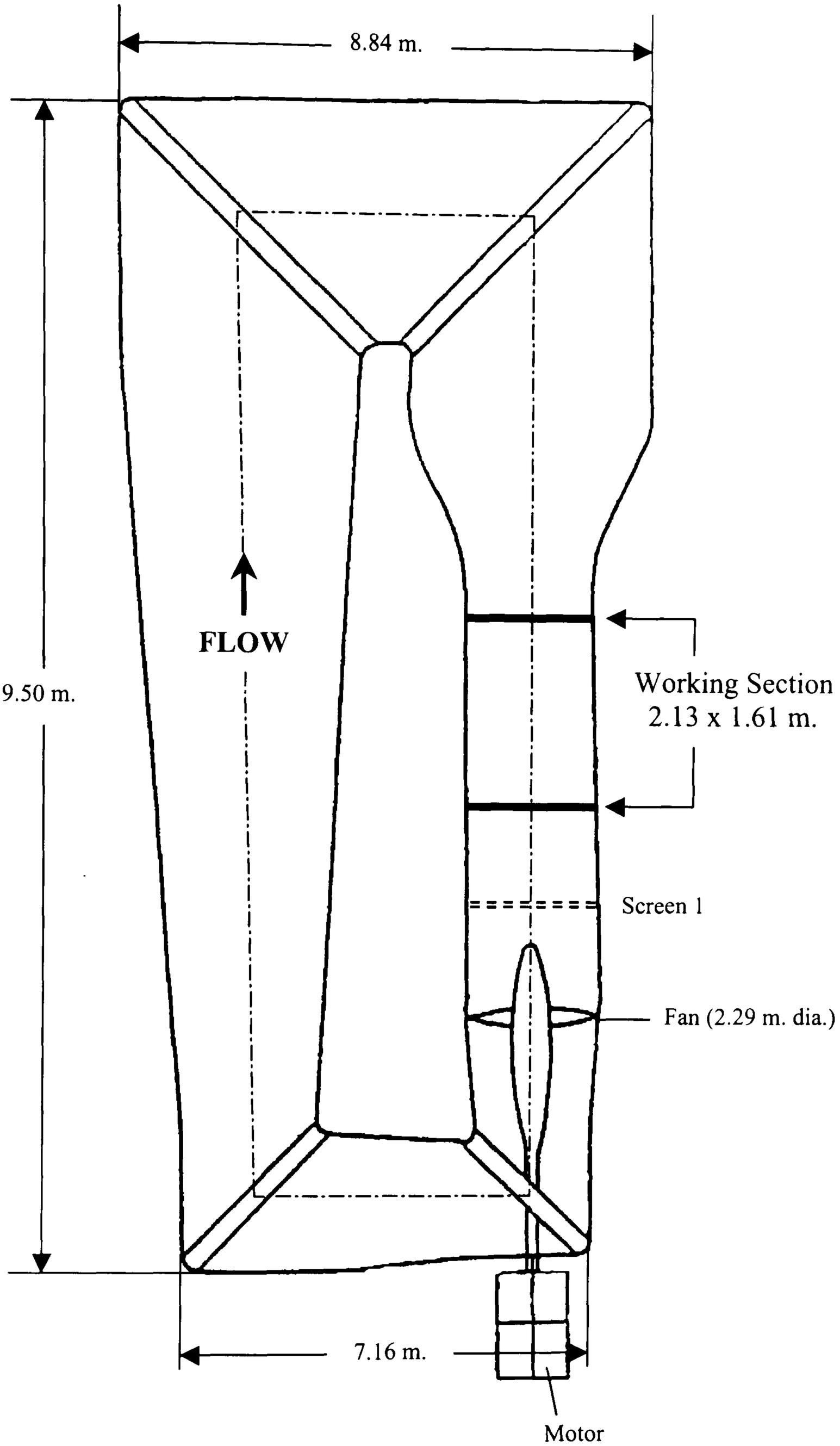

Figure A1. Plan view of the Glasgow University 'Handley Page' 2.13m x 1.61 m wind tunnel (***HPT***).

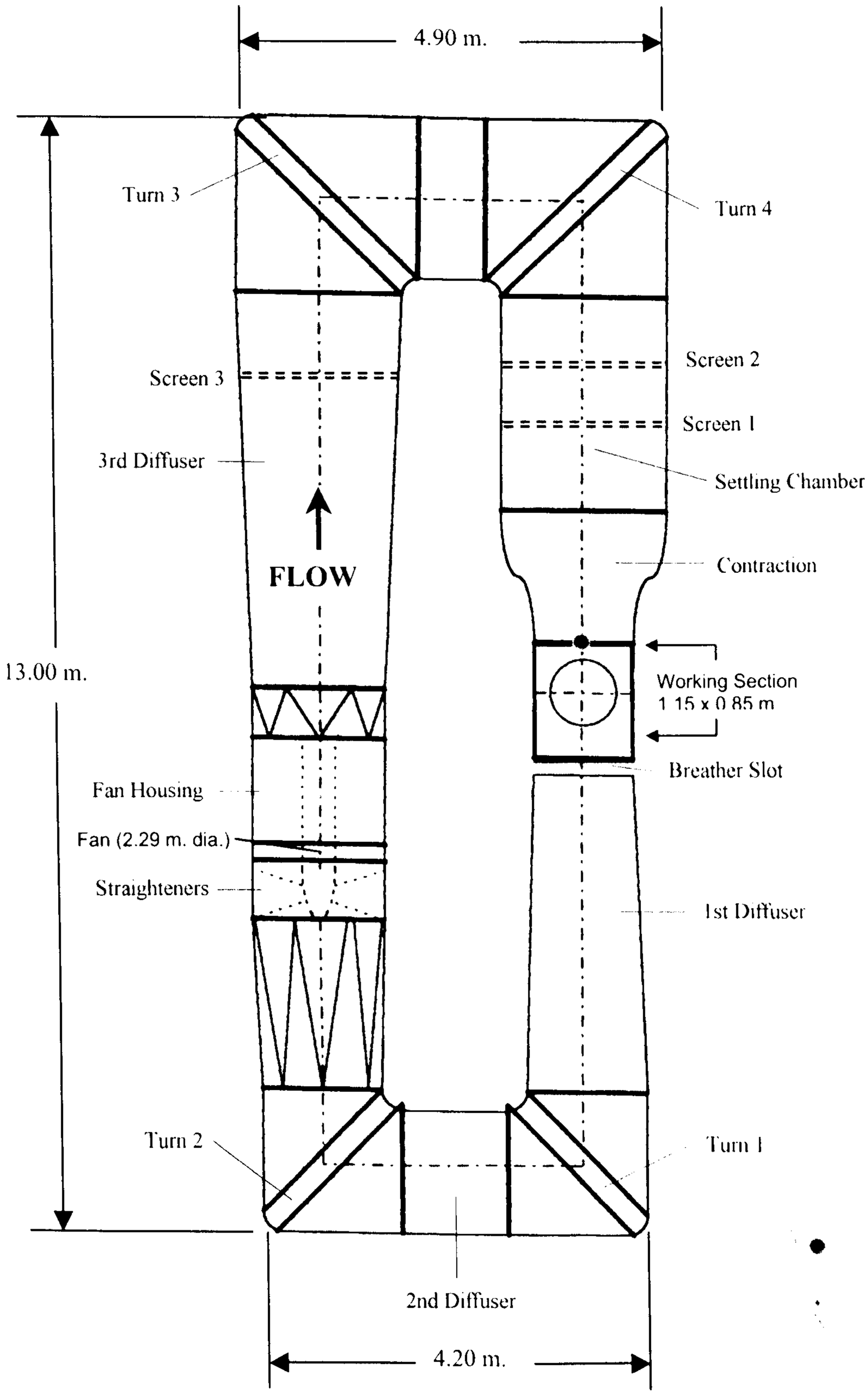

Figure A2. Plan view of the Glasgow University 'Anatomy building' 1.15m x 0.85 m wind tunnel (***AT***).

Screen configuration			Turbulent Intensity, %		
1	**2**	**3**	Hot-Wire Probe	Turbulence Sphere	PIV
			0.43	0.51	0.42
■			0.32	0.32	0.30
	■		0.32	0.34	0.31
		■	0.35	0.29	0.28
■		■	0.31	0.32	0.26
■	■		0.23	0.20	0.22

Table A1. The calculation of the turbulence intensity values measured in the middle section of the ***AT*** test-section for various screen configurations. The PIV results can be confirmed to have an accuracy of ±0.04% turbulence intensity.

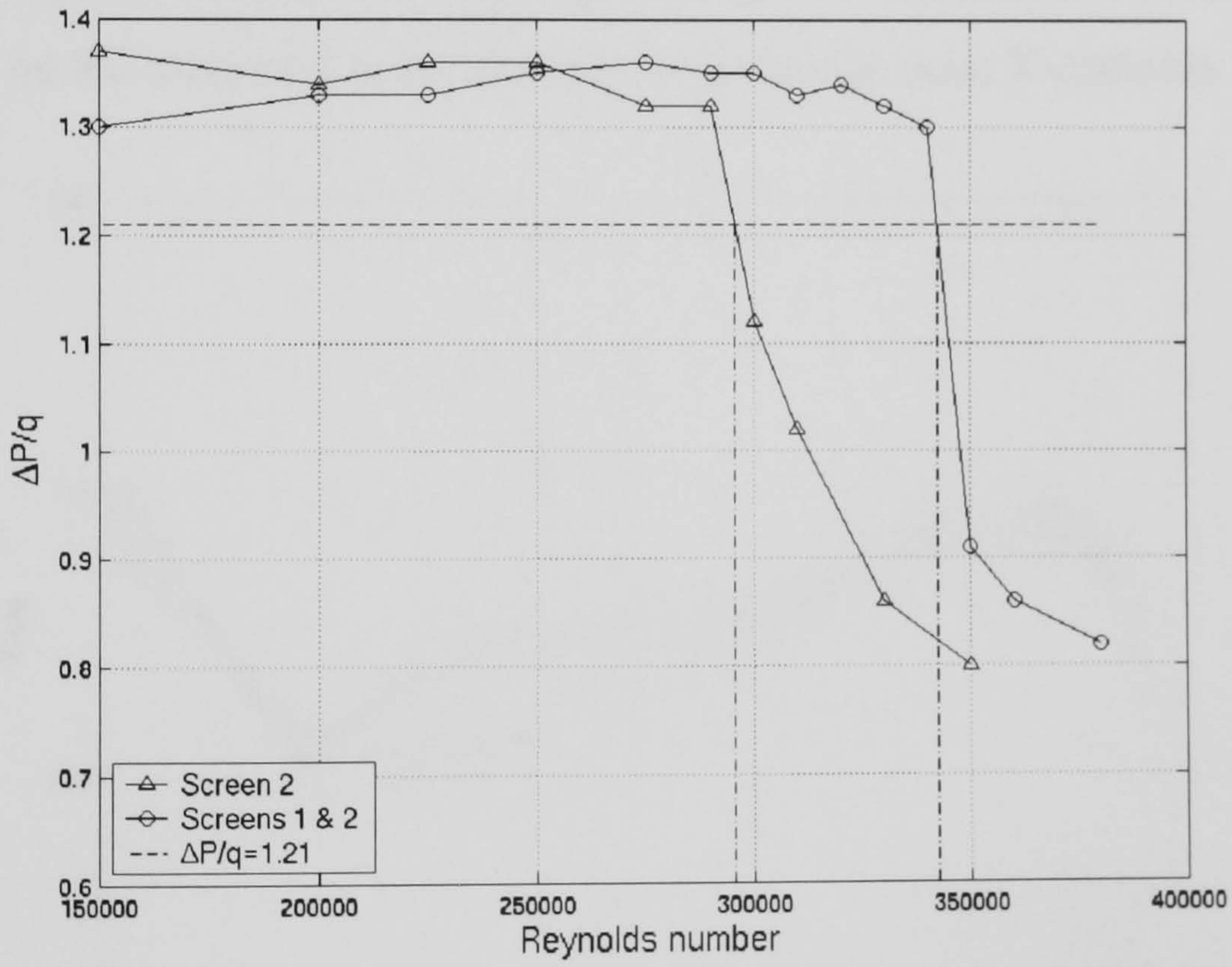

Figure A3. An example of the turbulence intensity calculation using the turbulence sphere. A sphere diameter of 0.225m was selected for the study, the corresponding critical Reynolds number for $\Delta p/q = 1.21$ relates to the turbulence factor, Barlow et al. 1999.

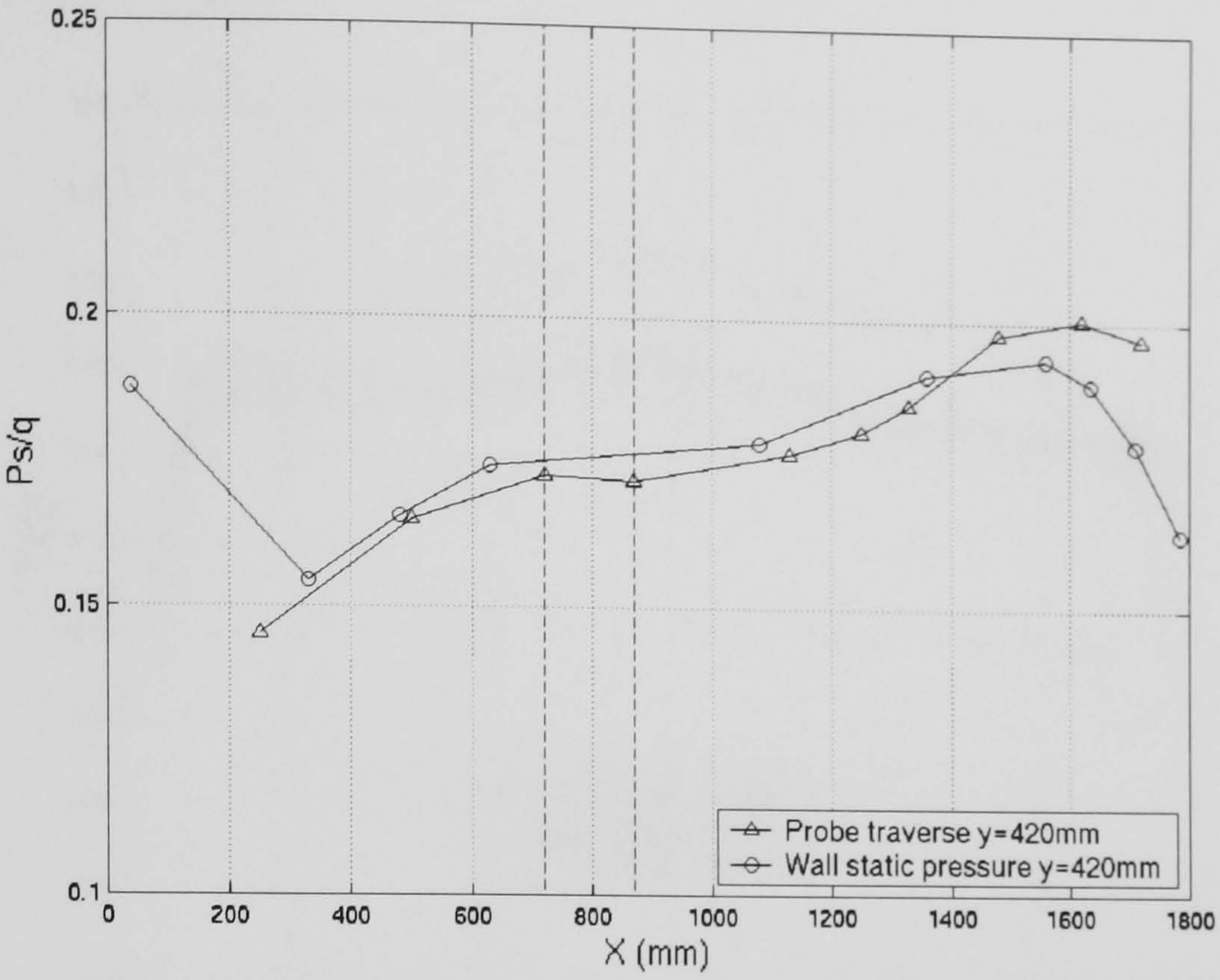

Figure A4. Static pressure gradient measured in the ***AT*** for $U_\infty = 28m/s$ with screens 1 and 2 up. The results from the wall tappings are shown in comparison to those measured on the traverse a small distance away for the same X-ordinate.

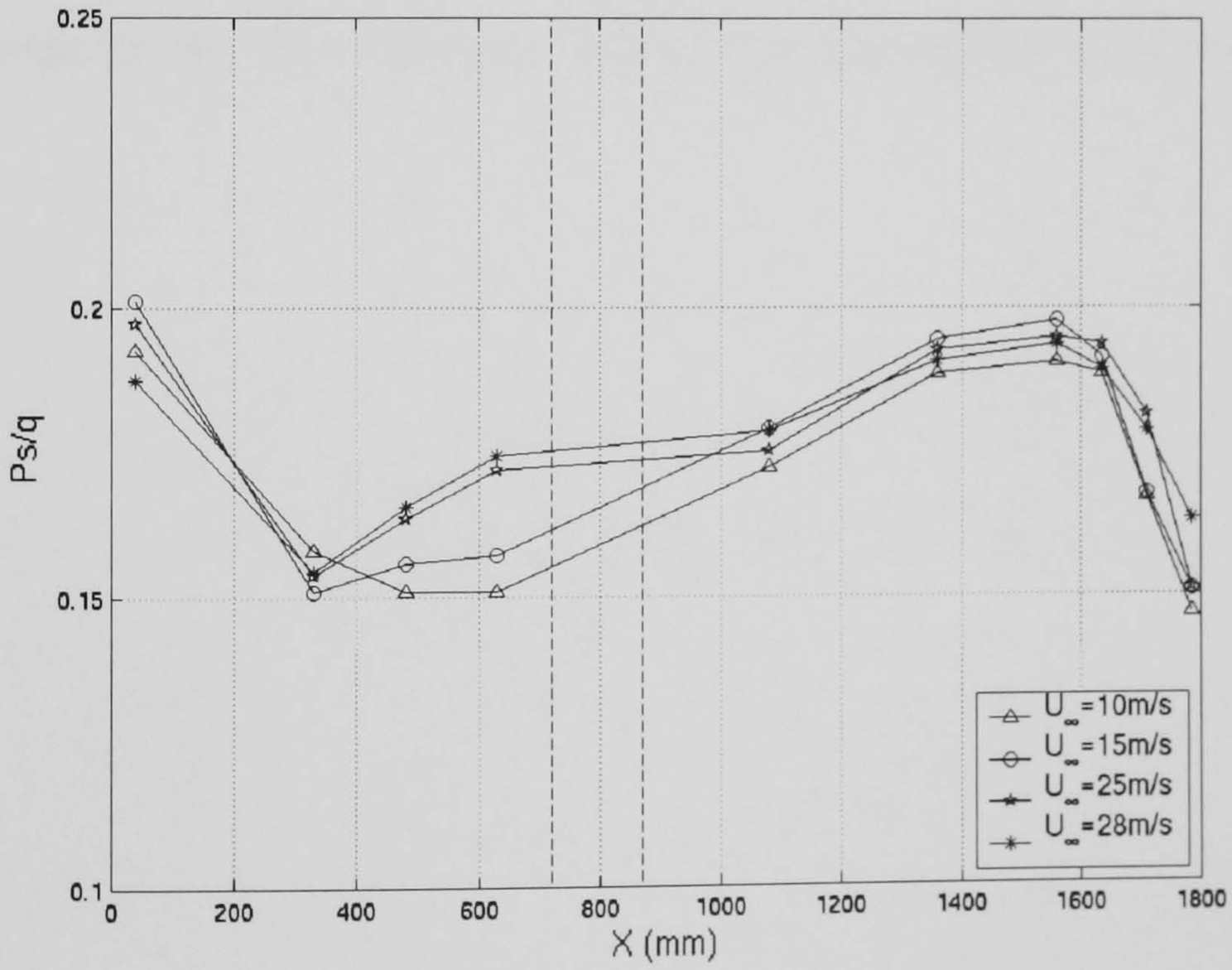

Figure A5. Static pressure gradient measured in the ***AT*** for a range of freestream velocity values for screens 1 and 2 up.

For figures A4 and A5 the static pressure tapping at $X = 850mm$ was broken.

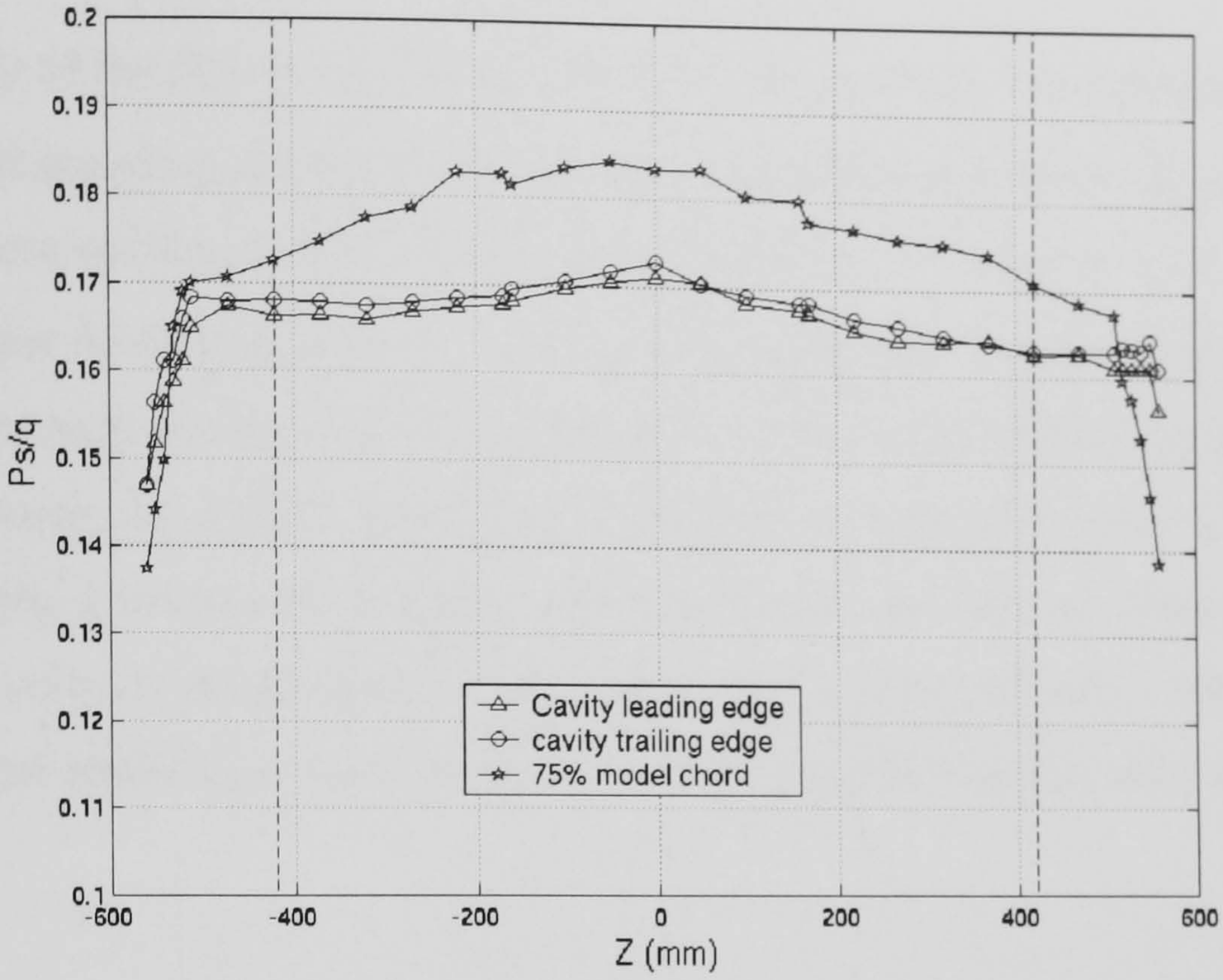

Figure A6. The static pressure profile recorded spanwise along the clean test section. Three measurement positions were chosen to correspond to locations for the model. These are the cavity entrance ($X = 720mm$) the cavity rear wall ($X = 870mm$) and 75% of the model chord ($X = 1230mm$). Dashed lines indicate the width of the model.

APPENDIX B: THE DERIVATIVE SCHEME

The accuracy of the derivative field measurement (in particular ω_z) depends primarily on the spatial sampling distance between the velocity data points (i.e. the spatial resolution between the in-plane velocity vector samples, Δ_{ij}) and on the accuracy of the velocity vector field measurements. Consequently these two factors depend on the measurement method employed to measure the velocity vector field samples. Thus in turn, the accuracy of velocity measurement depends on parameters set at the image acquisition phase such as the imaging spatial resolution, the ratio of seed particle diameter to vorticity distribution length scale and the seeding density. Only the computational method used to calculate ω_z can change the accuracy after image capture.

In principle the ω_z error can be decomposed into a bias error and a random error contribution. The velocity sampling separation is found to have a profound effect on the precise determination of ω_z by introducing a bias error. This bias error results in an underestimation of the peak vorticity. The random error transmission factor and the bias error cannot be minimized simultaneously since both depend on the velocity sampling separation with opposing effects.

For instance denoting ε as the absolute error, the measured velocity components become, $u^* = u + \varepsilon$ and $v^* = v + \varepsilon$. Applying this to the second order central difference scheme, equation [B1] it can be observed that the error in the measurement of vorticity depends on two components of a different nature.

$$\left(\frac{\partial v}{\partial x} - \frac{\partial u}{\partial y}\right)_{x,y} = \left(\frac{v^*_{i+1} - v^*_{i-1}}{2\Delta x} + \Delta x^2 \Re + \frac{\varepsilon}{\Delta x}\right) - \left(\frac{u^*_{i+1} - u^*_{i-1}}{2\Delta y} + \Delta y^2 \Re + \frac{\varepsilon}{\Delta y}\right) \qquad [B1]$$

where $\Re$ stands for higher order terms, from Lourenco et al. 1995.

The equation shows that the truncation error associated with the finite difference scheme is of the order $\left(\Delta x^2, \Delta y^2\right)$ while the absolute uncertainty in the velocity measurement is if the order $\left(1/\Delta x, 1/\Delta y\right)$. Thus we can expect a reduction in truncation error for an increase in spatial resolution, but an increase in the velocity uncertainty. For a given measurement error, ε, there exists a grid of optimal spacing which will

minimize the total error. The Richardson's extrapolation scheme seeks to take advantage of this behaviour.

If efforts are made to reduce the uncertainties in the velocity measurement, ε at the recording and processing stage it is possible to noticeably decrease the truncation error. Such errors are the inaccuracies due to the processing algorithm, bias introduced by large velocity gradients (Adrian 1988, Keane and Adrian 1990) and three-dimensional effects. Lesser errors are the distortion of the camera lens, the film resolution and optical aberrations.

The Richardson's extrapolation increases the order of the truncation error, and thus the accuracy of the derivative estimate, by combining values of derivatives evaluated in two different grids. For instance using the velocity component u :

$$f_8 = \frac{u_{j+8} - u_{j-8}}{16h} = f_{exact} + \frac{\varepsilon}{8h} + 64a_o h^2 + 4096a_1 h^4 + \ldots \qquad [B2]$$

$$f_4 = \frac{u_{j+4} - u_{j-4}}{8h} = f_{exact} + \frac{\varepsilon}{4h} + 16a_o h^2 + 256a_1 h^4 + \ldots \qquad [B3]$$

eliminating the second order term yields,

$$f_4^* = \frac{4f_4 - f_8}{3} + \frac{7\varepsilon}{24h} + 1024a_1 h^4 + \ldots \qquad [B4]$$

This process can proceed by calculating f_2^*, thus the forth order truncation error can be eliminated by $f_2^{**} = f_2^* - f_4^*$ and so on. The experimental error affecting each estimate remains the same and as such application of the scheme stops when the experimental uncertainty exceeds the truncation error. This is achieved by comparing derivative estimates of the same experimental error with derivative estimates of the same order truncation error. For the analysis shown above this would proceed as follows,

$$\left[f_8 - f_8^* < f_8 - f_4\right] \Rightarrow f_4^*$$

$$\left[f_4 - f_4^* < f_4^* - f_2^*\right] \Rightarrow f_2^* \qquad [B5]$$

$$\left[f_2^* - f_2^{**} < f_2^{**} - f^{**}\right] \Rightarrow f^{***}$$

where the left hand side indicates the derivative with the same experimental uncertainty and the right hand side represents the same order truncation error. By representing the velocity field using a local second order polynomial-fitting scheme (γ_{13}^2), see figure B1 it is possible to converge on a non-grid specific solution, allowing better error

minimisation. Incorporating the accuracy study performed by Fouras et al. 1998 it is possible to show that this procedure is more accurate than most other schemes by providing a balance between derivative profile and maximum derivative values.

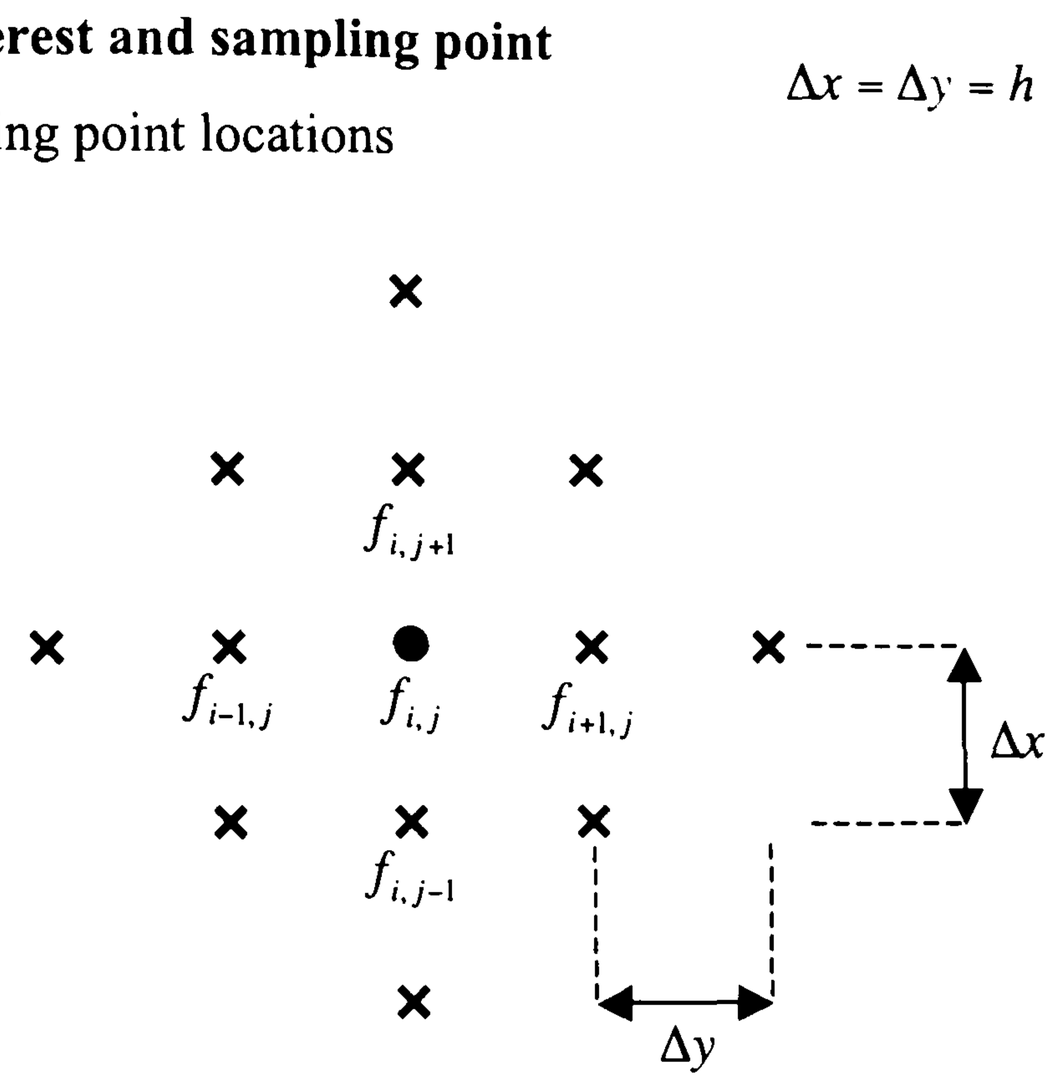

Figure B1. Grid pattern used for the γ_{13}^2 fit method on a regular Cartesian grid. These 12 local sampling points are used to fit a second order polynomial to the point of interest thus making the velocity field non-discrete allowing better truncation error reduction for a negligible increase in experimental error.

APPENDIX C: PRESSURE PORT POSITIONS ON CAVITY MODEL

NSXY			
Static port number	x (mm)	y(mm)	z (mm)
N1	-110.00	-0.10	0.00
N2	-140.00	-1.72	0.00
N3	-170.00	-5.63	0.00
N4	-200.00	-13.42	0.00
N5	-220.00	-30.00	0.00
N6	-200.00	-46.58	0.00
N7	-170.00	-54.36	0.00
N8	-140.00	-58.28	0.00
N9	-110.00	-59.90	0.00

Table C1. Physical location of the spanwise static pressure measurement ports around the model nose section.

NSXZ			
Static port number	x (mm)	y(mm)	z (mm)
N10	-110.00	-0.10	-350.00
N11	-110.00	-0.10	-280.00
N12	-110.00	-0.10	-210.00
N13	-110.00	-0.10	-140.00
N14	-110.00	-0.10	-70.00
N15	-110.00	-0.10	0.00
N16	-110.00	-0.10	70.00
N17	-110.00	-0.10	140.00
N18	-110.00	-0.10	210.00
N19	-110.00	-0.10	280.00
N20	-110.00	-0.10	350.00

Table C2. Physical location of the spanwise static pressure measurement ports along the model nose section.

CAVXZ								
Port	x (mm)	y (mm)	z (mm)	y/S	x/L			
					L/D=1.0	L/D=1.5	L/D=2.0	L/D=3.0
C1	25.00	-50.00	-415.00	-0.49	0.50	0.33	0.25	0.17
C2	25.00	-50.00	-390.00	-0.46	0.50	0.33	0.25	0.17
C3	25.00	-50.00	-360.00	-0.43	0.50	0.33	0.25	0.17
C4	25.00	-50.00	-330.00	-0.39	0.50	0.33	0.25	0.17
C5	25.00	-50.00	-300.00	-0.36	0.50	0.33	0.25	0.17
C6	25.00	-50.00	-270.00	-0.32	0.50	0.33	0.25	0.17
C7	25.00	-50.00	-240.00	-0.29	0.50	0.33	0.25	0.17
C8	25.00	-50.00	-210.00	-0.25	0.50	0.33	0.25	0.17
C9	25.00	-50.00	-180.00	-0.21	0.50	0.33	0.25	0.17
C10	25.00	-50.00	-150.00	-0.18	0.50	0.33	0.25	0.17
C11	25.00	-50.00	-120.00	-0.14	0.50	0.33	0.25	0.17
C12	25.00	-50.00	-90.00	-0.11	0.50	0.33	0.25	0.17
C13	25.00	-50.00	-60.00	-0.07	0.50	0.33	0.25	0.17
C14	25.00	-50.00	-30.00	-0.04	0.50	0.33	0.25	0.17
C15	25.00	-50.00	30.00	0.04	0.50	0.33	0.25	0.17
C16	25.00	-50.00	60.00	0.07	0.50	0.33	0.25	0.17
C17	25.00	-50.00	90.00	0.11	0.50	0.33	0.25	0.17
C18	25.00	-50.00	120.00	0.14	0.50	0.33	0.25	0.17
C19	25.00	-50.00	150.00	0.18	0.50	0.33	0.25	0.17
C20	25.00	-50.00	180.00	0.21	0.50	0.33	0.25	0.17
C21	25.00	-50.00	210.00	0.25	0.50	0.33	0.25	0.17
C22	25.00	-50.00	240.00	0.29	0.50	0.33	0.25	0.17
C23	25.00	-50.00	270.00	0.32	0.50	0.33	0.25	0.17
C24	25.00	-50.00	300.00	0.36	0.50	0.33	0.25	0.17
C25	25.00	-50.00	330.00	0.39	0.50	0.33	0.25	0.17
C26	25.00	-50.00	360.00	0.43	0.50	0.33	0.25	0.17
C27	25.00	-50.00	390.00	0.46	0.50	0.33	0.25	0.17
C28	25.00	-50.00	415.00	0.49	0.50	0.33	0.25	0.17

Table C3. Physical location of the spanwise static pressure measurement ports along the cavity floor.

CAVXY (L/D=3.0)				
Port	x (mm)	y(mm)	z (mm)	x/L
L1	-50.00	0.00	0.00	-0.33
L2	-35.00	0.00	0.00	-0.23
L3	-20.00	0.00	0.00	-0.13
L4	-5.00	0.00	0.00	-0.03
L5	0.00	-10.00	0.00	0.00
L6	0.00	-20.00	0.00	0.00
L7	0.00	-30.00	0.00	0.00
L8	10.00	-50.00	0.00	0.07
L9	15.00	-50.00	0.00	0.10
L10	20.00	-50.00	0.00	0.13
L11	25.00	-50.00	0.00	0.17
L12	40.00	-50.00	0.00	0.27
L13	45.00	-50.00	0.00	0.30
L14	50.00	-50.00	0.00	0.33
L15	55.00	-50.00	0.00	0.37
L16	65.00	-50.00	0.00	0.43
L17	75.00	-50.00	0.00	0.50
L18	80.00	-50.00	0.00	0.53
L19	90.00	-50.00	0.00	0.60
L20	95.00	-50.00	0.00	0.63
L21	100.00	-50.00	0.00	0.67
L22	110.00	-50.00	0.00	0.73
L23	125.00	-50.00	0.00	0.83
L24	135.00	-50.00	0.00	0.90
L25	150.00	-30.00	0.00	1.00
L26	150.00	-20.00	0.00	1.00
L27	150.00	-10.00	0.00	1.00
L28	155.00	0.00	0.00	1.03
L29	170.00	0.00	0.00	1.13
L30	185.00	0.00	0.00	1.23
L31	200.00	0.00	0.00	1.33
L32	215.00	0.00	0.00	1.43
L33	230.00	0.00	0.00	1.53
L34	245.00	0.00	0.00	1.63
L35	275.00	0.00	0.00	1.83
L36	305.00	0.00	0.00	2.03
L37	335.00	0.00	0.00	2.23

Table C4. Physical location of the longitudinal static pressure measurement ports across the cavity when $L/D = 3.0$.

CAVXY (L/D=2.5)				
Port	x (mm)	y(mm)	z (mm)	x/L
L1	-50.00	0.00	0.00	-0.40
L2	-35.00	0.00	0.00	-0.28
L3	-20.00	0.00	0.00	-0.16
L4	-5.00	0.00	0.00	-0.04
L5	0.00	-10.00	0.00	0.00
L6	0.00	-20.00	0.00	0.00
L7	0.00	-30.00	0.00	0.00
L8	10.00	-50.00	0.00	0.08
L9	15.00	-50.00	0.00	0.12
L10	20.00	-50.00	0.00	0.16
L11	25.00	-50.00	0.00	0.20
L12	40.00	-50.00	0.00	0.32
L13	45.00	-50.00	0.00	0.36
L14	50.00	-50.00	0.00	0.40
L15	55.00	-50.00	0.00	0.44
L16	65.00	-50.00	0.00	0.52
L17	75.00	-50.00	0.00	0.60
L18	80.00	-50.00	0.00	0.64
L19	90.00	-50.00	0.00	0.72
L20	95.00	-50.00	0.00	0.76
L21	100.00	-50.00	0.00	0.80
L22	110.00	-50.00	0.00	0.88
S1	125.00	-30.00	0.00	1.00
S2	125.00	-20.00	0.00	1.00
S3	125.00	-10.00	0.00	1.00
S4	130.00	0.00	0.00	1.04
S5	135.00	0.00	0.00	1.08
S6	140.00	0.00	0.00	1.12
S7	145.00	0.00	0.00	1.16
L28	155.00	0.00	0.00	1.24
L29	170.00	0.00	0.00	1.36
L30	185.00	0.00	0.00	1.48
L31	200.00	0.00	0.00	1.60
L32	215.00	0.00	0.00	1.72
L33	230.00	0.00	0.00	1.84
L34	245.00	0.00	0.00	1.96
L35	275.00	0.00	0.00	2.20
L36	305.00	0.00	0.00	2.44
L37	335.00	0.00	0.00	2.68

Table C5. Physical location of the longitudinal static pressure measurement ports across the cavity when $L/D = 2.5$.

CAVXY (L/D=2.0)				
Port	x (mm)	y(mm)	z (mm)	x/L
L1	-50.00	0.00	0.00	-0.50
L2	-35.00	0.00	0.00	-0.35
L3	-20.00	0.00	0.00	-0.20
L4	-5.00	0.00	0.00	-0.05
L5	0.00	-10.00	0.00	0.00
L6	0.00	-20.00	0.00	0.00
L7	0.00	-30.00	0.00	0.00
L8	10.00	-50.00	0.00	0.10
L9	15.00	-50.00	0.00	0.15
L10	20.00	-50.00	0.00	0.20
L11	25.00	-50.00	0.00	0.25
L12	40.00	-50.00	0.00	0.40
L13	45.00	-50.00	0.00	0.45
L14	50.00	-50.00	0.00	0.50
L15	55.00	-50.00	0.00	0.55
L16	65.00	-50.00	0.00	0.65
L17	75.00	-50.00	0.00	0.75
L18	80.00	-50.00	0.00	0.80
L19	90.00	-50.00	0.00	0.90
L20	95.00	-50.00	0.00	0.95
S8	100.00	-30.00	0.00	1.00
S9	100.00	-20.00	0.00	1.00
S10	100.00	-10.00	0.00	1.00
S11	105.00	0.00	0.00	1.05
S12	110.00	0.00	0.00	1.10
S13	115.00	0.00	0.00	1.15
S14	120.00	0.00	0.00	1.20
S15	130.00	0.00	0.00	1.30
S16	140.00	0.00	0.00	1.40
L28	155.00	0.00	0.00	1.55
L29	170.00	0.00	0.00	1.70
L30	185.00	0.00	0.00	1.85
L31	200.00	0.00	0.00	2.00
L32	215.00	0.00	0.00	2.15
L33	230.00	0.00	0.00	2.30
L34	245.00	0.00	0.00	2.45
L35	275.00	0.00	0.00	2.75
L36	305.00	0.00	0.00	3.05
L37	335.00	0.00	0.00	3.35

Table C6. Physical location of the longitudinal static pressure measurement ports across the cavity when $L/D = 2.0$.

CAVXY (L/D=1.5)				
Port	x (mm)	y(mm)	z (mm)	x/L
L1	-50.00	0.00	0.00	-0.67
L2	-35.00	0.00	0.00	-0.47
L3	-20.00	0.00	0.00	-0.27
L4	-5.00	0.00	0.00	-0.07
L5	0.00	-10.00	0.00	0.00
L6	0.00	-20.00	0.00	0.00
L7	0.00	-30.00	0.00	0.00
L8	10.00	-50.00	0.00	0.13
L9	15.00	-50.00	0.00	0.20
L10	20.00	-50.00	0.00	0.27
L11	25.00	-50.00	0.00	0.33
L12	40.00	-50.00	0.00	0.53
L13	45.00	-50.00	0.00	0.60
L14	50.00	-50.00	0.00	0.67
L15	55.00	-50.00	0.00	0.73
L16	65.00	-50.00	0.00	0.87
S17	75.00	-30.00	0.00	1.00
S18	75.00	-20.00	0.00	1.00
S19	75.00	-10.00	0.00	1.00
S20	80.00	0.00	0.00	1.07
S21	85.00	0.00	0.00	1.13
S22	90.00	0.00	0.00	1.20
S23	95.00	0.00	0.00	1.27
S24	105.00	0.00	0.00	1.40
S25	115.00	0.00	0.00	1.53
S26	125.00	0.00	0.00	1.67
S27	135.00	0.00	0.00	1.80
L28	155.00	0.00	0.00	2.07
L29	170.00	0.00	0.00	2.27
L30	185.00	0.00	0.00	2.47
L31	200.00	0.00	0.00	2.67
L32	215.00	0.00	0.00	2.87
L33	230.00	0.00	0.00	3.07
L34	245.00	0.00	0.00	3.27
L35	275.00	0.00	0.00	3.67
L36	305.00	0.00	0.00	4.07
L37	335.00	0.00	0.00	4.47

Table C7. Physical location of the longitudinal static pressure measurement ports across the cavity when $L/D = 1.5$.

CAVXY (L/D=1.0)				
Port	x (mm)	y(mm)	z (mm)	x/L
L1	-50.00	0.00	0.00	-1.00
L2	-35.00	0.00	0.00	-0.70
L3	-20.00	0.00	0.00	-0.40
L4	-5.00	0.00	0.00	-0.10
L5	0.00	-10.00	0.00	0.00
L6	0.00	-20.00	0.00	0.00
L7	0.00	-30.00	0.00	0.00
L8	10.00	-50.00	0.00	0.20
L9	15.00	-50.00	0.00	0.30
L10	20.00	-50.00	0.00	0.40
L11	25.00	-50.00	0.00	0.50
L12	40.00	-50.00	0.00	0.80
L13	45.00	-50.00	0.00	0.90
S28	50.00	-30.00	0.00	1.00
S29	50.00	-20.00	0.00	1.00
S30	50.00	-10.00	0.00	1.00
S31	55.00	0.00	0.00	1.10
S32	60.00	0.00	0.00	1.20
S33	65.00	0.00	0.00	1.30
S34	70.00	0.00	0.00	1.40
S35	80.00	0.00	0.00	1.60
S36	90.00	0.00	0.00	1.80
S37	100.00	0.00	0.00	2.00
S38	110.00	0.00	0.00	2.20
S39	120.00	0.00	0.00	2.40
S40	130.00	0.00	0.00	2.60
S41	140.00	0.00	0.00	2.80
L28	155.00	0.00	0.00	3.10
L29	170.00	0.00	0.00	3.40
L30	185.00	0.00	0.00	3.70
L31	200.00	0.00	0.00	4.00
L32	215.00	0.00	0.00	4.30
L33	230.00	0.00	0.00	4.60
L34	245.00	0.00	0.00	4.90
L35	275.00	0.00	0.00	5.50
L36	305.00	0.00	0.00	6.10
L37	335.00	0.00	0.00	6.70

Table C8. Physical location of the longitudinal static pressure measurement ports across the cavity when $L/D = 1.0$.

Transducer	x (mm)	y (mm)	z (mm)	x/L				
				L/D=1.0	L/D=1.5	L/D=2.0	L/D=2.5	L D=3.0
1	25.00	-50.00	0.00	0.50	0.33	0.25	0.20	0.17
2	L	-45.00	0.00	1.00	1.00	1.00	1.00	1.00

Table C9. Physical location of longitudinal dynamic pressure measurement.

Port	x-L (mm)	y (mm)	z (mm)	x/L				
				L/D=1.0	L/D=1.5	L/D=2.0	L/D=2.5	L/D=3.0
P1	5.00	0.00	100.00	1.10	1.07	1.05	1.04	1.03
P2	10.00	0.00	100.00	1.20	1.13	1.10	1.08	1.07
P3	15.00	0.00	100.00	1.30	1.20	1.15	1.12	1.10
P4	20.00	0.00	100.00	1.40	1.27	1.20	1.16	1.13
P5	25.00	0.00	100.00	1.50	1.33	1.25	1.20	1.17
P6	30.00	0.00	100.00	1.60	1.40	1.30	1.24	1.20
P7	35.00	0.00	100.00	1.70	1.47	1.35	1.28	1.23
P8	40.00	0.00	100.00	1.80	1.53	1.40	1.32	1.27
P9	45.00	0.00	100.00	1.90	1.60	1.45	1.36	1.30
P10	50.00	0.00	100.00	2.00	1.67	1.50	1.40	1.33
P11	55.00	0.00	100.00	2.10	1.73	1.55	1.44	1.37
P12	60.00	0.00	100.00	2.20	1.80	1.60	1.48	1.40
P13	65.00	0.00	100.00	2.30	1.87	1.65	1.52	1.43
P14	70.00	0.00	100.00	2.40	1.93	1.70	1.56	1.47
P15	75.00	0.00	100.00	2.50	2.00	1.75	1.60	1.50
P16	80.00	0.00	100.00	2.60	2.07	1.80	1.64	1.53
P17	85.00	0.00	100.00	2.70	2.13	1.85	1.68	1.57
P18	90.00	0.00	100.00	2.80	2.20	1.90	1.72	1.60
P19	95.00	0.00	100.00	2.90	2.27	1.95	1.76	1.63
P20	100.00	0.00	100.00	3.00	2.33	2.00	1.80	1.67
P21	110.00	0.00	100.00	3.20	2.47	2.10	1.88	1.73
P22	120.00	0.00	100.00	3.40	2.60	2.20	1.96	1.80
P23	130.00	0.00	100.00	3.60	2.73	2.30	2.04	1.87
P24	140.00	0.00	100.00	3.80	2.87	2.40	2.12	1.93
P25	150.00	0.00	100.00	4.00	3.00	2.50	2.20	2.00
P26	160.00	0.00	100.00	4.20	3.13	2.60	2.28	2.07
P27	170.00	0.00	100.00	4.40	3.27	2.70	2.36	2.13
P28	180.00	0.00	100.00	4.60	3.40	2.80	2.44	2.20
P29	190.00	0.00	100.00	4.80	3.53	2.90	2.52	2.27

Table C10. Physical location of the longitudinal static pressure measurement ports for Preston tube measurements. The total head probe was located at the same (x,y,z) positions.

Port	x-L (mm)	y (mm)	z (mm)
P30	20.00	0.00	-100.00
P31	20.00	0.00	-90.00
P32	20.00	0.00	-80.00
P33	20.00	0.00	-70.00
P34	20.00	0.00	-60.00
P35	20.00	0.00	-50.00
P36	20.00	0.00	-40.00
P37	20.00	0.00	-30.00
P38	20.00	0.00	-20.00
P39	20.00	0.00	-10.00
P40	20.00	0.00	0.00
P41	20.00	0.00	10.00
P42	20.00	0.00	20.00
P43	20.00	0.00	30.00
P44	20.00	0.00	40.00
P45	20.00	0.00	50.00
P46	20.00	0.00	60.00
P47	20.00	0.00	70.00
P48	20.00	0.00	80.00
P49	20.00	0.00	90.00
P50	20.00	0.00	100.00

Table C11. Physical location of the spanwise static pressure measurement ports for Preston tube measurements. The total head probe was located at the same (x,y,z) positions.